rptu.de

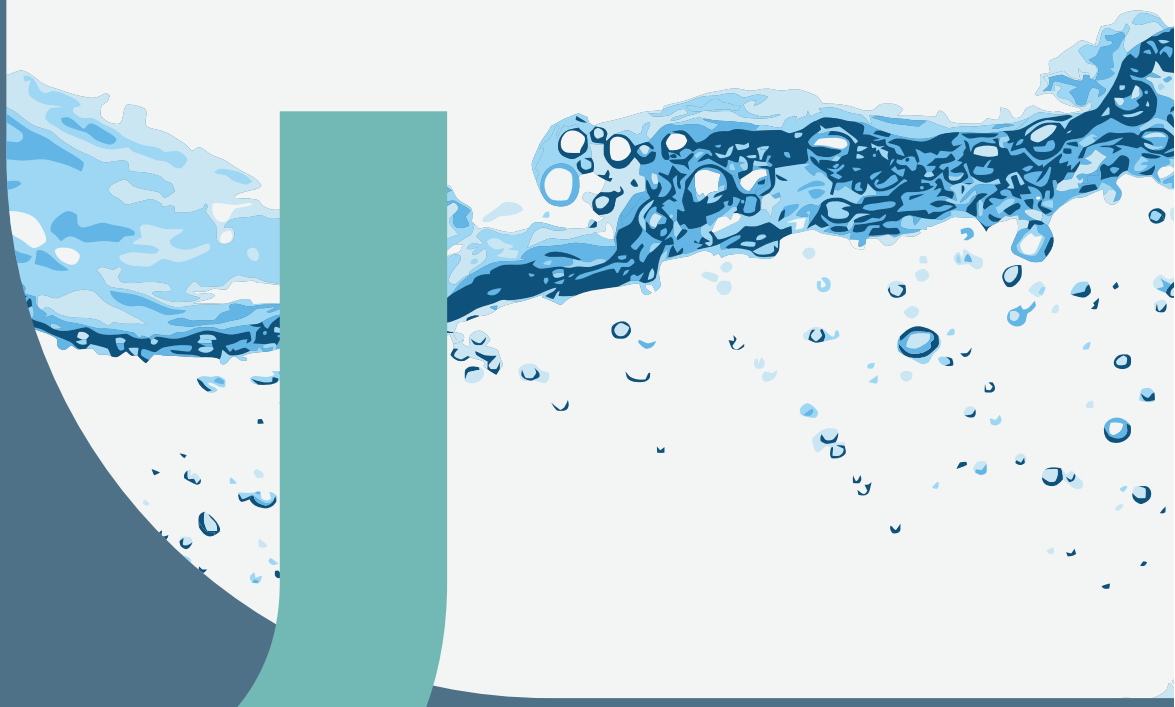

Erik von Harbou

Quantitative NMR methods for reaction and process monitoring

Laboratory of Reaction and Fluid Process Engineering
Band 1 | 2024
Herausgeber: Prof. Dr.-Ing. Erik von Harbou
Habilitation thesis

RPTU | LRF

Quantitative NMR methods for reaction and process monitoring

Vom Fachbereich Maschinenbau und Verfahrenstechnik

der Technischen Universität Kaiserslautern

zur Erlangung der

Lehrbefugnis

auf dem Gebiet der

chemischen Thermodynamik

genehmigte

Habilitation

von

Dr.-Ing. Erik von Harbou

aus Rotenburg / Wümme

Betreuer: Prof. Dr.-Ing. Hans Hasse

Abstract

In this work, new methods are presented that facilitate the application of Nuclear Magnetic Resonance (NMR) spectroscopy for monitoring of reactions and processes. NMR spectroscopy has the advantage that it enables both elucidation of species and their following quantification in a reacting mixture in situ without the need of prior calibration. New post-processing methods were developed that enable handling of large sets of NMR spectra and that reduce influence of the user on the outcome of the measurements of the composition. Furthermore, a spectral analysis method was introduced and tested that allows evaluating the acquired NMR signals quantitatively even if the peaks in the NMR spectrum are distorted and the concentration of analytes becomes very small. As the standard NMR equipment is mostly designed for structure elucidation purposes but not for reaction and process monitoring, the apparatuses were tailored in this work. A liquid thermostatted NMR probe head is presented, in which fast reactions can be monitored under isothermal conditions. Methods and experimental procedures were established to investigate chemical equilibria of different industrial relevant systems in situ. Examples are: the formation of intermediates in the reaction system that is found in the synthesis of crotonaldehyde from acetaldehyde and water, and the reaction that take place in aqueous methyl diethanolamine solutions when loaded with carbon dioxide. Furthermore, an inline analysis method for monitoring dynamic processes reliably with a high chemical and temporal resolution is presented. To demonstrate the potential of this method, the complex interactions of reaction and separation in a fixed-bed chromatographic reactor process were studied. Furthermore, a benchtop NMR spectrometer was employed to study liquid-liquid phase equilibria in situ in different systems. This new type of spectrometer are an interesting alternative to the high-field NMR spectrometer because of its smaller size and lower costs. The results show that benchtop NMR spectrometers have the potential to widen the range of application of NMR spectroscopy for reaction and process monitoring significantly. This works demonstrate that NMR spectroscopy is a useful tool in chemical reaction engineering as it enables detailed insights into complex reactions and processes and provides data that is essential for the development of reliable process models.

Kurzfassung

In dieser Arbeit werden Methoden präsentiert, die die Anwendung der Kernresonanzspektroskopie (NMR) für das Reaktions- und Prozessmonitoring ermöglichen. Die NMR-Spektroskopie bietet den Vorteil, dass sowohl unbekannte Spezies aufgeklärt werden können, als auch deren Konzentrationen anschließend in reaktiven Mischungen bestimmt werden können, ohne dass zuvor eine Kalibrierung der Analysemethode notwendig ist. Neue Methoden zur Nachbearbeitung der NMR-Signalen wurden entwickelt, mit deren Hilfe eine große Anzahl an aufgenommenen Spektren bearbeitet werden können und die den Einfluss des Benutzers auf das Ergebnis der Konzentrationsmessung reduzieren. Außerdem wurde eine Spektralanalysemethode eingeführt und getestet, die es ermöglicht, auch dann noch NMR-Signale quantitativ auszuwerten, wenn die Peaks im Spektrum verzerrt sind oder die Konzentration des Analyten sehr gering ist. Da die Standard-NMR-Geräte hauptsächlich zum Zwecke der Strukturaufklärung entwickelt wurden, aber nicht für das Reaktions- und Prozessmonitoring, wurden die experimentellen Aufbauten in dieser Arbeit speziell für diese Aufgaben angepasst. Ein flüssigkeitsthermostatisierter NMR-Probenkopf wird präsentiert, mit dem schnelle Reaktionen unter isothermen Bedingungen untersucht werden können. Außerdem wurden Methoden und Prozeduren etabliert, um chemische Gleichgewichte in situ in verschiedenen industriell relevanten Systemen zu untersuchen. Beispiele sind: die Bildung von Intermediaten, welche bei der Synthese von Crotonaldehyde aus Acetaldehyde und Wasser auftreten oder die Reaktionen, die in mit Kohlendioxid beladenen wässrigen Methyldiethanolamin-Lösungen vorkommen. Zusätzlich wird eine inline-Methode für die quantitative Analyse dynamischer Prozesse mit hoher örtlicher und zeitlicher Auflösung präsentiert. Um das Potential dieser Methode zu demonstrieren, wurden das komplexe Zusammenspiel von Reaktion und Stofftrennung in einem chromatographischen Festbettreaktor untersucht. Des Weiteren wurde ein Benchtop-NMR-Spektrometer für in situ Studien von Flüssig-flüssig Phasengleichgewichten in verschiedenen Stoffsystemen eingesetzt. Benchtop-NMR-Spektrometer sind aufgrund der kleineren Abmaße und der geringeren Kosten eine interessante Alternative zu den üblicherweise eingesetzten Hochfeldspektrometern. Die Ergebnisse belegen, dass Benchtop-NMR Spektrometer das Potential haben, den Anwendungsbereich der NMR-Spektroskopie für das Reaktions- und Prozessmonitoring deutlich zu erweitern. Diese Arbeit zeigt, dass die NMR-Spektroskopie ein mächtiges Werkzeug im Bereich der Reaktionstechnik ist, da sie detaillierte Einblicke in komplexe Reaktionen und Prozesse ermöglicht und dabei Daten liefert, die essentiell für die Entwicklung von verlässlichen Prozessmodellen sind.

Table of contents

Summary

Motivation

Nuclear Magnetic Resonance (NMR) spectroscopy is a very versatile technique with great importance in many fields. The Nobel prize lectures of Richard R. Ernst (1991), K. Wüthrich (2002), and P.C. Lauterbur and P. Mansfield (2003) provide an excellent overview on the development of NMR spectroscopy and its significance for various fields of application [15, 29, 53]. In chemistry and biology, the application of NMR spectroscopy for elucidation of chemical structures and identification of species is well known. For that reason, it has become a standard method for structural analysis in both academia and industries [26]. Additionally, NMR spectroscopy features many properties that make it a perfect tool for the investigation and monitoring of reactions and processes (see e.g. [4, 10, 16, 32–34]). Despite the fact that already many applications of NMR in this field have been reported in the literature, NMR spectroscopy is still far away from being a standard tool in Chemical Engineering. Not only the large investment costs and the severe requirements of the superconducting high-field NMR spectrometers on the laboratory infrastructure are strong hindrances for the wide application of NMR spectroscopy for reaction and process monitoring but also the lack of appropriate experimental apparatuses and evaluation methods of the acquired data. For that reason, the development of quantitative NMR methods and their application for the investigation of complex reactive systems and for monitoring of processes is presented in this work. The method development and application is not restricted to high-field NMR spectrometers but also comprises the new class of medium-field benchtop NMR spectrometers.

NMR spectroscopy for reaction and process monitoring

Compared to standard analytical methods such as titration or chromatographic methods, NMR spectroscopy has the great advantage that manifold information of a given fluid mixture can be obtained from the acquired signals. Like optical spectroscopic methods, NMR is a non-invasive technique. Encoded in the signals are information on the chemical structure of the different species and their concentration in the given sample. Thus, NMR spectroscopy can be applied for the identification and following quantification of intermediates or products in reactive mixtures. In contrast to optical spectroscopic methods, the concentration of the analytes can be directly obtained from the NMR signals without the need of

prior calibration [33]. This feature is very important for the investigation of reactive systems. In these systems, reactive intermediates or reaction products are often present that cannot be isolated from the mixture or cannot be purchased as pure components. Hence, the preparation of calibration samples with known composition is very difficult (if not impossible) (see e.g. [9, 14, 27, 50]). In these cases, NMR spectroscopy is often the only method that enables a quantification of the composition of the mixture. Furthermore, as a non-invasive method it facilitates in situ analysis of reactions and processes without sampling. Thus, the investigated processes, which are often very sensitive to any change of temperature, pressure or amount (hold-up), are not disturbed [3, 14]. Additionally, NMR spectroscopy facilitates spatial resolution of the chemical composition (that is concentration mapping), which widens its applicability for studying chemical processes even further [19]. Harbou et al. [23] gives a short overview on recent trends in the development of both optical and NMR spectroscopic in situ analysis techniques and their application for studying reactions (see Publication von Harbou et al., 2017 enclosed with this work).

Post-processing of NMR signals

Because of this versatility concerning both qualitative and quantitative analysis, NMR spectroscopy is well suited for example for the determination of chemical equilibria or reaction kinetics in complex systems (i.e. a large number of reactions and/or of intermediates that cannot be isolated from the reaction mixture). The requirements for the realisation of these investigations on both hardware and software is very different compared to the requirements for sole structural analysis. To give an example: in a typical experiment for the determination of reaction kinetics, the reactants are mixed in a NMR tube. Then, the reaction is started e.g. by adding a catalyst and NMR spectra of the reacting mixture are repeatedly acquired,which yields a large array of spectra at the end of the experiment (see e.g. [4, 9, 17]). To obtain the change of the composition of the mixture as a function of time, which correlates with the rate of the occurring reactions, each spectrum has to be evaluated quantitatively. Before this evaluation can be done, each spectrum must be processed, that is at least the phase and the baseline must be corrected [32]. If only a structural analysis of a given sample is desired, this post-processing is comparably simple as in general, the number of acquired spectra is significantly smaller compared to the number acquired for reaction monitoring. Furthermore, errors in the correction of the phase and baseline have only little impact on the outcome. In this case, the post-processing is well supported by standard software used for the visualisation and analysis of the NMR spectra. In contrast, the number of spectra acquired for reaction and process monitoring is significantly larger and even small phase or baseline errors can add up to large errors in the determination of the areas under the NMR peaks that are required to determine the concentration of

the analytes [35]. Therefore, even handling of large amount of data is demanding for the standard NMR analysis software and the provided post-processing algorithms regularly lead to unacceptably large errors in the quantitative analysis. Consequently, the acquired spectra are often corrected manually, which is a very time-consuming procedure. Furthermore, this manual correction is not feasible when NMR spectroscopy is employed as detector for process control and spectra are continuously acquired over a long period of time [38].

For that reason, we developed an automatic algorithm for simultaneous phase and baseline correction (SINC) that can handle large quantities of NMR spectra without manual input, which distinguishes this method from other approaches [40]. The method is based on multi-objective optimization or Pareto optimization that finds the best compromise between different objective functions. We showed that this method yields improved results (that is a higher accuracy in the determination of the composition of a given mixture) compared to consecutively applied correction steps [40] (see Publication Sawall et al., 2018 enclosed with this work).

In several studies, we showed that the algorithm gives robust results and is well-suited for processing large sets of spectra that are acquired to monitor reactions and processes [49]. In an in-house round robin test, spectra of different mixtures with known composition were corrected manually by different operators and then quantitatively analysed (i.e. the areas under the peaks were determined by integration). The results show that different manual corrections of the spectra by different operators lead to significant variations in the determined concentrations of the analytes. In contrast, the correction of the spectra with the SINC method yield in average a better accuracy of the concentration measurements [49].

Nevertheless, if the operator uses test mixtures with known composition, which are similar or equal to the investigated chemical system, to optimise the acquisition parameters and the post-processing procedure, the accuracy of the concentration measurements is comparable to other analysis methods such as gas chromatography (GC) or refractive index (RI) measurements (see e.g. [3, 8, 18]).

After the phase and baseline of each spectrum has been corrected, the spectra can be evaluated quantitatively. If the peaks in the NMR spectra, which correspond to the different analytes, are well separated, the procedure is straightforward: the areas under the different peaks are calculated by integration and the concentration of the analytes (normally as mole fractions) are determined from the ratios of the peak areas. When reactions and processes are monitored or when a medium-field spectrometer is used, this simple analysis, however, is often not possible. Reasons for the difficulties of the quantitative evaluations of the different peaks are manifold. Overlapping of peaks, shifting of peaks caused for example by changes of the pH-value during the reaction, small concentrations of analytes i.e. low signal-to-noise ratio (SNR) or distorted peaks caused e.g. by inhomogeneities of the magnetic field are

just a few examples. To analyse spectra with overlapping peaks quantitatively, the spectra are often modelled with physically motivated Gauss-Lorenzian functions [2, 27, 36]. These functions are fitted to the measured spectra and the obtained parameters are directly used to get information on the composition of the investigated sample. Drawback of this method is that in principle only symmetrical peaks can be described by these functions [55]. Distorted peaks, which are often encountered during reaction and process monitoring, can only be modelled by elaborate work-arounds for example by introducing additional peaks (that is in principle an addition of pseudo-components) as it can be done for example in the Indirect Hard Modelling (IHM) approach [2]. Furthermore, these methods require accurately phased spectra with good baseline correction. Even with advanced algorithms, such as the SINC method presented above [40], the accuracy of the phase and baseline correction is limited when data with low SNR is processed. For that reason, we developed an algorithm that analysis the NMR data directly in the time-domain [37] (see Publication Matviychuk et al., 2017 enclosed with this work). This approach provides effective mechanisms for automatic baseline and phase correction. Furthermore, it allows to account easily for any line shape distortions possibly caused by inhomogeneity of the external magnetic field or other factors. Bayesian statistics are used to estimate the model parameters. They smoothly incorporate any prior knowledge about the studied system into the model and provide a principle way to estimate the uncertainty of results. With this approach we were able to quantify the composition of samples reliably even when the peaks in the spectrum overlapped and even when the SNR was so low that the classical methods, which rely on a correct phasing of the spectra, failed [37].

NMR probe for kinetic measurements

To enable the investigation of reactions and processes by NMR spectroscopy not only new processing and analysis methods but also dedicated experimental apparatuses are required [32]. While kinetics of slow reactions, which have a small enthalpy of reaction, can be easily determined by following the change of composition of a reacting sample that has been filled into an standard NMR sample tube [4, 9], fast reactions or reactions with large enthalpy of reaction cannot be studied with this simple set-up. The time required to fill the reactants into the NMR sample tube, mix them, and insert the tube into the spectrometer takes at least 30 seconds. Furthermore, the sample tube is coiled / heated by a nitrogen gas stream. Typically, the reacting mixture in the sample tube cannot be stirred during the experiment. Thus the heat transfer from the reacting mixture to the gas stream is limited [22] (see Publication von Harbou et al., 2017a enclosed with this work). To ensure a good mixing of the reactants and to provide a good control of the temperature of the reacting mixture, an external reactor, for example a stirred tank, which is equipped with a sample loop, can be

used for that purpose. The sample loop is connected to a special NMR probe that is equipped with a flow cell. The reacting mixtures are pumped through the sample loop to the NMR spectrometer and then through the flow cell, where the NMR analysis takes place [27, 33, 56]. Drawback of such a set-up is that it takes several minutes until the sample reaches the flow cell in the NMR after it has left the reactor. Thus, this set-up is not applicable for studying reactions that reach equilibrium within a few minutes. To enable studies of fast reactions and ensure at the same time a good control of the temperature of the reacting mixture, we developed a new type of NMR probe [6] (see Publication Brächer et al., 2014 enclosed with this work). The NMR probe can be operated in two different modes: the stopped-flow mode (the reactor characteristics are basically like a batch reactor) and the flow mode (the reactor characteristics are like a tubular reactor). In both modes, the reactants are fed separately into the NMR probe and mixed with a micro-mixer just before they reach the flow cell. Thus, in the stopped-flow mode, the time delay between mixing that is the start of reaction and analysis in the flow cell is just seconds and reactions that reaches equilibrium in less than a minute can be analysed [7] (see Publication Brächer et al., 2016 enclosed with this work). Brächer et al. [7] showed that the reaction kinetics of an esterification reaction obtained by means of the new NMR probe are in good agreement with kinetic measurements of the same reactions reported in the literature, which were determined with completely different analysis methods and set-ups. The NMR probe features a thermostatisation of the complete feed lines, the micro-mixer and the flow cell with a special oil. This oil is not visible in the proton spectrum and thus it does not disturb the NMR measurements. Simulations of the temperature profiles in different NMR set-ups during the reaction showed that the control of temperature in the micro-reactor NMR probe is much more efficient than in standard NMR sample tubes. Therefore, even exothermal or endothermal reactions can be investigated under isothermal conditions with this new NMR probe [22].

In addition to the investigation of the esterification reactions mentioned above, we applied the micro-reactor NMR probe in two more studies to determine the rate of reaction under conditions that are relevant for industrial applications. The formation of poly(oxymethylene) glycols in aqueous formaldehyde systems are of great relevance for many chemical production processes [24]. Hahnenstein et al. [20] studied the reaction kinetics of that complex system under various conditions (start composition, temperature, and pH-value) using both NMR spectroscopic measurements in a simple sample tube set-up and a densimetric method. However, for temperature higher than 40 °C and for pH-values in the acidic or alkaline range, which are relevant for industrial applications, the reaction kinetics are so fast that Hahnenstein et al. [20] were not able to study them with their chosen methods. Thus, the micro-reactor NMR probe was used to expand the experimental data of the reaction kinetics in that system to conditions that could not be studied so far [22] (see Publication von Harbou et al., 2017a enclosed with this work). The experimental results confirm the kinetic model proposed by Hahnenstein et al. [20].

Acetaldehyde is an important intermediate in the chemical industry. It is used for the production of for example crotonaldehyde, ethyl acetate or acetic anhydride. Similar to aqueous formaldehyde solutions mixtures of acetaldehyde and water are reactive multi-component systems because poly(oxymethylmethylene) glycols are formed. The kinetics of the formation of these oligomers were studied using the micro-reactor NMR probe [44] (see Publication Scheithauer et al., 2014 enclosed with this work). In this system, the application of the micro-reactor NMR probe head was beneficial because it enables a much better control of the temperature of the reaction mixture than a standard NMR sample tube [22] and it enables to run the reaction under elevated pressure to prevent evaporation of reactants or products [6]. On the basis of the acquired spectroscopic data data, a reaction kinetic model was developed and numbers for the kinetic constants of poly(oxymethylmethylene) glycol formation were determined together with a correlation that describes their dependence on the temperature and pH-value. The results of these two studies demonstrate that the micro-reactor NMR probe can be used to investigate kinetics of fast and complex reactions under conditions relevant to industrial applications.

Structure elucidation and in situ measurement of chemical equilibria

As mentioned above, NMR spectroscopy enables both qualitative and quantitative analysis of reacting mixtures. This beneficial feature was exploited in several projects for the elucidation of reaction networks and the following determination of the chemical equilibria in that system. Crotonaldehyde can be industrially produced from acetaldehyde and water using among others reactive distillation [46]. A commonly accepted picture of the reaction scheme was that two acetaldehyde molecules react in an addition reaction to acetaldol. Then, acetaldol reacts further to crotonaldehyde [46]. By means of NMR structure elucidation techniques Scheithauer et al. [43] proved the presence of an additional reaction: the formation of aldoxane from acetaldehyde and acetaldol (see Publication Scheithauer et al., 2014a enclosed with this work). The following determination of the composition of the reacting mixture using quantitative NMR spectroscopy showed that the chemical equilibrium of the aldoxane formation lies well on the product side. Thus, large amount of acetaldehyde can be chemically bound in aldoxane and its formation and presence in the industrial process cannot be neglected but has to be considered in the model of the physico-chemical properties. In addition, we found that acetaldehyde reacts with water and forms poly(oxymethylmethylene) glycols in a similar way as formaldehyde undergoes reactions in aqueous solutions [41] (see Publication Scheithauer et al., 2015 enclosed with this work). Also in this work, NMR spectroscopy was applied first to elucidate the reaction network and to identify the different oligomers and then to determine the equilibrium

composition of the reacting mixture for different temperatures and initial compositions. The measurements were used to parametrise temperature dependent correlation of the equilibrium constants in the reaction network. Based on these measurement results a model of the physico-chemical properties was developed. Using this model, Scheithauer et al. [42] was able to simulate the standard production process of crotonaldehyde, which includes among others a reactive and hetero-azeotropic distillation process, and to discover weaknesses in the conceptual design.

Using NMR spectroscopy, we investigated the true equilibrium composition of aqueous methyl diethanolamine (MDEA) solutions that were loaded with carbon dioxide (CO_2) [3] (see Publication Behrens et al., 2017 enclosed with this work). Aqueous MDEA solutions are widely employed as solvents in reactive absorption processes for scrubbing CO_2 or hydrogen sulfide (H_2S) from natural gas, synthesis gases, and refinery gases [25]. To enable loadings of the solvent with CO_2 that are relevant for technical applications, the sample had to be maintained under pressure of up to 11 bar and constant temperature of 298 K [5]. Thus, the amine solution was loaded with CO_2 directly in a valved NMR sample tube, which was inserted into the NMR spectrometer. This set-up enables to study the reactions that take place in the liquid phase upon absorption of CO_2 in situ. Therefore, the pressure and temperature can be kept constant during the whole investigation and the equilibrium composition is not disturbed by sampling. Using this set-up, we were able to identify monoalkylcarbonate as an additional reaction product. By quantitative NMR measurements, we showed that more than 10 mol-% of the absorbed CO_2 is chemically bound as monoalkylcarbonate under conditions relevant for technical applications. This result is astonishing, as the presence of monoalkylcarbonate in this industrially important and well-studied reaction system has been widely ignored in the literature so far.

Inline analysis of dynamic processes

NMR spectroscopy is well-suited for inline analysis since it delivers the composition of a process stream with high accuracy and high temporal resolution. Thus, we applied quantitative inline NMR spectroscopy to study the dynamic behaviour of a fixed-bed chromatographic process [8] (see Publication Brächer et al., 2018 enclosed with this work). The hydrolysis of methyl formate and the hydrolysis of methyl acetate were chosen as test systems. In previous works, this fixed-bed chromatographic reactor was intensively studied in combination with these two reaction systems by Seidel-Morgenstern and co-workes [51, 52]. They employed a refractive index detector to analyse the product stream and to obtain the chromatograms. In this work, the NMR set-up had to be customised to ensure both a high sensitivity of the analysis and a well-defined residence time distribution of the sample in the product line. The concentration profiles of the reactants and products in the reactor outlet

could be measured with high accuracy even when the two hyrolysis reactions took place in parallel and the chromatograms of the different species strongly overlapped. These results illustrate the superiority of NMR analysis compared to other inline methods typically used such as refractive index detection. From the measured concentration profiles, we obtained detailed insights into the reaction and separation processes occurring simultaneously in the chromatographic reactor. This information is important for the development of reliable process models that can be used to optimise the process.

Application of benchtop NMR spectrometers

Since a couple of years, a new class of NMR spectrometers – the so-called benchtop NMR spectrometers – are on the market. In contrast to high field NMR spectrometers, which use cryogenically cooled super-conducting magnets to generate the required magnetic field, benchtop NMR spectrometers are based on permanent magnets [12, 28, 31]. Thus, the investment costs for benchtop NMR spectrometers are significantly lower compared to the investment and running costs of high field magnets. Without the need of cryogenic media and because of their small size, benchtop NMR spectrometers are flexible and easily applicable in every day laboratories. For example, they can be placed directly inside a fume hood next to a reactor vessel [11]. An additional advantage of most of the available types of benchtop NMR spectrometers is that they are equipped with a simple through-hole. It enables to insert not only the typical NMR sample tubes but also different types of pipes (e.g. teflon capillaries) into the NMR coil, where the measurement take place. Thus, different kinds of vessels can be easily connected with the benchtop NMR spectrometer through a simple sample line and they do not need a special probe as it is normally the case for high field NMR spectrometers. The lower magnetic field strength and less homogeneity of the magnetic field, however, entail lower sensitivity and chemical resolution compared to high field NMR spectrometers [48, 55].

To demonstrate that the accuracy of concentration measurements with a benchtop NMR spectrometer is sufficient for studying physico-chemical properties of liquid systems, we applied it to determine liquid-liquid equilibria (LLE) in different ternary systems [18] (see Publication Friebel et al., 2017 enclosed with this work). In this study, we exploited the feature of the benchtop NMR spectrometer that the samples can be easily inserted and its position inside the magnet can be swiftly varied. Hence, the composition of the coexisting phases can be investigated in situ by shifting the sample tube so that either phase is placed inside the NMR coil where its composition can be determined. Therefore, no sampling from the different phases and calibration of the analysis method is necessary. Both reduces the experimental error and the time effort. Moreover, the new method enables a simple

determination of the time that is needed for equilibration of the phases just by repeated measurements. The composition of the coexisting phases measured with the presented method agreed well with data from literature. In addition, Schmitz et al. [45] applied this method to study the LLE in binary and ternary mixtures of water, methylal and poly(oxymethylene) dimethyl ethers. The results of the in situ measurements agreed well with results obtained from samples, which were analysed ex situ using a gas chromatograph.

Thanks to the ability to change the location of the sample in the spectrometer within seconds so that the composition of both phases can be analysed repeatedly, reactions can be monitored in both phases almost simultaneously. We used this technique to follow the reaction of acetic anhydride with water to acetic acid both in the aqueous phase as well as in the organic phase [18]. The results show that the accuracy of the concentration measurements by benchtop NMR spectroscopy can compete with classical analysis methods. To conclude, the proposed in situ analysis method is a valuable tool to receive a swift overview of the physico-chemical properties of biphasic multicomponent systems.

Composition mapping with NMR

The great benefit of NMR is that it cannot only be used for spectroscopy but also for imaging as it is widely done for example in medicine. Imaging with NMR has the advantage compared to optical methods that it can probe optically opaque environments like reactors. For example, velocity maps of the flow within packed-bed reactors can be obtained by NMR imaging [19]. These maps can be used to test CFD modelling and simulation approaches [39]. The combination of spectroscopy with imaging methods yields maps of the composition that give for example spatial information on the conversion of reactants in a catalyst bed [47, 54]. These composition maps can be used to gain a rigorous understanding of chemical reactions and mass transfer processes. The acquisition time needed to obtain a multidimensional, fully sampled composition map, however, may take several hours, which can be detrimental [1]. First, the process has to be operated steadily for several hours. Second, transient phenomena that take place within minutes cannot be studied with this technique. For that reason, we developed a method for accelerating the acquisition of spatially resolved composition maps based on compressed sensing [21] (see Publication von Harbou et al., 2015 enclosed with this work). Compressed sensing enables the accurate reconstruction of an under-sampled signal by utilising the prior knowledge that the signal is compressible. As under-sampled signals can be used, compressed sensing provides a method of reducing the data acquisition times of imaging techniques significantly [13, 30]. The method was applied to simple test samples that contained binary mixtures with known composition. The method enabled acquisition of quantitative maps of the chemical composition in as little as 8 min, when a full chemical shift image at the same resolution would require 17 h. As for NMR

spectroscopy, no calibration is necessary prior to the analysis in order to get quantitative results. The accuracy was with about ±2 mol-% acceptable. With better hardware that yield more precise control of the magnetic field gradients and with a reconstruction algorithm that can compensate for inhomogeneities in the static magnetic field higher accuracy of the concentration measurements should be achievable in future work.

Conclusion and outlook

To conclude, the results reported in this work demonstrate that NMR spectroscopy is a valuable tool to gather detailed information about complex chemical systems and processes. The obtained data is important to get a comprehensive understanding of the processes and to be able to develop reliable process models. In many cases, customised apparatuses and analysis methods are necessary to acquire the data in the desired chemical, temporal or spatial resolution and with the desired accuracy of quantification. Applying these set-ups and methods, manifold qualitative and quantitative information about reaction and processes are accessible. Benchtop NMR spectrometers, though having lower sensitivity and resolution compared to high field spectrometers, widen the range of application of NMR for reaction and process monitoring significantly. They have the potential to become a standard analysis tool in chemical reaction engineering.

Literature

[1] Belinda S. Akpa et al. “In situ ^{13}C DEPT-MRI as a tool to spatially resolve chemical conversion and selectivity of a heterogeneous catalytic reaction occurring in a fixed-bed reactor”. In: *Chemical Communications* X.21 (2005), pp. 2741–2743. ISSN: 1359-7345.

[2] Frank Alsmeyer, Hans-Jürgen Koß, and Wolfgang Marquardt. “Indirect Spectral Hard Modeling for the Analysis of Reactive and Interacting Mixtures”. In: *Applied Spectroscopy* 58.8 (2004), pp. 975–985.

[3] Richard Behrens et al. “Monoalkylcarbonate Formation in Methyldiethanolamine-H_2O-CO_2”. In: *Industrial & Engineering Chemistry Research* 56.31 (Aug. 2017), pp. 9006–9015. ISSN: 0888-5885. (Visited on 08/14/2017).

[4] Michael A. Bernstein, Marijan Štefinović, and Chris J. Sleigh. “Optimising reaction performance in the pharmaceutical industry by monitoring with NMR”. en. In: *Magnetic Resonance in Chemistry* 45.7 (July 2007), pp. 564–571. ISSN: 1097-458X. (Visited on 04/27/2016).

[5] Wolfram Böttinger, Michael Maiwald, and Hans Hasse. “Online NMR Spectroscopic Study of Species Distribution in MDEA-H2O-CO2 and MDEA-PIP-H2O-CO2”. In: *Industrial & Engineering Chemistry Research* 47.20 (Oct. 2008), pp. 7917–7926. ISSN: 0888-5885. (Visited on 06/23/2015).

[6] A. Brächer et al. “Thermostatted micro-reactor NMR probe head for monitoring fast reactions”. In: *Journal of Magnetic Resonance* 242 (May 2014), pp. 155–161. ISSN: 1090-7807. (Visited on 05/29/2017).

[7] Alexander Brächer et al. “Application of a new micro-reactor ^{1}H NMR probe head for quantitative analysis of fast esterification reactions”. In: *Chemical Engineering Journal* 306 (2016), pp. 413–421. ISSN: 1385-8947. (Visited on 08/10/2016).

[8] Alexander Brächer et al. “Application of quantitative inline NMR spectroscopy for investigation of a fixed-bed chromatographic reactor process”. In: *Chemical Engineering Journal* 336 (Mar. 2018), pp. 518–530. ISSN: 1385-8947.

[9] Marie-Christine Brochier Salon et al. “Kinetics of hydrolysis and self condensation reactions of silanes by NMR spectroscopy”. In: *Colloids and Surfaces A: Physicochemical and Engineering Aspects* 312.2–3 (Jan. 2008), pp. 83–91. ISSN: 0927-7757. (Visited on 04/27/2016).

[10] Ian M. Clegg et al. “NMR reaction monitoring during the development of an active pharmaceutical ingredient”. en. In: *Analytical Methods* 4.6 (May 2012), pp. 1498–1506. ISSN: 1759-9679. (Visited on 04/28/2016).

[11] E. Danieli et al. “On-Line Monitoring of Chemical Reactions by using Bench-Top Nuclear Magnetic Resonance Spectroscopy”. en. In: *ChemPhysChem* 15.14 (2014), pp. 3060–3066. ISSN: 1439-7641. (Visited on 03/24/2015).

[12] Ernesto Danieli et al. “Kleine Magnete für NMR-Spektroskopie vor Ort”. de. In: *Angewandte Chemie* 122.24 (June 2010), pp. 4227–4229. ISSN: 1521-3757. (Visited on 03/26/2015).

[13] D.L. Donoho. “Compressed sensing”. In: *Information Theory, IEEE Transactions on* 52.4 (2006), pp. 1289–1306. ISSN: 0018-9448.

[14] Viktor Ermatchkov, Álvaro Pérez-Salado Kamps, and Gerd Maurer. “Chemical equilibrium constants for the formation of carbamates in (carbon dioxide + piperazine + water) from 1H-NMR-spectroscopy”. In: *The Journal of Chemical Thermodynamics* 35.8 (Aug. 2003), pp. 1277–1289. ISSN: 0021-9614. (Visited on 02/06/2015).

[15] Ernst Richard R. “Nuclear Magnetic Resonance Fourier Transform Spectroscopy (Nobel Lecture)”. In: *Angewandte Chemie International Edition in English* 31.7 (Dec. 2003), pp. 805–823. ISSN: 0570-0833.

[16] David A. Foley et al. “Online NMR and HPLC as a Reaction Monitoring Platform for Pharmaceutical Process Development”. In: *Analytical Chemistry* 85.19 (2013), pp. 8928–8932. ISSN: 0003-2700. (Visited on 04/27/2016).

[17] Foley David A., Dunn Anna L., and Zell Mark T. “Reaction monitoring using online vs tube NMR spectroscopy: seriously different results”. In: *Magnetic Resonance in Chemistry* 54.6 (Aug. 2015), pp. 451–456. ISSN: 0749-1581.

[18] Anne Friebel et al. “In situ measurement of liquid-liquid equilibria by medium field nuclear magnetic resonance”. In: *Fluid Phase Equilibria* 438 (Apr. 2017), pp. 44–52. ISSN: 0378-3812. (Visited on 02/28/2017).

[19] Lynn F. Gladden et al. “MRI: Operando measurements of temperature, hydrodynamics and local reaction rate in a heterogeneous catalytic reactor”. In: *Catalysis Today*. Recent Developments in Operando Spectroscopy 155.3–4 (2010), pp. 157–163. ISSN: 0920-5861. (Visited on 10/27/2016).

[20] Immanuel Hahnenstein et al. “NMR Spectroscopic and Densimetric Study of Reaction Kinetics of Formaldehyde Polymer Formation in Water, Deuterium Oxide, and Methanol”. In: *Industrial & Engineering Chemistry Research* 34.2 (Feb. 1995), pp. 440–450. ISSN: 0888-5885. (Visited on 02/08/2017).

[21] Erik von Harbou et al. “Quantitative mapping of chemical compositions with MRI using compressed sensing”. In: *Journal of Magnetic Resonance* 261 (2015), pp. 27–37. ISSN: 1090-7807. (Visited on 02/17/2016).

[22] Erik von Harbou et al. “Studying Fast Reaction Kinetics with Online NMR Spectroscopy”. en. In: *Chemie Ingenieur Technik* 89.4 (Apr. 2017), pp. 369–378. ISSN: 1522-2640. (Visited on 04/06/2017).

[23] Erik von Harbou et al. “Technische Chemie 2016”. en. In: *Nachrichten aus der Chemie* 65.3 (2017), pp. 367–374. ISSN: 1868-0054. (Visited on 03/06/2017).

[24] Hans Hasse and G. Maurer. “Kinetics of the poly(oxymethylene) glycol formation in aqueous formaldehyde solutions”. In: *Industrial & Engineering Chemistry Research* 30 (1991), pp. 2195–2200.

[25] Hans Hasse and Inga Tönnies. “Post Combustion Capture”. In: *Carbon Capture and Storage in Europe*. Halle (Saale): EASAC Secretariat, Deutsche Akademie der Naturforscher Leopoldina, 2013.

[26] J. Keeler. *Understanding NMR Spectroscopy*. Wiley, 2002.

[27] E. J. Kibrik et al. “On-Line NMR Spectroscopic Reaction Kinetic Study of Urea-Formaldehyde Resin Synthesis”. In: *Industrial & Engineering Chemistry Research* 53.32 (Aug. 2014), pp. 12602–12613. ISSN: 0888-5885. (Visited on 03/26/2015).

[28] Simon K. Küster et al. “High-resolution NMR spectroscopy under the fume hood”. en. In: *Physical Chemistry Chemical Physics* 13.29 (July 2011), pp. 13172–13176. ISSN: 1463-9084. (Visited on 03/26/2015).

[29] Paul C. Lauterbur. “All Science is Interdisciplinary-from Magnetic Moments to Molecules to Men”. en. In: *Bioscience Reports* 24.3 (June 2004), pp. 165–178. ISSN: 0144-8463, 1573-4935. (Visited on 04/03/2018).

[30] Michael Lustig, David Donoho, and John M. Pauly. “Sparse MRI: The application of compressed sensing for rapid MR imaging”. In: *Magnetic Resonance in Medicine* 58.6 (Dec. 2007), pp. 1182–1195. ISSN: 1522-2594.

[31] Burkhard Luy. “Transportable hochauflösende NMR-Spektrometer”. de. In: *Angewandte Chemie* 123.2 (Jan. 2011), pp. 371–373. ISSN: 1521-3757. (Visited on 03/26/2015).

[32] Michael Maiwald. *Hochauflösende Online-NMR-Spektroskopie für das Reaktions- und Prozeßmonitoring Beispiele zur Anwendung in der Verfahrenstechnik*. 1st ed. Göttingen: Cuvillier Verlag, 2012. ISBN: 978-3-95404-136-7.

[33] Michael Maiwald et al. “Quantitative high-resolution on-line NMR spectroscopy in reaction and process monitoring”. In: *Journal of Magnetic Resonance* 166.2 (Feb. 2004), pp. 135–146. ISSN: 1090-7807. (Visited on 10/17/2014).

[34] Michael Maiwald et al. “Quantitative NMR spectroscopy of complex technical mixtures using a virtual reference: chemical equilibria and reaction kinetics of formaldehyde–water–1,3,5–trioxane”. en. In: *Analytical and Bioanalytical Chemistry* 385.5 (July 2006), pp. 910–917. ISSN: 1618-2642, 1618-2650. (Visited on 03/20/2018).

[35] F. Malz and H. Jancke. “Validation of quantitative NMR”. In: *Journal of Pharmaceutical and Biomedical Analysis*. Quantitative NMR Spectroscopy principles and applications 38.5 (Aug. 2005), pp. 813–823. ISSN: 0731-7085. (Visited on 03/26/2015).

[36] Ian Marshall et al. “Use of voigt lineshape for quantification of in vivo1H spectra”. en. In: *Magnetic Resonance in Medicine* 37.5 (1997), pp. 651–657. ISSN: 1522-2594. (Visited on 06/03/2015).

[37] Yevgen Matviychuk, Erik von Harbou, and Daniel J. Holland. “An experimental validation of a Bayesian model for quantification in NMR spectroscopy”. In: *Journal of Magnetic Resonance* 285.Supplement C (Dec. 2017), pp. 86–100. ISSN: 1090-7807. (Visited on 11/08/2017).

[38] Klas Meyer et al. “Process control with compact NMR”. In: *TrAC Trends in Analytical Chemistry*. SI: Compact NMR 83, Part A (2016), pp. 39–52. ISSN: 0165-9936. (Visited on 02/03/2017).

[39] David J. Robbins et al. “CFD modeling of single-phase flow in a packed bed with MRI validation”. en. In: *AIChE Journal* 58.12 (2012), pp. 3904–3915. ISSN: 1547-5905. (Visited on 08/17/2016).

[40] Mathias Sawall et al. “Multi-objective optimization for an automated and simultaneous phase and baseline correction of NMR spectral data”. In: *Journal of Magnetic Resonance* 289 (Apr. 2018), pp. 132–141. ISSN: 1090-7807.

[41] Andreas Scheithauer et al. “^{1}H- and ^{13}C-NMR spectroscopic study of chemical equilibria in the system acetaldehyde + water”. en. In: *AIChE Journal* 61.1 (Jan. 2015), pp. 177–187. ISSN: 1547-5905. (Visited on 03/26/2015).

[42] Andreas Scheithauer et al. “Modeling, simulation and analysis of a process for the production of crotonaldehyde”. In: *Chemical Engineering and Processing: Process Intensification* 101 (2016), pp. 101–111. ISSN: 0255-2701. (Visited on 02/15/2016).

[43] Andreas Scheithauer et al. “NMR Spectroscopic Study of the Aldoxane Formation in Aqueous Acetaldehyde Solutions”. In: *Industrial & Engineering Chemistry Research* 53.20 (2014), pp. 8395–8403. ISSN: 0888-5885. (Visited on 03/26/2015).

[44] Andreas Scheithauer et al. “Online ^{1}H NMR Spectroscopic Study of the Reaction Kinetics in Mixtures of Acetaldehyde and Water Using a New Microreactor Probe Head”. In: *Industrial & Engineering Chemistry Research* 53.45 (Nov. 2014), pp. 17589–17596. ISSN: 0888-5885. (Visited on 03/26/2015).

[45] Niklas Schmitz et al. “Liquid-liquid equilibrium in binary and ternary mixtures containing formaldehyde, water, methanol, methylal, and poly(oxymethylene) dimethyl ethers”. In: *Fluid Phase Equilibria* 425 (2016), pp. 127–135. ISSN: 0378-3812. (Visited on 12/08/2016).

[46] R. Schulz, J. Blumenstein, and C. Kohlpaintner. “Crotonaldehyde and Crotonic acid”. In: *Ullmann's Encyclopedia of Industrial Chemistry*. 6th. Weinheim: Wiley-CH, 2005.

[47] Andrew J. Sederman et al. “In Situ MRI Study of 1-octene Isomerisation and Hydrogenation within a Trickle-bed Reactor”. In: *Catalysis Letters* 103.1-2 (2005), pp. 1–8. ISSN: 1011-372X.

[48] Silva Elipe, Maria Victoria and Milburn, Robert R. “Monitoring chemical reactions by low-field benchtop NMR at 45 MHz: pros and cons”. In: *Magnetic Resonance in Chemistry* 54.6 (Jan. 2015), pp. 437–443. ISSN: 0749-1581.

[49] Ellen Steimers et al. “Application of an new method for a simultaneous phase and baseline correction of NMR signals (SINC)”. In: *in preparation* – (–).

[50] Oliver Steinhof et al. “Quantitative and qualitative ^{1}H, ^{13}C, and ^{15}N NMR spectroscopic investigation of the urea-formaldehyde resin synthesis”. en. In: *Magnetic Resonance in Chemistry* 52.4 (Apr. 2014), pp. 138–162. ISSN: 1097-458X. (Visited on 07/07/2015).

[51] Tien Vu. “Analysis of Heterogeneously Catalyzed Ester Hydrolysis Reactions in a Fixed-Bed Chromatographic Reactor”. PhD thesis. Otto-von-Guericke-University Magdeburg, Germany, 2007.

[52] Tien D. Vu and A. Seidel-Morgenstern. “Quantifying Temperature and Flow Rate Effects on the Performance of a Fixed-Bed Chromatographic Reactor”. In: *J. Chromatogr. A* 1218 (2011), pp. 8097–8109. ISSN: 0021-9673.

[53] Kurt Wüthrich. “Nobel Lecture: NMR Studies of Structure and Function of Biological Macromolecules”. en. In: *Bioscience Reports* 23.4 (Aug. 2003), pp. 119–168. ISSN: 0144-8463, 1573-4935. (Visited on 04/03/2018).

[54] E.H.L. Yuen, A.J. Sederman, and L.F. Gladden. “In situ magnetic resonance visualisation of the spatial variation of catalytic conversion within a fixed-bed reactor”. In: *Applied Catalysis A: General* 232.1–2 (June 2002), pp. 29–38. ISSN: 0926-860X.

[55] Nicolai Zientek et al. “Automated data evaluation and modelling of simultaneous ^{19}F-^{1}H medium-resolution NMR spectra for online reaction monitoring”. en. In: *Magnetic Resonance in Chemistry* 54.6 (June 2016), pp. 513–520. ISSN: 1097-458X. (Visited on 10/21/2016).

[56] Nicolai Zientek et al. “Simultaneous ^{19}F-^{1}H medium resolution NMR spectroscopy for online reaction monitoring”. In: *Journal of Magnetic Resonance* 249 (2014), pp. 53–62. ISSN: 1090-7807. (Visited on 03/28/2015).

Declaration of authorship

The manuscripts presented in this work have been published previously. In the following, these publications are listed together with a statement on the contributions of the author of the present habilitation thesis.

- R. Behrens, E. von Harbou, W.R. Thiel, W. Böttinger, T. Ingram, G. Sieder, H. Hasse: Monoalkylcarbonate Formation in Methyldiethanolamine - H_2O-CO_2, Industrial & Engineering Chemistry Research 56 (2017) 9006-9015.

  The author supervised the experimental work and the model development. The author contributed to the algorithms used to solve the non-linear equations. The author has contributed to the manuscript.

- A. Brächer, R. Behrens, E. von Harbou, H. Hasse: Application of a new micro-reactor ^{1}H NMR probe head for quantitative analysis of fast esterification reactions, Chemical Engineering Journal 306 (2016) 413-421.

  The author supervised the experimental work. The author contributed to the algorithm used to estimate the kinetic parameters. The author has contributed to the manuscript.

- A. Brächer, S. Hoch, K. Albert, H.J. Kost, B. Werner, E. von Harbou, H. Hasse: Thermostatted micro-reactor NMR probe head for monitoring fast reactions, Journal of Magnetic Resonance 242 (2014) 155-161.

  The author supervised the development of the NMR probe and set-up, and the experimental work. The author carried out experiments in the flow mode. The author has contributed to the manuscript.

- A. Brächer, L.M. Kreußer, S. Qamar, A. Seidel-Morgenstern, E. von Harbou: Application of quantitative inline NMR spectroscopy for investigation of a fixed-bed chromatographic reactor process, Chemical Engineering Journal 336 (2018) 518-530.

  The author supervised the experimental work. The author implemented the model of the reactor in Matlab and contributed to the development of the algorithm used to solve the partial differential equation system. The author carried out the simulations and evaluated the results. The author wrote the manuscript.

- A. Friebel, A. Fröscher, K. Münnemann, E. von Harbou, H. Hasse: In situ measurement of liquid-liquid equilibria by medium field nuclear magnetic resonance, Fluid Phase Equilibria 438 (2017) 44-52.

The author developed the basic principle of the in situ analysis method. The author set-up the pulse sequence for the spatially resolved measurements. The author supervised the experimental work and the evaluation of the results. The author has contributed to the manuscript.

- E. von Harbou, R. Behrens, J. Berje, A. Brächer, H. Hasse: Studying Fast Reaction Kinetics with Online NMR Spectroscopy, Chemie Ingenieur Technik 89 (2017) 369-378.

  The author carried out the kinetic measurements in the flow mode. The author carried out the velocity mapping in collaboration with Alexander Brächer. The author supervised the remaining experimental work. The author developed the model, implemented the solver and carried out the simulation of the thermal effects in the different NMR set-ups. The author wrote the manuscript.

- E. von Harbou, H.T. Fabich, M. Benning, A.B. Tayler, A.J. Sederman, L.F. Gladden, D.J. Holland: Quantitative mapping of chemical compositions with MRI using compressed sensing, Journal of Magnetic Resonance 261 (2015) 27-37.

  The author carried out the experiments, developed the model and wrote the corresponding code. The author carried out the reconstructions and evaluated the results. The author wrote the manuscript.

- E. von Harbou, O. Wachsen, E. Klemm, C. Dreiser: Technische Chemie 2016, Nachrichten aus der Chemie 65 (2017) 367-374.

  The author wrote the section "'In-situ-Analytik in der Reaktionstechnik"'.

- Y. Matviychuk, E. von Harbou, D.J. Holland: An experimental validation of a Bayesian model for quantification in NMR spectroscopy, Journal of Magnetic Resonance 285 (2017) 86-100.

  The author supervised the experimental work and contributed to the evaluation of the results. The author has contributed to the manuscript.

- M. Sawall, E. von Harbou, A. Moog, R. Behrens, H. Schröder, J. Simoneau, E. Steimers, K. Neymeyr: Multi-objective optimization for an automated and simultaneous phase and baseline correction of NMR spectral data, Journal of Magnetic Resonance 289 (2018) 132-141.

  The author advised M. Sawall, A. Moog, and H. Schröder in the development of the algorithm. The author supervised the experimental work and contributed to the evaluation of the results. The author has contributed to the manuscript.

- A. Scheithauer, A. Brächer, T. Grützner, D. Zollinger, W.R. Thiel, E. von Harbou, H. Hasse: Online ^{1}H NMR Spectroscopic Study of the Reaction Kinetics in Mixtures of Acetaldehyde and Water Using a New Microreactor Probe Head, Industrial & Engineering Chemistry Research 53 (2014) 17589-17596.

The author advised A. Scheithauer during the experiments and their evaluation. The author has contributed to the manuscript.

- A. Scheithauer, T. Grützner, C. Rijksen, D. Zollinger, E. von Harbou, W.R. Thiel, H. Hasse: NMR Spectroscopic Study of the Aldoxane Formation in Aqueous Acetaldehyde Solutions, Industrial & Engineering Chemistry Research 53 (2014) 8395-8403.

  The author advised A. Scheithauer during the experiments and their evaluation. The author has contributed to the manuscript.

- A. Scheithauer, E. von Harbou, H. Hasse, T. Grützner, C. Rijksen, D. Zollinger, W.R. Thiel: ^{1}H- and ^{13}C-NMR spectroscopic study of chemical equilibria in the system acetaldehyde + water, AIChE Journal 61 (2015) 177-187.

  The author advised A. Scheithauer during the experiments and their evaluation. The author has contributed to the manuscript.

Student theses

The following student theses were prepared under the direct supervision of the author of the present habilitation:

- Rivera, E. B.: Morphologial analysis and optimisation of heterogeneously catalysed reactive distillation of complex chemical systems with side reactions. Master thesis, Laboratory of Engineering Thermodynamics (LTD), University of Kaiserslautern (2014).
- Poree, K.: Analysen zur Modellierung und Simulation von reaktiven Trennwandkolonnen. Master thesis, Laboratory of Engineering Thermodynamics (LTD), University of Kaiserslautern (2014).
- Steimers, E.: Modellierung und Simulation nicht-idealer Laborreaktoren. Bachelor thesis, Laboratory of Engineering Thermodynamics (LTD), University of Kaiserslautern (2015).
- Kunz, L.: Planung verfahrenstechnischer Versuche mit Hilfe multikriterieller Optimierung. Master thesis, Laboratory of Engineering Thermodynamics (LTD), University of Kaiserslautern (2015).
- Kreußer, J., Kiepfer, H., Kremers, A.: Verwendung von Abgasen aus der Koks- und Stahlproduktion als Synthesegas in der chemischen Industrie, BCI student project, Laboratory of Engineering Thermodynamics (LTD), University of Kaiserslautern (2015).
- Kreußer, J.: Development of a model of steam methane reformer. Bachelor thesis, Laboratory of Engineering Thermodynamics (LTD), University of Kaiserslautern (2016).
- Kreußer, L. M.: Modelling and simulation of a chromatographic fixed-bed reactor. Research project, Department of Applied Mathematics and Theoretical Physics, University of Cambridge (2016).
- Klein, M.: Auslegung von Destillationskolonnen unter Unsicherheiten in den Stoffdaten. Research project, Laboratory of Engineering Thermodynamics (LTD), University of Kaiserslautern (2017).
- Kreußer, J.: Simualtion of a Three Way Catalyst for Downsized Engines. Research project, Laboratory of Engineering Thermodynamics (LTD), University of Kaiserslautern (2017).

Selected publications

von Harbou et al., 2017a

Reprinted with permission from: E. von Harbou, O. Wachsen, E. Klemm, C. Dreiser, Technische Chemie 2016, Nachrichten aus der Chemie, Volume 65, 2017, Pages 367-374, DOI 10.1002/nadc.20174057518

Technische Chemie 2016

In-situ-Analytik, technische Elektrochemie und Prozesstechnik sind Schwerpunkte im Trendbericht der Processnet-Fachgruppe Reaktionstechnik. Erneuerbare Energien, nachwachsende Rohstoffe und neue Produkte erfordern neue Verfahren und Methoden. Sie unterstützen Unternehmen, globaler, innovativer und nachhaltiger zu agieren.

In-situ-Analytik in der Reaktionstechnik

◆ In-situ-Analytik trägt dazu bei, Prozesse in chemischen Reaktoren zu verstehen. Dieses Prozessverständnis erlaubt, chemische Reaktoren zu entwickeln, dem richtigen Maßstab anzupassen und zu optimieren. Entwicklungstrends der In-situ-Analysetechnik sind:

- die Empfindlichkeit sowie
- das örtliche und zeitliche Auflösungsvermögen zu verbessern,
- robuste Analysetechniken zu entwickeln, die sich für eine industrielle Umgebung eignen.

Beispiele und Herausforderungen

◆ Spektroskopische Messverfahren, etwa Raman-, Infrarot(IR)- oder Kernspinresonanz(NMR)-Spektroskopie, sind für die In-situ-Analytik reaktionstechnischer Systeme besonders geeignet, weil diese Verfahren nichtinvasiv messen. Als In-situ-Analytik werden in diesem Bericht alle Messungen der chemischen Zusammensetzung am Ort des Prozesses ohne Probennahme aufgefasst.

Die Forschungsarbeiten von Kubis et al. über neue rutheniumbasierte homogene Katalysatoren für die Hydroformulierung von Alkenen zeigen die Vorteile der In-situ-Analytik in der Reaktionstechnik:[1)] Da der Katalysator in situ in einer Reformierungsreaktion mit Kohlenmonoxid im Reaktor entsteht, lassen sich die Umwandlung des Precursors und der Fortschritt der Hydroformulierungsreaktion auch nur in situ beobachten. Die Messung des Umsatzes einer enzymkatalysierten Synthese von Polyestern aus 1,3-Propandiol in einem Blasensäulenreaktor mit einer IR-Sonde ist ein weiteres Beispiel für In-situ-Analysen, die komplexe Prozesse aufklären.[2)]

Abbildung 1 zeigt am Beispiel der Untersuchung eines chromatographischen Festbettreaktors, wie aus den in regelmäßigen Intervallen gemessenen Spektren (in diesem Fall NMR-Spektren) die Änderung der Konzentration der Analyten über die Zeit bestimmbar ist. In diesem Beispiel ist die Auswertung der Spektren direkt möglich, da die Signale (Peaks) der einzelnen Komponenten getrennt voneinander sind. In vielen Fällen lassen sich die Spektren jedoch nur über mathematische Verfahren auswerten.

Spektroskopische Daten, denen das Lambert-Beersche Gesetz zugrunde liegt, lassen sich mit Methoden der multivariaten Analyse auswerten. Ziel ist es, aus den Spektren

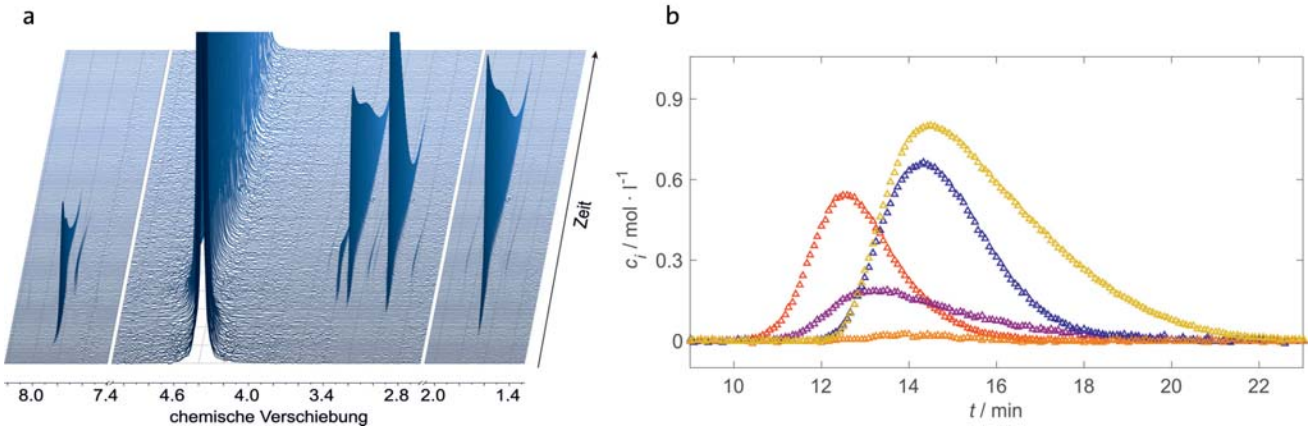

Abb. 1. Nachverfolgung eines chromatographischen Festbettreaktorprozesses mit NMR-Spektroskopie. a) Veränderung der Spektren über der Zeit, b) Konzentration der Analyten als Funktion der Zeit, die aus den Spektren abgeleitete wurde.

den Konzentrationsverlauf der Analyten zu erhalten. Die Lösung dieses mathematischen Rekonstruktionsproblems ist häufig nicht eindeutig, und viele Lösungen sind möglich. Ein zurzeit intensiv untersuchter Forschungszweig befasst sich mit der Ausnutzung von zusätzlichem Wissen für die Rekonstruktion der Spektren, um dadurch möglichst eindeutige Ergebnisse zu erhalten. Wenn etwa kinetische Modelle die zeitliche Änderung der Zusammensetzung beschreiben, dann hilft die Rekonstruktion, bei der Bestimmung des Konzentrationsverlaufs simultan die Kinetikkonstanten anzupassen.[3)]

Eine andere Möglichkeit, die Spektren einer Mehrkomponentenmischung zu analysieren, besteht darin, die Signale durch eine gewichtete Summe von Peaks aus den Einzelkomponenten darzustellen. Nach Kalibrierung der Signale der Einzelkomponenten lassen sich mit dieser Methode zudem die Zusammensetzungen komplexer Mischungen bestimmen, bei denen die Signale überlagern. Für die Analyse solcher Spektren hat sich vor allem Indirect Hard Modeling (IHM) als wertvoll erwiesen. Mit dieser Methode lassen sich Spektren auch dann quantitativ auswerten, wenn sich die Peaks von Spektrum zu Spektrum verschieben oder sie ihre Form ändern.[4,5)]

Wenn bei der Untersuchung reagierender Systeme Zwischenprodukte oder Produkte entstehen, die sich nicht aus der Lösung isolieren lassen und auch als Reinstoff nicht erhältlich sind, ist die NMR-Spektroskopie häufig die einzige Möglichkeit, diese Systeme quantitativ zu untersuchen. Denn im Gegensatz zur optischen ist bei der NMR-Spektroskopie in der Regel keine Kalibrierung notwendig. Zudem kann die NMR-Spektroskopie Strukturen aufklären, sodass neue Reaktionsprodukte direkt zu identifizieren sind. Zum Beispiel untersuchten Scheithauer et al. mit NMR-Spektroskopie das komplexe Reaktionssystem, das in wässrigen Acetaldehydlösungen auftritt.[6–8)] Sie fanden so mehrere Intermediate wie Aldoxan und Poly(oxymethylmethylen)glykole sowie die dazugehörigen Reaktionsgleichgewichte und Reaktionskinetiken.

Mikroreaktionstechnik

◆ Die Verknüpfung von In-situ-Analytik mit Mikroreaktionstechnik ist ein weiterer Entwicklungstrend. Der Vorteil von Mikroreaktoren liegt unter anderem darin, dass sich die Prozessbedingungen wie Reaktortemperatur und Hydrodynamik definiert einstellen lassen. So haben Brächer et al. einen NMR-Probenkopf entwickelt, mit dem sich die Kinetiken schneller Reaktionen bei isothermen Bedingungen untersuchen lassen (Abbildung 2).[9,10)] Dabei kommen die Edukte erst im NMR-Probenkopf über einen Mikromischer in Kontakt, sodass direkt nach dem Start der Reaktion der Reaktionsfortschritt nachverfolgbar ist. Mikroreaktionstechnik ist notwendig, damit die Komponenten ins NMR-Spektrometer passen sowie die effektive Vermischung der Edukte und gute Temperierung des Reaktors gewährleistet sind.

Fräulin et al. haben Mikroreaktionstechnik mit In-situ-Analytik verknüpft, um den Reaktionsmechanismus der selektiven Oxidation von Cyclohexan mit Raman-Spektroskopie zu untersuchen.[11)] Zudem ermöglicht der Mikroreaktor einen optischen Zugang zum Strömungskanal. Somit lässt sich die Konzentrationsmessung ortsaufgelöst durchführen. Die Konzentrationsprofile von Reaktanden und Reaktionsprodukten – ermittelt im einphasigen Betrieb entlang der Länge des Mikrokanals – zeigten, dass trotz der geringen Konzentration der Analyten die Messgenauigkeit ausreichend ist, um Aussagen über den Mechanismus und die Kinetik der Reaktionen zu treffen. Das Besondere bei diesem Versuchsaufbau ist, dass mit konfokaler Ramanspektroskopie die Konzentration der Analyten nicht nur entlang der Kanallänge, sondern auch in der Kanalbreite und -tiefe bestimmbar ist.

Die gleiche Arbeitsgruppe untersucht im Rahmen des DFG Schwerpunktprogramms 1740 „Reaktive Blasenströmungen“ auch Taylor-Strömung in Mikrokanälen. Dafür entwickelt sie ein Laser-Ramansystem, das wegen der kurzen Pulsdauer von 10 µs die Zusammensetzung der Flüssigkeitspfropfen ermittelt. Erste Ergebnisse zeigen, dass die Empfindlichkeit der Messtechnik ausreicht, um die Konzentration von Cyclohexan in einer Mischung mit Methanol bis zu 0,2 Massen-% quantitativ zu bestimmen.[12)] Weitere Forschungsarbeiten sollen diese Technik so verfeinern, dass die Zusammensetzung der Flüssigphase direkt im Nachlauf der

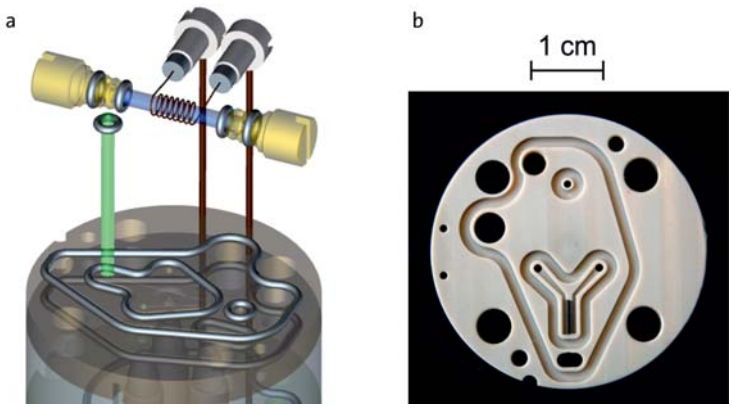

Abb. 2. Mikroreaktor NMR-Probenkopf zur Vermessung schneller Reaktionskinetiken. a) CAD-Zeichnung des NMR-Probenkopfes, b) Foto des im NMR-Probenkopf eingesetzten Mikromischers. Foto: TU Kaiserslautern

Blase untersucht werden kann. So lässt sich das Zusammenspiel von Stofftransport und Reaktion untersuchen.

Am Fraunhofer-Institut für Chemische Technologie wurde ein neuartiger Quantenkaskadenlaser entwickelt und mit einem Mikroreaktor gekoppelt. Damit lassen sich über IR-Spektroskopie mit hoher zeitlicher Auflösung Reaktionen auch in stark absorbierenden Medien wie Lösungsmitteln oder Polymeren untersuchen. Diese Technik lieferte etwa die Reaktionssequenz einer Knoevenagel-Kondensation in einem Mikroreaktor.[13)] Eine Zeilenkamera (push broom imaging) ermöglicht es zudem, chemischen Reaktionen mit einer hohen örtlichen Auflösung in einem kontinuierlich betriebenen Mikroreaktor zu verfolgen.[14)]

Im Gegensatz zur Raman- oder IR-Spektroskopie ist eine örtlich aufgelöste Messung der Zusammensetzung mit NMR-Spektrometer auch dann möglich, wenn es keinen optischen Zugang zum Reaktionsgemisch gibt. Voraussetzung dafür ist, dass der Reaktor ins NMR-Spektrometer passt und sich dort betreiben lässt. Deshalb lassen sich mit dieser Technik beispielsweise ortsaufgelöst die Strömungsgeschwindigkeiten, Konzentrations- und Temperaturprofile in lichtundurchlässigen Festbettreaktoren[15)] und in monolithischen Reaktoren bestimmen.[16)]

Neue Analysetechniken für industrielle Prozesse

◆ Durchflusszellen oder Reaktorgeometrien, die einen optischen Zugang zur Reaktionsmischung ermöglichen, sind in einem Laborreaktor einfach zu realisieren. Die Umsetzung im industriellen Maßstab ist schwieriger. Dies war bisher ein Hindernis für spektroskopische Methoden in der Prozessanalytik. Kürzlich wurde eine Prozesssonde für die Ramanspektroskopie vorgestellt, die sich direkt an die Schaugläser der Anlagen anbringen lässt und darüber die Reaktionsmischung optisch zugänglich macht.[17)]

Seit einigen Jahren sind Benchtop-NMR-Spektrometer auf dem Markt, die das Magnetfeld statt mit einem supraleitenden Elektromagneten wie bei Hochfeld-NMR-Spektrometern mit einem Permanentmagneten erzeugen. Benchtop-NMR-Spektrometer sind daher sowohl in der Anschaffung als auch im Unterhalt günstiger.[18,19)] Außerdem benötigen sie keine spezielle Infrastruktur oder Umgebung, und sie sind kompakter gebaut als Hochfeld-NMR-Spektrometer. Deshalb haben Benchtop-NMR-Spektrometer das Potenzial, nicht nur als Standardwerkzeug für In-situ-Analytik in Forschung und Entwicklung, sondern auch in der Prozessanalytik eingesetzt zu werden.

Forschungsarbeiten zeigten bereits, dass sich Benchtop-NMR-Spektrometer für Reaktionsuntersuchungen eignen.[5,20–23)] Benchtop-NMR-Spektrometer, die Prozesse innerhalb von containerbasierten modularen Produktionsanlagen überwachen und regeln, werden im Rahmen des EU-Projekts Consens (Integrated Control and Sensing) erforscht. Laborexperimente zeigen die Leistungsfähigkeit des Sensorkonzepts am Beispiel einer aromatischen Substitutionsreaktion.[24)]

Neben der Integration des Spektrometers in die Prozessumgebung ist die zuverlässige Auswertung der NMR-Daten schwierig. Probleme machen die große Datenmenge sowie die geringere Empfindlichkeit und spektrale Auflösung der Benchtop- gegenüber den Hochfeld-NMR-Spektrometern.[25)] Daher ist es wichtig, die mathematischen Analyseverfahren der spektroskopischen Messdaten aus dem Reaktions- und Prozessmonitoring weiterzuentwickeln.

Technische Elektrochemie

◆ Aus der Elektrochemie sollen drei aktuelle Forschungsgebiete herausgegriffen werden:

- Redoxflussbatterien,
- CO_2-H_2O-Coelektrolyse,
- Plasmachemie.

Redoxflussbatterien

◆ Redoxflussbatterien, mit denen sich elektrische Energie in Form von Ionenlösungen speichern lässt, sind in der elektrochemischen Forschung weiterhin wichtig. Vor allem das „all vanadium“-System mit Ionen der Wertigkeitsstufen V^{2+} bis V^{5+} wird bereits technisch angewendet und in seiner Leistungsfähigkeit kontinuierlich verbessert (Abbildung 3). Als Kernkomponente mit dem höchs-

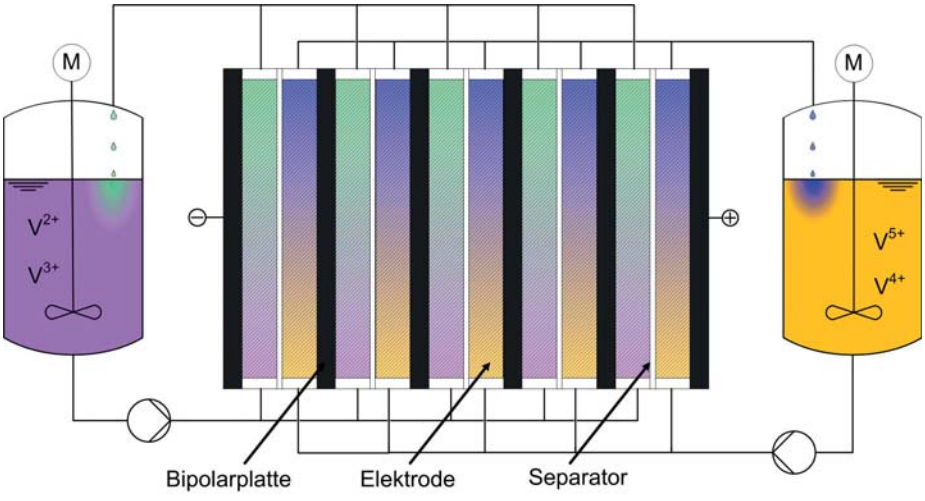

Abb. 3. Prinzipskizze einer Vanadium-Redoxflussbatterie.

ten Zellwiderstand wird die Membran besonders intensiv untersucht. Neben einer hohen ionischen Leitfähigkeit soll insbesondere der Durchtritt (crossover) der verschiedenen Vanadiumspezies möglichst gering sein. Es gibt viele Arbeiten zur Entwicklung von neuartigen Membranmaterialien und detaillierten Membranmodellen.[26] Bei Zellen mit größeren Abmessungen ist der Druckverlust bei der Durchströmung der Zellen mit den Elektrolytlösungen zunehmend wichtig. Deshalb müssen geeignete Strömungsfelder entwickelt werden.[27]

Um die Gleichverteilung von Stromdichte und Potenzial in den Zellen sicherzustellen, bieten sich ortsaufgelöste Messungen an,[28] mit denen sich Zellenmodelle und Simulationsrechnungen validieren lassen. Langfristig ist es wünschenswert, den teuren Vanadiumelektrolyten durch preiswertere Materialien zu ersetzen. In diesem Zusammenhang hat sich in den letzten zwei Jahren eine neue Forschungsrichtung etabliert, die organische Redoxsysteme wie Chinone entwickelt und vielversprechende Ergebnisse erzielt hat.[29]

H_2O-CO_2-Coelektrolyse

◆ Bei der H_2O-CO_2-Coelektrolyse werden an der Kathode H_2O und CO_2 miteinander umgesetzt, sei es unter Bildung von Synthesegas (CO-H_2-Gemischen), Methanol, Ameisensäure oder höherer Kohlenwasserstoffe wie Ethen und Ethanol.[30] Für die technische Machbarkeit einer Demonstrations- oder Produktionsanlage sind in erster Linie hohe Stromdichten (>100 mA·cm^{-2} beziehungsweise >1 A·cm^{-2}) und hohe Standzeiten erforderlich, um über viele 100 oder 1000 Stunden einige Kilogramm Produkt pro Stunde oder mehr herzustellen. Für die Wirtschaftlichkeit der H_2O-CO_2-Coelektrolyse sind zudem hohe Faraday-Effizienzen (Selektivitäten bezogen auf Elektronen als „Edukt“) und hohe Energie-Effizienzen (minimale Zellspannungen) erforderlich. Verma et al. (Arbeitsgruppe Paul Kenis) zeigten in einer technoökonomischen Studie, welche Werte diese Größen erreichen müssen, um einen technisch realisierbaren sowie wirtschaftlichen Produktionsprozess zu ergeben.[31] Demnach sollte die elektrochemische Produktion von Ameisensäure und CO bald kommerzialisierbar sein.[31]

Der Forschungsbedarf in der H_2O-CO_2-Coelektrolyse lässt sich in drei Themengebiete einteilen:

- Katalysatoren und Mechanismus,
- Elektrodendesign,
- Zellendesign.

Am Beispiel der H_2O-CO_2-Coelektrolyse zu Ameisensäure soll auf alle drei Themengebiete kurz eingegangen werden. Als bevorzugter Katalysator dient Zinn/Zinnoxid, das nanopartikulär oder nanostrukturiert eingesetzt wird. So wurden beispielsweise dendritische Zinn-Zinnoxid-Nanostrukturen durch Elektroabscheidung hergestellt. Im Gegensatz zu konventionellen Zinn-Vollelektroden haben sie eine hohe Aktivität (–13,5 mA·cm^{-2} bei –1 V Elektrodenpotenzial der reversiblen Wasserstoffelektrode) und erlauben einen stabilen Betrieb über 18 Stunden.[32] Weitere Beispiele zum Einfluss der Nanomorphologie der Elektrokatalysatoren stehen im Übersichtsartikel von Kumar et al.[33]

Vielversprechend sind heteroatomdotierte Kohlenstoffmaterialien, sei es als Träger oder als metallfreie Elektrokatalysatoren.[33] Mechanistische Einblicke in die elektrochemische CO_2-Reduktion an Zinnelektroden lieferte die Arbeitsgruppe von Andrew Bocarsly mit In-situ-ATR-IR-Spektroskopie.[34] An der Oberfläche des Zinns befindet sich unter den Bedingungen der kathodischen Reduktion entgegen der vorherrschenden Meinung eine metastabile und katalytisch relevante Zinnoxid-Schicht, an der CO_2 als Carbonat adsorbiert. Dieses ist das elektroaktive Intermediat und wird zu Formiat reduziert.

Das Elektrodendesign ist zentral, um hohe Stromdichten und gleichzeitig hohe Faraday-Effizienzen zu erhalten. Sobald eine Stofftransportbegrenzung für CO_2 einsetzt, bildet sich an der Kathode vermehrt unerwünschter Wasserstoff. Kopljar et al. zeigten, dass Gasdiffusionselektroden (Abbildung 4) durch ein optimales Design Stromdichten von bis zu 500 mA·cm^{-2} bei gleichzeitig hohen Faraday-Effizienzen zu Ameisensäure von mehr als 80 Prozent an auf Ruß geträgerten Zinn-Nanopartikeln ermöglichen.[35,36] Auch Whipple et al. setzen Gasdiffusionselektroden ein. Sie bringen analog zu den Elektroden bei PEM-Brennstoffzellen den Katalysator als katalytische Schicht auf ein Kohlepapier auf und erhalten damit bis zu 100 mA·cm^{-2} bei einer Faraday-Effizienz von etwa 89 Prozent.[37] Auf ähnliche Art erreichen Castillo et al. etwa 90 mA·cm^{-2} mit 70 Prozent Faraday-Effizienz.[38]

Beim Zellendesign sind vor allem die Übertragung auf einen

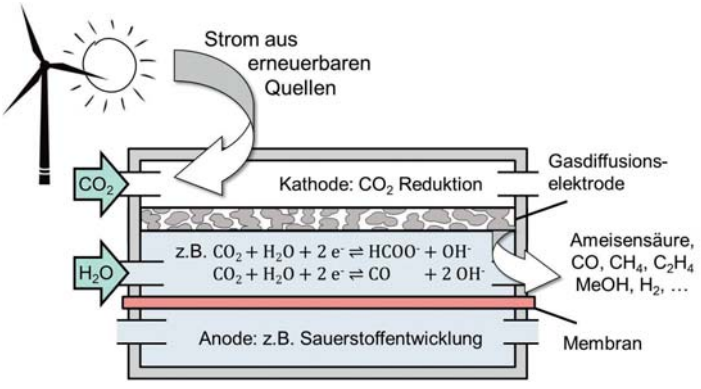

Abb. 4. Prinzipskizze einer Gasdiffusionselektrode für die H_2O-CO_2-Coelektrolyse.

kontinuierlichen Betrieb und die Scale-up-Fähigkeit zentral. Verschiedene Formen sind möglich: vom eher klassischen Elektrolyseurdesign[39] über mikrostrukturierte Elektrolytkanäle[36] bis hin zur mikrofluidischen Zelle.[37] Wichtig sind dabei eine hohe Leitfähigkeit des Elektrolyten und ein geringer Elektrodenabstand, um ohmsche Verluste und somit die Zellspannung so gering wie möglich zu halten. Für das Zellendesign und die Wirtschaftlichkeit des Prozesses muss zudem die Anodenseite betrachtet werden. So können Elektroden verwendet werden, um Wasser sauer oder alkalisch zu Sauerstoff zu oxidieren (oxygen evolution reaction, OER). Aufgrund der geforderten hohen Stromdichten auf der Kathodenseite müssen vor allem die Stromdichten für die alkalische Wasseroxidation weiterentwickelt werden.

Plasmaverfahren

◆ Plasmaverfahren, die schon vor mehr als 110 Jahren erstmals industriell der Prozesschemie dienten, sind wieder modern.[40] Niedertemperaturplasmen sowie moderne Katalyse- und Reaktorkonzepte ermöglichen eine Prozessintensivierung, vor allem erhöhen sie den zentralen Prozessparameter Energieeffizienz.

Die Herstellung von Dünger aus Luft (N-Fixierung) und grüner Windenergie ist ein Beispiel, an dem Evonik Industries und die TU Eindhoven (Arbeitsgruppe Hessel) zusammen arbeiten. In einem Gliding-arc-Plasma entsteht bei Raumtemperatur aus Luftstickstoff NO_x (NO und NO_2).[41] Absorbiert in wässrigen Lösungen bildet sich daraus Salpetersäure (HNO_3) oder Nitratdünger (etwa KNO_3). Hiermit stehen viele Türen für eine neue Verwertung offen, darunter die direkte Verwendung dieser Lösungen als Dünger oder Düngerzusatz oder eine dezentrale Düngererzeugung in kompakten, mobilen Containeranlagen; dies ist vor allem für Regionen interessant, die Dünger nur schwer und begrenzt importieren können, aber über große, weit auseinander liegende Landwirtschaftsflächen verfügen wie Zentralafrika. Begleitende und leitende Nachhaltigkeitsstudien (Kosten, Lebenzyklusbetrachtung) belegen die Kosteneffizienz und Umweltverträglichkeit der neuen Plasmaverfahren für die N-Fixierung zu Dünger.[42]

Prozesstechnik

◆ Drei wesentliche Pfeiler neuer Prozesstechniken sind

- integrale Technologieplattformen,
- Product-by-process-Konzepte und
- tolerante Prozesse.

Die Informationstechnik bietet mit der vierten industriellen Revolution[43] – Industrie 4.0 – zudem Chancen für gleichermaßen disruptive Anlagenkonzepte und Geschäftsmodelle (Abbildung 5).

Integrale Technologieplattformen

◆ Sonnen- und Windenergie, nachwachsende Rohstoffe, rezyklierte Materialien und Kohlenstoffdioxid als schrittweise zu implementierende Alternativen in der kohlenstoffbasierten Rohstoffsicherung[45] erfordern gleichermaßen neuartige Prozesse, realisiert durch integrale Technologieplattformen. Hierbei müssen interdisziplinär Einzelschritte aus Reaktionstechnik, Katalyse, Biotechnik und Downstreamprocessing entwickelt und nach einem ganzheitlichen End-to-end-Ansatz zu Produktionsanlagen kombiniert werden. Qualitätsschwankungen und Verfügbarkeiten von Rohstoffen und Energien erfordern dabei robuste Prozesse, die wirtschaftlich, zuverlässig, qualitativ hochwertig sowie mit hohen Umwelt- und Sicherheitsstandards produzieren. Circular Economy und Zero Liquid Discharge sind Begriffe, die damit eng verknüpft sind. Einige Forschungsarbeiten haben bereits industrielle Reife erreicht.

Neben Kohlenstoffdioxidabscheidung und -speicherung wird die direkte stoffliche Nutzung wirtschaftlich bedeutender. Hier ist das vom Bundesministerium für Bildung und Forschung geförderte

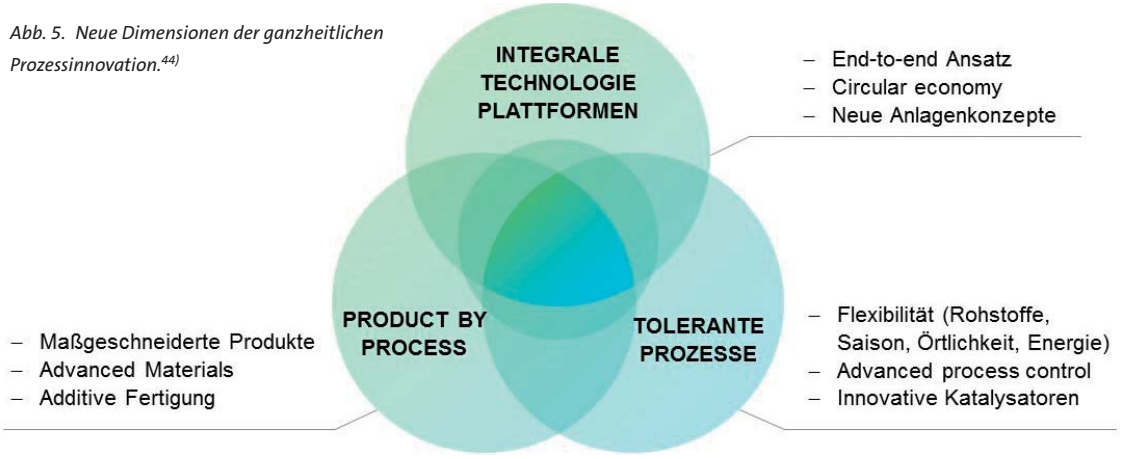

Abb. 5. Neue Dimensionen der ganzheitlichen Prozessinnovation.[44]

Verbundforschungsprojekt Carbon2Chem ein Beispiel, das die Herstellung chemischer Grundstoffe aus CO_2 und die gleichzeitige Reduzierung von CO_2-Emmissionen in Stahlwerken bis zum Jahr 2030 kombiniert. Kern des Projekts ist die hüttenbasierte Produktion von Methanol, anderen Alkoholen, Polymeren oder Oxymethylenether. Dazu kommen interdisziplinäre Themen. So hängt der Erfolg anschließender katalytischer Prozesse ab von der Aufarbeitung der Hüttengase, darunter das Entfernen von Schwefelverbindungen[46,47] und weiterer Verunreinigungen aus dem metallurgischen Prozess.

Schwankende Zusammensetzungen der Hauptkomponenten des Gasstroms sind ebenfalls kritisch für katalytische Folgeprozesse. Solche Schwankungen machen es notwendig, die Mischungsverhältnisse anzupassen oder zusätzlichen Wasserstoff bereit zu stellen. Flexible Elektrolyseverfahren und alternative Wasserstoffquellen sind ebenso entscheidend für Nachhaltigkeit und Wirtschaftlichkeit. Die neuen Prozesse konkurrieren mit den Verfahren auf petrochemischer Basis.

Vor allem die Rückgewinnung strategischer Metalle, die für technische Produkte unverzichtbar sind, ist ein wesentlicher Aspekt der Diskussion zur Kreislaufwirtschaft. Diese Rückgewinnung wird aus der Gasphase,[48] durch hybride, elementspezifische Prozesse und Membranverfahren aus Laugenlösungen,[49] über Flüssig-Flüssig-Extraktion[50] oder die Kombination von physikochemischen und biotechnischen Prozessen[51,52] erforscht.

Agrarreststoffe als Rohstoffe für Bioethanol der zweiten Generation, andere Flüssigkraftstoffe sowie für Basis- und Feinchemikalien erfordern tolerante Prozesse, die lokale Randbedingungen berücksichtigen. Verfahren wie der Karlsruher Bioliq-Prozess und der Sunliquid-Prozess von Clariant sind Beispiele neuer Prozessrouten, die auf erneuerbaren Rohstoffen basieren. Während der Bioliq-Prozess Biomasse in die petrochemische Stoffkette der Basischemikalien überführt, werden beim Sunliquid-Prozess Agrarreststoffe biochemisch in Zucker überführt. Diese bilden die Basis für die Herstellung von Bioethanol und anderer biobasierter Chemikalien.

Die Verfahren und Strategien, um CO_2, pflanzliche Rohstoffe oder rezykliertes Material zu nutzen, sind individuell und ganzheitlich zu bewerten. Dabei soll die synthetische Vorleistung der Natur nicht verloren gehen, und die Materialien sollen sicher verfügbar sein.[45]

Modularer Anlagenbau beschleunigt Markteintritte unter erhöhter Produktflexibilität. Der Modularisierung von Produktionsprozessen nimmt sich der temporäre Arbeitskreis „Modulare Anlagen“ von Processnet an. Beteiligt sind Chemieunternehmen, Hochschulen und Zulieferer. Themen sind Prozesseintensivierung, eine einheitliche Nomenklatur, Standardisierung sowie die rechtlichen Rahmenbedingungen und disruptiven Geschäftsmodelle für Anlagenbauer und Betreiber.[53] Modularität und einfache Skalierbarkeit sind insbesondere für klassische Grundoperationen herausfordernd.[53] Die Demonstration modularer Anlagenkonzepte für Mehrphasenanwendungen erfolgt derzeit am Beispiel der Absorption.[54]

Product-by-process

◆ Der Markt stellt höhere Anforderungen an Produkteigenschaften von neuen Hochleistungsmaterialien wie Nanopartikel und -tubes, Polymere oder Komposite für Anwendungen wie Automobil, Gesundheit oder Elektronik. Der Trend, industrielle Prozesse vom Satzbetrieb in den kontinuierlichen Betrieb umzustellen, hält dabei an. Die Modularisierung trägt wesentlich zur Flexibilisierung kontinuierlicher Herstellungsprozesse für maßgeschneiderte Produkte bei. Solche kontinuierlichen Mehrzweckanlagen erlauben es vor allem, die Produkteigenschaften maßzuschneidern. Prozessseitig zählen mikroskalige und modulare Reaktoren zunehmend zum etablierten Apparatebaukasten.[55,56] Allerdings bedarf es eines intensiven Austauschs zwischen Materialwissenschaftlern und Verfahrenstechnikern, um die Leistungsfähigkeit der Prozesse den Anforderungen des Marktes anzupassen und das Potenzial in kommerziell erfolgreiche Produkte umzusetzen.

Die additive Fertigung hält auch in der Chemieindustrie nach und

Erik von Harbou, Jahrgang 1981, studierte Verfahrenstechnik an der TU Hamburg und promovierte im Jahr 2012 an der TU Kaiserslautern. Nach einem Postdoc-Aufenthalt an der University of Cambridge hat er seit dem Jahr 2013 die Juniorprofessur für Chemische Systemtechnik an der TU Kaiserslautern. In seiner Forschung beschäftigt er sich mit der Untersuchung komplexer reaktiver mehrphasiger Systeme mit In-situ-Analytik, etwa der quantitativen NMR-Spektroskopie. erik.vonharbou@mv.uni-kl.de

Christian Dreiser, Jahrgang 1985, studierte in den Jahren 2006 bis 2010 Bio- und Umweltverfahrenstechnik an der TU Kaiserslautern und promovierte dort in thermischer Verfahrenstechnik. Seit dem Jahr 2015 arbeitet er im Segment Process Innovation bei Clariant.
christian.dreiser@clariant.com

Elias Klemm, Jahrgang 1965, studierte von 1985 bis 1991 Chemieingenieurwesen an der Universität Erlangen-Nürnberg und promovierte 1995 bei Gerhard Emig. Nach der Habilitation im Jahr 2001 und einer Industrietätigkeit von zwei Jahren bei der damaligen Degussa nahm er im Jahr 2003 einen Ruf auf die C4-Professur Technische Chemie der TU Chemnitz an. Seit dem Jahr 2009 leitet er das Institut für Technische Chemie an der Universität Stuttgart.
elias.klemm@itc.uni-stuttgart.de

Olaf Wachsen, Jahrgang 1967, studierte von 1986 bis 1991 Chemie an der TU Berlin. Er promovierte 1996 bei Karl-Heinz Reichert in der technischen Chemie. Nach diversen Tätigkeiten in der Ekato-Gruppe, bei Hoechst und Clariant ist er heute Leiter von Group Process Technology bei Clariant.
olaf.wachsen@clariant.com

Abb. 6. Chemiefabrik der Zukunft.

Abbildung: Mimi Potter, Fotolia

nach Einzug und beschleunigt die Prozess- und Apparateentwicklung sowie -intensivierung. Periodische zelluläre Strukturen als Katalysatorträger verdeutlichen,[57] wie Werkzeuge aus der rechnergestützten Entwicklung (computer-aided engineering, CAE) verfahrenstechnisch relevante Geometrien optimieren und damit die Fertigung unterstützen. Auch neue Rohstoffe für die additive Fertigung, etwa funktionalisierte Polymere, bereitzustellen, ist anspruchsvoll, bietet aber auch neue Rahmenbedingungen für apparative Gestaltung. So gibt es Kombinationen aus Polymeren und Enzymen, beispielsweise in einer modularen Reaktorkaskade.[58]

Tolerante Prozesse

◆ Der Rohstoffwandel und die wechselnden Marktanforderungen verlangen einen Paradigmenwechsel hin zu toleranten Prozessen. Neue Anforderungen entstehen vor allem durch die Substitution von konventionellen Rohstoffen durch beispielsweise erneuerbare, wässrige Lösungen mit schwankender Zusammensetzung aus biochemisch erschlossenen Quellen.

Zudem sind klassische thermische Aufarbeitungstechniken, die Zielkomponenten isolieren, in ihren Betriebsfenstern begrenzt. Es besteht dringender Forschungsbedarf bezüglich der Flexibilisierung von Reaktoren und verfahrenstechnischen Grundoperationen sowie der toleranten Prozessauslegung auch im systemverfahrenstechnischen Gesamtentwurf. Die Apparateauslegung legt dabei neben der Effizienz zunehmend Wert auf Flexibilität als gleichberechtigtes Kriterium.[59] Konzepte der instationären,[60] und erzwungen periodischen Betriebsweise[61] werden nach vielen Jahren wieder diskutiert und dazu genutzt, Reaktorleistungen robust zu erhöhen.

Digitalisierung der technischen Chemie

◆ Wie Industrie 4.0 auf die Produktion in der Chemieindustrie wirkt, wird intensiv diskutiert (Abbildung 6). Advanced Process Control und die Handhabung von Big Data sind besonders wichtig, um Prozesse zu optimieren und zu intensivieren. Zielführend ist allerdings nicht nur gesamte Standorte zu digitalisieren, sondern auch den Nutzen zunächst an Fallbeispielen zu zeigen.[62] Vision und Realität digitaler Anlagen und smarter Sensoren stehen im Dechema-Whitepaper „Digitalisierung in der Chemieindustrie“ und in der Technologie-Roadmap „Prozesssensoren 4.0“, die Interessengemeinschaft Automatisierungstechnik der Prozessindustrie Namur und die VDI/VDE-Gesellschaft Mess- und Automatisierungstechnik gemeinsam veröffentlichten.

Der allgemeine Nutzen für die Verfahrensentwicklung entlang der gesamten Wertschöpfungskette liegt darin, Prozessdaten nutzbar zu machen und neuen Planungsmöglichkeiten in der digitalen Anlage zu liefern. Beispiele sind Aufstellungsplanung, Personalschulung und betriebliche Optimierung an einem digitalen Zwilling[63] einer verfahrenstechnischen Anlage. Kinetiken und weitere Informationen aus der Verfahrensentwicklung sowie Prozessdaten lassen sich anschließend mit den Designdaten zur kontinuierlichen Prozessverbesserung und Online-Steuerung verknüpfen.

Chemieunternehmen haben wie andere Industrien die Chance, sich in der Wertschöpfungskette neu zu positionieren und so Geschäftsmodelle zu beeinflussen, wenn sie flexibel auf die Anforderungen von Kunden und Lieferanten reagieren. Für eine flexible und wirtschaftliche Produktion von maßgeschneiderten Spezialitäten sind modulare Steuerungselemente und Automatisierung wesentlich.

Bei der CAE ist die numerische Strömungssimulation zunehmend Bestandteil des Standardwerkzeugkastens eines Entwicklungsingenieurs, wie es vor Jahren für Prozesssimulationssoftware der Fall war. Zudem lohnt sich die Betrachtung der Multiskalen-Modellierung, bei der heutzutage beispielsweise quantenmechanische Betrachtungen am Katalysator mit der Strömung und Wärmeabfuhr im Reaktor simultan simuliert werden können.[64] ➜

Literatur

1) *C. Kubis, I. Profir, I. Fleischer et al.*, Chem. Eur. J. *2016*, 22, *2746–2757*.
2) *J. Gebhard, D. Sellin, L. Hilterhaus, A. Liese*, Chem. Ing. Tech. *2013*, 85, *1016–1022*.
3) *H. Schröder, M. Sawall, C. Kubis et al.*, Anal. Chim. Act. *2016*, 927, *21–34*.
4) *J. Meyer-Kirschner, M. Kather, A. Pich et al.*, Appl. Spectrosc. *2016*, 70, *416–426*.
5) *N. Zientek, C. Laurain, K. Meyer et al.*, Magn. Reson. Chem. *2016*, 54, *513–520*.
6) *A. Scheithauer, T. Grützner, C. Rijksen et al.*, Ind. Eng. Chem. Res. *2014*, 53, *8395–840*.
7) *A. Scheithauer, E. von Harbou, H. Hasse et al.*, AIChE J. *2015*, 61, *177–187*.
8) *A. Scheithauer, A. Brächer, T. Grützner et al.*, Ind. Eng. Chem. Res. *2014*, 53, *17589–17596*.
9) *A. Brächer, S. Hoch, K. Albert et al.*, J. Magn. Reson. *2014*, 242, *155–161*.
10) *A. Brächer, R. Behrens, E. von Harbou, H. Hasse*, Chem. Eng. J. *2016*, 306, *413–421*.
11) *C. Fräulin, G. Rinke, R. Dittmeyer, G. Waters, M. Nilles*, Chem. Ing. Tech. *2014*, 86, *524–528*.
12) *D. Schurr, J. Guhathakurta, S. Baroud, G. Rinke, R. Dittmeyer*, Proceedings of 9th International Conference on Multiphase Flow, *2016*.
13) *R. Ostendorf, L. Butschek, S. Hugger et al.*, Photonics *2016*, 3, *28*.
14) *S. Panic, D. Boskovic, S. Loebbecke*, Proceedings of 12th International Conference on Microreaction Technology (IMRET 12), *2012*.
15) *L. F. Gladden, F. J. R. Abegão, C. P. Dunckley et al.*, Recent Dev. Operando Spectrosc. *2010*, 155, *157–163*.
16) *J. Ulpts, W. Dreher, L. Kiewidt, M. Schubert, J. Thöming*, Catal. Today *2016*, 273, *91–98*.
17) *F. Braun, R. Schalk, J. Brunner et al.*, Tm – Tech. Mess. *2016*, 83, *593*.
18) *S. K. Küster, E. Danieli, B. Blümich, F. Casanova*, Phys. Chem. Chem. Phys. *2011*, 13, *13172–13176*.
19) *B. Luy*, Angew. Chem. Int. Ed. *2011*, 50, *354–356*.
20) *E. Danieli, J. Perlo, A. L. L. Duchateau et al.*, ChemPhysChem *2014*, 15, *3060–3066*.
21) *N. Zientek, C. Laurain, K. Meyer et al.*, J. Magn. Reson. *2014*, 249, *53–62*.
22) *V. Sans, L. Porwol, V. Dragone, L. Cronin*, Chem. Sci. *2015*, 6, *1258–1264*.
23) *A. M. R. Hall, J. C. Chouler, A. Codina et al.*, Catal. Sci. Technol. *(in press)*.
24) *S. Kern, K. Meyer, M. Maiwald*, Smart Sensors, *Vulkan-Verlag, 2016*.
25) *K. Meyer, S. Kern, N. Zientek, G. Guthausen, M. Maiwald*, Trends Anal. Chem. *2016*, 83, *39–52*.
26) *M. Paidar, V. Fateev, K. Bouzek*, Electrochim. Acta *2016*, 209, *737*.
27) *D. Reed, E. Thomsen, B. Li et al.*, J. Power Sources *2016*, 306, *24*.
28) *M. Becker, N. Bredemeyer, N. Tenhumberg, T. Turek*, J. Power Sources *2016*, *370, 826*.
29) *K. Lin, R. Gómez-Bombarelli, E. S. Beh et al.* Nat. Energ. *2016*, 1, *16102*.
30) *Y. Hori, Modern Aspects of Electrochemistry (Hrsg. C. Vayenas, R. White, M. Galboa-Aldeco), Vol. 42, Springer Science and Business Media, New York, 2008*.
31) *S. Verma, B. Kim, H.-R. Jhong et al.*, ChemSusChem *2016*, 9, *1*.
32) *D. H. Wong, C. H. Choi, J. Chung et al.*, ChemSusChem *2015*, 8, *3092*.
33) *B. Kumar, J. Brian, V. Atla et al.*, Catal. Today *2016*, 270, *19*.
34) *M. Baruch, J. Pander III, J. White, A. Bocarsly*, ACS Catal. *2015*, 5, *3148*.
35) *D. Kopljar, A. Inan, P. Vindayer, N. Wagner, E. Klemm*, J. Appl. Electrochem. *2014*, 44, *1107*.
36) *D. Kopljar, N. Wagner, E. Klemm*, Chem. Eng. Technol. *2016*, 39, *2042*.
37) *D. Whipple, E. Finke, P. Kenis*, Electrochem. and Solid-State Lett. *2010*, 13, *B109*.
38) *A. Del Castillo, M. Alvarez-Guerra, J. Solla-Gullon et al.*, Appl. Energy *2015*, 157, *165*.
39) *A. Agarwal, Y. Zhai, D. Hill, N. Sridhar*, ChemSusChem *2011*, 4, *1301*.
40) *B. S. Patil, Q. Wang, V. Hessel, J. Lang*, Catal. Today *2015*, 256, *49*.
41) *B. S. Patil, J. Rovira Palau, V. Hessel, J. Lang, Q. Wang*, Plasma Chem. Plasma Process. *2016*, 36, *241*.
42) *A. Anastasopoulou, S. D. Butala, J. Lang, V. Hessel, Q. Wang*, Ind. Eng. Chem. Res. *2016*, 55, *8141*.
43) *McKinsey & Company, Industry 4.0 – How to navigate digitization of the manufacturing sector, McKinsey Digital 2015*.
44) *M. Vollmer, Festvortrag, Processnet Jahrestagung 2016*.
45) *G. H. Vogel*, Chem. Ing. Tech. *2014*, 8, *2135–2149*.
46) *E. Speelmanns, M. Rieger, H. Thielert, G. Wozny, Chem. Ing. Tech. 2014, 86, 1609*.
47) *E.vM. Speelmanns, M. Rieger, H. Thielert, J.-U. Repke*, Chem. Ing. Tech. *2016*, 88, *1339–1340*.
48) *M. Binnewies, K. Bokelmann, C. Gellermann, S. Gäth, R. Stauber*, Chem. Ing. Tech. *2015*, 87, *1486–1497*.
49) *K. Meschke, B. Daus, R. Haseneder, J.-U. Repke*, Chem. Ing. Tech. *2016*, 88, *1344*.
50) *R. Vostl, P. Fröhlich, M. Bertau*, Chem. Ing. Tech. *2016*, 88, *1347*.
51) *R. Kermer, S. Hedrich, B. Brett et al.*, Adv. Mat. Res. *2015*, 1130, *296–299*.
52) *A. Schippers, S. Hedrich, J. Vasters et al.*, Adv. Biochem. Eng. Biotechnol. *2014*, 141, *1–47*.
53) *F. Stenger, D. Schmalz, T. Bieringer et al.*, Chem. Ing. Tech. *2016*, 88, *1217*.
54) *S. Müller, S. Lier, M. Grünewald*, Chem. Eng. Res. Des. *2015*, 99, *256–264*.
55) *G. J. Lichtenegger, V. Tursic, H. Kitzler et al.*, Chem. Ing. Tech. *2016*, 88, *1518–1523*.
56) *N. Kockmann*, Chem. Ing. Tech. *2015*, 87, *1173–1184*.
57) *E. Bianchi, W. Schwieger, H. Freund*, Adv. Eng. Mater. *2016*, 18, *608–614*.
58) *F. Kazenwadel, E. Biegert, J. Wohlgemuth, H. Wagner, M. Franzreb*, Eng. Life Sci. *2016*, 16, *560–567*.
59) *H. Mothes*, Chem. Ing. Tech. *2015*, 87, *1159–1172*.
60) *R. Lange, M. Schubert, W. Dietrich, M. Grünewald*, Chem. Eng. Sci. *2004*, 59, *5355–5361*.
61) *D. Nikolic, A. Seidel-Morgenstern, M. Petkovska*, Chem. Eng. Sci. *2015*, 137, *40–58*.
62) *J. Appel, C. Colombo, U. Dätwyler, Y. Chen, N. Kerimoglu*, Chimia *2016*, 70, *621–627*.
63) *J. Kaeser, Digitales Neuland (Hrsg.: T. Becker, T. Knop)*, Springer Fachmedien, *Wiesbaden, 2015*.
64) *S. Matera, S. Blomberg, M.J. Hoffmann et al.*, ACS Catal. *2015*, 5, *4514–4518*.

Die Autoren danken für die Unterstützung und Zuarbeit: Dusan Boskovic (Fraunhofer ICT), Roland Dittmeyer (KIT), Robert Franke (Evonik), Volker Hessel (TU Eindhoven), Michael Maiwald (BAM), Mathias Sawall (Uni Rostock) und Thomas Turek (TU Clausthal-Zellerfeld). Die Aufzählung in alphabetischer Reihenfolge erhebt keinen Anspruch auf Vollständigkeit.

Sawall et al., 2018

Reprinted with permission from: M. Sawall, E. von Harbou, A. Moog, R. Behrens, H. Schröder, J. Simoneau, E. Steimers, K. Neymeyr, Multi-objective optimization for an automated and simultaneous phase and baseline correction of NMR spectral data, Journal of Magnetic Resonance, Volume 289, 2018, Pages 132-141, ISSN 1090-7807, DOI 10.1016/j.jmr.2018.02.012

Journal of Magnetic Resonance 289 (2018) 132–141

Contents lists available at ScienceDirect

Journal of Magnetic Resonance

journal homepage: www.elsevier.com/locate/jmr

Multi-objective optimization for an automated and simultaneous phase and baseline correction of NMR spectral data

Mathias Sawall [a], Erik von Harbou [b], Annekathrin Moog [a], Richard Behrens [b], Henning Schröder [a], Joël Simoneau [d], Ellen Steimers [b], Klaus Neymeyr [a,c,*]

[a] Universität Rostock, Institut für Mathematik, Ulmenstraße 69, 18057 Rostock, Germany
[b] Technische Universität Kaiserslautern, Lehrstuhl für Thermodynamik, Erwin-Schrödinger-Straße 44, 67663 Kaiserslautern, Germany
[c] Leibniz-Institut für Katalyse e.V. an der Universität Rostock, Albert-Einstein-Straße 29a, 18059 Rostock, Germany
[d] Université de Sherbrooke, Department of Chemical & Biotechnological Engineering, 2500 Blvd. de L'Université, Sherbrooke, Canada

ARTICLE INFO

Article history:
Received 1 December 2017
Revised 12 February 2018
Accepted 13 February 2018
Available online 21 February 2018

Keywords:
NMR data preprocessing
Automated phase correction
Automated baseline correction
Multi-objective minimization
Whittaker smoother

ABSTRACT

Spectral data preprocessing is an integral and sometimes inevitable part of chemometric analyses. For Nuclear Magnetic Resonance (NMR) spectra a possible first preprocessing step is a phase correction which is applied to the Fourier transformed free induction decay (FID) signal. This preprocessing step can be followed by a separate baseline correction step. Especially if series of high-resolution spectra are considered, then automated and computationally fast preprocessing routines are desirable.

A new method is suggested that applies the phase and the baseline corrections simultaneously in an automated form without manual input, which distinguishes this work from other approaches. The underlying multi-objective optimization or Pareto optimization provides improved results compared to consecutively applied correction steps. The optimization process uses an objective function which applies strong penalty constraints and weaker regularization conditions. The new method includes an approach for the detection of zero baseline regions. The baseline correction uses a modified Whittaker smoother. The functionality of the new method is demonstrated for experimental NMR spectra. The results are verified against gravimetric data. The method is compared to alternative preprocessing tools. Additionally, the simultaneous correction method is compared to a consecutive application of the two correction steps.

1. Introduction

NMR spectroscopy is of extraordinary importance for many research fields in science and medicine. The Nobel lectures of Richard R. Ernst (1991), K. Wüthrich (2002) and P.C. Lauterbur and P. Mansfield (2003) provide an excellent overview on the development of NMR spectroscopy and its significance for various fields of application [10,27,17].

This paper focuses on NMR spectroscopy in chemistry or chemical engineering and the problem that NMR spectra often suffer from various types of misadjustment, distortions and noise. The zero-order misadjustment refers to the phase difference of the reference phase and the phase which is used by the FID signal recording detector [4]. The first-order misadjustment can be caused by different sources, e.g., by the delay between excitation and detection or by phase shifts induced by noise-reducing filters [6]. NMR spectra also suffer from baseline distortions which can be caused for example by the nonlinearity of the filter-phase response, instrumental instabilities, background signals or the discrete nature of the Fourier transformation, see [12]. An efficient and reliable correction of the zero- and first-order misadjustments (phase correction) and a correction of the baseline are prerequisites to facilitate the acquisition of quantitative results from the NMR spectrum [18]. Especially the application of NMR spectroscopy for reaction and process monitoring or process control, which has gained importance over the last years not only due to the development of benchtop NMR spectrometer [16], necessitate automatic and robust correction algorithms that can handle large data sets [3,19].

In this paper we present a new preprocessing approach for NMR spectral data which allows to correct the zero- and first-order misadjustments in a simultaneous way together with the baseline by means of a multi-objective optimization. The simultaneous optimization is a characteristic trait of this new approach.

* Corresponding author at: Universität Rostock, Institut für Mathematik, Ulmenstraße 69, 18057 Rostock, Germany.
E-mail address: klaus.neymeyr@uni-rostock.de (K. Neymeyr).

https://doi.org/10.1016/j.jmr.2018.02.012
1090-7807/

1.1. Organization of the paper

The paper is organized as follows. Section 2 introduces the optimization-based preprocessing approach. To this end, an objective function is suggested which includes penalty and regularization terms. Its minimization amounts to a simultaneous phase and baseline correction. In Sections 3 and 4 we discuss the step-by-step methods for the phase correction and for the baseline correction. The simultaneous correction method is presented in Section 5. The new method is tested for experimental NMR spectra in Section 6. This results are compared to the outcome of a computation in which the two correction steps are applied in consecutive manner. Finally, the results are compared to other phase correction methods.

1.2. Notation

We use the following notation for the NMR signal functions.

d^{ft} denotes a complex valued raw NMR spectrum gained by a Fourier transformation of the free induction decay (FID).

d^{pha} is a complex NMR signal after a phase correction step. However, only its real part is considered as the NMR spectrum.

d^{final} is a real-valued NMR signal either after step-wise or simultaneous phase and baseline correction.

d stands for a general real-valued NMR signal with or without prior application of correction steps.

2. Optimization-based data preprocessing

The focus of this paper is on a simultaneous and automated correction of the phase and the baseline of NMR spectra. To this end we use a multi-objective optimization which is a common approach for the implementation of competing constraints, see for example [4] where an entropy minimization approach is used for phase corrections of NMR spectra. It is a well-known fact that a multi-objective optimization problem with competing or even conflicting objective functions often has no single solution which optimizes each constraint. In such cases, the objective functions are called conflicting and the solution of the simultaneous optimization (also known as multi-objective optimization or Pareto optimization) represents a trade-off between the conflicting constraints.

Here we consider an objective function which is a weighted sum of penalty functions and regularizing conditions. This approach makes possible a simultaneous optimization. If all but one of the weight factors are set to zero, then the optimization is applied only to a single constraint. The active constraint can be changed and then the optimization can be restarted. The constraint functions either penalize negative entries of the spectra or are used to regularize the resulting spectra, e.g., in the sense of a small integral or the smoothness of the spectra. If $d \in \mathbb{R}^n$ denotes a real-valued (discrete) spectrum, then the objective function $f : \mathbb{R}^n \to \mathbb{R}$ reads

$$f(d) = \sum_{i=1}^{3} \gamma_i g_i(d/\|d\|_{\max}). \tag{1}$$

Therein the $\gamma_i \geqslant 0$ for $i = 1, 2, 3$ are real weight factors and $\|d\|_{\max} = \max_{i=1,\dots,n}|d_i|$ is the maximum norm. The three functions g_i are

$$g_1(d) = \sum_{j=1}^{n} \big(\min(0, d_j + \varepsilon_1)\big)^2, \quad g_2(d) = \sum_{j=1}^{n} \big(\max(0, |d_j| - \varepsilon_2)\big)^2,$$

$$g_3(d) = \sum_{j=2}^{n-1} \big(d_{j-1} - 2d_j + d_{j+1}\big)^2.$$

For the function g_1 we use a relative large weight factor γ_1 so that g_1 can be considered as a penalty function. For the functions g_2 and g_3 we take smaller weight factors which results in a regularizing effect in the optimization process. The function g_1 is applied in order to enforce nonnegative results in the optimization process. The constraint function g_1 is constructed in a way that only negative portions of d which are smaller than $-\varepsilon_1$ are square-summed up and are used for penalization. In other words, small negative entries whose absolute values are smaller than ε_1 are not penalized. The function g_2 is used in order to find a solution with a small integral (case of sharp and isolated peaks). More precisely, the function g_2 accesses the discrete integral in terms of sums of squares. In a similar way to g_1 all entries of $|d|$ which are smaller than ε_2 do not contribute to this constraint. Thus ε_2 can be considered as a level of accepted deviation of the baseline from the ideal zero-baseline. Finally, the function g_3 sums up the squares of discrete second derivatives of the data. In this way non-smooth solutions are penalized and smooth solutions are favored in the usual way of Tikhonov regularizations. The relations $\gamma_1 \gg \gamma_2, \gamma_3$ for the weight factors guarantee that nonnegativity is a stronger constraint (penalization) whereas a small integral and smoothness of the solutions are weaker constraints (regularizations). For the case of weakly perturbed spectra and if sharp peaks (small integral with low smoothness) are desired, then we use $\gamma_1 = 10, \gamma_2 = 10^{-2}$ and $\gamma_3 = 0$ as typical values for the weight constants. If γ_3 is increased, e.g. $\gamma_3 = 0.1$ together with $\gamma_1 = 10, \gamma_2 = 10^{-2}$, then somewhat wider peaks with a slightly increased smoothness are favored.

The control parameter $\varepsilon_1 \geqslant 0$ in the penalty function g_1 is used in order to weaken the nonnegativity constraint in a way that only negative components which are smaller than $-\varepsilon_1$ contribute to the sum of squares. The control parameter $\varepsilon_2 \geqslant 0$ in g_2 has a similar effect. Only components of d with $|d_j| \geqslant \varepsilon_2$ are taken into consideration for the sum of squares. Thus ε_2 is used to ignore the influence of small entries of the spectrum which are close to zero and which potentially can be traced back to noise or other perturbations. However, even $\varepsilon_1 = \varepsilon_2 = 0$ leads in many cases to useful results. In (1) the functions g_i are applied to normalized spectra $d/\|d\|_{\max}$. Hence ε_1 and ε_2 can be defined in a scaling-independent way. Otherwise, the magnitudes of these control parameters must be adapted to the signal intensity of the spectrum d. If the spectrum includes large perturbations or other systematic biases, then additional functions g_i can be added and further control parameters ε_i can be introduced in order to control or to remove the influence of these perturbations.

For the numerical minimization of f we use a combination of a genetic optimization algorithm with population sizes of 20 with 20 generations and an adaptive nonlinear least-squares solver, namely the ACM routine NL2SOL [8]. Our computationally fast program code is written in C and FORTRAN. An implementation in MATLAB by using the routines fminsearch, a gradient-free simplex minimization algorithm, or lsqnonlin, a nonlinear least-squares solver which uses a subspace trust-region method, is also possible. The optimization-based phase correction, see Section 3, and the baseline correction, see Section 4, result in preprocessed NMR spectra which fulfill to some extent the various constraints depending on the weight factors. The optimization process can implicitly determine further parameters which belong to the optimal solution. Examples are the optimal phase parameters φ_0^* and φ_1^* which are optimized in the phase correction, see Section 3. The correction steps can be applied consecutively, see Sections 3 and 4, or simultaneously, see Section 5.

3. The automated phase correction

This section recapitulates in short form the step of an automated phase correction for the Fourier transformed spectrum. This

phase correction is well-understood, see for example [25,4,7,1]. In Section 5 this correction procedure is a building block of the new simultaneous correction scheme. The phase correction fixes two misadjustments of zero- and of first-order by solving an optimization problem for the objective function f given in (1).

3.1. Misadjustments and automated phase correction

Let $d^{\mathrm{ft}} \in \mathbb{C}^n$ be the Fourier-transformed FID signal. The aim is to correct the misadjustments of zero-order and of first-order [4,6]. The fundamental relationship of d^{ft} to the real and imaginary parts of the phase-corrected spectrum $d^{\mathrm{pha}} \in \mathbb{C}^n$ is $d^{\mathrm{pha}} = (d^{\mathrm{ft}}, e^{i\phi})$ with the Euclidean product $(\cdot,\cdot)$ so that the real and imaginary parts are

$$\begin{aligned} \mathrm{Re}(d_j^{\mathrm{pha}}) &= \mathrm{Re}\left(d_j^{\mathrm{ft}}\right)\cos(\phi_j) - \mathrm{Im}\left(d_j^{\mathrm{ft}}\right)\sin(\phi_j), \\ \mathrm{Im}(d_j^{\mathrm{pha}}) &= \mathrm{Im}\left(d_j^{\mathrm{ft}}\right)\cos(\phi_j) + \mathrm{Re}\left(d_j^{\mathrm{ft}}\right)\sin(\phi_j) \end{aligned} \tag{2}$$

for $j = 1,\ldots,n$, see [25,1]. The vector ϕ depends on the two real-valued adjustment parameters φ_0 and φ_1

$$\phi_j = \varphi_0 + \varphi_1 \frac{j-1}{n}, \quad j = 1,\ldots,n. \tag{3}$$

The optimal phase angle φ_0^* and phase parameter φ_1^* minimize the objective function f by (1) in a way that

$$f\left(\mathrm{Re}\left(d^{\mathrm{pha}}(\varphi_0^*,\varphi_1^*)\right)\right) = \min_{\substack{\varphi_0\in[-\pi,\pi),\\ \varphi_1\in[-n\pi,n\pi)}} f\left(\mathrm{Re}(d^{\mathrm{pha}}(\varphi_0,\varphi_1))\right)$$

and result in the phase corrected spectrum.

3.2. Ambiguity of the phase correction angles

Nonnegativity of the real part $\mathrm{Re}(d^{\mathrm{pha}})$ is not a sufficient constraint for getting unique phase correction parameters φ_0 and φ_1. A formal mathematical argument shows that uniqueness cannot be expected: An ideal NMR spectrum is strictly positive since it is a linear combination with nonnegative coefficients of the (strictly positive) Lorentz profiles [15]. Additionally the relations (2) and (3) are continuous mappings. Thus nonnegativity of $\mathrm{Re}(d^{\mathrm{pha}})$ is guaranteed at least in a small neighborhood of any pair (φ_0,φ_1) which represents a positive function $\mathrm{Re}(d^{\mathrm{pha}})$. This yields a continuum of feasible solutions. Similar regions of feasible solutions with respect to the nonnegativity constraint are well-known from other fields of chemometrics; see e.g. [13,23,14,24] for the area of feasible solutions in multivariate curve resolution. However, the ambiguity of φ_0 and φ_1 is often not very large and uniqueness can be enforced if an additional regularization as by g_2 or g_3 is switched on or if for example an entropy regularization is used [4].

4. The automated baseline correction

The automated baseline correction consists of two steps. In the first step, intervals on the chemical shift axis are detected in which the baseline dominates in the sense that the NMR signals by the chemical sample are of minor importance. In a second step a smooth baseline function on the complete chemical shift axis is fitted to the already identified "pure baseline intervals". The first step is the more difficult one. The correctness of the complete baseline sensitively depends on the correct detection of the pure baseline intervals. In this section we always assume that the NMR spectrum d^{pha} has already undergone (a more or less successful) phase correction. Moreover, we consider while referring to d^{pha} only its real part.

4.1. Detection of pure baseline intervals

In this section we call a chemical shift value (on the abscissa of an NMR spectrum) a *pure-baseline value* if its associated signal intensity cannot be assigned to characteristic NMR signals of the chemical sample. Neighboring pure baseline values can be aggregated to pure baseline intervals. Before running the baseline detection procedure, a Savitzky-Golay filter [22,21] is applied to the NMR spectrum d^{pha}. The Savitzky-Golay filter is well-known to increase the signal-to-noise ratio and to preserve the characteristic form of the signal. The degree of the approximating polynomial is ℓ and the width of the moving window is $2m_1+1$. Thus $2m_1+1$ consecutive components of the vector d^{pha} are filtered by polynomial approximations with the polynomial degree of at most ℓ. If $d^{\mathrm{pha}} \in \mathbb{R}^n$, then the Savitzky-Golay filter computes for each integer number $i = m_1+1, m_1+2, \ldots, n-m_1$ a polynomial p_i of degree ℓ (or less) which approximates the points (of the moving window)

$$(x_j, d_j^{\mathrm{pha}}), \quad j = i-m_1,\ldots,i+m_1,$$

in the least-squares sense. The x_j are the discrete values on the abscissa. The least-squares approximation p_i is evaluated within the moving window and yields the smoothed data $\tilde{d} \in \mathbb{R}^n$ as

$$\tilde{d}_i = p_i(x_i), \quad j = i-m_1,\ldots,i+m_1,$$

and $\tilde{d}_i = d_i$ for all remaining indices which do not belong to the moving window. For the remaining abscissa values x_i with $i \leqslant m_1$ respectively $i \geqslant n-m_1$ the points $(x_j, d_j^{\mathrm{pha}})$ with $j = 1,\ldots,2m_1+1$ respectively $j = n-2m_1,\ldots,n$ are used for computing p_i. The smoothed approximations are given again in the form $\tilde{d}_i = p_i(x_i)$.

The next step is to detect abscissa values of the smoothed signal $\tilde{d}$ whose signal intensities are close to their local mean values. To this end we compute the quantities

$$z_i = \sum_{j=i-m_2}^{i+m_2} \left(\tilde{d}_j - \sum_{j=i-m_2}^{i+m_2} \tilde{d}_j\right)^2. \tag{4}$$

which is the sum of the squares of the deviations of $\tilde{d}_j$ from its mean in a window of the width $2m_2+1$ and where the outer sum runs again through the $2m_2+1$ indices of the window which is centered at x_i. The z_i are computed for the indices $i = m_2+1, m_2+2,\ldots,n-m_2$.

Remark 4.1. Only the components z_i with $i = m_2+1, m_2+2, \ldots, n-m_2$ are defined. We set $z_i = 0$ for $i = 1,\ldots,m_2$ and $i = m_2+1,\ldots,n-m_2$ in order to work (for convenience) only with n-dimensional vectors. The baseline detection procedure only needs the components $z_i, i = m_2+1,\ldots,n-m_2$.

Next the indices are determined for which the (nonnegative) components of z are smaller than a given threshold value. By (4) a component of z vanishes if a consecutive series of components of $\tilde{d}$ in a window with the width $2m_2+1$ satisfy a linear relation. We assume such a linear behavior to occur in pure baseline intervals. The selection criterion is as follows: With the control parameters $\alpha_{\mathrm{crit}} \in (0,1)$ and $\delta_{\mathrm{crit}} > 0$ we define the set of indices which belong to baseline values as

$$M_{\mathrm{bl}} = \{i : z_i/z_{\mathrm{thres}} \leqslant \delta_{\mathrm{crit}}\}.$$

Therein z_{thres} is a threshold value which is computed as follows: First the $n-2m_2$ real numbers $z_{m_2+1},\ldots,z_{n-m_2}$ are sorted in ascending order. Then we take the $\lceil \alpha_{\mathrm{crit}}(n-2m_2)\rceil$th value of this sequence of sorted numbers. Therein $\lceil\cdot\rceil$ denotes the ceiling function which is

the nearest integer to the argument of the ceiling function which is greater than or equal to its argument. In simple words, the set M_{bl} contains all indices which belong to windows of the index-width $2m_2+1$ in which the components behave linearly or nearly linearly.

Appropriate control parameters are $m_1 = 20, m_2 = 40, \alpha_{\text{crit}} = 0.95$ and $\delta_{\text{crit}} = 1.1$ for the case a step-by-step correction of the phase and the baseline. Appropriate values for simultaneous correction steps are $m_1 = 20, m_2 = 40$, $\alpha_{\text{crit}} = 0.5$ and $\delta_{\text{crit}} = 1.1$.

4.2. Baseline computation

The requirements for the baseline are as follows: On the one hand the baseline should be a smooth function and on the other hand the baseline should fit the data d^{pha} for all indices in the set M_{bl}. For experimental and noisy data these requirements can be somewhat contradictory as d^{pha} with respect to M_{bl} may be non-smooth. We use the baseline recognition process suggested in [9,5], which is very similar to the Whittaker smoother [26]. The idea is to consider a baseline u which is given by the vector $u \in \mathbb{R}^n$. Hence the baseline is a continuous function which for each $i = 1, \ldots, n-1$ is given by the linear interpolation of u_i and u_{i+1} on the interval $[x_i, x_{i+1}]$. The aim is that the u_i approximate the given values d_i^{pha} for $i \in M_{\text{bl}}$ and which is as smooth as possible. Then the associated Lagrange function reads

$$L(u,\lambda) = \sum_{i=1}^{n-1} \delta_{i,M_{\text{bl}}} (d_i^{\text{pha}} - u_i)^2 + \lambda \left(\frac{u_{i+1}-u_i}{x_{i+1}-x_i} \right)^2 .$$

Therein $\delta_{i,M_{\text{bl}}}$ is the Kronecker delta and λ the Lagrange multiplier. The first summand is the error of the approximation of d_i^{pha} by u only for indices in M_{bl} and the second summand is a measure for the smoothness of the piecewise linear baseline.

The necessary condition for an extremum of $\nabla_u L = 0$ yields the linear system of equations

$$(M + \lambda B)u = M d^{\text{pha}}. \tag{5}$$

Therein $M \in \mathbb{R}^{n\times n}$ is a diagonal matrix with the diagonal elements

$$M_{ii} = \begin{cases} 1, & \text{if } i \in M_{\text{bl}}, \\ 0, & \text{if } i \notin M_{\text{bl}} \end{cases},$$

and $B \in \mathbb{R}^{n\times n}$ is the tridiagonal matrix

$$B = \begin{pmatrix} 1 & -1 & & & \\ -1 & 2 & -1 & & \\ & \ddots & \ddots & \ddots & \\ & & -1 & 2 & -1 \\ & & & -1 & 1 \end{pmatrix}.$$

Remark 4.2. The system of linear Eqs. (5) is symmetric and trilinear. It can be solved by a direct solver with low costs which increase only linearly in the dimension n.

Having found the baseline u, we compute the baseline corrected spectrum d^{final} by a subtraction of the baseline $d^{\text{final}} = d^{\text{pha}} - u$. The choice of the Lagrange multiplier is still a degree of freedom; $\lambda = 1000$ is a reasonable choice.

4.3. Incompleteness of M_{bl}

An appropriate construction of the set M_{bl} is decisive for a successful baseline identification. It is no problem if single or even several indexes of pure-baseline regions are not included in M_{bl} as the baseline construction algorithm uses a linear interpolation over these missing points. The other case, namely that indices belong to M_{bl} which are associated with the true NMR signals of the chemical components, is very annoying. Then the baseline contains parts of the spectrum and the baseline subtraction distorts the spectrum. Therefore our index selection algorithm works in a defensive manner. Only those indexes are added to M_{bl} which belong to pure baseline regions of the spectrum.

4.4. Simplicity of the phase and baseline correction

The various steps of the phase and the baseline corrections might appear to be technical. However, all computational steps are very simple, can easily be programmed and require low computation times. The algorithm should be as robust, stable and general as possible and should work especially for experimental NMR spectra. The method in [4] is a prominent example of a simple and stable method.

4.5. The problem of data-overfitting

Ideally NMR spectra can be assumed to consist of finite sums of Lorentz profiles [15]. Lorentz profiles decay much more slowly than Gauss profiles. These facts seem to contradict our approach for the baseline detection. It identifies regions in which signal contributions from the chemical sample are ignored. In these regions the baseline subtraction forces the spectrum to zero whereas Lorentzians are always nonzero. Thus our baseline approach can lead to small inconsistencies for simulated NMR spectra, if a global or interval-wise integration of the spectrum is applied and if these integrals are compared with the integrals of the preprocessed data. However, we cannot confirm comparable small inconsistencies of experimental NMR spectra, see the results in Section 6 on the ratios of integrals of different peaks which represent concentration data on some of the chemical components.

4.6. Algorithmic variations

The suggested approach for the baseline correction opens a variety of possibilities for improvements. Other strategies for the detection of M_{bl} and for the baseline regularization can be used. Further, the baseline detection can use a wavelet-based smoothing instead of the Savitzky-Golay filtering. See also [5,29,28].

5. Simultaneous automated phase and baseline correction

This section explains how the automated phase correction, see Section 3, and the automated baseline correction, see Section 4, can be integrated into a simultaneous optimization procedure. Such a simultaneous optimization, which is also called a multi-objective optimization or Pareto-optimization, is well known to produce better solutions of optimization problems with competing or even conflicting objective functions [20]. The key observation is that the optimal solution with respect to one constraint is usually not optimal with respect to the other constraints and vice versa. Therefore, the optimal solution of the multi-objective optimization represents a trade-off between the conflicting constraints. We call our program code SINC, which stands for **si**multaneous **N**MR (signal) **c**orrection.

5.1. Idea of the approach

For the simultaneous optimization we use again the objective function f of Eq. (1). In contrast to applying consecutive preprocessing steps, now the spectrum is evaluated by a minimization

of f not until the baseline correction is applied. The optimization with respect to the variables φ_0 and φ_1 includes baseline corrections as internal computations. We fix the index set M_{bl}, which specifies the pure baseline regions of the spectrum, by means of an initial baseline step. There is no benefit to re-compute M_{bl} in each cycle of the simultaneous optimization as its changes are expected to be marginal, but may cause instabilities.

5.2. The algorithm of SINC

The algorithm of the simultaneous phase and baseline correction (SINC) starts with a given Fourier transformed FID signal $d^{\mathrm{ft}} \in \mathbb{C}^n$ and reads:

1. An initial phase correction is applied to d according to Section 3. The result is denoted by d^{pha}.
2. The set of baseline indices M_{bl} is computed for d^{pha}.
3. The simultaneous optimization for the parameters φ_0 and φ_1 is started by minimizing the objective function $f(\varphi_0, \varphi_1)$:

   (a) Compute the phase corrected spectrum $d^{\mathrm{pha}} = \mathrm{Re}(\varphi_0, \varphi_1)$.
   (b) Compute the baseline u for d^{pha} with respect to the fixed index set M_{bl}.
   (c) Evaluate the objective value $f(d^{\mathrm{pha}} - u)$.

Remark 5.1. The functions g_i in (1) are applied to normalized spectra $d/\|d\|_{\max}$. Further, the automatic detection of the baseline intervals is independent of the normalization of d^{pha}. The resulting baseline correction step is homogeneous of order 1 with respect to the input data. Thus the resulting algorithm of the automated and simultaneous phase and baseline correction is independent of the signal scaling. Thus the weighting parameters γ_i in (1) do not have to be scaled with a changing amplitude of the data.

5.3. Impact and selection of the control parameters

The SINC algorithm works with various control parameters. In the objective function (1) the Lagrange multipliers γ_1, γ_2 and γ_3 determine the relative weighting of the constraint functions. Most important is the nonnegativity of the data so that γ_1 has to be larger than γ_2, γ_3. Reasonable values are given in Section 2. The parameter ε_1 in g_1 is the acceptance level for relative negative entries. For medium up to large noise levels a maximal value of $\varepsilon_1 = 0.05$ is suggested in order to allow for larger negative (noise-) entries. A similar parametrization is suggested for ε_2, which controls noisy or shifted baselines in the regularization function g_2.

The baseline detection is a crucial part of the SINC method. The degree of the polynomial used by the Savitzky-Golay filter should be small, e. g. $\ell \in \{1, 3\}$. The band-width parameter m_1 depends mainly on the number n of channels but also on the width of the peaks. Typical values $m_1 \in \{10, \ldots, 30\}$ are suggested if n is large. For small n we use $m_1 \leq 10$. The value m_2 controls the band width for the comparison process in order to decide whether or not a channel belongs to a pure baseline interval. A typical choice for m_2 is $m_2 = 2m_1$. Further decisive parameters for the detection of pure baseline intervals are α_{crit} and δ_{crit}. If α_{crit} is large, then more channels are considered for the baseline correction. If $\alpha_{\mathrm{crit}} = 1$, then all channels are declared as pure baseline intervals which is not acceptable. The other extreme is $\alpha_{\mathrm{crit}} = 0$ which means that no baseline correction can be applied. For data including low up to medium noise levels we use $\alpha_{\mathrm{crit}} \in \{0.3, 0.95\}$. For a higher noise level we suggest $\alpha_{\mathrm{crit}} \leq 0.7$. The parameter δ_{crit} is closely linked to α_{crit}. A large value of δ_{crit} increases the length of pure baseline intervals. For data including a low or a medium noise level we use $\delta_{\mathrm{crit}} \in \{1.0, 2.0\}$. For a higher noise level we suggest $\delta_{\mathrm{crit}} \leq 1.25$.

The actual correction of the baseline is controlled by the Lagrange multiplier λ. If the pure baseline intervals are determined properly, then we use $\lambda \in [10^{-2}, 10^{6}]$ and observe only a minor impact of the choice of λ on the computational results.

6. Numerical results for experimental NMR spectra

Next the new method is tested for experimental NMR spectra. We compare the results of the new simultaneous preprocessing not only with the results of consecutive phase and baseline corrections, but also with an exclusive phase correction. We also compare the results with the entropy minimization approach [4] and the two-stages-tuning as introduced in [1]. The program codes of these two methods are combined with the adaptive iteratively re-weighted penalized least squares approach from [9,11]. We have applied these methods with and also without their baseline correction algorithms. Additonally we have applied the software package Mnova by Mestrelab.

6.1. Experimental NMR spectra

The ^{1}H NMR spectra of the first two sample mixtures are taken with a medium field NMR spectrometer (Spinsolve Carbon, Magritek, Wellington/New Zealand) using a 1 Tesla permanent magnet so that the proton Larmor frequency equals 42.5 MHz. The spectra are taken with a flip angle of 90°, a repetition time of 30 s, a number of 32 scans and an acquisition time of 6.4 s. The Fourier transformed FID contains a number of $n = 65,536$ data points. The ^{13}C spectrum for sample mixture 3 is taken with a Bruker Ascend 400 MHz (console Avance 3 HD 400, probe CyroProbe Prodigy, Bruker Biospin, Rheinstetten/Germany) NMR spectrometer using a 9.4 Tesla vertical superconducting magnet with a proton Larmor frequency of 400.25 MHz. The spectrum is taken with a ^{13}C inverse gated pulse sequence, a flip angle of 60°, a relaxation delay of 100 s, a number of 512 scans, and an acquisition time of 1.36 s.

Sample mixture 1. The ^{1}H NMR spectrum is taken from a sample containing 0.66 g of 2-propanol (Sigma-Aldrich, anhydrous, $\geqslant$ 99.5 mass%) and 0.266 g of toluene (Merck, Uvasol, $\geqslant$ 99.9 mass%). The resulting mole fractions of 2-propanol (PrOH) and toluene (Tol) in the mixture are: $x_{\mathrm{PrOH}} = 0.7918 \pm 0.0007$ mol/mol and $x_{\mathrm{Tol}} = 0.2082 \pm 0.0007$ mol/mol, respectively. The real and the imaginary parts of the Fourier transformed spectrum are presented in the left subplot of Fig. 1.

Sample mixture 2. The ^{1}H NMR spectrum is taken from a sample containing 0.594 g of ethyl acetate (Sigma-Aldrich, $\geqslant$ 99.5 mass%) and 0.428 g of toluene (Merck, Uvasol, $\geqslant$ 99.9 mass%). The resulting mole fractions of ethyl acetate (EtAc) and toluene in the mixture are $\widetilde{x}_{\mathrm{EtAc}} = 0.5921 \pm 0.0008$ mol/mol and $\widetilde{x}_{\mathrm{Tol}} = 0.4079 \pm 0.0008$ mol/mol, respectively. The real and the imaginary parts of the Fourier transformed spectrum are shown in the right subplot of Fig. 1.

Sample mixture 3. The ^{13}C NMR spectrum is taken from a sample containing 0.09040 ± 0.0001 mol/mol of N-Methyldiethanolamine (Sigma-Aldrich, $\geqslant$ 99 mass%), 0.0099 ± 0.0001 mol/mol of sodium carbonate (Th. Geyer, $\geqslant$ 99.8 mass%), 15.0083 g of water (deionized and purified with a water purification system (Milli-Q Refer-

ence A+ System, Merck Millipore, Billerica/US-MA)). Sodium carbonate was dried for 12 h at 120 °C before using and all other chemicals were used without further purification. For details on the sample see [2].

The uncertainties of all mole fractions of the components in the two sample mixtures are estimated from the given accuracy of the laboratory balance and the uncertainties of the purities of the samples.

6.2. Application of the phase and baseline corrections

The NMR spectra for the two mixtures as described in the sample mixture 1 and 2 are subjected to three different preprocessing methods. The control parameters for these computations, namely the weight factors γ_i and the truncation parameters ε_i, are already given in Section 2. The preprocessed NMR spectra are plotted in Figs. 2 and 3. The blue spectrum results from an application of only the phase correction to either the NMR spectrum of the 2-propanol mixture with toluene, see Fig. 2, or to the NMR spectrum of the ethyl acetate mixture with toluene, see Fig. 3. Especially for the largest peaks some positive dispersion is still present. The green spectra in these two figures represent the results of a consecutive application of the phase and baseline correction steps. The new simultaneous phase and baseline correction algorithm yields in Fig. 2 and in Fig. 3 the red spectrum. The Pareto optimal solution of the simultaneous correction is always the best correction.

Fig. 4 shows the pure baseline regions in blue color along the complete chemical shift axis for the two sample mixtures. As explained in Section 4.3 it is of crucial importance that the index sets are not too large. It is much better to omit some data points of pure baseline regions (which are then filled by linear interpolation) than to assign data points at peak flanks incorrectly to the baseline. This would result in significant distortions of the spectrum, see Section 4.4.

Fig. 5 shows a comparison of the four preprocessing methods for sample mixture 3. These methods are the simultaneous phase and baseline correction (SINC), the entropy minimization approach

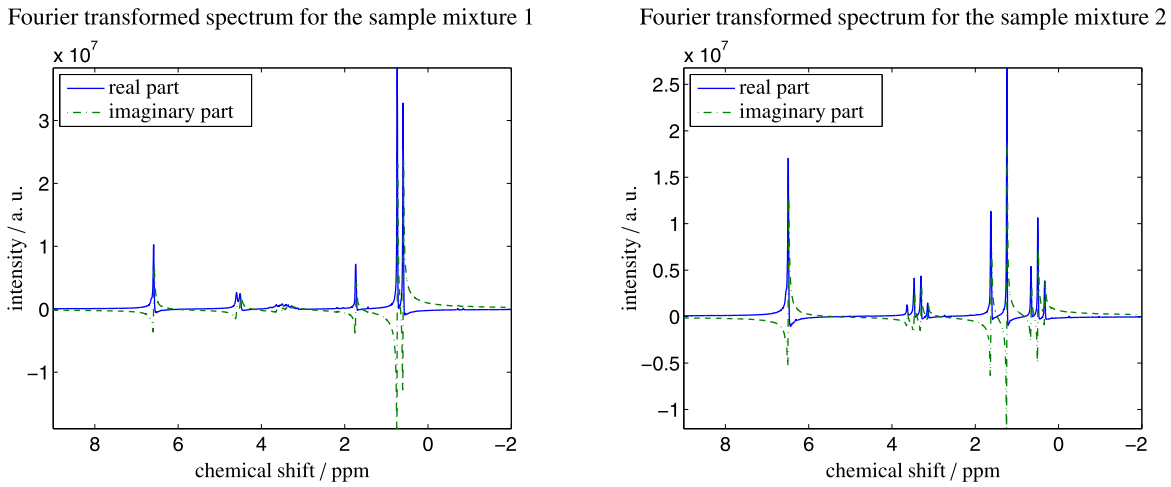

Fig. 1. The Fourier transformed ^{1}H-spectra for the two chemical sample mixtures 1 and 2, see Section 6.1, prior to any phase and baseline corrections. The spectra are plotted only for the relevant ppm-intervals.

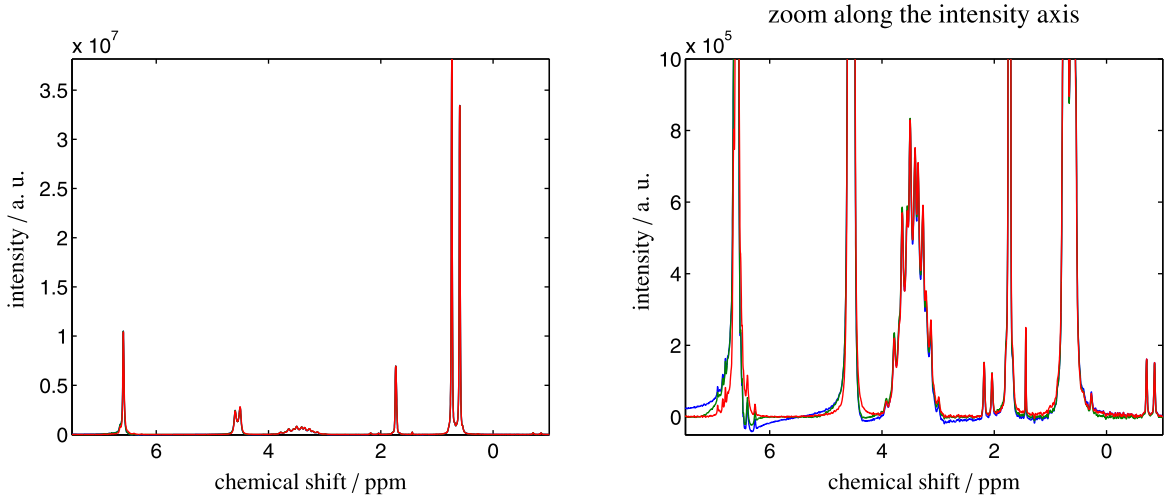

Fig. 2. NMR spectra for the binary mixture of 2-propanol and toluene, see the sample mixture 1, after application of three forms of data preprocessing. Left: the NMR spectrum on the relevant 7–(-1) ppm range. Right: zoom along the ordinate-direction. The blue spectrum results from exclusive application of the phase correction, and the green spectrum is the outcome of a consecutive application of the phase and baseline correction steps. The new simultaneous phase and baseline correction algorithm yields the red spectrum. Obviously the best spectrum results from the simultaneous correction algorithm. (For interpretation of the references to colour in this figure legend, the reader is referred to the web version of this article.)

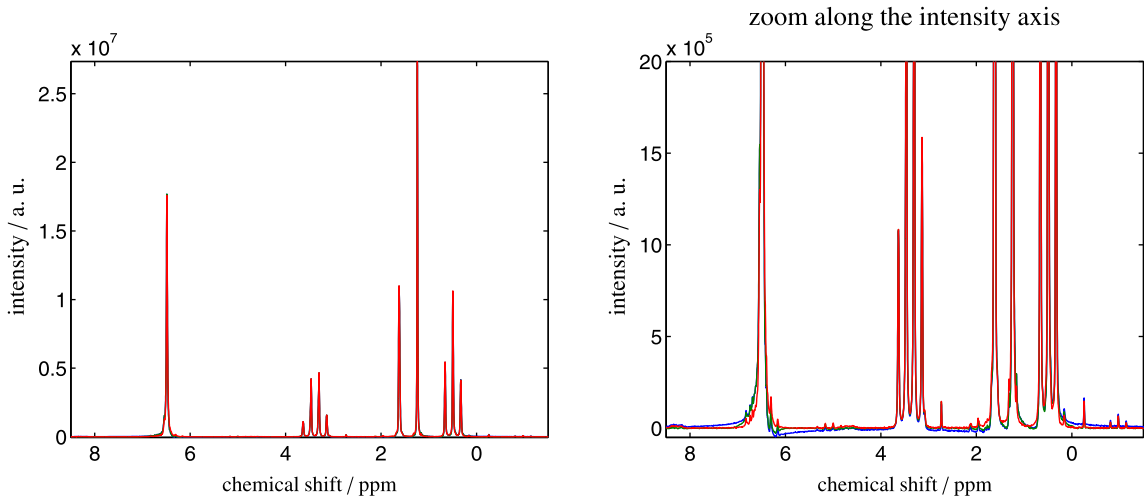

Fig. 3. NMR spectra for the ethyl acetate mixture with toluene, see the sample mixture 2, after application of three forms of data preprocessing. Left: the NMR spectrum on the relevant 8.5–(-1.5) ppm range. Right: zoom along the ordinate-direction. The blue spectrum results from exclusive application of the phase correction, and the green spectrum is the outcome of a consecutive application of the phase and baseline correction steps. The new simultaneous phase and baseline correction algorithm yields the red spectrum. As in Fig. 2 the best results are obtained by the simultaneous correction algorithm. (For interpretation of the references to colour in this figure legend, the reader is referred to the web version of this article.)

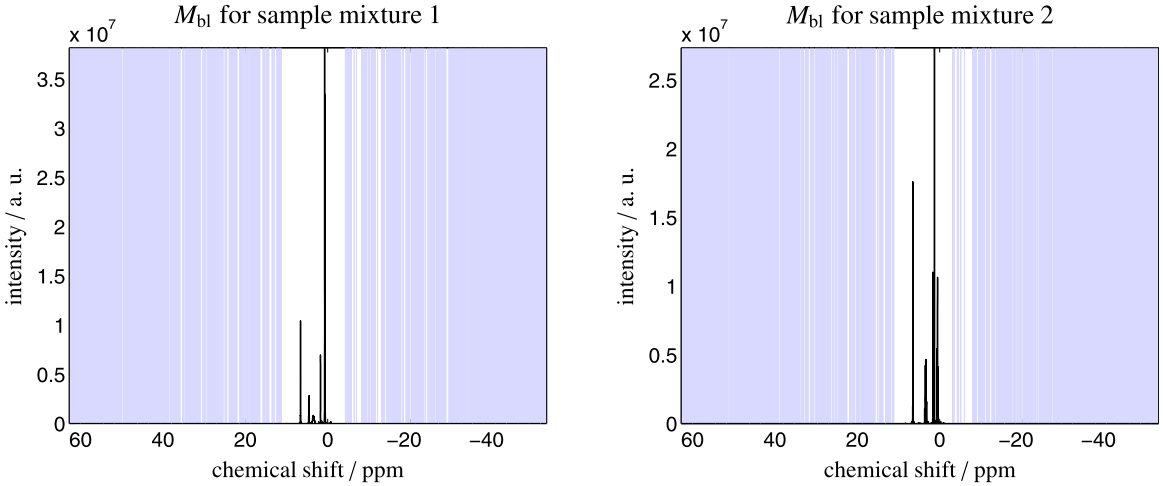

Fig. 4. The automatically detected pure baseline intervals are colored blue (along the ordinate) for the two sample mixtures 1 and 2. (For interpretation of the references to colour in this figure legend, the reader is referred to the web version of this article.)

[4] including a simple baseline correction and the two-stages tuning [1] including a simple baseline correction. We also corrected the spectrum with standard algorithms provided in the software package Mnova (Mestrelab, Santiago de Compostela, Spain). For brevity, this method will be called Mnova in the following. In Mnova we applied for the phase correction the automatic consecutive algorithms "Global", "Minimum Entropy", "Selective", "Baseline Optimization", "Metabonomics", "Region Analysis", and "Whitening". We also used the settings "Filter: Autodetect" and "Smooth Factor: Autodetect" for the consecutive baseline correction. The results gained by SINC and Mnova are almost identical. A detail enlargement of the peak close to 167.9 ppm shows small deviations of the results of these two methods compared to entropy minimization and two-stages tuning.

Remark 6.1. The SINC method, the entropy minimization approach and also the two-stages-tuning method use the Fourier transformed FID signal as the data input for the their respective preprocessing steps. In contrast to this, the highly elaborated and powerful Mnova software typically takes the raw FID signal as input and additionally applies FID preprocessing steps as drift correction, apodization, zero filling, linear prediction and further steps. For the purpose of comparison we imported the Fourier transformed FID signal to Mnova and applied its preprocessing steps. We are aware that this does not capitalize the full strength of data preprocessing implemented in Mnova.

6.3. Verification of the results

The gravimetric values on the portions of NMR-resonant hydrogen nuclei in the sample mixtures 1 and 2 are used in order to verify the results of the new method, cf. [18]. To this end we have to know which peaks belong to which of the two chemical compounds in the respective mixture. Then the integrals for the single peaks as well as their relations are computed. Finally the deviations to the expected gravimetric values are calculated. These integral calculations are also executed for the spectra which result

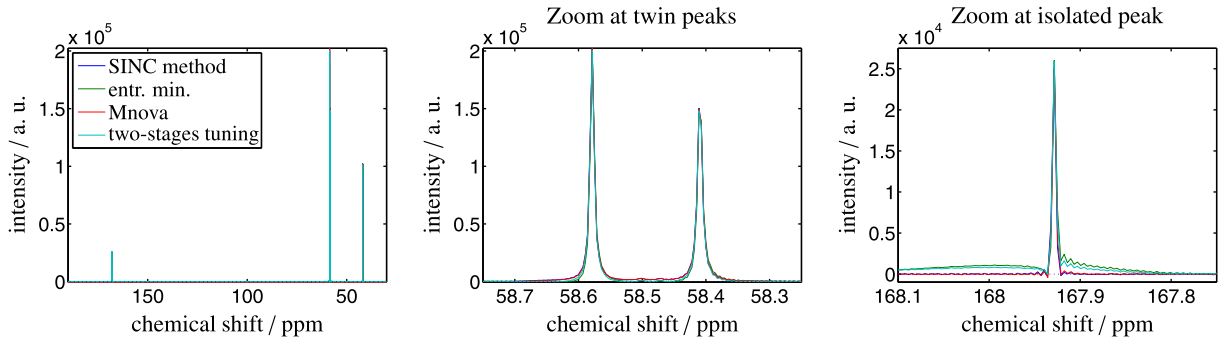

Fig. 5. The four preprocessing methods are compared for the sample mixture 3. The color code is as follows: the new SINC-method (blue), the entropy minimization approach [4] including a simple baseline correction (green), the two-stages-tuning method [1] including a simple baseline correction (cyan) and Mnova (red). Mnova is directly applied to the Fourier transformed FID signal, see Remark 6.1. SINC and Mnova yield nearly the same results, whereas the other two methods show small deviations especially for the peak close to 167.9 ppm. (For interpretation of the references to colour in this figure legend, the reader is referred to the web version of this article.)

from an exclusive application of the phase correction and also for the spectra which result from a consecutive application of the phase and baseline correction steps. Additionally, we apply this comparative gravimetric analysis to the spectra which are attained by the entropy minimization approach [4], the two-stages-tuning method [1] and Mnova.

The gravimetric analysis is first applied to the sample mixture 1. We consider only the peaks or peak group which are centered at 0.66, 1.7, 3.5, 4.6 and 6.6 ppm. The second and the fifth peak group belong to toluene and the remaining ones belong to 2-propanol. The numbers of the associated protons are $p = [6, 3, 1, 1, 5]$. The following chemical shift intervals are used for the integration:

$$\mu_1 = [0.3, 0.9]\ \text{ppm}, \quad \mu_2 = [1.5, 1.9]\ \text{ppm},$$
$$\mu_3 = [2.8, 4.0]\ \text{ppm}, \quad \mu_4 = [4.2, 5.0]\ \text{ppm}, \quad \mu_5 = [6.0, 7.1]\ \text{ppm}.$$

For the sample mixture 1 we consider six verification values $\delta_i = x_i^{\text{NMR}} - x_{\text{Tol}}$ for $i = 1, \ldots, 6$. The index i represents the different combinations of peak areas A_j that can be applied to calculate the mole fraction x_i^{NMR}. The index j runs through the five chemical shift intervals. We calculate the following combinations of the mole fraction of toluene:

$$x_1^{\text{NMR}} = A_2/(A_1 + A_2), \quad x_2^{\text{NMR}} = A_2/(A_3 + A_2), \quad x_3^{\text{NMR}} = A_2/(A_4 + A_2),$$
$$x_4^{\text{NMR}} = A_5/(A_1 + A_5), \quad x_5^{\text{NMR}} = A_5/(A_3 + A_5), \quad x_6^{\text{NMR}} = A_5/(A_4 + A_5).$$

Therein the A_j are $A_j = I(d^{\text{final}}(\mu_j))/p_j,\ i = j, \ldots, 5$, where $I(d^{\text{final}}(\mu_i))$ is a numerical approximation of the peak area in spectrum d^{final} on the integration interval μ_i which is divided by the number of the associated protons p_i.

The gravimetric analysis is also applied to the sample mixture 2 with the six verification values $\widetilde{\delta}_i = \widetilde{x}_i^{\text{NMR}} - \widetilde{x}_{\text{Tol}}$. For this example the selected peak groups are contained in the chemical shift intervals

$$\widetilde{\mu}_1 = [0.2, 0.8]\ \text{ppm}, \quad \widetilde{\mu}_2 = [0.9, 1.4]\ \text{ppm},$$
$$\widetilde{\mu}_3 = [1.5, 1.8]\ \text{ppm}, \quad \widetilde{\mu}_4 = [3.0, 3.8]\ \text{ppm}, \quad \widetilde{\mu}_5 = [6.0, 7.0]\ \text{ppm}.$$

The associated numbers of protons for these five peak groups are $p = [3, 3, 3, 2, 5]$. The peaks in the intervals $\widetilde{\mu}_1, \widetilde{\mu}_2$ and $\widetilde{\mu}_4$ belong to ethyl acetate, and the peaks in $\widetilde{\mu}_3$ and $\widetilde{\mu}_5$ belong to toluene. The $\widetilde{x}_i^{\text{NMR}}$ for this mixture are as follows:

$$\widetilde{x}_1^{\text{NMR}} = A_3/(A_1 + A_3) \quad \widetilde{x}_2^{\text{NMR}} = A_3/(A_2 + A_3), \quad \widetilde{x}_3^{\text{NMR}} = A_3/(A_4 + A_3),$$
$$\widetilde{x}_4^{\text{NMR}} = A_5/(A_1 + A_5), \quad \widetilde{x}_5^{\text{NMR}} = A_5/(A_2 + A_5), \quad \widetilde{x}_6^{\text{NMR}} = A_5/(A_4 + A_5).$$

Remark 6.2. Some entries of the preprocessed spectra can be negative especially if only a phase correction is applied, see e.g. the blue spectra in Figs. 2 and 3. All negative entries are set to zero prior to the numerical integration process in order to avoid major errors - but there is no necessity for this cut-off of negative entries.

Table 1 lists the verification values for the sample mixture 1 for eight different preprocessing techniques. The analogous values for the sample mixture 2 are given in Table 2. Fig. 6 is a semi-logarithmic plot of all these verification values. The final conclusion is:

1. The phase correction approach as used here is very similar to the one presented in [4] on the basis of an entropy minimization (see the columns 1 and 4 in Tables 1 and 2).

Table 1
The table lists the verification values δ_i, $i = 1, \ldots, 6$, which are the deviations from the numerical integration approximations from the gravimetric value 0.2082 mol/mol. Eight different preprocessing techniques are considered. The new simultaneous multi-objective optimization in the fourth column gains in most instances the smallest error. The last row contains the mean values of the absolute verification values. Mnova is directly applied to the Fourier transformed FID signal, cf. Remark 6.1.

Verif. value	New method (multi-objective opt.)			Min. entropy approach [4]		Two-stages-tuning [1]		Mnova
	No baseline corr.	Consec. opt.	Simult. opt.	No baseline	Sep. baseline	No baseline	Sep. baseline	Incl. baseline
δ_1	$1.3 \cdot 10^{-3}$	$3.4 \cdot 10^{-3}$	$4.0 \cdot 10^{-3}$	$1.3 \cdot 10^{-3}$	$6.4 \cdot 10^{-3}$	$-1.9 \cdot 10^{-3}$	$7.3 \cdot 10^{-3}$	$-1.2 \cdot 10^{-3}$
δ_2	$5.0 \cdot 10^{-3}$	$-8.6 \cdot 10^{-4}$	$3.3 \cdot 10^{-4}$	$5.0 \cdot 10^{-3}$	$5.4 \cdot 10^{-3}$	$8.4 \cdot 10^{-3}$	$8.7 \cdot 10^{-3}$	$7.0 \cdot 10^{-3}$
δ_3	$-2.6 \cdot 10^{-3}$	$-1.6 \cdot 10^{-3}$	$2.7 \cdot 10^{-4}$	$-2.6 \cdot 10^{-3}$	$1.1 \cdot 10^{-3}$	$5.6 \cdot 10^{-3}$	$5.3 \cdot 10^{-3}$	$-2.0 \cdot 10^{-3}$
δ_4	$5.4 \cdot 10^{-3}$	$7.3 \cdot 10^{-3}$	$4.1 \cdot 10^{-3}$	$5.4 \cdot 10^{-3}$	$1.2 \cdot 10^{-2}$	$-8.2 \cdot 10^{-3}$	$2.2 \cdot 10^{-3}$	$2.2 \cdot 10^{-3}$
δ_5	$9.2 \cdot 10^{-3}$	$3.0 \cdot 10^{-3}$	$3.8 \cdot 10^{-4}$	$9.2 \cdot 10^{-3}$	$1.1 \cdot 10^{-2}$	$1.9 \cdot 10^{-3}$	$3.6 \cdot 10^{-3}$	$1.1 \cdot 10^{-2}$
δ_6	$1.4 \cdot 10^{-3}$	$2.2 \cdot 10^{-3}$	$3.2 \cdot 10^{-4}$	$1.4 \cdot 10^{-3}$	$7.0 \cdot 10^{-3}$	$-8.4 \cdot 10^{-4}$	$2.0 \cdot 10^{-4}$	$1.3 \cdot 10^{-3}$
$\frac{1}{6}\sum\lvert\delta_i\rvert$	$4.18 \cdot 10^{-3}$	$3.05 \cdot 10^{-3}$	$1.57 \cdot 10^{-3}$	$4.18 \cdot 10^{-3}$	$7.28 \cdot 10^{-3}$	$4.48 \cdot 10^{-3}$	$4.55 \cdot 10^{-3}$	$4.05 \cdot 10^{-3}$

Table 2
The table lists the verification values $\widetilde{\delta}_i$, $i = 1, \ldots, 6$, which are the deviations from the numerical integration approximations from the gravimetric value 0.4079 mol/mol. Eight different preprocessing techniques are considered. The new simultaneous multi-objective optimization in the fourth column gains in most instances the smallest error. The last row contains the mean values of the absolute verification values. Mnova is directly applied to the Fourier transformed FID signal, cf. Remark 6.1.

Verif. value	New method (multi-objective opt.)			Min. entropy approach [4]		Two-stages-tuning [1]		Mnova
	No baseline corr.	Consec. opt.	Simult. opt.	No baseline	Sep. baseline	No baseline	Sep. baseline	Incl. baseline
$\widetilde{\delta}_1$	$-7.9 \cdot 10^{-3}$	$-3.9 \cdot 10^{-3}$	$1.2 \cdot 10^{-4}$	$-7.9 \cdot 10^{-3}$	$-2.0 \cdot 10^{-3}$	$-2.0 \cdot 10^{-2}$	$-1.1 \cdot 10^{-2}$	$-7.4 \cdot 10^{-3}$
$\widetilde{\delta}_2$	$-5.5 \cdot 10^{-3}$	$-4.1 \cdot 10^{-3}$	$1.6 \cdot 10^{-4}$	$-5.6 \cdot 10^{-3}$	$-3.4 \cdot 10^{-3}$	$-1.2 \cdot 10^{-2}$	$-1.4 \cdot 10^{-2}$	$-4.0 \cdot 10^{-3}$
$\widetilde{\delta}_3$	$-7.9 \cdot 10^{-4}$	$-3.4 \cdot 10^{-3}$	$-1.1 \cdot 10^{-3}$	$-8.0 \cdot 10^{-4}$	$-2.5 \cdot 10^{-4}$	$-1.3 \cdot 10^{-2}$	$-2.4 \cdot 10^{-3}$	$5.0 \cdot 10^{-3}$
$\widetilde{\delta}_4$	$-3.0 \cdot 10^{-3}$	$1.9 \cdot 10^{-3}$	$4.1 \cdot 10^{-4}$	$-3.0 \cdot 10^{-3}$	$5.8 \cdot 10^{-3}$	$-9.3 \cdot 10^{-3}$	$1.0 \cdot 10^{-1}$	$-9.9 \cdot 10^{-3}$
$\widetilde{\delta}_5$	$-6.3 \cdot 10^{-4}$	$1.7 \cdot 10^{-3}$	$4.5 \cdot 10^{-4}$	$-6.5 \cdot 10^{-4}$	$4.4 \cdot 10^{-3}$	$-1.2 \cdot 10^{-3}$	$1.0 \cdot 10^{-1}$	$-6.5 \cdot 10^{-3}$
$\widetilde{\delta}_6$	$4.1 \cdot 10^{-3}$	$2.4 \cdot 10^{-3}$	$-8.0 \cdot 10^{-4}$	$4.1 \cdot 10^{-3}$	$7.6 \cdot 10^{-3}$	$-1.8 \cdot 10^{-3}$	$1.1 \cdot 10^{-1}$	$2.4 \cdot 10^{-3}$
$\frac{1}{6}\sum\lvert\widetilde{\delta}_i\rvert$	$3.66 \cdot 10^{-3}$	$2.90 \cdot 10^{-3}$	$5.03 \cdot 10^{-4}$	$3.68 \cdot 10^{-3}$	$3.92 \cdot 10^{-3}$	$9.70 \cdot 10^{-3}$	$5.78 \cdot 10^{-2}$	$5.87 \cdot 10^{-3}$

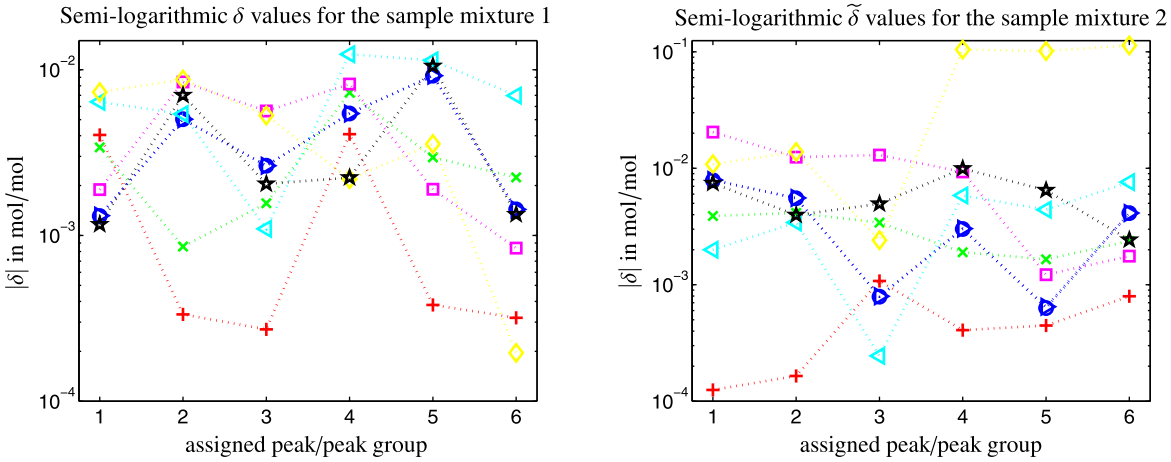

Fig. 6. The deviations δ_i from the gravimetric values 0.2082 mol/mol and the deviations $\widetilde{\delta}_i$ from 0.4079 mol/mol for the eight different preprocessing methods. The numerical values are listed in Tables 1 and 2. The color code is as follows: (○) for the new method but only with a phase correction, (×) for consecutive phase and baseline corrections by the new method, and (+) for the simultaneous phase correction by the multi-objective optimization. Further, (▷) represent only the phase correction by minimum entropy approach, (◁) for the minimum entropy approach with a separate baseline correction step, (□) for only the phase correction by the two-stages-tuning approach, (◇) for the two-stages-tuning approach with a separate baseline correction step and (☆) for the phase and baseline correction by Mnova. Mnova is directly applied to the Fourier transformed FID signal, cf. Remark 6.1. (For interpretation of the references to colour in this figure legend, the reader is referred to the web version of this article.)

2. The simultaneous phase and baseline correction by multi-objective optimization produces the best results for the given experimental NMR spectra. The separate baseline correction step improves in all cases the results for previous phase correction steps. The smallest deviations in the gravimetric analysis are observed for the simultaneous correction scheme.

7. Conclusion

Competing or even conflicting objectives arise in many optimization problems. In most cases such optimization problems cannot successfully be solved by optimizing each objectives in a step-by-step manner as no single solution can be found which simultaneously optimizes all constraints. Instead, a trade-off is needed between the objectives. The new algorithm for the phase and baseline correction of NMR spectra demonstrates how the multi-objective optimization methodology improves the data preprocessing for NMR data. A characteristic trait of the suggested algorithm is that the detection of pure baseline regions is done only in an initial phase.

The new method is tested for two NMR spectra and shows clear improvements compared to a consecutive optimization. In a following paper we plan to present an extensive and systematic comparison for various data sets. Further algorithmic variations, e.g. the use of wavelets for the detection of the pure baseline regions, are possible and the topic of future research.

Acknowledgment

We thank Dan Holland and Yevgen Matviychuk from the University of Canterbury in New Zealand for fruitful discussions. E. von Harbou and K. Neymeyr acknowledge the financial support of the present study by the Deutsche Forschungsgemeinschaft DFG. The project number of von Harbou is HA 7582/1-1.

References

[1] Q. Bao, J. Feng, L. Chen, F. Chen, Z. Liu, B. Jiang, C. Liu, A robust automatic phase correction method for signal dense spectra, J. Magn. Reson. 234 (2013) 82–89.
[2] R. Behrens, E. von Harbou, W.R. Thiel, W. Böttinger, T. Ingram, G. Sieder, H. Hasse, Monoalkylcarbonate formation in methyldiethanolamine–H_2O–CO_2, Ind. Eng. Chem. Res. 56 (31) (2017) 9006–9015.
[3] A. Brächer, R. Behrens, E. von Harbou, H. Hasse, Application of a new micro-reactor ^{1}H NMR probe head for quantitative analysis of fast esterification reactions, Chem. Eng. J. 306 (2016) 413–421.
[4] L. Chen, Z. Weng, L. Goh, M. Garland, An efficient algorithm for automatic phase correction of NMR spectra based on entropy minimization, J. Magn. Reson. 158 (2002) 164–168.
[5] J.C. Cobas, M.A. Bernstein, M. Martín-Pastor, P.G. Tahoces, A new general-purpose fully automatic baseline-correction procedure for 1D and 2D NMR data, J. Magn. Reson. 183 (1) (2006) 145–151.

[6] E.C. Craig, A.G. Marshall, Automated phase correction of FT NMR spectra by means of phase measurement based on dispersion versus absorption relation (DISPA), J. Magn. Reson. 76 (3) (1988) 458–475.
[7] H. de Brouwer, Evaluation of algorithms for automated phase correction of NMR spectra, J. Magn. Reson. 201 (2) (2009) 230–238.
[8] J. Dennis, D. Gay, R. Welsch, An adaptive nonlinear least-squares algorithm, ACM Trans. Math. Softw. 7 (1981) 348–368.
[9] P.H.C. Eilers, A perfect smoother, Anal. Chem. 75 (14) (2003) 3631–3636.
[10] R.R. Ernst, Nuclear magnetic resonance Fourier transform spectroscopy (nobel lecture), Angew. Chem. Int. Ed. Engl. 31 (7) (1992) 805–823.
[11] F. Gan, G. Ruan, J. Mo, Baseline correction by improved iterative polynomial fitting with automatic threshold, Chemom. Intell. Lab. Syst. 82 (2006) 59–65.
[12] S. Golotvin, A. Williams, Improved baseline recognition and modeling of FT NMR spectra, J. Magn. Reson. 146 (1) (2000) 122–125.
[13] A. Golshan, H. Abdollahi, M. Maeder, Resolution of rotational ambiguity for three-component systems, Anal. Chem. 83 (3) (2011) 836–841.
[14] A. Jürß, M. Sawall, K. Neymeyr, On generalized Borgen plots. I: From convex to affine combinations and applications to spectral data, J. Chemom. 29 (7) (2015) 420–433.
[15] J. Keeler, Understanding NMR Spectroscopy, John Wiley, 2010
[16] S.K. Küster, E. Danieli, B. Blümich, F. Casanova, High-resolution NMR spectroscopy under the fume hood, Phys. Chem. Chem. Phys. 13 (29) (2011) 13172–13176.
[17] P.C. Lauterbur, All science is interdisciplinary – from magnetic moments to molecules to men, Biosci. Rep. 24 (3) (2004) 165–178.
[18] F. Malz, H. Jancke, Validation of quantitative NMR, J. Pharm. Biomed. Anal. 38 (5) (2005) 813–823 (Quantitative NMR Spectroscopy).
[19] K. Meyer, S. Kern, N. Zientek, G. Guthausen, M. Maiwald, Process control with compact NMR, TrAC, Trends Anal. Chem. 83 (2016) 39–52.
[20] P.M. Pardalos, A. Zilinskas, J. Zilinskas, Non-convex Multi-objective Optimization, Springer International Publishing, New York, 2017.
[21] W.H. Press, et al., Numerical Recipes, The Art of Scientific Computing, third ed., Cambridge University Press, 2007.
[22] A. Savitzky, M.J.E. Golay, Smoothing and differentiation of data by simplified least squares procedures, Anal. Chem. 36 (8) (1964) 1627–1639.
[23] M. Sawall, A. Börner, C. Kubis, D. Selent, R. Ludwig, K. Neymeyr, Model-free multivariate curve resolution combined with model-based kinetics: algorithm and applications, J. Chemom. 26 (2012) 538–548.
[24] M. Sawall, A. Jürß, H. Schröder, K. Neymeyr, On the analysis and computation of the area of feasible solutions for two-, three- and four-component systems, in: C. Ruckebusch (Ed.), Data Handling in Science and Technology, Resolving Spectral Mixtures, vol. 30, Elsevier, Cambridge, 2016, pp. 135–184 (Chapter 5).
[25] C.H. Sotak, C.L. Dumoulin, M.D. Newsham, Automatic phase correction of Fourier transform NMR spectra based on the dispersion versus absorption (DISPA) lineshape analysis, J. Magn. Reson. 57 (3) (1984) 453–462.
[26] E.T. Whittaker, On new method of graduation, Proc. Edinburgh Math. Soc. 41 (1923) 63–75.
[27] K. Wüthrich, Nmr studies of structure and function of biological macromolecules, Biosci. Rep. 23 (4) (2003) 119–168.
[28] Z.-M. Zhang, S. Chen, Y.-Z. Liang, Baseline correction using adaptive iteratively reweighted penalized least squares, Analyst 135 (5) (2010) 1138–1146.
[29] Z.-M. Zhang, S. Chen, Y.-Z. Liang, Z.-X. Liu, Q.-M. Zhang, L.-X. Ding, F. Ye, H. Zhou, An intelligent background-correction algorithm for highly fluorescent samples in Raman spectroscopy, J. Raman Spectrosc. 41 (6) (2010) 659–669.

Matviychuk et al., 2017

Reprinted with permission from: Y. Matviychuk, E. von Harbou, D. J. Holland, An experimental validation of a Bayesian model for quantification in NMR spectroscopy, Journal of Magnetic Resonance, Volume 285, 2017, Pages 86-100, ISSN 1090-7807, DOI 10.1016/j.jmr.2017.10.009

Journal of Magnetic Resonance 285 (2017) 86–100

Contents lists available at ScienceDirect

Journal of Magnetic Resonance

journal homepage: www.elsevier.com/locate/jmr

An experimental validation of a Bayesian model for quantification in NMR spectroscopy

Yevgen Matviychuk [a,*], Erik von Harbou [b], Daniel J. Holland [a]

[a] University of Canterbury, Private Bag 4800, Cristchurch 8140, New Zealand
[b] Technische Universität Kaiserslautern, Erwin-Schrödinger-Straße 44, 67663 Kaiserslautern, Germany

ARTICLE INFO

Article history:
Received 7 July 2017
Revised 20 October 2017
Accepted 21 October 2017
Available online 23 October 2017

2010 MSC:
00-01
99-00

Keywords:
NMR spectroscopy
Quantification
Bayesian analysis

ABSTRACT

The traditional peak integration method for quantitative analysis in nuclear magnetic resonance (NMR) spectroscopy is inherently limited by its ability to resolve overlapping peaks and is susceptible to noise. The alternative model-based approaches not only extend quantification capabilities to these challenging examples but also provide a means for automation of the entire process of NMR data analysis. In this paper, we present a general model for an NMR signal that, in a principled way, takes into account the effects of chemical shifts, relaxation, lineshape imperfections, phasing, and baseline distortions. We test the model using both simulations and experiments, concentrating on simple spectra with well-resolved peaks where we expect conventional analysis to be effective. Our results of quantifying mixture compositions compare favorably with the established methods. At high SNR (> 40 dB), all approaches usually achieve for these test systems an absolute accuracy of at least 0.01 mol/mol for the concentrations of all species. Our model-based approach is successful even for SNR < 20 dB; it achieves 0.05—0.1 mol/mol accuracy in cases where precise phasing is practically impossible due to high levels of noise in the data.

1. Introduction

Nuclear magnetic resonance (NMR) spectroscopy is a popular non-destructive technique in analytical chemistry and related fields. Different chemical species produce distinct signatures in NMR spectra owing to differences in magnetic shielding and, as a result, chemical shifts. Their line intensities are proportional to the amounts of related nuclei, which provides a means for fast and non-destructive quantitative characterization of chemical mixtures.

In the traditional quantification approach, the concentrations of mixture constituents can be determined by numerical integration of corresponding peaks in the spectra. This intuitive technique, however, is limited by its ability to resolve overlapping peaks and requires certain preprocessing steps of the acquired spectra, such as phasing and baseline correction. They are particularly challenging with noisy signals and hinder the analysis of large datasets with many complex spectra, not uncommon, for example, in chemical reaction monitoring [1–3]. Furthermore, advances in benchtop NMR make compact instruments an interesting option for industrial applications. They provide the functionality of conventional superconducting magnets at much lower cost. Unfortunately, the lower field strengths of benchtop instruments decrease the signal-to-noise ratio and spectral resolution. In spectra acquired on such instruments, multiple resonances often overlap and baseline distortions become more common [4–6]. These factors make established peak integration procedures inapplicable for accurate analysis in many systems. Furthermore, robust and automatic analysis methods that require only minimal interaction with operators are essential to facilitate the application of NMR spectroscopy for process analysis and quality control [7]. All in all, this calls for development of novel data processing techniques.

Recently proposed model-based methods are an excellent alternative that allows us to speed up and automate the analysis of spectroscopic data [8,9]. Advanced spectral processing algorithms, such as Indirect Hard Modeling [10–12] and Global Spectral Deconvolution [13], can readily handle overlapping peaks and mild lineshape distortions, but these methods usually operate on accurately phased spectra with good baseline correction – a serious limitation for processing noisy data. On the other hand, black-box methods exist that do not assume any prior knowledge about the acquired signal other than it being composed of a number of exponentially decaying sinusoids. Black box methods estimate the parameters

* Corresponding author.
E-mail address: eugene.matviychuk@canterbury.ac.nz (Y. Matviychuk).

https://doi.org/10.1016/j.jmr.2017.10.009
1090-7807/

of the sinusoids by solving certain singular value decomposition (SVD) problems in state space. These algorithms, such as liner prediction SVD (LPSVD) [14] or Hankel matrix decomposition SVD (HSVD) [15] provide a fast and accurate way for processing simple spectra with non-overlapping peaks, but they become less reliable when the noise increases or multiple peaks overlap.

Finally, a large class of other methods view an entire raw NMR signal as an instance generated by a model with certain parameters and reduce the problem of quantification to that of parameter estimation. Effectively, this makes them less susceptible to noise and often improves the quantification results. In the multitude of proposed techniques [16–19], the methods of Bayesian statistics have been shown to be particularly effective for the purpose of estimating the model parameters [20–22]. They smoothly incorporate any prior knowledge about the studied system into the model and provide a principled way to estimate the uncertainty of results. This paper aims to summarize these approaches and presents a new general Bayesian solution to the parameter estimation problem. In contrast to the other methods introduced above that are based on Bayesian statistics [20–22], our approach provides effective mechanisms for automatic baseline and phase correction. Furthermore, it allows us to easily account for any lineshape distortions possibly caused by inhomogeneity of the external magnetic field or other factors. This is an important feature for analyzing data obtained from medium-field spectrometers or during reaction and process monitoring.

The method is tested using simulations as well as experimental spectra of simple binary mixtures acquired using high-field (9.4 T) and medium-field (1 T) spectrometers. The quantification results are compared with the conventional peak integration in the Fourier domain and with the black-box method HSVD. In the chosen examples, where peaks are well separated, peak integration readily achieves almost perfect quantification results. Yet we show that even in this challenging competition, our model-based estimation performs as well, and usually slightly better. Most importantly, it easily extends to noisy conditions, where phasing required for integrating peak areas is practically impossible.

In the next section, we present a definition of a general mathematical model for an NMR signal that we later use to establish our quantification method. Section 3 describes the set up for our simulations and laboratory experiments; their results are presented in Section 4.

2. Theory

This section provides a theoretical background for our method. In this work, we assume that the species in the studied mixture are known – the number of chemicals K and the individual NMR spectra of pure components are supplied by the user as input information – and we are interested in quantifying the relative mole fractions of the mixture constituents. For this, we define a mathematical model for a general NMR signal of a chemical mixture. The quantification relies on estimating parameters of this model by fitting it to the observed data. We consider a Bayesian approach for the model fitting and derive its solution here.

2.1. A mathematical model of FID signals

In our method, we define a parametric model for a free induction decay signal (FID) acquired in time domain. It contains the same information as its more common spectral-based representation, but from the modeling point of view, the time-domain description has a certain advantage: it leads to simpler readily interpretable equations. Furthermore, postulated in terms of the raw unprocessed FID, our model directly includes phase and baseline correction terms obviating the need for performing these challenging procedures separately. We emphasize, however, that one may derive the equivalent frequency-domain formulation related to our model by the Fourier transform, leading to the same result under the least-squares criterion.

Thus, for a mixture of K chemical species, the FID signal acquired using the principles of quadrature detection and sampled at time instances $\mathbf{t} \in \mathbb{R}^{N\times 1}$ can be represented as a complex-valued vector $\mathbf{x} \in \mathbb{C}^{N\times 1}$ defined as:

$$\mathbf{x} = e^{i\varphi_0}\mathrm{s}(\mathbf{t}+\tau,\xi)\sum_{k=1}^{K} c_k \mathrm{u}_k(\mathbf{t}+\tau,\theta_k) + c_0 e^{i\varphi_0}\cdot \mathrm{v}(\mathbf{t}+\tau,\vartheta). \quad (1)$$

In the above equation, the response of each chemical specie k is represented by a complex-valued function of time $\mathrm{u}_k(t,\theta_k)$ parameterized with a set of scalar parameters θ_k and related to the nature of a particular compound; its intensity c_k is proportional to the amount of substance of specie k. The global phase shift φ_0 and the ringdown delay τ bear the meaning of the zero- and first-order phasing terms, respectively. The other time-dependent components, $\mathrm{s}(t,\xi)$ and $\mathrm{v}(t,\vartheta)$, parameterized by their own sets of parameters ξ and φ, encompass any possible deviations from the ideal FID, such as lineshape imperfections or baseline distortions.

2.1.1. The base model for an ideal NMR signal component

The common assumption that an FID is a superposition of exponentially decaying complex sinusoids leads to the model for individual species

$$\mathrm{u}_k(t,\theta_k) = \sum_{l_k=1}^{L_k} b_{l_k} e^{[i\omega_{l_k}-\alpha_{l_k}]t}. \quad (2)$$

This gives rise to the familiar Lorentzian-shaped peaks in the spectrum with areas under the curve proportional to the coefficients b_{l_k}. The angular frequencies $\omega_{l_k} = 2\pi\left(f_{l_k} - f_0\right)$ are defined with respect to some (absolute) reference f_0 offset by the frequencies of chemical shifts f_{l_k} (in Hz). The decay rates α_{l_k}, also expressed in Hz, are related to the full width at half maximum (FWHM) of each peak and the relaxation time T_2^* through $\alpha_{l_k} = \pi\mathrm{FWHM} = 1/T_2^*$. These parameters constitute the set $\theta_k = \{b_{l_k}, \omega_{l_k}, \alpha_{l_k}\}_{l_k=1}^{L_k}$ with b_{l_k} possibly known and fixed. Alternatively, one may specify ω_{l_k} in terms of the corresponding chemical shifts and j-coupling constants, and include any other parameters relevant for a particular chemical, if desired.

2.1.2. Modeling signal distortions

In practice, the ideal Lorentzian shape of spectral lines is often distorted by any inhomogeneity of the external magnetic field. In such cases, Gaussian and Voigt functions have been used in NMR spectroscopy to describe spectral lines [23]. Furthermore, Hutton et al. proposed a polynomial model to minimize the effect of distortions in strong solvent peaks, which facilitates quantitative analysis of high dynamic range spectra [24]. On the other hand, non-parametric lineshape adaptation filters [25] can potentially compensate for inaccuracies between the assumed model and the data.

In our model, to account for the effects of distortions, we introduce the lineshape correction term $\mathrm{s}(t,\xi)$ in Eq. (1). For simplicity of explanation and in all our experiments, it is assumed that all peaks in the spectrum are equally affected by the distortions; however, we note that extension of the model attributing different correction terms $\mathrm{s}_k(t,\xi_k)$ to each signal component is straightforward. Following the approach of [24], we require $\mathrm{s}(t,\xi)$ to be a smooth function of time and model it as a polynomial of order Q,

$$\mathrm{s}(t,\xi)=\exp\left\{\sum_{q=2}^{Q}\xi_q t^q\right\}, \tag{3}$$

where linear and zero-order terms are left out, but are otherwise included in Eqs. (1) and (2) as the decay and phasing terms. The complex-valued coefficients $\xi=\{\xi_p\}_{q=2}^{Q}$ allow us to model not only deviations in the amplitude but also in the phase of the FID and ensure that even asymmetric peaks can be described accurately (see Fig. 1 for examples). Popular Gaussian and Voigt lineshape models can be seen as special cases of Eq. (3) for certain values of ξ_q limited to symmetric peaks. We note that, in principle, there are no inherent constraints on the form of the lineshape function $\mathrm{s}(t,\xi)$. The representational capabilities of the model can potentially be expanded by using more complex formulations for $\mathrm{s}(t,\xi)$, e.g. rational functions of polynomials or sums of harmonic components, to account for even severe distortions such as peak splitting. Increase of the model complexity, however, entails difficulties in finding its optimal parameters and the possibility of overfitting. Thus, using simpler lineshape correction mechanisms, if any, is normally preferred; in this paper we consider only unimodal, but potentially asymmetric, peaks.

Finally, we account for baseline imperfections by including the additive component $\mathrm{v}(t,\vartheta)$ weighted by c_0 in Eq. (1). For example, to remove a uniform baseline offset, we alter the first time sample of the signal by setting $\mathrm{v}(t,\vartheta)=[\vartheta,0,\ldots,0]$ and estimating ϑ as another free parameter. Similarly, one may remove an offset in the time domain or define more complex (e.g. polynomial) models for $\mathrm{v}(t,\vartheta)$, if necessary.

2.1.3. An overview of model fitting

An acquired FID signal $\mathbf{y}$ can be viewed as an instance of the above model evaluated with some combination of parameters and possibly affected by additive noise, i.e. $\mathbf{y}=\mathbf{x}+\mathbf{n}$. In what follows, we assume that $\mathbf{n}\in\mathbb{C}^N$ is a zero-mean circularly-symmetric Gaussian random vector $\mathbf{n}\sim\mathcal{N}(\mathbb{0},\sigma^2\mathbf{I})$ [20], and introduce a compact matrix notation:

$$\mathbf{y}=\mathbf{Z}\mathbf{c}e^{i\varphi_0}+\mathbf{n}, \tag{4}$$

where $\mathbf{Z}\in\mathbb{C}^{N\times K+1}$ is a model matrix with entries $\mathrm{Z}_{n,k}=\mathrm{s}(\mathrm{t}_n+\tau,\xi)\mathrm{u}_k(\mathrm{t}_n+\tau,\theta_k)$ for $k=1,\ldots,K$ and $\mathrm{Z}_{n,0}=\mathrm{v}(\mathrm{t}_n+\tau,\vartheta)$; similarly, $\mathbf{c}\in\mathbb{R}^{K+1\times 1}$ is a vector of intensities, $\mathbf{c}=[c_0,c_1,\ldots,c_K]$. We note that $\mathbf{Z}$ implicitly depends on all model parameters, θ_k,ξ,ϑ, and τ. For compactness, in the upcoming discussion, we aggregate them into a single set $\Theta=\{\theta_k,\xi,\vartheta,\tau\}$ for all $k=1,\ldots,K$.

The main idea of any model-based quantification method is to find the model that explains the observed data best in some sense, which then provides a straightforward way for determining the mole fractions $\chi_k=\frac{c_k}{\sum_k c_k}$ of chemical species in the mixture. Such model fitting is performed by many popular quantification algorithms, such as AMARES [16], QUEST [17], AQSES [26], and others [27,28,19,29]. Probabilistic Bayesian methods, instead of looking for point estimates of the underlying parameters, view them as random variables and aim to reconstruct their entire posterior distributions [20–22]. Although this more extensive problem often comes with an inevitable increase in computational complexity, it allows us to seamlessly incorporate prior knowledge about the sought parameters into the problem and provides a principled way to quantify the uncertainty of results. We proceed by deriving a Bayesian solution for the NMR quantification problem.

2.2. Bayesian estimation of the model parameters

The idea of Bayesian inference for parameter estimation was first introduced to NMR spectroscopy by Bretthorst [20]. Specifically, in this framework, one aims to recover the joint posterior distribution of all model parameters consistent with the observed data $\mathcal{D}=\{\mathbf{y}_n\}$ and any prior assumptions. By invoking Bayes theorem, we express the posterior as:

$$p(\Theta,\mathbf{c},\varphi_0,\sigma^2\mid\mathcal{D})\propto p(\mathcal{D}\mid\Theta,\mathbf{c},\varphi_0,\sigma^2)p(\Theta,\mathbf{c},\varphi_0,\sigma^2), \tag{5}$$

where $p(\mathcal{D}\mid\Theta,\mathbf{c},\varphi_0,\sigma^2)$ is the likelihood (as a function of the parameters Θ) and $p(\Theta,\mathbf{c},\varphi_0,\sigma^2)$ is the prior probability distribution that specifies any initial beliefs about the model and the variance of noise; assuming the model and the noise are independent, it factors into $p(\Theta,\mathbf{c},\varphi_0,\sigma^2)=p(\Theta,\mathbf{c},\varphi_0)p(\sigma^2)$. In the present work, we also treat the concentrations, global phasing terms, and the rest of model parameters as independent variables, which eventually factors the prior as $p(\Theta,\mathbf{c},\varphi_0,\sigma^2)=p(\Theta)p(\mathbf{c})p(\varphi_0)p(\sigma^2)$. We emphasize, however, that the general model formulation in Eq. (5) permits any mutual relationship of some or all parameters. For example, if relevant, dependence between a chemical shift and a concentration can be incorporated into the model with a more complex *joint* prior. However, it is unlikely to lead to the simple closed form solutions presented next, which makes parameter estimation possible only with numerical simulations.

The likelihood function is determined by assumptions about the noise, and for Gaussian noise with variance σ^2 it is

$$p(\mathcal{D}\mid\Theta,\mathbf{c},\varphi_0,\sigma^2)=\frac{1}{(\pi\sigma^2)^N}\exp\left\{-\frac{1}{\sigma^2}(\mathbf{y}-\mathbf{Z}\mathbf{c}e^{i\varphi_0})^{\mathrm{H}}(\mathbf{y}-\mathbf{Z}\mathbf{c}e^{i\varphi_0})\right\}, \tag{6}$$

where $[\cdot]^{\mathrm{H}}$ denotes the Hermitian transpose. We proceed by assigning specific prior distributions to the parameters and find the

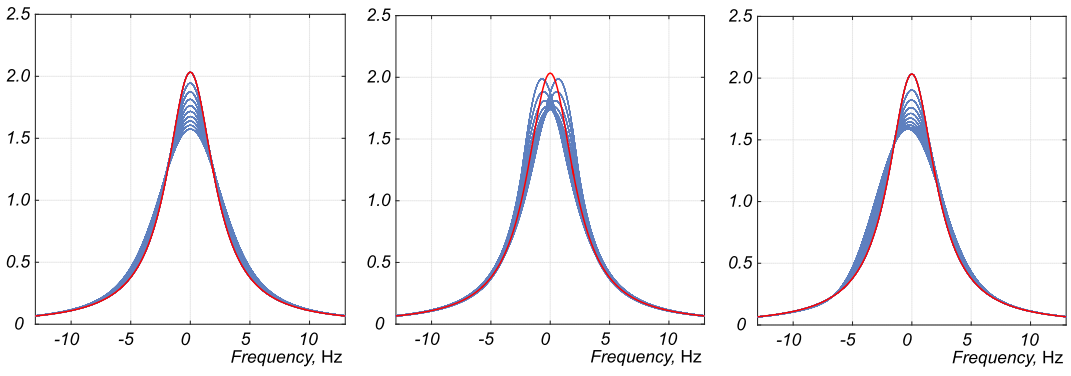

Fig. 1. Examples of peaks generated using different values of lineshape correction coefficients ξ_q and $\alpha=15\ \mathrm{s}^{-1}$. Left: $\xi_2=-50,\ldots,0$; middle: $\xi_2=-25e^{-i\pi/2},\ldots,-25e^{i\pi/2}$; right: $\xi_3=-350,\ldots,0,\xi_2=-25e^{-i\pi/3},\ldots,0$. In each case, the red lines correspond to the pure Lorentzian peak. Note the asymmetry in peaks with complex values of ξ_q. (For interpretation of the references to color in this figure legend, the reader is referred to the web version of this article.)

posterior estimates of the components' intensities $\widehat{\mathbf{c}}$, the global phase shift $\widehat{\varphi_0}$, and the variance of noise $\widehat{\sigma^2}$. In these derivations, we assume that the estimates of the nonlinear model parameters, i.e. chemical shifts, peak widths, baseline and lineshape correction terms, are known and used in the corresponding matrix $\widehat{\mathbf{Z}}$. They are found by maximizing or sampling the resulting posterior as summarized in Algorithm 1.

2.3. Our implementation of the Bayesian approach

Parameter estimation of the FID model in Eq. (1) (or its related formulations) have been considered in several previous works. Most notably, following the works of Bretthorst [20,30–32], Rubtsov and Griffin find closed form solutions for the intensities of components and the variance of noise [21]. Hutton et al. consider the problem of baseline correction and lineshape modeling, specifically for spectra containing strong solvent peaks [24]. Finally, Bydder constrains the phase of spectral components and derives an expression for the zero-order phasing term optimal in the least squares sense [33], although without probabilistic assumptions. Here, we review and combine these approaches, including the lineshape and baseline correction terms according to Section 2.1.2, and present a comprehensive parameter estimation procedure that we use in our experiments.

2.3.1. Estimation of the absolute intensities

Due to the specific form of the likelihood, the vector of component intensities $\mathbf{c}$ is typically modeled as normally distributed, $\mathbf{c} \sim \mathcal{N}\left(\mathbf{m}_0, \frac{\sigma^2}{2}\boldsymbol{\Sigma}_0\right)$ with some prior mean $\mathbf{m}_0$ and covariance matrix $\frac{\sigma^2}{2}\boldsymbol{\Sigma}_0$. With this conjugate prior, after substituting Eq. (6) into Eq. (5) and completing the square in the exponent, we find that the posterior distribution of intensities is Gaussian $p(\mathbf{c} \mid \mathcal{D}) = \mathcal{N}(\mathbf{m}, \sigma^2\boldsymbol{\Sigma})$ with the mean $\mathbf{m} = \boldsymbol{\Sigma}\left[\boldsymbol{\Sigma}_0^{-1}\mathbf{m}_0 + Re\left(\widehat{\mathbf{Z}}^{\mathrm{H}}\mathbf{y}e^{-i\varphi_0}\right)\right]$ and the covariance matrix $\boldsymbol{\Sigma} = \left[\boldsymbol{\Sigma}_0^{-1} + Re\left(\widehat{\mathbf{Z}}^{\mathrm{H}}\widehat{\mathbf{Z}}\right)\right]^{-1}$. The remaining posterior becomes:

$$p(\Theta, \varphi_0, \sigma^2 \mid \mathcal{D}) \propto \frac{\sqrt{\det\boldsymbol{\Sigma}}}{(\pi\sigma^2)^N\sqrt{\det\boldsymbol{\Sigma}_0}} \times \exp\left\{-\frac{1}{\sigma^2}\left(\mathbf{y}^{\mathrm{H}}\mathbf{y} + \mathbf{m}_0^{\mathrm{T}}\boldsymbol{\Sigma}_0^{-1}\mathbf{m}_0 - \mathbf{m}^{\mathrm{T}}\boldsymbol{\Sigma}^{-1}\mathbf{m}\right)\right\} \cdot p(\Theta)\cdot p(\varphi_0)\cdot p(\sigma^2). \tag{7}$$

The choice of $\mathbf{m}_0$ and $\boldsymbol{\Sigma}_0$ reflects any knowledge about the mixture composition. Furthermore, one may introduce another hyperparameter g, related to the expected SNR, and set $\boldsymbol{\Sigma}_0 = g\left[\widehat{\mathbf{Z}}^{\mathrm{H}}\widehat{\mathbf{Z}}\right]^{-1}$ [34,21]. In our experiments, we let $g \to \infty$, which effectively corresponds to a vague assumption about the components' intensities $\mathbf{c}$ in the absence of any prior knowledge. This leads to $\boldsymbol{\Sigma}_0^{-1} \to \mathbb{0}$ and, consequently,

$$\mathbf{m} = \boldsymbol{\Sigma}Re\left(\widehat{\mathbf{Z}}^{\mathrm{H}}\mathbf{y}e^{-i\varphi_0}\right) \tag{8}$$

with $\boldsymbol{\Sigma} = Re\left(\widehat{\mathbf{Z}}^{\mathrm{H}}\widehat{\mathbf{Z}}\right)^{-1}$. We note that the choice of a Gaussian prior for the vector $\mathbf{c}$ is dictated primarily by the simple closed form solution for the given likelihood function, but unfortunately, it implies that the obtained concentrations can be negative, which is physically meaningless. If this happens in practice (for example, if the signal intensity of a chemical is comparable to the noise level, or if the model is not fitted properly), we set the corresponding entries in $\mathbf{m}$ to 0, which accounts for the absence of the chemical in the mixture. In general, one may chose a one-sided prior distribution for $\mathbf{c}$, but in this case, the integration can be performed only numerically.

2.3.2. Estimation of the global phase shift

The prior distribution of the global zero-order phase shift φ_0 is uniform over $[-\pi, \pi]$. With this assumption, we note that in order to maximize the above posterior in Eq. (7), one may consider maximizing $\mathbf{m}^{\mathrm{T}}\boldsymbol{\Sigma}^{-1}\mathbf{m}$ as a function of φ_0 [33,35] instead. After substituting the expression for $\mathbf{m}$ (Eq. (8)) and differentiating, we obtain:

$$\frac{d}{d\varphi_0}\mathbf{m}^{\mathrm{T}}\boldsymbol{\Sigma}^{-1}\mathbf{m} = 2Im\left[\widehat{\mathbf{Z}}^{\mathrm{H}}\mathbf{y}e^{-i\varphi_0}\right]^{\mathrm{T}}\boldsymbol{\Sigma}Re\left[\widehat{\mathbf{Z}}^{\mathrm{H}}\mathbf{y}e^{-i\varphi_0}\right] = Im\left\{\left[\widehat{\mathbf{Z}}^{\mathrm{H}}\mathbf{y}\right]^{\mathrm{T}}\boldsymbol{\Sigma}\left[\widehat{\mathbf{Z}}^{\mathrm{H}}\mathbf{y}\right]e^{-i2\varphi_0}\right\}.$$

Similarly, the second derivative is

$$\frac{d^2}{d\varphi_0^2}\mathbf{m}^{\mathrm{T}}\boldsymbol{\Sigma}^{-1}\mathbf{m} = -Re\left\{\left[\widehat{\mathbf{Z}}^{\mathrm{H}}\mathbf{y}\right]^{\mathrm{T}}\boldsymbol{\Sigma}\left[\widehat{\mathbf{Z}}^{\mathrm{H}}\mathbf{y}\right]e^{-i2\varphi_0}\right\}.$$

To find the maximum, we set the first derivative to 0 and require that the second derivative is negative. The real part of a complex number is positive and its imaginary part is zero if and only if its argument is also zero, leading to:

$$\widehat{\varphi_0} = \frac{1}{2}\angle\left\{\left[\widehat{\mathbf{Z}}^{\mathrm{H}}\mathbf{y}\right]^{\mathrm{T}}\boldsymbol{\Sigma}\left[\widehat{\mathbf{Z}}^{\mathrm{H}}\mathbf{y}\right]\right\}, \tag{9}$$

where $\angle[\cdot]$ denotes the argument of a complex number. With this estimate of the phase, we can readily obtain an estimate of the vector of intensities

$$\widehat{\mathbf{c}} = Re\left(\widehat{\mathbf{Z}}^{\mathrm{H}}\widehat{\mathbf{Z}}\right)^{-1}Re\left(\widehat{\mathbf{Z}}^{\mathrm{H}}\mathbf{y}e^{-i\widehat{\varphi_0}}\right) \tag{10}$$

and subsequently compute the sought mole fractions.

2.3.3. Estimation of the variance of noise

In many practical cases, a good estimate of the noise variance $\widehat{\sigma^2}$ can be obtained from a signal-free region of the spectrum. This value can then be used in place of σ^2 in Eq. (5), and the posterior is then maximized with respect to the rest of the parameters. To account for possible uncertainty in $\widehat{\sigma^2}$, or if it is completely unknown, it can be modeled parametrically. Choosing an inverse-gamma prior, $\sigma^2 \sim IG(\alpha_\sigma, \beta_\sigma)$, allows us to integrate out the variance of noise with $p(\sigma^2 \mid \mathcal{D}) = IG(\alpha_\sigma, \beta_\sigma + \mathbf{y}^{\mathrm{H}}\mathbf{y} - \mathbf{m}^{\mathrm{T}}\boldsymbol{\Sigma}^{-1}\mathbf{m})$ and find its estimate as the mean of the inverse-gamma distribution, $\widehat{\sigma^2} = \frac{\beta_\sigma + \mathbf{y}^{\mathrm{H}}\mathbf{y} - \mathbf{m}^{\mathrm{T}}\boldsymbol{\Sigma}^{-1}\mathbf{m}}{\alpha_\sigma - 1}$. This leaves the marginal posterior $p(\Theta \mid \mathcal{D})$ that depends only on the nonlinear parameters of the model (note that both $\boldsymbol{\Sigma}$ and $\mathbf{m}$ implicitly depend on Θ):

$$p(\Theta \mid \mathcal{D}) \propto \frac{\sqrt{\det\boldsymbol{\Sigma}}}{\pi^N}\left[\beta_\sigma + \mathbf{y}^{\mathrm{H}}\mathbf{y} - \mathbf{m}^{\mathrm{T}}\boldsymbol{\Sigma}^{-1}\mathbf{m}\right]^{-(\alpha_\sigma + N)} \cdot p(\Theta). \tag{11}$$

The rest of the model parameters Θ, in general, cannot be eliminated from the problem analytically, and their estimation relies on numerical methods. For example, maximizing Eq. (11) with respect to Θ using any available non-linear optimization algorithm results in their maximum aposteriori (MAP) estimates. Unfortunately, with complicated multi-modal posteriors, there is no guarantee of convergence to the global optimum, and the results crucially depend on the initialization. Alternatively, although more computationally demanding, the entire posterior can be sampled with Markov chain Monte-Carlo (MCMC) methods; the sought parameter estimates are then found as sample means or medians of the respective distributions, possibly equipped with their confidence intervals, if desired. For example, Dou and Hodgson [36,37] propose to use Gibbs sampling and to alternate between estimating different parameters. Other methods employ the

Metropolis-Hastings algorithm or its modifications for this purpose [38,39]. Finally, Wilson et al. [22] use point estimates of the non-linear model parameters and then only sample the component intensities from the corresponding Gaussian distributions. We discuss our algorithmic approach in detail in the next section.

2.4. An outline of the proposed algorithmic approach

In this section, we describe the proposed algorithmic procedure used in our experiments. We summarize it in the most general form in the following table.

Algorithm 1. The proposed quantification algorithm

Input: FID data $\mathcal{D}$ as a vector $\mathbf{y}$ sampled at times $\mathbf{t}$, list of chemical species, initial values of parameters Θ_0, maximum number of iterations M.

Output: Estimates of mole fractions $\widehat{\chi}_k$.

1: $\widehat{\Theta} \leftarrow \Theta_0$ ▷ Initialize the model parameters

2: **for** $m := 1 \dots M$ ▷ Iterative maximization

3: Split the parameters into two disjoint subsets, $\widehat{\Theta} = \left\{\widetilde{\Theta}, \overline{\Theta}\right\}$. Fix $\overline{\Theta}$.

4: $\widetilde{\Theta} \leftarrow \underset{\widetilde{\Theta}}{\operatorname{argmax}}\, p\left(\widetilde{\Theta}, \overline{\Theta} \mid \mathcal{D}\right)$ ▷ Maximize the posterior in Eq. (11)

5: $\widehat{\Theta} \leftarrow \left\{\widetilde{\Theta}, \overline{\Theta}\right\}$ ▷ Update the estimates of parameters

6: **end for**

7: $\mathbf{Z} \leftarrow \begin{bmatrix} \mathrm{v}\left(\mathbf{t} + \widehat{\tau}, \widehat{\vartheta}\right) \\ \mathrm{s}\left(\mathbf{t} + \widehat{\tau}, \widehat{\xi}\right)\mathrm{u}_k\left(\mathbf{t} + \widehat{\tau}, \widehat{\theta}_k\right) \end{bmatrix}^{\mathrm{T}}$ ▷ Compute $\mathbf{Z}$ based on values in $\widehat{\Theta}$

8: $\widehat{\varphi_0} \leftarrow \frac{1}{2}\angle\left(\left[\mathbf{Z}^{\mathrm{H}}\mathbf{y}\right]^{\mathrm{T}}\boldsymbol{\Sigma}\left[\mathbf{Z}^{\mathrm{H}}\mathbf{y}\right]\right)$ ▷ Find the global phase shift (Section 2.3.2)

9: $\widehat{\mathbf{c}} \leftarrow Re\left(\mathbf{Z}^{\mathrm{H}}\mathbf{Z}\right)^{-1} Re\left(\mathbf{Z}^{\mathrm{H}}\mathbf{y}e^{-i\widehat{\varphi_0}}\right)$ ▷ Find the intensities (Section 2.3.1)

10: $\widehat{\chi}_k \leftarrow \widehat{\mathrm{c}}_k / \sum_k \widehat{\mathrm{c}}_k$ for $k = 1, \dots, K$ ▷ Estimate the mole fractions

11: *Optional.* Run MCMC simulations to sample the posterior in Eq. (11) with respect to all model parameters and estimate their sample means (medians), standard deviations, and confidence intervals, if desired.

In addition to the raw spectrometer data, the algorithm is supplied with signature NMR spectra of the K quantified chemical species. If after fitting them to the data, some resonances remain unexplained, additional components can be introduced to the model. However, we note that it is not always necessary to model all mixture components; unspecified peaks sufficiently far away from the spectral region of interest do not affect the model fitting process and the quantification results. If desired, such peaks can be filtered out on a preprocessing step, or the fitting can be performed using an objective function localized in the frequency domain. In contrast, if some peaks overlap with the quantified components, excluding them from the model will necessarily introduce an error. Thus, when analyzing crowded spectral regions, all neighboring peaks must be considered.

Initialization of parameters includes specifying their prior distributions and starting values for optimization. Specifically, in our experiments in this paper, we set uniform prior distributions for all non-linear parameters allowing chemical shifts of the peaks to vary in the range of up to ± 1 ppm of their reference values. Likewise, exponential decay rates α_{l_k} are modeled with uniform distributions on the interval $[0, 250]\ \mathrm{s}^{-1}$ in our ^{1}H experiments ($[0, 25]\ \mathrm{s}^{-1}$ in ^{13}C experiments) and are initialized with small values corresponding to narrow peaks ($\approx 5\ \mathrm{s}^{-1}$ and $\approx 0.5\ \mathrm{s}^{-1}$ respectively). Alternatively, one may manually identify the peaks in the spectrum, measure their widths directly, and then use these values to obtain possibly more accurate parameter initialization. However, in our simple examples, we found the algorithm to be robust to misspecification of the initial parameter values in their respective ranges, and thus such preprocessing is deemed unnecessary.

The complex-valued lineshape parameters ξ_q are modeled with their magnitudes and angles uniformly distributed on the intervals $[-50, 50]$ and $[-\pi, \pi]$ respectively, and the ringdown delay τ is uniform on the interval $\tau_0 \pm 10^{-5}$ s, where τ_0 is the delay time found in the spectrometer acquisition protocol. In principle, using informative prior distributions that give strong preference to certain parameter values (e.g. truncated Gaussian) can increase the robustness of the algorithm, however, if an incorrectly chosen prior dominates the measured data, this may easily lead to overfitting and false results. For this reason, prior assumptions in this work are limited only to the ranges of parameters.

To keep computational complexity low while achieving accurate quantification results, we maximize the marginal posterior of Eq. (11) sequentially over smaller subsets of parameters rather than in the overall large parameter space at once. We note that many of the variables are likely to be mutually independent (for example, small changes in chemical shift or width of one peak do

not significantly affect other distant unrelated peaks); this governs the choice of subsets of optimized parameters at Step 4 of the algorithm. For example, with two non-overlapping peaks in the spectrum, on the first iteration, we optimize the chemical shift and width of the first peak, $\widetilde{\Theta} = \{\delta_1, \alpha_1\}$, while keeping the second peak fixed, $\overline{\Theta} = \{\delta_2, \alpha_2\}$. During the second iterative step, the found $\widehat{\delta}_1$ and $\widehat{\alpha}_1$ are fixed and included in the set $\overline{\Theta}$ while optimizing the parameters of the second peak, $\widetilde{\Theta} = \{\delta_2, \alpha_2\}$. However, when several (k) peaks overlap and can affect each other, fitting them simultaneously as a group may prove to be more beneficial (i.e. using $\widetilde{\Theta} = \{\delta_1, \ldots, \delta_k, \alpha_1, \ldots, \alpha_k\}$). Furthermore, as one may expect, starting the fitting with parameters corresponding to larger components in the signal is preferable. Finally, it is suggested that the lineshape correction parameters ξ_q are fitted, if desired, only after good Lorentzian approximations for all peaks are found. Therefore, the choice of the optimized parameters on Step. 3 of the algorithm is highly case-dependent.

Maximizing the posterior distribution of Eq. (11) results in its mode – the set of most probable model parameters given the prior knowledge and the observed data. The use of point estimators is primarily motivated by the assumption that each parameter (e.g. peak frequencies) is associated with a single true value. However, Bayesian methods allow one to fully take advantage of the probabilistic problem formulation and summarize the obtained results more comprehensively. By analyzing the entire posterior distribution, the appropriate point estimates of parameters (e.g. mean, mode, or median) can be additionally equipped with credible intervals to express their uncertainty, if desired. Unfortunately, theoretical analysis of large posteriors is rarely possible in practice, and one must resort to numerical methods for their integration. A broad class of Markov Chain Monte-Carlo algorithms is designed to draw samples from potentially large parameter spaces according to complex distributions. The uncertainties in the found parameters can then be estimated as sample deviations or quantile measures. Here, we suggest running the Goodman-Weare affine-invariant ensemble sampler [40,41] on the final step of the algorithm. However, instead of exploring the entire posterior, we initialize the chain in the vicinity of the found maximum, assuming it is a good approximation to the sought true parameter values; this facilitates convergence and reduces the computational burden of notoriously slow MCMC algorithms. Furthermore, additional care should be taken when working with multimodal posteriors, as often arise in spectroscopy applications. Blindly sampling the entire parameter space may lead to unexpected results if the found mean estimate falls into a low-probability area between separate modes [42,43]. In such cases, marginal maximum a posteriori estimators can provide more faithful results. Also note that the MCMC sampling is only required if an estimate of the uncertainty in the quantification is needed; if a point estimate is sufficient, then the maximum a posteriori estimator is sufficient.

We implement our method in MATLAB and use the standard Sequential Quadratic Programming (SQP) algorithm for model fitting called within the global search routine to increase the chance of converging to the global solution. Convergence is typically achieved after $M = 3$ iterative loops over all model parameters. The code is available from the authors on request.

3. Materials and methods

3.1. Settings for simulations

In Section 4.1 we use several simulated datasets to compare the performance of our quantification approach with the traditional peak integration in frequency domain and the black-box HSVD algorithm [15]. For this, we generate spectra containing two overlapping peaks according to the model of Eq. (1), where we use $s = 1$ and $c_0 = 0$. The integration of peak areas in these experiments is performed in MATLAB; to obviate the need for phasing, we set $\tau = \varphi_0 = 0$, but we assume these parameters are unknown in HSVD and in our method. In each case, we obtain $2^{13} = 8192$ FID samples with the dwell time of 200 μs and then add Gaussian noise to them.

The distance between the peaks is varied in the range $\Delta f = 0 \ldots 32$ Hz and their widths FWHM $= 1.25 \ldots 70$ Hz to achieve different degree of overlap, which we quantify as the inner product between the corresponding data vectors, $\mu^o = \frac{z_1^H z_2}{\|z_1\| \|z_2\|}$. Thus, two completely overlapping peaks have $\mu^o = 1$, while for two well separated peaks, $\mu^o \to 0$. We note that this measure summarizes the effects of the distance between the peaks as well as their widths.

3.2. Sample preparation and data acquisition

In this work, with the intention to isolate and analyze essential properties of the algorithms, we consider only very simple spectra containing single well resolved peaks. Such cases are notably easy to deal with using the traditional peak integration as well state-space algorithms for analysis of harmonic signals, such as HSVD [15,44,45]. Nevertheless, we show that our method of Bayesian estimation performs at least as good, and often better, than its competitors. The improvement is more significant with increasing levels of noise.

First, we validate our quantification method with an example, in which relative peak intensities are known exactly. For this, we prepare 0.1M solution of creatine in D_2O and study its proton spectrum. Specifically, we estimate the intensities of its peaks appearing at 2.9 and 3.8 ppm and compare their ratio with the true value. These experiments are performed on a 400 MHz Agilent 400MR spectrometer equipped with a OneNMR probe. We acquire ^{1}H FID signals with 2^{14} points and dwell time of 312.5 μs using a one-pulse sequence with pulse angle of 45° and no repetitions. We use only a standard pre-programmed shimming procedure, which typically results in lower field homogeneity than in the rest of our examples and notably distorted spectral lines. This allows us to study the effectiveness of the lineshape correction mechanism in our model.

Next, we consider a mixture of acetonitrile and dioxane. Both of these chemicals exhibit single peaks in their proton spectra located at 1.7 ppm and 3.7 ppm for acetonitrile and dioxane respectively. In carbon spectra, dioxane shows a single peak and acetonitrile two peaks. In our experiments the frequency scale was adjusted so that the dioxane peak occurred at 67.2 ppm and the peaks of acetonitrile at 116 ppm and 0 ppm. The two peaks of acetonitrile have equal areas but typically an order of magnitude different widths. For spectral integration we use only the peak at 0 ppm as the highest and thus less affected by noise; in our model-based method and in HSVD, we consider both peaks, when possible. We prepared a binary mixture with gravimetrically determined mole fraction of dioxane, $\chi_{\text{Diox}}^{\text{grav}} = 0.344$ mol/mol. By means of the accuracy of the laboratory balances, which is provided in the calibration protocol of the manufacturer, and error propagation, the uncertainty of the gravimetrically determined mole fraction was estimated to be 10^{-4} mol/mol. With such samples, modern spectrometers readily achieve very high signal-to-noise ratios (SNR) even with single scans and short excitation pulses (e.g. 10—30°). Thus to be able to study a wide range of noise conditions, we prepare four additional samples of the same mixture diluted with

heavy water in proportions (by mass) equal to $1:2, 1:5, 1:10$, and $1:50$. This controllably decreases the peaks' heights with respect to the noisy baseline but leaves their chemical shifts and widths unchanged. In all our experiments, we report only the relative mole fractions of these two primary components and ignore a small additional peak at 4.75 ppm in ^{1}H spectra appearing due to residual hydrogen in D_2O.

For another set of experiments, we prepare a series of cyclohexane-dioxane mixtures, with gravimetric mole fractions of dioxane, $\chi_{\text{Diox}} = 0.799, 0.599, 0.400, 0.199, 0.100, 0.012$ mol/mol. The uncertainty in the gravimetrically estimated mole fractions does not exceed 10^{-4} mol/mol. The peaks of cyclohexane are located at 1.4 and 27.1 ppm in ^{1}H and ^{13}C spectra respectively. All considered chemical species have simple spectra, which allows us to model them with decaying complex sinusoids (see Eq. (2)). When processing data of uncoupled proton experiments, we found it necessary to take into account the ^{13}C satellites to slightly improve quantification with our method at very high signal-to-noise ratios. This is especially relevant when processing medium field data, where these peaks may overlap.

Cyclohexane, dioxane, and deuterated water were purchased from Sigma-Aldrich, and acetonitrile was purchased from Carl Roth ROTISOLV HPLC. All chemicals except for dioxane have reported purities of 99.9%; the purity of dioxane is 99.8%. The samples of approximately 1—2 g in each case were prepared gravimetrically using a Mettler Toledo AX205 balance with instrument accuracy of 0.1 mg (provided in the calibration protocol of the manufacturer). The uncertainties of the gravimetrically determined mole fractions of the analytes are estimated from purity range of the chemicals specified by the supplier and the accuracy of the laboratory balances by means of an error propagation. The uncertainties of the gravimetrically determined mole fractions of dioxane in all samples are at least one order of magnitude lower than the difference between the values determined from the NMR measurements and the gravimetric values.

To study the effect of noise in a wide SNR range, the data was acquired on two different high-field NMR spectrometers with 9.4 T vertical superconducting magnets (Ascend 400, console: Avance 3 HD 400, Bruker Biospin, Rheinstetten, Germany), which correspond to a proton Larmor frequency of 400.25 MHz. One spectrometer was equipped with a standard probe (BBFO, Bruker Biospin, Rheinstetten, Germany) and the other was equipped with a probe whose electronics are cryogenically cooled (CryoProbe Prodigy, Bruker Biospin, Rheinstetten, Germany). In proton NMR experiments, we use a simple one-pulse sequence with pulse angle of 10°. Depending on the particular case, we collect 2^{13}—2^{14} points with dwell times of 330—500 μs and use a relaxation delay of 10 s in repeated experiments. In ^{13}C experiments, we collected 2^{17} points with dwell time of 133 μs using an inverse-gated decoupling sequence with pulse length corresponding to flip angles of 60° (cryo probe) and 90° (BBFO probe); datasets with one and four scans were acquired with relaxation delay of 60 s. Both instruments were tuned and shimmed individually for each sample.

Additionally, the same samples were used to acquire data on two medium-field Magritek Spinsolve-Carbon benchtop spectrometers operating at a ^{1}H frequency of 43.6 MHz. In ^{1}H experiments, we collected 2^{15} time points with dwell time DW = 200 μs (2^{12} points with DW = 400 μs for ^{13}C). Proton experiments were run with single scans and varied pulse angles, 30°, 60°, or 90°; in ^{13}C experiments, we use 90° pulse angle and acquire up to 1024 repetitive scans with the relaxation delay of 60 s. While collecting the data, both Spinsolve instruments were periodically recalibrated using the standard shimming protocol to ensure the best field homogeneity.

3.3. Data processing and quantification

All computational analysis in this work was performed on an Intel Core i7-4790 desktop computer operating at CPU frequency of 3.60 GHz with 16 GB RAM installed. Peak integration was carried out with the software Mnova (version 11.0, Mestrelab Research, Santiago de Compostela, Spain). In each case, automatic phase (global, whitening) and baseline (Whittaker smoother) corrections were applied followed by visual inspection and manual adjustment where necessary. To improve SNR in ^{13}C experiments, exponential line-broadening of 1 Hz was applied. Integration boundaries for each peak are chosen based on their full width at half-maximum (FWHM) and are set at least 50 × FWHM, or wider, to include all ^{13}C satellite peaks if needed [46].

Finally, for comparison, we use another popular quantification algorithm, HSVD [47,15]. This fast method based on singular value decomposition of a Hankel matrix, automatically extracts frequencies and damping rates of exponentially decaying sinusoids in a multicomponent signal. The recovered components are then assigned to their closest peaks in the reference spectra with intensities estimated using the least squared fit. Unfortunately, costly matrix decomposition operations that underly high resolution state-space algorithms, such as HSVD, impose limitations on their ability to analyze large datasets. Indeed, due to the memory limitations, processing signals with more than 2^{14} time samples was found infeasible using the full singular value decomposition algorithm. This obstacle can be overcome with certain complexity reduction procedures, such as decimation and localization [48]. Alternatively, since only a few largest singular values are retained in the HSVD method, one may look for a low-rank approximation of the Hankel matrix with one of several fast algorithms [49,50]. Specifically, in this work, we use the MATLAB's svd command with the "economy size" decomposition option; this allows us to perform computations on signals with up to 2^{19} time samples.

3.4. Estimation of SNR

In both simulations and laboratory experiments, we report the results of quantification with respect to estimated signal-to-noise ratio expressed in dB as

$$\text{SNR} = 10 \log \left(\frac{P_s}{P_n} \right), \tag{12}$$

where P_s and P_n are the energies of the useful signal and the background noise respectively. To find P_s, we rely on the signal estimate found with our model-based method, $P_s = \sum_{n=1}^{N} \widehat{x}_n^2$. On the other hand, for Gaussian noise, $P_n = N\widehat{\sigma}^2$, where N is the total number of samples and $\widehat{\sigma}^2$ is the estimated noise variance. In addition to estimating $\widehat{\sigma}^2$ as described in Section 2.3.3, one may measure it in any signal-free region of the spectrum assuming the power spectral density is uniform over the entire frequency range. Unlike the ratio of the peak height to the noise floor in the spectrum, this usual SNR definition accounts for contributions of all signal components. Indeed, this is important, since in many cases, even if any small peaks cannot be directly observed and measured due to noise, intensities of other stronger components in the spectrum may provide indirect information about the corresponding mole fractions.

4. Results and discussion

In this section, we compare performance of the proposed model-based method with the traditional approach of peak integration and with the black-box HSVD algorithm on several simulated and real-world datasets.

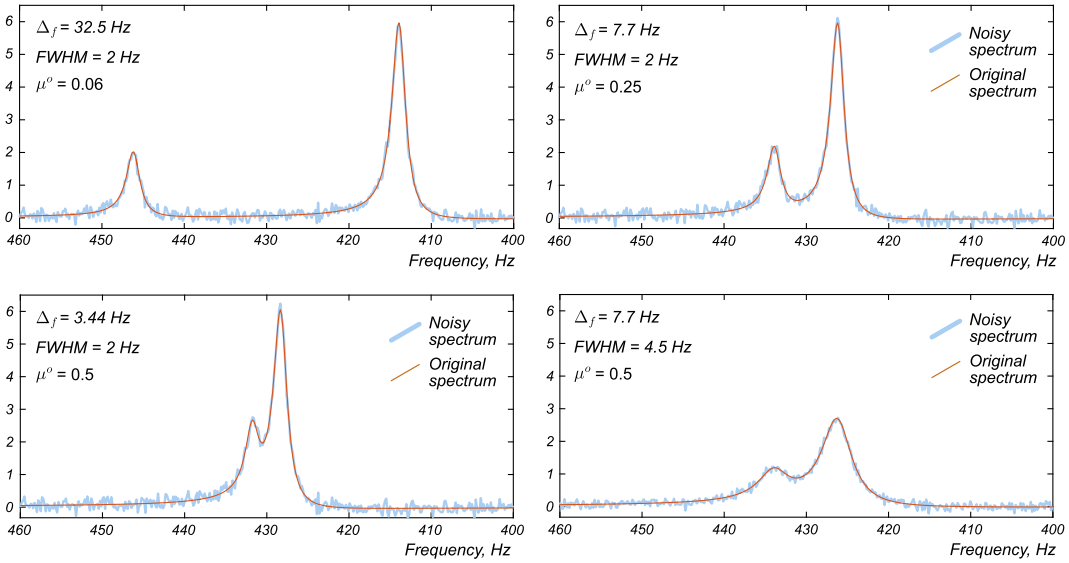

Fig. 2. Simulated examples of spectra containing two peaks with intensities in the 3 : 1 ratio. The numbers on each plot indicate the difference in frequency between the peaks Δf, their width FWHM, and the resulting measure of overlap μ^o. In these examples, SNR = 0 dB.

4.1. Results of simulations

Before proceeding with data from real samples, we look at the performance of the studied methods in controlled simulated experiments. Specifically, we consider the simplest problem of estimating relative intensities of two separate peaks, and with this example, we study the robustness of different quantification methods to noise. Furthermore, by changing peaks' widths and frequencies, we look at the effects of their overlap, which we quantify with the inner product measure μ^o (please see Section 3 for detail). Several exemplar spectra used in this section are shown in Fig. 2. As the peaks approach each other or become wider, the parameter μ^o increases. The bottom plots in Fig. 2 demonstrate that two pairs of peaks with $\Delta_f = 3.44$ Hz and FWHM = 2 Hz, and $\Delta_f = 7.7$ Hz and FWHM = 4.5 Hz have the same value of $\mu^o = 0.5$, which characterizes the same degree of peak overlap in these spectra.

We start by simulating spectra of two peaks with fixed positions, such that $\Delta f = 3.44$ Hz, and width set to FWHM = 2 Hz, which results in $\mu^o \approx 0.5$ overlap (as in the bottom left plot in Fig. 2). We consider three cases of relative peaks' intensities, $1:1, 3:1$, and $19:1$. To compute the reported errors in the estimated mole fractions, we attribute these ratios to the intensities b in Eq. (2) and assume coefficients $c_1 = c_2 = 1$ in Eq. (1), and thus $\chi_1^{\text{true}} = \chi_2^{\text{true}} = 0.5$. That is, one may think about Fig. 2 as spectra of two chemical species present in the mixture in equal molar amounts, but having one and three magnetically equivalent active NMR nuclei. Next, we add white Gaussian noise to this data and vary its intensity. The same simulations are run 100 times with different noise realizations for each SNR level, and the average absolute errors of estimation, $|\widehat{\chi}_1 - \chi_1^{\text{true}}|$, are plotted in Fig. 3. The results of the peak integration correspond to the best case scenario with known exact positions and widths of the peaks (the integration windows of ± 32 FWHM are centered at the true peaks' frequencies; where they overlap, the integration boundary is set at the midpoint between the peaks). Nevertheless, Fig. 3 reveals a systematic error in this method when integrating a small peak overshadowed by a closely located strong one. Similarly, the HSVD algorithm cannot always faithfully identify the smallest peak in the noise floor and is more likely to fail at SNR < 3 dB. One may readily observe that the Bayesian approach is effective over the entire considered range of SNRs and leads to significant improvement over its competitors when the noise level increases.

In the second set of simulations, the widths of both peaks are again fixed at FWHM = 2 Hz, but their relative positions are allowed to vary leading to changing overlap (i.e. μ^o). The noise level is set to be equal to the level of the signal, i.e. $P_s = P_n$ and SNR = 0 dB. The quantification results in Fig. 4 reveal that the case of two very close peaks with similar intensities is the most challenging for both HSVD and the Bayesian approach, although the latter performs notably better. Quantification is most accurate

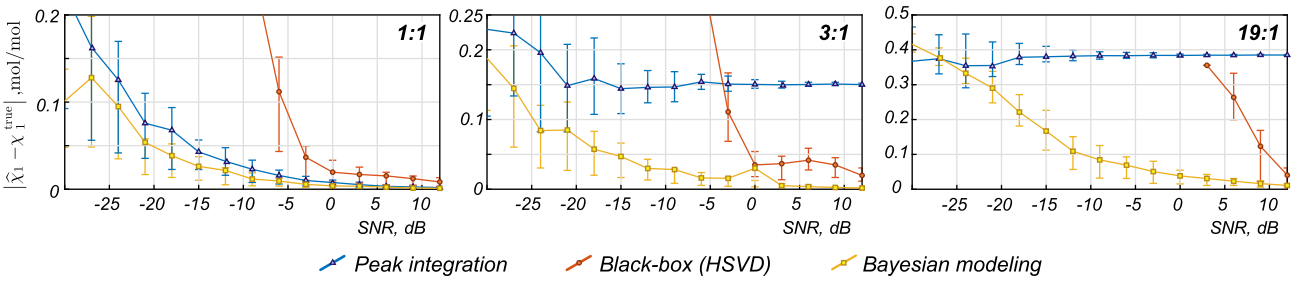

Fig. 3. Average absolute errors of estimating mole fractions in a simulated binary mixture with respect to SNR (assuming $\chi^{\text{true}} = 0.5$ in each case); the errorbars mark the first and the third quartiles in the simulated datasets with 100 realisations of random noise. In each case, the widths of both peaks are set to FWHM = 2 Hz and the distance between them to $\Delta f = 3.44$ Hz, which results in $\mu^o = 0.5$. Different plots correspond to different relative intensities of the peaks b_1/b_2, from left to right, $1:1, 3:1$, and $19:1$. The Bayesian modeling approach is effective over the entire considered range of SNRs.

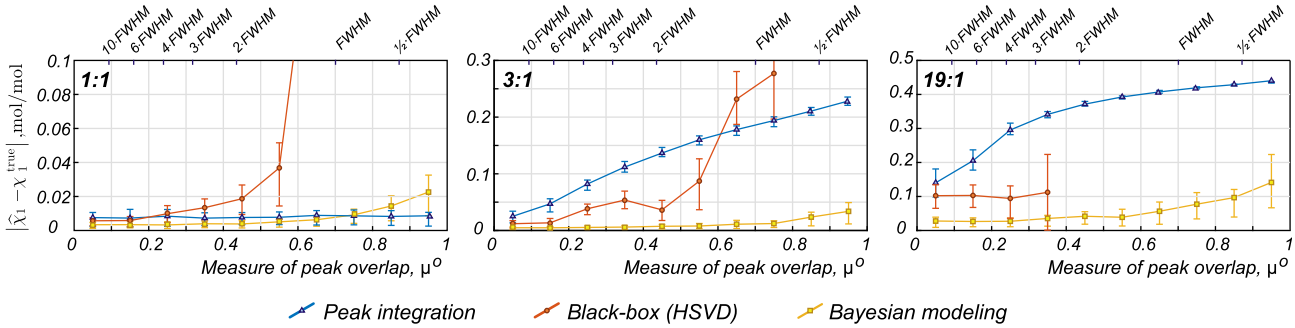

Fig. 4. Average absolute quantification errors in the example of two peaks with same widths but varying frequencies plotted with respect to the measure of peaks' overlap μ^o; the errorbars mark their first and the third quartiles. The second horizontal axis indicates the distance between the peaks in terms of their full widths at half maxima (FWHM). Different plots show cases of peaks with different relative intensities.

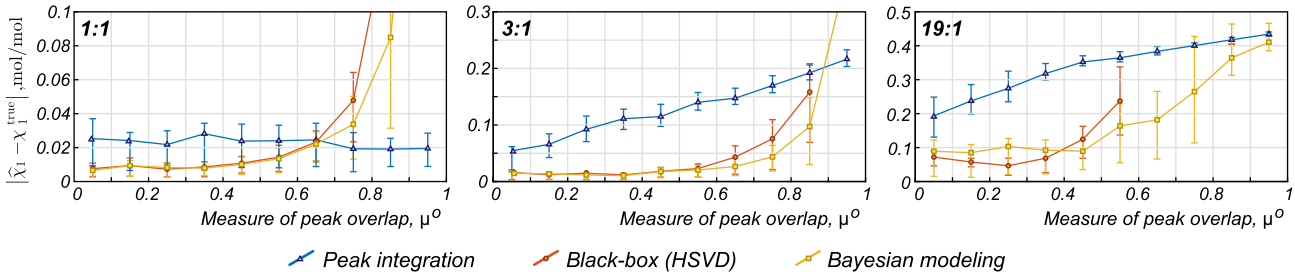

Fig. 5. Average absolute errors of quantification in the example of two peaks with randomly chosen positions and width; the errorbars mark their first and the third quartiles. The horizontal axis indicate the values of the measure of peak overlap μ^o, and different plots correspond to different relative peaks' intensities. SNR in these experiments is set to 0 dB.

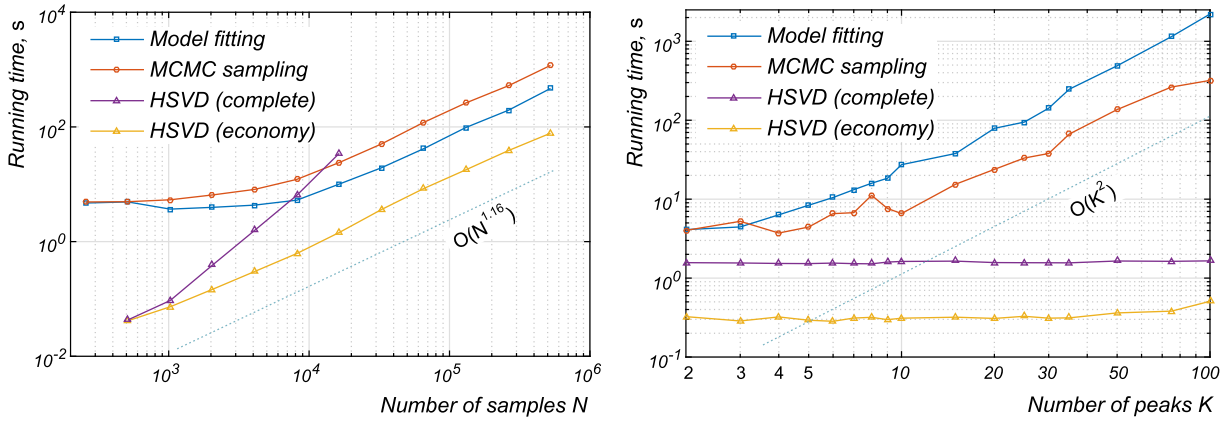

Fig. 6. An empirical analysis of computational complexity of the studied methods with respect to the number of samples in the dataset N and the number of fitted peaks K. Left: $N = 2^8, \ldots, 2^{19}, K = 3$; right: $N = 2^{12}, K = 2, \ldots, 100$. The model fitting and the MCMC sampling steps of our method, while taking notably longer to run than the HSVD algorithm, scale similarly with the number of samples.

when separation between the peaks is higher than their FWHM, but the estimation quality degrades quickly after a certain critical value of μ^o (≈ 0.4 for HSVD, and ≈ 0.8 for the Bayesian method). This transition is notably more gradual if the peaks' intensities differ substantially. The breaking point of the integration method obviously depends on one's ability to distinguish two overlapping peaks in the noisy spectrum and to specify the integration boundaries properly, which cannot be modeled in these idealized examples. Furthermore, when the peaks have the same intensities, and the integration boundary is chosen at the middle point between them, as we did here, the effect of their mutual overlap effectively cancels in the integrals. For that reason, the peak integration method performs equally well in the entire range of peak overlap when a mixture with relative peak intensities of $1:1$ is analyzed.

In practice, when the true peaks' parameters are unknown, we would expect the peak integration method to perform worse. Similar trends are observed when the peaks are allowed to change their positions and widths simultaneously (see Fig. 5), but with the HSVD algorithm performing almost as well as the Bayesian method in this case.

Finally, in Fig. 6 we study the experimental computational complexity of our method, where we consider the model fitting and the optional MCMC sampling steps separately; we compare them with the HSVD algorithm run with the complete decomposition of the Hankel matrix and also using the "economy" SVD algorithm in MATLAB. First, we generate datasets with $K = 3$ peaks and different numbers of time samples N. In the second example, the number of samples is held fixed ($N = 2^{12}$), but the number of resonances

changes instead. During the model fitting, we optimize the chemical shifts and decay rates for each peak in the spectrum separately and repeat this process four times to ensure convergence. The multivariate posterior function is then sampled about this optimum with the Goodman-Weare MCMC sampler [40] over all $2K$ parameters simultaneously; the number of MCMC samples is chosen as $2500K$ to account for increasing complexity of the posterior when more peaks are added to the spectrum.

We note that for relatively large numbers of points ($N > 2^{13}$), the complexities of both steps of our approach as well as the economy HSVD algorithm scale similarly with n, approximately as $\mathrm{O}\left(N^{1.16}\right)$. Fitting a three-peak model to a dataset with 2^{14} points takes less than 10 s, and the optional MCMC sampling accounts for ≈ 24 s. The complete SVD algorithm scales as $\mathrm{O}\left(N^2\right)$, as expected, but it cannot handle cases with more than 2^{14} points due to memory constraints. The economy HSVD algorithm executes in only 1.4 s for $N = 2^{14}$ but cannot run if the number of points exceeds 2^{19}; the model fitting method has notably lower memory footprint for large N.

With more peaks present in the spectrum, the increase of complexity is dominated by operations on $K \times K$ matrices (e.g. $\mathbf{Z}^{\mathrm{H}}\mathbf{Z}$) as well as by the necessity to run more model fitting iterations and to obtain more MCMC samples of the higher-dimensional posterior. The HSVD algorithm is less affected by these circumstances and exhibits almost constant running time with respect to the number of peaks (1.5—1.9 s), whereas the duration of model fitting crucially depends on the number of optimized parameters and the number of iterations. In our experiments, its complexity scales approximately as $\mathrm{O}\left(K^{2.25}\right)$, and for the MCMC sampling, $\mathrm{O}\left(K^{1.75}\right)$. These empirical estimates are in agreement with previous theoretical analysis of a similar system with complexity $\mathrm{O}\left(NK^2 + K^3\right)$ [22].

To conclude, the results of simulations show that our model-based approach (which includes peak fitting and intensity estimation) is effective over a wide range of SNRs and is less susceptible to the problem of peak overlap than other algorithms. It quantitatively differentiates two peaks with overlap $\mu^o > 0.8$ – higher than the black-box HSVD algorithm. Most importantly, it can successfully operate even at very low signal-to-noise ratios (e.g. down to −20 dB), where peak integration becomes critically affected by the uncertainty in the signal phase. We confirm these findings with experimental results in the upcoming sections.

4.2. An example with known peak ratios

To validate our quantification approach in an experimental setting, we look at peaks attributed to different nuclei of the same compound, creatine. The ratios of the peaks' intensities are determined by the molecular structure and thus are known exactly. From the quantification point of view, this effectively eliminates the influence of any gravimetric errors possible during sample preparation and provides a perfect benchmark for an unbiased comparison of different algorithms. Creatine contains an ethyl and a methyl group that are not coupled, and thus its proton spectrum exhibits two single peaks with intensities in the $2:3$ ratio. We define $\chi_{\mathrm{CH_3}}$ as the fraction of the number of $\mathrm{CH_3}$ groups to the number of $\mathrm{CH_3}$ and $\mathrm{CH_2}$ groups and compare our found estimates with the true value $\chi^{\mathrm{true}}_{\mathrm{CH_3}} = 0.5$. High SNR in the acquired data (SNR = 52.9 dB in the example below) means that any errors in the estimates are less likely attributed to the effect of noise but result from other sources, such as lineshape imperfections caused by magnetic field inhomogeneity. Thus, this example allows us to fully appreciate the effectiveness of the lineshape correction mechanism embedded in our model.

Fig. 7 shows an acquired FID and the corresponding ^{1}H spectrum of creatine in $\mathrm{D_2O}$. One can readily note the deviation of the FID envelope from the ideal exponential decay, and the same effect manifests itself in the frequency domain at the bases of the peaks. Including the lineshape correction term in the model leads to accurate fitting of the data. In this example, a sixth-order polynomial in Eq. (3) allows us to reduce the absolute estimation error by more than an order of magnitude (from $4 \cdot 10^{-3}$ mol/mol to $3 \cdot 10^{-4}$ mol/mol) when compared to the model that does not take into account lineshape imperfections. Further increase of the model complexity does not lead to any noticeable improvement. We observe the non-zero imaginary part in the resulting correcting term $\mathrm{s}(t)$. Effectively, it plays the role of an additional phase correction and is essential for fitting asymmetric peaks, which is otherwise impossible with simpler (real-valued) Gaussian or Voigt models. In this example, where peaks are well separated and the SNR is high, the mole fractions estimated with the peak integration approach and the HSVD algorithm are $\chi^{\mathrm{FT}}_{\mathrm{CH_3}} = 0.5003$ mol/mol and $\chi^{\mathrm{HSVD}}_{\mathrm{CH_3}} = 0.498$ mol/mol, respectively (resulting in the corresponding absolute errors of $3 \cdot 10^{-4}$ mol/mol and $2 \cdot 10^{-3}$ mol/mol). The results of peak integration, however, critically depend on the accuracy of phasing; our approach does not have this shortcoming. Furthermore, we process the data with another Bayesian model-based approach, CRAFT [51], which is a part of the VnmrJver.4.2 software used to acquire this dataset; this results in $\chi^{\mathrm{CRAFT}}_{\mathrm{CH_3}} = 0.505$ mol/mol. We note, however, that this package is designed primarily for analyzing complex multicomponent spectra with many overlapping peaks (e.g. metabolites) and may be suboptimal for our simpler problem. It also does not model non-ideal line shapes.

4.3. Dilution series of an acetonitrile-dioxane mixture with heavy water

Our next example concerns a binary mixture of acetonitrile and dioxane. The main goal of this set of experiments is to study the performance of quantification algorithms under varying noise conditions in a practical setting. The errors reported in this and the next section are computed with respect to gravimetrically obtained values. Fig. 8 shows examples of spectra of the studied mixture acquired on a high-field Bruker spectrometer with a cryogenically cooled probe and on a medium-field Spinsolve instrument.

The estimation results of the mole fractions of dioxane with respect to the SNR are plotted in Fig. 9. Here we aggregate results obtained in different experiments (^{1}H,^{13}C, with varying number of scans and flip angles) to reveal leading trends. On the entire range of SNRs, our Bayesian estimation leads to slightly more accurate results than both peak integration and the HSVD algorithm. Since it does not rely on any data preprocessing, our method is successful even at very high noise levels that typically hinder precise phasing and integration. Furthermore, at SNRs lower than ≈ -5 dB, the black-box HSVD algorithm that does not assume any prior information about the signal struggles to find the correct harmonic components, which makes subsequent peak assignment impossible. However, at high SNR levels (e.g. SNR > 60 dB in proton NMR using cryo high-field probe) all three methods perfectly tackle the simple task of analyzing two non-overlapping peaks. All computational methods are generally in a good agreement on the estimated $\widehat{\chi}_{\mathrm{Diox}}$ and achieve very low estimation errors with respect to the gravimetrically calculated values. With SNR > 40

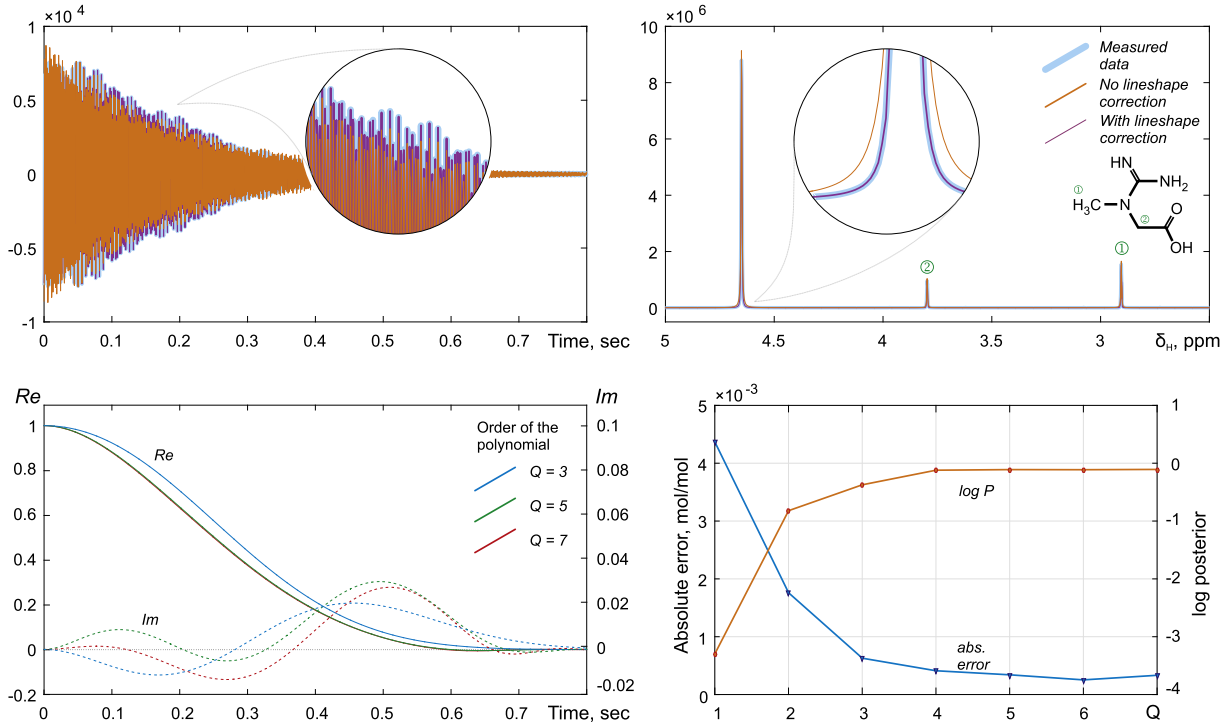

Fig. 7. Top: An FID signal and the corresponding spectrum of creatine in D_2O along with our model fitting results. Taking into account the lineshape imperfections with a sixth-order polynomial produces significantly better agreement between the model and the experimental data. Bottom, left: The real and imaginary parts of the lineshape correcting terms $s(t)$ in the fitted model for different orders of the polynomial in Eq. (3) (please note the difference in the scales for real and imaginary terms). Bottom, right: the improvement of quantification results with increasing model complexity (polynomial order Q). Note the that $Q = 1$ corresponds to zero and first-order phase correction only. The goodness of model fit is measured with log of (unnormalized) posterior function in Eq. (11). In these examples, SNR = 52.9 and $\mu^o = 0.004$.

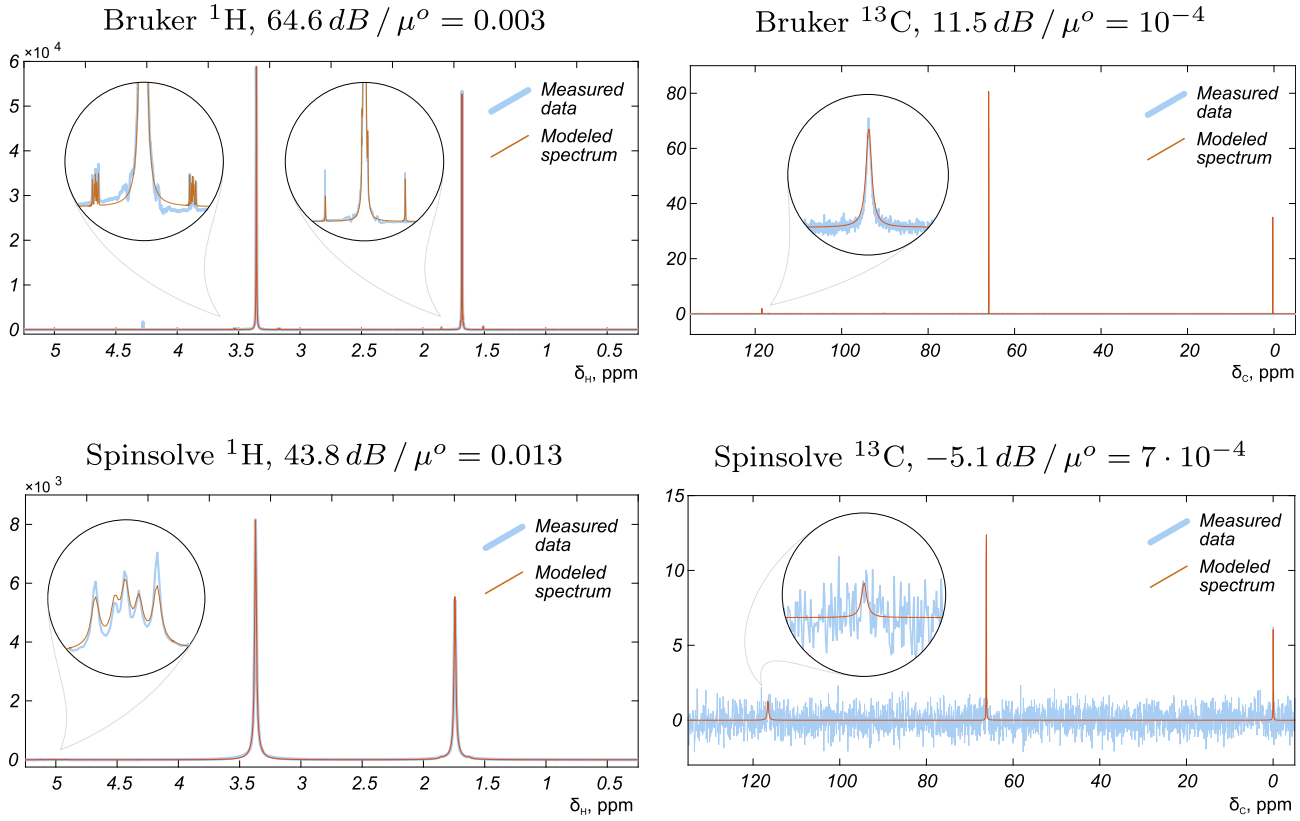

Fig. 8. Left: Examples of ^{1}H NMR spectra of the mixture of acetonitrile and dioxane diluted with D_2O. Right: Examples of ^{13}C spectra of the same sample shown without line broadening (exponential broadening was applied to improve quantification with all methods). Numbers indicate estimated SNR and the measure of overlap μ^o.

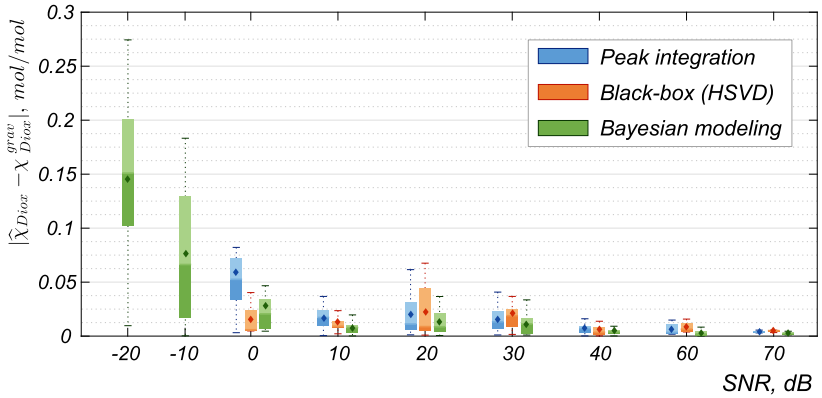

Fig. 9. The results of estimating mole fraction of dioxane χ_{Diox} in a mixture with acetonitrile diluted with heavy water. This plot aggregates data from a series of experiments run on different instruments and modes (^{1}H and ^{13}C). For each experiment, the absolute errors are computed with respect to the gravimetric value $\chi^{\text{grav}}_{\text{Diox}} = 0.344$ mol/mol and averaged over ±5 dB windows in SNR (15–20 points in each case); their centers are indicated on the horizontal axis. Lineshape correction in our method was applied for all data at SNR > 20 dB. The lines on the bars correspond to, from bottom to top, the first quartile q_1, sample median, and the third quartile q_3; the whiskers on each side mark 1.5 of interquartile range $IQR = q_3 - q_1$, and the diamonds indicate sample means.

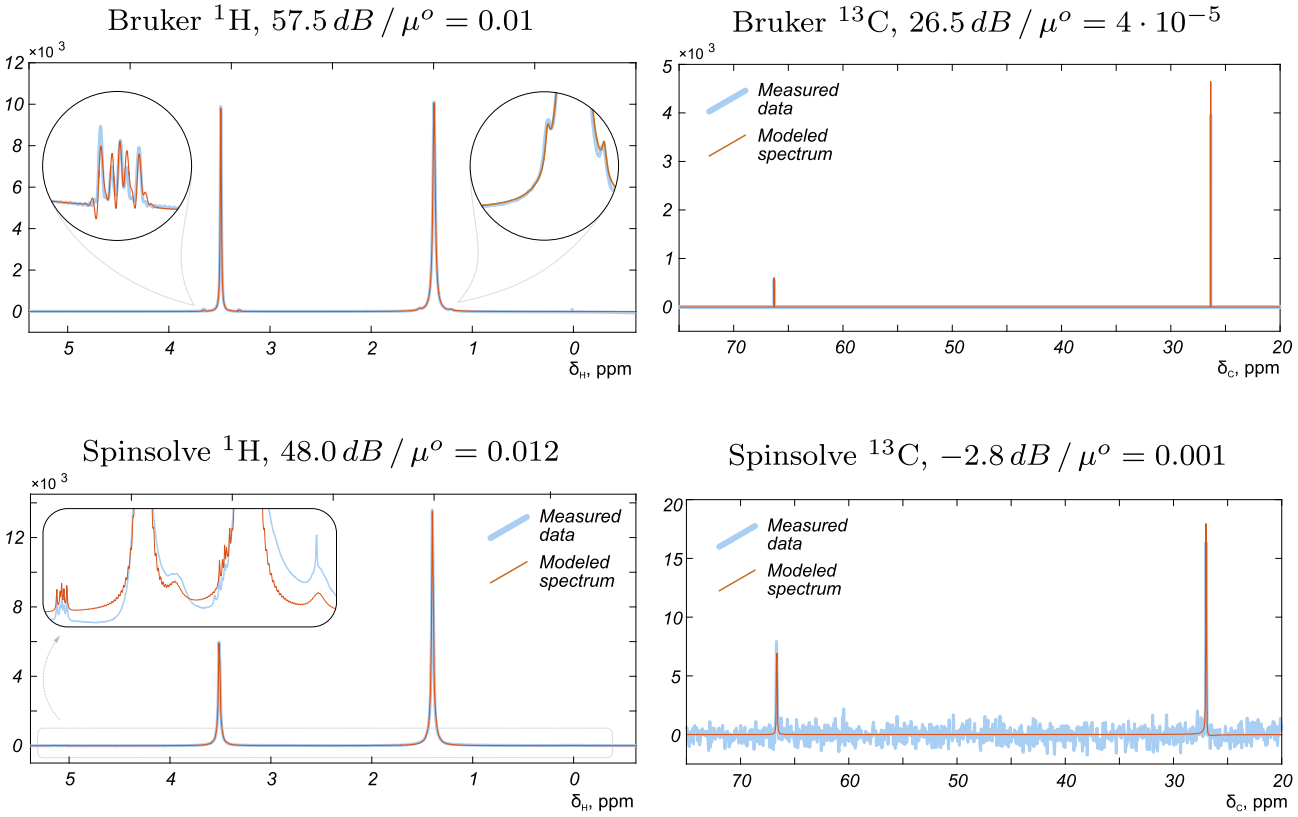

Fig. 10. Left: Examples of ^{1}H NMR spectra of the mixture of cyclohexane and dioxane with gravimetric molar fraction of the latter $\chi^{\text{grav}}_{\text{Diox}} = 0.399$ mol/mol. Right: Examples of ^{13}C spectra of the same sample averaged over four scans. These spectra were measured on a high-field Bruker instrument with cryogenically cooled probe (top row) and on a medium-field Spinsolve instrument (bottom row). Numbers indicate estimated SNR and the measure of overlap μ^o.

dB, the lineshape correction in our model becomes especially effective and allows us to notably improve the results.

4.4. Binary mixtures of cyclohexane and dioxane

Finally, we consider binary mixtures of cyclohexane and dioxane with different compositions. Exemplar spectra of one of these samples are shown in Fig. 10 along with fitted models found with our approach. The results of quantification with different methods are analyzed in Fig. 11. For each of the six samples, absolute errors with respect to the corresponding gravimetric values are averaged over multiple experiments of the same type (proton or carbon) run on either of the instruments. In most cases, all considered methods agree on the estimated values of mole fractions. Their correlation with respect to the gravimetric values is measured with the squared Pearson coefficient r^2 – a measure of linear correlation between two variables with $r^2 = 1$ for perfectly correlated variables and $r^2 = 0$ in case of absence of linear correlation; it is indicated in the left top corner of the plots. We note that the proposed Bayesian approach usually produces tighter estimates showing

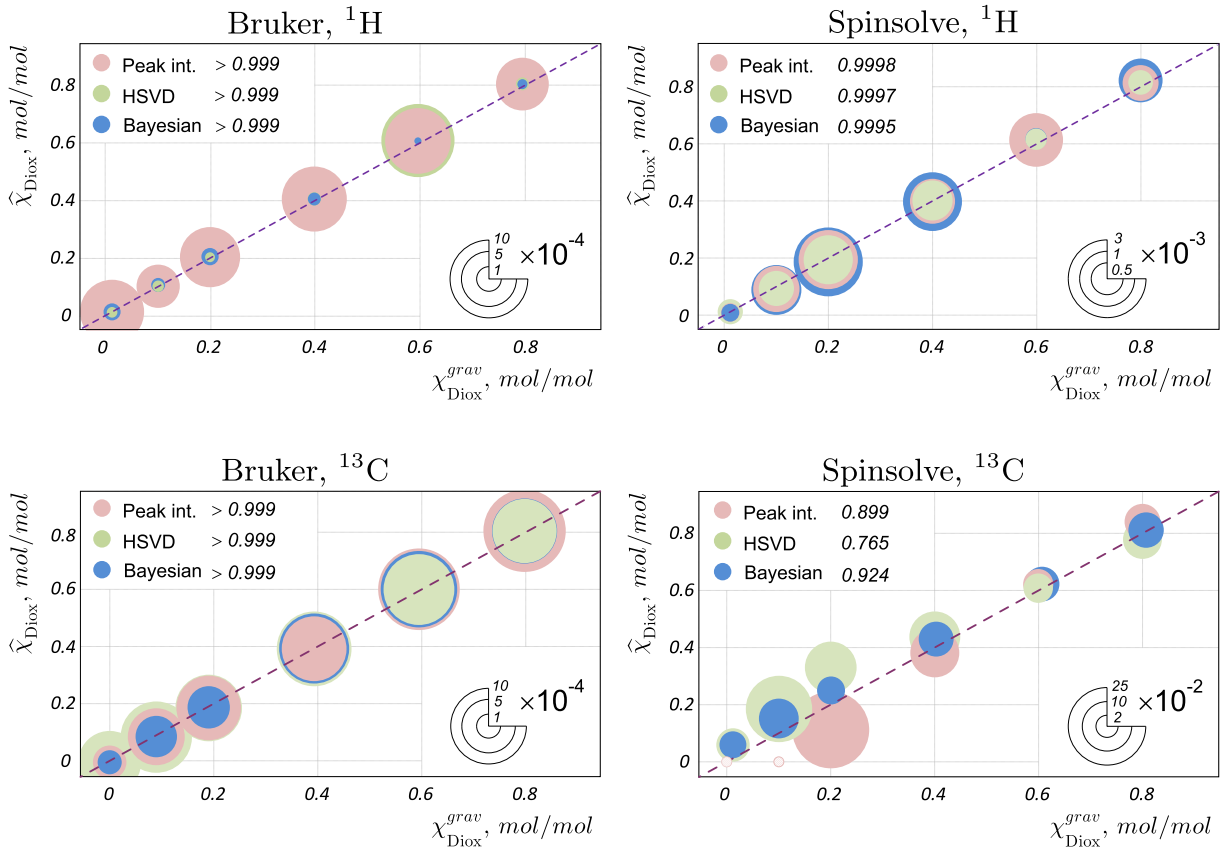

Fig. 11. Results of estimating mole fractions of dioxane in six different mixtures with cyclohexane. The centers of the bubbles indicate the estimated mole fractions χ_{Diox} plotted against the gravimetric values (averaged over 7–10 experiments for each sample); their areas are proportional to standard deviations of the estimates (please note that for improved visibility, plots have different scales). Reliable phasing and peak integration of medium-field ^{13}C spectra of samples with low dioxane concentration are impossible due to high levels of noise. Numbers in the top left corner of each plot indicate the squared Pearson correlation coefficient r^2 computed with respect to the gravimetric values.

high correlation with the gravimetric values. The strong deviation of the peak integration method and the HSVD algorithm seen in the ^{13}C data acquired on the Spinsolve instruments is primarily due to high levels of noise in these experiments (SNR = 0 . . . 10 dB). This is especially conspicuous with samples having lower fraction of dioxane, whose four carbon atoms contribute to the peak of lower intensity than that of cyclohexane.

As the relative error of quantification decreases below 1%, it is important to consider ^{13}C satellite peaks in uncoupled proton spectra. Although, in many practical cases their contribution cancels in the resulting mole fractions, at lower field strength and decreased spectral resolution, satellites of one component may fall onto the main peak of another (e.g. as happens in the cyclohexane/dioxane and acetonitrile/dioxane mixtures at the 43 MHz operating frequency of the Spinsolve instruments). Typically, such a situation would be hard to detect and resolve in the traditional peak integration approach, but these additional peaks can be easily handled as extra components in our model, even where they overlap (please see Figs. 8 and 10 for examples of fitting ^{13}C satellites). In some cases, notably in dioxane, carbon satellites have rather complicated patterns. Their inclusion into the model, unnecessarily complicates fitting. The application of ^{13}C-decoupled sequences would enable the use of much simpler models. On the other hand, it requires a more complicated pulse sequence and longer relaxation delays between repeated measurements. A study of the effect of ^{13}C-decoupled sequences on the performance of the different quantification approaches, however, was not in the scope of the present study and will be considered in future work.

5. Conclusions

This paper reviews the problem of signal processing and quantification in NMR spectroscopy, particularly with the goal of estimating concentrations of chemicals in mixtures. The proposed approach is based on a time-domain model of a general NMR signal, whose parameters are estimated with methods of Bayesian statistics. This approach seamlessly incorporates any prior knowledge about the studied system, such as spectral patterns, chemical shifts and widths of the peaks. Furthermore, our model directly includes the baseline and phase correction terms and obviates the need to perform these difficult data preprocessing steps separately. This not only simplifies the workflow, but most importantly, improves the consistency of results in comparison with the traditional peak integration method and other algorithms that operate on processed spectra and thus are heavily affected by the influence of user input. The robustness to noise of our method allows it to successfully operate on noisy data and achieve 0.1 mol/mol accuracy of mole fraction estimation in cases where precise phasing is practically impossible (e.g. SNR < -5 dB). Finally, our model automatically adjusts to lineshape distortions possibly caused by non-ideal homogeneity of the magnetic field or other factors and easily handles even mildly non-symmetric peaks, further improving the quantification results and bringing the absolute errors in mole fraction estimates to as low as $25 \cdot 10^{-5}$ mol/mol.

We remark that all examples in this paper were intentionally chosen to be very simple. Spectra with only a few well separated single peaks do not normally require sophisticated processing

algorithms and peak integration is the typical method of choice here. Indeed, we see that it performs very well at SNR > 60 dB and satisfactorily at SNR > 20 dB. When the noise increases further, but the peaks are sufficiently well resolved (e.g. $\mu^0 < 0.5$), they may be detected with a black-box algorithm and then quantified with the least-squares fit. Such approach is less susceptible to peak overlap but may detect spurious peaks or miss valid components. The unreliability of the black-box method poses a significant challenge in practical applications, often making correct peak assignment impossible.

The results of the Bayesian modeling are usually in good agreement with the other two methods and with the gravimetric values or the ground truth, where available. At SNR > 40 dB, it achieves similar quantification errors as the peak integration approach (as low as 0.005—0.01 mol/mol with respect to gravimetric values in real mixtures and on the order of 10^{-4} mol/mol when comparing peaks of known intensities); the deviation of estimated mole fractions between different measurements of the same sample are often much lower with our method. However, it reveals its full potential at very low SNRs (e.g. SNR < 0 dB) and by easily disentangling peaks with up to $\mu^o = 0.8$ overlap. In such cases, using prior information available about the studied system is essential for accurate quantification.

Thus, our model-based approach has the potential to facilitate robust quantitative analysis of difficult spectra (e.g. more complicated mixtures with many overlapping peaks acquired at low SNR). Its independence on the user input makes it a perfect choice for processing large complex datasets with many spectra, e.g. obtained in reaction and process monitoring. Thus, the method helps to expand the range of application of quantitative NMR analysis significantly.

Acknowledgements

The authors would like to thank Silvie Müller, Anne Friebel, and Richard Behrens for their help with preparing samples and acquiring data. Financial support of the present study by the New Zealand Ministry of Business, Innovation and Employment and Deutsche Forschungsgemeinschaft DFG (project number: HA 7582/1-1) is gratefully acknowledged.

References

[1] É.J. Kibrik, O. Steinhof, G. Scherr, W.R. Thiel, H. Hasse, On-line NMR spectroscopic reaction kinetic study of urea-formaldehyde resin synthesis, Ind. Eng. Chem. Res. 53 (32) (2014) 12602–12613, https://doi.org/10.1021/ie5001746. <http://pubs.acs.org/doi/abs/10.1021/ie5001746>.

[2] A. Brächer, R. Behrens, E. von Harbou, H. Hasse, Application of a new microreactor 1H NMR probe head for quantitative analysis of fast esterification reactions, Chem. Eng. J. 306 (2016) 413–421, https://doi.org/10.1016/j.cej.2016.07.045. <http://linkinghub.elsevier.com/retrieve/pii/S1385894716309913>.

[3] M.A. Bernstein, M. Stefinovic, C.J. Sleigh, Optimising reaction performance in the pharmaceutical industry by monitoring with NMR, Magn. Reson. Chem. 45 (7) (2007) 564–571, https://doi.org/10.1002/mrc.2007. <http://doi.wiley.com/10.1002/mrc.2007>.

[4] S.K. Küster, E. Danieli, B. Blümich, F. Casanova, High-resolution NMR spectroscopy under the fume hood, PCCP 13 (29) (2011) 13172–13176, https://doi.org/10.1039/c1cp21180c. <http://xlink.rsc.org/?DOI=c1cp21180c>.

[5] T.H. Rehm, C. Hofmann, D. Reinhard, H.-J. Kost, P. Löb, M. Besold, K. Welzel, J. Barten, A. Didenko, D.V. Sevenard, B. Lix, A.R. Hillson, S.D. Riegel, Continuous-flow synthesis of fluorine-containing fine chemicals with integrated benchtop NMR analysis, React. Chem. Eng. 2 (3) (2017) 315–323, https://doi.org/10.1039/C7RE00023E. <http://xlink.rsc.org/?DOI=C7RE00023E>.

[6] M.V. Silva Elipe, R.R. Milburn, Monitoring chemical reactions by low-field benchtop NMR at 45 MHz: pros and cons, Magn. Reson. Chem. 54 (6) (2016) 437–443, https://doi.org/10.1002/mrc.4189.

[7] K. Meyer, S. Kern, N. Zientek, G. Guthausen, M. Maiwald, Process control with compact NMR, TrAC – Trends Anal. Chem. 83 (Part A) (2016) 39–52, https://doi.org/10.1016/j.trac.2016.03.016. <https://doi.org/10.1016/j.trac.2016.03.016>.

[8] S.M. Ackermann, K. Dolsophon, Y.B. Monakhova, T. Kuballa, H. Reusch, T. Thongpanchang, M. Bunzel, D.W. Lachenmeier, Automated multicomponent analysis of soft drinks using 1D 1H and 2D 1H-1H J-resolved NMR spectroscopy, Food Anal. Methods 10 (3) (2017) 827–836, https://doi.org/10.1007/s12161-016-0643-y. <http://link.springer.com/10.1007/s12161-016-0643-y>.

[9] S. Ravanbakhsh, P. Liu, T.C. Bjorndahl, R. Mandal, J.R. Grant, M. Wilson, R. Eisner, I. Sinelnikov, X. Hu, C. Luchinat, R. Greiner, D.S. Wishart, Accurate, fully-automated NMR spectral profiling for metabolomics, PLoS One 10 (7) (2015) e0132873, https://doi.org/10.1371/journal.pone.0132873. <http://linkinghub.elsevier.com/retrieve/pii/S002437951000368X>.

[10] E. Kriesten, F. Alsmeyer, A. Bardow, W. Marquardt, Fully automated indirect hard modeling of mixture spectra, Chemomet. Intell. Lab. Syst. 91 (2) (2008) 181–193, https://doi.org/10.1016/j.chemolab.2007.11.004.

[11] F. Alsmeyer, H.-J. Koß, W. Marquardt, Indirect spectral hard modeling for the analysis of reactive and interacting mixtures, Appl. Spectrosc. 58 (8) (2004) 975–985, https://doi.org/10.1366/0003702041655368. <http://journals.sagepub.com/doi/10.1366/0003702041655368>.

[12] N. Zientek, C. Laurain, K. Meyer, A. Paul, D. Engel, G. Guthausen, M. Kraume, M. Maiwald, Automated data evaluation and modelling of simultaneous 19 F- 1 H medium-resolution NMR spectra for online reaction monitoring, Magn. Reson. Chem. 54 (6) (2016) 513–520, https://doi.org/10.1002/mrc.4216. <http://doi.wiley.com/10.1002/mrc.4216>.

[13] T. Schoenberger, S. Menges, M.A. Bernstein, M. Pérez, F. Seoane, S. Sýkora, C. Cobas, Improving the performance of high-precision qNMR measurements by a double integration procedure in practical cases, Anal. Chem. 88 (7) (2016) 3836–3843, https://doi.org/10.1021/acs.analchem.5b04911.

[14] R. Kumaresan, D. Tufts, Estimating the parameters of exponentially damped sinusoids and pole-zero modeling in noise, IEEE Trans. Acoust., Speech Signal Process. 30 (6) (1982) 833–840, https://doi.org/10.1109/TASSP.1982.1163974.

[15] S.Y. Kung, K.S. Arun, D.V.B. Rao, State-space and singular-value decomposition-based approximation methods for the harmonic retrieval problem, J. Opt. Soc. Am. 73 (12) (1983) 1799, https://doi.org/10.1364/JOSA.73.001799. <https://www.osapublishing.org/josa/abstract.cfm?uri=josa-73-12-1799>.

[16] L. Vanhamme, A. van den Boogaart, S. van Huffel, Improved method for accurate and efficient quantification of MRS data with use of prior knowledge, J. Magn. Reson. 129 (1) (1997) 35–43, https://doi.org/10.1006/jmre.1997.1244 (San Diego, Calif.: 1997) <http://europepmc.org/abstract/med/9405214>.

[17] H. Ratiney, Y. Coenradie, S. Cavassila, D. Van Ormondt, D. Graveron-Demilly, Time-domain quantitation of 1H short echo-time signals: background accommodation, Magn. Reson. Mater. Phys., Biol. Med. 16 (6) (2004) 284–296, https://doi.org/10.1007/s10334-004-0037-9.

[18] J.-B. Poullet, D.M. Sima, A.W. Simonetti, B.D. Neuter, L. Vanhamme, P. Lemmerling, S.V. Huffel, An automated quantitation of short echo time MRS spectra in an open source software environment: AQSES, NMR Biomed. 20 (2007) 493–504, https://doi.org/10.1002/nbm.1112.

[19] S.W. Provencher, Automatic quantitation of localized in vivo1h spectra with lcmodel, NMR Biomed. 14 (4) (2001) 260–264, https://doi.org/10.1002/nbm.698. <https://doi.org/10.1002/nbm.698>.

[20] G.L. Bretthorst, Bayesian Spectrum Analysis and Parameter Estimation, 1988.

[21] D.V. Rubtsov, J.L. Griffin, Time-domain Bayesian detection and estimation of noisy damped sinusoidal signals applied to NMR spectroscopy, J. Magn. Reson. 188 (2) (2007) 367–379, https://doi.org/10.1016/j.jmr.2007.08.008. <http://linkinghub.elsevier.com/retrieve/pii/S1090780707002467>.

[22] A.G. Wilson, Y. Wu, D.J. Holland, S. Nowozin, M.D. Mantle, L.F. Gladden, A. Blake, Bayesian Inference for NMR Spectroscopy with Applications to Chemical Quantification. Available from: arXiv preprint <arXiv:1402.3580>.

[23] J.F. Kielkopf, New approximation to the Voigt function with applications to spectral-line profile analysis, J. Opt. Soc. Am. (1917–1983) 63 (1973) 987–995.

[24] W.C. Hutton, G.L. Bretthorst, J.R. Garbow, J.J. Ackerman, High dynamic-range magnetic resonance spectroscopy (MRS) time-domain signal analysis, Magn. Reson. Med. 62 (4) (2009) 1026–1035, https://doi.org/10.1002/mrm.22084. <http://doi.wiley.com/10.1002/mrm.22084>.

[25] S. Ye, E. Aboutanios, Efficient peak extraction of proton NMR spectroscopy using lineshape adaptation, in: 2014 IEEE International Conference on Acoustics, Speech and Signal Processing (ICASSP), IEEE, 2014, pp. 5661–5665, https://doi.org/10.1109/ICASSP.2014.6854687. <http://ieeexplore.ieee.org/document/6854687>/.

[26] J.B. Poullet, D.M. Sima, S. Van Huffel, MRS signal quantitation: a review of time- and frequency-domain methods, J. Magn. Reson. 195 (2) (2008) 134–144, https://doi.org/10.1016/j.jmr.2008.09.005.

[27] Y. Hiltunen, M. Ala-Korpela, J. Jokisaari, S. Eskelinen, K. Kiviniitty, M. Savolainen, Y.A. Kesäniemi, A lineshape fitting model for 1h nmr spectra of human blood plasma, Magn. Reson. Med. 21 (2) (1991) 222–232, https://doi.org/10.1002/mrm.1910210207. <https://doi.org/10.1002/mrm.1910210207>.

[28] R. Laatikainen, M. Niemitz, U. Weber, J. Sundelin, T. Hassinen, J. Vepsäläinen, General strategies for total-lineshape-type spectral analysis of NMR spectra using integral-transform iterator, J. Magn. Reson., Ser. A 120 (1) (1996) 1–10, https://doi.org/10.1006/jmra.1996.0094. <http://www.sciencedirect.com/science/article/pii/S1064185896900947>.

[29] J. Slotboom, C. Boesch, R. Kreis, Versatile frequency domain fitting using time domain models and prior knowledge, Magn. Reson. Med. 39 (6) (1998) 899–911, https://doi.org/10.1002/mrm.1910390607. <https://doi.org/10.1002/mrm.1910390607>.

[30] G. Bretthorst, Bayesian analysis. I. Parameter estimation using quadrature NMR models, J. Magn. Reson. (1969) 88 (3) (1990) 533–551, https://doi.org/

10.1016/0022-2364(90)90287-J. <http://linkinghub.elsevier.com/retrieve/pii/002223649090287J>.
[31] G. Bretthorst, Bayesian analysis. III. Applications to NMR signal detection, model selection, and parameter estimation, J. Magn. Reson. (1969) 88 (3) (1990) 571–595, https://doi.org/10.1016/0022-2364(90)90289-L. <http://linkinghub.elsevier.com/retrieve/pii/002223649090289L>.
[32] G. Bretthorst, Bayesian analysis. II. Signal detection and model selection, J. Magn. Reson. (1969) 88 (3) (1990) 552–570, https://doi.org/10.1016/0022-2364(90)90288-K. <http://linkinghub.elsevier.com/retrieve/pii/002223649090288K>.
[33] M. Bydder, Solution of a complex least squares problem with constrained phase, Linear Algebra Appl. 48 (Suppl. 2) (2010) 1–6, https://doi.org/10.1016/j.laa.2010.07.011. <http://www.sciencedirect.com/science/article/pii/S002437951000368X>.
[34] A. Zellner, On assessing prior distributions and Bayesian regression analysis using g-prior distributions, in: Bayesian Inference and Decision Techniques: Essays in Honor of Bruno de Finetti, 1986, pp. 233–243.
[35] I. Markovsky, On the complex least squares problem with constrained phase, SIAM J. Matrix Anal. Appl. 32 (3) (2011) 987–992, https://doi.org/10.1137/110826497. <https://doi.org/10.1137/110826497>.
[36] L. Dou, R. Hodgson, Bayesian inference and Gibbs sampling in spectral analysis and parameter estimation. i, Inverse Prob. 11 (5) (1995) 1069.
[37] L. Dou, R. Hodgson, Bayesian inference and Gibbs sampling in spectral analysis and parameter estimation. ii, Inverse Prob. 12 (1996) 121–137.
[38] M. Andrec, J.H. Prestegard, A metropolis Monte Carlo implementation of Bayesian time-domain parameter estimation: application to coupling constant estimation from antiphase multiplets, J. Magn. Reson. 130 (2) (1998) 217–232, https://doi.org/10.1006/jmre.1997.1304. <http://www.sciencedirect.com/science/article/pii/S1090780797913045>.
[39] W. Astle, M. De Iorio, S. Richardson, D. Stephens, T. Ebbels, A Bayesian model of NMR spectra for the deconvolution and quantification of metabolites in complex biological mixtures, J. Am. Stat. Assoc. 107 (500) (2012) 37–41, https://doi.org/10.1080/01621459.2012.695661, Available from: <arXiv:1105.220> <http://arxiv.org/abs/1105.2204>.
[40] J. Goodman, J. Weare, Ensemble samplers with affine invariance, Commun. Appl. Math. Comput. Sci. 5 (1) (2010) 65–80, https://doi.org/10.2140/camcos.2010.5.65.
[41] D. Foreman-Mackey, D.W. Hogg, D. Lang, J. Goodman, emcee: The MCMC Hammer, Publ. Astron. Soc. Pac. 125 (925) (2013) 306–312, https://doi.org/10.1086/670067, Available from: <arXiv:1202.366> <http://arxiv.org/abs/1202.3665>.
[42] S. Godsill, A. Doucet, M. West, Maximum a Posteriori Sequence Estimation Using Monte Carlo Particle Filters, 2001, https://doi.org/10.1023/A:1017968404964. <http://link.springer.com/article/10.1023/A:1017968404964>.
[43] A. Doucet, S.J. Godsill, C.P. Robert, Marginal maximum a posteriori estimation using Markov chain Monte Carlo, Stat. Comput. 12 (1) (2002) 77–84, https://doi.org/10.1023/A:1013172322619. <http://link.springer.com/article/10.1023/A:1013172322619>.
[44] H. Yan, J.C. Gore, The relation of HSVD to LPSVD for fitting time-domain signals, J. Magn. Reson. (1969) 80 (2) (1988) 324–327, https://doi.org/10.1016/0022-2364(88)90303-4. <http://linkinghub.elsevier.com/retrieve/pii/0022236488903034>.
[45] H. Barkhuijsen, R. de Beer, D. van Ormondt, Improved algorithm for noniterative time-domain model fitting to exponentially damped magnetic resonance signals, J. Magn. Reson. (1969) 73 (3) (1987) 553–557, https://doi.org/10.1016/0022-2364(87)90023-0. <http://www.sciencedirect.com/science/article/pii/0022236487900230>.
[46] F. Malz, H. Jancke, Validation of quantitative NMR, J. Pharm. Biomed. Anal. 38 (5) (2005) 813–823, https://doi.org/10.1016/j.jpba.2005.01.043. <http://linkinghub.elsevier.com/retrieve/pii/S0731708505001597>.
[47] H. Barkhuijsen, R. de Beer, D. van Ormondt, Improved algorithm for noniterative time-domain model fitting to exponentially damped magnetic resonance signals, J. Magn. Reson. (1969) 73 (3) (1987) 553–557, https://doi.org/10.1016/0022-2364(87)90023-0.
[48] S.-E. Fotinea, I. Dologlou, G. Carayannis, Decimation and SVD to estimate exponentially damped sinusoids in the presence of noise, in: Proc. of IEEE International Conference on Acoustics, Speech, and Signal Processing ICASSP-2001, vol. V, Salt Lake City, Utah, USA, 2001, pp. 3073–3076.
[49] A. Frieze, R. Kannan, S. Vempala, Fast Monte-Carlo algorithms for finding low-rank approximations, J. ACM 51 (6) (2004) 1025–1041, https://doi.org/10.1145/1039488.1039494. <http://doi.acm.org/10.1145/1039488.1039494>.
[50] D. Achlioptas, F. Mcsherry, Fast computation of low-rank matrix approximations, J. ACM 54 (2) (2007), https://doi.org/10.1145/1219092.1219097. <http://doi.acm.org/10.1145/1219092.1219097>.
[51] K. Krishnamurthy, CRAFT (complete reduction to amplitude frequency table) – robust and time-efficient Bayesian approach for quantitative mixture analysis by NMR, Magn. Reson. Chem. 51 (12) (2013) 821–829, https://doi.org/10.1002/mrc.4022.

Brächer et al., 2014

Reprinted with permission from: A. Brächer, S. Hoch, K. Albert, H.J. Kost, B. Werner, E. von Harbou, H. Hasse, Thermostatted micro-reactor NMR probe head for monitoring fast reactions, Journal of Magnetic Resonance, Volume 242, 2014, Pages 155-161, ISSN 1090-7807, DOI 10.1016/j.jmr.2014.02.013

Journal of Magnetic Resonance 242 (2014) 155–161

Contents lists available at ScienceDirect

Journal of Magnetic Resonance

journal homepage: www.elsevier.com/locate/jmr

Thermostatted micro-reactor NMR probe head for monitoring fast reactions

A. Brächer [a], S. Hoch [a,1], K. Albert [b], H.J. Kost [c], B. Werner [c,2], E. von Harbou [a,*], H. Hasse [a]

[a] University of Kaiserslautern, Kaiserslautern, Germany
[b] Eberhard Karls University, Tübingen, Germany
[c] Institut für Mikrotechnik Mainz GmbH, Mainz, Germany

ARTICLE INFO

Article history:
Received 18 December 2013
Revised 10 February 2014
Available online 1 March 2014

Keywords:
Online NMR spectroscopy
Micro-reaction technology
Capillary flow NMR
Reaction kinetics
Reaction monitoring
Thermostatted micro-reactor

ABSTRACT

A novel nuclear magnetic resonance (NMR) probe head for monitoring fast chemical reactions is described. It combines micro-reaction technology with capillary flow NMR spectroscopy. Two reactants are fed separately into the probe head where they are effectively mixed in a micro-mixer. The mixed reactants then pass through a capillary NMR flow cell that is equipped with a solenoidal radiofrequency coil where the NMR signal is acquired. The whole flow path of the reactants is thermostatted using the liquid FC-43 (perfluorotributylamine) so that exothermic and endothermic reactions can be studied under almost isothermal conditions. The set-up enables kinetic investigation of reactions with time constants of only a few seconds. Non-reactive mixing experiments carried out with the new probe head demonstrate that it facilitates the acquisition of constant highly resolved NMR signals suitable for quantification of different species in technical mixtures. Reaction kinetic measurements on a test system are presented that prove the applicability of the novel NMR probe head for monitoring fast reactions.

1. Introduction

NMR spectroscopy is a powerful tool as it facilitates non-invasive in situ analysis of complex fluid mixtures without sample preparation. The method has a high resolution and enables resolving species that are chemically similar. Contrary to most optical spectroscopy methods, no prior calibration is needed for quantitative analysis. Thus, even unstable intermediates can be quantified by NMR spectroscopy [1–3]. Furthermore, NMR spectroscopy is an excellent tool for identifying unknown components such as side products [4,5]. Online NMR techniques have the advantage that the liquid compositions during reactions or in equilibria are not disturbed by sampling and that the temperature and pressure can be maintained [2,6–8]. Thus, when complex reaction systems with unknown and/or unstable intermediates have to be monitored, online NMR spectroscopy is often not only the best choice but also the sole analytical method that will yield the desired detailed quantitative data, see e.g. [2,9–11].

Often, NMR tubes are used to monitor chemical reactions by NMR spectroscopy. This simple set-up, however, has many drawbacks, for example the long delay between external mixing of the reactants, inserting the tube into the NMR and starting the acquisition of the spectra. Furthermore, it is difficult to control the pressure and temperature within the NMR tube.

To overcome these disadvantages, conventional reactors have been coupled to NMR flow probes, for details; see e.g. Maiwald et al. [11,12]. The reaction mixture is pumped from the external reactor, typically a stirred tank reactor, through a sample loop to the NMR flow probe head, where the composition of the reacting mixtures is analyzed. Numerous studies using similar flow set-ups have been carried out by several groups; see e.g. [13–18]. Furthermore, this type of set-up was used for pharmaceutical research [14,19] and to investigate complex reaction networks from industrial organic chemistry [10,11,20,21,3].

The characteristics of flowing samples, e.g. the signal intensity and the resolution as a function of the flow rate were investigated for example by Sudmeier et al. [22] and Haner et al. [23]. As the quality of the NMR signal (e.g. signal-to-noise ratio, resolution of the spectra) is strongly influenced by the geometry of the radio frequency (RF) coil, e.g. planar, solenoidal or stripline design, and the diameter of the RF coil, these parameters were investigated and optimized in several studies [24–26]. As discussed by Webb [27] and Fratila and Velders [28] the miniaturization of the RF coils

* Corresponding author. Address: Laboratory of Engineering Thermodynamics, P.O. Box 3049, 67653 Kaiserslautern, Germany.
E-mail address: erik.vonharbou@mv.uni-kl.de (E. von Harbou).
[1] Present address: Bayer Technology Service GmbH, Leverkusen, Germany.
[2] Present address: Boehringer Ingelheim GmbH, Ingelheim, Germany.

http://dx.doi.org/10.1016/j.jmr.2014.02.013
1090-7807/

can have several advantages such as increasing sensitivity and decreasing mass limitations for detection.

The set-ups consisting of a combination of external reactors with NMR flow cells, however, have considerable disadvantages. For quantitative analysis, a certain residence time of the sample in the permanent magnetic field of the spectrometer (B_0 field) is required. Thus, the maximum flow rate in the sample loop is limited and thus there is a time delay between the moment when the sample leaves the external reactor and it is analyzed in the NMR probe head. Hence, the set-up with external reactors is difficult to apply for kinetic studies of reactions with time constants below approximately 10 min [11,12,29]. In order to enable investigations of fast reactions with online NMR spectroscopy, a novel NMR probe head was developed in the present work. Several groups have applied micro-reaction technology either in combination with conventional NMR cells (volume 60–120 μl) or with miniaturised NMR flow cells (volume from 50 μl down to picoliters) [30–39]. Because of differences in the quality of the micro-mixer, in the reactor volume, in the RF coil geometry, in the pressure and temperature range, and in the applied thermal management, the set-ups differ significantly in their performance. In many publications, however, no specifications are given concerning these parameters. Often, the temperature is controlled with air as cooling or heating medium, which is common for standard NMR probe heads. Even for studies of mildly exo- or endothermic reactions, this temperature control turns out to be insufficient in maintaining isothermal conditions. To our knowledge, the present work describes for the first time a design of a NMR probe head in which the whole flow path of the reactants is liquid thermostatted to ensure efficient thermostatisation of the reactants.

In this NMR probe head, a liquid thermostatted micro-mixer is coupled with a capillary NMR flow cell and mounted directly in the probe head. Hence, the residence time between mixing of the reactants and analysis in the NMR flow cell is significantly reduced compared to the set-up with external reactor. At the same time, the residence time within the B_0 field is sufficiently long so that quantitative studies of fast reactions in technical mixtures (highly concentrated solutions relevant to industrial applications) with time constants of only seconds can be studied. The focus of this work was to develop a robust measurement method, and an easy to use set-up and probe head which can be applied without long preparations and large adjustments in different laboratories and different spectrometers.

In this work, the design of the novel NMR probe head is presented in detail. After assessing the quality of the NMR measurements (signal-to-noise ratio, limit of detection, RF homogeneity), the novel NMR probe head was tested in two different studies. In the first study, measurements with a non-reacting mixture of acetone and ethanol were carried out to determine the resolution of acquired spectra and the accuracy of the probe head for quantitative concentration measurements in the flow mode. In the second study, the kinetics of the homogeneously catalyzed esterification of methanol with acetic acid were measured with the probe head both in the stopped flow and in the flow mode.

2. Micro-reactor probe head

2.1. Design

The basic units of the new probe head are the micro-mixer, the dwell unit, and the NMR flow cell. These units are mounted in a cylindrical block made of PEEK (poly(etheretherketone)). The probe head (i.e. the PEEK block) has a height of 80 mm and an outer diameter of 38 mm. PEEK was chosen as it is inert regarding most chemicals, it has good mechanical properties in a wide temperature range, and, in addition, is non-magnetic. The probe head is assembled together with the supply tubes in a housing (made of brass). Fig. 1 gives an overview of the assembled probe.

The probe head consists of five segments, which are shown in Fig. 2: bottom plate (I), micro-mixer (II), dwell unit (III), NMR flow cell (IV), and top plate (V). The bottom plate (I) is the connection between the feed tubes and the PEEK block. Screws reaching from the bottom plate (I) to the top plate (V) give stability to the whole block and apply the pressure needed for a proper sealing of the reactants and the thermostatting liquid. The two feed tubes of the reactants (both made of PEEK) are connected to passage channels, which are milled into the bottom plate (I) of the probe head, so that they enter the micro-mixer (II) separately. The micro-mixer is a crawler-type mixer developed by the Institut für Mikrotechnik Mainz (IMM), Germany [40]. A special design was tailored by the IMM for this probe head to meet the given requirements (flow rates, density, surface tension, etc. of the reactants). The micro-mixer consists of two PEEK plates with mixing channels on the micro-scale, which are fabricated via laser ablation. While passing through the micro-mixer, the two incoming flows are split and recombined 39 times to achieve an efficient mixing. The total volume of the micro-mixer is only 0.27 μl. The mixed fluid flows through a short capillary made of PEEK (outer diameter 1/16 in., length 23 mm), the dwell unit (see Fig. 3, III, vertical line). By using capillaries of different inner diameters (from 0.025 mm to 1.3 mm), it is possible to adjust the volume of the dwell unit and therefore the volume between mixer and NMR flow cell in a range of 18 μl to 48 μl. After having passed the dwell unit, the reactants enter the NMR flow cell (see Fig. 3, IV, horizontal line), which is oriented perpendicular to the B_0 field. It consists of a capillary made of silica glass (inner diameter 1 mm) with a total volume of 12 μl. A solenoidal micro-RF coil made of copper is wrapped around the

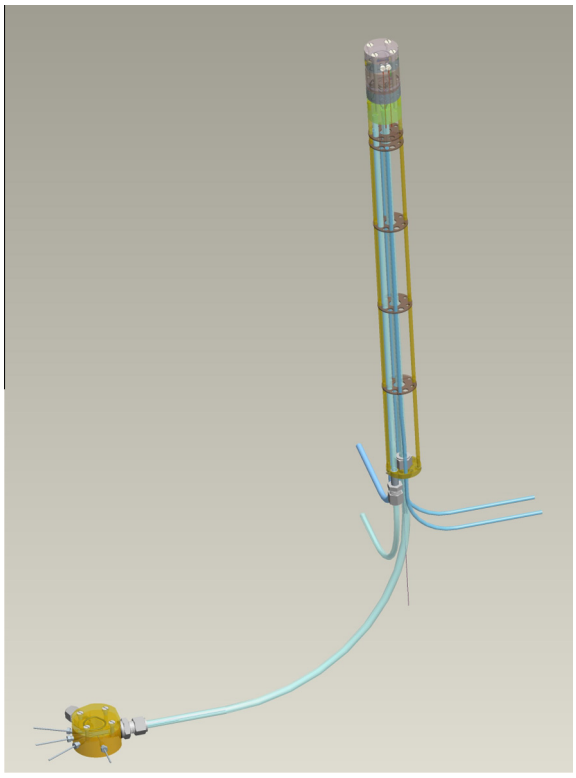

Fig. 1. Overview of the NMR probe including the micro-reactor probe head (top), supply lines (blue) and connection box for the feed and product lines (bottom left). (For interpretation of the references to color in this figure legend, the reader is referred to the web version of this article.)

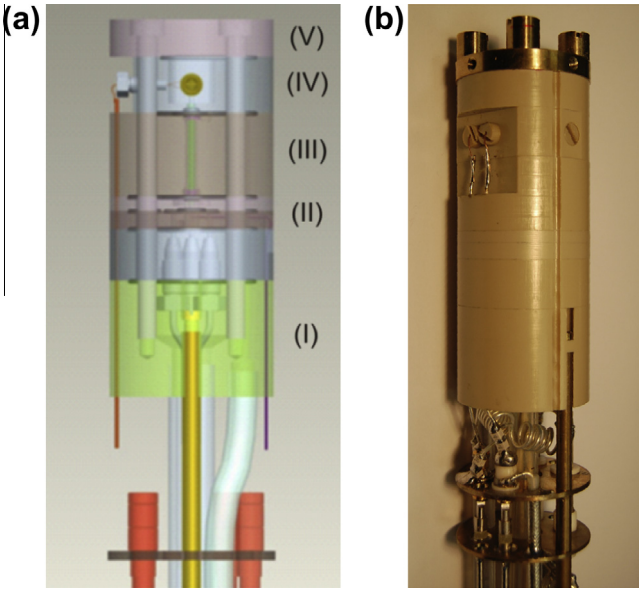

Fig. 2. (a) Drawing of the micro-reactor probe head (PEEK block) including bottom plate (I), micro-mixer plate (II), dwell unit (III), NMR flow cell (IV), and top plate (V). (b) Photograph of the micro-reactor probe head.

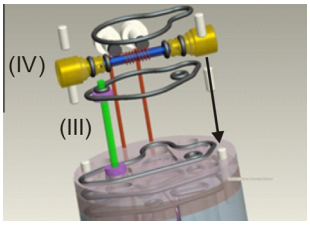

Fig. 3. Dwell unit (III) and NMR flow cell (IV) of the micro-reactor probe head visualized without the surrounding PEEK. The gray loops show the sealings. The arrow indicates the direction of the reactants leaving the NMR flow cell. The same numbering as in Fig. 2 is used.

capillary, resulting in a NMR active volume of approximately 5 µl. In the present set-up, only a ^{1}H NMR RF circuit is installed. An upgrade for the observation of ^{13}C nuclei is in preparation.

After passing the NMR flow cell, the fluid mixture leaves the probe head through the bottom plate (I) via milled channels in the PEEK block. Finally, the reactants leave the NMR probe through the connected lines (see Fig. 2).

The new probe head is designed in a way that the whole flow path of the reactants including the feed tubes, the micro-mixer plates, the dwell unit, and the NMR flow cell is thermostatted. Liquid perfluorotributylamine (FC-43) was chosen as thermostatting fluid. FC-43 is a favorable choice for NMR applications because of several reasons. First, FC-43 is fully fluorinated so that it causes no ^{1}H NMR signals, which would interfere with the measurements, and, in addition, the signals of FC-43 in the ^{13}C spectrum are shifted far from the regions commonly investigated in NMR spectroscopy. Second, the magnetic susceptibility of the RF coil, the glass and FC-43 is very different from that of air. Thus by replacing air with FC-43 the differences in magnetic susceptibility of the materials surrounding the sample are smaller and therefore the spectral resolution is improved as shown by Subramanian et al. [33]. Additionally, it is well suited as thermostatting liquid because of its low melting and high boiling point (operating range at ambient pressure about −40 °C to 120 °C). The temperature of the reactants is monitored by means of a calibrated thermocouple, which is installed in the PEEK block directly underneath the micro-mixer. The temperature of the FC-43 is controlled by a cryostat. The standard air-based temperature control of the NMR spectrometer is employed for cooling the electronic components in the probe head, which are mounted below the PEEK block. The probe head is designed for pressures up to 60 bar. The range of the operating temperature is limited both by the properties of the FC-43 as well as the fact that an efficient cooling of the electronics must be guaranteed. It is approximately −20 °C to 100 °C.

2.2. Operating modes

The micro-mixer probe head can be used in two different operating modes: the stationary flow mode and the stopped flow (non-steady) mode. In the stationary flow mode, the probe head is operated as a continuous tubular reactor with the two feeds being set to constant flow rates. After the reactor has reached steady-state, the NMR measurements are started and spectra are acquired which yield information on the composition of the liquid in the NMR active volume (volume of the capillary which is wrapped by the RF coil, see above). As the operation is stationary, in principle any time is available for collecting the spectra so that using ^{13}C NMR with long acquisition times poses no problem. By adjusting the flow rates of the reactants, both the inlet composition and the residence time within the reactor can be varied so that reaction kinetics can be measured at different conversion rates and compositions. Shifting the reference frame and moving it with the sample, a mean time can be assigned to each experiment which elapses between the mixing and the analysis in the flow cell. This assignment is not trivial and involves determining residence and flow characteristics of the studied system by measurements of residence time distributions. This work is in progress. For the purposes of the present study, a simple first estimate is used: it is assumed that the acquired NMR signal corresponds to the position in the middle of the active volume of the NMR flow cell (1), that the mixing takes place instantaneously in the micro-mixer (2) and that the flow pattern corresponds to plug flow. Thus, the corresponding residence time is found by dividing the volume between (1) and (2) by the volumetric flow rate.

In the stopped flow mode, the reactants are fed into the reactor at high flow rates so as to minimize the time that elapses between the mixing and the filling of the NMR flow cell with the reacting mixture. After the NMR flow cell is filled with the reacting mixture, the flow is stopped abruptly and the signal acquisition is started. Thus, the NMR flow cell is operated as a batch reactor, i.e. the operation is non-steady and the composition of the reacting mixture is obtained as function of time. By means of this composition profile, the reaction kinetics can be calculated.

Both operating modes have advantages and disadvantages. In the stationary flow mode, as stated above, the composition of the sample in the active volume of the NMR flow cell is constant. Thus, multiple scans and time-consuming measurements such as ^{13}C NMR or two-dimensional methods with high resolution can be applied to obtain qualitative or quantitative data. In the stopped flow mode, however, these time-consuming measurements are only possible for slow reactions. But as ^{1}H NMR spectroscopy enables obtaining spectra that yield good quantitative data at intervals of about 1 s, also the stopped flow mode is suited for kinetic studies of comparatively fast reactions. Furthermore, it is easier to control the temperature of exo- and endothermic reactions in the stationary flow mode than in the stopped flow mode, as in the stopped flow mode hardly any convection occurs inside the cell and as the cryostat has a limited control response time.

The stopped flow mode has the advantage that reactions can be monitored within one experiment over a long period of time starting from the first acquisition after the flow was stopped (typically

after a few seconds) and ending after several hours. In the stationary flow mode, the window of the feasible residence times in the reactor is limited. At low flow rates of the reactants, the accuracy and stability of the pumps may cause problems and/or the micro-mixer may be outside its operating range, so that the reactants are not well mixed. In contrast, at high flow rates of the reactants, the resolution of the spectrum deteriorates for several reasons. First, the residence time in the NMR flow cell is short and the excited nuclei are rapidly flushed out of the NMR active volume during acquisition. This rapid flushing results in a faster decay of the NMR signal and it leads to a line broadening in the spectrum compared to low flow rates [41,22]. The line broadening caused by flushing out exited nuclei can be easily estimated assuming plug flow in the probe head [29,12]. The resulting difference of the peak widths for flow and stopped flow is less than about 3.5 Hz for the volume flow rates applicable in the probe head presented in this work. Second, the mixing of two reactants with different magnetic susceptibilities can cause local inhomogeneities in the B_0 field that in turn results in a faster decay of the signal and hence in a line broadening of the peaks. Furthermore, if the residence time of the nuclei in the premagnetisation volume is too short, the nuclei are not fully Boltzmann equilibrated before their excitation in the RF coil. This can imply that the spectral information is not quantitative any longer without prior calibration [12]. Finally, the pressure drop over the probe head increases significantly with high flow rates. Regarding the mentioned constraints, the probe head design used in this work facilitates residence times of the reactants in the reactor volume from 2 s to approximately 5 min.

3. Experimental section

3.1. Experimental set-up

The experiments were carried out using a 400 MHz NMR spectrometer (Unity Inova 400, Varian, Palo Alto, USA), which was equipped with the new micro-mixer probe as described in Section 2. The measured spectra were processed with the MestReNova 6.0 software package (Mestrelab Research, Santiago de Compostela, Spain) including phasing, baseline correction and integration.

Fig. 4 shows the set-up used for the NMR experiments. Two syringe pumps (pump A and pump B; Dual 260d, Teledyne Isco, Lincoln, USA, accuracy 0.5% of setpoint) are used to feed two mixtures or two pure liquids (here called A and B) pulsation-free, via PEEK capillaries (inner diameter 0.8 mm) into the NMR probe. In the present work, a capillary with a diameter of 0.75 mm is installed in the dwell unit resulting in a total volume of the micro-reactor of 34 µl. To prevent plugging of the capillaries or the micro-mixer structure by impurities (e.g. dust, precipitated solids), 0.5 µm filters (stainless steel frits, type number A-103, Upchurch Scientific Inc., Oak Harbor, USA) are installed in the feed lines of NMR probe. The purge tube leaving the NMR probe is connected to a vessel that is pressurized with nitrogen to apply a back-pressure. This vessel is important for the stopped flow mode. In that mode, unavoidable small fluctuations of the temperature would lead to large pressure changes if dilatation of the liquid volume were not enabled. Hence, a constant pressure can be applied in the micro-reactor both in the flow mode and in the stopped flow mode. The pressure is measured in the two feed tubes and in the purge tube. Valves (V1-V4, cf. Fig. 4) are used to switch between the different operating modes (stationary flow mode and stopped flow mode, see Section 2.2).

The feed and the purge lines are embedded in silicon tubes (outer diameter 8 mm). This silicon tube is filled with water outside of the NMR and it is connected to a cryostat (F12-ED, Julabo GmbH, Seelbach, Germany) to control the temperature of the reactants. In a second circuit, the silicon tube is filled with the thermostatting liquid FC-43 (see Fig. 4) and it is connected via the connection box with the NMR probe (see Fig. 1) and a second cryostat (Petite Fleur, Two to Tango, Huber Kältemaschinenbau GmbH, Offenburg, Germany, temperature range −40 °C to 200 °C, accuracy ±0.01 °C), so that the whole flow path of the reactants in the probe, including the feed lines, the micro-mixer, the dwell unit, the NMR flow cell, and the purge lines are surrounded by a constant flow of the thermostatting liquid FC-43 to assure a good thermostatisation. The thermocouple, which is installed directly beneath the micro-mixer and which is used as control variable for the cryostat, was calibrated on the temperature of the reactants within the NMR flow cell prior to the experiments. The temperature of the reactants was measured by means of the temperature dependence of the proton resonance frequency shift between the two peaks of

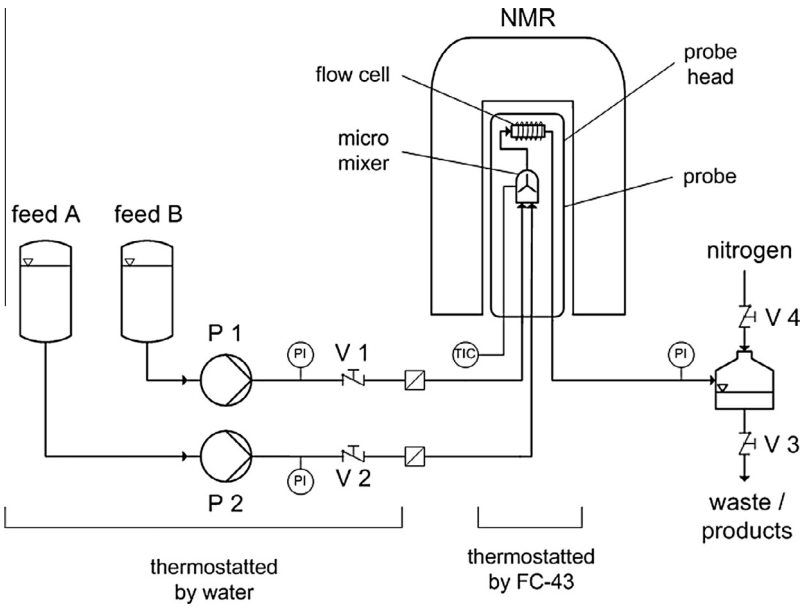

Fig. 4. Flow diagram of the experimental set-up for online NMR measurements with the micro-reactor probe head.

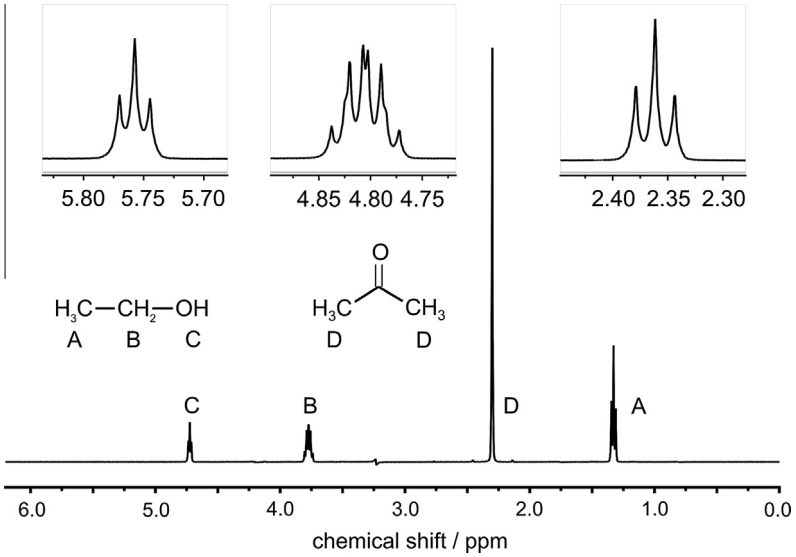

Fig. 5. ^{1}H NMR spectrum of an ethanol/acetone mixture ($x_{ethanol}$ = 0.5 mol/mol, T = 20 °C) acquired in stopped flow mode (single scan, acquisition time 1 s, flip angle 45°).

ethane-1,2-diol [42]. The measurement showed that the calibration of the thermocouple on the temperature of the reactants depends only weakly on the flow rate of the reactants. Thus, the temperature of the reactants can be measured by the thermocouple within an accuracy of ±0.5 °C.

Methanol, acetone, ethanol, acetic acid, sulfuric acid (all analytical grade) were purchased from Sigma Aldrich (St. Louis, Missouri, USA) and were used as received. Water was taken from a Milli-Q water purification system from Millipore (Bedford, Massachusetts, USA). The thermostatting liquid FC-43 was from 3M (St. Paul, Minnesota, USA).

3.2. Non-reactive measurements

First, sensitivity measurements were carried out with a solution of sucrose in D_2O (10 mM) [36]. Single scan spectra with an acquisition time (AT) of 2 s, a relaxation delay (RD) of 59 s and a pulse width of 10 μs (RF power of 58 dB) were acquired, yielding a SNR (signal-to-noise ratio) of 70. For the micro-reactor probe head a $nLOD_m$ of 0.1 μmol was determined using the method described by Krojanski et al. [36]. The peak area ratio $A_{810°}/A_{90°}$, which is a measure for the RF homogeneity of the coil, was 68%.

The non-reactive measurements were carried out as follows. First, the probe head was filled with a mixture of acetone and ethanol and measurements in the stopped flow mode were carried out. 60 single scans were acquired with an AT of 1 s, a RD of 59 s and a pulse width of 14 μs, which corresponds to a flip angle (β) of 45° (RF power of 50 dB). Second, a mixture of acetone and ethanol was fed into the probe head at a constant flow rate of 100 μl/min. ^{1}H NMR spectra (60 signal scans, AT 1 s, RD 59 s, β = 45°) were taken every minute to test the long term stability of the acquisition in the stationary flow mode. As a premixed feed was used, there was no influence of mixing effects on the spectra. Last, pump A was filled with acetone and pump B with ethanol so that both species were fed separately into the probe head and first mixed in the micro-mixer (non-premixed feeds). The flow rate of each pump was set to 50 μl/min resulting in a total flow rate of 100 μl/min and ^{1}H NMR spectra (60 signal scans, AT 1 s, RD 59 s, β = 45°) were taken every minute. By comparing the results of the experiments with premixed feeds and the results of the experiments with two non-premixed feeds insight in the stability and accuracy of the pumps and the micro-mixer were gained. The mole fraction of acetone was calculated for all experiments from the peak areas of the CH_3 groups of acetone and ethanol. The values shown here are the means of the repeated scans.

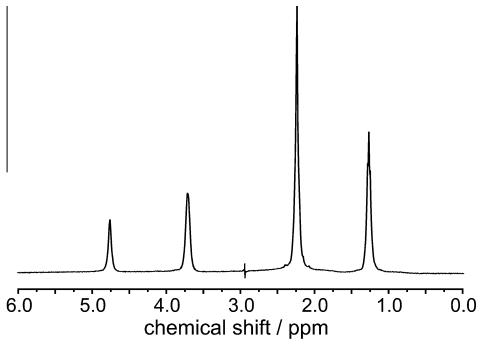

Fig. 6. ^{1}H NMR spectrum acquired in the stationary flow mode with two non-premixed feeds of ethanol (flow rate 50 μl/min) and acetone (flow rate 50 μl/min) ($x_{ethanol}$ = 0.56 mol/mol, T = 20 °C). Acquisition parameters: single scan, acquisition time 1 s, flip angle 45°. The FWHM is approximately 12 Hz.

Fig. 5 depicts the ^{1}H NMR spectrum of the mixture of acetone and ethanol acquired in the stopped flow mode. The single scan measurements yield a well resolved fine structure of ethanol with a full width at half maximum (FWHM) of approximately 2 Hz. Fig. 6 shows the ^{1}H NMR spectrum in the flow mode experiment with acetone and ethanol being fed separately into the probe head. The resulting peaks are broader (FWHM of 12 Hz) than in the stopped flow experiments (cf. Fig. 5). This line broadening is expected. As mentioned above, the line broadening is mainly caused by two effects. First, the excited nuclei are flushed out of the NMR active volume during acquisition which causes a faster decay of the NMR signal and thus a line broadening of the peaks compared to the spectra acquired in the stopped flow mode [41,22]. Second, the mixing of two species with different magnetic susceptibilities introduces local inhomogeneities of the B_0 field that causes line broadening. In the present case, the contribution to the broadening of the spectra by flushing out nuclei is less than 2 Hz thus the dominating effect is the mixing of the species with different susceptibilities.

Table 1 gives an overview of the non-reactive measurements. The measured mole fraction of acetone is in good agreement with

Table 1
Comparison of measured and the expected mole fractions of acetone for the non-reactive experiments in different operation modes. The ranges given for the measure mole fractions are the 95% confidence interval of the repeated measurements.

Experiment	Mole fraction of acetone		
	Expected	Measured	Rel. error (%)
Stopped flow mode	0.499	0.500 ± 0.0004	0.2
Flow mode: premixed feeds	0.443	0.442 ± 0.0004	0.2
Flow mode: non-premixed feeds	0.443	0.436 ± 0.0013	1.6

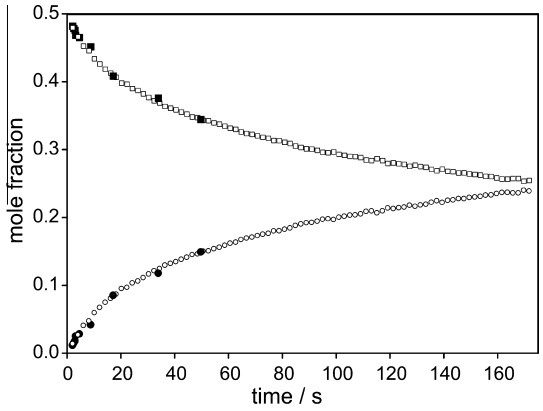

Fig. 7. Comparison of experimental reaction kinetic data for the esterification of methanol and acetic acid carried out in the stationary flow mode (filled symbols) and in the stopped flow mode (open symbols) at 50 °C (equimolar feed with 0.04 g/g sulfuric acid). (■/□) mole fraction of methanol. (●/○) mole fraction of methyl acetate.

the expected mole fraction of acetone. The relative error is approximately 0.2% for the stopped flow mode and for the flow mode with premixed feeds, and 1.6% for the flow mode with non-premixed feeds, cf. Table 1. The small variance of the measurements (indicated by the small 95% confidence interval of 4×10^{-4} mol/mol) both in the stopped flow mode and in the flow mode with premixed feeds demonstrates that stable spectra can be acquired over a long period of time and that the flow of thermostatting liquid around the NMR coil has no adverse effects on the spectra. The only minor increase of the variance for the measurements in the flow mode with the non-premixed feeds (the 95% confidence interval is 1.3×10^{-3} mol/mol) shows that the pumps and the mixer introduce hardly any fluctuation. To conclude, the results of this study prove that the probe head facilitates the acquisition of constant, high-resolved, and quantitative NMR signals.

3.3. Reactive measurements

To demonstrate that the probe head is suited for the investigation of fast reactions, the homogeneously catalyzed esterification of methanol with acetic acid was studied in this work at 50 °C using both the stationary flow mode and the stopped flow mode.

The experiments were carried out as follows. One pump was filled with methanol and the other pump was filled with a mixture of acetic acid and the catalyst sulfuric acid. The ratio of the flow rates of the two pumps was set so that an equimolar feed ratio was achieved. The concentration of sulfuric acid in the reacting mixture was 0.04 g/g. Before the acquisition was started, the set-up was thermostatted for at least 1 h to ensure that the temperature was in steady-state. During the stopped flow measurements, a large number of ^{1}H NMR spectra were acquired at intervals of 2 s (AT 1 s, RD 1 s, $\beta = 45°$) to follow the reaction and obtain the composition of the reactants as a function of time. The experiments in the stationary flow mode were carried out at seven different flow rates (35 µl/min to 800 µl/min), i.e. with seven different residence times (2–47 s). For each flow rate, an array of 30 single scan ^{1}H NMR spectra was acquired (AT 1 s, RD 59 s, $\beta = 45°$) and the peak areas were averaged. During all measurements (stationary flow and stopped flow mode), fluctuations in the temperature were less than ±0.5 °C.

Fig. 7 depicts the results for the reaction kinetics measurements carried out both in the stationary flow mode and in the stopped flow mode. The concentration profiles of methanol and methyl acetate are plotted as function of time (stopped flow mode) and as function of the residence time (stationary flow mode), respectively. Both concentration profiles agree well, hence, both operating modes yield consistent results. The first data points were taken only 2 s after the reaction had started (cf. Fig. 7). This shows that the probe head facilitates quantitative measurements and kinetic studies of fast reactions.

4. Conclusion

A novel NMR probe head design for non-invasive investigation of fast reactions is presented. The probe head combines a micro-mixer with a solenoidal capillary NMR flow cell. The total volume of the micro-reactor used in the present work is 34 µl. The temperature of the whole flow path of the reactants is controlled by a thermostatting liquid, so that also exo- and endothermic reactions can be studied under isothermal conditions. Non-reactive mixing experiments with the new probe head demonstrate that highly resolved spectra can be acquired and that the concentration of different species in technical mixtures can be measured accurately with a relative error less than 2%. Using the esterification of methanol with acetic acid as test system, the applicability of the probe head for measurements of reaction kinetics under isothermal conditions was demonstrated. The two possible operating modes of the probe head (stationary flow mode and non-steady stopped flow mode) yield consistent results. First data points were obtained 2 s after the reaction had started. The novel micro-mixer probe head is a useful device for online monitoring of fast reactions with NMR spectroscopy under industrially relevant conditions.

Acknowledgments

We gratefully acknowledge financial support of this project by DFG. We thank Berthold Mrawek, University of Kaiserslautern and Paul Schuler, Eberhard Karls University, Tübingen, for technical support.

References

[1] I. Hahnenstein, M. Albert, H. Hasse, C.G. Kreiter, G. Maurer, NMR spectroscopic and densimetric study of reaction kinetics of formaldehyde polymer formation in water, deuterium oxide, and methanol, Ind. Eng. Chem. Res. 34 (1995) 440–450.
[2] M. Maiwald, H.H. Fischer, M. Ott, R. Peschla, C. Kuhnert, C.G. Kreiter, G. Maurer, H. Hasse, Quantitative NMR spectroscopy of complex liquid mixtures: methods and results for chemical equilibria in formaldehyde–water–methanol at temperatures up to 383 K, Ind. Eng. Chem. Res. 42 (2003) 259–266.
[3] M. Maiwald, T. Grützner, E. Ströfer, H. Hasse, Quantitative NMR spectroscopy of complex technical mixtures using a virtual reference: chemical equilibria and reaction kinetics of formaldehyde-water-1,3,5-trioxane, Anal. Bioanal. Chem. 385 (2006) 910–917.
[4] W. Böttinger, M. Maiwald, H. Hasse, Online NMR spectroscopic study of species distribution in MEA-H2O-CO2 and DEA-H2O-CO2, Fluid Phase Equilib. 263 (2008) 131–143.
[5] C.A. Fyfe, L. Vanveen, Flow nuclear magnetic resonance investigation of the intermediates formed during the bromination of phenols in acetic acid, J. Am. Chem. Soc. 99 (1977) 3366–3371.
[6] C.A. Fyfe, M. Cocivera, S.W.H. Damji, T.A. Hostetter, D. Sproat, J. O'Brien, Apparatus for the measurement of transient species and effects in flowing systems by high-resolution nuclear magnetic resonance spectroscopy, J. Magn. Reson. 23 (1976) 377–384.

[7] M. Maiwald, H. Li, T. Schnabel, K. Braun, H. Hasse, On-line ^{1}H NMR spectroscopic investigation of hydrogen bonding in supercritical and near critical CO2-methanol up to 35 MPa and 403 K, J. Supercrit. Fluids 43 (2007) 267–275.

[8] W. Böttinger, M. Maiwald, H. Hasse, Online NMR spectroscopic study of species distribution in MDEA-H2O-CO2 and MDEA-PIP-H2O-CO2, Ind. Eng. Chem. Res. 47 (2008) 7917–7926.

[9] O. Steinhof, NMR-spektroskopische Aufklärung des bei der Umsetzung von Harnstoff mit Formaldehyd auftretenden Reaktionsnetzwerks, Ph.D. thesis, University Stuttgart, 2010.

[10] E.J. Kibrik, O. Steinhof, G. Scherr, W.R. Thiel, H. Hasse, Proof of ether-bridged condensation products in UF resins by 2D NMR spectroscopy, J. Polym. Res. 20 (79) (2013) 1–10.

[11] M. Maiwald, H.H. Fischer, Y. Kim, K. Albert, H. Hasse, Quantitative high-resolution on-line NMR spectroscopy in reaction and process monitoring, J. Magn. Reson. 166 (2004) 135–146.

[12] M. Maiwald, Hochauflösende Online NMR-Spektroskopie für das Reaktions- und Prozessmonitoring, Cuvillier Verlag, Göttingen, 2012.

[13] M. Ott, H.H. Fischer, M. Maiwald, K. Albert, H. Hasse, Kinetics of oligomerization reactions in formaldehyde solutions: NMR experiments up to 373 K and thermodynamically consistent model, Chem. Eng. Process. 44 (2005) 653–660.

[14] M.A. Bernstein, M. Stefinovic, C.J. Sleigh, Optimising reaction performance in the pharmaceutical industry by monitoring with NMR, Magn. Reson. Chem. 45 (2007) 564–571.

[15] H. Weber, L. Brecker, Online NMR for monitoring biocatalysed reactions, Curr. Opin. Biotechnol. 11 (2000) 572–578.

[16] D.W. Jones, T. Child, Advances in Magnetic Resonance, Academic Press, New York, 1976.

[17] P.A. Keifer, Flow techniques in NMR spectroscopy, Annu. Rep. NMR Spectrosc. 62 (2007) 1–47.

[18] H. Fischer, K. Albert, Online LC NMR and Related Techniques, John Wiley & Sons, New York, 2003. pp. 195–218.

[19] U. Holzgrabe, I. Wawer, B. Diehl, NMR Spectroscopy in Pharmaceutical Analysis, Elsevier, Amsterdam, 2008.

[20] M. Maiwald, H.H. Fischer, Y.-K. Kim, H. Hasse, Quantitative on-line high-resolution NMR spectroscopy in process engineering applications, Anal. Bioanal. Chem. 375 (2003) 1111–1115.

[21] W. Neudert, E. Ströfer, On-line NMR in process engineering, Magn. Reson. Chem. 24 (1986) 1089–1092.

[22] J.L. Sudmeier, U.L. Günther, K. Albert, W.W. Bachovchin, Sensitivity optimization in continuous-flow FTNMR, J. Magn. Reson. Series A 118 (1996) 145–156.

[23] R.L. Haner, W. Llanos, L. Mueller, Small volume flow probe for automated direct-injection NMR analysis: design and performance, J. Magn. Reson. 143 (2000) 69–78.

[24] K.R. Minard, R.A. Wind, Solenoidal microcoil design. Part I: optimizing RF homogeneity and coil dimensions, Concepts Magn. Reson. 13 (2001) 128–142.

[25] A.P.M. Kentgens, J. Bart, P.J.M. van Bentum, A. Brinkmann, E.R.H. van Eck, J.G.E. Gardeniers, J.W.G. Janssen, P. Knijn, S. Vasa, M.H.W. Verkuijlen, High-resolution liquid- and solid-state nuclear magnetic resonance of nanoliter sample volumes using microcoil detectors, J. Chem. Phys. 128 (052202) (2008) 1–17.

[26] A.G. Webb, Radiofrequency microcoils for magnetic resonance imaging and spectroscopy, J. Magn. Reson. 229 (2013) 55–66.

[27] A.G. Webb, Radiofrequency microcoils in magnetic resonance, Prog. Nucl. Magn. Reson. Spectrosc. 31 (1997) 1–42.

[28] R.M. Fratila, A.H. Velders, Small-volume nuclear magnetic resonance spectroscopy, Annu. Rev. Anal. Chem. 4 (2011) 227–249.

[29] F. Dalitz, M. Maiwald, G. Guthausen, Considerations on the design of flow cells in by-pass systems for process analytical applications and its influence on the flow profile using NMR and CFD, Chem. Eng. Sci. 75 (2012) 318–326.

[30] D.L. Olson, J.A. Norcross, M. O'Neil-Johnson, P.F. Molitor, D.J. Detlefsen, A.G. Wilson, T.L. Peck, Microflow NMR: concepts and capabilities, Anal. Chem. 76 (2004) 2966–2974.

[31] H. Wensink, F. Benito-Lopez, D.C. Hermes, W. Verboom, H.J.G.E. Gardeniers, D.N. Reinhoudt, A. van den Berg, Measuring reaction kinetics in a lab-on-a-chip by microcoil NMR, Lab Chip 5 (2005) 280–284.

[32] M. Kakuta, D.A. Jayawickrama, A.M. Wolters, A. Manz, J.V. Sweedler, Micromixer-based time-resolved NMR: applications to ubiquitin protein conformation, Anal. Chem. 75 (2003) 956–960.

[33] R. Subramanian, W.P. Kelley, P.D. Floyd, Z.J. Tan, A.G. Webb, J.V. Sweedler, A microcoil NMR probe for coupling microscale HPLC with on-line NMR spectroscopy, Anal. Chem. 71 (1999) 5335–5339.

[34] K. Ehrmann, K. Pataky, M. Stettler, F.M. Wurm, J. Brugger, P.A. Besse, R. Popovic, NMR spectroscopy and perfusion of mammalian cells using surface microprobes, Lab Chip 7 (2007) 381–383.

[35] J. Bart, A.J. Kolkman, A.J. Oosthoek-de Vries, K. Koch, P.J. Nieuwland, H.J.W.G. Janssen, J.P.J.M. van Bentum, K.A.M. Ampt, F.P.J.T. Rutjes, S.S. Wijmenga, H.J.G.E. Gardeniers, A.P.M. Kentgens, A microfluidic high-resolution NMR flow probe, J. Am. Chem. Soc. 131 (2009) 5014–5015.

[36] H.G. Krojanski, J. Lambert, Y. Gerikalan, D. Suter, R. Hergenröder, Microslot NMR probe for metabolomics studies, Anal. Chem. 80 (2008) 8668–8672.

[37] O. Gökay, K. Albert, From single to multiple microcoil flow probe NMR and related capillary techniques: a review, Anal. Bioanal. Chem. 402 (2012) 647–669.

[38] M. Gal, M. Mishkovsky, L. Frydman, Real-time monitoring of chemical transformations by ultrafast 2D NMR spectroscopy, J. Am. Chem. Soc. 128 (2006) 951–956.

[39] E. Harel, A. Pines, Spectrally resolved flow imaging of fluids inside a microfluidic chip with ultrahigh time resolution, J. Magn. Reson. 193 (2008) 199–206.

[40] F. Schönfeld, V. Hessel, C. Hofmann, An optimised split-and-recombine micro-mixer with uniform 'chaotic' mixing, Lab Chip 4 (2004) 65–69.

[41] D.A. Laude, C.L. Wilkins, Direct-linked analytical scale high-performance liquid chromatography/nuclear magnetic resonance spectrometry, Anal. Chem. 56 (1984) 2471–2475.

[42] C. Ammann, P. Meier, A. Merbach, A simple multi-nuclear NMR thermometer, J. Magn. Reson. 46 (1982) 319–321.

Brächer et al., 2016

Reprinted with permission from: A. Brächer, R. Behrens, E. von Harbou, H. Hasse, Application of a new micro-reactor ^{1}H NMR probe head for quantitative analysis of fast esterification reactions, Chemical Engineering Journal, Volume 306, 2016, Pages 413-421, ISSN 1385-8947, DOI 10.1016/j.cej.2016.07.045

Chemical Engineering Journal 306 (2016) 413–421

Contents lists available at ScienceDirect

Chemical Engineering Journal

journal homepage: www.elsevier.com/locate/cej

Application of a new micro-reactor ^{1}H NMR probe head for quantitative analysis of fast esterification reactions

Alexander Brächer, Richard Behrens, Erik von Harbou *, Hans Hasse

Laboratory of Engineering Thermodynamics, University of Kaiserslautern, Erwin-Schrödinger-Strasse 44, 67663 Kaiserslautern, Germany

HIGHLIGHTS

- Application of a new micro-reactor NMR probe head for reaction kinetic investigations.
- Micro-reactor NMR probe head is operated at constant temperature and pressure.
- Comparison of experimental results agree well with kinetic models.
- Fast reaction kinetics in the order of seconds are accessible using the new set-up.

GRAPHICAL ABSTRACT

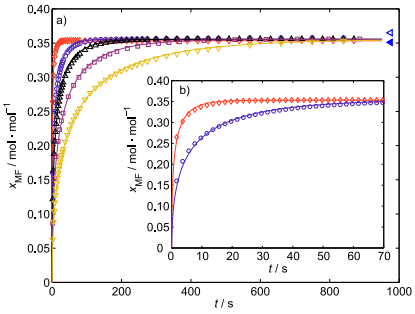

ARTICLE INFO

Article history:
Received 20 April 2016
Received in revised form 9 July 2016
Accepted 12 July 2016
Available online 15 July 2016

Keywords:
Online NMR spectroscopy
Fast reactions
Reaction kinetics
NMR probe development
Micro-reactor
Esterification reactions

ABSTRACT

A fully liquid-thermostatted micro-reactor probe head for ^{1}H NMR spectroscopic studies of fast reaction kinetics, which was recently developed, is tested in the present work by studying fast esterification kinetics in the stopped flow mode. It is shown that reliable kinetic data can be obtained using this set-up for reactions with time constants down to a few seconds. The two test systems are the formation of methyl acetate (MA) and methyl formate (MF). Both are homogeneously catalyzed by sulfuric acid, which is added to the educts in different amounts. The temperatures of the kinetic studies are chosen between 303 and 333 K. The reaction kinetic data for both systems is correlated by activity-based kinetic models. For the MA formation, reference data from the literature is available, however only for regimes with time constants of minutes to hours. That data fits well to the results of the present study. The MF formation was studied here at conditions in which the time constants are of the order of seconds and therefore no reference data is available. The new probe head substantially extends the range in which NMR spectroscopy can be used for studies of fast reaction kinetics.

1. Introduction

Reaction kinetics are important for designing chemical processes but are often not available. Batch reactors are widely used for studying reaction kinetics. As homogeneous and heterogeneous catalysis can be applied, batch reactors have been widely used for the investigation of esterification reactions, for some examples see [1–9]. In those experiments the rate of reaction is determined by measuring the change of the composition of the reacting mixture over time. The composition of the mixture is often determined ex situ by gas chromatography or titration methods. In the case of homogeneously catalysed reactions, normally the reaction has to be stopped prior to the analysis. This can be done by adding an inhibitor [10,11] or by cooling down the sample rapidly [12]. This procedure, however, is laborious and error-prone and not suitable if the reaction kinetics are too fast. In this case, an analytical method that can measure the extent of the reaction online without the need for sampling and ex situ analysis is often the only possible option for studying the reaction kinetics.

* Corresponding author.
E-mail address: erik.vonharbou@mv.uni-kl.de (E. von Harbou).

http://dx.doi.org/10.1016/j.cej.2016.07.045
1385-8947/

NMR spectroscopy is an interesting tool for studying reaction kinetics, especially in complex systems with many components. As no calibration is needed, it lends itself to such quantitative studies. In cases in which unstable intermediates occur, or in which the components are chemically similar, it is often the only analytical method that facilitates reliable measurements of the composition of the investigated mixture [13–18]. NMR spectroscopy can be used for the ex situ analysis of samples taken, for example, from a batch reactor [18,19]. As described above, the sampling and the ex situ analysis, however, have several drawbacks. For that reason, online NMR spectroscopy has been applied in several studies to determine reaction kinetics [3,19–26]. In a typical online NMR spectroscopy set-up, a batch reactor is connected by a sample loop to the NMR spectrometer equipped with a flow probe so that no sampling and ex situ analysis is necessary. This set-up, however, cannot be used for studying fast reactions, due to the time delay caused by the sample transport from the reactor to the spectrometer. First spectra of the reaction can be obtained approximately 3–5 min after the reaction has been started. Thus, the method is limited to reactions with time constants of about 10 min [23,27]. Similar restrictions apply to kinetic studies in which the reactants are filled into an NMR sample tube outside the spectrometer, which is then inserted into the spectrometer and used as batch reactor while the extent of the reaction is monitored online by repeated NMR spectroscopic measurements. To use the NMR sample tube directly as batch reactor has the additional drawback that the temperature of the reaction sample is difficult to control especially for fast reactions that occur at elevated temperatures and are strongly exo- or endothermal.

To overcome these hurdles a novel micro-reactor NMR probe head has been recently developed by our group [28]. It is fully liquid-thermostatted and designed for the investigation of fast reaction kinetics. In our previous work [28], only results from preliminary tests were reported. In the present work, that micro-reactor probe head is tested more thoroughly to demonstrate its usefulness and fields of application.

To operate the micro-reactor probe head, two reactants are fed separately into the probe head. Therein, the reactants are mixed in a micro-mixer. The reacting mixture is then led through a short capillary into the NMR flow cell which is equipped with a solenoidal microcoil for detection. The delay between the start of the reaction, which is initiated by mixing the reactants, and the analysis in the NMR flow cell is short. The actual delay depends on the residence time in the capillary i.e. on the inner diameter of the capillary and the flow rate of the reactant and can be as low as about 2 s in the present set-up. The entire set-up including the micro-mixer and the NMR flow cell is liquid-thermostatted by the thermo oil FC 43 (perfluorotributylamine) to ensure isothermal kinetic investigations.

In the last decades, the development of new NMR probe heads had a focus on microcoil research to improve the sensitivity. Thorough overviews of the field of microcoil research and microcoil based probe heads are available [29,30]. While a number of very sensitive probe heads exist [31–35], they often lack accurate temperature and pressure control during experiments and are not available with integrated micro-mixers making them unsuitable for the investigation of fast reaction kinetics. Similar approaches, using miniaturized devices, were conducted in the field of vibrational spectroscopy. Hence, the use of micro-mixing units coupled to infrared (IR) [36–38] and Raman spectroscopy [39] for reaction monitoring is reported as well as the implementation of miniaturized flow cells for LC-IR (liquid chromatography) applications [40].

In general, NMR flow probes can be used in two different ways for reaction kinetic studies. In the non-steady state stopped flow mode, the reactants are fed to the micro-mixer in the desired ratio at high flow rates so that there is only a short delay before the mixed reactants reach the NMR flow cell. When the NMR flow cell is completely filled with reactants, the flow is stopped and the composition of the reacting mixture in the active volume of the NMR flow cell is measured repeatedly as a function of time. In that case, the thermostatted NMR flow cell can be considered as a batch reactor. That mode was used in the present study. As a transient process is monitored, measuring in that mode requires fast acquisitions of NMR spectra with sufficient quality. The acquisition of a quantifiable spectrum takes about 1 s using ^{1}H NMR spectroscopy. Depending on the relaxation time T_1 of the investigated species and the applied pulse flip angle the fastest possible pulse repetition rate for quantitative measurements is about 2 s.

An alternative operation mode is the stationary flow mode. In that mode the reactants are fed to the micro-mixer in a desired ratio with given flow rates. When steady state is reached, spectra are acquired while the reactants are still in motion. By varying the total flow rate or the inner diameter of the capillary, at constant reactant ratio, the residence time in the probe head, i.e. the time between the mixing of the reactants and the analysis in the NMR flow cell is varied. Thus, by acquiring spectra for each steady state, the composition of the reactants is measured as a function of the residence time. In this case, the probe head is operated as a continuous tubular reactor. Measuring reaction kinetics in the stationary flow mode, however, is time-consuming as the flow rate of the reactants has to be changed several times to get sufficient information on the reaction kinetics. In contrast, using the non-steady state stopped flow mode an entire composition profile, from the start of the reactions until equilibrium is reached, can be recorded in one experimental run. Thus, in the present study, only the stopped flow mode was applied. For more details on the advantages and disadvantages of the two operating modes see [28].

In a first application of the new micro-reactor probe head, the reactions of acetaldehyde with water forming poly(oxymethylmethylene) glycols were recently investigated [41]. It is shown that the analysis of this multi-component system, which is relevant for industrial processes [42], yielded new kinetic data that is not accessible by the use of vibrational spectroscopy. In general, the use of the micro-mixer probe head is recommended for homogeneously catalysed reaction systems. Investigations of multi-phase reactions, e.g. transesterifications [43] for liquid–liquid reactions, are difficult to investigate as heterogeneously dispersed samples cause unwanted inhomogenieties in the magnetic flux. However, an application using slug flow reactors for liquid–liquid [44] or gas–liquid phase [45] systems that use separated slugs of the two phases is conceivable.

In the present work, we focus on a systematic testing of the probe head considering the limits of the analytical method and the set-up. For the tests, two reaction systems are chosen. The first system is the rather slow but well-investigated esterification of methanol (MeOH) with acetic acid (AA) to methyl acetate (MA) homogeneously catalyzed by sulfuric acid. In literature, besides autocatalysis [12], various homogeneous catalysts were used in reaction kinetic studies of the MA formation: HI [46], HCl [2] and sulfuric acid [10,47–50]. Most of these studies were carried out in diluted aqueous solution, whereas in the present work undiluted equimolar mixtures of MeOH and AA were used as feed. These conditions are similar to the ones used by Dörhöfer [10].

The second system is the esterification reaction of MeOH and formic acid (FA) to methyl formate (MF) homogeneously catalysed by sulfuric acid. Compared to the MA formation, this reaction is much faster. Kinetic investigations of the MF formation are, to our knowledge, only reported by Smith [2] and Tischmeyer [11]. Smith [2] investigated the esterification of aliphatic acids with methanol catalysed by HCl using a batch reactor and a titration method for analysis of the conversion of the aliphatic acids. The reactants were diluted in water for the study and a rather

low concentration of HCl (5 mmol/l) was used. Thus, the kinetics of the MF formation are considerably slower in the experiments of Smith [2] than under the conditions investigated in the present study. Tischmeyer [11] investigated the autocatalysis of the MF formation by MeOH and FA using feed mixtures of MeOH and FA of various compositions. The reaction was so slow that a batch reactor set-up and an ex situ analysis of the samples could be used. Thus, this study is considered here only for comparison of the composition of the reaction mixture in chemical equilibrium.

It would have been desirable to have a well-studied test system of a homogenously catalysed liquid phase reaction with fast reaction kinetics (time constants of the order of seconds) for the tests. As we are not aware of such a system, the strategy with two test systems, as described above, was chosen. Our aim is not to provide a thorough reaction kinetic study of these systems, but is rather to demonstrate the general feasibility of such studies with the new equipment and to characterize that equipment.

2. Reaction systems and kinetic model

2.1. Reaction systems

In the present work, two reaction systems for kinetic test studies under homogeneously catalysis of sulfuric acid are investigated. The MA formation (Reaction 1) and the MF formation (Reaction 2).

$$\underset{\text{AA}}{CH_3COOH} + \underset{\text{MeOH}}{CH_3OH} \overset{H^+}{\rightleftharpoons} \underset{\text{MA}}{CH_3COOCH_3} + \underset{\text{W}}{H_2O} \quad (1)$$

$$\underset{\text{FA}}{HCOOH} + \underset{\text{MeOH}}{CH_3OH} \overset{H^+}{\rightleftharpoons} \underset{\text{MF}}{HCOOCH_3} + \underset{\text{W}}{H_2O} \quad (2)$$

Both reactions are weakly exothermic (MA formation: $\Delta_R h^{\ominus} = -7.3$ kJ/mol [51], MF formation: $\Delta_R h^{\ominus} = -8.0$ kJ/mol [51]).

2.2. Kinetic model

To describe reaction kinetics of homogeneously catalyzed esterifications, it is common to use second order type models [10–12,47]. Different approaches are employed to describe the influence of the catalyst and the influence of the amount of water on the catalyst activity. The model used in the present work is shown in (3), in which 'acid' stands either for FA or AA and 'ester' refers either to MF or to MA.

$$r = \frac{1}{x_W} \cdot \left[k_f(T, x_{H_2SO_4}) a_{MeOH} a_{acid} - k_b(T, x_{H_2SO_4}) a_{ester} a_W \right] \quad (3)$$

r is the rate of reaction which is related here to the total amount of substance. x_i is the mole fraction and a_i the activity of the species i. k_f and k_b are the rate constants of the forward and backward reaction, respectively. The influence of the catalyst is considered to be dependent on the mole fraction of water x_W in the system as suggested by Liu et al. [47]. The model is based on activities a_i, so that the reaction proceeds to the thermodynamic chemical equilibrium. The corresponding activity coefficients γ_i are calculated using the UNIQUAC model. The UNIQUAC parameters for both systems are given in the Appendix A.1.

The temperature dependency of the rate constant k_f and k_b is described by the Arrhenius equation.

$$k_i(T, x_{H_2SO_4}) = k_i^0(x_{H_2SO_4}) \exp\left(-\frac{E_{A,i}}{RT}\right) \quad \text{for} \quad i = f, b \quad (4)$$

with the pre-exponential factors k_i^0 and the activation energy $E_{A,i}$. The rate constants of the forward and backward reaction k_b and k_f are connected via the thermodynamic equilibrium constant K_a.

$$K_a = \frac{k_f}{k_b} \quad (5)$$

The applied activity coefficients γ_i do not consider the influence of the sulfuric acid (cf. Appendix A.1). Thus, a dependancy of K_a on the concentration of sulfuric acid is expected.

The temperature dependancy of K_a, is modeled by the Van't-Hoff equation assuming that the reaction enthalpy $\Delta_R h$ is constant.

$$K_a = K_a^* \exp\left(\frac{\Delta_R h}{RT}\right) \quad (6)$$

3. Experimental section

3.1. Chemicals

Formic acid (FA, $\geqslant 0.98$ g/g), acetic acid (AA, $\geqslant 0.99$ g/g), methanol (MeOH, $\geqslant 0.998$ g/g), methyl formate (MF, $\geqslant 0.99$ g/g) and methyl acetate (MA, $\geqslant 0.998$ g/g) were purchased from Sigma Aldrich (Munich, Germany) in p.a. quality. Sulfuric acid ($\geqslant 0.96$ g/g) was purchased from Roth (Karlsruhe, Germany). The thermostatting liquid perfluorotributylamine (FC 43) for the micro-reactor probe head was purchased from 3M (St. Paul, MN, USA). The chemicals were used without further purification.

3.2. Thermostatted micro-reactor probe head

The thermostatted micro-reactor probe head used in this study is described in detail by Brächer et al. [28]. Thus, only a brief description is given here. Fig. 1 shows a detailed view of the probe head. The probe head consists of several segments that are made of PEEK. They include an integrated micro-mixer, a dwell unit and an

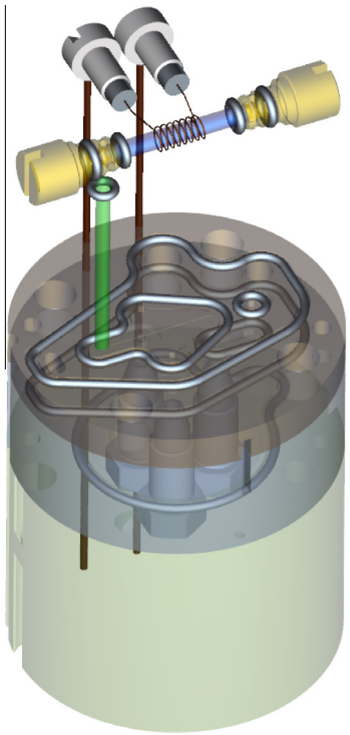

Fig. 1. Details of the thermostatted micro-reactor probe head showing the vertically orientated dwell unit (green tube) and the horizontally orientated NMR flow cell (blue tube). The top circular segment contains the micro-mixer. The grey loops are seals and indicate the different segments of the probe head. (For interpretation of the references to colour in this figure legend, the reader is referred to the web version of this article.)

NMR flow cell. The two reactants are fed separately via the feed lines into the probe head and are mixed in the micro-mixer. After the micro-mixer, the reacting mixture passes through the dwell unit and flows into the NMR flow cell. From the NMR flow cell, the reacting mixture leaves the probe head via the product line which is made of PEEK, too.

The micro-mixer is a crawler-type mixer (developed by Institute of Microtechnology Mainz, Germany, now ICT-IMM Fraunhofer [52]) with a total mixing volume of 0.27 µl. The dwell unit is a PEEK capillary with an inner diameter of 0.75 mm, which corresponds to a volume of about 10 µl.

By installing capillaries with different inner diameters, it is possible to change the volume of the dwell unit and therefore the residence time of the mixture in the dwell unit. The NMR flow cell consists of a capillary made of silica glass (inner diameter of 1 mm). A solenoidal micro radiofrequency (RF) coil enwinds the capillary yielding an NMR active volume of approximately 5 µl.

All educt and product lines, the micro-mixer, the dwell unit as well as the NMR flow cell are surrounded by thermostatting liquid (FC 43) to maintain an efficient thermal management of the entire probe head. FC 43 is chosen as thermostatting liquid as it contains no ^{1}H atoms and thus does not disturb the ^{1}H NMR signals of the reacting mixture. The total reaction volume V_R, from the micro-mixer to the middle of the RF coil, is 27.7 µl. The probe head can be operated at temperatures up to 120 °C and pressures up to 60 bar. It is inert against many aggressive media such as acids and bases.

In contrast to earlier studies [28,41], the main parts of the electronics of the probe head were modified in order to optimize the tuning and matching circuits as well as to facilitate ^{13}C NMR measurements. This work was carried out by Bruker BioSpin GmbH (Rheinstetten, Germany). In addition, the body of the probe head was renewed using a special brass alloy. Due to these changes, the baseline of the spectra and the handling of the tuning and matching process of the probe head were further improved. The sensitivity of the renewed probe head is within the published values of our former study [28].

3.3. Experimental set-up and procedure

The kinetic experiments in this work are carried out in the stopped flow mode. The flow diagram of the used set-up is shown in Fig. 2. Prior to the kinetic experiments, the liquid reactants are degased in an ultrasonic bath. The sulfuric acid is added to the acetic acid for kinetic studies of the MA formation. To prevent the decomposition of formic acid to carbon monoxide in the presence of sulfuric acid, the sulfuric acid is added to methanol for kinetic studies of the MF formation. The reactants are filled separately into the two syringe pumps A and B (Dual 260D, Teledyne Isco, Lincoln, NE, USA, accuracy of the flow rate 0.5% of setpoint). The pumps deliver the reactants pulsation-free through the feed lines to the micro-reactor NMR probe head. The composition of the reactants after the micro-mixer is set by adjusting the flow rates of the two pumps accordingly. The feed lines are equipped with 0.5 µm filters to prevent clogging of the micro-mixer structure or the capillaries. The reaction products leaving the NMR probe head are collected in the product vessel at the outlet that is pressurized by nitrogen (cf. Fig. 2). The pressure is measured in the product vessel and the feed lines. During the experiments the pressure in the product vessel is maintained above 4 bar so that evaporation of reactants is prevented.

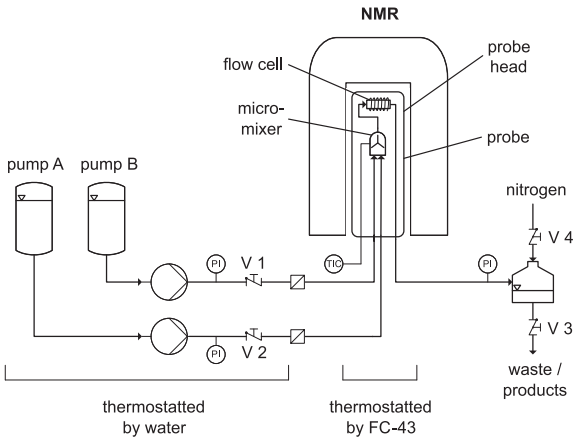

Fig. 2. Online NMR set-up using the micro-reactor probe head as reactor and detector.

Outside the NMR spectrometer, the feed lines are thermostatted with water. The temperature of water is controlled by a cryostat (F12-ED, Julabo GmbH, Seelbach, Germany). Inside the NMR, all feed and product lines, the micro-mixer, the dwell unit and the NMR flow cell are thermostatted by FC 43. The temperature of the FC 43 is controlled using another cryostat (Petite Fleur, Two to Tango, Huber Kältemaschinenbau GmbH, Offenburg, Germany).

To determine the temperature of the reacting mixture, a thermocouple (type K, nickel–chromium and nickel–aluminum alloy) is used that is located underneath the micro-mixer. The temperature measured by the thermocouple is correlated to the temperature inside the NMR flow cell. This correlation was determined prior to the kinetic experiments as follows: Methanol is filled in the NMR flow cell. Then the thermostatting liquid FC 43 is set to different temperatures in the range between 283 and 333 K. By measuring the temperature-dependent chemical shift of the OH-group of methanol [53] the temperature of the methanol inside the NMR flow cell is determined. This value is then correlated to the temperature measured by the thermocouple. The procedure is carried out when methanol is flowing as well as when the flow is stopped while the temperature of the FC 43 is kept constant. Thereby, no significant effect of the convection of methanol on the temperature in the NMR flow cell was observed. The accuracy of the measurement of the temperature inside the NMR flow cell by using the thermocouple together with this correlation is estimated to be ±1 K.

The uncertainty of the pump flowrate was tested gravimetrically in pre-runs, yielding a maximum deviation of 0.4% compared to the setting of the adjusted flowrate. Thus, the flow rate is directly adjusted via the pumps and no additional flow meter is used. In order to ensure an efficient mixing of the reactants, a total flow rate of both pumps $\dot{V}_{tot}$ (sum of flow rates) of 1000 µl/min is chosen for all experiments. This results in a residence time between the micro-mixer and the NMR flow cell of 1.7 s.

By raising the total flow rate, the residence time could be further decreased. However, if the residence time is too short, the magnetization of the sample before its excitation in the microcoil decreases. A reduction of the flow rate results in higher residence times, which are undesired here. It could also cause inefficient mixing. The operating point was chosen so as to avoid problems at both ends.

To obtain a steady-state inside the NMR flow cell, the pumps were operated for about 10 min at the desired flow rate. Only then the flow is stopped and the batch experiment is started. The reaction time t starts after the mixing of the reactants, which is considered to be instantaneous, i.e. the conversion of the reactants is zero. The reaction time t has to be matched precisely with the points in time when the NMR spectra are acquired. This is done as follows: The time of the experiment t' is recorded using a digital clock (Prisma 200, Hanhart, Gütenbach, Germany). t' is zero when the acquisition is started, i.e. for the first spectrum.

At $t' = t_{stop}$ the flow is stopped. The reaction time t is related to t' as given in (7).

$$t = t' - t_{stop} + t_{dwell} \tag{7}$$

Therein, t_{dwell} is the residence time of the reacting mixture in the reactor volume, i.e. the residence time between the micro-mixer and the middle of the NMR flow cell.

In the experiments presented here, the residence time in the dwell unit t_{dwell} is 1.7 ± 0.1 s. The error is estimated from the error propagation of the uncertainty of the total reactor volume and the uncertainty of the volumetric flow rate. Due to the errors in the time measurement of the stop time t_{stop} and the uncertainties in the residence time t_{dwell}, the uncertainty of the reaction time t is estimated to be ±1 s.

3.4. NMR spectroscopy and data analysis

^{1}H NMR experiments are carried out using a 400 MHz NMR spectrometer (magnet: Ascend 400, console: Avance 3 HD 400, Bruker Biospin, Rheinstetten, Germany). The NMR spectra are processed with MestReNova (Mestrelab Research, Santiago de Compostela, Spain). All spectra for the measurements of the reaction kinetics are acquired using single scans with a flip angle of 10° (corresponding to a duration of the pulse of 1.5 µs), an aquisition time of 1 s and a spectral width of 25 ppm. The shortest possible pulse repetition time, that yields quantitative results is found to be 2 s. During the kinetic experiments, the pulse repetition time is varied between 2 s at the beginning and 480 s at the end of the experiments, when the reacting mixture is close to the equilibrium.

For each reaction kinetic measurement an array of 100–180 single scans is acquired. As an example, Fig. 3 shows a stacked plot of the ^{1}H NMR spectra as a function of the reaction time t that were acquired during a MF formation experiment.

Because of overlapping peaks, not all peaks are used for the quantitative analysis, but only the peaks of the educt MeOH (≈3.21 ppm) and the CH_3-group signal of the corresponding product esters MA (≈3.38 ppm) or MF (≈3.45 ppm). Based on these signals, the extent of reaction λ is determined. The mole fraction of species x_i is then calculated from the initial mole fraction of species $x_{i,0}$ (i.e. the composition of the reactants in the micro-mixer at t = 0 s) and the extent of reaction λ:

$$x_i(t) = x_{i,0} + \nu_i \lambda(t) \tag{8}$$

Thereby, ν_i is the stoichiometric coefficient of the species i in the reaction (here either −1 or 1). The extent of reaction λ is calculated using (9).

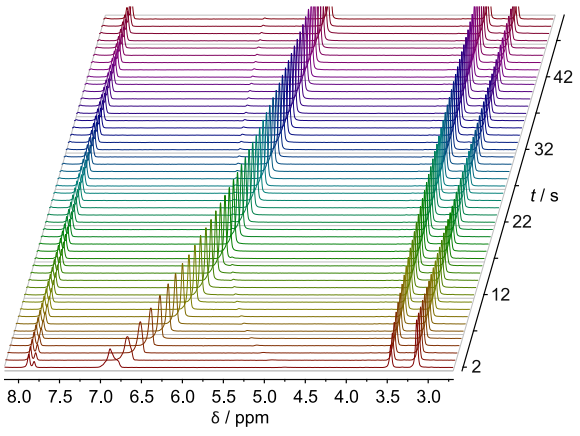

Fig. 3. Stacked plot of ^{1}H NMR spectra as a function of the reaction time. The spectra are acquired during the kinetic experiment of the MF formation using 2 mass-% of sulfuric acid at 333 K.

$$\lambda(t) = \zeta_{ester}(t)(x_{ester,0} + x_{MeOH,0}) - x_{ester,0} \tag{9}$$

with

$$\zeta_{ester}(t) = \frac{n_{ester}(t)}{n_{ester}(t) + n_{MeOH}(t)} \tag{10}$$

Therein, the molar ratio ζ_{ester}, as defined in (10), can be directly computed at a given point in time from the areas under the peaks of the CH_3 groups of MeOH $A^{CH_3}_{MeOH}$ and the ester $A^{CH_3}_{ester}$ respectively in the spectrum.

$$\zeta_{ester}(t) = \frac{A^{CH_3}_{ester}(t)}{A^{CH_3}_{ester}(t) + A^{CH_3}_{MeOH}(t)} \tag{11}$$

Thus, the extent of reaction λ at a given point in time can be directly determined from the initial composition and from the NMR spectrum at that point in time. The areas under the peaks are determined in this work by direct integration of the peaks. The initial composition of the reactants $\underline{x}_0$ is calculated from the compositions of the mixture filled in pump A and pump B, their densities and from the flow rates of the pumps $\dot{V}_A$ and $\dot{V}_B$. To calculate the density of the mixtures filled in the pumps, non-ideal mixing effects are neglected.

Each stopped flow experiment is carried out three times using identical experimental parameters (flow rates, temperatures, initial weights, etc.) and acquisition parameters (acquisition time, relaxation delays, etc.). Thus the molar ratio ζ_{ester} (cf. (10)) is determined for each point in time three times and its average is calculated for evaluation.

The three single runs of each kinetic experiment are compared to each other. The 95% confidence interval of the mean of the molar ratios ζ_{MA} and ζ_{MF} at a given point in time measured in the three single runs of each kinetic experiment is about ±0.005 mol/mol. The largest absolute deviation of a single data point from the mean of the three runs is less than 0.015 mol/mol. The small 95% confidence interval of the repeated measurements together with the small absolute deviations from the mean of the three runs demonstrate the high reproducibility of the measurements.

As described in Section 3.3, a total flow rate of 1000 µl/min of the reactants is applied. At that flow rate, the nuclei are not fully magnetized before they reach the NMR flow cell. As the T_1 relaxation time of the different nuclei used for the quantification in this work are similar (T_1^{MF} = 6.1 s, T_1^{MA} = 5.5 s, T_1^{MeOH} = 4.5 s), the degree of magnetization of the different nuclei is similar, too. So, the composition of the mixture can be directly determined from the ratio of the peak areas in the acquired NMR spectrum. As described above, the pulse repetition time, however, is chosen large enough to ensure a sufficient relaxation of the nuclei prior to their excitation.

The uncertainty of the mole fraction of the reactants in these experiments is estimated from the uncertainty in the initial composition of the reaction mixture (error in the volumetric flow rate, initial weight, etc.) and from uncertainties in the molar ratio of the ester ζ_{ester} (cf. (10)), i.e. errors in the peak area determination (peak integration error, phasing errors, etc.). The uncertainty of the mole fraction of the reactants is determined to be ±0.015 mol/mol.

3.5. Parameter estimation procedure

In order to obtain rate constants from the measured NMR data, the following procedure is carried out. Considering the NMR flow cell as a batch reactor, the change of the extent of reaction λ with time is directly related to the rate of reaction r:

$$\frac{d\lambda}{dt} = r(t) \tag{12}$$

Solving the differential equation, the extent of reaction λ is given as a function of $t, \underline{x}_0, k_f$ and k_b. Thus, the rate constants k_f and k_b are determined for each kinetic experiment individually by means of a parameter estimation procedure that uses the sum of squared errors (SSE) as objective function for the minimization problem:

$$\mathrm{SSE} = \sum_{k=1}^{M_{obs}} \left(\lambda^{obs}_{ester,k}(t_k, \underline{x}_0) - \lambda^{model}_{ester,k}(t_k, \underline{x}_0, k_f, k_b) \right)^2 \stackrel{!}{=} \min \qquad (13)$$

With M_{obs} as the number of spectra taken in one kinetic experiment and t_k as the corresponding point in time of this spectrum, λ^{obs} is the observed extent of reaction that is calculated as given in (9). λ^{model} is the extent of reaction described by the differential equation given in (12). The experimental data is fitted individually for every kinetic experiment at isothermal conditions.

3.6. Preliminary test

In order to evaluate the accuracy of the analysis method for the kinetic experiments, non-reactive test measurements in the stopped flow mode were carried out both for a binary mixture of MeOH and MF, as well as for MeOH and MA. Therefore, pure MeOH was filled into pump A, pure ester (MA or MF respectively) into pump B and both are subsequently mixed in the micro-mixer at a total flow rate of 1000 µl/min and at a temperature of 303 K. The composition of the mixture is analyzed by quantitative ^{1}H NMR spectroscopy over a time span of 1 h after the flow was stopped. Therefore, 200 single scan spectra using the same parameters as in a reactive kinetic experiments are acquired. The mole fraction of the ester measured by ^{1}H NMR spectroscopy is compared to the mole fraction of ester that is expected from the chosen volumetric flow rates of the pumps. These non-reactive stopped flow experiments give information on the propagation of uncertainties from the volumetric flow rates of the pumps and from the determination of the areas under the peaks (phasing, baseline correction, integration etc.). The results including the 95% confidence interval of the repeated measurements and the relative deviation between the measured and expected values are reported in Table 1. The mean of the measured mole fraction of MA and MF are in good agreement with the expected value. These results show that the calculation of the composition of the reactants leaving the micro-mixer, based on the density of the reactants and the flow rates of the pumps, is appropriate. The very small 95% confidence intervals of the mean values for MA and MF indicate the high stability and accuracy of the applied experimental method.

4. Results and discussion

4.1. Methyl acetate formation

Kinetic experiments of the MA formation were carried out at 313 K using an undiluted equimolar feed of MeOH and AA with 1.3 and 3.5 mass-% of sulfuric acid as catalyst, respectively. Details on the experimental parameters are given in the Appendix A.2. The experimental results and the results of the kinetic parameter estimation carried out in this work are presented in Fig. 4. The concentration profile of MA determined by the NMR spectroscopic measurements is smooth and shows no outliers which demonstrates the robustness of the applied analysis method. In comparison to other analytical methods, such as gas chromatography or titration, more data points per time unit can be obtained. The mean absolute deviation between the experimental data and the model prediction parametrized in this work is small (see Fig. 4). This result indicates that the applied model, that comprises both the reactor model and the kinetic model, is consistent with the experimental data. The results of the estimation of the kinetic parameters of the MA formation carried out in this work are listed in Table 2.

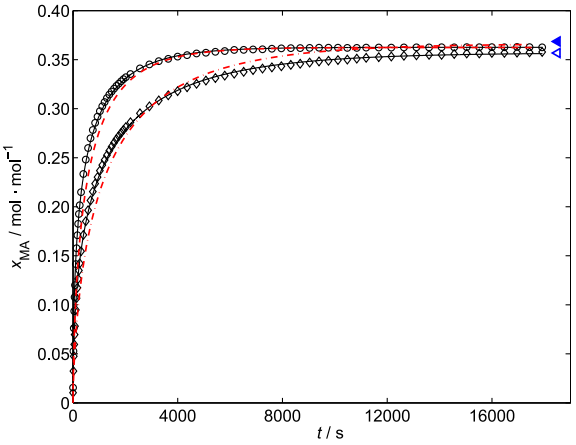

Fig. 4. Mole fraction of MA as a function of time for kinetic experiments of the MA formation carried out at 313 K. Symbols: experimental data using 1.3 mass-% (◊) and 3.5 mass-% (○) of sulfuric acid as catalyst. Predictions of the concentration profile of MA: model parameterized in this work (–) and model of Dörhöfer [10] using 1.3 mass-% (– · –) and 3.5 mass-% (– – –) of sulfuric acid as catalyst. Predicted mole fraction of MA in the chemical equilibrium: at 313 K by the model of Pöpken et al. [12] (◀) and at 333 K by the model of Liu et al. [47] (◁). For clarity, only every third experimental data point is shown.

Fig. 4 also shows the prediction of the concentration profile of MA using the model of Dörhöfer [10] (for more information see Appendix A.4) to describe the kinetics of the reaction. This model prediction agrees well with the experimental data. The small difference between the measured and predicted concentration profile of MA at 1.3 mass-% of sulfuric acid is probably attributable to the fact that Dörhöfer [10] carried out a global parameter estimation using data from kinetic experiments that were carried out in a wide range of temperatures, initial compositions of the reactants and the amount of catalyst. As a result, Dörhöfer [10] reports deviations between his experimental data and the model predictions that are in the same range as the deviation between the experimental data and the model prediction of this work. The prediction of the mole fraction of MA in chemical equilibrium using the model of Pöpken et al. [12] and the model of Liu et al. [47] is shown as well in Fig. 4. The values are in good agreement with the data from the present work. The concentration profile of MA was also

Table 1
Results of the tests with binary non-reactive mixtures of MeOH with MA and MF respectively. The uncertainty of the mole fraction of ester observed by NMR is calculated from the 95% confidence interval of the repeated measurements.

Experiment	Mole fraction		Relative deviation
	Observed mean	Expected mean	
MA	0.398 ± 0.001	0.401	0.7%
MF	0.393 ± 0.002	0.389	0.4%

Table 2
Results of the estimation of the kinetic parameters of the MA formation at 313 K using the experimental data of this work. The uncertainty given is the 95% confidence interval of the parameter estimation.

$x^{(m)}_{H_2SO_4}$ mass-%	k_f mol/(mol · s)	k_b mol/(mol · s)
1.3	$3.06 \times 10^{-4} \pm 4 \times 10^{-6}$	$9.93 \times 10^{-6} \pm 3 \times 10^{-7}$
3.5	$7.77 \times 10^{-4} \pm 9 \times 10^{-6}$	$2.03 \times 10^{-5} \pm 4 \times 10^{-7}$

predicted using the kinetic model of Ganesh et al. [50]. Up to a reaction time of 4000 s, this prediction agrees well with our experimental data. But the prediction of the composition in chemical equilibrium by the model of Ganesh et al. [50] does not agree with the experimental data of this work and with other literature studies [10,12,47]. Thus, the model prediction using the model of Ganesh et al. [50] is not shown in Fig. 4.

To summarize, the experimental data of this work and the predictions using different kinetic models that were determined with completely different set-ups than the one used in this work are in good agreement. These results show that the method applied in this work to determine the reaction kinetics including both the NMR spectroscopic analysis and the modeling of the NMR flow cell as a batch reactor yields reliable results.

4.2. Methyl formate formation

Kinetic experiments of the MF formation were carried out at 303 K, 313 K, 323 K and 333 K using an undiluted equimolar feed of MeOH and FA with 2 mass-% of sulfuric acid as catalyst. To further increase the reaction rate, an additional experiment was carried out at 333 K using 6 mass-% of sulfuric acid as catalyst. Details on the experimental parameters are given in the Appendix A.2. The results of these studies and the results of the kinetic parameter estimation carried out in this work are shown in Fig. 5.

As for the MA formation and despite the fact that the MF formation is much faster than the MA formation, the measured concentration profile of MF is smooth and shows no outliers. The fast acquisition enables to follow the reaction kinetics even in the case of the fastest reaction progress at 333 K using 6 mass-% of sulfuric acid. Under these conditions the chemical equilibrium is reached in less than 20 s. The mean absolute deviation between the experimental data and the corresponding predictions using the kinetic model parameterized in this work is also small (see Fig. 5). The kinetic parameters determined in this work are listed in Table 3. Additionally, the predicted mole fraction of MF in chemical equilibrium using the model of Tischmeyer [11] is depicted in Fig. 5, which is also in good agreement with the experimental data.

The small 95% confidence intervals of the estimated kinetic parameters indicate a high goodness of fit. This high goodness of fit is a result of the small scattering of the experimental data about the model prediction. Moreover, it shows that the chosen model, including both the model of the rate of reaction and the batch reactor model, can describe the experimental data well.

Table 3
Results of the estimation of the rate constants and the corresponding values of the equilibrium constant K_a for the kinetic experiments of the MF formation. Linear regression of the Arrhenius plot yields an apparent activation energy $E_{A,f}$ of 60.6 kJ/mol and a preexponential factor k_f^0 of 18.9 mol/(mol·s).

T	$x_{H_2SO_4}^{(m)}$	k_f	k_b	K_a
K	mass-%	mol/(mol s)	mol/(mol s)	(–)
303	2	$5.59 \times 10^{-3} \pm 4 \times 10^{-5}$	$1.63 \times 10^{-4} \pm 3 \times 10^{-6}$	34.4
313	2	$1.19 \times 10^{-2} \pm 2 \times 10^{-4}$	$3.70 \times 10^{-4} \pm 8 \times 10^{-6}$	32.2
323	2	$2.50 \times 10^{-2} \pm 2 \times 10^{-4}$	$8.15 \times 10^{-4} \pm 1 \times 10^{-5}$	30.7
333	2	$4.83 \times 10^{-2} \pm 9 \times 10^{-4}$	$1.65 \times 10^{-3} \pm 4 \times 10^{-5}$	29.3
333	6	$2.70 \times 10^{-1} \pm 6 \times 10^{-3}$	$8.04 \times 10^{-3} \pm 2 \times 10^{-4}$	33.6

Fig. 6 shows the Arrhenius plot of the rate constants of the forward reaction at 303 K, 313 K, 323 K and 333 K using 2 mass-% of sulfuric acid as catalyst. The Arrhenius plot gives a straight line. Linear regression yields an apparent activation energy $E_{A,f}$ of 60.6 kJ/mol and a preexponential factor k_f^0 of 18.9 mol/(mol·s). The obtained value for $E_{A,f}$ is within the range of values reported for the esterification of methanol with lower aliphatic acids: 65.1 kJ/mol by Tischmeyer [11] for the MF formation and 61.0 kJ/mol by Liu et al. [47] as well as 63.5 kJ/mol by Pöpken et al. [12] for the MA formation. The results demonstrate that the micro-reactor NMR probe head is well suited for studies of reaction kinetics at different temperatures.

The enthalpy of reaction $\Delta_R h$ is determined via the Van't-Hoff plot (cf. Fig. 7). The results are listed together with literature data in Table 4. The values of this work deviate slightly from the literature data, depending on the source, but are within the expected error range.

As described above, to our knowledge, no suitable experimental data and models of the reaction kinetics, which are applicable under the given conditions, are available in the literature. A possible explanation for the lack of data and models in the literature is the fact that only few analytical techniques exist that enable to track such fast reactions. Thus, only a comparison with the prediction of the chemical equilibrium with models from literature is possible, which gave good results as already discussed above. The presented results demonstrate that fast reaction kinetics, with time constants in the order of seconds, can be studied reliably using the new micro-reactor probe head. Thus, this set-up extends

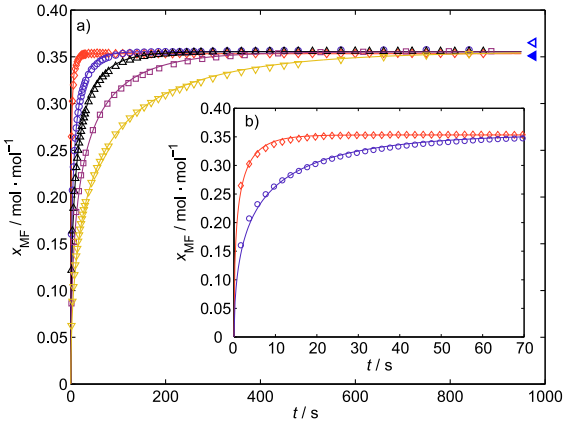

Fig. 5. Results of the kinetic experiments of the MF formation given as an overview of all experiments in (a) and as a zoom of the two fastest observed reaction kinetics in (b). Experimental data using 2 mass-% of sulfuric acid as catalyst at 303 K (▽), 313 K (□), 323 K (△), 333 K (○) and using 6 mass-% of catalyst at 333 K (◇). Lines: prediction by the model developed in this work. Mole fractions of MF in the chemical equilibrium predicted by the model of Tischmeyer [11] at 313 K (◁) and 333 K (◀). In (a), for clarity, only every third experimental data point is shown.

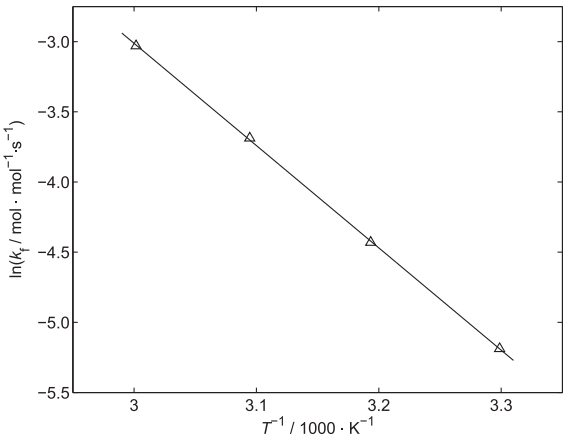

Fig. 6. Arrhenius plot of the rate constant k_f of the MF formation at 303 K to 333 K using 2 mass-% of sulfuric acid as catalyst. Symbols: experimental data. Line: linear regression.

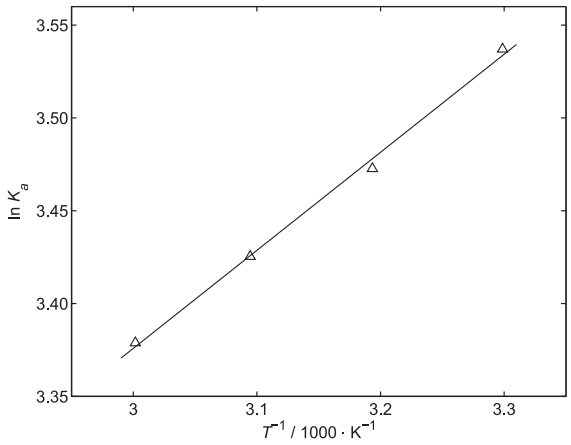

Fig. 7. Van't-Hoff plot of the equilibrium constant K_a of the MF formation at 303 K to 333 K using 2 mass-% of sulfuric acid as catalyst. Symbols: experimental data. Line: linear regression.

Table 4
Reaction enthalphy $\Delta_R h$ of the MF formation determined in this work and comparison to literature data.

Source	$\Delta_R h$ / kJ mol^{-1}
Enthalpy of formation: DIPPR [51] (298.15 K)	−7.3
Enthalpy of formation: HSC databank [54] (298.15 K)	−5.4
Linear regression of Van't Hoff: this work (303–333 K)	−4.4

the application range of kinetic investigations using NMR spectroscopy to fast reactions that reach equilibrium in less than one minute.

5. Conclusion

The design of chemical processes requires reliable data on reaction kinetics which is difficult to obtain for fast reactions, especially in the case of complex systems with many reactants. In this work, the novel micro-reactor probe head is applied for the investigation of the homogeneously catalysed MA and MF formation with the focus on a thorough test of the limits and accuracy of the presented set-up for the investigation of fast reaction kinetics. Therefore, the homogeneously catalysed formation of MA and MF were chosen as test systems.

For both systems the experiments using the new probe head yield reliable kinetic data with a high temporal resolution and a high reproducibility. The accuracy of the analysis method under the chosen conditions is similar to established methods like gas chromatography or titration, whereas the temporal resolution is higher. Even in the case of the very fast reaction of the MF formation at 333 K using 6 mass-% of sulfuric acid, that reached equilibrium within 20 s, the course of reaction could be followed using the presented set-up.

Kinetic models are parameterized in this work using the experimental data of this work. The model predictions and the experimental data correlate well. Furthermore, the experimental data of the MA formation is in good agreement with predictions using models from the literature. In addition, the apparent activation energy of the MF formation determined in this work is in good agreement with literature data on esterification reactions. These results show that the micro-reactor NMR probe head can be used to determine reaction kinetics at different temperatures reliably even for fast reactions.

As the new set-up enables an in situ analysis of the composition of a reacting mixture at constant temperature and pressure, it extends the range in which NMR spectroscopy can be applied for studies of fast reaction kinetics. The new technique is an attractive alternative to an ex situ analysis in an NMR sample tube or to the commonly applied online NMR spectroscopy set-ups using a sample loop to the NMR spectrometer for the investigation of reaction kinetics. Gaining both, quantitative and qualitative information at the same time by the use of NMR spectroscopy, the new technique is especially advantageous for studying complex reacting systems with many components. Such systems will be a focus of future kinetic studies using the new micro-reactor probe head.

Acknowledgement

We gratefully acknowledge Frank Engelke, Hartmut Glauner and Jürgen Ganz (Bruker BioSpin GmbH, Rheinstetten, Germany) for their support during the development of the new probe head electronics. We further gratefully acknowledge the technical support of Berthold Mrawek and Julian Peter. Erik von Harbou thanks Max Buchner Research Foundation for its support.

Appendix A. Supplementary data

Supplementary data associated with this article can be found, in the online version, at http://dx.doi.org/10.1016/j.cej.2016.07.045.

References

[1] R.P. Bell, A.L. Dowding, J.A. Noble, The kinetics of ester hydrolysis in concentrated aqueous acids, J. Chem. Soc. (1955) 3106–3110.
[2] H.A. Smith, Kinetics of the catalyzed esterification of normal aliphatic acids in methyl alcohol, J. Am. Chem. Soc. 61 (1939) 254–260.
[3] S. Grob, H. Hasse, Reaction kinetics of the homogeneously catalyzed esterification of 1-butanol with acetic acid in a wide range of initial compositions, Ind. Eng. Chem. Res. 45 (2006) 1869–1874.
[4] J. Lilja, D. Murzin, T. Salmi, J. Aumo, P. Mäki-Arvela, M. Sundell, Esterification of different acids over heterogeneous and homogeneous catalysts and correlation with the taft equation, J. Mol. Catal. A: Chem. 182-183 (2002) 555–563.
[5] J. Holtbruegge, M. Leimbrink, P. Lutze, A. Górak, Synthesis of dimethyl carbonate and propylene glycol by transesterification of propylene carbonate with methanol: catalyst screening, chemical equilibrium and reaction kinetics, Chem. Eng. Sci. 104 (2013) 347–360.
[6] R. Tesser, M. Di Serio, M. Guida, M. Nastasi, E. Santacesaria, Kinetics of oleic acid esterification with methanol in the presence of triglycerides, Ind. Eng. Chem. Res. 44 (2005) 7978–7982.
[7] E. von Harbou, A. Yazdani, M. Schmitt, C. Großmann, H. Hasse, Reaction kinetics for reactive distillation using different laboratory reactors, Ind. Eng. Chem. Res. 52 (2013) 624–637.
[8] M. Mazzotti, B. Neri, D. Gelosa, M. Morbidelli, Dynamics of a chromatographic reactor: esterification catalyzed by acidic resins, Ind. Eng. Chem. Res. 36 (1997) 3163–3172.
[9] P.T. Mai, T.D. Vu, K.X. Mai, A. Seidel-Morgenstern, Analysis of heterogeneously catalyzed ester hydrolysis performed in a chromatographic reactor and in a reaction calorimeter, Ind. Eng. Chem. Res. 43 (2004) 4691–4702.
[10] T. Dörhöfer, Gestaltung und Effektivität von Bodenkolonnen für die Reaktivrektifikation, TU München, 2006 (Ph.D. thesis).
[11] M. Tischmeyer, Messung und Berechnung von Phasengleichgewichten reaktiver Systeme, University Erlangen, 2004 (Ph.D. thesis).
[12] T. Pöpken, L. Götze, J. Gmehling, Reaction kinetics and chemical equilibrium of homogeneously and heterogeneously catalyzed acetic acid esterification with methanol and methyl acetate hydrolysis, Ind. Eng. Chem. Res. 39 (2000) 2601–2611.
[13] M. Maiwald, H.H. Fischer, M. Ott, R. Peschla, C. Kuhnert, C.G. Kreiter, G. Maurer, H. Hasse, Quantitative NMR spectroscopy of complex liquid mixtures: methods and results for chemical equilibria in formaldehyde-water-methanol at temperatures up to 383 K, Ind. Eng. Chem. Res. 42 (2003) 259–266.
[14] W. Böttinger, M. Maiwald, H. Hasse, Online NMR spectroscopic study of species distribution in MDEA-H2O-CO2 and MDEA-PIP-H2O-CO2, Ind. Eng. Chem. Res. 47 (2008) 7917–7926.
[15] M.A. Bernstein, M. Stefinovic, C.J. Sleigh, Optimising reaction performance in the pharmaceutical industry by monitoring with NMR, Magn. Reson. Chem. 45 (2007) 564–571.
[16] E.J. Kibrik, O. Steinhof, G. Scherr, W.R. Thiel, H. Hasse, Proof of ether-bridged condensation products in UF resins by 2D NMR spectroscopy, J. Polym. Res. 20:79 (2013) 1–10.

[17] M. Maiwald, Hochauflösende Online NMR-Spektroskopie für das Reaktions- und Prozessmonitoring, Cuvillier Verlag, Göttingen, 2012.
[18] I. Hahnenstein, M. Albert, H. Hasse, C.G. Kreiter, G. Maurer, NMR spectroscopic and densimetric study of reaction kinetics of formaldehyde polymer formation in water, deuterium oxide, and methanol, Ind. Eng. Chem. Res. 34 (1995) 440–450.
[19] M. Maiwald, T. Grützner, E. Ströfer, H. Hasse, Quantitative NMR spectroscopy of complex technical mixtures using a virtual reference: chemical equilibria and reaction kinetics of formaldehyde-water-1,3,5-trioxane, Anal. Bioanal. Chem. 385 (2006) 910–917.
[20] M. Ott, H.H. Fischer, M. Maiwald, K. Albert, H. Hasse, Kinetics of oligomerization reactions in formaldehyde solutions: NMR experiments up to 373 K and thermodynamically consistent model, Chem. Eng. Process. 44 (2005) 653–660.
[21] H. Fischer, K. Albert, Online LC NMR and Related Techiques, John Wiley & Sons, New York, 2003. pp. 195–218.
[22] N. Zientek, C. Laurain, K. Meyer, M. Kraume, G. Guthausen, M. Maiwald, Simultaneous ^{19}F-^{1}H medium resolution NMR spectroscopy for online reaction monitoring, J. Magn. Reson. 249 (2014) 53–62.
[23] F. Dalitz, M. Cudaj, M. Maiwald, G. Guthausen, Process and reaction monitoring by low-field NMR spectroscopy, Prog. Nuc. Mag. Res. Spectrosc. 60 (2012) 52–70.
[24] H. Wensink, F. Benito-Lopez, D.C. Hermes, W. Verboom, H.J.G.E. Gardeniers, D. N. Reinhoudt, A. van den Berg, Measuring reaction kinetics in a lab-on-a-chip by microcoil NMR, Lab. Chip 5 (2005) 280–284.
[25] L. Ciobanu, D.A. Jayawickrama, X. Zhang, A.G. Webb, J.V. Sweedler, Measuring reaction kinetics by using multiple microcoil NMR spectroscopy, Angew. Chem. Int. Ed. Eng. 42 (2003) 4669–4672.
[26] I.M. Clegg, C.M. Gordon, D.S. Smith, R. Alzaga, A. Codina, NMR reaction monitoring during the development of an active pharmaceutical ingredient, Anal. Methods 4 (2012) 1498–1506.
[27] M. Maiwald, H.H. Fischer, Y. Kim, K. Albert, H. Hasse, Quantitative high-resolution on-line NMR spectroscopy in reaction and process monitoring, J. Magn. Reson. 166 (2004) 135–146.
[28] A. Brächer, S. Hoch, K. Albert, H. Kost, B. Werner, E. von Harbou, H. Hasse, Thermostatted micro-reactor NMR probe head for monitoring fast reactions, J. Magn. Reson. 242 (2014) 155–161.
[29] A.G. Webb, Radiofrequency microcoils in magnetic resonance, Prog. Nucl. Magn. Reson. Spectrosc. 31 (1997) 1–42.
[30] R.M. Fratila, A.H. Velders, Small-volume nuclear magnetic resonance spectroscopy, Annu. Rev. Anal. Chem. 4 (2011) 227–249.
[31] A.P.M. Kentgens, J. Bart, P.J.M. van Bentum, A. Brinkmann, E.R.H. van Eck, J.G.E. Gardeniers, J.W.G. Janssen, P. Knijn, S. Vasa, M.H.W. Verkuijlen, High-resolution liquid- and solid-state nuclear magnetic resonance of nanoliter sample volumes using microcoil detectors, J. Chem. Phys. 128 (2008) 052202.
[32] H.G. Krojanski, J. Lambert, Y. Gerikalan, D. Suter, R. Hergenröder, Microslot NMR Probe for metabolomics studies, Anal. Chem. 80 (2008) 8668–8672.
[33] M.E. Lacey, R. Subramanian, D.L. Olson, A.G. Webb, J.V. Sweedler, High-resolution NMR spectroscopy of sample volumes from 1 nL to 10 μL, Chem. Rev. 99 (1999) 3133–3152.
[34] M. Kakuta, D.A. Jayawickrama, A.M. Wolters, A. Manz, J.V. Sweedler, Micromixer-based time-resolved nmr: applications to ubiquitin protein conformation, Anal. Chem. 75 (2003) 956–960.
[35] D.L. Olson, M.E. Lacey, J.V. Sweedler, High-resolution microcoil NMR for analysis of mass-limited, nanoliter samples, Anal. Chem. 70 (1998) 645–650.
[36] M.L. Kieke, J.W. Schoppelrei, T.B. Brill, Spectroscopy of hydrothermal reactions. 1. The CO2-H2O system and kinetics of urea decomposition in an FTIR spectroscopy flow reactor cell operable to 725 K and 335 bar, J. Phys. Chem. 100 (1996) 7455–7462.
[37] P. Hinsmann, J. Frank, P. Svasek, M. Harasek, B. Lendl, Design, simulation and application of a new micromixing device for time resolved infrared spectroscopy of chemical reactions in solution, Lab Chip 1 (2001) 16–21.
[38] T.M. Floyd, M.A. Schmidt, K.F. Jensen, Silicon micromixers with infrared detection for studies of liquid-phase reactions, Ind. Eng. Chem. Res. 44 (2005) 2351–2358.
[39] J.W. Schoppelrei, M.L. Kieke, T.B. Brill, Spectroscopy of hydrothermal reactions. 2. Reactions and kinetic parameters of [NH3OH]NO3 and equilibria of (NH4) 2CO3 determined with a flow cell and FT raman spectroscopy, J. Phys. Chem. 100 (1996) 7463–7470.
[40] J. Kuligowski, G. Quintás, M. de la Guardia, B. Lendl, Analytical potential of mid-infrared detection in capillary electrophoresis and liquid chromatography: a review, Anal. Chim. Acta 679 (2010) 31–42.
[41] A. Scheithauer, A. Brächer, T. Grützner, D. Zollinger, W. Thiel, E. von Harbou, H. Hasse, Online ^{1}H NMR spectroscopic study of the reaction kinetics in mixtures of acetaldehyde and water using a new microreactor probe head, Ind. Eng. Chem. Res. 53 (2014) 17589–17596.
[42] A. Scheithauer, T. Grützner, D. Zollinger, E. von Harbou, H. Hasse, Modeling, simulation and analysis of a process for the production of crotonaldehyde, Chem. Eng. Process. 101 (2016) 101–111.
[43] B. Likozar, A. Pohar, J. Levec, Transesterification of oil to biodiesel in a continuous tubular reactor with static mixers: Modelling reaction kinetics, mass transfer, scale-up and optimization considering fatty acid composition, Fuel Process. Technol. 142 (2016) 326–336.
[44] G. Dummann, U. Quittmann, L. Gröschel, D.W. Agar, O. Wörz, K. Morgenschweis, The capillary-microreactor: a new reactor concept for the intensification of heat and mass transfer in liquid-liquid reactions, Catal. Today 79-80 (2003) 433–439.
[45] N. Aoki, S. Tanigawa, K. Mae, Design and operation of gas-liquid slug flow in miniaturized channels for rapid mass transfer, Chem. Eng. Sci. 66 (2011) 6536–6543.
[46] R. Rönnback, T. Salmi, A. Vuori, H. Haario, J. Lehtonen, A. Sundqvist, E. Tirronen, Development of a kinetic model for the esterification of acetic acid with methanol in the presence of a homogeneous acid catalyst, Chem. Eng. Sci. 52 (1997) 3369–3381.
[47] Y. Liu, E. Lotero, J. Goodwin, Effect of water on sulfuric acid catalyzed esterification, J. Mol. Catal. A Chem. 245 (2006) 132–140.
[48] V. Agreda, L. Partin, W. Heise, High-purity methyl acetate via reactive distillation, Chem. Eng. Prog. 86 (1990) 40–46.
[49] S. Elgue, A. Devatine, L.E. Prat, P. Cognet, M. Cabassud, C. Gourdon, F. Chopard, Intensification of ester production in a continuous reactor, Int. J. Chem. React. Eng. 7 (2009) A24.
[50] B. Ganesh, K. Yamuna Rani, B. Satyavathi, C. Venkateswarlu, Development of kinetic models for acid-catalyzed methyl acetate formation reaction: effect of catalyst concentration and water inhibition, Int. J. Chem. Kinet. 43 (2011) 263–277.
[51] American Institute of Chemical Engineers, Design Institute for Physical Properties Research (DIPPR), Project 801, 2006.
[52] F. Schönfeld, V. Hessel, C. Hofmann, An optimised split-and-recombine micro-mixer with uniform 'chaotic' mixing, Lab Chip 4 (2004) 65–69.
[53] C. Ammann, P. Meier, A. Merbach, A simple multinuclear NMR thermometer, J. Magn. Reson. 46 (1982) 319–321.
[54] A. Roine, HSC chemistry 7.0, Outokumpu Research Oy: Pori, 2009.

von Harbou et al., 2017

Reprinted with permission from: E. von Harbou, R. Behrens, J. Berje, A. Brächer, H. Hasse, Studying Fast Reaction Kinetics with Online NMR Spectroscopy, Chemie Ingenieur Technik, Volume 89, 2017, Pages 369-378, DOI 10.1002/cite.201600068

Studying Fast Reaction Kinetics with Online NMR Spectroscopy

Erik von Harbou*, Richard Behrens, Jürgen Berje, Alexander Brächer, and Hans Hasse

DOI: 10.1002/cite.201600068

On the occasion of the Hanns-Hofmann Prize awarded at the European Symposium on Chemical Reaction Engineering, Fürstenfeldbruck, October 2015

Dedicated to Prof. Dr.-Ing. Andreas Seidel-Morgenstern on the occasion of his 60th birthday

A liquid thermostated microreactor Nuclear Magnetic Resonance (NMR) probe head is presented that facilitates the investigation of kinetics of fast reactions. With this setup, reaction kinetics can be studied in a broad temperature (–20 – 100 °C) and pressure range (0 – 60 bar). The setup and NMR probe head are discussed from a reaction engineering standpoint based on experiments and simulations. The microreactor probe head widens significantly the range of applications of online NMR spectroscopy for reaction and process monitoring.

Keywords: Micro-reaction technology, Online NMR spectroscopy, Reaction kinetics

Received: June 06, 2016; *revised:* September 16, 2016; *accepted:* November 21, 2016

1 Introduction

For the model-based design, scale-up, and optimization of chemical processes, reliable kinetic models of the involved reactions are a key prerequisite. Normally, these reaction kinetics are determined in laboratory reactors. The analysis required to determine the composition of the reactants is normally carried out using ex situ analysis methods such as gas chromatography. The application of noninvasive analysis methods is advantageous as they enable studying the reaction kinetics in situ in the laboratory reactor so that sampling is not necessary. Frequently applied noninvasive analysis methods are IR, Raman and UV-Vis spectroscopy, and nuclear magnetic resonance (NMR) spectroscopy. In contrast to most optical spectroscopic methods, NMR spectroscopy has the advantage that no calibration is necessary prior to the analysis to obtain quantitative results. Hence, the composition of mixtures that contain species that cannot be isolated or that are not available in pure form can also be determined. Furthermore, NMR spectroscopy has a high spectral resolution and can distinguish even between chemically similar species. Hence, online NMR spectroscopy is often not only the best choice but also the sole analytical method that will yield the desired detailed quantitative data when complex reaction systems with unknown and/or unstable intermediates are studied [1].

A variety of setups and NMR methods exist that can be applied to monitor reactions. The simplest and most often used method is to fill and mix the reactants directly inside the NMR sample tube and follow then the progress of reaction by repeated acquisition of NMR spectra. For details, see, e.g., [2 – 6]. Another widely used setup is an external reactor that is connected via a sample loop with the NMR spectrometer. The NMR spectrometer is equipped with a flow cell where the sample is analyzed. Also in this case, the progress of reaction is monitored by repeated acquisitions of spectra. Compared to the NMR sample tube the external reactor has the advantage that it facilitates a very good control of the temperature and the pressure in the reactor. Some examples for the application of this setup are given in [1, 7 – 9].

In both methods (NMR sample tube and external reactor with sample loop) the time delay between the mixing of the reactants, i.e., the start of the reaction and the earliest time the reaction can be monitored in the NMR spectrometer is at least 1 – 4 min [1]. Thus, fast reactions with a half-life of less than 2 – 8 min cannot be studied with these methods. Several alternative methods have been developed in the past to overcome this limitation. One option is to inject the reactants rapidly into the NMR sample tube, which was placed inside the NMR spectrometer before, see, e.g., [10 – 12]. This rapid injection NMR method reduces the time delay between mixing of the reactants and the start of the moni-

Dr. Erik von Harbou, Richard Behrens, Jürgen Berje, Alexander Brächer, Prof. Hans Hasse,
erik.vonharbou@mv.uni-kl.de
Technische Universität Kaiserslautern, Lehrstuhl für Thermodynamik (LTD), Erwin-Schrödinger-Straße 44, 67663 Kaiserslautern, Germany.

toring of the reaction by NMR spectroscopy significantly down to less than a second.

However, to enable the measurement of fast reaction kinetics that are transferable to the kinetics in industrial reactors not only the time delay between mixing and analysis is of importance but also other reaction engineering aspects. Usually laboratory reactors are designed so that it can be assumed that the reactions take place under isothermal conditions and that the laboratory reactor can be described by an ideal reactor model such as batch reactor model, continuous stirred tank reactor model, or plug flow reactor model. The design of a setup that fulfills these requirements and facilitates online NMR spectroscopic analysis is especially challenging for fast reactions, which are exo- or endothermic, as it has to be assured among others that the reactants are perfectly and instantaneously mixed (i.e., much faster than the time constant of the reaction), the hydrodynamic conditions are well defined (i.e., no dead-zones, bypasses, etc.) in the reactor, and that the change of the temperature of the reactants both over time and space is negligible.

Recently, we presented a NMR probe head that is designed to measure the kinetics of fast reactions under conditions that are transferable to industrial applications. The NMR probe head combines micro-reaction technology with capillary flow NMR spectroscopy [13, 14]. Two reactants are fed separately into the NMR probe head and they first come into contact inside the NMR using a micromixer. The mixed reactants then pass through a capillary NMR flow cell where the NMR signal is acquired and the sample is analyzed. The whole flow path of the reactants is liquid thermostated so that reactions can be investigated in a broad temperature range (–20 – 100 °C). Moreover, the microreactor NMR probe head is designed for pressures up to 60 bar. The microreactor NMR probe head was already used to study the kinetics of the industrially relevant reaction of acetaldehyde with water [15]. Here, the challenge was not the fast reaction but to avoid evaporation of the reactants and to control the temperature efficiently in a large range.

As it is difficult to determine the temperature of the reaction mixture that is located inside the NMR spectrometer simultaneously with the measurements of the reaction kinetics, an important (and often unanswered) question is whether the assumption that the reactions take place under isothermal conditions is justified for the used NMR setups. For this reason, both the microreactor NMR probe head and the NMR sample tube are modeled in this work as non-isothermal reactors under consideration of the thermostatization of the setups. Using these models, the temperature change caused by the reaction and its influence on the concentration profiles are predicted. In a parameter study it is assessed for which reaction (time constants, i.e., half-life of the reaction, enthalpy of reaction, and activation energy of the reaction) these two setups can be applied. In addition, the behavior of the microreactor NMR probe head is characterized from a reaction engineering standpoint. For that purpose, performance test of the micromixer, measurements of the velocity profile in the reactor, and residence time distribution (RTD) measurements are carried out.

Finally, the results from kinetic studies are presented. By comparing the kinetics of the esterification of methanol to methyl acetate determined with the microreactor NMR probe head with the kinetics reported in literature, the accuracy of the measurement method is demonstrated. The applicability of the probe head for studying fast reactions is tested using the homogeneously catalyzed esterification of methanol to methyl formate as example. In addition, to demonstrate that the microreactor NMR probe head widens the range of application of online NMR spectroscopy significantly, the results from a kinetic study of the industrially relevant formation of poly(oxymethylene) glycols in aqueous formaldehyde solutions is shown. These kinetic experiments were carried out under conditions that were not observable using conventional setups because of the fast reaction kinetics in this system.

2 Micromixer NMR Probe Head

2.1 Description

The microreactor probe head consists basically of three main units: the micromixer, the reactor, and the NMR flow cell. The feed streams are efficiently mixed in the micromixer. After the micromixer, the reactants enter the reactor unit which is simply a short capillary. From the reactor unit the reactants pass through the NMR flow cell, which is also a capillary. The NMR flow cell is wrapped by the radio frequency coil that is used to excite the sample and to receive the NMR signals. Hence, the composition of the mixture is determined in the NMR flow cell. After the NMR flow cell the reactants leave the NMR probe head through a capillary. A drawing of the NMR probe head highlighting the mixer unit, the reactor unit, and the NMR flow cell is shown in Fig. 1. The total reactor volume can be adapted using capillaries with different inner diameter in the reactor unit.

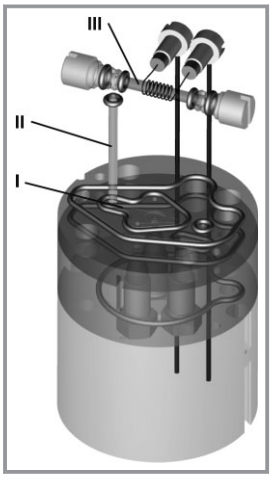

Figure 1. Microreactor NMR probe head: mixer unit (I), reactor unit (II), NMR flow cell (III).

Thus, the total reactor volume counted from the micromixer to the middle of the NMR flow cell, where the analysis of the mixture takes place, is in the range of 25 – 55 µL. The NMR flow cell is made of glass, all other units are made of poly(etherether) ketone (PEEK). The microreactor NMR probe head was manufactured at the Fraunhofer ICT-IMM, Mainz, Germany. The electronics (i.e., the resonant circuit) required for the NMR measurements were installed by Bruker, Rheinstetten, Germany.

The NMR microreactor probe head is mounted inside the 54 mm bore of the NMR spectrometer. Two reactants are feed separately into the NMR probe head. In this work, two high precision syringe pumps (Dual 260d, Teledyne Isco, Lincoln, USA) are used. The reactants are brought into contact in the micromixer for the first time. All units along the flow path of the reactants, i.e., the pumps, the feed lines, the micromixer, the reactor unit, the NMR flow cell, and the product line, are liquid thermostated. Water is used outside the NMR spectrometer as thermostatization medium. The choice of the thermostatization medium that can be used inside the NMR spectrometer is not trivial as it should not interfere with the NMR spectroscopic measurements. Thus, perfluorotributylamine (FC-43), which is a fully fluorinated polymer, is used in this work. A schematic drawing of the experimental setup is depicted in Fig. 2. More details on the microreactor NMR probe head as well as on the whole experimental setup are given in [13, 14].

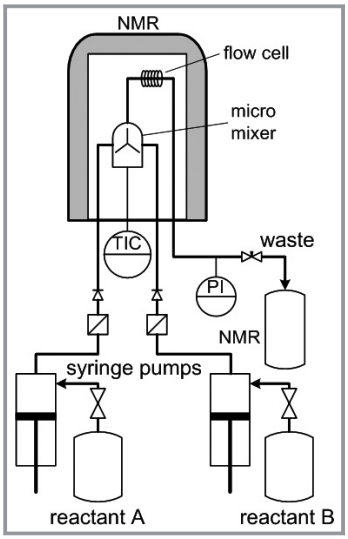

Figure 2. Scheme of the experimental setup for the measurement of reaction kinetics using the microreactor NMR probe head.

Two operation modes can be applied to measure the rate of reaction: the stopped flow mode and the flow mode. In the stopped flow mode, the two reactants are fed with high flow rates into the microreactor NMR probe head, where they pass through the micromixer, the reactor unit, and the NMR flow cell as described above. After the flow has been stopped abruptly, the change of the composition of the reacting mixture inside the NMR flow cell is followed over time by repeated acquisition of NMR spectra. Because of the very short residence time of the reactants in the reactor unit, the time delay between mixing of the reactants (i.e., start of the reaction) and first analysis of the composition of the reacting mixture is about two seconds only.

In the flow mode, the reactants are fed into the microreactor NMR probe head with a constant flow rate. When steady-state is reached, the composition of the reacting mixture is analyzed in the NMR flow cell without stopping the flow of reactants. Then the flow rate of the reactants, i.e., the residence time in the reactor is changed and the reacting mixture is analyzed again after steady-state has been reached. By repeating this procedure several times, the composition of the reacting mixture is determined as a function of the residence time.

The advantage of the flow mode is that the analysis is carried out under steady-state conditions. In contrast to the stopped flow mode, the composition of the reactants does not change during the analysis and thus also methods with long acquisitions times such as multi-scan or 2D spectroscopic methods can be applied. On the other hand, the analysis of flowing mixtures has unfavorable effects on the quality of the obtained NMR spectra [16]. In certain circumstances this can mean that the information obtained from the spectra are not quantitative any longer. As a rule of thumb, the accuracy of the quantitative measurement with the microreactor NMR probe head diminishes at flow rates higher than 1000 µL min^{-1}. Even higher flow rates are possible but they require a calibration to account for the effect of the flowing sample on the obtained NMR signals. The lower limit of applicable flow rates of the reactants is not determined by NMR spectroscopic effects but by the performance of the micromixer to achieve an efficient mixing of the reactants. This value depends both on the chosen chemical system (viscosity, surface tension, etc.) and on the used type of mixer. The influence of the mixer design on the mixing of the reactants is discussed in detail in the next section. All in all, the range of flow rates that can be realized with this NMR probe head in the flow mode corresponds to a residence time of the reactants of about 2 – 150 s (counted from the micromixer to the NMR flow cell). Another disadvantage of the flow mode is that the determination of reaction kinetics is more time-consuming than in the stopped flow mode. After each change of the flow rate of the reactants the microreactor probe head has to be operated for several minutes until steady-state is reached again and a NMR spectrum can be acquired. In contrast, in the stopped-flow within one experimental run the whole concentration profile is obtained. A detailed discussion on the advantages and disadvantages of the two different operation modes is given in [13].

In order to be able to describe the reactor in both flow modes by a well-defined reactor model that facilitates the deduction of the rate of reaction from the measured concentration profiles, the micromixer has to fulfill two important requirements. First, the reactants leaving the mixer should be perfectly mixed in a large range of flow rates. Second, the mixing time should be significantly shorter than

the time constant of the reaction. That means the volume of the micromixer must be small in comparison to the total reactor volume.

In this work, two different types of micromixers were tested: a split-and-recombine mixer and an interdigital mixer. A schematic drawing of both mixer types is shown in Fig. 3 together with a picture of the implementation in the microreactor NMR probe head. In the split-and-recombine mixer the two feeds are passing through a crawler-shaped structure, where they are split and recombined 39 times to ensure a good mixing (cf. Fig. 3a). In the interdigital mixer, the two feeds are passing separately through 21 or 22 microchannels arranged in parallel. The outlet of these microchannels is collected in a small mixing chamber where the two feeds are brought into contact. From the mixing chamber the reactants leave the micromixer and flow into the reactor unit (cf. Fig. 3b). The micromixers were designed and manufactured at the Fraunhofer ICT-IMM, Mainz, Germany. More details on the two different types of mixer are given, e.g., in [17, 18].

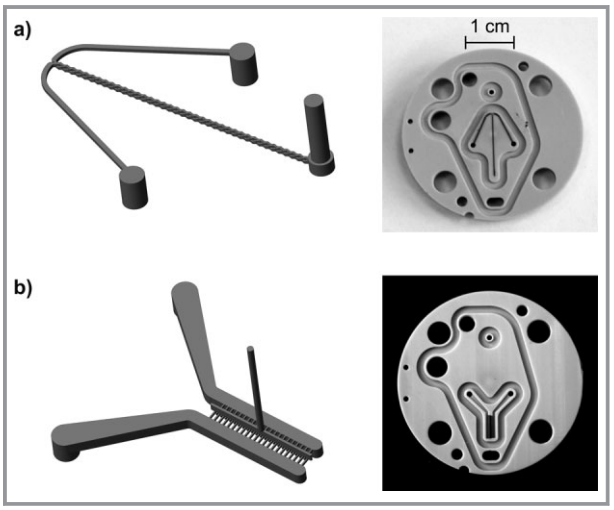

Figure 3. Drawings of the micromixers (left hand side) and pictures of the whole micromixer unit (right hand side) that is installed in the microreactor probe head: a) split-and-recombine mixer, b) interdigital mixer.

The volume of the liquid inside the micromixer is 0.14 µL for the interdigital mixer and 0.27 µL for the split-and-recombine mixer. Thus, the volume is less than one percent of the total reactor volume and the mixing time is indeed negligible compared to the residence time in the reactor unit (assuming the reactants are fully mixed when they leave the micromixer).

2.2 Performance Tests of the Micromixer

The test of the performance of the micromixer is not trivial as the micromixers can only be used when they are installed in the probe head so that the outlet of the micromixer cannot be directly accessed. However, when a blend of two pure liquids that is not completely mixed and contains inhomogeneities passes through the NMR flow cell, the magnetic flux density is usually disturbed because of the susceptibility differences of the two liquids. These inhomogeneities in the magnetic flux density cause strong artefacts and distortions of the peaks in the acquired NMR spectra. This effect is exploited in this work to test the performance of the two different mixers.

These mixing experiments were carried out in this work using the setup depicted in Fig. 2. Pump A and pump B were filled with two different substances that do not react when they come into contact. The two pure substances are fed continuously into the microreactor NMR probe head that is either equipped with the split-and-recombine or the interdigital mixer. Different combinations of substances were used as feeds: acetone/cyclohexane, water/acetone, methyl formate/methanol, and ethanol/acetone. Starting with a high total flow rate of about 2000 µL min^{-1} the flow rate was decreased stepwise and each time an ^{1}H NMR spectra of the product stream was acquired in the flow mode. Fig. 4 depicts the ^{1}H NMR spectra of the mixture of acetone and cyclohexane acquired at a flow rate of 400 µL min^{-1} using the split-and-recombine mixer (Fig. 4a) or the interdigital mixer (Fig. 4b). The form of the peaks in the spectrum in Fig. 4a indicates that both liquids are well-mixed. The determined composition of the mixture is with a relative error of about 1 % in good agreement with the value expected from the flow rates of the two pumps. More details on the accuracy of the measurement method are presented in [13]. In contrast, the distorted peaks in the ^{1}H NMR spectrum in Fig. 4b reveal that the two liquids are not well-mixed. The outcomes of the mixing experiment using the other combination of substances as feeds are similar. These results are confirmed by means of spatially resolving NMR spectroscopy experiments that were carried

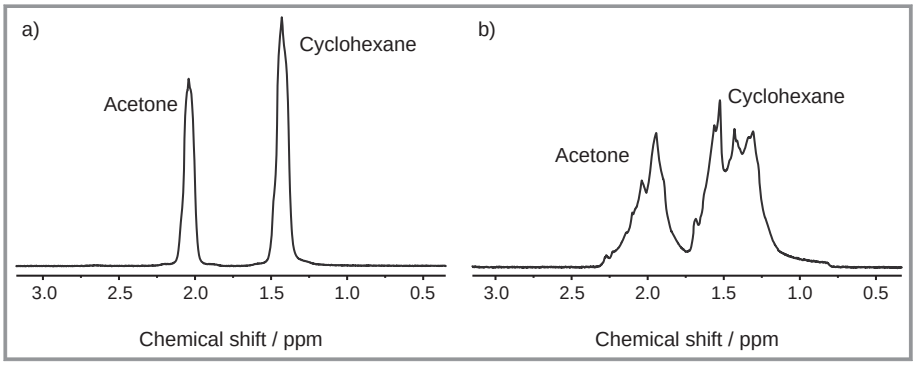

Figure 4. ^{1}H NMR spectrum acquired with the microreactor NMR probe head in the mixing experiments at a total flow rate of 400 µL min^{-1} using acetone and cyclohexane as feed. Used mixer type: a) split-and-recombine mixer, b) interdigital mixer.

out at the Magnetic Resonance Research Centre of the University of Cambridge, UK. It was found in these experiments that strong concentration gradients exist perpendicular to the flow direction (i.e., the liquids are not homogeneously mixed) for systems that show a NMR spectrum as depicted in Fig. 4b.

The minimal flow rate required for a good mixing of the tested binary mixtures was 15 μL min^{-1} for the split-and-recombine mixer and 500 μL min^{-1} for the interdigital mixer used in this work. Obviously, the performance of the split-and-recombine mixer with regards to the requirements in this project is much better. Assuming that the results are similar for mixing other liquids than thus tested in this work all further experiments of this work were carried out with the split-and-recombine mixer.

2.3 Flow Characterization and Residence Time Distribution Measurements

As the flow characteristics inside the NMR probe head influence significantly its behavior as reactor, the velocity profile in the NMR flow cell was measured by Magnetic Resonance Velocimetry (MRV). These experiments were also carried out at the Magnetic Resonance Research Centre of the University of Cambridge, UK. Pure water was continuously pumped at different flow rate through the microreactor NMR probe head using both pumps. For each flow rate, the two dimensional velocity profiles were determined through a plane that was oriented perpendicular to the flow direction and was located in the middle of the NMR flow cell. The observed velocity profile is depicted in Fig 5a for a total flow rate of 100 μL min^{-1}. The measured velocity profile has a parabolic shape (cf. Fig. 5b). The same holds for other flow rates tested in this work. These findings indicate that a fully developed laminar flow profile exists in the NMR flow cell and no strong nonideal flow effects like backmixing or dead zones are introduced by the change of the flow direction and the inner diameter of the capillaries in the transition from the reactor unit to the NMR flow cell (cf. Fig. 1).

To determine the flow characteristics in the whole microreactor probe head residence time distribution (RTD) measurements were carried out by applying a step input at the micromixer inlet. The application of the step input is not trivial because the inlet of micromixer is not directly accessible when the probe head is mounted inside the NMR spectrometer. For that reason the step input was created by changing abruptly the feed ratio of the two pumps, which were filled with two different mixtures (acetone in pump A and cyclohexane in pump B), while keeping the total flow rate constant. Using a fast NMR acquisition method the concentration change in the NMR flow cell, i.e., the step response was determined, see Fig. 6. The results show that the RTD in the microreactor probe head can be well described by an axial dispersion model or a tanks-in-series model. The obtained values of the axial dispersion coefficient and the numbers of tanks, respectively are in the range that can be expected from the correlation of stream line flow in pipes given in [19]. Using the tank-in-series model the measured RT summation functions can be fitted depending on the overall flow rate with a number of 6 – 25 tanks. By means of a sensitivity study it was shown that

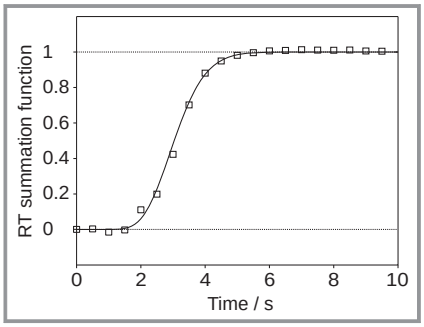

Figure 6. Step response of the microreactor NMR probe head at a total flow rate of 500 μL min^{-1}. Symbols: Experimental results. Line: Prediction with tank-in-series model with a number of tanks of $N_{tanks} = 20$.

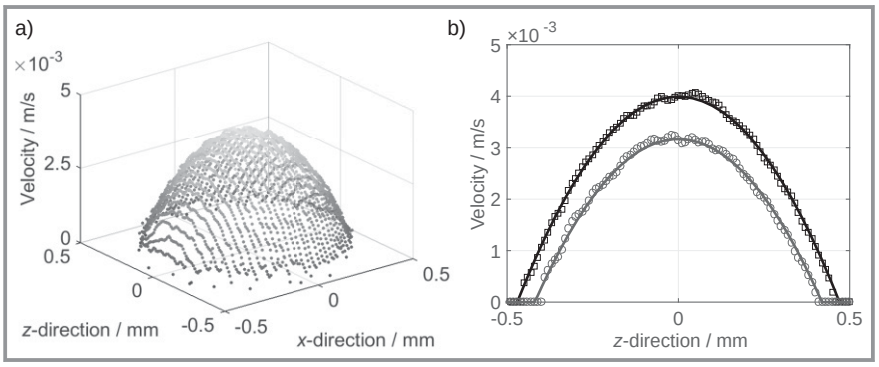

Figure 5. Velocity profile of pure water in the NMR flow cell at a flow rate of 100 μL min^{-1}. a) Results of the 2D measurements using MR velocimetry. b) Comparison of the experimental results (symbols) with a parabolic flow profile (solid lines) at different positions in the x-direction.

even for the case when the behavior of the reactor deviates most from a plug flow reactor (i.e., it behaves as 6 tanks in series) an ideal plug flow reactor model is still applicable for reaction with a half-life of more than about 100 s. The error introduced by this simplification is in the range of the accuracy of the NMR analysis.

3 Modeling of Thermal Effects

Isothermal operation of the reactor is favorable for the analysis of the con-

centration profiles of the reactants, which are obtained by online NMR spectroscopy. In reality, perfectly isothermal conditions are difficult to achieve in the setups, especially for systems that have a high enthalpy of reaction. To compare the performance of the microreactor NMR probe head with that of the standard NMR sample tube with respect to their thermostatization, the temperature profile and the concentration profile in the different setup heads is simulated. Based on these results, the errors in the determined rate constants that are caused by the nonisothermal operation are assessed.

Two different model approaches are chosen to describe the microreactor NMR probe head and its thermostatization in the stopped flow mode and in the flow mode. In the stopped flow mode, only the reactants in the NMR flow cell and the glass capillary of the NMR flow cell are considered. It is assumed that the reactants are a stationary fluid so that heat transfer occurs by conduction only and no convection takes place. Furthermore, only heat conduction in the radial direction of the NMR flow cell is considered. The rate of the reaction is described by a first-order kinetic model. The temperature dependence of the rate constant is taken into account using the Arrhenius equation. Diffusion of the reactants is not considered. Thus, if spatial temperature gradients occur in the fluid, spatial concentration gradients are the consequence. In the glass capillary, only heat conduction is considered. The heat transfer coefficient used to describe the heat transfer from the glass capillary to the surrounding thermostatization oil caused by forced convection is estimated using Nusselt correlations [20]. All properties (heat conductivity, enthalpy of reaction, heat capacity, etc.) are assumed to be constant and are taken from [20]. The energy and component balances, describing this problem, result in three coupled partial differential equations of the concentration and the temperature of the reactants, and of the temperature of the glass capillary. The partial differential equations were solved numerically with MATLAB (MathWorks, Natick, USA) using the method-of-line together with a finite volume method for the spatial discretization. The same model approach can be used to describe the thermal effects that occur during the kinetic measurements using the NMR sample tube. Here, the heat transfer coefficient from the NMR sample tube to the air passing by was determined in a cooling experiment with a nonreactive mixture. The temperature change in the NMR sample tube was measured in situ with the so-called NMR thermometer as described in [21].

The assumption, that no convective heat transfer and no diffusion take place in the reacting fluid, is certainly an over-simplification of the real conditions present in the NMR flow cell. This simplification, however, is justified to get a worst-case estimation of the maximal temperature differences and the associated concentration differences in the NMR flow cell in the stopped flow mode.

To obtain the temperature and concentration profiles in the microreactor NMR probe head for the flow mode, a nonisothermal steady-state plug flow reactor model was used and the heat transfer from the reactor to the thermostatization oil was described using Nusselt correlations [20]. A publication on the details of the modelling of the thermal effects and simulation of the NMR setups is currently in preparation.

If the concentration profiles that are observed in an NMR experiment inside the NMR flow cell or the NMR sample tube respectively are evaluated under the assumption of isothermal operation of the setup, the obtained apparent rate constants deviates from the true rate constants. To estimate the influence of the nonisothermal operation during the experiment on the measured apparent rate constants, a first-order kinetic model was fitted to the simulated concentration profile of the reactants inside the NMR flow cell or the NMR sample tube respectively. The obtained apparent rate constant is compared to the true rate constant that was used for the nonisothermal simulation and that was evaluated at the start temperature of the reacting mixture. If the temperature gradients in the reactor are large, the difference between the two rate constants is large as well. By means of a parameter study based on this simulation method, the applicability of the microreactor NMR probe head both in the stopped-flow and in the flow mode and of the NMR sample tube for measuring kinetics of exo- or endothermic reactions is evaluated. The investigated parameters are the rate of reaction (here expressed as half-life of the reaction), the enthalpy of reaction, and the activation energy. The results are depicted in Fig. 7, for the microreactor NMR probe head both in the stopped flow mode, in the flow mode, and for the NMR sample tube. A relative error of more than 20 % in the rate constants corresponds to a maximum temperature difference in the reactor of about 10 K or more. The results show that the microreactor probe head provides a much better thermostatization than the standard NMR sample tube. Note that the range of the *x*-axis and *y*-axis in Fig. 7 are different for the NMR sample tube and for the microreactor NMR probe head. Even reactions with a large enthalpy of reaction ($> 100\,\mathrm{kJ\,mol^{-1}}$) can be investigated without causing large temperature gradients and large errors in the obtained rate constants. Using the NMR sample tube, the investigated reaction must be much slower and/or the enthalpy of reaction must be much lower to keep the error in the obtained rate constant at a similar value compared to measurements with the microreactor NMR probe head. Only if very fast reactions with large activation energy, enthalpy of reaction, and rate constants are investigated, the NMR microreactor probe head is not applicable. In a well-designed external reactor, which is connected with the NMR spectrometer via a sample loop, a good control of the temperature of the reactants should be possible, even for reactions with large enthalpy of reaction. But as mentioned above, this setup is not applicable for fast reactions because of the time delay between start of reaction and analysis in the NMR spectrometer. To our knowledge, however, no NMR setup exists so far that fulfills all requirements necessary to measure very fast and highly endo-/exothermic reactions under isothermal conditions.

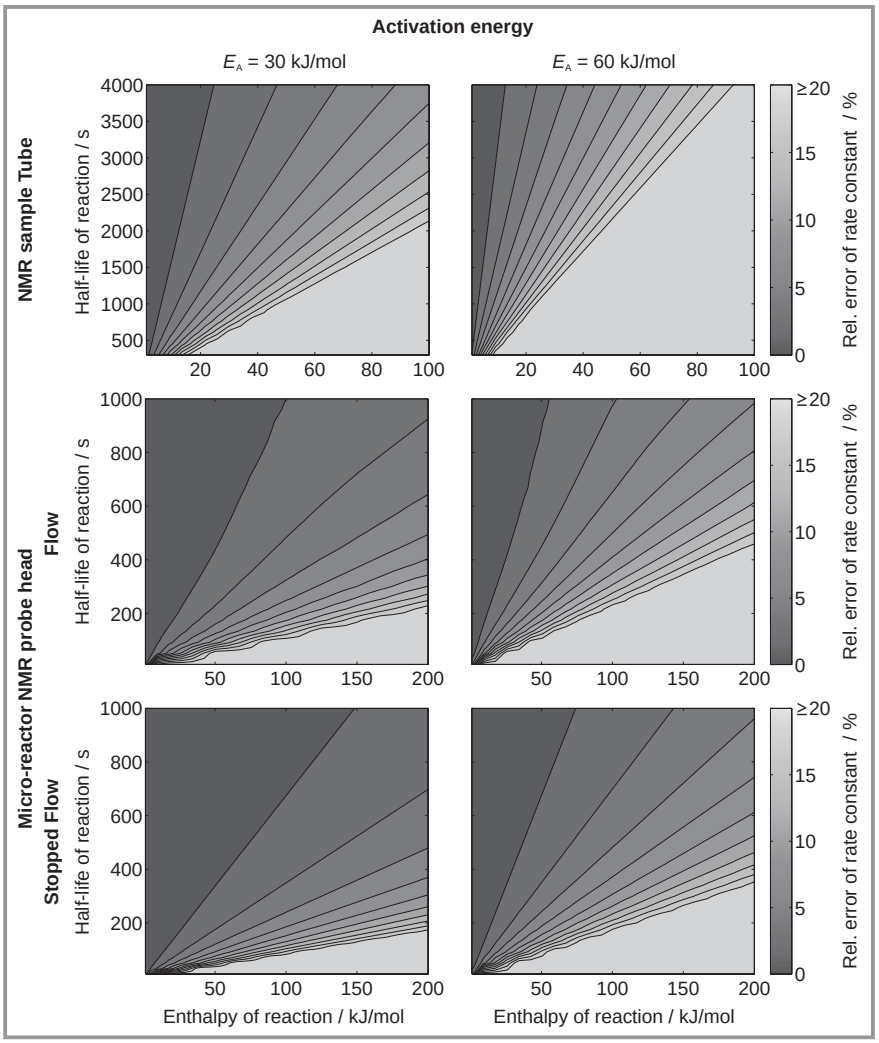

Figure 7. Results of the simulative parameter study for different NMR setups on the error in the apparent rate constant that is determined from the experiment if isothermal conditions are assumed. The concentration and temperature profiles, which are defined here as true results, are simulated by nonisothermal reactor models that consider the thermostatization of the NMR setup.

4 Kinetic Measurements

4.1 Esterification Reactions

To test the applicability of the microreactor NMR probe head for measuring reaction kinetics, the esterification of methanol to methyl acetate, homogeneously catalyzed by sulfuric acid, was studied at different temperatures in both operation modes. The experimental results are depicted in Fig. 8. They show that the first observation of the composition of the reaction mixture is obtained only seconds after the reaction has been started. The small scattering of the data over a long period of time (cf. Fig. 8a) demonstrates the robustness of the analysis method.

The concentration of the reactants in the NMR flow cell are predicted using an isothermal batch reactor model for the stopped flow mode and an isothermal tank-in-series model for the flow mode as described in Sect. 2.3. The results are also plotted in Fig. 8. The assumption of an isothermal operation is motivated by the small enthalpy of reaction (about –6 kJ mol^{-1}) and the simulation results presented in the previous section. To describe the rate of reaction the kinetic model of Dörhöfer [22] was applied. Dörhöfer [22] determined the kinetics of that reaction system in a batch reactor with ex situ GC analysis. The predicted concentration profiles are also plotted in Fig. 8. The good agreement between the experimental results of this work and the results from the literature that are based on completely different measurement methods demonstrate that reliable kinetic data of fast reactions can be determined with the microreactor NMR probe head.

Another test system was the faster esterification reaction of methanol to methyl formate, homogeneously catalyzed by sulfuric acid. To demonstrate that kinetics in technical solutions, i.e., highly concentrated solutions relevant to industrial applications, can be reliably determined with the microreactor NMR probe head, an undiluted equimolar feed of methanol and formic acid was used. The result of the kinetic studies carried out under various conditions (temperature and concentration of catalyst) are shown in Fig. 9 together with the prediction using a kinetic model that was parameterized based on this experimental data. The kinetic model is a simple second-order approach based on activities with the kinetic constant of the forward and the backward reaction as the two model parameters (for details see [14]). The results show that the microreactor NMR probe head is well-suited for studying the kinetics of reactions under conditions relevant for industrial applications that reaches chemical equilibrium within about 20 s.

4.2 Reactions in the System Formaldehyde and Water

The formation of poly(oxymethylene) glycols in aqueous formaldehyde systems are of great relevance for many industrial applications [23]. Hahnenstein et al. [5] studied the

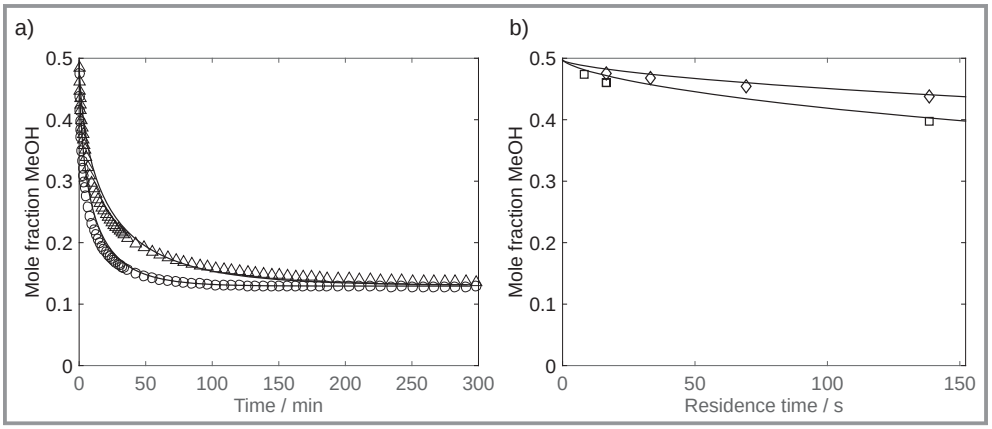

Figure 8. Results of the kinetic measurement of the esterification of methanol (MeOH) to methyl acetate using the microreactor NMR probe head. a) Experiments in the stopped flow mode with a temperature of 40 °C using 0.02 g g^{-1} (△) and 0.05 g g^{-1} (○) sulfuric acid as catalyst. b) Experiments in the flow mode with a temperature of 30 °C (◇) and 50 °C (□) using 0.01 g g^{-1} sulfuric acid as catalyst. Lines: Prediction using the kinetic model of Dörhöfer [22].

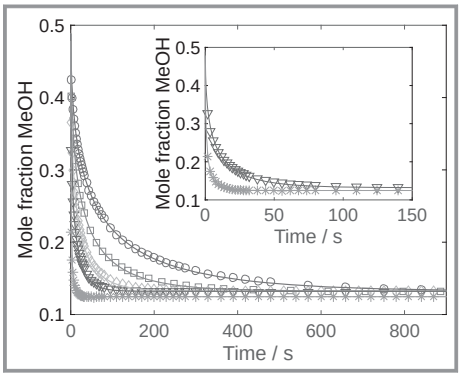

Figure 9. Results of the kinetic measurements of the esterification of methanol (MeOH) to methyl formate using the microreactor NMR probe head in the stopped flow mode. Large diagram: overview of the concentration profiles of MeOH; inserted diagram: concentration profiles of MeOH for the two fastest observed reaction kinetics. Symbols: Experimental results using 0.02 g g^{-1} of sulfuric acid as catalyst at 30 °C (○), 40 °C (□), 50 °C (◇), and 60 °C (▽) and using 0.06 g g^{-1} sulfuric acid at 60 °C (∗). Lines: predictions using a kinetic model parameterized with this experimental data.

reaction kinetics of that complex system under various conditions (start composition, temperature, and pH-value) using both NMR spectroscopic measurements in the NMR sample tube and densimetric methods. However, for temperature higher than 40 °C and for pH-values in the acidic or alkaline range, which are relevant for industrial applications, the reaction kinetics were too fast so that they could not be studied with these methods. Thus, the microreactor NMR probe head was used to expand the experimental data of the reaction kinetics in that system to conditions that could not be studied so far. Some results of that study are depicted in Fig. 10 together with an excerpt of an NMR spectrum of the reactants and the peak assignment. The experimental results depicted in Fig. 10 confirm the kinetic model proposed by Hahnenstein et al. [5]. Furthermore, the results demonstrate that the microreactor NMR probe head can be used to study the kinetics of fast and complex reactions under conditions relevant to industrial applications.

5 Conclusions

A microreactor NMR probe head is presented. The probe head facilitates studies of kinetics of fast reactions with quantitative NMR spectroscopy. Based on the results from mixing experiments an optimal design of a micromixer is chosen that ensures an efficient mixing of the reactants in a large range of flow rates. The behavior of the probe head as reactor is characterized in this work by measurements of the velocity profile and the residence time distribution. Based on this characterization, well-defined reactor models of the probe head are developed.

By means of a simulative parameter study, the deviation from isothermal operation of the NMR setups (microreactor NMR probe head and NMR sample tube) during the kinetic measurements is estimated and it is assessed for which reaction (time constants, i.e., half-life of the reaction, enthalpy of reaction, and activation energy) the setups are applicable. The results confirm that the thermostatization of the microreactor probe head is more efficient than that of the standard NMR sample tube which is often used to study reaction kinetics with NMR spectroscopy. Thus, also fast exo-/endothermic reactions can be studied with this setup without large deviation from an isothermal operation. Very fast reactions (half-life of less than 10 s) and highly exo-/endothermic reactions (enthalpy of reaction greater than 50 kJ mol^{-1}), however, cannot be studied quantitatively with any of the NMR setups discussed in this work. The development of an NMR based setup that facilitates quantitative studies under these conditions will be part of future research work.

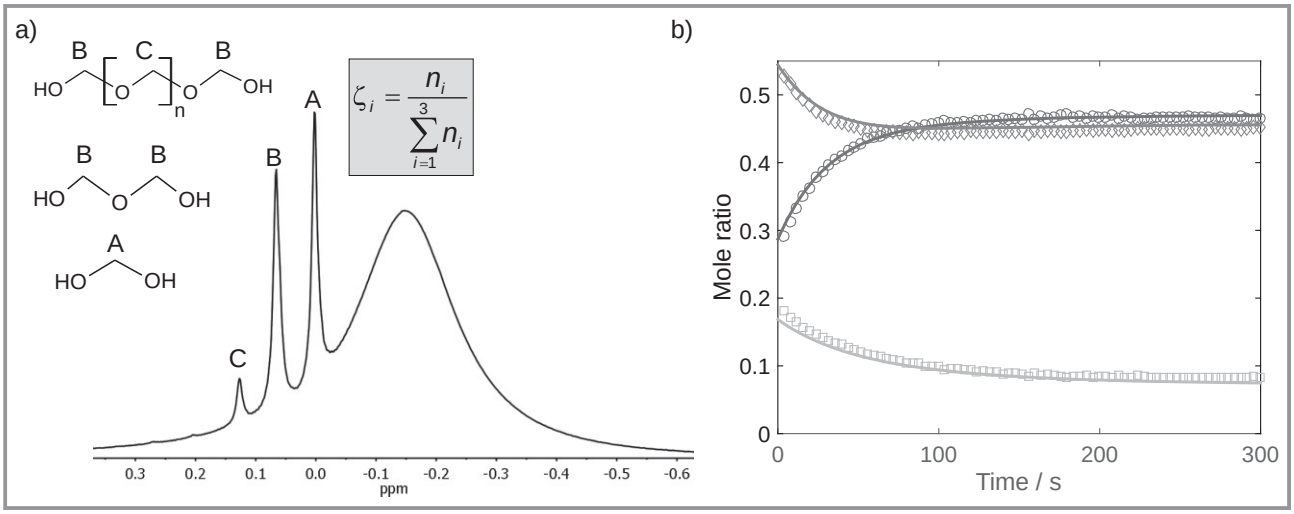

Figure 10. Results of the kinetic measurements of the formation of poly(oxymethylene) glycols in aqueous formaldehyde solution using the microreactor NMR probe head in the stopped flow mode carried out at T = 60 °C and pH = 3.8, initial weight ratio of formaldehyde to water of 0.15 g g^{-1}. a) Excerpt of a ^{1}H NMR spectrum of the reacting mixture together with the peak assignment. The dominant peak represents water. b) Mole ratio ζ_i of the three groups defined in a) as a function of time. Symbols: experimental data. Lines: Prediction using the kinetic model of Hahnenstein et al. [5].

The experimental results of the reaction kinetic measurements carried out with the microreactor NMR probe head are in good agreement with data from the literature. These results show that the probe head enables reliable kinetic measurements of fast reactions. The probe head was used to study the kinetics of the formation of poly(oxymethylene) glycols in aqueous formaldehyde systems. The fact that the probe head facilitates the investigations of those reaction systems under conditions, which are relevant for industrial applications but have not been realizable with the experimental setups and methods existing so far, demonstrates the usefulness of this new device. The microreactor probe head widens significantly the range of applications of online NMR spectroscopy for reaction and process monitoring. Hence, it is a very useful tool with a great range of applications for the research and development in the chemical and in the pharmaceutical industries.

We thank Frank Engelke, Hartmut Glauner, and Jürgen Ganz (Bruker BioSpin GmbH, Rheinstetten, Germany) for their support installing the electronics of the probe head. We further thank Hans-Joachim Kost and Patrick Löb (Fraunhofer ICT-IMM, Mainz, Germany) for the cooperation with developing the micromixers used in the NMR probe head. Furthermore, we thank the team from the Magnetic Resonance Research Centre at the University of Cambridge, UK in particular Daniel Holland, Andy Sederman, and Lynn Gladden for giving us the opportunity to conduct experiments in Cambridge and for their kind support. Erik von Harbou gratefully acknowledges the Max Buchner Research Foundation for its support.

References

[1] M. Maiwald, H. H. Fischer, Y.-K. Kim, K. Albert, H. Hasse, *J. Magn. Reson.* **2004**, *166 (2)*, 135 – 146. DOI: 10.1016/j.jmr.2003.09.003

[2] M. A. Vargas, M. Cudaj, K. Hailu, K. Sachsenheimer, G. Guthausen, *Macromolecules* **2010**, *43 (13)*, 5561 – 5568. DOI: 10.1021/ma1006599

[3] M.-C. Brochier Salon, P.-A. Bayle, M. Abdelmouleh, S. Boufi, M. N. Belgacem, *Colloids Surf., A* **2008**, *321 (2 – 3)*, 83 – 91. DOI: 10.1016/j.colsurfa.2007.06.028

[4] A. Scheithauer, T. Grützner, C. Rijksen, D. Zollinger, E. von Harbou, W. R. Thiel, H. Hasse, *Ind. Eng. Chem. Res.* **2014**, *53 (20)*, 8395 – 8403. DOI: 10.1021/ie5004043

[5] I. Hahnenstein, M. Albert, H. Hasse, C. G. Kreiter, G. Maurer, *Ind. Eng. Chem. Res.* **1995**, *34 (2)*, 440 – 450. DOI: 10.1021/ie00041a003

[6] I. M. Clegg, C. M. Gordon, D. S. Smith, R. Alzaga, A. Codina, *Anal. Methods* **2012**, *4 (6)*, 1498 – 1506. DOI: 10.1039/C1AY05384A

[7] É. J. Kibrik, O. Steinhof, G. Scherr, W. R. Thiel, H. Hasse, *Ind. Eng. Chem. Res.* **2014**, *53 (32)*, 12602 – 12613. DOI: 10.1021/ie5001746

[8] D. A. Foley, J. Wang, B. Maranzano, M. T. Zell, B. L. Marquez, Y. Xiang, G. L. Reid, *Anal. Chem.* **2013**, *85 (19)*, 8928 – 8932. DOI: 10.1021/ac402382d

[9] N. Zientek, C. Laurain, K. Meyer, M. Kraume, G. Guthausen, M. Maiwald, *J. Magn. Reson.* **2014**, *249*, 53 – 62. DOI: 10.1016/j.jmr.2014.10.007

[10] J. Kind, C. M. Thiele, *J. Magn. Reson.* **2015**, *260*, 109 – 115. DOI: 10.1016/j.jmr.2015.09.008

[11] S. E. Denmark, B. J. Williams, B. M. Eklov, S. M. Pham, G. L. Beutner, *J. Org. Chem.* **2010**, *75 (16)*, 5558 – 5572. DOI: 10.1021/jo100837a

[12] G. E. Wagner, P. Sakhaii, W. Bermel, K. Zangger, *Chem. Commun.* **2013**, *49*, 3155 – 3157. DOI: 10.1039/C3CC39107H

[13] A. Brächer, S. Hoch, K. Albert, H. J. Kost, B. Werner, E. von Harbou, H. Hasse, *J. Magn. Reson.* **2014**, *242*, 155 – 161. DOI: 10.1016/j.jmr.2014.02.013
[14] A. Brächer, R. Behrens, E. von Harbou, H. Hasse, *Chem. Eng. J.* **2016**, *306*, 413 – 421. DOI: 10.1016/j.cej.2016.07.045
[15] A. Scheithauer, A. Brächer, T. Grützner, D. Zollinger, W. R. Thiel, E. von Harbou, H. Hasse, *Ind. Eng. Chem. Res.* **2014**, *53 (45)*, 17589 – 17596. DOI: 10.1021/ie5033556
[16] M. Maiwald, *Hochauflösende Online-NMR-Spektroskopie für das Reaktions- und Prozeßmonitoring*, 1st ed., Cuvillier, Göttingen, Germany **2012**.
[17] F. Schönfeld, V. Hessel, C. Hofmann, *Lab Chip* **2004**, *4*, 65 – 69. DOI: 10.1039/B310802C
[18] V. Hessel, S. Hardt, H. Löwe, F. Schönfeld, *AIChE J.* **2003**, *49 (3)*, 566 – 577. DOI: 10.1002/aic.690490304
[19] O. Levenspiel, *Chemical Reaction Engineering*, 3rd ed., Wiley, New York **1999**.
[20] *VDI-Wärmeatlas*, 11th ed., Springer, Heidelberg **2013**.
[21] C. Ammann, P. Meier, A. Merbach, *J. Magn. Reson.* **1982**, *46 (2)*, 319 – 321. DOI: 10.1016/0022-2364(82)90147-0
[22] T. Dörhöfer, *Ph.D. Thesis*, Technische Universität München **2006**.
[23] H. Hasse, G. Maurer, *Ind. Eng. Chem. Res.* **1991**, *30 (9)*, 2195 – 2200. DOI: 10.1021/ie00057a022

Scheithauer et al., 2014

Reprinted with permission from: A. Scheithauer, A. Brächer, T. Grützner, D. Zollinger, W. R. Thiel, E. von Harbou, H. Hasse, Online ^{1}H NMR Spectroscopic Study of the Reaction Kinetics in Mixtures of Acetaldehyde and Water Using a New Microreactor Probe Head, Industrial & Engineering Chemistry Research, Volume 53, 2014, Pages 17589-17596, DOI 10.1021/ie5033556

I&EC research
Industrial & Engineering Chemistry Research

Article

pubs.acs.org/IECR

Online ^{1}H NMR Spectroscopic Study of the Reaction Kinetics in Mixtures of Acetaldehyde and Water Using a New Microreactor Probe Head

Andreas Scheithauer,[†] Alexander Brächer,[†] Thomas Grützner,[‡] Daniel Zollinger,[‡] Werner R. Thiel,[§] Erik von Harbou,*[,†] and Hans Hasse[†]

[†]Laboratory of Engineering Thermodynamics, University of Kaiserslautern, Erwin-Schrödinger-Strasse 44, 67663 Kaiserslautern, Germany

[‡]Lonza AG, Rottenstrasse 6, 3930 Visp, Switzerland

[§]Department of Chemistry, University of Kaiserslautern, Erwin-Schrödinger-Strasse 54, 67663 Kaiserslautern, Germany

Supporting Information

ABSTRACT: Mixtures of acetaldehyde and water are reactive multicomponent systems because poly(oxymethylmethylene) glycols are formed. A study on the kinetics of the formation of these oligomers was carried out using a new microreactor NMR probe head that combines online flow ^{1}H NMR spectroscopy with microreaction technology. The study covers temperatures between 278 and 298 K and pH values between 3.5 and 10.3. From the peak areas in the ^{1}H NMR spectra, quantitative results for the conversion of acetaldehyde were obtained. On the basis of the new data, a reaction kinetic model was developed and numbers for the kinetic constants of poly(oxymethylmethylene) glycol formation were determined together with a correlation that describes their dependence on the temperature and pH value.

INTRODUCTION

Acetaldehyde (AA) is an important intermediate in the chemical industry and is used for the production of various substances like acetic acid, ethyl acetate, acetic anhydride, peracetic acid.[1] Acetaldehyde is used in mixtures with water (W),[1] which are reactive multicomponent systems because acetaldehyde and water yield ethane-1,1-diol [$HO(CH(CH_3)O)H$, MMG_1] and higher oligomeric species, the poly(oxymethylmethylene) glycols [$HO(CH(CH_3)O)_nH$, MMG_n].

Mixtures of acetaldehyde and water can already be present in the production of acetaldehyde, when it is obtained from acetylene, by oxidation from ethanol, and even in direct oxidation from ethylene.[1] Acetaldehyde is widely used in aldol condensations to obtain different products. In these condensation reactions, water is a byproduct, so that mixtures containing acetaldehyde and water are present. Furthermore, sometimes acetaldehyde is deliberately used in aqueous solutions rather than in pure form because the solutions are easier to handle. There can also be reaction technological reasons for using acetaldehyde in aqueous solutions, e.g., to avoid high temperatures in exothermal reactions of acetaldehyde. An example for this use is the production of crotonaldehyde from acetaldehyde.[2]

The reactions of acetaldehyde with water are similar to those of formaldehyde with water.[3−8] It is known from formaldehyde process design that the models of the properties of mixtures of formaldehyde and water should explicitly include the formation of oligomers in that system.[4,7,9−13] The same is true for the system acetaldehyde and water. Unfortunately, in contrast to mixtures of formaldehyde and water, the quantitative information on the speciation in mixtures of acetaldehyde and water available in the literature is rather spotty and not adequate for developing engineering models. Table 1 gives an overview of the available studies of the kinetics of the reactions in the acetaldehyde with water system. A review of the equilibrium data was recently presented in ref 14. Most of these studies were carried out in dilute solutions. Probably for this reason, most of the authors do not take the formation of higher oligomers ($MMG_{n>1}$) into account. To the best of the authors' knowledge, no literature study on the temperature dependence of reaction kinetics in the studied system is available. A more detailed discussion of the literature studies is given in the Supporting Information (SI).

Table 1. Literature Data on the Reaction Kinetics of the Formation of Poly(oxymethylmethylene) Glycols in Mixtures of Acetaldehyde and Water

species	method	kinetics
MMG_1	NMR[a]	24 and 27−30
	UV/vis	17, 26, and 30−33
	calorimetry	25, 31, 34, and 35
	others	30, 36, and 37
$MMG_{n>1}$	NMR[a]	24 and 28

[a] ^{1}H NMR, except for ref 27, in which ^{17}O NMR was used.

In a previous study of our group,[14] a combination of ^{1}H and ^{13}C NMR spectroscopy was used for investigating the chemical equilibrium in mixtures of acetaldehyde and water and a model

Received: August 24, 2014
Revised: October 14, 2014
Accepted: October 16, 2014
Published: October 16, 2014

dx.doi.org/10.1021/ie5033556 | Ind. Eng. Chem. Res. 2014, 53, 17589−17596

was provided with which the true species mole fractions in equilibrium can be calculated from the overall acetaldehyde mole fraction $\tilde{x}_{AA}$ at a given temperature.

The present work ties in that study and extends it to reaction kinetics. Only ^{1}H NMR spectroscopy can be used for this purpose because the acquisition of ^{13}C NMR spectra takes too long to follow the reactions that are of interest here. A microreactor NMR probe head with a ^{1}H NMR coil that was recently presented by Bräcker et al.[15] was used in the present work. It was the first time that this new equipment was used for a systematic study of an industrially relevant system. On the basis of the new data, a kinetic model was developed that accounts for the formation of both MMG_1 and $MMG_{n>1}$.

Two different ways for specifying compositions are used in the present work. The overall mole fractions of acetaldehyde ($\tilde{x}_{AA}$) and water ($\tilde{x}_W$) are known from the feed ratio of the pure educts. In constrast, true mole fractions x_i (i = AA, W, MMG_1, MMG_2, MMG_3, ...) are those that relate to the true speciation of the mixture.

REACTION SYSTEM

Acetaldehyde and water undergo oligomerization reactions that yield poly(oxymethylmethylene) glycols. Ethane-1,1-diol (MMG_1) is the smallest oligomer:

$$\underbrace{CH_3{-}CHO}_{AA} + \underbrace{H_2O}_{W} \rightleftharpoons \underbrace{HO{-}(CH(CH_3){-}O{-})H}_{MMG_1} \quad (I)$$

In further reactions, higher oligomers ($MMG_{n>1}$) are formed:[14,16]

$$\underbrace{HO{-}(CH(CH_3){-}O{-})_{n-1}H}_{MMG_{n-1}} + \underbrace{CH_3{-}CHO}_{AA} \rightleftharpoons \underbrace{HO{-}(CH(CH_3){-}O{-})_nH}_{MMG_n} \quad (II)$$

Reactions (I) and (II) always take place in mixtures of acetaldehyde and water. They are catalyzed by both bases and acids.[17] At pH values above about 10.2, the aldol addition of acetaldehyde occurs whereby acetaldol and aldoxane are formed.[18] In strong acidic media, acetaldehyde forms paraldehyde.[19] Therefore, the conditions in the present work were chosen so that no side products are formed. For more detailed information, see ref 2.

EXPERIMENTS

Chemicals. Acetaldehyde (≥0.995 g/g) was purchased from Sigma-Aldrich, Munich, Germany, as an A.C.S. reagent. Ultrapure water was produced using a Milli-Q integral water purification system from Merck Millipore, Darmstadt, Germany. Caustic soda pellets were purchased from Roth, Karlsruhe, Germany, in p.a. quality. The thermostatting liquid FC-43 for the NMR probe head was purchased from 3M, St. Paul, MN. The chemicals were used without further purification.

NMR Spectroscopy and Spectra Evaluation. The experiments were carried out using a 400 MHz NMR spectrometer (Unity Inova 400, Varian, Palo Alto, CA), which was equipped with a microreactor NMR probe head. The NMR spectra were processed with MestReNova (Mestrelab Research, Santiago de Compostela, Spain). The acquisition time was 1 s, the relaxation delay 39 s, and the pulse width 45°. No T_1 values were measured directly, but it was verified by comparison with experiments with higher relaxation delays that they were high enough. Even smaller values could have been used. To enable monitoring of the fast reactions, only one scan was recorded for each spectrum. Because of the high concentration of reactants, one single scan yields a signal-to-noise ratio sufficient for quantitative evaluation of the spectra. ^{13}C NMR spectroscopy cannot be applied to monitor the fast reactions studied here.

Figure 1 shows a typical ^{1}H NMR spectrum of a mixture of acetaldehyde and water with peak assignment. An overview of the peaks in

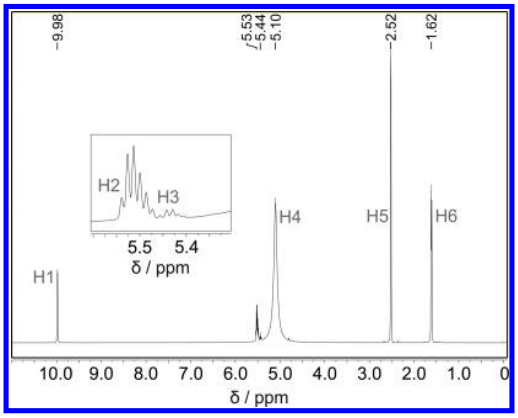

Figure 1. ^{1}H NMR spectrum of an acetaldehyde/water mixture ($\tilde{x}_{AA}$ = 0.245 mol/mol) at 293 K (for peak assignment, cf. Table 2).

Table 2. Peak Assignment in the ^{1}H NMR Spectra and Corresponding Components[2]

peak name	component	group	δ (ppm)	peak area
H1	AA	C*H*O	9.98	
H2	MMG_1	C*H*	5.53	
H3	MMG_n (n > 1)	C*H*	5.44	
H4	W	H_2O	5.10	
	MMG_n (n ≥ 1)	O*H*	5.10	
H5	AA	CH_3	2.52	A_{AA}
H6	MMG_n (n ≥ 1)	CH_3	1.62	A_{MMG_n}

the ^{1}H NMR spectra with their chemical shifts and related nomenclature is given in Table 2. For more detailed information, see ref 14. Because of the overlap of the CH peaks of the different oligomers among each other and with the water peak, it is not possible to gain information on the distribution of different oligomers from these ^{1}H NMR resonances. Additionally, the peaks broaden as the reactions become faster. Therefore, only the CH_3 peaks were used for quantification. There are two methyl peaks, one resulting from monomeric acetaldehyde and one from acetaldehyde bound in the oligomers (without distinguishing which oligomer). The corresponding areas of these peaks (H5 and H6 in Table 2) are labeled as A_{AA} and A_{MMG_n}. From these peak areas, the peak area fractions of the signals of the methyl groups in the oligomers ζ_{MMG_n} are calculated:

$$\zeta_{MMG_n} = \frac{A_{MMG_n}}{A_{AA} + A_{MMG_n}} \quad (1)$$

Experimental Setup and Procedure. The flow diagram of the setup used in the experiments is shown in Figure 2. Two syringe pumps (Dual 260d, Teledyne Isco, Lincoln, NE; accuracy 0.5% of the set point) deliver pure acetaldehyde and pure water pulsation-free to the microreactor NMR probe head. A scheme of the probe head is shown in Figure 3. In the feed capillaries of the NMR probe head, 0.5 μm filters are installed to prevent plugging of the micromixer structure or the capillaries because of contaminants. The educt tubes are connected via a connection box to the NMR probe head. The educt streams enter the NMR probe head and are mixed in the micromixer (crawler-type, developed by the Mainz Institute for Microtechnology, Mainz, Germany).[20] The dwell unit (volume of about 10 μL) connects the micromixer with the NMR flow cell (active volume of about 5 μL). The reaction mixture passes the dwell unit and NMR flow cell capillary and is collected in a vessel at the outlet (cf. Figure 2). The educt and product lines outside the NMR spectrometer are embedded in silicon tubes and liquid-thermostated by water. Also all lines inside the NMR probe as well as the micromixer, dwell unit, and flow cell are liquid-thermostated. For this purpose, FC-43 was chosen because it is fully fluorinated so that it causes no ^{1}H NMR

dx.doi.org/10.1021/ie5033556 | Ind. Eng. Chem. Res. 2014, 53, 17589−17596

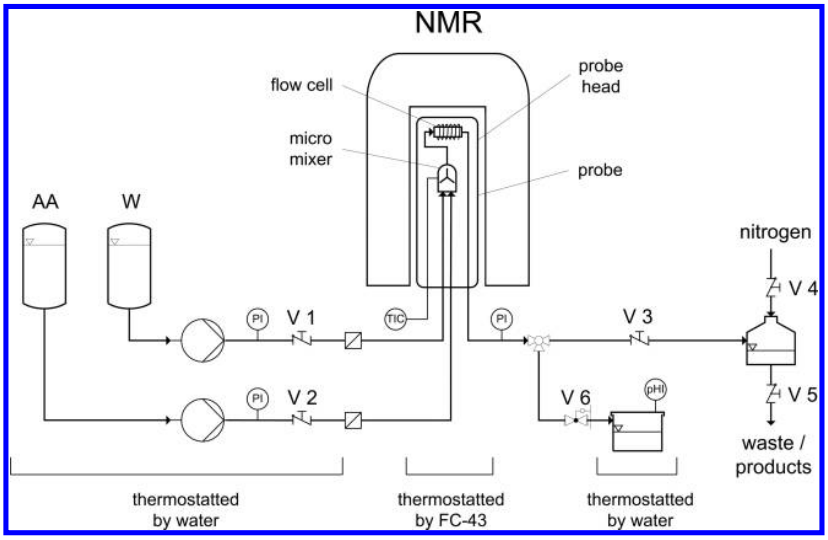

Figure 2. Flowsheet of the experimental setup to study the reaction kinetics of the oligomer formation in mixtures of acetaldehyde and water.

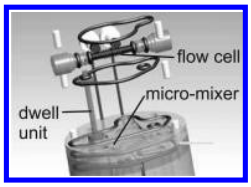

Figure 3. Details of the microreactor NMR probe head to study the reaction kinetics in mixtures of acetaldehyde and water.

signals in the spectrum that would interfere with those from the measurements.

The microreactor NMR probe head was operated in the stopped-flow mode. In that mode, first high educt flow rates are used so that the NMR flow cell is quickly filled with the reacting mixture of the desired overall composition. Then, the flow is stopped, and the NMR flow cell is used as a batch reactor in which the instationary reaction is monitored online.

The outlet line of the NMR probe head is connected to a vessel, which is pressurized with nitrogen to apply a back-pressure and thus to adjust the system pressure. This vessel is important because the stopped-flow mode is applied. Small fluctuations of the temperature in the probe head, which are not avoidable, would cause large pressure fluctuations if expansion of the liquid was hindered. The pressure was measured in both the feed tubes and outlet line.

For pH measurement, the NMR probe outlet was temporarily rerouted into a pH measurement cell (cf. Figure 2). Details on the pH measurement are described in the SI.

The educts acetaldehyde and water were precooled and placed at 280 K in the piston pumps, which supply the educt streams to the NMR probe head. The flow rates of the educt streams were $\dot{V}_{AA}$ = 254 μL/min and $\dot{V}_{W}$ = 748 μL/min at 280 K to obtain a mixture with $\tilde{x}_{AA}$ = 0.1 mol/mol after mixing. That concentration of acetaldehyde in the feed was chosen because, for more dilute solutions, less higher oligomers ($MMG_{n>1}$) are formed and, for more concentrated mixtures, it is difficult to maintain isothermal conditions in the NMR flow cell because of the strongly exothermic reactions, despite cooling. Additionally, for more concentrated mixtures, larger shifts in the pH value occur and the peaks broaden more strongly. The investigated mixtures at the start of the reaction and the mixtures at the end of the reaction differ in their magnetic susceptibility. Therefore, an investigation of the whole reaction is only possible by optimizing the magnetic field based on one particular state of the reaction. The field was optimized for the equilibrated state at the end of the reaction because during the reaction there are no stable conditions. This results in a peak broadening in the spectra that are obtained during the reaction. This peak broadening is pronounced especially at the beginning and when the acetaldehyde concentration is high.

The pH value was adjusted by adding caustic soda to the educt water. The required amount of caustic soda was determined in preliminary experiments. The residence time between the micromixer and NMR flow cell was about 2 s. This time was added to the experimental time in the evaluation in order to calculate the total reaction time. All valves, except V5 and V6 (cf. Figure 2), were opened until stationarity was reached. Then, valve V3 was closed and valve V6 opened at the same time, and a sample for the pH measurement was collected. For more information, see the SI. Subsequently, valve V6 was closed and valve V3 opened, and the stationarity was checked again. Then, valves V1 and V2 were closed, and the acquisition of an array of ^{1}H NMR spectra was started. During the entire procedure, the system pressure was maintained at about 6 bar.

Because of the strong exothermic reactions, it is difficult to maintain isothermal conditions in a standard NMR probe head, where the reactions take place in a sample tube. In contrast, the good thermal management provided by the setup of the microreactor probe head facilitates isothermal conditions during the experiments. Additionally, the reactants in the microreactor probe head can be pressurized to avoid evaporation of the reactants. Furthermore, with the setup of the present work, it is possible to monitor the reaction kinetics already a

Table 3. Overview of the Parameters of the Experiments on Reaction Kinetics of the Formation of Poly(oxymethylmethylene) Glycols[a]

	experiment										
	E1	E2	E3	E4	E5	E6	E7	E8	E9	E10	E11
pH	3.5	3.6	3.7	5.4	5.4	5.3	6.7	6.4	6.3	10.3	10.2
T (K)	278	288	298	278	288	298	278	288	298	278	288

[a]All experiments were carried out at $\tilde{x}_{AA}$ = 0.1 mol/mol.

dx.doi.org/10.1021/ie5033556 | Ind. Eng. Chem. Res. 2014, 53, 17589−17596

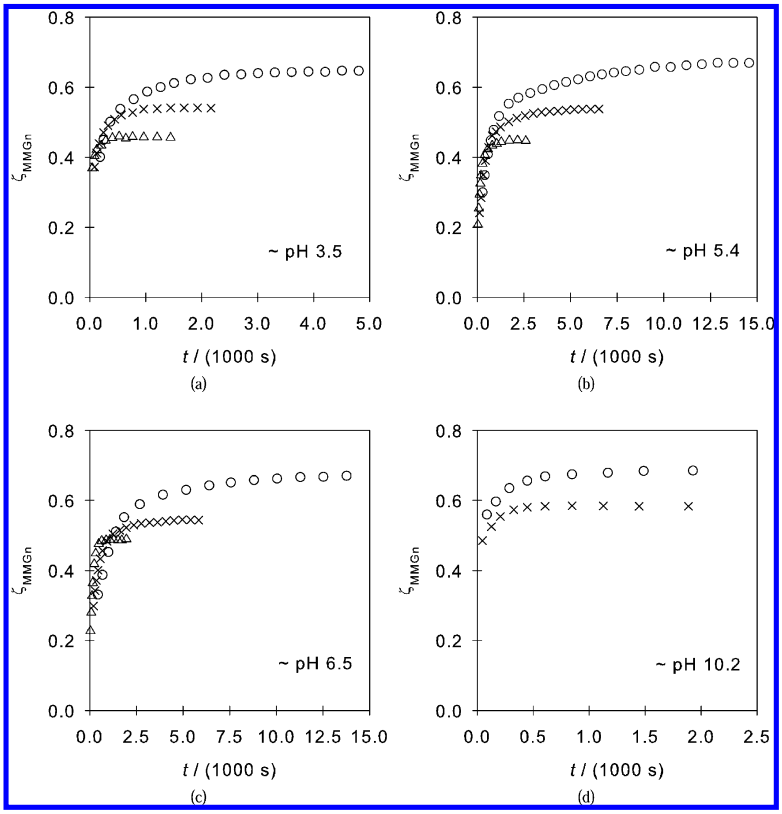

Figure 4. Peak area fractions of acetaldehyde bound in oligomers ζ_{MMGn} as determined in the reaction kinetic study of the oligomer formation in mixtures of acetaldehyde and water. Comparison of experiments with different temperatures (278 K (○), 288 K (×), and 298 K (Δ)) and similar pH values: (a) E1 (○), E2 (×), E3 (Δ); (b) E4 (○), E5 (×), E6 (Δ); (c) E7 (○), E8 (×), E9 (Δ); (d) E10 (○), E11 (×) (cf. Table 3).

few seconds after the educts were mixed, whereas an investigation in a standard probe head needs mixing of the reactants in advance without isothermal conditions and has a delay of a few minutes until the first NMR spectra are taken. For more information about the probe head, see ref 15.

EXPERIMENTAL RESULTS

Table 3 gives an overview of the experiments carried out in the present work and used for development of the kinetic model. A further experiment at 298 K and pH 10.3 is not included because the formation of acetaldol or aldoxane[18] was observed.

A reproduction was carried out for all experiments. Typical deviations between the peak area fractions ζ_{MMG_n} of the experiments and the reproductions are about 2%, and the largest deviation between two single values is smaller than 11%.

No experiments were carried out at pH values between 7 and 9 because the equivalence point of the acetaldehyde and water mixtures is located in this range. In that pH range, small variations of the composition cause a strong change of the pH value. Therefore, this pH range is difficult to access experimentally without the use of buffer solutions, which could cause an undesired impact on the kinetics.

At the beginning of the experiment, the peaks broaden strongly because the conversion of acetaldehyde is very high. This fact is challenging in the evaluation of the NMR peaks because some peaks at the beginning of an experiment are so broad that they cannot be evaluated quantitatively.

The experimental results are shown in Figure 4, where the experimental peak area fractions of acetaldehyde bound in oligomers ζ_{MMGn} are plotted as a function of time. When the temperature is increased by 10 K, the time needed to reach the equilibrium decreases by about a factor of 2. The overall acetaldehyde conversion decreases with increasing temperature. The overall conversion of acetaldehyde is only a function of the temperature and not of the pH value. At both low (cf. Figure 4a) and high pH values (cf. Figure 4d), the reaction is much faster than that at pH values between 5 and 7. The results indicate that the minimum of the reaction rate is at about pH 6.

MODEL

The kinetic experiments yield peak area fractions as a function of time. The kinetic model yields the true mole fractions of all components as a function of time. From the mole fractions, peak area fractions can be determined. Peak area fractions are therefore well suited for a direct comparison between the experiment and model and were used here for the parametrization and validation of the model. The influence of the pressure on the reaction kinetics is low in the liquid phase at moderate pressures[21] and neglected here.

Kinetic Model. The reaction rates are modeled for reactions (I) ($n = 1$) and (II) ($n > 1$) by

$$r_n(t, T, \mathrm{pH}) = k_{f,n}(T, \mathrm{pH}) \prod_{\text{all } i}^{\text{educts}} x_i(t)^{|\nu_{i,n}|} - k_{r,n}(T, \mathrm{pH}) \prod_{\text{all } i}^{\text{products}} x_i(t)^{|\nu_{i,n}|} \quad (2)$$

where

$$r_n(t) = \frac{1}{V_R} \frac{d\xi_n(t)}{dt} \quad (3)$$

dx.doi.org/10.1021/ie5033556 | Ind. Eng. Chem. Res. 2014, 53, 17589−17596

Table 4. Model Parameters of the Arrhenius Equation (eq 4) for Calculation of the Reaction Rates of the Oligomer Formation in Mixtures of Acetaldehyde and Water [cf. Reactions (I) and (II)]

reaction	$k^0_{f,n}$ [mol/(dm^3 s)]	$E_{A,f,n}$ (J/mol)	$C_{1,n}$	$C_{2,n}$
$n = 1$	5.812×10^9	59214	8.263×10^3	7.054×10^{-10}
$n > 1$	3.208×10^6	45000	1.247×10^4	6.513×10^{-10}

and $\xi_n(t)$ is the extent of reaction (n) (for calculation, cf. the SI), V_R is the reaction volume, and $\nu_{i,n}$ is the stoichiometric coefficient of component i in reaction (n). The kinetic constants of the forward reaction $k_{f,n}(T,\text{pH})$ and the reverse reaction $k_{r,n}(T,\text{pH})$ depend on the temperature and pH value. This dependence is described for the kinetic constants of the forward reactions by

$$k_{f,n}(T, \text{pH}) = k^0_{f,n} \exp\left(-\frac{E_{A,f,n}}{RT}\right)(1 + C_{1,n} \times 10^{-\text{pH}} + C_{2,n} \times 10^{\text{pH}}) \quad (4)$$

The parameters $C_{1,n}$ and $C_{2,n}$ describe the pH dependence of the kinetics. Such a model was used before by Hahnenstein et al.[5]

The kinetic parameters of the forward reaction $k_{f,n}$ and the reverse reaction $k_{r,n}$ are coupled by the chemical equilibrium constant $K_n(T)$:

$$k_{r,n}(T, \text{pH}) = \frac{k_{f,n}(T, \text{pH})}{K_n(T)} \quad (5)$$

From the reaction rates, initial composition, temperature, and pH value, the time dependence of the mole numbers $n_i(t)$, and, hence, the mole fractions $x_i(t)$ can be obtained, as described in the SI.

von Harbou et al.[22] found that it is favorable to rearrange reaction kinetic equations like those given above and introduced reference temperatures[23] for the purpose of parameter fitting. The procedure of von Harbou et al.[22] was adopted here; for details, see the SI.

Peak Area Fractions. The peak area fractions ζ_{MMG_n}, as defined in eq 1, can also be calculated from the mole fractions of the MMGs and acetaldehyde because the true mole numbers of the species acetaldehyde and MMG_n are proportional to the peak areas A_{AA} and A_{MMG_n}:

$$A_{AA} = \beta_{AA} \times 3n_{AA} \quad (6)$$

$$A_{MMG_n} = \beta_{MMG_n} \times 3\sum_n n\, n_{MMG_n} \quad (7)$$

With the common assumption that the proportionality factors of all methyl groups are equal

$$\beta_{AA} = \beta_{MMG_n} \quad (8)$$

the peak area fraction of the overall methyl peak of the oligomers ζ_{MMG_n} can be obtained from

$$\zeta_{MMG_n} = \frac{\sum_n n\, x_{MMG_n}}{x_{AA} + \sum_n n\, x_{MMG_n}} \quad (9)$$

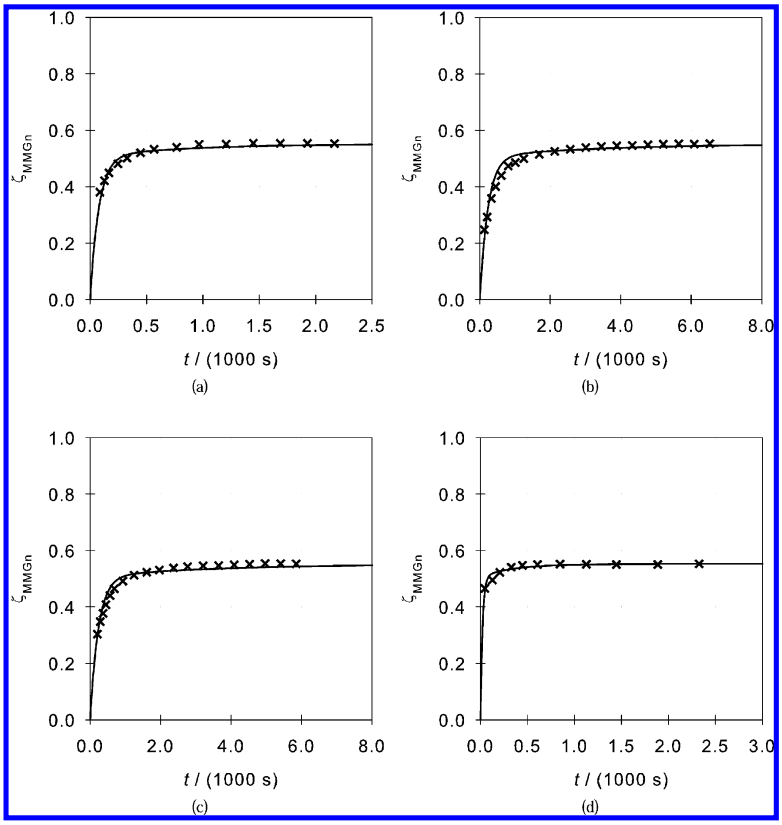

Figure 5. Peak area fractions ζ_{MMG_n} as a function of time at 288 K at different pH values. Lines are correlations of experimental data obtained in the present work (with correlation from eqs 1−9 and parameters from Table 4), and symbols are the related experimental values (×) for (a) E2, (b) E5, (c) E8, and (d) E11.

dx.doi.org/10.1021/ie5033556 | Ind. Eng. Chem. Res. 2014, 53, 17589−17596

Parameter Fit. The experimental and calculated peak area fractions ζ_{MMG_n} were compared in order to determine the parameters of the Arrhenius equation (cf. eq 4). A Matlab routine was used to minimize the objective function:

$$SSE = \sum_{k=1}^{M} \sum_{\text{all } l} (\zeta^{\text{exp}}_{MMG_n,k,l} - \zeta^{\text{calc}}_{MMG_n,k,l})^2 \stackrel{!}{=} \min \quad (10)$$

wherein k stands for the experiment ($k = 1, ..., M$) and l stands for the number of the experimental values at time t determined in that experiment.

Only n_{max} oligomers are considered. The number for n_{max} was set to 5 because the amount of acetaldehyde that is chemically bound in MMGs with $n > 5$ is negligible for the conditions used in the present work; cf. ref 14. This choice was made after the fitting procedure was conducted with higher numbers for n_{max}, and the resulting model parameters did not change significantly.

It is assumed that all kinetic constants for $n > 1$ are equal:

$$k_{f,n>1} = k_{f,2} = k_{f,3} = ... = k_{f,n\,max} \quad (11)$$

This choice was made after preliminary tests. It simplifies the model without compromising its quality. The equilibrium constants of reactions (I) and (II), K_1 and $K_{n>1}$, are available.[14]

Prior to the kinetic fit, the data from the present work were reconciled. This was necessary because the results for the equilibrium obtained in the present study do not fully match those from the dedicated equilibrium study.[14] The deviations are about 10% in the conversion of acetaldehyde and probably result from the fact that only much cruder information on the equilibrium was available in the present study than in ref 14. For details, see the SI.

To obtain a correlation that describes the temperature and pH dependence of the kinetics of the poly(oxymethylmethylene) glycol formation, a parameter fit was conducted including all experiments, with eq 10 as the objective function based on eqs 4 and 5. The full model has eight parameters ($k^0_{f,n}$, $E_{A,f,n}$, $C_{1,n}$, and $C_{2,n}$ for $n = 1$ and $n > 1$) using the assumptions described above.

Because at $\tilde{x}_{AA} = 0.1$ mol/mol only small amounts of higher oligomers are formed, the following fitting procedure was used. The two parameters $k_{f,1}$ and $k_{f,n}$ were fitted to each single experiment. From these results, the activation engergy of the formation of higher oligomers $E_{A,f,n}$ was estimated, evaluating an Arrhenius plot for the experiments E4, E5, E7, and E8. The estimated activation energy was fixed, and a global fit, including all experiments, was carried out.

RESULTS AND DISCUSSION

The results of the parameter fit are presented in Table 4. Figure 5 shows the peak area fraction ζ_{MMG_n} at 288 K as a function of time calculated using the model of the present work in comparison to the reconciled experimental data. The corresponding diagrams for 278 and 298 K are given in the SI.

In Figure 6, the values of the kinetic constants $k_{f,1}$ (cf. Figure 6a) and $k_{f,n}$ (cf. Figure 6b) are plotted as a function of the pH value. The vertex of the parabola is located at pH 6.

As an example for the application of the model, the mass fractions of the reactants as a function of time are calculated for the conditions used in experiment E4 (pH = 5.4 and T = 278 K). The results are shown in Figure 7. The maximum of the concentration of MMG_1 is reached after about 2000 s. The formation of higher oligomers takes much longer. After about 60000 s, equilibrium is almost reached.

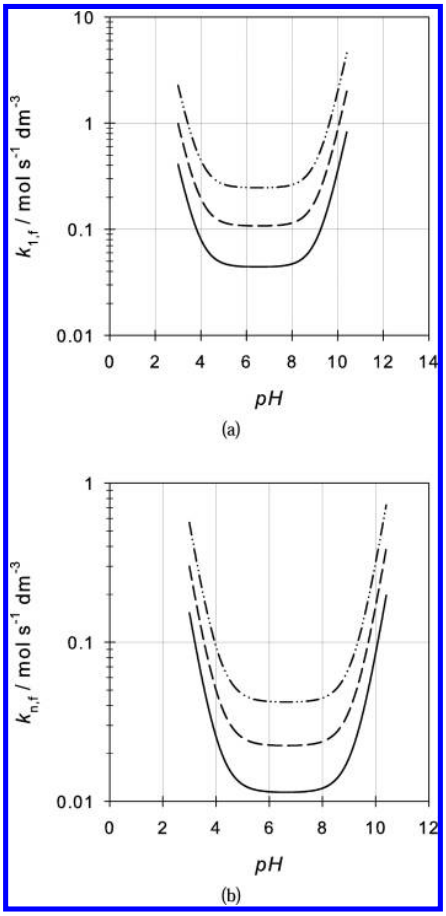

Figure 6. Kinetic constants for the forward reaction of (a) the MMG_1 formation [cf. reaction (I)] and (b) the $MMG_{n>1}$ formation [cf. reaction (II)] as a function of the pH value, calculated using the model of the present work. Different lines are correlations for 278 K (—), 288 K (– –), and 298 K (–·–·–).

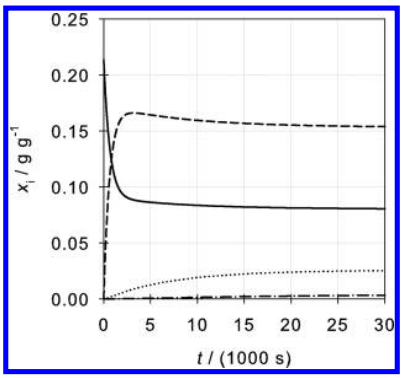

Figure 7. Mass fractions of the components AA (—), MMG_1 (– –), MMG_2 (···), and MMG_3 (–·–) as a function of time, calculated using the model of the present work, for the conditions of experiment E4 (T = 278 K and pH = 5.4). Results for $MMG_{n>3}$ are not shown because of low mass fractions.

In the following, the results obtained in the present work are compared to the results from the literature. The minimum of the reaction kinetics of the formation of MMG_1 is found here at about pH 6. This result is consistent with the results obtained from Sørensen and Jencks.[17] Ahrens and Strehlow[24] state that

dx.doi.org/10.1021/ie5033556 | Ind. Eng. Chem. Res. 2014, 53, 17589−17596

the kinetics of the MMG_2 formation are "similar" to that of the MMG_1 formation. This is confirmed by the results of the present work regarding the dependence on the pH value and temperature (cf. Figure 6); however, the rate constants of the formation of $MMG_{n>1}$ are found to be smaller than those of the MMG_1 formation.

Bell et al.[25] report half-life times of acetaldehyde between 6 and 60 s at 298 K, which is in good agreement with the values of the present work. Furthermore, data for the initial reaction rate of the formation of MMG_1 at 298 K can be obtained from refs 17 and 25−27 and compared to the present results. For a comparison of the data from different sources, the initial reaction rates $r^0_{MMG_1}$ were normalized by the initial overall molarity of acetaldehyde $\tilde{c}^0_{AA}$. The literature data and the results from the present work agree well for pH values between about 5 and 7, where the literature data for $r^0_{MMG_1}/\tilde{c}^0_{AA}$ are between about 0.4 and 1.7×10^{-2} s^{-1} and show no clear influence of the pH value. The results from the model of the present work are about 0.5×10^{-2} s^{-1}.

Outside that pH range, the literature data are spotty and contradictive so that a comparison in that range is not considered here.

A comparison with further studies from the literature on the kinetics of MMG formation (see Table 1) is not carried out because the authors claim agreement with studies discussed above or the presented information is not sufficient for a comparison.

CONCLUSION

Mixtures of acetaldehyde and water are reactive multicomponent systems because poly(oxymethylmethylene) glycols (MMG_1 and $MMG_{n>1}$) are formed. Quantitative data on the reaction kinetics of this system are scarce in the literature, and most studies were only carried out in dilute acetaldehyde solutions at 298 K and only the formation of MMG_1 was considered. In the present work, the reaction kinetics were studied for the formation of not only MMG_1 but also $MMG_{n>1}$. For the experimental work, a new microreactor NMR probe head was used that combines the advantages of online flow ^1H NMR spectroscopy with microreaction technology. A reaction kinetic model was developed, and the rate constants were fitted to the new experimental data. The results extend the knowledge on the reaction kinetics in the industrially important system studied.

It would, in principle, be desirable to extend the present study to a wider range of feed compositions, temperatures, and pH values. Such extensions would be difficult with the experimental setup used in the present work. An extension of the range to lower temperatures is difficult at least as long as pure water is used as one of the educts because of its melting point at 273 K. An extension of the range to higher temperatures is difficult because the reactions become too fast. The same holds for both ends of the studied pH range. Furthermore, outside of the pH range studied here, side reactions become important. The concentration range could probably be extended. However, at lower acetaldehyde concentrations, the concentration of higher oligomers becomes very small, and at higher acetaldehyde concentrations, it is questionable whether the experiments could be carried out under isothermal conditions with the present approach because of the strongly exothermic effects upon mixing acetaldehyde with water. This could possibly be circumvented by changing the strategy of initializing the kinetic experiments. Instead of mixing pure acetaldehyde with water, concentrated mixtures of acetaldehyde and water could be diluted with water. The results from such experiments would probably yield more information on the kinetics of the reactions in which $MMG_{n>1}$ are involved, which is hard to retrieve from the present data because the concentrations of $MMG_{n>1}$ are low.

The kinetic model developed in the present work enables, for the first time ever, a description of the kinetic effects in the system acetaldehyde and water in a wide temperature and pH range.

ASSOCIATED CONTENT

Supporting Information

Overview of literature studies, pH measurements, model details, modelling results, and a table and figures. This material is available free of charge via the Internet at http://pubs.acs.org.

AUTHOR INFORMATION

Corresponding Author

*E-mail: erik.vonharbou@mv.uni-kl.de.

Notes

The authors declare no competing financial interest.

ACKNOWLEDGMENTS

We gratefully acknowledge financial support of this work by Lonza AG, Visp, Switzerland.

REFERENCES

(1) Eckert, M.; Fleischmann, G.; Jira, R.; Bolt, H. M.; Golka, K. Acetaldehyde. *Ullmann's Encyclopedia of Industrial Chemistry*, 6th ed.; Wiley-VCH: Berlin, 2006.

(2) Scheithauer, A. Physico-Chemical Data and Conceptual Design of a Crotonaldehyde Production Process. Ph.D. Thesis, Laboratory of Engineering Thermodynamics, University of Kaiserslautern, Kaiserslautern, Germany, 2014; Vol. *13*; Scientific Report Series, ISBN 978-3-944433-12-7.

(3) Hahnenstein, I.; Hasse, H.; Kreiter, C.; Maurer, G. ^1H- and ^{13}C-NMR Spectroscopic Study of Chemical Equilibria in Solutions of Formaldehyde in Water, Deuterium Oxide, and Methanol. *Ind. Eng. Chem. Res.* **1994**, *33*, 1022−1029.

(4) Hahnenstein, I.; Hasse, H.; Liu, Y.-Q.; Maurer, G. *AIChE Symposium Series 298*; AIChE: New York, 1994; Vol. *90*, pp 141−157.

(5) Hahnenstein, I.; Albert, M.; Hasse, H.; Kreiter, C. G.; Maurer, G. NMR Spectroscopic and Densimetric Study of Reaction Kinetics of Formaldehyde Polymer Formation in Water, Deuterium Oxide, and Methanol. *Ind. Eng. Chem. Res.* **1995**, *34*, 440−450.

(6) Maiwald, M.; Fischer, H. H.; Ott, M.; Peschla, R.; Kuhnert, C.; Kreiter, C. G.; Maurer, G.; Hasse, H. Quantitative NMR Spectroscopy of Complex Liquid Mixtures: Methods and Results for Chemical Equilibria in Formaldehyde−Water−Methanol at Temperatures up to 383 K. *Ind. Eng. Chem. Res.* **2003**, *42*, 259−266.

(7) Ott, M.; Fischer, H. H.; Maiwald, M.; Albert, K.; Hasse, H. Kinetics of Oligomerization Reactions in Formaldehyde Solutions: NMR Experiments up to 373 K and Thermodynamically Consistent Model. *Chem. Eng. Process.* **2005**, *44*, 653−660.

(8) Kuhnert, C.; Albert, M.; Breyer, S.; Hahnenstein, I.; Hasse, H.; Maurer, G. Phase Equilibrium in Formaldehyde Containing Multicomponent Mixtures: Experimental Results for Fluid Phase Equilibria of (Formaldehyde plus (Water or Methanol) plus Methylal) and (Formaldehyde plus Water plus Methanol plus Methylal) and Comparison with Predictions. *Ind. Eng. Chem. Res.* **2006**, *45*, 5155−5164.

(9) Schilling, K.; Sohn, M.; Ströfer, E.; Hasse, H. Reactive Evaporation of Formaldehyde-containing Mixtures and Process Monitoring by Online NMR-Spectroscopy. *Chem. Ing. Tech.* **2003**, *75*, 240−244.

(10) Maiwald, M.; Fischer, H. H.; Kim, Y.-K.; Albert, K.; Hasse, H. Quantitative High-Resolution On-line NMR Spectroscopy in Reaction and Process Monitoring. *J. Magn. Reson.* **2004**, *166*, 135−146.
(11) Grützner, T.; Hasse, H.; Lang, N.; Siegert, M.; Ströfer, E. Development of a New Industrial Process for Trioxane Production. *Chem. Eng. Sci.* **2007**, *62*, 5613−5620.
(12) Drunsel, J.-O.; Renner, M.; Hasse, H. Experimental Study and Model of Reaction Kinetics of Heterogeneously Catalyzed Methylal Synthesis. *Chem. Eng. Res. Des.* **2012**, *90*, 696−703.
(13) Burger, J.; Ströfer, E.; Hasse, H. Chemical Equilibrium and Reaction Kinetics of the Heterogeneously Catalyzed Formation of Poly(oxymethylene) Dimethyl Ethers from Methylal and Trioxane. *Ind. Eng. Chem. Res.* **2012**, *51*, 12751−12761.
(14) Scheithauer, A.; Grützner, T.; Rijksen, C.; Zollinger, D.; von Harbou, E.; Thiel, W.; Hasse, H. ^{1}H- and ^{13}C-NMR Spectroscopic Study of Chemical Equilibria in the System Acetaldehyde + Water. *AIChE J.* **2014**, DOI: 10.1002/aic.14623.
(15) Brächer, A.; Hoch, S.; Albert, K.; Kost, H.; Werner, B.; von Harbou, E.; Hasse, H. Thermostatted Micro-Reactor NMR Probe Head for Monitoring Fast Reactions. *J. Magn. Reson.* **2014**, *242*, 155−161.
(16) Podo, F.; Viti, V. A PMR Study of Hydration Products in Aqueous Acetaldehyde Solutions. *Org. Magn. Reson.* **1970**, *3*, 259−261.
(17) Sørensen, P.; Jencks, W. Acid- and Base-Catalyzed Decomposition of Acetaldehyde Hydrate and Hemiacetals in Aqueous Solution. *J. Am. Chem. Soc.* **1987**, *109*, 4675−4690.
(18) Scheithauer, A.; Grützner, T.; Rijksen, C.; Zollinger, D.; von Harbou, E.; Thiel, W.; Hasse, H. NMR Spectroscopic Study of the Aldoxane Formation in Aqueous Acetaldehyde Solutions. *Ind. Eng. Chem. Res.* **2014**, *53*, 8395−8403.
(19) Busfield, W. K.; Lee, R. M.; Merigold, D. Gas Phase Equilibrium between Acetaldehyde and Paraldehyde, Thermodynamic Values for the Trimerisation of Acetaldehyde and the Polymerisability of Paraldehyde. *J. Chem. Soc., Faraday Trans. 1* **1973**, *69*, 936−940.
(20) Schönfeld, F.; Hessel, V.; Hofmann, C. An Optimised Split-and-Recombine Micro-Mixer with Uniform 'Chaotic' Mixing. *Lab Chip* **2004**, *4*, 65−69.
(21) Lewis, C. A.; Wolfenden, R. Influence of Pressure on the Equilibrium of Hydration of Aliphatic Aldehydes. *J. Am. Chem. Soc.* **1973**, *95*, 6685−6688.
(22) von Harbou, E.; Yazdani, A.; Schmitt, M.; Großmann, C.; Hasse, H. Reaction Kinetics for Reactive Distillation Using Different Laboratory Reactors. *Ind. Eng. Chem. Res.* **2013**, *52*, 624−637.
(23) Buzzi-Ferraris, G.; Manenti, F. *Interpolation and Regression Models for the Chemical Engineer: Solving numerical problems*; Wiley-VCH: Weinheim, Germany, 2010.
(24) Ahrens, M.; Strehlow, H. Acid Catalyzed Hydration of Acetaldehyde. *Discuss. Faraday Soc.* **1965**, *39*, 112−120.
(25) Bell, R.; Rand, M. H.; Wynne-Jones, K. M. A. Kinetics of the Hydration of Acetaldehyde. *Trans. Faraday Soc.* **1956**, *52*, 1093−1102.
(26) Bell, R. P.; Evans, P. G. Kinetics of the Dehydration of Methylene Glycol in Aqueous Solution. *Proc. R. Soc. London A* **1966**, *291*, 297−323.
(27) Greenzaid, P.; Luz, Z.; Samuel, D. A Nuclear Magnetic Resonance Study of the Reversible Hydration of Aliphatic Aldehydes and Ketones. II. The Acid-Catalyzed Oxygen Exchange of Acetaldehyde. *J. Am. Chem. Soc.* **1967**, *89*, 756−759.
(28) Socrates, G. Hydration Study of Acetaldehyde and Propionaldehyde. *J. Org. Chem.* **1969**, *34* (10), 2958−2961.
(29) Cheshnovsky, D.; Navon, G. Nuclear Magnetic Resonance Studies of Carbonic Anhydrase Catalyzed Reversible Hydration of Acetaldehyde by the Saturation Transfer Method. *Biochemistry* **1980**, *19*, 1866−1873.
(30) Evans, P.; Miller, G.; Kreevoy, M. Comparison of Nuclear Magnetic Resonance, Thermal Maximum, and Scavenging Techniques for Rate Measurement. *J. Phys. Chem.* **1965**, *69*, 4325−4327.
(31) Gruen, L.; McTigue, P. Kinetics of Hydration of Aliphatic Aldehydes. *J. Chem. Soc.* **1963**, 5224−5229.
(32) Pocker, Y.; Meany, J. E. The Catalytic Versatility of Carbonic Anhydrase from Erythrocytes. The Enzyme-Catalyzed Hydration of Acetaldehyde. *J. Am. Chem. Soc.* **1965**, *87*, 1809−1811.
(33) Buschmann, H.-J.; Dutkiewicz, E.; Knoche, W. The Reversible Hydration of Carbonyl Compounds in Aqueous Solution. Part II: The Kinetics of the Keto/Gem-diol Transition. *Ber. Bunsenges. Phys. Chem.* **1982**, *86*, 129−134.
(34) Bell, R. P.; Clunie, J. C. Binary and Ternary Mechanisms in the Hydration of Acetaldehyde. *Proc. R. Soc. London A* **1952**, *212*, 33−37.
(35) Kurz, J. L.; Coburn, J. I. The Hydration of Acetaldehyde. II. Transition-State Characterization. *J. Am. Chem. Soc.* **1967**, *89*, 3528−3537.
(36) Bell, R. P.; Higginson, W. C. E. The Catalyzed Dehydration of Acetaldehyde Hydrate, and the Effect of Structure on the Velocity of Protolytic Reactions. *Proc. R. Soc. London A* **1949**, *197*, 141−159.
(37) Schuchmann, M. N.; von Sonntag, C. The Rapid Hydration of the Acetyl Radical. A Pulse Radiolysis Study of Acetaldehyde in Aqueous Solution. *J. Am. Chem. Soc.* **1988**, *110*, 5698−5701.

Scheithauer et al., 2014a

Reprinted with permission from: A. Scheithauer, T. Grützner, C. Rijksen, D. Zollinger, E. von Harbou, W. R. Thiel, H. Hasse, NMR Spectroscopic Study of the Aldoxane Formation in Aqueous Acetaldehyde Solutions, Industrial & Engineering Chemistry Research, Volume 53, 2014, Pages 8395-8403, DOI 10.1021/ie5004043

I&EC research
Industrial & Engineering Chemistry Research

Article

pubs.acs.org/IECR

NMR Spectroscopic Study of the Aldoxane Formation in Aqueous Acetaldehyde Solutions

Andreas Scheithauer,[†] Thomas Grützner,[‡] Christiaan Rijksen,[‡] Daniel Zollinger,[‡] Erik von Harbou,[†] Werner R. Thiel,[§] and Hans Hasse*[,†]

[†]Laboratory of Engineering Thermodynamics and [§]Department of Chemistry, University of Kaiserslautern, 67663 Kaiserslautern, Germany

[‡]Lonza AG, 3930 Visp, Switzerland

Supporting Information

ABSTRACT: Crotonaldehyde is an interesting intermediate in the chemical industry. It is usually produced from aqueous acetaldehyde in a two step process in which the first step is carried out under basic and the second step under acidic conditions. It is commonly assumed that acetaldehyde is converted in the first step to acetaldol and that acetaldol is subsequently dehydrated in the second step to crotonaldehyde. We demonstrate by ^{1}H and ^{13}C NMR spectroscopic studies that acetaldol is hardly present in the reacting solutions at lower temperatures and that the key intermediate is aldoxane (2,6-dimethyl-1,3-dioxane-4-ol). For the first time, data on the chemical equilibrium of the aldoxane formation in aqueous acetaldehyde solutions is provided. Furthermore, preliminary information on the kinetics of that reaction is presented.

INTRODUCTION

Acetaldehyde (AA) is an important intermediate in chemical industry and used, among others, for the production of acetic acid, acetic anhydride, ethyl acetate, 1-butanol, and pentaerythritol.[1] In the present work, the chemical route leading from acetaldehyde to crotonaldehyde (CA) is studied. Crotonaldehyde is an intermediate in many chemical value-added chains[2] and used for producing chemicals like sorbic acid and crotonic acid.[3]

The established production process for obtaining crotonaldehyde from acetaldehyde is described in some detail in ref 3. Efforts for improving that process have led to a number of patents, for example, refs 4−9. For a rational process design, the physicochemical fundamentals of the process have to be known. The present work aims at contributing to this by supplying reaction equilibrium and reaction kinetic data.

In industrial crotonaldehyde production, acetaldehyde is supplied in aqueous solution. Aqueous acetaldehyde solutions are highly reactive multicomponent mixtures. Similar to formaldehyde,[10] also acetaldehyde is chemically bound in aqueous solutions. Acetaldehyde and water react to ethane-1,1-diol (MMG_1). The reaction has been studied by different authors.[11−19] The addition of further acetaldehyde molecules yields poly(oxymethylmethylene) glycols (MMG_n). The formation of oligomers in aqueous acetaldehyde solutions is explicitly accounted for in the present work, based on the results presented in the work of Scheithauer.[20] It is assumed that monomeric acetaldehyde is the reacting species, i.e. that acetaldehyde bound in the oligomers does not directly take part in the main reactions discussed here, but only after their cleavage. Hence, the interpretation of the experimental results is based on true species mole fractions x_i. To characterize feeds and products also the overall mole fractions $\tilde{x}_i$ are used, where it is assumed that the oligomers are completely decomposed into water and acetaldehyde.

It is commonly assumed that acetaldehyde is converted under basic conditions to form acetaldol (ADL). The aldol addition reaction is usually catalyzed by a homogeneous catalyst in liquid phase. Commonly used catalysts are sodium hydroxide and potassium hydroxide.[21] The reaction is typically carried out at about 293−298 K[21] and pH-values of 10−13.[22]

After shifting to acidic conditions (pH values of about 2−7[23]), at higher temperatures (about 373 K[24]), acetaldol reacts in a dehydration reaction to yield crotonaldehyde. Then, the basic catalyzed addition reaction is stopped. For shifting the pH value from basic to acidic conditions, typically acetic acid or mineral acids are used.[3] The formation of crotonaldehyde is usually carried out in a reactive distillation column,[3] and the resulting heteroazeotropic mixture consisting of mostly crotonaldehyde and water is separated in a heteroazeotropic distillation sequence.

In earlier studies in the literature partly conflicting conclusions about the aldol addition reaction were published. Bell and McTigue[25] attributed this to the complicated reaction system involving the formation of intermediate products. There is no agreement on whether the aldol addition reaction is irreversible or reversible.[25,26] Also different reaction orders relating to the concentration of acetaldehyde were found in various publications[25,27,28] on that reaction.

Despite these discrepancies, the simple reaction scheme described above is used in previous models of the reactions leading from acetaldehyde to crotonaldehyde.[3,22,26,29,30] These models have several shortcomings. First, most neglect the presence of the poly(oxymethylmethylene) glycols and are based on overall concentrations. Abundant experience with

Received: January 28, 2014
Revised: April 15, 2014
Accepted: April 16, 2014
Published: April 16, 2014

dx.doi.org/10.1021/ie5004043 | Ind. Eng. Chem. Res. 2014, 53, 8395−8403

reacting formaldehyde solutions[10,31−38] shows that it is more favorable to set up such models using true concentrations, as it is done in the present study.

More importantly, the simple two step picture of crotonaldehyde production is an oversimplification. There have been previous reports that, besides acetaldol, another intermediate product occurs, namely aldoxane (ALX).[39−42] This ring structure is formed from acetaldehyde and acetaldol in basic as well as in neutral or acidic medium. Also the existence of paraldol (PADL), another ring structure similar to aldoxane which is formed by two acetaldol molecules, has been reported.[43−46]

The experimental data from the present work clearly shows that aldoxane is not just a side component but a main component in the conversion of acetaldehyde to crotonaldehyde and that, while typically large amounts of aldoxane are present in reacting acetaldehyde mixtures, the amount of acetaldol is low. Hence, a more detailed reaction model for the crotonaldehyde process must be developed. It must explicitly include aldoxane. It is also shown that the paraldol formation is not important in the technical process.

Therefore, in the present work, experiments were carried out in order to study the chemical equilibrium of the aldoxane formation. Acetaldehyde in aqueous solution of different compositions was converted to acetaldol and aldoxane using the basic heterogeneous catalyst Amberlyst A26 OH (product of Rohm and Haas (currently Dow Chemical), Paris, France). The samples were analyzed at different temperatures by ^{13}C NMR spectroscopy. The peak area fractions of the peaks in the ^{13}C NMR spectra were acquired and the composition of the samples was calculated. From the data the equilibrium constant of the aldoxane formation was determined and a model describing the chemical equilibrium was developed.

Furthermore, preliminary experiments were carried out to study the reaction kinetics of the aldoxane formation. For this purpose the homogeneously catalyzed addition reaction of acetaldehyde was monitored online.

REACTION SYSTEM

In the following, the reactions in aqueous acetaldehyde solutions are described. The chemical structures of the components are shown in Figure 1.

Acetaldol (ADL) is formed in an addition reaction of two acetaldehyde (AA) molecules under basic conditions:

$$\underbrace{2\,CH_3{-}CHO}_{AA} \overset{OH^-}{\rightleftharpoons} \underbrace{CH_3{-}CH(OH){-}CH_2{-}CHO}_{ADL} \quad (I)$$

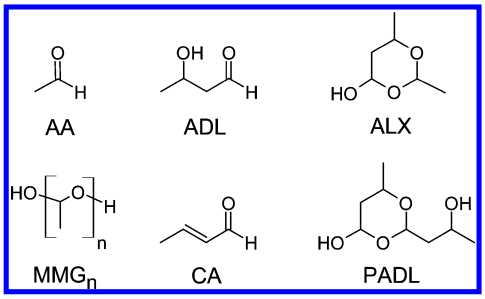

Figure 1. Chemical structure of the components in the aldol condensation reaction scheme, with abbreviations.

Acetaldehyde and acetaldol form the cyclic aldoxane (ALX) no matter the pH value.

$$\underbrace{CH_3{-}CHO}_{AA} + \underbrace{CH_3{-}CH(OH){-}CH_2{-}CHO}_{ADL} \rightleftharpoons \underbrace{C_6H_{12}O_3}_{ALX} \quad (II)$$

On the basis of the simplified reaction scheme with acetaldol as the sole product, studies of the addition reaction of acetaldehyde have been carried out, for example, refs 22 and 25−27. They report apparent reaction kinetic constants based on molarities from which overall kinetic constants can be calculated. These are based on an analysis of overall concentrations, e.g. acetaldehyde concentrations from gas chromatography. As it is not clear what influence the presence of aldoxane has on the results obtained with these methods, we refrain from using this data to retrieve information on the equilibrium of the acetaldol formation (reaction I) using our new data on the aldoxane formation (reaction II). For technical applications, this is no serious drawback. Reaction I only occurs under basic conditions, under which typically also important side reactions are observed, that hinder the direct study of the equilibrium of reaction I. In industrial reactors for the addition reaction of acetaldehyde, therefore, the reaction is stopped by shifting the pH when the conversion is about 50−60%.[21,24] So detailed information on the equilibrium of reaction I is not mandatory for process design. Furthermore, the results from the present work show that the equilibrium constant of reaction II is very large at temperatures around 293 K, where the industrial aldol addition reaction is carried out so that hardly any acetaldol is present, which is a further hindrance of studies of the equilibrium of reaction I.

It is important to consider aldoxane in industrial process design. On the one hand, the formation of aldoxane limits the selectivity of the crotonaldehyde formation. On the other hand, acetaldehyde is bound in the higher boiling aldoxane and thus the reverse reaction (of reaction II) has to be supported in order to recycle unreacted acetaldehyde. Therefore, the separation becomes much more challenging.

Because acetaldehyde is supplied in aqueous solution, the formation of poly(oxymethylmethylene) glycols has to be taken into account. Ethane-1,1-diol (MMG_1) is formed in a reaction of acetaldehyde with water:

$$\underbrace{CH_3{-}CHO}_{AA} + \underbrace{H_2O}_{W} \rightleftharpoons \underbrace{HO{-}(CH(CH_3){-}O{-})H}_{MMG_1} \quad (III)$$

The formation of the higher oligomers can be described in general as follows:

$$\underbrace{HO{-}(CH(CH_3){-}O{-})_{n-1}H}_{MMG_{n-1}} + \underbrace{CH_3{-}CHO}_{AA} \rightleftharpoons \underbrace{HO{-}(CH(CH_3){-}O{-})_nH}_{MMG_n} \quad (n \geq 2) \quad (IV)$$

In the present model, only MMG_1 and MMG_2 are considered, as at the temperatures and compositions studied here, higher oligomers (MMG_n, with $n > 2$) are not present.[20] Reactions III and IV are catalyzed both by acids and bases but occur also in neutral media. The formation of paraldol from acetaldol has not been observed and is, hence, not considered. Also the formation of crotonaldehyde

$$\underbrace{CH_3{-}CH(OH){-}CH_2{-}CHO}_{ADL} \rightleftharpoons \underbrace{CH_3{-}CH{=}CH{-}CHO}_{CA} + \underbrace{H_2O}_{W} \quad (V)$$

is not considered, because, in the experiments of the present work, it was only observed in some cases as a byproduct in small amounts.

dx.doi.org/10.1021/ie5004043 | Ind. Eng. Chem. Res. 2014, 53, 8395−8403

EXPERIMENTAL STUDY OF THE ALDOXANE EQUILIBRIUM

Chemicals. Acetaldehyde was delivered by Sigma-Aldrich, Munich, Germany, as an A.C.S. reagent (≥0.995 g/g). Ultrapure water was produced using a Milli-Q integral water purification system from Merck Millipore, Darmstadt, Germany. The heterogeneous catalyst Amberlyst A26 OH of Rohm and Haas (currently Dow Chemical), Paris, France, was used to catalyze the aldol addition reaction of acetaldehyde. The technical data of Amberlyst A26 OH is given in the Supporting Information.

NMR Spectroscopy. All samples were analyzed by ^{1}H and ^{13}C NMR spectroscopy using a 400 MHz Unity Nova NMR spectrometer of Varian, Palo Alto, USA, equipped with a Varian 400 AutoSW PFG 4 nuclei probe head. Proton decoupled ^{13}C NMR spectra with an acquisition time of about 10 s, a relaxation delay of 60 s, and a pulse width of 45° with at least 265 scans were acquired and averaged in the equilibrium experiments. The NOE was suppressed during the ^{13}C NMR spectroscopic experiments. Because no aldehyde signals were quantitatively evaluated, which should have the longest T1 values, and due to the 45° pulse width, the relaxation delay was more than enough for quantitative evaluation of the ^{13}C NMR spectra. This was checked in experiments with the same sample and other values for the relaxation delay. The digitalization of the ^{13}C NMR spectra was about 0.1 Hz/pt or less and thus enough for quantitative evaluation. The ^{1}H NMR spectra had an acquisition time of 1 s, a relaxation delay of 30 s, and a pulse width of 45°. At least 4 scans were recorded and averaged.

For peak assignment of aldoxane, besides ^{1}H and ^{13}C NMR spectroscopy, two-dimensional NMR spectroscopy was applied. HH-Cosy- and Hmqc-NMR spectra were recorded. For these experiments an Avance 600 MHz NMR spectrometer from Bruker, Rheinstetten, Germany, was used.

Because of the high vapor pressure of acetaldehyde (normal boiling point: 294 K), pressure resistant NMR tubes from WILMAD, Vineland, NJ, were used. It was verified by tests with pure acetaldehyde at 353 K for 7 days that no losses occur from these tubes. Typical liquid sample volumes were 1.5 mL. It was verified that the shift of the mole fractions of the liquid sample by evaporation in the sample tubes is small, even under unfavorable conditions, and can be neglected.

Peak Assignment in ^{1}H and ^{13}C NMR Spectra. In order to assign the peaks of aldoxane in the ^{1}H and ^{13}C NMR spectra, acetaldehyde ($\tilde{x}_{AA}$ = 0.8 mol/mol) was partially converted to aldoxane using Amberlyst A26 OH. The catalyst was separated from the mixture and unreacted acetaldehyde was distilled off from the product mixture in a batch distillation device at 10 mbar and 298 K. The residue of the distillation was analyzed by ^{1}H, ^{13}C, HH-Cosy-, and Hmqc-NMR spectroscopy. The structure of aldoxane with group numbers as used for the interpretation is shown in Figure 2. The 1,3-dioxane ring of aldoxane has three chirality centers, groups 2, 4, and 6. Two diastereomeric forms of aldoxane are distinguishable in the NMR spectra. Therefore, normally two peaks for each proton in the ^{1}H NMR spectrum and each carbon in the ^{13}C NMR spectrum are obtained.

The ^{1}H NMR spectrum of the residue of the distillation is shown in Figure 3. The numbers in the spectrum refer to the group numbers of the aldoxane molecule in Figure 2. The assignment was carrried out based on the HH-Cosy-NMR spectrum (see the Supporting Information). The two

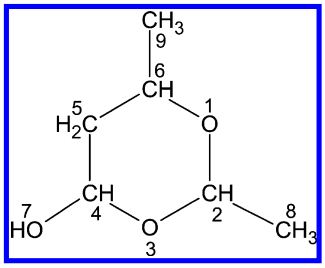

Figure 2. Chemical structure of aldoxane with group numbering as used for the peak assignment in the ^{1}H and ^{13}C NMR spectra.

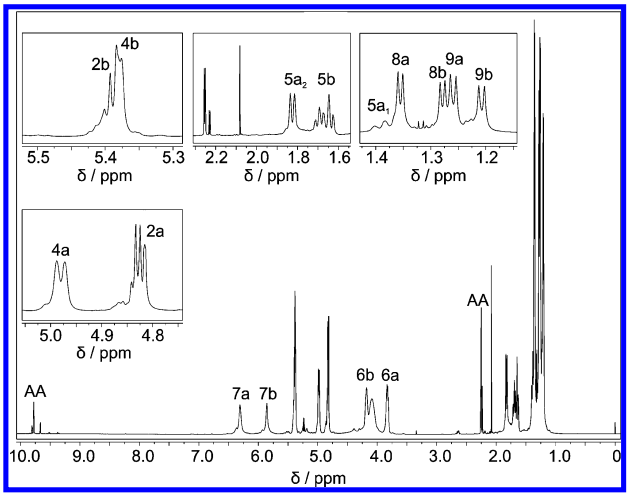

Figure 3. ^{1}H NMR spectrum (600 MHz) of the residue of a batch distillation (cf. text), containing aldoxane, water, and acetaldehyde at 293 K with peak assignment according to Figure 2. The two distinguishable diastereomeric forms of aldoxane are labeled with a and b. Peaks that are not labeled are side components which result from the sample production.

distinguishable diastereomeric forms of aldoxane are labeled with a and b. Figure 4 shows the ^{13}C NMR spectrum of the residue of the batch distillation together with the peak assignment, based on the peak assignment in the ^{1}H and Hmqc-NMR spectra (see the Supporting Information).

For quantitative evaluation of the NMR spectra, it is desirable to identify at least one isolated peak for aldoxane, acetaldol, acetaldehyde, MMG_1, and MMG_2. After the evaluation, the true mole fraction of water can be calculated from the mass balances and the known overall feed composition. The ^{1}H NMR spectra were not quantitatively evaluated to avoid problems resulting from the overlapping peaks. The peaks in the ^{13}C NMR spectra that were chosen for the experimental evaluation are listed in Table 1. In the following, the two peaks of aldoxane, resulting from the two distinguishable diastereomeric forms are labeled ALX_A and ALX_B. For more comprehensive information on the peak assignment of aldoxane in the ^{13}C and ^{1}H NMR spectra, see the Supporting Information.

Sample Preparation. Mixtures of acetaldehyde and water, with overall acetaldehyde mole fractions of $\tilde{x}_{AA}$ = 0.4, 0.3, 0.2, and 0.1 mol/mol (sample P1−P4), were prepared gravimetrically using a precision balance (Mettler Toledo XS603S, Greifensee, Switzerland). Before the preparation of the samples, the starting materials were cooled to 275 K to prevent losses of acetaldehyde by evaporation during the preparation. The

dx.doi.org/10.1021/ie5004043 | Ind. Eng. Chem. Res. 2014, 53, 8395−8403

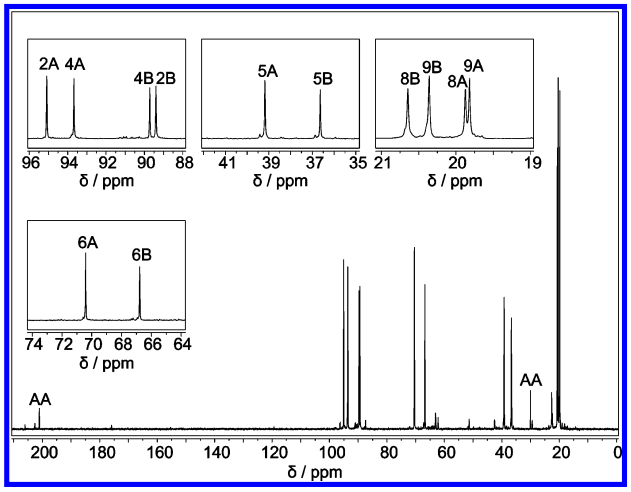

Figure 4. ^{13}C NMR spectrum (600 MHz) of the residue of a batch distillation (cf. text), containing aldoxane, water, and acetaldehyde at 293 K with peak assignment according to Figure 2. The two distinguishable diastereomeric forms of aldoxane are labeled with A and B. Peaks that are not labeled are side components which result from the sample production.

Table 1. Chemical Shifts of the Peaks in the ^{13}C NMR Spectrum Which Are Used for Quantitative Calculation of the Chemical Equilibrium of the Aldoxane Formation

component	carbon group	δ/ppm
aldoxane	C in group 6[a]	70.5/66.8[b]
acetaldol	CH_3–CH(OH)–$\underline{C}H_2$–CHO	51
acetaldehyde	$\underline{C}H_3$–CHO	30
MMG_1	HO–(CH($\underline{C}H_3$)–O–)H	23.5
MMG_2	HO–(CH($\underline{C}H_3$)–O–)$_2$H	22.5

[a]See Figure 2. [b]Two distinguishable diastereomers, peaks labeled as ALX_A and ALX_B in the following.

cooling is important as the mixing of acetaldehyde and water goes along with the formation of poly(oxymethylmethylene) glycols (reactions III and IV), which is exothermal.[12,18,20,47] About 2 g of Amberlyst A26 OH were added to about 30 mL of the acetaldehyde and water mixture, to start the acetaldehyde addition reaction. The reacting mixture was thermostated in a glass vessel at 278 K. After about 6 h, the catalyst was removed. Even though Amberlyst A26 OH was deactivated during the experiments, its activity was high enough to convert a considerable amount of acetaldehyde. From the resulting mixture, samples of about 1.5 mL were taken for studies of the chemical equilibrium of the aldoxane formation. The ratio of the overall mole number of water and acetaldehyde $\tilde{n}^0_W/\tilde{n}^0_{AA}$ in the sample is not changed by the reaction and, hence, known from the preparation. Details on the base catalyzed reaction are not important as long as it yields acetaldol, as all educts and products of the aldoxane formation are quantified by NMR spectroscopy in the equilibrium. By removing the catalyst, reaction I is stopped and only reaction II and the formation of poly(oxymethylmethylene) glycols (reactions III and IV) can occur.

NMR Experiments. The samples were equilibrated at the desired temperature in an oven for about 1 h. Subsequently, they were analyzed at the same temperature by ^{13}C NMR spectroscopy. The samples P1–P4 were analyzed at 313, 333, 353, and 363 K. The samples could not be analyzed at temperatures higher than 363 K, for two reasons. On the one hand, at high temperatures the formation of crotonaldehyde becomes important and cannot be neglected anymore. On the other hand, with increasing temperature the signal-to-noise ratio gets worse and thus the NMR spectra become difficult to evaluate.

The NMR spectra were quantitatively evaluated using the peak assignment as described above. For the integration of the peaks MestReNova (MestreLabs, Santiago de Compostela, Spain) was used and a baseline and phase correction was applied. It was assumed that the area below each peak is proportional to the mole number of the corresponding group and that the proportionality constants are the same for all peaks of the groups CH, CH_2, and CH_3. This was justified by comparing the peak areas of the CH and CH_2 groups of aldoxane. The primary data on the peak areas are reported in the work of Scheithauer.[20]

Small amounts of crotonaldehyde were found in some samples which were exposed to high temperatures (x_{CA} < 0.01 mol/mol) but were neglected in the evaluation.

DATA EVALUATION AND CORRELATION

The experimental data on the peak areas was used to determine the true mole fractions in the studied mixtures. The true mole numbers of each component in equilibrium n_i can be calculated from the extents of reaction ξ_j of all considered reactions j (reaction I–IV):

$$n_W = \tilde{n}^0_W - \xi_{III} \quad (1)$$

$$n_{AA} = \tilde{n}^0_{AA} - 2\xi_I - \xi_{II} - \xi_{III} - \xi_{IV} \quad (2)$$

$$n_{ALX} = \xi_{II} \quad (3)$$

$$n_{ADL} = \xi_I - \xi_{II} \quad (4)$$

$$n_{MMG1} = \xi_{III} - \xi_{IV} \quad (5)$$

$$n_{MMG2} = \xi_{IV} \quad (6)$$

$\tilde{n}^0_W$ and $\tilde{n}^0_{AA}$ are the initial mole numbers of water and acetaldehyde, respectively. The ratio of the mole number of component i and the mole number of acetaldehyde is calculated from the peak areas:

$$\frac{n_{ALX}}{n_{AA}} = \frac{A_{ALXA} + A_{ALXB}}{A_{AA}} \quad (7)$$

$$\frac{n_{ADL}}{n_{AA}} = \frac{A_{ADL}}{A_{AA}} \quad (8)$$

$$\frac{n_{MMG1}}{n_{AA}} = \frac{A_{MMG1}}{A_{AA}} \quad (9)$$

$$\frac{n_{MMG2}}{n_{AA}} = \frac{A_{MMG2}}{A_{AA}} \quad (10)$$

where A_i denotes the peak area of the characteristic peak of component i as defined in Table 1. Aldoxane has two peaks, because of the two distinguishable diastereomeric forms. Equations 1–10 are 10 equations for 10 unknowns (6 mole numbers n_i and 4 reaction extents ξ_j) assuming that $\tilde{n}^0_W$ and $\tilde{n}^0_{AA}$ as well as the peak areas A_i are known. Either $\tilde{n}^0_W$ or $\tilde{n}^0_{AA}$ can be chosen freely, the other is then determined by the known feed ratio $\tilde{n}^0_W/\tilde{n}^0_{AA}$. From the true mole numbers, the true mole

dx.doi.org/10.1021/ie5004043 | Ind. Eng. Chem. Res. 2014, 53, 8395–8403

Table 2. Overall Mole Fraction of Acetaldehyde $\tilde{x}_{AA}$ in the Aqueous Feed Solution and Mole Fractions x_i in Chemical Equilibrium at Different Temperatures, Determined by ^{13}C NMR Spectroscopy

sample	$\tilde{x}_{AA}$	T	x_W	x_{AA}	x_{MMG1}	x_{MMG2}	x_{ADL}	x_{ALX}
	mol/mol	K	mol/mol					
1	0.4	313.15	0.786	0.034	0.012	0.004	0.008	0.154
		333.13	0.764	0.077	0.010	0	0.018	0.131
		353.15	0.734	0.120	0.012	0	0.038	0.096
		363.15	0.723	0.123	0.017	0	0.058	0.079
2	0.3	313.15	0.808	0.075	0.030	0.002	0.002	0.082
		333.15	0.799	0.102	0.020	0	0.007	0.072
		353.15	0.777	0.140	0.018	0	0.014	0.052
		363.15	0.767	0.153	0.018	0	0.020	0.042
3	0.2	313.15	0.873	0.049	0.027	0.004	0.001	0.047
		333.15	0.867	0.068	0.017	0.003	0.005	0.040
		353.15	0.848	0.099	0.017	0	0.009	0.027
		363.15	0.846	0.100	0.014	0	0.019	0.021
4	0.1	313.15	0.928	0.034	0.020	0.001	0.001	0.016
		333.15	0.926	0.042	0.014	0.002	0.003	0.013
		353.15	0.921	0.052	0.011	0.002	0.007	0.008
		363.15	0.917	0.061	0.008	0.001	0.008	0.005

fractions can be calculated for each experiment. Table 2 gives an overview over the results.

The calculation of the equilibrium constant of the aldoxane formation is based on mole fractions here as no activity model describing nonidealities in the liquid phase is available in literature for this system. Because the reaction only takes place in the liquid phase, the influence of the pressure on the chemical equilibrium is neglected. The equilibrium constant of the aldoxane formation (reaction II) is

$$K_x = \frac{x_{ALX}}{x_{ADL} x_{AA}} \tag{11}$$

wherein x_i is the mole fraction of component i. The chemical equilibrium of the aldoxane formation strongly depends on temperature. The van't Hoff equation is used to describe the dependence of the equilibrium constant of the aldoxane formation (eq 11) on the temperature:

$$\ln K_x(T) = \ln K_{x,0} - \frac{\Delta_R h}{R} \frac{1}{T} \tag{12}$$

The parameters $K_{x,0}$ and $\Delta_R h$ of eq 12 were fitted to the equilibrium constants which can be calculated for each experiment from eq 11 and the data in Table 2. A MATLAB routine was used for the fit in which the absolute error in K_x was minimized, applying the least-squares method

$$\mathrm{SSE} = \sum_{k=1}^{M} w_k \left(K_{x,i}^{\mathrm{exp}} - K_{x,i}^{\mathrm{calc}}\right)^2 \stackrel{!}{=} \min \tag{13}$$

where M is the number of experiments and w_k is the weighting factor of experiment k:

$$w_k = \sqrt{x_{ADL,k}} \tag{14}$$

This weighting factor takes into account that the experiments with high acetaldol concentrations are less influenced by errors. The result of the parameter fit is shown in Table 3. The reaction enthalpy indicates that the aldoxane formation is strongly exothermal. In Figure 5 the individual experimental data for K_x are compared to the correlation with eq 12, the agreement is good.

Table 3. Parameters of the van't Hoff Equation (Equation 12) for the Calculation of the Equilibrium Constant K_x of the Aldoxane Formation (Reaction II)

$K_{x,0}$	$\Delta_R h$/kJ·mol^{-1}
3.923×10^{-10}	−72.811

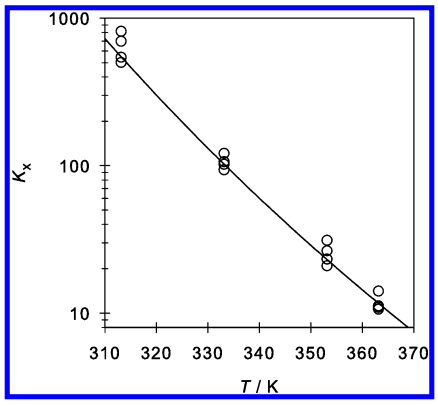

Figure 5. Chemical equilibrium constant K_x of the aldoxane formation as a function of the temperature: (symbols) experimental data; (line) correlation with the van't Hoff equation (eq 12).

To assess the quality of the parameter fit, the following procedure was used. From the experimental results of the true mole fractions the data of aldoxane and acetaldol were removed. Taking the remaining data together with the correlation of $K_x(T)$ and the summation equation of the mole fractions, numbers for x_{ALX} and x_{ADL} can be calculated. These numbers are compared to the experimental data in Figure 6. The parity plots show good agreement.

Furthermore, the experimental data provides information on the ratio of the two distinguishable diastereomeric forms of aldoxane. The peak area of ALX_A related to the total peak area of aldoxane is plotted as a function of temperature in Figure 7. Despite a scattering of the experimental values, it can be concluded that about 70% of aldoxane are present as ALX_A form. Within the temperature range covered by the experiments no dependence of this fraction on temperature is observed.

dx.doi.org/10.1021/ie5004043 | Ind. Eng. Chem. Res. 2014, 53, 8395−8403

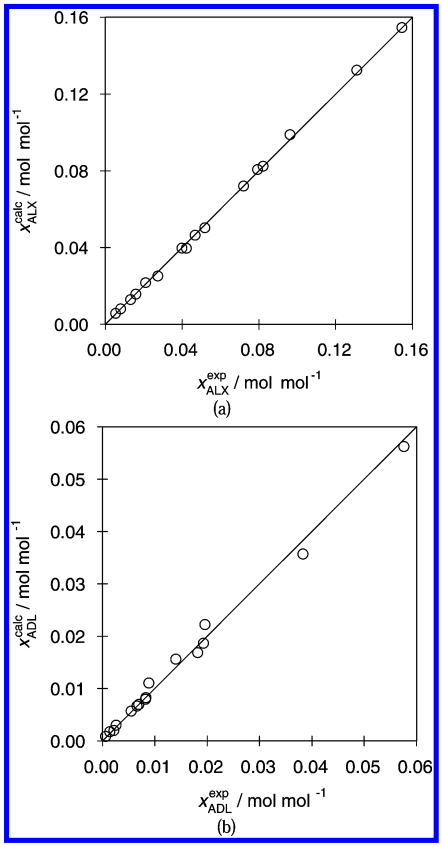

Figure 6. Comparison of the experimental and the calculated mole fractions of aldoxane (a) and acetaldol (b) of all samples.

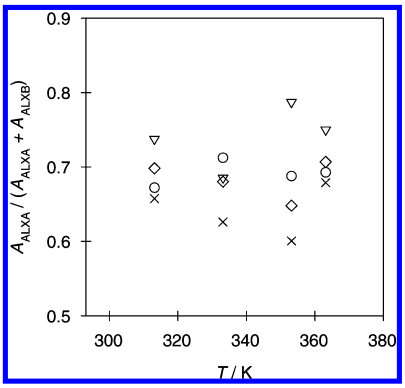

Figure 7. Peak area fraction of the diastereomer ALX_A of aldoxane in relation to the sum of the peak areas of the two distinguishable diastereomeric forms as a function of the temperature: (symbols) experimental data of the samples P1 (×), P2 (◇), P3 (▽), and P4 (○).

Moreover, the experimental data contains information on the chemical equilibrium of the formation of the poly(oxymethylmethylene) glycols. Therefore, the equilibrium constants of the formation of MMG_1

$$K_{x,\mathrm{MMG1}} = \frac{x_{\mathrm{MMG1}}}{x_{\mathrm{W}} x_{\mathrm{AA}}} \tag{15}$$

were calculated for each experiment. The calculated values are plotted together with the model results from the work of Scheithauer,[20] which were obtained in a dedicated comprehensive NMR study of the system acetaldehyde and water, in Figure 8. The experimental values of the equilibrium constant

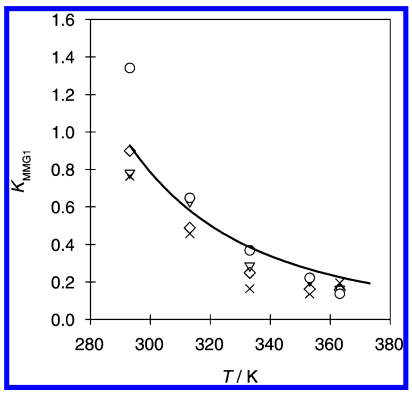

Figure 8. Equilibrium constants of the formation of MMG_1 (cf. eq 15) as a function of the temperature: (symbols) experimental data from the present work of the samples P1 (×), P2 (◇), P3 (▽), and P4 (○); (line) model.[20]

are in good agreement with the model. As only small amounts of MMG_2 are formed, the calculation of $K_{x,\mathrm{MMG2}}$ from the data obtained in the present study is subject to large errors, so that a comparison to the model of the work of Scheithauer[20] shows no insights and is therefore not presented here.

PRELIMINARY STUDY OF THE KINETICS OF ALDOXANE FORMATION

As a hypothesis it is assumed that the kinetics of the formation of aldoxane from acetaldehyde and acetaldol (reaction II) are fast so that the aldol addition reaction (reaction I) is the rate-limiting step of the acetaldehyde conversion in basic medium. Namely, it is assumed that reaction II is so fast that it can be described by its equilibrium constant in the reaction network of the acetaldehyde conversion. To prove this hypothesis, two kinds of experiments were carried out.

In the first experiment, the conversion of acetaldehyde to acetaldol (and aldoxane respectively) (reactions I and II) was homogeneously catalyzed by caustic soda. The sample was analyzed by online ^{1}H NMR spectroscopy, and the acetaldol peak was monitored during the experiment. If at all times the equilibrium condition of reaction II is fulfilled, it can be concluded that the hypothesis holds.

In the second experiment, a sample was prepared as described in the equilibrium experiments and Amberlyst A26 OH was removed after the heterogeneously catalyzed conversion. After equilibration, the sample was heated in the NMR spectrometer, and during the heating, the sample was analyzed by ^{1}H NMR spectroscopy. As a reference, the same sample was analyzed in equilibrated state at different temperatures. The peak area ratios of the acetaldol peak to the peak area of an internal standard were evaluated and compared to those of the equilibrated state. The purpose of this experiment was to check if the aldoxane formation (reaction II) is in equilibrium at all times during the transient heating experiment.

Homogeneously Catalyzed Kinetics. An aqueous solution of acetaldehyde and water was prepared and equilibrated at 293 K for several hours. Then a small amount of an aqueous caustic soda solution was added to start the aldol addition reaction. The overall acetaldehyde mole fraction and the pH value of the starting solution were $\tilde{x}_{\mathrm{AA}}$ = 0.25 mol/mol

dx.doi.org/10.1021/ie5004043 | Ind. Eng. Chem. Res. 2014, 53, 8395−8403

and pH = 10.3. A sample of 1 mL was taken, filled in an NMR tube, and introduced in the NMR spectrometer at 293 K. After τ = 60 s, the recording of the ^{1}H NMR spectra was started and an array of NMR spectra, with one spectrum every 10 s, was acquired.

The results are shown in Figure 9. The peak of the methyl group of acetaldehyde ($\delta_{AA,C\underline{H}3}$ = 2.2 ppm) decreases as well as

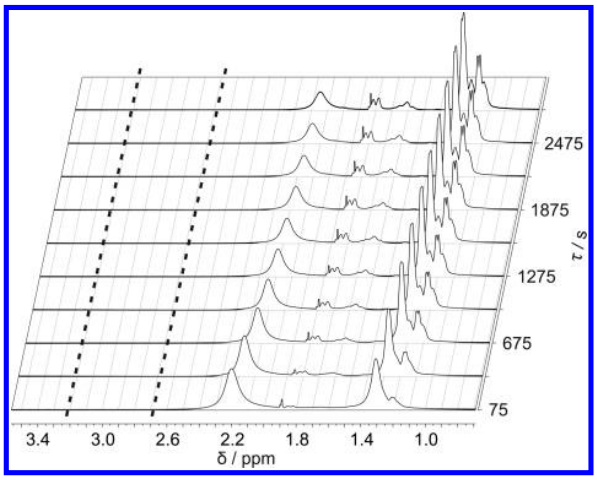

Figure 9. Array of ^{1}H NMR spectra (400 MHz) acquired to analyze the formation of acetaldol at 293 K during the aldol addition reaction of acetaldehyde in aqueous solution ($\tilde{x}_{AA}$ = 0.25 mol/mol), homogeneously catalyzed by dilute caustic soda (pH = 10.3, experimental details, cf. text). No acetaldol peak is observed (that peak would be expected at about δ = 2.7−3.2 ppm).

the methyl peak of the poly(oxymethylmethylene) glycols ($\delta_{MMG,C\underline{H}3}$ = 1.3 ppm). The aldoxane peaks increase ($\delta_{ALX,C\underline{H}3}$ = 1.2 ppm, $\delta_{ALX,C\underline{H}2}$ = 1.6 and 1.8 ppm). No acetaldol peak is observed (The protons of the CH_2 group of acetaldol would be expected at $\delta_{ADL,C\underline{H}_2}$ = 2.7−3.2 ppm).

At 293 K the equilibrium constant of the aldoxane formation is very large (cf. Figure 5) so that in equilibrium almost no acetaldol is present. If the aldoxane formation was kinetically limited, then, as obviously large amounts of acetaldehyde were converted, also acetaldol should have been detected in the solution. The fact that this is not the case supports the hypothesis. Hence, it is concluded that the kinetics of the aldoxane formation (reaction II) are much faster than those of the addition reaction (reaction I) and the hypothesis is confirmed.

No acetaldol was detected in the NMR spectra. The limit of detection of acetaldol is given by the signal-to-noise ratio and is about $x_{ADL} < 5.0 \times 10^{-4}$ mol/mol.

Heterogeneously Catalyzed Kinetics. A sample of a mixture of aldoxane, water, and acetaldehyde was prepared as in the experiments for determination of the chemical equilibrium of the aldoxane formation. 3-(Trimethylsilyl)propionic-2,2,3,3-*d*4 acid sodium salt (TMSP) as internal standard and ethane-1,2-diol were added in a sealed capillary tube in the NMR tube. After the equilibration for 1 h at 293 K, the experiment was started. In the experiment the sample was heated up from 293 to 363 K in about 15 min. For more details see the work of Scheithauer.[20] ^{1}H NMR-spectra were acquired at different times. Two independent transient heating experiments were carried out. For a comparison, equilibrated samples were examined at different temperatures, in the same range. The temperature of the sample was detected through the chemical shift of the two ethane-1,2-diol peaks by the method of Ammann et al.[48] in both sets of experiments. ^{1}H NMR spectra were acquired in the experiments and the peak area ratio of the CH_2 peak of acetaldol to the peak of TMSP was determined. The result is presented in Figure 10. Figure 10a shows the

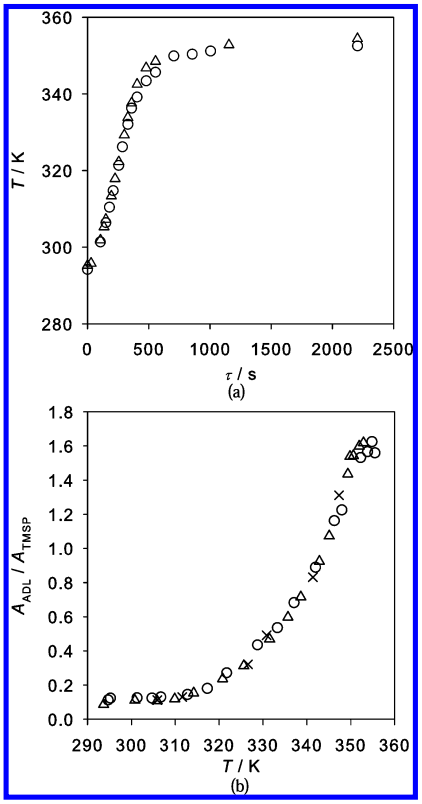

Figure 10. Evaluation of the aldoxane formation kinetics indicated by a temperature shift from 293 to 363 K. (a) Temperature determined using the method of Ammann et al.[48] as a function of time: (symbols) values from two independent transient experiments (Δ, ○). (b) Ratio of the peak areas of acetaldol (CH_2 group) to TMSP as a function of the temperature: (symbols) results from the transient experiments (Δ, ○) and the equilibrium experiments (×).

temperature during the heating as a function of time, and Figure 10b shows the results of the comparison of the peak areas obtained in the transient experiments to those of the equilibrium experiments. Within the experimental error, there is no difference in the peak area ratios of the equilibrium experiments compared to those of the transient experiments. Therefore, the reaction kinetics of aldoxane formation (reaction II) are significantly faster than reaction I and it can be assumed that the equilibrium is established instantaneously. Thus, it can be concluded that reaction II is in equilibrium in the transient experiments with rate constants of the order of minutes.

■ CONCLUSION

In the literature it is usually assumed that crotonaldehyde is formed from aqueous acetaldehyde solutions in a two step process with acetaldol as intermediate. The present work shows that this is an oversimplification and that the formation of aldoxane has to be taken into account. The equilibrium constant of the aldoxane formation is reported for the first time.

dx.doi.org/10.1021/ie5004043 | Ind. Eng. Chem. Res. 2014, 53, 8395−8403

A preliminary reaction kinetic study indicated that the aldoxane formation is not the rate-limiting step in the studied reaction network. It can be assumed that the chemical equilibrium of the aldoxane formation is always established in transient processes with time constants of the order of minutes.

■ ASSOCIATED CONTENT

Supporting Information

Technical data of Amberlyst A26 OH, HH-Cosy, Hmqc NMR spectra and peak assignment, Tables S.1 and S.2, and Figures S.1 and S.2. This material is available free of charge via the Internet at http://pubs.acs.org/.

■ AUTHOR INFORMATION

Corresponding Author

*E-mail: hans.hasse@mv.uni-kl.de.

Notes

The authors declare no competing financial interest.

■ ACKNOWLEDGMENTS

We gratefully acknowledge financial support of this work by Lonza AG, Visp, Switzerland. We thank Rohm and Haas (currently Dow Chemical), Paris, France, for providing the catalyst Amberlyst A26 OH and Christian Noti, Lonza AG, and Christoph Seubert, University of Kaiserslautern, for fruitful discussions.

■ REFERENCES

(1) Eckert, M.; Fleischmann, G.; Jira, R.; Bolt, H. M.; Golka, K. Acetaldehyde. *Ullmann's Encyclopedia of Industrial Chemistry*, 6th ed.; Wiley-VCH, 2006.

(2) Fernandez, J.; Salomons, T. Crotonaldehyde. *Chem. Rev.* **1962**, *5*, 485−502.

(3) Schulz, R.; Blumenstein, J.; Kohlpaintner, C. Crotonaldehyde and Crotonic Acid. *Ullmann's Encyclopedia of Industrial Chemistry*, 6th ed.; Wiley-VCH, 2000.

(4) Alhéritière, L. Process for Producing Acetaldol. Patent US 2489608, 1949.

(5) Alhéritière, L. Manufacture of Aldol and/or Crotonaldehyde. Patent CA 511225D, 1955.

(6) Craven, E.; Gell, W. Improvements in or Relating to the Production of Aldol and Crotonaldehyde. Patent GB 704854, 1950.

(7) Heinz, W.; McLean, A. Aldol Condensation Reactions. Patent US 3077500, 1963.

(8) Guimei, Y.; Hongwei, L. Process for Preparation of Crotonaldehyde. Patent CN 100344598C, 2006.

(9) Mueller-Cunradi, M. Verfahren zur Herstellung von Crotonaldehyd. Patent DE 907888, 1954.

(10) Hahnenstein, I.; Hasse, H.; Kreiter, C.; Maurer, G. ^{1}H- and ^{13}C-NMR Spectroscopic Study of Chemical Equilibria in Solutions of Formaldehyde in Water, Deuterium Oxide, and Methanol. *Ind. Eng. Chem. Res.* **1994**, *33*, 1022−1029.

(11) Ahrens, M.; Strehlow, H. Acid Catalyzed Hydration of Acetaldehyde. *Discuss. Faraday Soc.* **1965**, *39*, 112−120.

(12) Bell, R. P.; Clunie, J. C. The Hydration of Acetaldehyde in Aqueous Solution. *Trans. Faraday Soc.* **1952**, *48*, 439−442.

(13) Bell, R. P.; Clunie, J. C. Binary and Ternary Mechanisms in the Hydration of Acetaldehyde. *Proc. R. Soc. Lond. A* **1952**, *212*, 33−37.

(14) Podo, F.; Viti, V. A PMR Study of Hydration Products in Aqueous Acetaldehyde Solutions. *Org. Magn. Reson.* **1970**, *3*, 259−261.

(15) Socrates, G. Hydration Study of Acetaldehyde and Propionaldehyde. *J. Org. Chem.* **1969**, *34* (10), 2958−2961.

(16) Sørensen, P.; Jencks, W. Acid- and Base-Catalyzed Decomposition of Acetaldehyde Hydrate and Hemiacetals in Aqueous Solution. *J. Am. Chem. Soc.* **1987**, *109*, 4675−4690.

(17) Lombardi, E.; Sogo, P. NMR Study of Acetaldehyde-Water Mixtures. *J. Chem. Phys.* **1960**, *32*, 635−636.

(18) Kurz, J. L. The Hydration of Acetaldehyde. I. Equilibrium Thermodynamic Parameters. *J. Am. Chem. Soc.* **1967**, *89*, 3524−3528.

(19) Fujiwara, Y.; Fujiwara, S. Nuclear Magnetic Resonance Study of Acetaldehyde Aqueous Solution. *Bull. Chem. Soc. Jpn.* **1963**, *36*, 574−578.

(20) Scheithauer, A. Physico-Chemical Data and Conceptual Design of a Crotonaldehyde Production Process. Ph.D. thesis, Laboratory of Engineering Thermodynamics, University of Kaiserslautern, 2014; Scientific Report Series 13, ISBN 978-3-944433-12-7.

(21) Kohlpaintner, C.; Schulte, M.; Falbe, J.; Lappe, P.; Weber, J. Aldehydes, Aliphatic. *Ullmann's Encyclopedia of Industrial Chemistry*, 6th ed.; Wiley-VCH, 2005.

(22) Anderson, J.; Peters, M. Acetaldehyde Aldol Condensation Kinetics. *J. Chem. Eng. Data* **1960**, *5*, 359−364.

(23) Newby, H. Improvements in the Production of Crotonaldehyde. Patent GB 660972, 1951.

(24) Horn, O. Products with Commercial Possibilities from Reactions of Crotonaldehyde. *Ind. Eng. Chem.* **1959**, *51*, 655−658.

(25) Bell, R.; McTigue, P. Kinetics of the Aldol Condensation of Acetaldehyde. *J. Chem. Soc.* **1960**, 2983−2994.

(26) Guthrie, J. The Aldol Condensation of Acetaldehyde: The Equilibrium Constant for the Reaction and the Rate Constant for the Hydroxide Catalyzed RetroAldol Reaction. *Can. J. Chem.* **1974**, *52*, 2037−2040.

(27) Atalay, F.; Atalay, S. Kinetics of Acetaldol Production. *Chem. Ing. Tech.* **1991**, *63*, 933−934.

(28) Matsuyama, H. Thermal Analysis of the Aldol Condensation. *Proc. Jpn. Acad.* **1951**, *27*, 552−555.

(29) Atalay, S.; Atalay, F. S. Production of Crotonaldehyde from Acetaldol. *Dev. Chem. Eng. Miner. Process* **1994**, *2*, 58−60.

(30) González Alafita, O. Investigación sobre la cinética del proceso de transformación del acetaldol a butiraldehído. *J. Mex. Chem. Soc.* **1997**, *41*, 8−14.

(31) Hahnenstein, I.; Hasse, H.; Liu, Y.-Q.; Maurer, G. *AIChE Symposium Series: Thermophysical Properties for Industrial Process Design*; AIChE: New York, 1994; Vol. *90*, 298, pp 141−157.

(32) Ott, M.; Schoenmakers, H.; Hasse, H. Distillation of Formaldehyde Containing Mixtures: Laboratory Experiments, Equilibrium Stage Modeling and Simulation. *Chem. Eng. Process.* **2005**, *44*, 687−694.

(33) Schilling, K.; Sohn, M.; Ströfer, E.; Hasse, H. Reactive Evaporation of Formaldehyde-containing Mixtures and Process Monitoring by Online NMR-Spectroscopy. *Chem. Ing. Tech.* **2003**, *75*, 240−244.

(34) Grützner, T.; Lang, N.; Ströfer, E.; Hasse, H. Entwicklung eines neuen Trioxanverfahrens. *Chem. Ing. Tech.* **2004**, *76*, 1342−1342.

(35) Maiwald, M.; Fischer, H. H.; Kim, Y.-K.; Albert, K.; Hasse, H. Quantitative High-Resolution On-line NMR Spectroscopy in Reaction and Process Monitoring. *J. Magn. Reson.* **2004**, *166*, 135−146.

(36) Grützner, T.; Hasse, H.; Lang, N.; Siegert, M.; Ströfer, E. Development of a New Industrial Process for Trioxane Production. *Chem. Eng. Sci.* **2007**, *62*, 5613−5620.

(37) Drunsel, J.-O.; Renner, M.; Hasse, H. Experimental Study and Model of Reaction Kinetics of Heterogeneously Catalyzed Methylal Synthesis. *Chem. Eng. Res. Des.* **2012**, *90*, 696−703.

(38) Burger, J.; Ströfer, E.; Hasse, H. Chemical Equilibrium and Reaction Kinetics of the Heterogeneously Catalyzed Formation of Poly(oxymethylene) Dimethyl Ethers from Methylal and Trioxane. *Ind. Eng. Chem. Res.* **2012**, *51*, 12751−12761.

(39) Späth, E.; Lorenz, R.; Freund, E. Über ein Additionsprodukt des Acetaldehyds an Acetaldol (V. Mitteil. über Derivate des Aldols und des Crotonaldehyds). *Ber. Dtsch. Chem. Ges.* **1943**, *76*, 57−68.

(40) Späth, E.; Lorenz, R.; Freund, E. Zur Kenntnis der Aldoxane (XII. Mitteil. über Derivate des Aldols und des Crotonaldehyds). *Ber. Dtsch. Chem. Ges.* **1944**, *77*, 354−361.

(41) Hanschke, E. Zur Kenntnis des Aldols. Über eine Verbindung aus Aldol und Acetaldehyd. *Ber. Dtsch. Chem. Ges.* **1943**, *76*, 180−182.

(42) Saunders, R. H.; Murray, M. J. The Aldol Condensation. III. Aldol-aldehyde Addition Products and their Derivatives. *J. Am. Chem. Soc.* **1944**, *66*, 206−208.
(43) Späth, E.; Schmid, H. Über die Konstitution des Paraldols (III. Mitteil. über Derivate des Aldols und des Crotonaldehyds). *Ber. Dtsch. Chem. Ges.* **1941**, *74*, 859−866.
(44) Vogel, M.; Rhum, D. The Structure of Paraldol. *J. Org. Chem.* **1966**, *31*, 1775−1780.
(45) Späth, E.; Lorenz, R.; Freund, E. Über das Gleichgewicht zwischen monomerem und dimerem Acetaldol in wässeriger Lösung. *Monatsh. Chem.* **1946**, *76*, 83−85.
(46) Owen, L. N. The Polymerisation of Acetaldol. *J. Chem. Soc.* **1943**, 445−446.
(47) Cheshnovsky, D.; Navon, G. Nuclear Magnetic Resonance Studies of Carbonic Anhydrase Catalyzed Reversible Hydration of Acetaldehyde by the Saturation Transfer Method. *Biochemistry* **1980**, *19*, 1866−1873.
(48) Ammann, C.; Meier, P.; Merbach, A. A Simple Multinuclear NMR Thermometer. *J. Magn. Reson.* **1982**, *46*, 319−321.

Scheithauer et al., 2015

Reprinted with permission from: A. Scheithauer, E. von Harbou, H. Hasse, T. Grützner, C. Rijksen, D. Zollinger, W. R. Thiel, ^{1}H- and ^{13}C-NMR spectroscopic study of chemical equilibria in the system acetaldehyde + water, AIChE Journal, Volume 61, 2015, Pages 177-187, DOI 10.1002/aic.14623

^{1}H- and ^{13}C-NMR Spectroscopic Study of Chemical Equilibria in the System Acetaldehyde + Water

Andreas Scheithauer, Erik von Harbou, and Hans Hasse
Dept. of Mechanical and Process Engineering, Laboratory of Engineering Thermodynamics, University of Kaiserslautern, Kaiserslautern, Germany

Thomas Grützner, Christiaan Rijksen, and Daniel Zollinger
Lonza AG, Visp, Switzerland

Werner R. Thiel
Dept. of Chemistry, University of Kaiserslautern, Kaiserslautern, Germany

DOI 10.1002/aic.14623
Published online September 30, 2014 in Wiley Online Library (wileyonlinelibrary.com)

Acetaldehyde is an important intermediate in the chemical industry and often used in mixtures with water. These mixtures are reactive multicomponent systems, as acetaldehyde forms oligomers with water. Quantitative studies of the resulting speciation are scarce in the literature and limited to the formation of the smallest oligomer, ethane-1,1-diol. Therefore, in the present work, a comprehensive study of chemical equilibria in mixtures of acetaldehyde and water was carried out by quantitative ^{1}H- and ^{13}C-NMR spectroscopy. The study covers temperatures between 275 and 338 K and overall acetaldehyde mole fractions between about 0.05 and 0.95 mol/mol. The peak assignment is given for both the ^{1}H- and ^{13}C-NMR spectra. From the speciation data, obtained from the peak area fractions, numbers for the chemical equilibrium constants of the oligomer formation are obtained and a correlation is presented. © 2014 American Institute of Chemical Engineers *AIChE J*, 61: 177–187, 2015

Keywords: poly(oxymethylmethylene) glycols, acetaldehyde + water, chemical equilibrium, experiments and modeling, quantitative NMR spectroscopy

Introduction

Acetaldehyde (AA) is an important intermediate in chemical industry. It is used, for example, for the production of acetic acid, acetic anhydride, ethyl acetate, peracetic acid, 2-ethylhexanol, butanol, pentaerythritol.[1] In these and other processes, acetaldehyde is often used in mixtures with water.[1] These solutions are reactive mixtures, in which acetaldehyde undergoes similar reactions as formaldehyde in aqueous solutions.[2–7]

The reaction of acetaldehyde with water yields ethane-1,1-diol (MMG_1, HO—(CH(CH$_3$)—O—)H), which is the first member of the series of the poly(oxymethylmethylene) glycols (MMG_n, HO—(CH(CH$_3$)—O—)$_n$H). This reaction has been studied previously by many authors with different analytical methods: nuclear magnetic resonance (NMR) spectroscopy, ultraviolet and visible (UV/VIS) spectroscopy, calorimetry, and others. An overview of the literature studies is given in Table 1. Sørensen and Jencks[25] give an overview of equilibrium constants of the formation of ethane-1,1-diol reported in literature. Information on reaction kinetics is available in the references in Table 1 as well. Most of these studies were carried out in dilute aqueous solutions of acetaldehyde, in which MMG_1 is the predominant reaction product of acetaldehyde and water, so that most authors have ignored the presence of longer poly(oxymethylmethylene) glycols (MMG_n). Ahrens and Strehlow[14] studied mixtures of acetaldehyde and water with up to 0.6 mol/mol acetaldehyde using a NMR line broadening technique and concluded that MMG_2 is present. Socrates[15] and Podo and Viti[8] confirmed in their studies the existence of MMG_2 by ^{1}H-NMR spectroscopy. Socrates[15] found that MMG_2 is formed, even in dilute aqueous acetaldehyde solutions. Podo and Viti[8] reported estimates for the equilibrium constant of the formation of MMG_2 and assumed that higher oligomers are present, too. Greenzaid et al.[9,16] have used ^{17}O-NMR spectroscopy to study the oligomer formation in aqueous acetaldehyde solutions, but could not gain more information than with ^{1}H-NMR spectroscopy. That information is limited because of the superposition of the proton peaks of the CH and the CH$_3$ groups of the poly(oxymethylmethylene) glycols.

To the best of the authors' knowledge, there are no reports in the literature on studies of the speciation of acetaldehyde and water mixtures with ^{13}C-NMR spectroscopy. This is astonishing, as this method has been applied successfully for studies of the speciation in the closely related system formaldehyde and water.[2–7,35–38]. Therefore, we carried out a comprehensive study of the speciation in mixtures of acetaldehyde and water in chemical equilibrium by quantitative ^{1}H- and ^{13}C-NMR spectroscopy. The study covers temperatures between 275 and 338 K and overall acetaldehyde mole fractions between about 0.05 and 0.95 mol/mol.

Correspondence concerning this article should be addressed to H. Hasse at hans.hasse@mv.uni-kl.de.

Table 1. Literature Data on the Speciation of Mixtures of Acetaldehyde and Water

Species	Method	Equilibrium	Kinetics
MMG_1	NMR[a]	8–13	14–18
	UV/VIS	19–24	18,25–29
	Calorimetry	19,20	26,30–32
	Others		18,33,34
$MMG_{n>1}$	NMR[a]	8	14,15

[a]^{1}H-NMR, except Refs. 9 and 16 which used ^{17}O-NMR, no ^{13}C-NMR.

Also, the kinetics of the reactions in mixtures of acetaldehyde and water can be studied with NMR spectroscopy. The present work on chemical equilibria establishes a basis for such kinetic studies, which themselves are, however, not in its scope.

It is well known from formaldehyde process design that models of the properties of mixtures containing formaldehyde and water should explicitly account for the formation of oligomers in that system.[3,6,37,39–42] The same is true for mixtures of acetaldehyde and water. Unfortunately, contrarily to mixtures of formaldehyde and water, the quantitative information on the speciation in mixtures of acetaldehyde and water, which is available in the literature, is only spotty and not sufficient for developing a reliable model of the equilibrium speciation. Most authors only considered the formation of MMG_1, and most of the data are only for dilute solutions and were obtained near room temperature or below (some examined a broad temperature range[19,20]). Ahrens and Strehlow,[14] Socrates,[15] and Podo and Viti[8] took the formation of MMG_2 into account, but not the formation of higher oligomers (MMG_n, $n > 2$).

Based on the comprehensive new data, in the present work, chemical equilibrium constants were determined not only for the formation of MMG_1 and MMG_2 but also for the formation of all higher oligomers (MMG_n, $n > 2$). Two versions of the model are presented. The first uses equilibrium constants based on mole fractions and is straightforward to apply, but based on the assumption of the ideality of the mixture. In the second model that assumption is dropped and the equilibrium constants are based on activities with activity coefficients estimated by the UNIFAC group contribution method.[43]

Throughout the present work, two different ways of specifying the concentration are used. Overall mole fractions of acetaldehyde and water ($\tilde{x}_{AA}$ and $\tilde{x}_W$) are those that are known from gravimetric preparation of the samples, that is, they disregard in which form acetaldehyde or water is present in the mixture. Conversely, mole fractions x_i ($i = AA$, W, MMG_1, MMG_2, $MMG_3, \ldots$) are used which refer to the true speciation of the mixture.

Reaction System

Acetaldehyde (AA) undergoes chemical reactions with water (W) which yield poly(oxymethylmethylene) glycols (MMG_n). The reactions are similar to those of formaldehyde with water.[2] The smallest poly(oxymethylmethylene) glycol is ethane-1,1-diol (MMG_1)

$$\underbrace{CH_3{-}CHO}_{AA} + \underbrace{H_2O}_{W} \rightleftharpoons \underbrace{HO{-}(CH(CH_3){-}O{-})H}_{MMG_1} \qquad (I)$$

MMG_2 is formed in a reaction of MMG_1 with acetaldehyde

$$\underbrace{HO{-}(CH(CH_3){-}O{-})H}_{MMG_1} + \underbrace{CH_3{-}CHO}_{AA} \rightleftharpoons \underbrace{HO{-}(CH(CH_3){-}O{-})_2H}_{MMG_2} \qquad (II)$$

and in a similar manner higher oligomers MMG_n ($n \geq 2$) are obtained

$$\underbrace{HO{-}(CH(CH_3){-}O{-})_{n-1}H}_{MMG_{n-1}} + \underbrace{CH_3{-}CHO}_{AA} \rightleftharpoons \underbrace{HO{-}(CH(CH_3){-}O{-})_nH}_{MMG_n} \qquad (III)$$

These reactions always occur in mixtures of acetaldehyde and water. They can be accelerated both by the addition of acids and bases.[25] As no side products were observed in the present work, the issue of side product formation is not discussed here. For more information see Ref. 43.

Experimental Section

Chemicals

Acetaldehyde (≥ 0.995 g/g) was delivered by Sigma-Aldrich as A.C.S. reagent. Ultrapure water was produced using a Milli-Q integral water purification system from Merck Millipore.

For the two-dimensional (2-D) NMR studies, 3-(trimethylsilyl)propionic-2,2,3,3-d4 acid sodium salt (TMSP, ≥ 0.98 g/g) and deuterium oxide (D_2O, ≥ 0.999 mol/mol) were purchased from Sigma-Aldrich.

Chemical equilibrium experiments

The mixtures of acetaldehyde and water were prepared gravimetrically using a Mettler Toledo XS603S precision balance. The educts were cooled to 275 K to prevent losses by evaporation of acetaldehyde. The overall acetaldehyde mole fractions $\tilde{x}_{AA}$ in the samples are listed in Table 2. After mixing and sealing, the samples were stored at constant temperature in the NMR tubes for about 24 h to establish the chemical equilibrium. Subsequently, the samples were analyzed at the same temperature by ^{1}H-NMR and ^{13}C-NMR spectroscopy. The studied temperatures were 275, 293, 308, 323, and 338 K. The overall uncertainty of temperatures reported here is estimated to be about ± 1 K.

Because of the high vapor pressure of acetaldehyde (normal boiling point: 294 K) pressure resistant NMR tubes (Wilmad quick pressure valve NMR tubes) were used. It was verified by tests with pure acetaldehyde in an oven at 353 K for 7 days, that no losses from these tubes occur, as checked gravimetrically. Typical liquid sample volumes were 1.5 cm^3. It was verified that the shift of the mole fraction of the liquid samples by evaporation in the sample tubes is small, even under unfavorable conditions, and can be neglected.

Table 2. Overall Mole Fraction of Acetaldehyde in the Studied Samples

Sample	$\tilde{x}_{AA}$ (mol/mol)
1	0.046
2	0.100
3	0.249
4	0.499
5	0.748
6	0.899
7	0.952

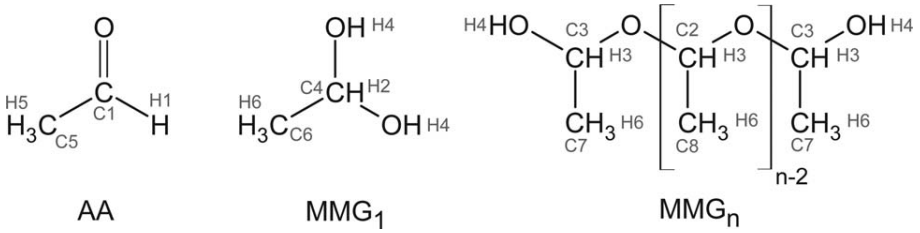

Figure 1. Chemical structure of the components in mixtures of acetaldehyde and water with peak names as used in peak assignment (cf. Table 3, Figures 2 and 4).

NMR spectroscopy

All samples were analyzed by ^{1}H- and ^{13}C-NMR spectroscopy using a 400 MHz Unity Nova NMR spectrometer from Varian, equipped with a Varian 400 AutoSW PFG 4 nuclei probe head. Proton decoupled ^{13}C-NMR spectra were acquired with an acquisition time of 3 s, a relaxation delay of 40 s, and a pulse width of 45°. An inverse-gated decoupling sequence was used with a decoupling power of about 44 W. During the relaxation delay, the decoupler was off to ensure the suppression of the nuclear overhauser effect (NOE) and enable quantification. At least, 128 scans were recorded and averaged. Because only signals of the same type of groups were evaluated and because of the 45° pulse width, the relaxation delay was high enough for quantitative evaluation of the ^{13}C-NMR spectra. As no $T1$ values were measured directly, this was verified in experiments with higher values for the relaxation delay analyzing the same sample. The ^{1}H-NMR spectra were acquired with an acquisition time of 3 s, a relaxation delay of 15 s, and a pulse width of 45°. At least, four scans were recorded and averaged. For the peak assignment in the NMR spectra, 2-D NMR spectroscopy was applied. HH-Cosy- and Hmqc-NMR spectra were acquired. For these experiments, an Avance 600 MHz NMR spectrometer from Bruker was used.

The postprocessing of the acquired spectra was carried out with the MestReNova software from MestreLabs, Santiago de Compostela, Spain. For the baseline correction, a Whittaker Smoother algorithm[44] was used, and for the phasing the so-called "global method" (MestReNova). The integration range was about 20 times of the linewidth of the signal. In the evaluation of the ^{1}H-NMR spectra, care was taken that the ^{13}C-satellites were outside the integration range. Every experiment was evaluated individually using the processing described above. The uncertainty of the determination of the peak areas introduced by the postprocessing is estimated to be about 3%.

Peak assignment

The structures of all relevant components are shown in Figure 1 together with the abbreviations used here. For the peak assignment in the ^{1}H-NMR and the ^{13}C-NMR spectra, an aqueous acetaldehyde solution with an overall mole fraction of acetaldehyde of $\tilde{x}_{AA}=0.245$ mol/mol was prepared, as described above. A capillary tube containing a dilute solution of 3-(trimethylsilyl)propionic-2,2,3,3-d4 acid sodium salt (TMSP) in D_2O was added to the NMR tube filled with the sample in the 2-D NMR experiments for auto locking and shimming. TMSP was used as reference component for the chemical shift. The sample was equilibrated for about 24 h at 293 K, and then analyzed at the same temperature. ^{1}H-, ^{13}C-, HH-Cosy-, and Hmqc-NMR spectra were acquired. The peaks in the ^{1}H-NMR spectrum (see Figure 2) were assigned using the information on the proton–proton interactions from the HH-Cosy-NMR spectrum (see Figure 3). The results are presented in Figure 2 and Table 3.

The signals from the protons of the CH group of the different oligomers overlap (see zoom in Figure 2) and they also overlap with the water peak, so that it is difficult to obtain reliable quantitative data on the different oligomers from the ^{1}H-NMR spectra. It is, however, possible to obtain information on the amount of acetaldehyde which is present as monomer.

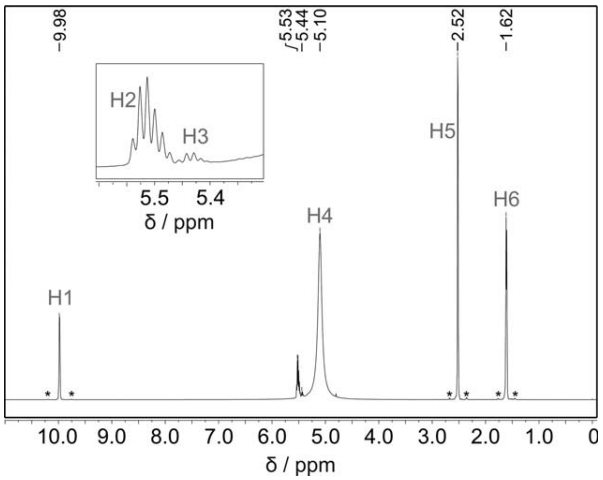

Figure 2. ^{1}H-NMR spectrum (600 MHz) of a mixture of acetaldehyde and water ($\tilde{x}_{AA}=0.245$ mol/mol) at 293 K (peak assignment cf. Figure 1 and Table 3).

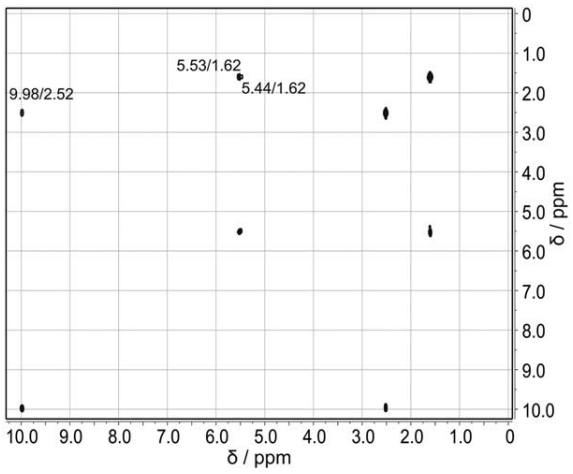

Figure 3. HH-Cosy-NMR spectrum (600 MHz) of a mixture of acetaldehyde and water ($\tilde{x}_{AA}=0.245$ mol/mol) at 293 K (peak assignment cf. Table 3).

Table 3. Peak Assignment in the ^{1}H-NMR and ^{13}C-NMR Spectra with Corresponding Components, Used for Peak Evaluation in the Equilibrium Experiments

Spectrum	Peak Name	Component	Group	δ (ppm)	Peak Area
^{1}H-NMR	H1	AA	$\underline{\mathrm{C}}\mathrm{HO}$	9.98	
	H2	MMG_1	$\underline{\mathrm{C}}\mathrm{H}$	5.53	
	H3	MMG_n $(n \geq 2)$	$\underline{\mathrm{C}}\mathrm{H}$	5.44	
	H4	W	$\mathrm{H}_2\underline{\mathrm{O}}$	5.10	
		MMG_n $(n \geq 1)$	$\underline{\mathrm{O}}\mathrm{H}$	5.10	
	H5	AA	$\mathrm{C}\underline{\mathrm{H}}_3$	2.52	$A^{1\mathrm{H}}_{\mathrm{AA,CH_3}}$
	H6	MMG_n $(n \geq 1)$	$\mathrm{C}\underline{\mathrm{H}}_3$	1.62	$A^{1\mathrm{H}}_{\mathrm{MMG}_n,\mathrm{CH_3}}$
^{13}C-NMR	C1	AA	$\underline{\mathrm{C}}\mathrm{HO}$	208.4	
	C2	MMG_n $(n \geq 3)$	M-$\underline{\mathrm{C}}\mathrm{H}$	97.07	$A^{13\mathrm{C}}_{\mathrm{MMG}_n,\mathrm{M\text{-}CH}}$
	C3	MMG_n $(n \geq 2)$	E-$\underline{\mathrm{C}}\mathrm{H}$	93.54	$A^{13\mathrm{C}}_{\mathrm{MMG}_n,\mathrm{E\text{-}CH}}$
	C4	MMG_1	$\underline{\mathrm{C}}\mathrm{H}$	91.39	$A^{13\mathrm{C}}_{\mathrm{MMG}_1,\mathrm{CH}}$
	C5	AA	$\underline{\mathrm{C}}\mathrm{H}_3$	33.36	$A^{13\mathrm{C}}_{\mathrm{AA,CH_3}}$
	C6	MMG_1	$\underline{\mathrm{C}}\mathrm{H}_3$	26.72	$A^{13\mathrm{C}}_{\mathrm{MMG}_1,\mathrm{CH_3}}$
	C7	MMG_n $(n \geq 2)$	E-$\underline{\mathrm{C}}\mathrm{H}_3$	25.84	$A^{13\mathrm{C}}_{\mathrm{MMG}_n,\mathrm{E\text{-}CH_3}}$
	C8	MMG_n $(n \geq 3)$	M-$\underline{\mathrm{C}}\mathrm{H}_3$	25.48	$A^{13\mathrm{C}}_{\mathrm{MMG}_n,\mathrm{M\text{-}CH_3}}$

The peaks in the ^{13}C-NMR spectrum (see Figure 4) were assigned with the information from the Hmqc-NMR spectrum (see Figure 5). The results are given in Figure 4 and Table 3. There are signals in the ^{13}C-NMR spectra from CH and CH_3 groups, respectively. Both for CH and CH_3, different signals are obtained. The signals from groups in monomeric acetaldehyde can be distinguished from those in MMG_1 and those in $\mathrm{MMG}_{n>1}$. Within the MMG_n, a distinction is possible between groups at the end (E) and those which are not at the end (middle (M)). Thereby, from the ^{13}C-NMR spectrum quantitative information on the distribution of oligomers can be obtained.

Quantification

From the peak areas in the acquired spectra, peak area fractions ζ_i^{exp} were determined. Peak area fractions can be related to fractions of the amount of substance of components. These fractions of the amount of substance of components can also be calculated from chemical equilibrium constants. Hence, from a comparison of the experimental and calculated numbers, equilibrium constants can be determined by a fit. Details on the calculation of the peak areas and the amounts of substance are given in Appendix A.

Model

Equilibrium constants

The thermodynamic equilibrium constant K_n of a reaction n can be split into a pseudo equilibrium constant $K_{x,n}$ and a correction term $K_{\gamma,n}$

$$K_n(T) = K_{x,n} \cdot K_{\gamma,n} \tag{1}$$

with

$$K_{x,n} = \prod_i x_{i,n}^{\nu_{i,n}} \tag{2}$$

and

$$K_{\gamma,n} = \prod_i \gamma_{i,n}^{\nu_{i,n}} \tag{3}$$

where i stands for species participating in the reaction with the stoichiometric coefficient $\nu_{i,n} > 0$ for products and

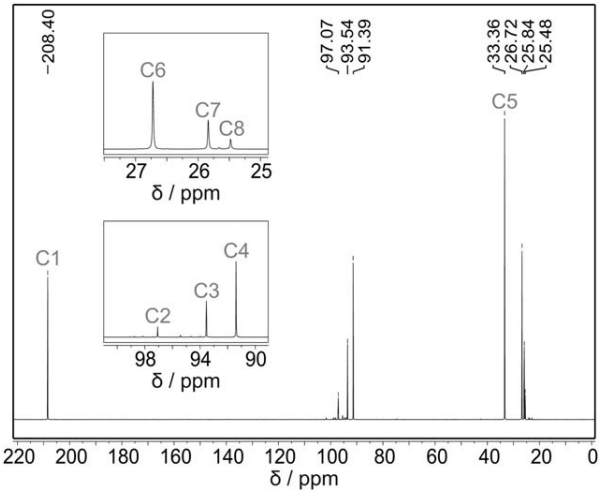

Figure 4. ^{13}C-NMR spectrum (600 MHz) of a mixture of acetaldehyde and water ($\tilde{x}_{\mathrm{AA}}$=0.245 mol/mol) at 293 K (peak assignment cf. Figure 1 and Table 3).

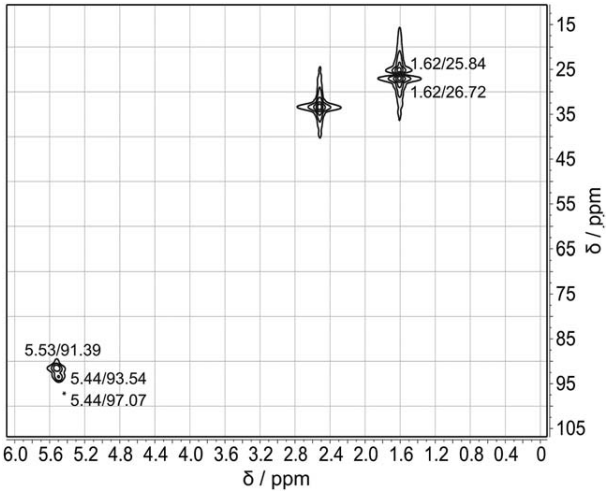

Figure 5. Zoom of a Hmqc-NMR spectrum (600 MHz) of a mixture of acetaldehyde and water ($\tilde{x}_{\mathrm{AA}}$=0.245 mol/mol) at 293 K (peak assignment cf. Table 3).

Table 4. UNIFAC Group Parameters Q and R and Group Assignment for the Components[46,47]

Group	H_2O	HCO[a]	OH	CH_3	CH	CHO[b]
Q	1.400	0.948	1.200	0.848	0.228	0.468
R	0.9200	0.9980	1.000	0.9011	0.4469	0.6908
W	1	0	0	0	0	0
AA	0	1	0	1	0	0
MMG_1	0	0	2	1	1	0
MMG_n $(n \geq 2)$	0	0	2	n	1	$n-1$

[a]Aldehyde group.
[b]Ether group.

$v_{i,n} < 0$ for educts. The dependence of the equilibrium constant on pressure is neglected here. K_n is, therefore, only a function of temperature whereas the numbers for $K_{x,n}$ and $K_{\gamma,n}$ may also depend on the composition of the mixture. For ideal solutions, $K_{\gamma,n}=1$. The temperature dependence of the equilibrium constant K_n is described here by van't Hoff's law

$$K_n(T)=K_{n,0}\cdot\exp\left(-\frac{\Delta_R h_n}{RT}\right) \tag{4}$$

For the formation of MMG_1 (Reaction I), the equilibrium condition in liquid phase is

$$K_1=\frac{x_{MMG_1}}{x_{AA}\cdot x_W}\cdot\frac{\gamma_{MMG_1}}{\gamma_{AA}\cdot\gamma_W} \tag{5}$$

The equilibrium constant of the formation of $MMG_{n>1}$ (Reaction III) is

$$K_n=\frac{x_{MMG_n}}{x_{AA}\cdot x_{MMG_{n-1}}}\cdot\frac{\gamma_{MMG_n}}{\gamma_{AA}\cdot\gamma_{MMG_{n-1}}} \tag{6}$$

For given equilibrium constants, Eqs. 5 and 6 are n equations for $n+2$ mole fractions. The mole fractions are coupled by the summation equation

$$x_W+x_{AA}+\sum_{n=1}^{n_{max}}x_{MMG_n}=1 \tag{7}$$

The mass balance yields a relation between the overall mole fractions of water and acetaldehyde and the true mole fractions

$$\frac{\tilde{x}_W}{\tilde{x}_{AA}}=\frac{x_W+\sum_{n=1}^{n_{max}}x_{MMG_n}}{x_{AA}+\sum_{n=1}^{n_{max}}n\cdot x_{MMG_n}} \tag{8}$$

From Eq. 5 to Eq. 8, the true mole fractions in mixtures of acetaldehyde and water can be calculated from the overall mole fraction of acetaldehyde and water and the equilibrium constants K_1 to K_n. For numerical reasons only n_{max} different MMG's are considered. The number for n_{max} was set here to

Table 5. UNIFAC Group Interaction Parameters $a_{i,j}$ (K)[46,47]

	Group j					
Group i	H_2O	HCO[a]	OH	CH_3	CH	CHO[b]
H_2O	0	−116.0	−229.1	300.0	300.0	540.5
HCO[a]	480.8	0	529.0	505.7	505.7	304.1
OH	353.5	−203.6	0	156.4	156.4	28.06
CH_3	1318.0	677.0	986.5	0	0	251.5
CH	1318.0	677.0	986.5	0	0	251.5
CHO[b]	−314.7	−7.838	237.7	83.36	83.36	0

[a]Aldehyde group.
[b]Ether group.

Table 6. Model Parameters $K_{0,n}$ and $\Delta_R h_n$ of the van't Hoff Equation 4 for the Reaction of Acetaldehyde with Water (cf. Reactions I–III and Eq. 4)

	Reaction	$K_{n,0}$	$\Delta_R h_n$ (kJ/mol)
Ideal	$n=1$	6.09×10^{-4}	−17.865
	$n>1$	1.95×10^{-3}	−13.158
Nonideal	$n=1$	1.77×10^{-4}	−17.730
	$n>1$	1.54×10^{-4}	−17.730

$n_{max}=10$ as the amount of acetaldehyde bound in MMG's with $n>10$ is negligible. This was verified by tests in which n_{max} was increased further and which show that the amount of acetaldehyde bound in oligomers with $n>10$ is negligible.

Hence, with known parameters $K_{n,0}$ and $\Delta_R h_n$ of all reactions n and the overall mole fractions, it is possible to obtain calculated peak area fractions ζ_i^{calc}. The parameters $K_{n,0}$ and $\Delta_R h_n$ were fitted by comparing the experimental peak area fractions ζ_i^{exp} to the peak area fractions calculated this way.

Von Harbou et al.[45] have shown that it is advantageous for the fitting procedure when an equation of the form as given in Eq. 4 is rearranged. The procedure of von Harbou et al.[45] is adopted here, for details see Appendix B.

Model of excess Gibbs energy

To describe the nonideality of the liquid phase, the UNIFAC group contribution model[46] is used, with model parameters from the Dortmund Data Bank.[47] The group assignment as well as the Q and R parameters of the groups are listed in Table 4. The UNIFAC group interaction parameters are shown in Table 5.

For the parameter fit based on the assumption of an ideal liquid phase, all activity coefficients γ_i equal one.

Parameter fit

For determination of the parameters in the van't Hoff equation (Eq. 4), measured and calculated peak area

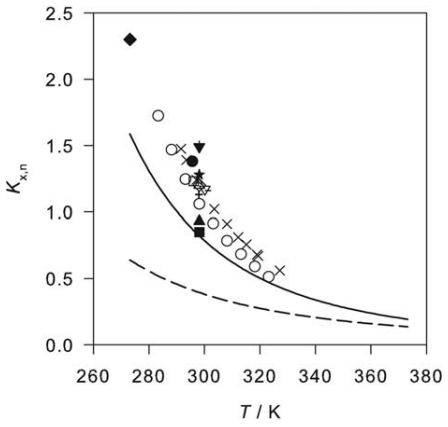

Figure 6. Chemical equilibrium constants of the formation of poly(oxymethylmethylene) glycols assuming ideal behavior as a function of temperature.

Lines are correlations of experimental data obtained in the present work with the van't Hoff equation: $K_{x,1}$ (—), $K_{x,n>1}$ (– –). Symbols are values of the equilibrium constants $K_{x,1}$ from literature: Ref. 27 (◆), Ref. 12 (•), Ref. 14 (□), Ref. 18 (⋆), Ref. 11 (▽), Ref. 10 (|), Ref. 20 (○), Ref. 23 (■), Ref. 24 (Δ), Ref. 28 (◇), Ref. 21 (▲), Ref. 19 (×), Ref. 29 (▼), Ref. 17 (–), and Ref. 22 (+).

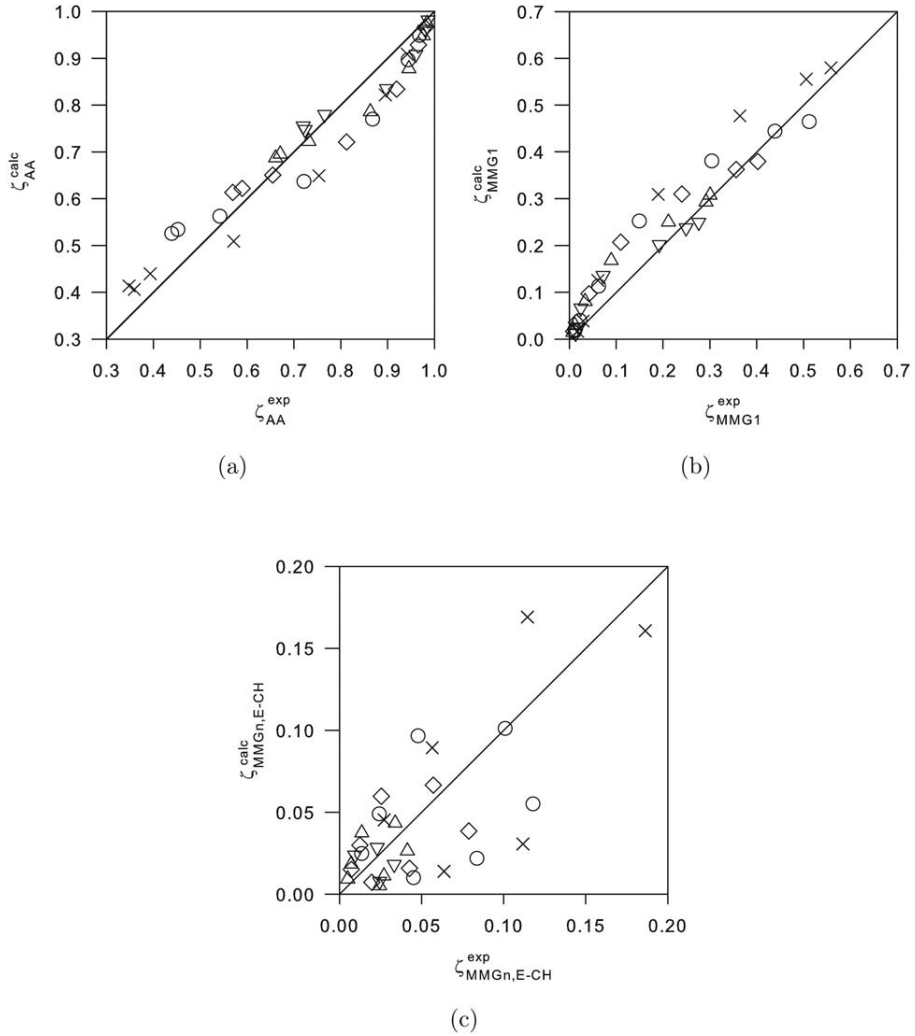

Figure 7. Peak area fractions calculated using the model assuming ideal liquid phase behavior plotted against the experimental values.

Data of the present work at different temperatures are shown (cf. Table A1): 275 K (×), 293 K (○), 308 K (◇), 323 K (Δ), and 338 K (▽).

fractions ζ_i, as defined in Appendix A, were compared. For the parameter fit, a MATLAB routine was used and the objective function was

$$\mathrm{SSE}=\sum_{k=1}^{M}\sum_{i=1}^{4} w_{i,k}\cdot\left(\zeta_{i,k}^{\mathrm{exp}}-\zeta_{i,k}^{\mathrm{calc}}\right)^2 \stackrel{!}{=} \min \tag{9}$$

wherein k stands for the experiment ($k=1\ldots M$) and i stands for the peak area fraction ($i=1\ldots 4$) determined in that experiment. The weighting factors $w_{i,k}$ were chosen as follows

$$w_{i,k}=\frac{1}{\zeta_{i,k}^{\mathrm{exp}}} \tag{10}$$

and $w_{i,k}$ was limited to a maximal value of 4 as otherwise the influence of small peaks would have been too large. This particular choice was made after tests of different options based on consideration of the uncertainity of the data and its evaluation.

The parameters of the model were determined both for the assumption of ideal liquid phase and nonideal liquid phase behavior.

It turns out, that the data from the present work can be described well by assuming that the equilibrium constants of the formation of higher poly(oxymethylmethylene) glycols ($\mathrm{MMG}_{n>1}$, cf. Reaction III) are equal: $K_{n>1}=K_2=K_3=\ldots K_{n\mathrm{max}}$. Hence, only four adjustable parameters remain: $K_{1,0}, K_{n>1,0}, \Delta_R h_1$, and $\Delta_R h_{n>1}$. Furthermore, for the case of a nonideal behavior of the liquid phase, it turned out to be sufficient to use equal reaction enthalpies $\Delta_R h_1=\Delta_R h_{n>1}$ without a significant loss in the quality of the fit. The relative deviation of the reaction enthalpies $\Delta_R h$ between the fit with and without this assumption is smaller than 5%.

Results and Discussion

Chemical equilibrium assuming ideal behavior

The model parameters determined as described above are listed in Table 6. The equilibrium constants as a function of temperature are plotted in Figure 6 together with literature data for $K_{x,1}$ which is discussed below.

Figure 7 shows a parity plot of the calculated peak area fractions ($\zeta_{\mathrm{AA}}, \zeta_{\mathrm{MMG}_1}, \zeta_{\mathrm{MMG}_n,\mathrm{E\text{-}CH}}$), in comparison to the experimental values. For ζ_{AA} and ζ_{MMG_1}, the absolute deviations are usually below about 0.1. There are some systematic trends in the deviations which could result from systematic

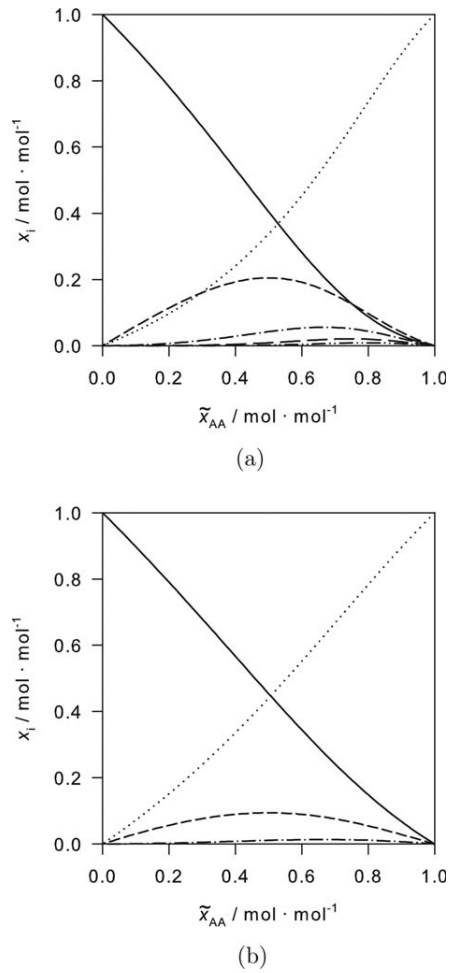

Figure 8. True mole fractions of all components in mixtures of acetaldehyde and water, calculated using the model assuming ideal liquid phase behavior, at (a) 275 K and (b) 323 K.

Lines are: AA (···), W (—), MMG_1 (−−), MMG_2 (− · −), MMG_3 (— —), and MMG_4 (− ··−). For clarity reasons, the trends of $MMG_{n\geq5}$, are not shown.

errors in the data evaluation, such as temperature calibration and peak integration. For more details on errors in quantitative NMR spectroscopy, see Ref. 48. We have refrained from refitting the model parameters with the sole objective of reducing these deviations. Also for $\zeta_{MMG_n,E\text{-}CH}$, the deviations are below about 0.1 but as the absolute numbers are small the relative deviations are quite large. This is unavoidable given the small peaks in the spectra.

The deviations of $\zeta_{MMG_n,M\text{-}CH}$ are similar to the ones of $\zeta_{MMG_n,E\text{-}CH}$, with a slightly larger scattering due to still smaller peak area values. For more comprehensive information see Ref. 43.

With the parameterized model (see Table 6), the true mole fractions of all components in mixtures of acetaldehyde and water can be calculated from the overall acetaldehyde mole fraction at a given temperature. In Figure 8, results for the true species mole fractions at 275 and 323 K are presented. At 275 K (see Figure 8a), the formation of poly(oxymethylmethylene) glycols is important and there is up to 0.2 mol/mol MMG_1. Also, MMG_n are present in amounts which decrease as n increases. At 323 K (see Figure 8b), the equilibrium state is shifted to the educts acetaldehyde and water. Fewer higher oligomers are present compared to the equilibrium composition at 275 K.

In Figure 9, the distribution of the overall acetaldehyde to the different species is plotted against the overall mole fraction of acetaldehyde at 275 and 323 K. It illustrates that an important fraction of acetaldehyde is bound in reaction products (up to about 60% at 275 K and 32% at 323 K).

The chemical equilibrium constants K_x from the present study are compared to literature data in Figure 6. For that purpose, numbers for K_x were calculated from the literature data. Most of the literature data were taken at around room temperature. The results scatter strongly. Furthermore, only data on $K_{x,1}$ for the formation of MMG_1 is available in the literature as most studies from the literature were carried out in dilute solutions of acetaldehyde. The equilibrium constants are given as molarity ratio of MMG_1 to acetaldehyde. To convert this ratio into K_x, the number for x_W has to be included as follows: $K_{x,1}=K^{lit}/x_W$. It was assumed that $x_W=1$ for the literature values in dilute solutions. The literature values for the equilibrium constant $K_{x,1}$ of MMG_1 formation

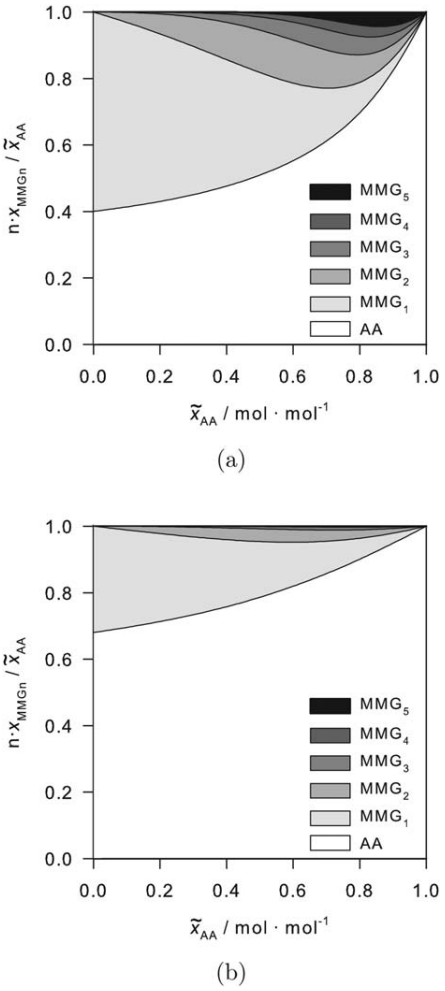

Figure 9. Distribution of the overall acetaldehyde in mixtures with water, bound in the different oligomers, calculated using the model assuming ideal liquid phase behavior, at (a) 275 K and (b) 323 K.

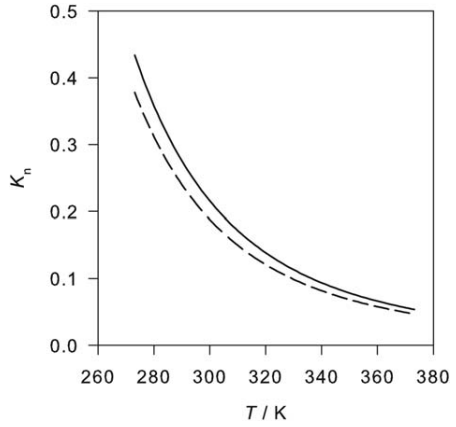

Figure 10. Chemical equilibrium constants of the formation of poly(oxymethylmethylene) glycols assuming nonideal behavior as a function of temperature.

Lines are correlations of experimental data obtained in the present work with the van't Hoff equation: K_1 (—), $K_{n>1}$ (– –).

are higher than the values from the present work. The deviation decreases with increasing temperature. The deviations are probably not related to the fact that the formation of MMG_n $(n>1)$ was neglected in the literature studies as $MMG_{n>1}$ are hardly present in dilute solutions (cf. Figure 9). It is more likely that they are related to the comparative simple experimental techniques that were used for the literature studies, which are over 30 years old. For example, NMR spectrometers with a proton resonance frequence of 100 MHz or below were used. Furthermore, also the different literature values scatter strongly (see values for 298 K in Figure 6) and there are large deviations between literature data from different sources.

Podo and Viti[8] published an equilibrium constant for the formation of MMG_2 on the basis of molarity. They do not specify the temperature, but it can be assumed that they measured at around room temperature. The equilibrium constant $K_{x,2}=1.05$ estimated from their data is higher than the one from the present work ($K_{x,n>1}=0.394$).

Chemical equilibrium assuming nonideal behavior

The results of the parameter fit are shown in Table 6. The corresponding equilibrium constants K_n as a function of temperature are shown in Figure 10. The results of the comparison of the experimental and the calculated peak area fractions ζ_i are similar to those for the model in which ideal liquid phase behavior is assumed (cf. Figure 7). Only for $\zeta_{MMG_n,E}$ and $\zeta_{MMG_n,M}$, slightly better results than those shown in Figure 7 are obtained. Also, the results for the true speciation are similar to those obtained with the model in which ideal behavior is assumed (cf. Figures 8 and 9). The corresponding plots showing the results from the model in which the nonideality is accounted for are therefore not presented here. They are available elsewhere.[43]

Figure 11 compares results for the equilibrium constants K_x obtained using Eqs. 5 and 6 for nonideal vs. ideal behavior. The results for K_x, which were obtained from the model assuming nonideal behavior, depend on the overall composition and therefore, cover a certain range in the plot of K_x over T (cf. gray area in Figure 11). The results agree fairly

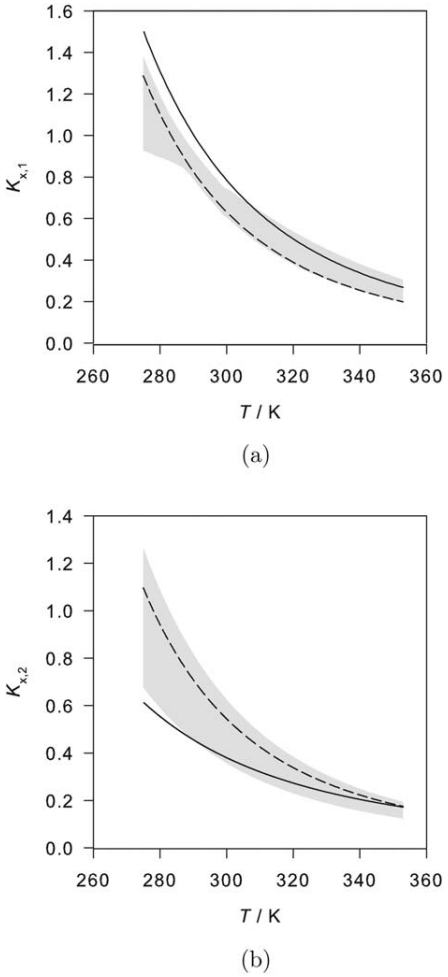

Figure 11. Chemical equilibrium constants K_x of the formation of MMG's (a) $K_{x,1}$ and (b) $K_{x,2}$.

Results from fits to NMR data from the present work in which: ideal behavior is assumed (—), the nonideality is accounted for (numbers for K_x are evaluated at infinite dilution of acetaldehyde) (– –). The shaded area also represents results from the fit in which the nonideality is accounted for and indicates the range in which numbers for K_x lie that are evaluated at overall acetaldehyde mole fractions up to 0.95 mol/mol.

well for K_x of the MMG_1 formation. The variation of K_x with the overall composition is predicted to be about $\pm 10\%$ by the model which takes the nonideality into account (cf. gray area in Figure 11a). That variation is larger for the equilibrium constant K_x of the $MMG_{n>1}$ formation at low temperatures where it is up to about $\pm 20\%$ (cf. gray area in Figure 11b). The results from the model in which ideality is assumed (full lines in Figure 11) are within the range of the predictions of the nonideal model or close to it.

Conclusion

In the present work, the speciation of mixtures containing acetaldehyde and water was studied by a combination of ^{1}H- and ^{13}C-NMR spectroscopy. The latter method was used for the first time to study this technically important system. It gives quantitative information not only on the formation of MMG_1 but also on that of $MMG_{n>1}$. Such data were previously unavailable. The NMR spectroscopic results were used

to determine the equilibrium constants of the formation of MMG_1 and $MMG_{n>1}$ in the system acetaldehyde and water. That information is needed for the development of physicochemical models of the thermodynamic properties of these widely used mixtures.

Acknowledgment

The authors gratefully acknowledge financial support of this work by Lonza AG, Visp, Switzerland.

Literature Cited

1. Eckert M, Fleischmann G, Jira R, Bolt HM, Golka K. *Acetaldehyde, Ullmann's Encyclopedia of Industrial Chemistry*, 6th ed. Weinheim, Germany: Wiley-VCH, 2006.
2. Hahnenstein I, Hasse H, Kreiter C, Maurer G. ^{1}H- and ^{13}C-NMR spectroscopic study of chemical equilibria in solutions of formaldehyde in water, deuterium oxide, and methanol. *Ind Eng Chem Res*. 1994;33:1022–1029.
3. Hahnenstein I, Hasse H, Liu YQ, Maurer G. Thermodynamic properties of formaldehyde containing mixtures for separation process design. *AIChE Symposium Series, Vol. 90, No. 298*. New York: AIChE, 1994:141–157.
4. Hahnenstein I, Albert M, Hasse H, Kreiter CG, Maurer G. NMR spectroscopic and densimetric study of reaction kinetics of formaldehyde polymer formation in water, deuterium oxide, and methanol. *Ind Eng Chem Res*. 1995;34:440–450.
5. Maiwald M, Fischer HH, Ott M, Peschla R, Kuhnert C, Kreiter CG, Maurer G, Hasse H. Quantitative NMR spectroscopy of complex liquid mixtures: methods and results for chemical equilibria in formaldehyde -water - methanol at temperatures up to 383 K. *Ind Eng Chem Res*. 2003;42:259–266.
6. Ott M, Fischer HH, Maiwald M, Albert K, Hasse H. Kinetics of oligomerization reactions in formaldehyde solutions: NMR experiments up to 373 K and thermodynamically consistent model. *Chem Eng Process*. 2005;44(6):653–660.
7. Kuhnert C, Albert M, Breyer S, Hahnenstein I, Hasse H, Maurer G. Phase equilibrium in formaldehyde containing multicomponent mixtures: experimental results for fluid phase equilibria of (formaldehyde plus (water or methanol) plus methylal) and (formaldehyde plus water plus methanol plus methylal) and comparison with predictions. *Ind Eng Chem Res*. 2006;45:5155–5164.
8. Podo F, Viti V. A PMR study of hydration products in aqueous acetaldehyde solutions. *Org Magn Reson*. 1970;3:259–261.
9. Greenzaid P, Luz Z, Samuel D. A nuclear magnetic resonance study of the reversible hydration of aliphatic aldehydes and ketones. I. Oxygen-17 and proton spectra and equilibrium constants. *J Am Chem Soc*. 1967;89:749–756.
10. Lombardi E, Sogo P. NMR study of acetaldehyde-water mixtures. *J Chem Phys*. 1960;32:635–636.
11. Fujiwara Y, Fujiwara S. Nuclear magnetic resonance study of acetaldehyde aqueous solution. *Bull Chem Soc Jpn*. 1963;36:574–578.
12. Lewis C, Wolfenden R. Antiproteolytic aldehydes and ketones: substituent and secondary deuterium isotope effects on equilibrium addition of water and other nucleophiles. *Biochemistry*. 1977;16(22):4886–4890.
13. Buschmann HJ, Füldner HH, Knoche W. The reversible hydration of carbonyl compounds in aqueous solution. Part I. The keto/gem-diol equilibrium. *Ber Bunsenges Phys Chem*. 1980;84(1):41–44.
14. Ahrens M, Strehlow H. Acid catalyzed hydration of acetaldehyde. *Discuss Faraday Soc*. 1965;39:112–120.
15. Socrates G. Hydration study of acetaldehyde and propionaldehyde. *J Org Chem*. 1969;34(10):2958–2961.
16. Greenzaid P, Luz Z, Samuel D. A nuclear magnetic resonance study of the reversible hydration of aliphatic aldehydes and ketones. II. The acid-catalyzed oxygen exchange of acetaldehyde. *J Am Chem Soc*. 1967;89:756–759.
17. Cheshnovsky D, Navon G. Nuclear magnetic resonance studies of carbonic anhydrase catalyzed reversible hydration of acetaldehyde by the saturation transfer method. *Biochemistry*. 1980;19:1866–1873.
18. Evans P, Miller G, Kreevoy M. Comparison of nuclear magnetic resonance, thermal maximum, and scavenging techniques for rate measurement. *J Phys Chem*. 1965;69:4325–4327.
19. Bell RP, Clunie JC. The hydration of acetaldehyde in aqueous solution. *Trans Faraday Soc*. 1952;48:439–442.
20. Kurz JL. The hydration of acetaldehyde. I. Equilibrium thermodynamic parameters. *J Am Chem Soc*. 1967;89:3524–3528.
21. Gruen L, McTigue P. Hydration equilibria of aliphatic aldehydes in H2O and D2O. *J Chem Soc*. 1963:5217–5223.
22. Xu H, Wentworth PJ, Howell NW, Joens JA. Temperature dependent near-UV molar absorptivities of aliphatic aldehydes and ketones in aqueous solution. *Spectrochim Acta A*. 1993;49(8):1171–1178.
23. Lienhard GE, Jencks WP. Thiol addition to the carbonyl group. Equilibria and kinetics. *J Am Chem Soc*. 1966;88(17):3982–3995.
24. Lewis CA, Wolfenden R. Influence of pressure on the equilibrium of hydration of aliphatic aldehydes. *J Am Chem Soc*. 1973;95(20):6685–6688.
25. Sørensen P, Jencks W. Acid- and base-catalyzed decomposition of acetaldehyde hydrate and hemiacetals in aqueous solution. *J Am Chem Soc*. 1987;109:4675–4690.
26. Gruen L, McTigue P. Kinetics of hydration of aliphatic aldehydes. *J Chem Soc*. 1963:5224–5229.
27. Pocker Y, Meany JE. The catalytic versatility of carbonic anhydrase from erythrocytes. The enzyme-catalyzed hydration of acetaldehyde. *J Am Chem Soc*. 1965;87(8):1809–1811.
28. Buschmann HJ, Dutkiewicz E, Knoche W. The reversible hydration of carbonyl compounds in aqueous solution part II: the kinetics of the keto/gem-diol transition. *Ber Bunsenges Phys Chem*. 1982;86(2):129–134.
29. Bell RP, Evans PG. Kinetics of the dehydration of methylene glycol in aqueous solution. *Proc R Soc A*. 1966;291(1426):297–323.
30. Bell RP, Clunie JC. Binary and ternary mechanisms in the hydration of acetaldehyde. *Proc R Soc London Math Phys Sci*. 1952;212(1108):33–37.
31. Bell R, Rand MH, Wynne-Jones KMA. Kinetics of the hydration of acetaldehyde. *Trans Faraday Soc*. 1956;52:1093–1102.
32. Kurz JL, Coburn JI. The hydration of acetaldehyde. II. Transition-state characterization. *J Am Chem Soc*. 1967;89(14):3528–3537.
33. Bell RP, Higginson WCE. The catalyzed dehydration of acetaldehyde hydrate, and the effect of structure on the velocity of protolytic reactions. *Proc R Soc London A*. 1949;197:141–159.
34. Schuchmann MN, von Sonntag C. The rapid hydration of the acetyl radical. A pulse radiolysis study of acetaldehyde in aqueous solution. *J Am Chem Soc*. 1988;110:5698–5701.
35. Albert M, Hahnenstein I, Hasse H, Maurer G. Vapor-liquid equilibrium of formaldehyde mixtures: new data and model revision. *AIChE J*. 1996;42(6):1741–1752.
36. Maiwald M, Fischer H, Kim YK, Hasse H. Quantitative on-line high-resolution NMR spectroscopy in process engineering applications. *Anal Bioanal Chem*. 2003;375(8):1111–1115.
37. Schilling K, Sohn M, Ströfer E, Hasse H. Reactive evaporation of formaldehyde-containing mixtures and process monitoring by online NMR-spectroscopy. *Chem Ing Tech*. 2003;75:240–244.
38. Maiwald M, Grützner T, Ströfer E, Hasse H. Quantitative NMR spectroscopy of complex technical mixtures using a virtual reference: chemical equilibria and reaction kinetics of formaldehyde - water - 1,3,5-trioxane. *Anal Bioanal Chem*. 2006;385(5):910–917.
39. Maiwald M, Fischer HH, Kim YK, Albert K, Hasse H. Quantitative high-resolution on-line NMR spectroscopy in reaction and process monitoring. *J Magn Reson*. 2004;166(2):135–146.
40. Grützner T, Hasse H, Lang N, Siegert M, Ströfer E. Development of a new industrial process for trioxane production. *Chem Eng Sci*. 2007;62:5613–5620.
41. Drunsel JO, Renner M, Hasse H. Experimental study and model of reaction kinetics of heterogeneously catalyzed methylal synthesis. *Chem Eng Res Des*. 2012;90(5):696–703.
42. Burger J, Ströfer E, Hasse H. Chemical equilibrium and reaction kinetics of the heterogeneously catalyzed formation of poly(oxymethylene) dimethyl ethers from methylal and trioxane. *Ind Eng Chem Res*. 2012;51(39):12751–12761.
43. Scheithauer A. Physico-chemical data and conceptual design of a crotonaldehyde production process. Ph.D. Thesis. Laboratory of Engineering Thermodynamics, University of Kaiserslautern. *Scientific Report Series*. 2014;13. ISBN 978-3-944433-12-7.
44. Cobas JC, Bernstein MA, Martín-Pastor M, Tahoces PG. A new general-purpose fully automatic baseline-correction procedure for 1D and 2D NMR data. *J Magn Reson*. 2006;183(1):145–151.
45. Von Harbou E, Yazdani A, Schmitt M, Großmann C, Hasse H. Reaction kinetics for reactive distillation using different laboratory reactors. *Ind Eng Chem Res*. 2013;52(2):624–637.

46. Fredenslund A, Gmehling J, Rasmussen P. Vapor-liquid equilibria by UNIFAC Group contribution method. Revision and extension 5. *Ind Eng Chem Res*. 1991;30:2352–2355.
47. Dortmund Data Bank. Oldenburg, Germany: DDBST GmbH, 2012.
48. Malz F, Jancke H. Validation of quantitative NMR. *J Pharm Biomed Anal*. 2005;38(5):813–823.
49. Buzzi-Ferraris G, Manenti F. Interpolation and regression models for the chemical engineer: solving numerical problems. Weinheim, Germany: Wiley-VCH, 2010.

Appendix A

The areas of the peaks H5, H6 (see Figure 2 and Table 3) and C2–C8 (see Figure 4 and Table 3) were used for the evaluation of the NMR spectra. Several choices are possible for the quantification as redundant information is available. To check the consistency of this information, redundant peak area fractions are shown in a parity plot in Figure A1. As can be seen in Figure A1, the results from the different methods are consistent. The present choice was motivated by a consideration of the errors introduced by the NMR spectra and more importantly by their evaluation. Figure A1a also shows that the ^{1}H-NMR and ^{13}C-NMR data are consistent.

The following procedure for the quantification was chosen. From the ^{1}H-NMR spectra, the ratio of acetaldehyde as monomer and acetaldehyde bound in $MMG_{n\geq 1}$ was derived using the peaks H5 and H6 specified in Table 3 and Figure 2. The distribution of acetaldehyde to the different MMG_n species was determined from the information of the CH part (peaks C2, C3, and C4) of the ^{13}C-NMR spectrum (cf. Table 3), because compared to the CH_3 part, the peaks are better separated and thus the baseline correction is more appropriate.

For the quantification and the parameter fit peak area fractions ζ_i were used

$$\zeta_i = \frac{\text{amount of substance of acetaldehyde bound in form } i}{\text{overall amount of substance of acetaldehyde}} \tag{A1}$$

where i is

- i = AA (monomeric AA)
- $i = MMG_1$
- $i = MMG_{n,E}$ (end group (E) in MMG_n, $n > 1$)
- $i = MMG_{n,M}$ (middle group (M) in MMG_n, $n > 2$)

so that

$$\sum_{I} \zeta_i = 1 \tag{A2}$$

The ζ_i are related to the peak areas by

$$\zeta_{AA} = \frac{A^{1H}_{AA,CH_3}}{A^{1H}_{AA,CH_3} + A^{1H}_{MMG_n,CH_3}} \tag{A3}$$

$$\zeta_{MMG_1} = \eta^{13C}_{MMG_1,CH} \cdot (1 - \zeta_{AA}) \tag{A4}$$

$$\zeta_{MMG_n,E\text{-}CH} = \eta^{13C}_{MMG_n,E\text{-}CH} \cdot (1 - \zeta_{AA}) \tag{A5}$$

$$\zeta_{MMG_n,M\text{-}CH} = \eta^{13C}_{MMG_n,M\text{-}CH} \cdot (1 - \zeta_{AA}) \tag{A6}$$

with the abbreviation η^{13C}_i

$$\eta^{13C}_{MMG_1,CH} = \frac{A^{13C}_{MMG_1,CH}}{A^{13C}_{MMG_{n\geq 1},CH}} \tag{A7}$$

$$\eta^{13C}_{MMG_n,E\text{-}CH} = \frac{A^{13C}_{MMG_n,E\text{-}CH}}{A^{13C}_{MMG_{n\geq 1},CH}} \tag{A8}$$

$$\eta^{13C}_{MMG_n,M\text{-}CH} = \frac{A^{13C}_{MMG_n,M\text{-}CH}}{A^{13C}_{MMG_{n\geq 1},CH}} \tag{A9}$$

and

$$A^{13C}_{MMG_{n\geq 1},CH} = A^{13C}_{MMG_1,CH} + A^{13C}_{MMG_n,E\text{-}CH} + A^{13C}_{MMG_n,M\text{-}CH} \tag{A10}$$

The peak areas A_i and the peak area fractions ζ_i are related to the true species amounts of substance by

$$A^{1H}_{AA,CH_3} = \xi^{1H}_{AA,CH_3} \cdot 3 \cdot n_{AA} \tag{A11}$$

$$A^{1H}_{MMG_n,CH_3} = \xi^{1H}_{MMG_n,CH_3} \cdot 3 \cdot \sum_{n=1}^{n_{max}} n \cdot n_{MMG_n} \tag{A12}$$

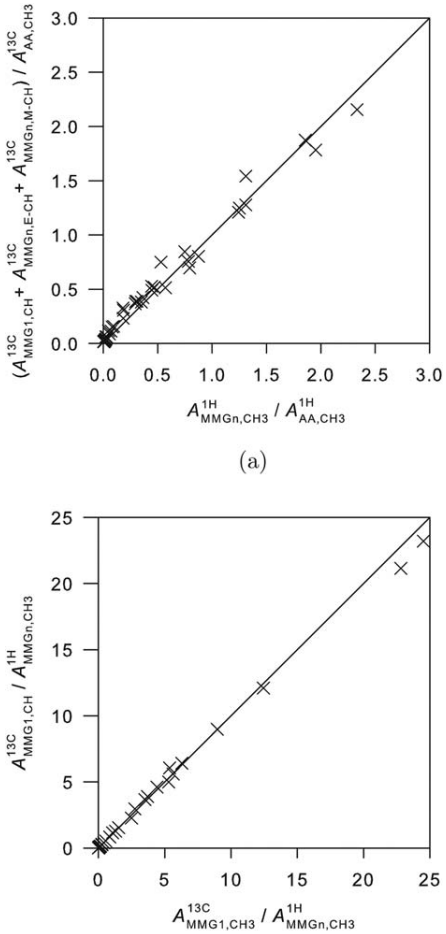

Figure A1. Comparison of redundant information from ^{1}H-NMR and ^{13}C-NMR spectra (peak assignment cf. Table 3).

The comparison is carried out for two different quantities: (a) the overall conversion of acetaldehyde to MMG_n and (b) the ratio of the amount of acetaldehyde bound in MMG_1 and monomeric acetaldehyde. The *x* axis indicates the results when only information from CH_3 groups is used. The *y* axis indicates the results when a combination of information from CH and CH_3 groups is used. There are no systematic differences between the results from the different methods.

Table A1. Experimental Peak Area Fractions Calculated from the Peak Areas of ^{1}H- and ^{13}C-NMR Spectra

T (K)	Sample	ζ_{AA}^{exp}	$\zeta_{MMG_1}^{exp}$	$\zeta_{MMG_n,E}^{exp}$	$\zeta_{MMG_n,M}^{exp}$
275	1	0.3594	0.5588	0.0636	0.0182
	2	0.3481	0.5056	0.1118	0.0345
	3	0.3935	0.3641	0.1894	0.0530
	4	0.5717	0.1897	0.1863	0.0523
	5	0.7534	0.0610	0.1146	0.0710
	6	0.8953	0.0291	0.0565	0.0191
	7	0.9419	0.0179	0.0272	0.0129
293	1	0.4393	0.5122	0.0451	0.0034
	2	0.4524	0.4391	0.0837	0.0248
	3	0.5419	0.3042	0.1179	0.0361
	4	0.7213	0.1494	0.1009	0.0284
	5	0.8678	0.0626	0.0478	0.0217
	6	0.9438	0.0223	0.0242	0.0097
	7	0.9684	0.0119	0.0135	0.0063
308	1	0.5696	0.4023	0.0197	0.0085
	2	0.5895	0.3563	0.0425	0.0117
	3	0.6548	0.2403	0.0787	0.0262
	4	0.8125	0.1100	0.0572	0.0204
	5	0.9192	0.0420	0.0255	0.0133
	6	0.9656	0.0152	0.0124	0.0068
	7	0.9798	0.0093	0.0072	0.0036
323	1	0.6609	0.3005	0.0244	0.0142
	2	0.6707	0.2916	0.0271	0.0106
	3	0.7321	0.2116	0.0413	0.0150
	4	0.8631	0.0894	0.0339	0.0136
	5	0.9454	0.0336	0.0135	0.0075
	6	0.9761	0.0113	0.0072	0.0055
	7	0.9844	0.0078	0.0050	0.0028
338	1	0.7237	0.2763	0.0000	0.0000
	2	0.7201	0.2494	0.0245	0.0060
	3	0.7658	0.1919	0.0333	0.0090
	4	0.8978	0.0724	0.0229	0.0069
	5	0.9602	0.0246	0.0093	0.0059
	6	0.9801	0.0199	0.0000	0.0000
	7	0.9863	0.0137	0.0000	0.0000

$$A_{MMG_1,CH}^{13C} = \xi_{MMG_1,CH}^{13C} \cdot n_{MMG_1} \tag{A13}$$

$$A_{MMG_n,E\text{-}CH}^{13C} = \xi_{MMG_n,E\text{-}CH}^{13C} \cdot 2 \cdot \sum_{n=2}^{n_{max}} n_{MMGn} \tag{A14}$$

$$A_{MMG_n,M\text{-}CH}^{13C} = \xi_{MMG_n,M\text{-}CH}^{13C} \cdot \sum_{n=3}^{n_{max}} (n-2) \cdot n_{MMG_n} \tag{A15}$$

wherein the formation of n_{max} oligomers is considered. It is assumed that the proportionality constants for the CH_3 peaks in the ^{1}H-NMR spectrum (cf. Eqs. A11 and A12) are equal

$$\xi_{AA,CH_3}^{1H} = \xi_{MMG_n,CH_3}^{1H} \tag{A16}$$

The same assumption is used for the CH peaks in the ^{13}C-NMR spectrum (cf. Eqs.A13–A15)

$$\xi_{MMG_1,CH}^{13C} = \xi_{MMG_n,E\text{-}CH}^{13C} = \xi_{MMG_n,M\text{-}CH}^{13C} \tag{A17}$$

This was checked by comparison of the redundant information in the NMR spectra (see Figure A1).

The peak area fractions were computed for all experiments using Eqs. A3–A10. The results are given in Table A1.

Appendix B

Von Harbou et al.[45] rearranged an equation of the form as given in Eq. 4 to improve the fit procedure. They introduced two reference temperatures T_{min} and T_{max} as proposed by Buzzi-Ferraris and Manenti.[49] The reparameterized van't Hoff equation is expressed by

$$K_n(T) = \exp\left[\frac{\left(\Theta_{1,n} \cdot \left(\frac{1}{T} - \frac{1}{T_{min}}\right) - \Theta_{2,n} \cdot \left(\frac{1}{T} - \frac{1}{T_{max}}\right)\right)}{\left(\frac{1}{T_{min}} - \frac{1}{T_{max}}\right)}\right] \tag{B1}$$

The parameters of the original van't Hoff equation (Eq. 4) can be calculated from the parameters $\vec{\Theta}$ of the reparameterized equation (Eq. B1)

$$K_{n,0} = \exp\left[\left(\frac{1}{T_{min}} - \frac{1}{T_{max}}\right)^{-1} \cdot \left(\frac{\Theta_{2,n}}{T_{max}} - \frac{\Theta_{1,n}}{T_{min}}\right)\right] \tag{B2}$$

$$\Delta_R h_n = R \cdot \left(\frac{1}{T_{min}} - \frac{1}{T_{max}}\right)^{-1} \cdot \left(\Theta_{2,n} - \Theta_{1,n}\right) \tag{B3}$$

Manuscript received Apr. 2, 2014, and revision received July 16, 2014.

Behrens et al., 2017

Reprinted with permission from: R. Behrens, E. von Harbou, W. R. Thiel, W. Böttinger, T. Ingram, G. Sieder, H. Hasse, Monoalkylcarbonate Formation in Methyldiethanolamine–H_2O–CO_2, Industrial & Engineering Chemistry Research, Volume 56, 2017, Pages 9006-9015, DOI 10.1021/acs.iecr.7b01937

I&EC research
Industrial & Engineering Chemistry Research

Article

pubs.acs.org/IECR

Monoalkylcarbonate Formation in Methyldiethanolamine–H_2O–CO_2

Richard Behrens,[†] Erik von Harbou,[*,†] Werner R. Thiel,[‡] Wolfram Böttinger,[†,§] Thomas Ingram,[¶] Georg Sieder,[¶] and Hans Hasse[†]

[†]Laboratory of Engineering Thermodynamics (LTD), University of Kaiserslautern, Erwin-Schrödinger-Straße 44, 67663 Kaiserslautern, Germany

[‡]Department of Chemistry, University of Kaiserslautern, Erwin-Schrödinger-Straße 54, 67663 Kaiserslautern, Germany

[¶]BASF SE RCP/TD, 67056 Ludwigshafen, Germany

[§]Wacker Chemie AG, 84489 Burghausen, Germany

Supporting Information

ABSTRACT: In this work, the monoalkylcarbonate ((*N*-hydroxyethyl)(*N*-methyl)(2-aminoethyl) hydrogen carbonate) formation in the system methyldiethanolamine (MDEA)–water (H_2O)–carbon dioxide (CO_2) is investigated by nuclear magnetic resonance (NMR) spectroscopy. Aqueous solutions containing 0.4 g/g of MDEA were loaded with CO_2 in valved NMR tubes, and the composition of the liquid phase in equilibrium was determined *in situ* at 298 K at pressures up to 11 bar. By two-dimensional NMR, the presence of monoalkylcarbonate was verified, which has been widely overlooked in the literature so far. The experimental data of this work and reevaluated NMR data obtained in previous work of our group were used to calculate chemical equilibrium constants of the proposed monoalkylcarbonate formation. A model taken from the literature that describes the solubility of CO_2 in aqueous solution of MDEA and the corresponding species distribution is extended so that it can account for the monoalkylcarbonate in the liquid phase as well. The extended model is validated using NMR data in the temperature range 273–333 K. The study shows that more than 10 mol % of the absorbed CO_2 is bound as monoalkylcarbonate under conditions relevant for technical applications.

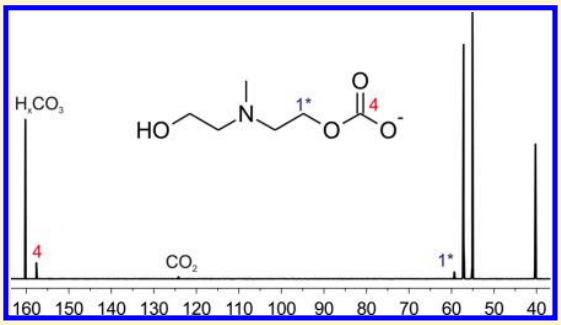

INTRODUCTION

Aqueous alkanolamine solutions are widely used as solvents in reactive absorption processes. They are applied for example for scrubbing carbon dioxide (CO_2) or hydrogen sulfide (H_2S) from natural gas, synthesis gases, and refinery gases. Further, they are currently discussed as solvents for the removal of CO_2 from flue gas of fossil fueled power plants.[1]

Process models that enable a reliable prediction are a prerequisite for the design, scale-up, and optimization of reactive absorption processes. The backbone of the process model is the model of the physicochemical properties of the pertinent reactive mixtures.[2] Here, the correct description of the species distribution in the solvent is of great importance. Depending on the type of aqueous alkanolamine solution used as a solvent, different reactions take place in the liquid phase when CO_2 is absorbed. A review of the possible reactions of CO_2 with all types of aqueous alkanolamines is given by Vaidya and Kenig.[3]

In this work, aqueous solutions containing the tertiary alkanolamine methyldiethanolamine (MDEA), which is widely used in the chemical industry,[3,4] are investigated. Unlike primary (e.g., monoethanolamine (MEA)) and secondary alkanolamines (e.g., diethanolamine (DEA)), tertiary alkanolamines do not form carbamates. Instead, tertiary alkanolamines mainly support the CO_2 hydrolysis reaction forming bicarbonates by a pH shift. Consequently, most of the models describing the chemical equilibrium in the liquid phase of the system tertiary alkanolamine–H_2O–CO_2 take four reactions into account: the autoprotolysis of water, the formation of bicarbonate (HCO_3^-) and carbonate (CO_3^{2-}), and the protonation of the tertiary alkanolamine to the ammonium ion. For the system MDEA–H_2O–CO_2, this results in a total of 8 species in the liquid phase: H_2O, CO_2, MDEA, H^+, OH^-, HCO_3^-, CO_3^{2-}, and $MDEAH^+$.[5−7]

Jørgensen and Faurholt[8] stated an additional species in CO_2 loaded aqueous solutions containing the tertiary alkanolamine triethanolamine (TEA). Results from precipitation studies let them assume that monoalkylcarbonate is formed in the liquid phase. Subsequent kinetic studies of Hikita et al.[9] in which TEA was rapidly mixed with CO_2 loaded water were in agreement with the proposed formation of monoalkylcarbonate. Contrarily, later kinetic studies on the absorption of CO_2 in aqueous solutions of TEA and in other tertiary alkanolamines were interpreted successfully without accounting for monoalkylcarbonates.[10−13] As a result, henceforth, the formation of

Received: May 10, 2017
Revised: June 29, 2017
Accepted: July 7, 2017
Published: July 7, 2017

DOI: 10.1021/acs.iecr.7b01937
Ind. Eng. Chem. Res. 2017, 56, 9006−9015

monoalkylcarbonate was neglected in models of the chemical equilibria in alkanolamine systems loaded with CO_2.[3] However, the true contribution of the formation of monoalkylcarbonate to the overall CO_2 absorption has never been investigated in detail. Instead, only overall reaction kinetics were determined by means of measurements of the exothermicity,[9] $^{14}CO_2$-tracer experiments,[10] pH-measurements,[11] or measurements of the overall absorption of CO_2.[12,13] To assess the true contribution of different reactions taking place in the liquid phase, the composition of the liquid phase has to be determined at different CO_2 loadings.

Suitable methods for the analysis of the composition of the liquid phase of aqueous alkanolamine solutions loaded with CO_2 are IR spectroscopy,[14] Raman spectroscopy,[15] or NMR spectroscopy.[4,6,16−21] Among those analysis methods, only NMR spectroscopy has the advantage that it enables quantitative measurements without prior calibration. Furthermore, NMR spectroscopy has a high chemical resolution and can distinguish even between chemically similar species.[22,23] An overview of the application of NMR spectroscopy for the investigation of alkanolamine−H_2O−CO_2 systems has been given recently by Perinu et al.[24] So far, however, NMR has not been used for the identification and quantification of monoalkylcarbonate in aqueous solutions of alkanolamines. The formation of additional species in the system tertiary alkanolamine−H_2O−CO_2 has been recognized before in different NMR experiments but has not been explicitly studied, and no monoalkylcarbonate was identified. Poplsteinova[25] called the additional species she observed impurities, whereas Böttinger et al.[4] called them byproducts. Böttinger et al.[4] assumed that the byproducts are formed by degradation reactions of MDEA, as they were reported by Chakma and Meisen.[26] Only for the anhydrous system tertiary alkanolamine−CO_2 the formation of monoalkylcarbonate was explicitly reported and quantified with ^{13}C NMR spectroscopy.[18]

The species distribution in aqueous solutions of MDEA loaded with CO_2 was investigated in the present work by NMR spectroscopy with a special focus on the elucidation of all species existent in the liquid phase. By means of two-dimensional NMR techniques, the presence of monoalkylcarbonate ((*N*-hydroxyethyl)(*N*-methyl)(2-aminoethyl)hydrogen carbonate) was identified. Furthermore, the experimental results show that the amount of monoalkylcarbonate formed under conditions relevant for technical applications is too large to be simply ignored in the models. Therefore, experiments were carried out to determine the chemical equilibrium of the formation of monoalkylcarbonate. Samples of aqueous solution of MDEA loaded with CO_2 (composition of the aqueous stock solution of MDEA 0.4 g/g, CO_2 loadings from 0.1 to 1.1 mol/mol as defined in eq 3) were prepared by loading aqueous stock solutions of MDEA directly inside valved NMR tubes at different partial pressures of CO_2. The experiments were carried out at 298 K.

Furthermore, the NMR data acquired by Böttinger et al.[4] was reevaluated considering the new knowledge on the monoalkylcarbonate formation. This yields comprehensive data on the composition of the liquid phase in chemical equilibirium including the concentration of monoalkylcarbonate at various conditions (temperatures 293, 313, and 333 K, composition of the aqueous stock solution of MDEA 0.2, 0.3, and 0.4 g/g, CO_2 loadings from 0.1 to 1.3 mol/mol).

The data is used to parametrize a model of the chemical equilibrium of the formation of monoalkylcarbonate. The chemical equilibria constants of the other reactions were taken from Ermatchkov and Maurer.[5] The strong thermodynamic nonidealities in the liquid phase are accounted for using an extended version of Pitzer's model as described in Ermatchkov and Maurer.[5] That model will simply be called Pitzer's model here for brevity. The model is able to predict the formation of monoalkylcarbonate and thus of all species present in the system MDEA−H_2O−CO_2 in the temperature range 273−333 K. However, in industrial amine solutions, more species may be present, for example, H_2S and reaction products of H_2S, degradation products, antifoaming additives, and impurities. No attempts were made in this work to include the prediction of those species as well. The results of this work prove that more than 10 mol % of the absorbed CO_2 is bound as monoalkylcarbonate under conditions relevant for technical applications.

REACTION SYSTEM

Aqueous tertiary alkanolamines mainly facilitate the CO_2 hydrolysis reaction forming bicarbonates through an acid−base buffer mechanism. Thus, the following reactions are commonly considered to describe the chemical equilibrium in the system MDEA−H_2O−CO_2:[5]

$$H_2O \rightleftharpoons H^+ + OH^- \quad \text{(I)}$$

$$CO_2 + H_2O \rightleftharpoons HCO_3^- + H^+ \quad \text{(II)}$$

$$HCO_3^- \rightleftharpoons CO_3^{2-} + H^+ \quad \text{(III)}$$

$$MDEAH^+ \rightleftharpoons MDEA + H^+ \quad \text{(IV)}$$

Figure 1 shows an exemplary ^{13}C spectrum of the liquid phase of an aqueous solution of MDEA loaded with CO_2.

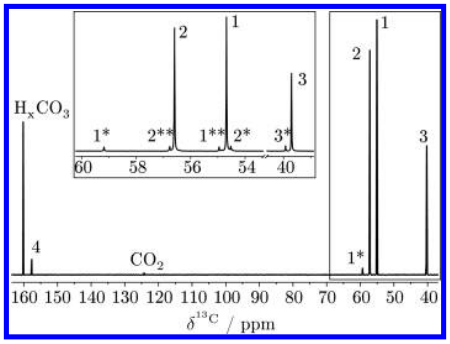

Figure 1. ^{13}C NMR spectrum of MDEA−H_2O−CO_2, for $x^{(m),0}_{MDEA}$ = 0.4 g/g, α_{CO_2} = 1.066 mol/mol, T = 298 K; notation of the peaks according to Figure 2. Peak H_xCO_3 results from H_2CO_3, HCO_3^-, and CO_3^{2-}.

Signals of CO_2 and all the other carbon-containing species in reactions I−IV can be found in the spectrum. Since NMR spectroscopy is too slow to follow protonation reactions, the carbon atoms of MDEA and $MDEAH^+$ are superimposed in peaks 1, 2, and 3 and HCO_3^- and CO_3^{2-} are superimposed in the H_xCO_3 peak. However, also additional peaks, which cannot be assigned to the species of reactions I−IV, are observed in the ^{13}C spectrum, from left to the right in Figure 1: peak 4, 1*, 2**, 1**, 2*, and 3*. In order to assign these peaks, the formation of additional species in the reaction network has to be postulated.

DOI: 10.1021/acs.iecr.7b01937
Ind. Eng. Chem. Res. 2017, 56, 9006−9015

Böttinger et al.[4] extended the reaction network (reactions I–IV) by the degradation reactions of MDEA to dimethyldiethanolammonium ($DMDEA^+$) and diethanolamine (DEA) with a subsequent protonation and carbamate formation of the DEA as described by Chakma and Meisen.[26] Böttinger et al.[4] assigned $DMDEA^+$ to peak 1* but considered DEA as well as its protonated form and the carbamate as not quantifiable. They were not able to assign peak 4 to any reaction product postulated by Chakma and Meisen.[26] Therefore, they followed the assumption of Poplsteinova[25] saying that peak 4 can be traced back to impurities. Nevertheless, peak 4 was evaluated by Böttinger et al.[4] and labeled as a byproduct. Due to the partial overlapping by the dominant MDEA/$MDEAH^+$ peaks, peaks 2**, 1**, 2*, and 3* were not identified and evaluated by Böttinger et al.[4]

By employing two-dimensional NMR techniques, we identified the monoalkylcarbonate of MDEA ((*N*-hydroxyethyl)(*N*-methyl)(2-aminoethyl)hydrogen carbonate) as an additional species in this work. Details on the two-dimensional NMR techniques are presented in the Supporting Information in Section 1. All peaks in the ^{13}C spectrum that could not be assigned to any species in reactions I–IV can be explained by the monoalkylcarbonate of MDEA (abbreviated $MDEACOO^-$). The structure of $MDEACOO^-$ and the numbering of its carbon atoms is depicted on the right-hand side of Figure 2. The nitrogen of $MDEACOO^-$ can protonate

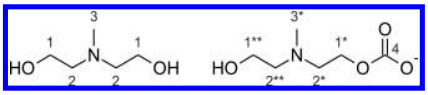

Figure 2. Chemical structure of MDEA (left) and of monoalyklcarbonate ((*N*-hydroxyethyl)(*N*-methyl)(2-aminoethyl)hydrogen carbonate), $MDEACOO^-$ (right) with notation of the groups used in this paper.

in the same way as MDEA can protonate. Following this, not only $MDEACOO^-$ is introduced in the reaction system but also its protonated form $MDEAH^+COO^-$:

$$MDEA + HCO_3^- \rightleftharpoons MDEACOO^- + H_2O \quad (V)$$

$$MDEAH^+ + HCO_3^- \rightleftharpoons MDEAH^+COO^- + H_2O \quad (VI)$$

There might be a small influence on the pK_a value of the remaining OH group after the formation of the monoalkylcarbonate of MDEA, since the nitrogen atom of MDEA should become protonated during this process. This nitrogen atom is only three bonds away from the OH group. We believe, however, that this influence should have a minor impact on the equilibria discussed in the present paper. Reactions V and VI are in line with with conclusions of Jørgensen and Faurholt[8] and Rainbolt et al.[18] Jørgensen and Faurholt[8] suggested the following overall reaction for the formation of the monoalkylcarbonate of triethanolamine in an basic aqueous medium:

$$N(CH_2CH_2OH)_3 + CO_2 + OH^- \rightleftharpoons N(CH_2CH_2OH)_2CH_2CH_2CO_3^- + H_2O$$

and reported the formation of monoalkylcarbonate when mixing aqueous solutions of triethanolamine with potassium bicarbonate and sodium carbonate, suggesting

$$N(CH_2CH_2OH)_3 + HCO_3^- \rightleftharpoons N(CH_2CH_2OH)_2CH_2CH_2CO_3^- + H_2O$$

Rainbolt et al.[18] were able to prove the existence of monoalkylcarbonate of neat dimethylethanolamine (DMEA) at elevated CO_2 pressure via ^{13}C NMR spectroscopy. Since no water is present, they explained the required deprotonation of the hydroxyethyl group by a proton transfer to the nitrogen:

$$N(CH_3)_2CH_2CH_2OH + CO_2 \rightleftharpoons NH^+(CH_3)_2CH_2CH_2CO_3^-$$

EXPERIMENTS

Chemicals. *N*-Methyldiethanolamine (MDEA, ≥99 mass %) was purchased from Sigma-Aldrich (Steinheim/Germany). Sodium carbonate (Na_2CO_3, ≥99.8 mass %) was purchased from Th. Geyer (Renningen/Germany). Water was deionized and purified with a water purification system (Milli-Q Reference A+ System, Merck Millipore, Billerica/US-MA). Carbon dioxide (CO_2 N45, 99.995 vol %) was purchased from Air Liquide (Düsseldorf/Germany). Methanol (≥99.8 mass %) was purchased from Merck (Darmstadt/Germany). Sodium carbonate was dried for 12 h at 120 °C before using. All other chemicals were used without further purification. The purities of all chemicals reported here were adopted from the product data sheets of the suppliers.

Experimental Procedure. Based on the work of Jakobsen et al.[16] and Tomizaki et al.,[27] a procedure was developed to prepare the CO_2 loaded samples. The procedure is briefly described in this section. More details are given in the Supporting Information in Section 2. An aqueous solution of MDEA, whose composition is known from the gravimetrical sample preparation using a laboratory balance (estimated accuracy of the mass fraction of MDEA 2×10^{-5} g/g), was loaded directly inside a valved NMR sample tube with CO_2 and equilibrated at a defined temperature (estimated accuracy 0.3 K). After the loading had been completed, the NMR sample tube was placed inside the NMR spectrometer. The temperature of the sample tube was controlled using a nitrogen gas flow provided by the NMR spectrometer. Prior to the NMR measurements, the temperature control of the nitrogen gas flow had been calibrated to the temperature inside the NMR sample tube in the range of 288 and 333 K with an estimated accuracy of ±0.5 K by making use of the temperature dependence of the ^1H chemical shift difference of the CH_3 and the OH group of a methanol sample as described by Ammann et al.[28]

In this work, the NMR data acquired by Böttinger et al.[4] was reevaluated considering the new knowledge on the monoalkylcarbonate. The procedure of Böttinger et al.[4] is briefly described here. Böttinger et al.[4] designed a special apparatus that mainly consisted of a thermostated view cell with plunger and stirrer in which about 350 mL of aqueous solutions of MDEA were loaded with CO_2. The view cell was connected with heated-loop capillaries to an NMR flow probe head, which was placed inside an NMR spectrometer (400 MHz Unity Inova, Varian, Palo Alto/US-CA). After loading the aqueous solutions of MDEA in the view cell with CO_2, the CO_2 loaded aqueous solution of MDEA was circulated in the loop with a HPLC pump for 1–2 h until steady-state conditions were reached. Then, the HPLC pump was stopped, and the NMR spectra were acquired.

DOI: 10.1021/acs.iecr.7b01937
Ind. Eng. Chem. Res. 2017, 56, 9006–9015

NMR Spectroscopy and Data Analysis. The composition of the liquid phase of the CO_2 loaded aqueous solution of MDEA was determined with quantitative NMR spectroscopy. In this work an NMR spectrometer with a 9.4 T vertical superconducting magnet corresponding to a proton Larmor frequency of 400.25 MHz equipped with a probe with cryogenically cooled electronics was used (magnet Ascend 400, console Avance 3 HD 400, probe CyroProbe Prodigy, Bruker Biospin, Rheinstetten/Germany). All quantitative measurements were carried out with a ^{13}C inverse gated pulse sequence: 60° flip angle, 30 s relaxation delay, and 512−1024 scans. The time-optimized relaxation delay for the chosen flip angle was checked for full relaxation of all species by repeating the analysis of a sample at high CO_2 loading and with very long relaxation delays where full relaxation is certainly ensured. For the additional measurements, a 60° flip angle with a relaxation delay of 100 s and a 90° flip angle with a relaxation delay of 180 s were chosen. No significant differences were found in the quantitative results for the three spectra of the sample. Details on the acquisition and processing parameters are presented in the Supporting Information in Section 3.

In this work, the speciation of the liquid phase for different CO_2 loadings were measured solely with ^{13}C NMR spectroscopy. All species except H_2O, H^+, and OH^- are quantifiable from ^{13}C NMR data. The determination of the true concentration of H_2O, H^+, and OH^- in the liquid phase from ^1H NMR data is error prone because of the superposition of fast exchanging protons and OH groups in the water peak as well as because of the broad water peak, which overlaps with other signals. Thus, only the carbon-containing species were quantified in this work. For that reason, the results are expressed here as molar ratio, ζ_i, of the true amount of species, i, related to the sum of the amount of all carbon-containing species:

$$\zeta_i = \frac{n_i}{\sum_{i=1}^{N_C} n_i}, \qquad N_C = \text{number of carbon-containing species} \tag{1}$$

Furthermore, the evaluation of the ^{13}C NMR spectra gives the CO_2 loading of the aqueous solution of MDEA. The CO_2 loading, α_{CO_2}, is defined as the overall amount of substance, $\tilde{n}_{CO_2}$, of absorbed CO_2 related to the overall amount of substance, $\tilde{n}_{MDEA}$, of MDEA in the liquid phase:

$$\alpha_{CO_2} = \frac{\tilde{n}_{CO_2}}{\tilde{n}_{MDEA}} \tag{2}$$

The CO_2 loading, α_{CO_2}, can be determined in principle also from the gravimetric sample preparation. The small amount of CO_2 that is absorbed into the aqueous solution of MDEA inside the valved NMR tube, however, causes large measurement errors. Thus, only the CO_2 loadings that were determined by NMR spectroscopy are reported in this work.

According to reactions I−VI, α_{CO_2} is calculated from the true amount of substances as follows:

$$\alpha_{CO_2} = \frac{n_{CO_2} + n_{HCO_3^-} + n_{CO_3^{2-}} + n_{MDEACOO^-} + n_{MDEAH^+COO^-}}{n_{MDEA} + n_{MDEAH^+} + n_{MDEACOO^-} + n_{MDEAH^+COO^-}} \tag{3}$$

The molar ratio, ζ_i, and the CO_2 loading, α_{CO_2}, were determined directly from the areas, A_i, under the peaks that correspond to the species i as described below. Figure 1 shows an exemplary ^{13}C spectrum of the liquid phase of an aqueous solution of MDEA loaded with CO_2. By employing two-dimensional NMR techniques, the peaks were assigned to the different species. Details on the two-dimensional NMR techniques are presented in the Supporting Information in Section 1. As NMR spectroscopy is too slow to follow protonation reactions, species present in a protonated and in an unprotonated form are superimposed in their corresponding peaks. For that reason, the index H_x is introduced where "x" represents the number of fast exchanging protons per molecule, which can be either 0 or 1 for $MDEAH_x$ and $MDEAH_xCOO^-$ and 0, 1, or theoretically 2 for H_xCO_3. Peak 3 corresponds to the CH_3 group of $MDEAH_x$, peak 3* corresponds to the CH_3 group of $MDEAH_xCOO^-$, and peak 4 corresponds to the COO^- group of $MDEAH_xCOO^-$. Because of the partial overlapping of peak 3 and peak 3*, both peaks were integrated together so that the total integral $A_3 + A_{3*}$ was determined.

Because of the chosen NMR sequence, the relation between the area, A_i, and the amount of substance, n_i, is described proportionally by the same constant for all species $i = 1...N_C$. Therefore, the observed values, ζ_i^{obs} and $\alpha_{CO_2}^{obs}$, were calculated directly from the peak areas in the ^{13}C NMR spectra:

$$\zeta_{MDEAH_x}^{obs} = \frac{A_3 + A_{3*} - A_4}{A_3 + A_{3*} + A_{H_xCO_3} + A_{CO_2}} \tag{4}$$

$$\zeta_{MDEAH_xCOO^-}^{obs} = \frac{A_4}{A_3 + A_{3*} + A_{H_xCO_3} + A_{CO_2}} \tag{5}$$

$$\zeta_i^{obs} = \frac{A_i}{A_3 + A_{3*} + A_{H_xCO_3} + A_{CO_2}}, \qquad i = H_xCO_3,\ CO_2 \tag{6}$$

$$\alpha_{CO_2}^{obs} = \frac{A_4 + A_{H_xCO_3} + A_{CO_2}}{A_3 + A_{3*}} \tag{7}$$

Only the molar ratios, ζ_i^{obs}, and the CO_2 loading, $\alpha_{CO_2}^{obs}$, were used for the estimation of the chemical equilibrium constants of reactions V and VI (see next section). For presentation reasons, the mole fractions, x_i^{obs}, were calculated as well. Since not all species are present in the ^{13}C NMR spectra, the total amount of substance, which is normally expressed as the sum of the true amount of all species, is not ascertainable from the NMR data. For that reason, the total amount of substance was expressed as the sum of the overall amounts of MDEA and H_2O and the true amount of molecular CO_2: $\tilde{n}_{MDEA}^{obs} + \tilde{n}_{H_2O}^{obs} + n_{CO_2}^{obs}$. The true amounts of H^+ and OH^- are negligible in the investigated pH range and were not considered in the calculation of the total amount of substance. In order to assess the overall amount of water, the initial mass fraction $x_{MDEA}^{(m),0,obs}$ of MDEA in the unloaded aqueous stock solution obtained from the gravimetric sample preparation is used. The mass fraction $x_{MDEA}^{(m),0,obs}$ of MDEA is converted to the molar loading $X_{H_2O,MDEA}^{(n),0,obs}$ of water in MDEA with the molar masses M_{MDEA} = 119.163 g/mol and M_{H_2O} = 18.015 g/mol. The mole fractions, x_i^{obs}, are calculated from the peak areas, A_i:

$$x_{MDEAH_x}^{obs} = \frac{A_3 + A_{3*} - A_4}{(A_3 + A_{3*})(X_{H_2O,MDEA}^{(n),0,obs} + 1) + A_{CO_2}} \tag{8}$$

DOI: 10.1021/acs.iecr.7b01937
Ind. Eng. Chem. Res. 2017, 56, 9006−9015

$$x^{\mathrm{obs}}_{\mathrm{MDEAH_xCOO^-}} = \frac{A_4}{(A_3 + A_{3*})(X^{(\mathrm{n}),0,\mathrm{obs}}_{\mathrm{H_2O,MDEA}} + 1) + A_{\mathrm{CO_2}}} \quad (9)$$

$$x^{\mathrm{obs}}_i = \frac{A_i}{(A_3 + A_{3*})(X^{(\mathrm{n}),0,\mathrm{obs}}_{\mathrm{H_2O,MDEA}} + 1) + A_{\mathrm{CO_2}}} \qquad i = \mathrm{H_xCO_3},\ \mathrm{CO_2} \quad (10)$$

The accuracy of the analysis method was evaluated with samples of sodium carbonate (Na_2CO_3) dissolved in aqueous stock solution of MDEA. The system MDEA−H_2O−Na_2CO_3 was chosen as it contains a subset of the species of the system MDEA−H_2O−CO_2. Moreover, it can be easily prepared on a laboratory scale with high accuracy, and it does not react under the given conditions. Therefore, the molar ratios, ζ_i, of the species MDEA and Na_2CO_3 can both be determined from the gravimetric sample preparation and from ^{13}C NMR data. Using the mass fraction $x^{(\mathrm{m}),0,\mathrm{obs}}_{\mathrm{MDEA}}$ of MDEA in the aqueous stock solution the mole fractions, x^{obs}_i, were calculated as well. By comparing the composition of the liquid phase determined with ^{13}C NMR spectroscopy with the composition determined from the gravimetric sample preparation, the accuracy of the ^{13}C NMR spectroscopy was found to be 11% for mole fractions $x_i <$ 0.001 mol/mol and 5% for mole fractions $x_i \geq$ 0.001 mol/mol. Details on the tests and the results of the evaluation of the accuracy of the analysis method are presented in the Supporting Information in Section 4.

The NMR raw data, the ^{13}C NMR peak areas, of Böttinger et al.[4] were taken and evaluated the same way as the new data (see eqs 4−10).

MODELING AND PARAMETER ESTIMATION

The chemical equilibrium of the reaction j (with j = I, ..., VI) is described here using molality based activities normalized similar to Henry's law for the solutes (including MDEA) and a mole fraction based activity normalized according to Raoult's law for water:

$$K_{\mathrm{a},j}(T) = \prod_i^N a_i^{\nu_{i,j}} \qquad \text{with} \quad a_{\mathrm{H_2O}} = x_{\mathrm{H_2O}}\gamma_{\mathrm{H_2O}}$$
$$\text{and} \quad a_i = \frac{m_i}{m^0}\gamma_i^{\mathrm{m}*} \ \text{for all}\ i \neq \mathrm{H_2O} \quad (11)$$

$\nu_{i,j}$ is the stoichiometric factor of the species, i, for the reaction, j. The dependence of the chemical potential on pressure is neglected so that the chemical equilibrium constant, $K_{\mathrm{a},j}$, is only a function of temperature. The temperature dependence of the chemical equilibrium constants is described by empirical correlations. For reactions I−IV, these correlations are taken from Ermatchkov and Maurer.[5] The activity coefficients, $\gamma_i^{\mathrm{m}*}$, of all species but water are described using an extended form of Pitzer's equation.[29,30] Where available, the interaction parameters are taken from Ermatchkov and Maurer.[5] The parameters describing the interaction of the new species $MDEACOO^-$ and $MDEAH^+COO^-$ with all other species are set to zero. Thus, the activity coefficients of these two species are described by the contribution from the Debye−Hückel-term (empirically modified by Pitzer[29,30]) only. The activity coefficient, $\gamma_{\mathrm{H_2O}}$, of water is calculated from the Gibbs−Duhem equation.

Using eq 11, the molar ratio, ζ_i^{model}, was calculated as a function of the $K_{\mathrm{a},j}$ for a given CO_2 loading, $\alpha^{\mathrm{obs}}_{\mathrm{CO_2}}$, and mass fraction, $x^{(\mathrm{m}),0,\mathrm{obs}}_{\mathrm{MDEA}}$, of the aqueous stock solution of MDEA. The chemical equilibrium constants for reactions V and VI were determined by solving the minimization problem using the sum of squared errors as objective function:

$$K_{\mathrm{a},j}(T_l) = \underset{K_{\mathrm{a},j}\in\mathbb{R}^+}{\arg\min} \sum_{k=1}^{M_l}\sum_{i=1}^{2} (\zeta^{\mathrm{obs}}_{i,k} - \zeta^{\mathrm{model}}_i(K_{\mathrm{a},j}(T_l), \alpha^{\mathrm{obs}}_{\mathrm{CO_2},k}, x^{(\mathrm{m}),0,\mathrm{obs}}_{\mathrm{MDEA},k}))^2$$
$$i = \{\mathrm{MDEAH_x}(1), \mathrm{MDEAH_xCOO^-}(2)\} \qquad k = 1 \ldots M_l \quad (12)$$

where M_l is the total number of observations carried out at the temperature T_l. In a preliminary study, the question was addressed whether both reactions V and VI are needed to adequately describe the measured species distributions. It was found that introducing only reaction V into the model results in an underestimation of the concentration of monoalkylcarbonate at high CO_2 loadings, while introducing only reaction VI results in an underestimation of the monoalkylcarbonate concentration at low CO_2 loadings. This result can be explained by the fact that most of the MDEA is present in its unprotonated form at low CO_2 loadings whereas the MDEA is mainly present in its protonated form $MDEAH^+$ at high CO_2 loadings. So even though the differently protonated forms of monoalkylcarbonate cannot be distinguished spectroscopically, it is possible to retrieve meaningful results on the equilibrium constants of reactions V and VI based on the results at different CO_2 loadings. The optimization problem was solved in MATLAB (The MathWorks, Natick/US-MA) using a trust-region algorithm embedded in the MATLAB solver lsqnonlin. ζ_i^{model} was calculated using a Newton−Raphson algorithm.

RESULTS AND DISCUSSION

Experimental Observation and Data Evaluation. As an example, Figure 3 shows the mole fractions of the different species in the system MDEA−H_2O−CO_2 in chemical equilibrium at 298 K determined by NMR spectroscopy as a function of the CO_2 loading. The results from the model developed in the present work are shown as well. The corresponding numerical values are listed together with the reevaluated data of Böttinger et al.,[4] which was measured at temperatures of 293, 313, and 333 K, in Tables S2 and S3 in the Supporting Information in Section 5.

The data of this work (experimental parameters: temperature of 298 K, composition of the aqueous stock solution of MDEA $x^{(\mathrm{m}),0,\mathrm{obs}}_{\mathrm{MDEA}}$ = 0.4 mol/mol) show good agreement with the reevaluated data of Böttinger et al.[4] (experimental parameters: temperature of 293 K, composition of the aqueous stock solution of MDEA $x^{(\mathrm{m}),0,\mathrm{obs}}_{\mathrm{MDEA}}$ = 0.395 mol/mol). Both experimental procedures, even though very different, and NMR spectroscopic analysis yield the same results. The data of this work show less scattering in the general trends of all species than the reevaluated data of Böttinger et al.[4] Moreover, highly dilute components like the molecular CO_2 are successfully quantified in this work at CO_2 loadings where Böttinger et al.[4] were not able to do so. Both findings indicate a better quality of the NMR data due to the technical advances in NMR spectroscopy. Particularly with regard to the fact that both the concentration of molecular CO_2 and of $MDEAH_x$, which differ by 100 orders of magnitude, can be determined simultaneously with a high accuracy demonstrates the good suitability of the NMR spectroscopic analysis for studying the chemical equilibria in these systems.

The experimental results (cf. Figure 3) show that the absorbed CO_2 is bound both as H_xCO_3 (bicarbonate and

DOI: 10.1021/acs.iecr.7b01937
Ind. Eng. Chem. Res. 2017, 56, 9006−9015

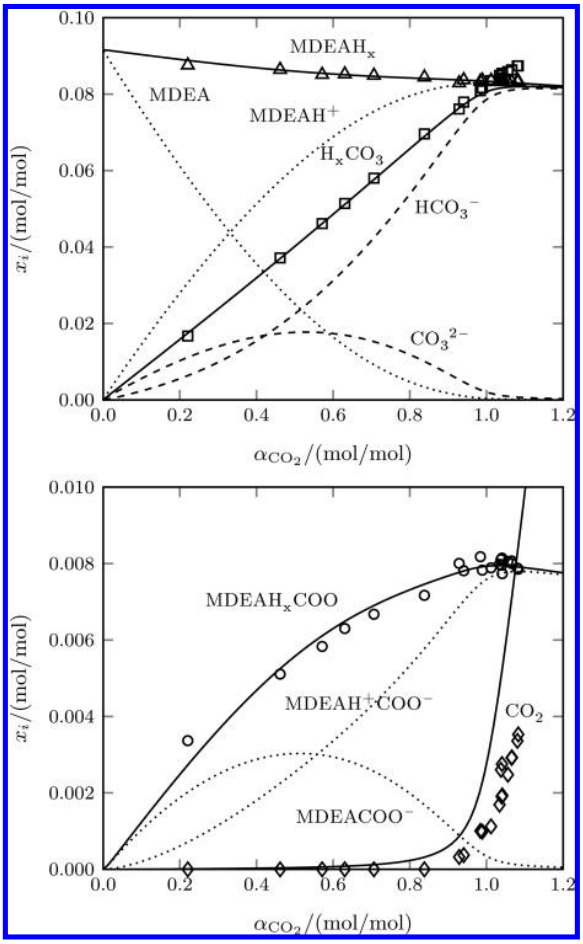

Figure 3. Composition of the liquid phase of the system MDEA–H_2O–CO_2 in chemical equilibrium, for $x^{(m),0}_{MDEA}$ = 0.4 g/g, T = 298 K. Symbols: experimental data from this work. Lines: model prediction.

carbonate) and as MDEAH$_x$COO$^-$ at CO_2 loadings below 1 mol/mol. Because of the formation of MDEAH$_x$COO$^-$, the mole fraction of MDEAH$_x$ decreases to the same extent as the mole fraction of MDEAH$_x$COO$^-$ increases. This observation confirms the occurrence of the two reactions V and VI, which are postulated in this work. At CO_2 loadings larger than 1 mol/mol, no additional MDEAH$_x$COO$^-$ is formed. Instead, molecular CO_2 is observed in quantifiable amounts. Furthermore, the experimental results show that the mole fraction of H$_x$CO$_3$ exceeds the mole fraction of MDEAH$_x$ at CO_2 loadings larger than 1 mol/mol.

The chemical equilibrium constants for reactions V and VI determined by solving the minimization problem given in eq 12 for the different data sets are listed in Table 1. The chemical equilibrium constants at 293 and 298 K are in good agreement

Table 1. Chemical Equilibrium Constants (on the Molality Scale) of the Formation of the Monoalkylcarbonate Determined at Different Temperatures

T (K)	$K_{a,V}$	$K_{a,VI}$
293.15	0.0155	0.0834
298.15	0.0139	0.0777
313.15	0.0114	0.0965
333.15	0.0187	0.0555

showing that the experimental procedure and NMR analysis of this work and of Böttinger et al.[4] yield the same results. The chemical equilibrium constants show no clear trend regarding the dependence on temperature. Because of the better quality of the data of the present work, the chemical equilibrium constant at 298 K is weighted higher than the chemical equilibrium constants at the other temperatures. The chemical equilibrium constants obtained from the uncertainty weighted mean are $K_{a,V}$ = 0.014 for reaction V and $K_{a,VI}$ = 0.082 for reaction VI in the temperature range 293–333 K.

Simulation Results. Figure 3 shows that the experimental results of all species are in good agreement with the simulation results in the range of the CO_2 loading that is relevant for technical application (typical CO_2 loading of the rich solution: α_{CO_2} = 0.6 mol/mol[31]). However, at overall CO_2 loadings larger than 0.9 mol/mol deviations between the experimental results and model prediction of H$_x$CO$_3$ and of dissolved molecular CO_2 become apparent, while MDEAH$_x$COO$^-$ and MDEAH$_x$ are still well described. The model overestimates the mole fraction of molecular CO_2 and underestimates the mole fraction of H$_x$CO$_3$ by the same extent. This discrepancy is found for the original version of the model of Ermatchkov and Maurer[5] as well. Therefore, the introduction of the formation of MDEAH$_x$COO$^-$ into the model did not cause this discrepancy. To elucidate the discrepancy, four hypothesis were tested and discussed in the Appendix. As reported there, all hypothesis were discarded.

Even without overcoming the discrepancy at high CO_2 loadings, the extension of the model proposed in this work is a decisive improvement as the new model is able to predict the formation of monoalkylcarbonate. Figure 4 shows the

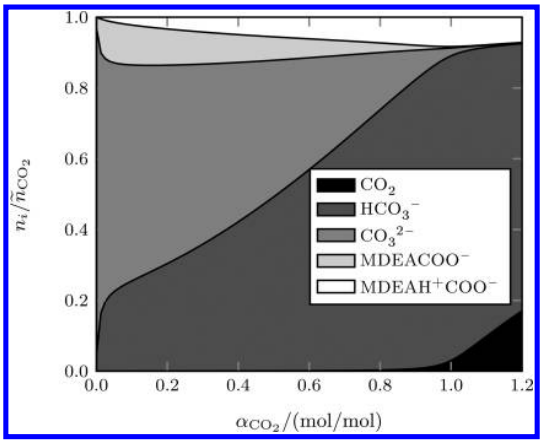

Figure 4. Relative distribution of the overall CO_2 of the different species determined by the present model, for $x^{(m),0}_{MDEA}$ = 0.4 g/g, T = 298 K.

distribution of the overall amount of absorbed CO_2 to the different species as predicted by the model at 298 K. It illustrates the significance of the monoalkylcarbonate formation. More than 10 mol % of the absorbed CO_2 is chemically bound as MDEAH$_x$COO$^-$. Monoalkylcarbonate is already formed at low CO_2 loadings, and it is present in the whole CO_2 loading range relevant for technical application ($\alpha_{CO_2} \leq$ 0.6 mol/mol[31]).

The model presented here can be understood as an extension of the model of Ermatchkov and Maurer[5] for describing the

DOI: 10.1021/acs.iecr.7b01937
Ind. Eng. Chem. Res. 2017, 56, 9006–9015

solubility of CO_2 in aqueous solution of MDEA. While the differences between the model of Ermatchkov and Maurer[5] and the new model are important regarding the speciation in the liquid phase, they are minor regarding the gas solubility. Figure 5 depicts the partial pressure, p_{CO_2}, of CO_2 and the total pressure, p, as a function of the CO_2 loading, α_{CO_2}, at 313 K for both models along with experimental data of Kuranov et al.,[32] Kamps et al.,[33] and Ermatchkov.[34] Obviously, the extension of the model with the two reactions V and VI has only minor effect on the predicted partial pressure, p_{CO_2}, of CO_2 and the total pressure, p (cf. Figure 5). The reason for this result is that neither the predicted activity of CO_2 nor that of H_2O is significantly changed because of the additional reactions in the model. Therefore, the extended Henry's law for CO_2 and the extended Raoult's law for H_2O yield almost the same partial pressure, p_{CO_2}, of CO_2 and the same total pressure, p. The present model, however, overestimated the concentration of CO_2 in the liquid phase as discussed above. If a new chemical equilibrium model was found that predicts the concentration of CO_2 in the liquid phase correctly, the predicted partial pressure of the CO_2 would be underestimated with the present activity model.

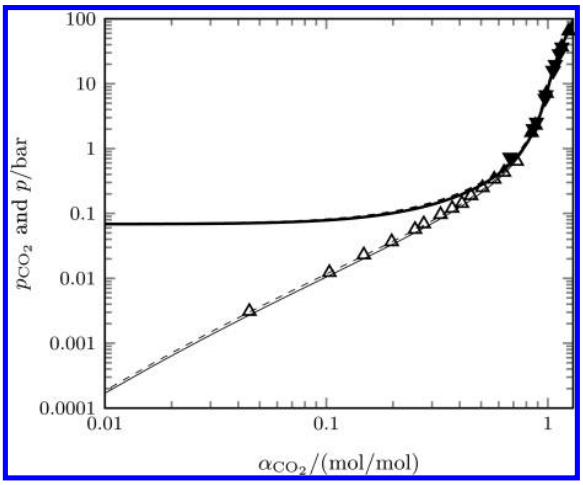

Figure 5. Model results of this work (solid lines) and model results of Ermatchkov and Maurer[5] (dashed lines) for both total pressure (thick lines) and partial pressure of CO_2 (thin lines) above CO_2 loaded aqueous solution of MDEA, for $x^{(m),0}_{MDEA}$ = 0.323 g/g, T = 313 K; (△) partial pressure p_{CO_2} from Ermatchkov;[34] (▲) total pressure p from Kamps et al.;[33] (▼) total pressure p from Kuranov et al.[32]

CONCLUSION

In this work, the equilibrium composition of the liquid phase of the system MDEA−H_2O−CO_2 was investigated. By means of two-dimensional NMR spectroscopy, the presence of monoalkylcarbonate ((*N*-hydroxyethyl)(*N*-methyl)(2-aminoethyl)-hydrogen carbonate) in the liquid phase, which has been widely ignored in the literature so far, is verified. A chemical equilibrium model was developed using experimental data of the composition of the liquid phase that was measured with quantitative NMR spectroscopy in this work and together with NMR data of Böttinger et al.,[4] which was reevaluated taking the presence of monoalkylcarbonate into account. The activities of the species in the liquid phase are described using Pitzer's model. No interaction parameters for the two new components $MDEACOO^-$ and $MDEAH^+COO^-$ were introduced in this work.

The extended model describes the speciation in the industrially relevant range of CO_2 loadings below 0.9 mol/mol for the reported experimental conditions (273−333 K) very well. At the industrially less important range of CO_2 loadings above 0.9 mol/mol, the experimental results and model predictions of the mole fraction of molecular CO_2 and the overall species H_xCO_3 deviates. These deviations are also observed when the model of Ermatchkov and Maurer[5] is used to predict the speciation of the liquid phase. Thus, the discrepancies between model prediction and experimental results are not related to the introduction of the new monoalkylcarbonate species in the reaction system, and they need to be investigated further.

The results obtained in this work prove that NMR spectroscopy is a very versatile tool for the *in situ* analysis of complex reacting systems. It enables not only the identification of unknown species and elucidation of the reaction system but also the accurate measurement of the composition of the reacting system even though the concentration of the species differs by orders of magnitude. Thus, the method can be applied in further work to clarify the remaining open questions in this system.

The study shows that more than 10 mol % of the absorbed CO_2 is bound as monoalkylcarbonate under conditions relevant for technical applications. Thus, the formation of monoalkycarbonate has to be considered in the model describing the liquid phase reactions in the system MDEA−H_2O−CO_2. Furthermore, the knowledge on the formation of monoalkycarbonate and additional species is important for the design of new solvents for the reactive absorption of CO_2. The consequences of the presence of the monoalkylcarbonate on an industrial absorption/desorption process remain to be studied. Also the impact of the formation of monoalkylcarbonate on the regeneration and on the recovery of the MDEA solution need to be investigated in future studies.

APPENDIX: DISCUSSION ON THE DISCREPANCY BETWEEN MODEL RESULTS AND EXPERIMENTAL DATA AT HIGH LOADINGS

To elucidate the discrepancy between the experimental results and model prediction of H_xCO_3 and of molecular dissolved CO_2 at CO_2 loadings larger than 0.9 mol/mol four hypothesis were tested.

The first hypothesis assumes that the chemical equilibrium constant of reaction II is wrong. For increasing the mole fraction of H_xCO_3 and decreasing the mole fraction of CO_2, the chemical equilibrium of reaction II would need to shift to the product side. According to reaction II along with the increased formation of HCO_3^- more protons would be formed as well. Those protons would need to be captured by shifting reactions III and IV to the side of the reactants. However, at loadings larger than 0.9 mol/mol, reactions III and IV are already on the side of the reactants according to the model results. So shifting reaction II to the product side would cause a decrease in pH, which is not observed. The first hypothesis is therefore rejected.

The second hypothesis assumes that the chemical equilibrium constants of reactions V and VI are wrong. In order to obtain more H_xCO_3, the chemical equilibrium constants of those reactions would have to be lower. Lower equilibrium constants of reactions V and VI, however, would deteriorate the

DOI: 10.1021/acs.iecr.7b01937
Ind. Eng. Chem. Res. 2017, 56, 9006−9015

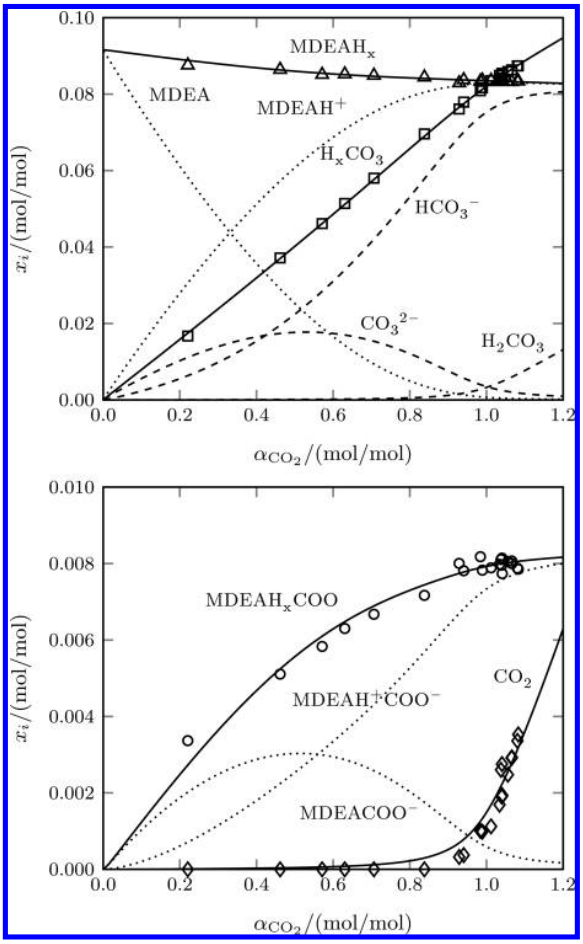

Figure 6. Composition of the liquid phase of the system MDEA–H_2O–CO_2 in chemical equilibrium assuming the formation of carbonic acid (H_2CO_3), for $x^{(m),0}_{MDEA}$ = 0.4 g/g, T = 298 K. Symbols: experimental data from this work. Lines: model prediction.

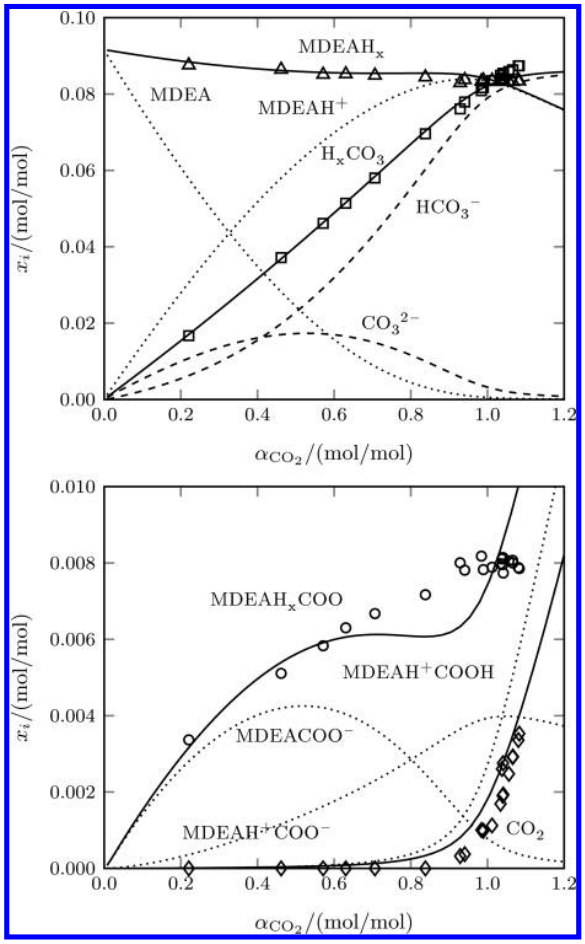

Figure 7. Composition of the liquid phase of the system MDEA–H_2O–CO_2 in chemical equilibrium assuming an additional protonation of the monoalkylcarbonate to monoalkylester (MDEAH$^+$COOH), for $x^{(m),0}_{MDEA}$ = 0.4 g/g, T = 298 K. Symbols: experimental data from this work. Lines: model prediction.

description of the formation of MDEAH$_x$ and MDEAH$_x$COO$^-$. Therefore, also the second hypothesis is rejected.

Obviously, the observations cannot be aligned with the presented reaction system (reactions I–VI). Thus, the third hypothesis assumes that the reaction network is not complete and that the formation of carbonic acid (H_2CO_3) takes place in significant amounts as well. The mole fraction of H_2CO_3 cannot be determined by NMR spectroscopy since it appears in the H_xCO_3 peak of the ^{13}C spectra. Nevertheless, the reaction system was extended with the following reaction of formation of H_2CO_3: $CO_2 + H_2O \rightleftharpoons H_2CO_3$. The formation of H_2CO_3 does not significantly influence the chemical equilibrium of the formation of MDEAH$^+$COO$^-$ and of MDEAHCOO$^-$. Therefore, the chemical equilibrium constants of reactions V and VI were not estimated again. The chemical equilibrium constant of the formation of H_2CO_3 is determined by solving the minimization problem (cf. eq 12) based on the experimental values of $\zeta^{obs}_{H_xCO_3}$ and $\zeta^{obs}_{CO_2}$:

$$K_{a,H_2CO_3}(T = 298.15\ \text{K}) = 2.35$$

As a result the mole fraction of H_xCO_3 and molecular CO_2 is well-described even at CO_2 loadings larger than 0.9 mol/mol. The predicted composition of the liquid phase in MDEA–H_2O–CO_2 assuming the formation of carbonic acid (H_2CO_3) is shown in Figure 6. The obtained chemical equilibrium constant of the formation of carbonic acid, however, is approximately 1300–1700 times higher than the reported value in literature at a temperature of 25 °C.[35,36] Therefore, we discard also the third hypothesis here.

The fourth hypothesis assumes that the monoalkylcarbonate undergoes an additional reaction: MDEAH$^+$COOH $\rightleftharpoons$ H$^+$ + MDEAH$^+$COO$^-$. Since the additional proton of the protonated form of the monoalkylester MDEAH$^+$COOH of MDEA is a fast exchanging proton, MDEAH$^+$COOH cannot be discriminated from the monoalkylcarbonate in the NMR spectra. Because monoalkylcarbonate is a reactant of this proposed reaction, the chemical equilibrium constant of reactions V and VI were estimated again. The resulting chemical equilibrium constants of reactions V and VI, as well as of the formation of MDEAH$^+$COOH, are

$$K_{a,V}(T = 298.15\ \text{K}) = 0.02$$

$$K_{a,VI}(T = 298.15\ \text{K}) = 0.04$$

$$K_{a,MDEAH^+COOH}(T = 298.15\ \text{K}) = 1 \times 10^7$$

DOI: 10.1021/acs.iecr.7b01937
Ind. Eng. Chem. Res. 2017, 56, 9006–9015

The predicted composition of the liquid phase is presented in Figure 7. The manual parameter estimation of the chemical equilibrium constants yielded a good fit for CO_2, but at the expense of the quality of fit of all other species. Thus, also the fourth hypothesis is rejected.

So up to now we cannot explain the experimental data at high CO_2 loadings. The discrepancy, however, occurred in a region that is not relevant in most technical applications.

■ ASSOCIATED CONTENT

Supporting Information

The Supporting Information is available free of charge on the ACS Publications website at DOI: 10.1021/acs.iecr.7b01937.

Structure Elucidation by 2D NMR Spectroscopy, Experimental Procedure, NMR Acquisition and Processing Parameters, Results from Tests with Sodium Carbonate Dissolved in Aqueous Stock Solution of MDEA, and Numerical Results (PDF)

■ AUTHOR INFORMATION

Corresponding Author

*E-mail: erik.vonharbou@mv.uni-kl.de. Phone: +49(0)631 205-4685.

ORCID

Richard Behrens: 0000-0002-4044-2909

Erik von Harbou: 0000-0001-9228-8942

Notes

The authors declare no competing financial interest.

■ ACKNOWLEDGMENTS

Dedicated to Prof. Dr. C. Kreiter on the occasion of his 80th birthday. We thank Philipp Haltenort for supporting us with the experiments presented in this work.

■ NOMENCLATURE

Abbreviations

DEA	diethanolamine
$DMDEA^+$	dimethyldiethanolammonium
H_x	sum of a molecule with different amount of fast exchanging protons (e.g., $MDEAH_x$ as the sum of MDEA and $MDEAH^+$)
HPLC	high-performance liquid chromatography
IR	infrared
MDEA	methyldiethanolamine
$MDEACOO^-$	monoalkylcarbonate of MDEA ((*N*-hydroxyethyl)(*N*-methyl)(2-aminoethyl)-hydrogen carbonate)
$MDEAH^+$	methyldiethanolammonium
$MDEAH^+COO^-$	ammonium ion of the monoalkylcarbonate of MDEA
$MDEAH^+COOH$	ammonium ion of the monoalkylester of MDEA
MEA	monoethanolamine
NMR	nuclear magnetic resonance
TEA	triethanolamine

Symbols and Indices

A_i	peak area under a peak in a ^{13}C NMR spectrum corresponding to the component i
a_i	activity of component i
$K_{a,j}$	chemical equilibirium constant of reaction j
m^0	hypothetical 1 molal solution of solute i in pure water as reference state
m_i	molality of component i in pure water
M_l	total number of observations carried out at temperature T_l
N	number of reactions
N_C	number of carbon-containing species
n_i	true amount of substance of component i
$\tilde{n}_i$	overall amount of substance of component i
T	temperature
$x^{(m),0}_{MDEA}$	mass fraction of MDEA in the unloaded aqueous stock solution
$X^{(n),0}_{H_2O,MDEA}$	molar loading of water in MDEA in the unloaded aqueous stock solution
x_i	mole fraction of component i
α_{CO_2}	CO_2 loading
γ_{H_2O}	mole fraction based activity coefficient of water
γ^{m*}_i	molality based activity coefficient of component i
$\delta^{13}C$	chemical shift of the ^{13}C spectrum in ppm
ζ_i	molar ratio of component i related to the sum of the amount of all carbon-containing species
$\nu_{i,j}$	stoichiometric factor of component i for the reaction j
model	index for an estimated value
obs	index for an observed value

■ REFERENCES

(1) Hasse, H.; von Harbou, I. Post Combustion Capture. In *Carbon Capture and Storage in Europe*; EASAC Secretariat, Deutsche Akademie der Naturforscher Leopoldina: Halle (Saale), 2013.

(2) Tönnies, I.; Mangalapally, H. P.; Hasse, H. Sensitivity Study for the Rate-Based Simulation of the Reactive Absorption of CO_2. *Energy Procedia* **2011**, *4*, 533−540.

(3) Vaidya, P. D.; Kenig, E. Y. CO_2-Alkanolamine Reaction Kinetics: A Review of Recent Studies. *Chem. Eng. Technol.* **2007**, *30*, 1467−1474.

(4) Böttinger, W.; Maiwald, M.; Hasse, H. Online NMR Spectroscopic Study of Species Distribution in MDEA-H_2L-CO_2 and MDEA-PIP-H_2L-CO_2. *Ind. Eng. Chem. Res.* **2008**, *47*, 7917−7926.

(5) Ermatchkov, V.; Maurer, G. Solubility of Carbon Dioxide in Aqueous Solutions of N-Methyldiethanolamine and Piperazine: Prediction and Correlation. *Fluid Phase Equilib.* **2011**, *302*, 338−346.

(6) Derks, P. W. J.; Hogendoorn, J. A.; Versteeg, G. F. Experimental and Theoretical Study of the Solubility of Carbon Dioxide in Aqueous Blends of Piperazine and N-Methyldiethanolamine. *J. Chem. Thermodyn.* **2010**, *42*, 151−163.

(7) Derks, P. W. J.; Huttenhuis, P. J. G.; van Aken, C.; Marsman, J.-H.; Versteeg, G. F. Determination of the Liquid-Phase Speciation in the MDEA - H_2L - CO_2 System. *Energy Procedia* **2011**, *4*, 599−605.

(8) Jørgensen, E.; Faurholt, C. Reactions between Carbon Dioxide and Amino Alcohols. II. Triethanolamine. *Acta Chem. Scand.* **1954**, *8*, 1141−1144.

(9) Hikita, H.; Asai, S.; Ishikawa, H.; Honda, M. The Kinetics of Reactions of Carbon Dioxide with Monoethanolamine, Diethanolamine and Triethanolamine by a Rapid Mixing Method. *Chemical Engineering Journal* **1977**, *13*, 7−12.

(10) Donaldson, T. L.; Nguyen, Y. N. Carbon Dioxide Reaction Kinetics and Transport in Aqueous Amine Membranes. *Ind. Eng. Chem. Fundam.* **1980**, *19*, 260−266.

(11) Barth, D.; Tondre, C.; Lappai, G.; Delpuech, J. J. Kinetic Study of Carbon Dioxide Reaction with Tertiary Amines in Aqueous Solutions. *J. Phys. Chem.* **1981**, *85*, 3660−3667.

(12) Blauwhoff, P. M. M.; Versteeg, G. F.; Van Swaaij, W. P. M. A Study on the Reaction between CO_2 and Alkanolamines in Aqueous Solutions. *Chem. Eng. Sci.* **1984**, *39*, 207−225.

DOI: 10.1021/acs.iecr.7b01937
Ind. Eng. Chem. Res. 2017, 56, 9006−9015

(13) Benitez-Garcia, J.; Ruiz-Ibanez, G.; Al-Ghawas, H. A.; Sandall, O. C. On the Effect of Basicity on the Kinetics of CO_2 Absorption in Tertiary Amines. *Chem. Eng. Sci.* **1991**, *46*, 2927−2931.
(14) Diab, F.; Provost, E.; Laloué, N.; Alix, P.; Souchon, V.; Delpoux, O.; Fürst, W. Quantitative Analysis of the Liquid Phase by FT-IR Spectroscopy in the System CO_2/Diethanolamine (DEA)/H_2L. *Fluid Phase Equilib.* **2012**, *325*, 90−99.
(15) Wong, M. K.; Bustam, M. A.; Shariff, A. M. Chemical Speciation of CO_2 Absorption in Aqueous Monoethanolamine Investigated by in Situ Raman Spectroscopy. *Int. J. Greenhouse Gas Control* **2015**, *39*, 139−147.
(16) Jakobsen, J. P.; Krane, J.; Svendsen, H. F. Liquid-Phase Composition Determination in CO_2-H_2L-Alkanolamine Systems: An NMR Study. *Ind. Eng. Chem. Res.* **2005**, *44*, 9894−9903.
(17) Böttinger, W.; Maiwald, M.; Hasse, H. Online NMR Spectroscopic Study of Species Distribution in MEA−H_2L−CO_2 and DEA−H_2L−CO_2. *Fluid Phase Equilib.* **2008**, *263*, 131−143.
(18) Rainbolt, J. E.; Koech, P. K.; Yonker, C. R.; Zheng, F.; Main, D.; Weaver, M. L.; Linehan, J. C.; Heldebrant, D. J. Anhydrous Tertiary Alkanolamines as Hybrid Chemical and Physical CO_2 Capture Reagents with Pressure-Swing Regeneration. *Energy Environ. Sci.* **2011**, *4*, 480−484.
(19) Perinu, C.; Arstad, B.; Jens, K.-J. ^{13}C NMR Experiments and Methods Used to Investigate Amine-CO_2-H_2L Systems. *Energy Procedia* **2013**, *37*, 7310−7317.
(20) Ciftja, A. F.; Hartono, A.; Svendsen, H. F. Amine Neutralized Amino Acid as CO_2 Absorbents: A Quantitative ^{13}C-NMR Study. *Int. J. Greenhouse Gas Control* **2014**, *27*, 169−177.
(21) Kortunov, P. V.; Siskin, M.; Baugh, L. S.; Calabro, D. C. In Situ Nuclear Magnetic Resonance Mechanistic Studies of Carbon Dioxide Reactions with Liquid Amines in Aqueous Systems: New Insights on Carbon Capture Reaction Pathways. *Energy Fuels* **2015**, *29*, 5919−5939.
(22) Hahnenstein, I.; Albert, M.; Hasse, H.; Kreiter, C. G.; Maurer, G. NMR Spectroscopic and Densimetric Study of Reaction Kinetics of Formaldehyde Polymer Formation in Water, Deuterium Oxide, and Methanol. *Ind. Eng. Chem. Res.* **1995**, *34*, 440−450.
(23) Scheithauer, A.; Brächer, A.; Grützner, T.; Zollinger, D.; Thiel, W. R.; von Harbou, E.; Hasse, H. Online ^1H NMR Spectroscopic Study of the Reaction Kinetics in Mixtures of Acetaldehyde and Water Using a New Microreactor Probe Head. *Ind. Eng. Chem. Res.* **2014**, *53*, 17589−17596.
(24) Perinu, C.; Arstad, B.; Jens, K.-J. NMR Spectroscopy Applied to Amine−CO_2−H_2L Systems Relevant for Post-Combustion CO_2 Capture: A Review. *Int. J. Greenhouse Gas Control* **2014**, *20*, 230−243.
(25) Poplsteinova, J. Absorption of Carbon Dioxide - Modeling and Experimental Characterization. Ph.D. thesis, NTNU, Trondheim, 2004.
(26) Chakma, A.; Meisen, A. Methyl-Diethanolamine Degradation — Mechanism and Kinetics. *Can. J. Chem. Eng.* **1997**, *75*, 861−871.
(27) Tomizaki, K.-y.; Kanakubo, M.; Nanjo, H.; Shimizu, S.; Onoda, M.; Fujioka, Y. ^{13}C NMR Studies on the Dissolution Mechanisms of Carbon Dioxide in Amine-Containing Aqueous Solvents at High Pressures toward an Integrated Coal Gasification Combined Cycle-Carbon Capture and Storage Process. *Ind. Eng. Chem. Res.* **2010**, *49*, 1222−1228.
(28) Ammann, C.; Meier, P.; Merbach, A. A Simple Multinuclear NMR Thermometer. *J. Magn. Reson. (1969-1992)* **1982**, *46*, 319−321.
(29) Pitzer, K. S. Thermodynamics of Electrolytes. I. Theoretical Basis and General Equations. *J. Phys. Chem.* **1973**, *77*, 268−277.
(30) Pitzer, K. S. *Activity Coefficients in Electrolyte Solutions*; CRC Press: Boca Raton, FL, 1991.
(31) Kohl, A. L.; Nielsen, R. *Gas Purification*; Gulf Pub.: Houston, Tex., 1997.
(32) Kuranov, G.; Rumpf, B.; Smirnova, N. A.; Maurer, G. Solubility of Single Gases Carbon Dioxide and Hydrogen Sulfide in Aqueous Solutions of N-Methyldiethanolamine in the Temperature Range 313−413 K at Pressures up to 5 MPa. *Ind. Eng. Chem. Res.* **1996**, *35*, 1959−1966.
(33) Kamps, Á. P.-S.; Balaban, A.; Jödecke, M.; Kuranov, G.; Smirnova, N. A.; Maurer, G. Solubility of Single Gases Carbon Dioxide and Hydrogen Sulfide in Aqueous Solutions of N-Methyldiethanolamine at Temperatures from 313 to 393 K and Pressures up to 7.6 MPa: New Experimental Data and Model Extension. *Ind. Eng. Chem. Res.* **2001**, *40*, 696−706.
(34) Ermatchkov, V. Phasengleichgewichte in Komplexen, Chemisch Reagierenden Systemen: NH_3 + SO_2 + H_2L + Salze Und CO_2 + H_2L + MDEA/Piperazin. Ph.D. thesis, TU Kaiserslautern, Kaiserslautern, 2006.
(35) Stumm, W.; Morgan, J. J. *Aquatic Chemistry: Chemical Equilibria and Rates in Natural Waters*; John Wiley & Sons: New York, 1996.
(36) Soli, A. L.; Byrne, R. H. CO_2 System Hydration and Dehydration Kinetics and the Equilibrium CO_2/H_2CO_3 Ratio in Aqueous NaCl Solution. *Mar. Chem.* **2002**, *78*, 65−73.

DOI: 10.1021/acs.iecr.7b01937
Ind. Eng. Chem. Res. 2017, 56, 9006−9015

Brächer et al., 2018

Reprinted with permission from: A. Brächer, M. Kreußer, S. Qamar, A. Seidel-Morgenstern, E. von Harbou, Application of quantitative inline NMR spectroscopy for investigation of a fixed-bed chromatographic reactor process, Chemical Engineering Journal, Volume 336, 2018, Pages 518-530, DOI 10.1016/j.cej.2017.12.004

Chemical Engineering Journal 336 (2018) 518–530

Contents lists available at ScienceDirect

Chemical Engineering Journal

journal homepage: www.elsevier.com/locate/cej

Application of quantitative inline NMR spectroscopy for investigation of a fixed-bed chromatographic reactor process

Alexander Brächer[a], Lisa Maria Kreußer[b], Shamsul Qamar[c,d], Andreas Seidel-Morgenstern[c,e], Erik von Harbou[a,*]

[a] Laboratory of Engineering Thermodynamics, University of Kaiserslautern, Erwin-Schrödinger-Straße 44, 67663 Kaiserslautern, Germany
[b] Department of Applied Mathematics and Theoretical Physics, Centre for Mathematical Sciences, Wilberforce Road, Cambridge CB3 0WA, United Kingdom
[c] Max Planck Institute (MPI) for Dynamics of Complex Technical Systems, Sandtorstraße 1, 39106 Magdeburg, Germany
[d] Department of Mathematics, COMSATS Institute of Information Technology, Park Road, Chak Shahzad, Islamabad, Pakistan
[e] Otto-von-Guericke-Universität, Institut für Verfahrenstechnik, Universitätsplatz 2, 39106 Magdeburg, Germany

GRAPHICAL ABSTRACT

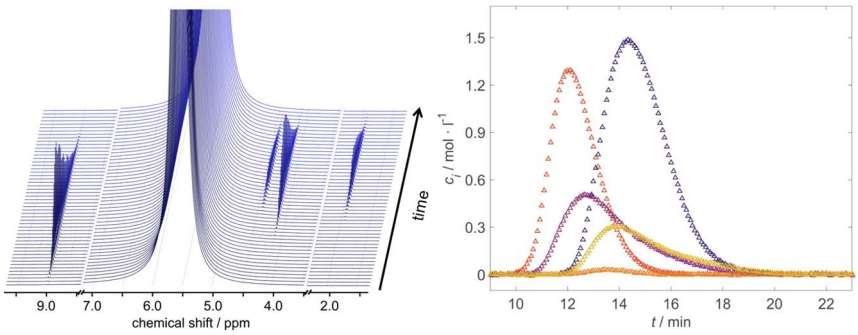

ARTICLE INFO

Keywords:
Fixed-bed chromatographic reactor
Inline NMR spectroscopy
Dynamic process
Modeling and simulation

ABSTRACT

A Nuclear Magnetic Resonance (NMR) spectroscopy method is presented that facilitates inline analysis of dynamic processes. Compared to other commonly used optical inline analysis methods, NMR spectroscopy has the advantage that it can resolve different species in complex multicomponent mixtures. An inline NMR spectroscopy method was optimized to enable analysis with high temporal resolution. The method was applied to study the dynamic behavior of a fixed-bed chromatographic reactor (FBCR) by monitoring the composition at the reactor outlet.

The heterogeneously catalyzed hydrolysis reactions of methyl acetate and methyl formate were chosen as test systems. The influence of different process parameters such as the concentration of reactants, reactor temperature and flow rate of the mobile phase (water) were systematically studied with the presented method. The concentration profiles of the different reactants and products could be determined accurately even though the two hydrolysis reactions proceeded simultaneously in the FBCR and the concentration profiles of the different species overlapped strongly. The measured concentration profiles are in good agreement with additional RI measurements which, however, do not facilitate a component specific analysis.

The accurate measurement of the concentration profiles enables to study the interaction of reaction and separation in the FBCR. At low concentrations of the reactants the measured concentration profiles agree well with predictions based on a model of the FBCR developed in previous works. At higher concentrations, however, the comparison of the predictions and experimental results reveals deficits in the model. The results demonstrate

* Corresponding author.
E-mail address: erik.vonharbou@mv.uni-kl.de (E. von Harbou).

https://doi.org/10.1016/j.cej.2017.12.004
Received 26 September 2017; Received in revised form 30 November 2017; Accepted 1 December 2017
Available online 06 December 2017

that the presented inline NMR spectroscopy method is a valuable tool to gain insights into complex dynamic processes and to gather accurate experimental data that is essential for the development of reliable process models.

1. Introduction

The startup and shutdown of chemical processes, or periodic operation of reactors [1], adsorbers [2,3] or distillation columns [4] are just a few examples of dynamic processes in the chemical industry. Advanced experimental techniques are needed to study such dynamic processes. These experimental studies are required to gather information concerning the operation and design of the process. In particular, they are needed to develop and parametrize models that can reliably predict the behavior of the process and that can be applied to scale-up and to optimize the process. To gather sufficient information on reactions and mass transfer, taking place during the process, it is often necessary to monitor the composition of feed and product streams with an high temporal resolution over a long period of time.

The fixed-bed chromatographic reactor (FBCR) is a good example to illustrate the analytical challenges that emerge when a highly dynamic process is experimentally investigated. FBCR is a hybrid process that combines reaction and separation in one apparatus. This combination has various potential advantages compared to conventional processes, in which the reaction and the separation of the reactants and products is carried out sequentially using different apparatuses. Especially, if the conversion of the reaction is limited by chemical equilibrium, reactive separation processes can be beneficial [5]. Chromatography is a very versatile and highly selective separation technique. Thus it is widely applied for analysis and purification in the food and pharmaceutical industries, and for the production of fine chemicals [6,7]. In a chromatographic process the separation of the species is based on their different adsorptivities to an adsorbent (the so-called stationary phase) that is immobilized in the chromatographic column. In a FBCR, the adsorbent is additionally catalytically active so that reaction and separation of the different species occur simultaneously in the column. Hence, high conversions of the reactants and good separation of the products can be obtained in a FBCR. Despite these advantages, reactive chromatography has not been widely adopted mainly because of its complexity and the resulting difficulties in designing and optimizing this process. Therefore, analytical methods are required that enable detailed experimental investigations of the different processes taking place in a FBCR.

In a typical reactive chromatography experiment, a fixed amount of reactants is injected into the stationary phase passing through the FBCR, and the outlet of the reactor is analyzed i.e. the chromatogram is recorded. Repeated sampling of the reactor outlet and offline analysis of the collected samples using e.g. gas chromatography [8–11] is only possible if the temporal change of the composition of the reactor outlet is slow so that a sampling rate of 1–2 samples per minute, which is feasible for offline analysis, is sufficient. Thus, to study highly dynamic processes, offline analysis methods are often not applicable, and inline analysis methods must be used. In this case, the reactor outlet is directly connected with a detector that is equipped with a flow cell so that the product stream leaving the reactor passes through that flow cell where its composition can be analyzed.

Refractive index detectors (RID) are often used for inline analysis [12–16,11]. Furthermore, the application of UV/Vis [17,13,18], IR [19] or Raman spectroscopy [20,21], either as single detection method or in combination with RID or offline GC for validation, is reported in literature. RI and UV/Vis detectors have several advantages: they have a high data acquisition rate (typically more than one data acquisition per second), they are sensitive and they are easy to use. The main drawback of these detectors is that the composition of multi-component mixtures cannot generally be obtained from the acquired signal. Hence, important information on the performance of the investigated process such as the conversion of the reactants, the yield of the different products or the product purity are not directly quantifiable from the measured chromatograms. Only if the species are well separated in the FBCR, so that the product stream consists effectively only of a binary mixture of an analyte and the mobile phase (e.g. water), the concentration profile of the analyte (that is the concentration of an analyte as function of time) can be determined from the RID measurements or the UV/Vis signal. If the species are not well separated and the measured signal is a superposition of the contribution of the different species, only model based data evaluation is possible [12]. In this case, first the concentration profiles in the reactor outlet are predicted by a process model and then the simulated concentration profiles are translated into the measurement signals using a calibration model of the analysis method. However, the validation of the process model by comparison of RID or UV/Vis signal with the simulation results is often ambiguous. That means the signal predicted by the process model is the same even if different values of the model parameters are applied. All in all, these disadvantages clearly limit the application of RI or UV/Vis detectors for studying these complex dynamic processes.

Compared to RI and UV/Vis detectors, ones based on IR or Raman spectroscopy have the advantage that different species can be distinguished in the acquired signals. The resulting peaks in the IR or Raman spectrum associated to the different species, however, are often overlapped [22,23]. The overlapping of peaks hinders the quantitative analysis of the spectrum and often requires extensive and tedious calibration procedures for all components within a wide concentration range.

Therefore, a method based on NMR spectroscopy is developed in this work that facilitates inline analysis of dynamic processes. NMR spectroscopy has the great advantage that it can often resolve different species in multi-component mixtures even though they are chemically similar. Moreover, little or no effort on calibration is needed to get quantitative results (that is the composition of the investigated mixture) from the acquired NMR spectra [24]. For that reason, quantitative NMR spectroscopy has manifoldly been used for example for monitoring reactions in a variety of different set-ups [25–33].

Coupling of NMR spectroscopy with liquid chromatography (LC) is a well-established technique [34–38]. LC and NMR spectroscopy, however, are not coupled to study the dynamic processes occurring in the LC column but to separate different species from a multi-component mixture and to elucidate successively the structure of the species by NMR spectroscopy methods. Often the flow through the LC column is even stopped when the species of interest has reached the NMR flow cell so that elaborate and time-consuming NMR pulse sequences can be applied. Hence, the application of NMR spectroscopy for studying dynamic processes such as FBCR requires different methods than the well-established methods used for LC-NMR applications.

Compared to the other analytical methods discussed above, NMR spectroscopy has the drawback that its sensitivity (that is the limit of detection) and its signal acquisition rate is typically lower. An enhancement of the signal acquisition rate is in most cases only possible at the cost of sensitivity. Furthermore, a short mean residence time with a narrow residence time distribution from the investigated process stream to the NMR flow cell is important. In that way, the influence of the detector on the concentration profiles is minimized and the measured concentration profiles are as close as possible to the concentration profiles of the investigated process stream. For this reason, an NMR detector was optimized in this work so that a good compromise between sensitivity, temporal resolution and residence time distribution was found.

The developed inline NMR spectroscopy method was applied to study the dynamic behavior of a FBCR. The heterogeneously catalyzed hydrolysis reactions of methyl formate and methyl acetate to methanol, formic acid and acetic acid, respectively were chosen as test systems. In previous studies, Vu and Seidel-Morgenstern[39,12] had investigated the behavior of these test systems in a FBCR by measuring the RI signal at the reactor outlet. The same FBCR was employed in this work so that a direct comparison with the data of Vu and Seidel-Morgenstern [12] is enabled.

In this work, the accuracy of the NMR spectroscopy method was carefully assessed among others by comparing the measurement results with results obtained using a RID. Thereafter, the influence of the temperature, the composition of the reactor feed and the volumetric flow rate on the performance of the FBCR were thoroughly investigated by measuring the concentration profiles of the different species in the product stream. The findings of this work are compared to the results reported by Vu and Seidel-Morgenstern [12]. Furthermore, the reliability of the model of the FBCR developed by Vu and Seidel-Morgenstern [12] was assessed by comparing the measured concentration profiles with model predictions. In this work, we did not only study the two hydrolysis reaction separately but also the parallel hydrolysis of methyl formate and methyl acetate in the FBCR. As the concentration profiles of the reactants and products can be accurately measured with the presented inline NMR analysis method we obtained detailed insights into the reaction and separation processes occurring in the FBCR. For example, we can conclude from the experimental data that the formation of methanol via the faster hydrolysis of methyl formate suppresses the rate of reaction the slower hydrolysis of methyl acetate. These results illustrate the superiority of the presented NMR analysis method compared to other inline methods such as RID. Thus, the NMR spectroscopy method is a valuable tool to gather accurate experimental data of complex processes that is essential to get a comprehensive understanding of the processes and to develop reliable process models.

2. Investigated reaction system

In this study, the heterogeneously catalyzed hydrolysis of methyl formate (MF) forming formic acid (FA) and methanol (MeOH) (see Reaction I), and the hydrolysis of methyl acetate (MA) forming acetic acid (AA) and methanol (see Reaction II) were chosen as suitable model reactions for testing the analytical technique. In both reactions the conversion is limited by chemical equilibrium. In preliminary investigations carried out in chromatographic reactors connected with UV-analysis no side reactions were observed under the applied conditions [39,12].

$$\underset{\text{MF}}{HCOOCH_3} + \underset{\text{W}}{H_2O} \overset{H+}{\rightleftharpoons} \underset{\text{FA}}{HCOOH} + \underset{\text{MeOH}}{CH_3OH} \quad \text{(I)}$$

$$\underset{\text{MA}}{CH_3COOCH_3} + \underset{\text{W}}{H_2O} \overset{H+}{\rightleftharpoons} \underset{\text{FA}}{CH_3COOH} + \underset{\text{MeOH}}{CH_3OH} \quad \text{(II)}$$

The same strongly acidic surface-sulfonated ion-exchange resin Dowex 50W-X8 as used in the studies of Vu [39] as well as of Vu and Seidel-Morgenstern [12] was employed as catalyst in the present work. The spherical catalyst particles have particle sizes between 37–74 μm. They were packed in laboratory scale HPLC columns (length: 250 mm, inner diameter: 4.6 mm) resulting in a porosity of the catalyst bed (when filled with water) of $\epsilon = 0.33$. Evaluating the results of preliminary investigation with pure compounds the following elution order of the different species in the column was found at room temperature using water as the mobile phase:

$$FA < AA < MeOH < MA < MF \quad (1)$$

The observed retention times were translated using classical methods into adsorption equilibrium constants (for details, see [39,12]).

3. Modeling and simulation of the FBCR

The concentration profiles of the analytes in the liquid phase of the FBCR can be described by a coupled system of partial differential equations (PDEs) that are derived from the mass balances of the analytes under the following assumptions:

- the catalyst bed is homogeneously packed,
- the volumetric flow rate is constant,
- no concentration gradients occur in radial direction,
- the temperature in the FBCR is constant,
- all effects broadening the RTD in the FBCR can be combined into an apparent dispersion coefficient,
- autocatalytic homogeneous reactions are negligible,
- the change of concentration of water is negligible,
- the rate of conversion of the reactants is determined by the reaction on the catalyst,
- the adsorption of the analytes from the liquid phase to the catalyst phase is always in equilibrium,
- the adsorption isotherms are linear.

More precisely, this mathematical model can be regarded as a system of convection-reaction-diffusion equations whose solution is a function of time and of the axial position in the FBCR. The injection of the analytes is modeled by a rectangular injection profile given by standard Danckwerts boundary conditions. Furthermore, it is assumed that initially only pure water is present in the liquid phase of the FBCR. Details on the model and its derivation are presented by Vu and Seidel-Morgenstern [12]. The values of all model parameters such as equilibrium and kinetic constants, the dispersion coefficient and the bed porosity are taken from Vu and Seidel-Morgenstern [12] and Vu [39]. All parameters were determined only at room temperature for the catalyst used in this work. However, to enable the simulation of the influence of the temperature, the relevant parameters (e.g. activation energy) were adopted from another catalyst (same ion exchange resin but different charge) that was also used for FBCR experiments and that was thoroughly studied by Vu [39]. All model parameters used in this study are listed in the Supplementary data in Table S.2.

To enable a direct comparison between the model predictions and the measurements by NMR and RID, the residence time distribution (RTD) in the detector unit (that is the RTD in the capillaries connecting the reactor outlet with the NMR and RID) has to be considered as well. This RTD is described by an axial dispersion model. This model is parameterized by RTD measurements carried out in this work. Details are given in Section 4.4.2. All model predictions of the concentration profiles reported in the work are calculated by solving the PDE of the FBCR and convoluting the measured concentration profiles with the residence time distribution function of the detector unit (for details, see Supplementary data Section S.3.1).

To solve numerically the system of PDEs forming the equilibrium dispersion model we use Strang splitting on an equidistant spatial grid, resulting in convection-diffusion equations as well as ordinary differential equations on fixed grid points. The former can be solved by combining the finite volume method and the flux-limiter method, while the latter can be solved by applying the explicit Euler scheme. Here the size of the time step has to be chosen in such a way that convergence of the numerical scheme can be guaranteed.

The scheme is implemented in Matlab (version 8.4, MathWorks, Natick, MA, USA) and 750 spatial grid points are considered. The accuracy of the numerical scheme is verified by comparing the simulation results to the analytical solution of a dispersion model describing the concentration profiles in the FBCR when no reaction occurs [40]. Furthermore, the error in the mass balance of amount of substance of the analytes (i.e. the stoichiometric error e_i^{stochi}) is calculated for each simulation result (details are given in the Supplementary data Section S.1.2). The relative stoichiometric error of all analytes was less than 1% for all simulation results.

4. Experimental section

4.1. Chemicals

Methyl formate (≥ 0.99 g/g), methyl acetate (≥ 0.998 g/g), formic acid (≥ 0.98 g/g) and acetic acid (≥ 0.99 g/g) were purchased from Sigma Aldrich, Munich, Germany, and methanol (≥ 0.998 g/g) from Merck, Darmstadt, Germany. Purified (deionised) water was taken from a Milli-Q system, Millipore, Massachusetts, USA. The chemicals were treated in an ultrasonic bath prior to the experiments for degasing. The Dowex 50 W-X8 ion exchange resinion exchange resin was purchased from Sigma-Aldrich, Munich, Germany.

4.2. Experimental apparatus and procedure

A schematic drawing of the experimental apparatus is shown in Fig. 1. The FBCR was built of a stainless steel column with a internal diameter of 4.6 mm and a length of 250 mm in which the catalyst particles were immobilized. The same FBCR was used by Vu and Seidel-Morgenstern [12] for reactive chromatography experiments. Details on the preparation of the catalyst bed and the experiments carried out with the FBCR are given in the PhD thesis of Vu [39].

The FBCR was submersed in a water bath for temperature control. To preheat the feed before entering the FBCR, about one metre of feed line (made of polyetheretherketone, PEEK) was coiled up and also thermostatted in the water bath. The temperature of the water bath was controlled using a cryostat (F12-ED, Julabo GmbH, Seelbach, Germany) with an accuracy of ±1 K. Since the hydrolysis reactions of methyl formate and methyl acetate (see Reaction I and II) are both only weakly endothermic [41], it is assumed that the temperature within the FBCR column was constant and that it corresponded to the temperature of the water bath which was measured by an additional thermometer (Pt100, testo 701, Testo SE & Co, Lenzkirch, Germany, accuracy of ±0.5 K). A HPLC pump (Smartline 1000, Knauer, Berlin, Germany) was used to feed the stationary phase, i.e. water, at a constant volumetric flow rate into the FBCR. The flow rate was monitored with a flow meter (Bronkhorst High-Tech B.V., mini Cori-Flow, Ruurlo, Netherlands, accuracy of the measured absolute mass flow within the observed flow regime of ±1% according to the manufacturer's information) that was installed directly after the pump. The maximum relative fluctuation of the detected volumetric flow rate was less than ±0.5%.

The products leaving the FBCR were fed into the so-called detector unit that comprises first the NMR spectrometer (Avance III HD 400, Bruker Biospin, Rheinstetten, Germany, operating at a ^{1}H resonance frequency of 400.25 MHz with a vertical 9.4 T superconducting magnet) and second the RID (Optilab T-rEX, Wyatt Technology Corporation, Santa Barbara, CA, USA). The product stream leaving the RID was collected in an unpressurized vessel.

To avoid an undesirable residence time distribution, the applied NMR probe (BBO Prodigy CryoProbe equipped with the CyroFit flow upgrade, Bruker Biospin, Rheinstetten, Germany) was customized in this work. Instead of the flow cell, designed by the manufacturer, a straight capillary made of PEEK with an inner diameter of 1 mm was mounted inside the CryoProbe. The chosen diameter of the capillary is the best compromise between a short residence time in the spectrometer and sensitivity of the NMR measurement. The filling factor of the RF coil in the customized set-up is reduced by a factor of 10 compared to the standard flow cells. This effect is partially compensated by the use of the CryoProbe. The electronics inside the CryoProbe are cooled with liquid nitrogen so that the sensitivity of the measurement is enhanced by a factor of three compared to standard NMR probes whose electronics are operated at room temperature.

Two injection valves both connected to a sample loop are installed within the set-up: the injection valve V1 (Rheodyne 7725i, 6-port, 2-way, IDEX, Oak Harbor, WA, USA) before the FBCR and the injection valve V2 (Rheodyne 7000, 6-port, 2-way, IDEX, Oak Harbor, WA, USA) just after the FBCR, see Fig. 1. The injection valve V1 is used to inject a mixture of reactants (water, methyl formate and/ or methyl acetate) into the reactor feed stream. The injection valve V2 is used to inject calibration samples with known composition into the detector unit. The injection volume of the mixtures of reactants, i.e. the volume of the sample loop connected to V1, is 540 µl ±10 µl. This volume was determined in preparatory calibration experiments (for details, see Supplementary data Section S.1.1). The injection volume of the calibration samples is about 5 ml. All lines installed in the set-up (with the exception of the capillary mounted inside the NMR probe) are standard PEEK capillaries with an inner diameter of 0.25 mm.

The experiments were carried out as follows. The pump, feeding the water into the FBCR, and the cryostat were started. After the water bath had reached the desired temperature and the flow rate had been steady for at least 10 min, different calibration samples with known composition were sequentially fed via the sample loop connected to the injection valve V2 into the detector unit. This procedure is called pre-calibration. Next, the main experiment was started by injecting a mixture of reactants with known composition via the sample loop connected to the injection valve V1 into the feed stream of the FBCR. To monitor the stability of the analysis method additional calibration samples were fed into the detector unit using injection valve V2 after a delay (about 5–30 min depending on the flow rate). The duration of the delay was chosen sufficiently long enough to ensure that the concentration of the analytes in the NMR flow cell was zero before the calibration sample entered. This procedure is called post-calibration. During the whole FBCR experiment comprising the pre-calibration, the main experiment, and the post-calibration, the flow rate and the temperature of the reactions was held constant. Furthermore, NMR spectra were acquired at frequent intervals and the RID was continuously measured.

The starting time of the experiment ($t = 0$) is defined as the time when the injection of the mixture of reactants was started by switching the injection valve V1. When the valve was switched the RID measurements were automatically started and the time of the experiment was internally recorded by the RID control unit. As the acquisition of NMR spectra had been initialized several minutes before the main experiment was started, the timestamp of the start of the NMR acquisition was referenced to the time of the experiments using a stop watch (Prisma 200, Hanhart, Gütenbach, Germany). Details on the whole sequence of a reactive chromatography experiment (FBCR experiment) including the pre- and post-calibration are given in the Supplementary data Section S.1.4.

The calibration samples and the mixtures of reactants, which were injected into the stationary phase, were prepared as follows: the desired amount of analyte (methyl formate, methyl acetate, methanol, formic acid or acetic acid) was filled into a measuring cylinder and the mass of sample was recorded using a laboratory balance (XS603S Delta Range, Mettler-Toledo GmbH, Gießen, Germany, accuracy of $\Delta m = \pm 0.01$ g). Then, water was added into the measuring cylinder to gain the desired concentration of analytes. The estimated error of the concentration of the analytes in the calibration samples and mixtures of reactants respectively is ± 0.005 mol/l.

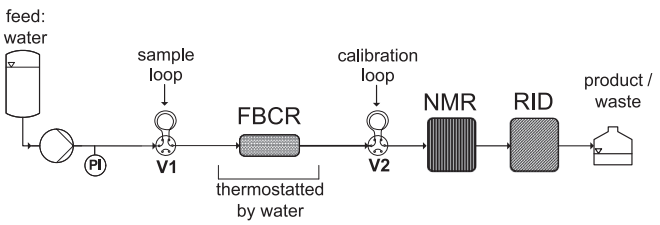

Fig. 1. Overview of the apparatus used for the FBCR experiments.

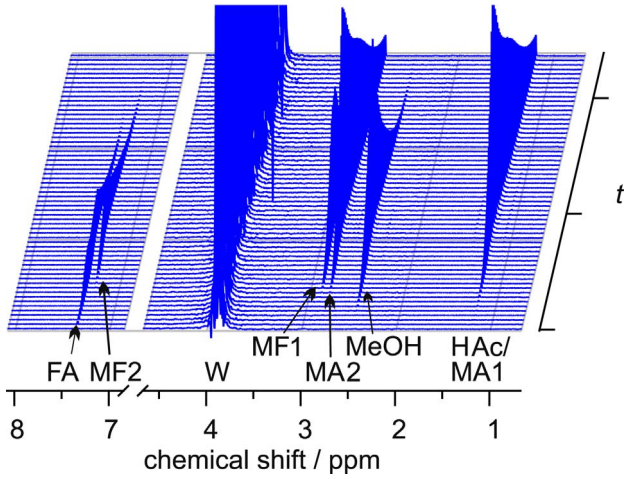

Fig. 2. Stacked plot of the NMR spectra acquired over time during a FBCR experiment (T= 25 °C, $\dot{V}$ = 300 µl/min and $c_{MF}^{inj} = c_{MA}^{inj}$ = 1.5 mol/l) showing the signal peaks of all species present in the two test systems.

4.3. Analysis methods

The ^{1}H NMR spectra were acquired with a flip angle of 30°, an acquisition time of 2 s and a pulse repetition time of 5 s. The small flip angle of only 30° was chosen as a compromise between high sensitivity (i.e. flip angle of 90°) and high pulse repetition rate (i.e. small flip angle). Preliminary tests were carried out to confirm that the delay between the repeated RF pulses was sufficiently long to ensure a full relaxation of the nuclei prior to their excitation. Fig. 2 shows an example of the NMR spectra acquired over time during a FBCR experiment. The NMR spectra were processed (i.e. baseline correction, phasing and peak integration) using the software package MestReNova (Mestrelab Research, Santiago de Compostela, Spain, version 6.0).

The concentration of the analytes c_i^{NMR} (with i= MF, MA, MeOH, FA and AA) was determined from the NMR signal S_i^{NMR} corresponding to the analyte i using a one-point calibration as given in Eq. (2). The NMR signal of the analyte S_i^{NMR} was calculated from the areas under the corresponding peaks in the NMR spectrum as explained in detail in the Appendix A in Table 2. The peak areas were determined by direct integration of the NMR spectrum.

$$c_i^{NMR} = k_i^{NMR} \cdot S_i^{NMR} \quad \text{with:} \quad k_i^{NMR} = \frac{c_i^{cal}}{\overline{S}_i^{NMR,\,cal}} \tag{2}$$

Given by the high linearity of the NMR method, the calibration factors k_i^{NMR} are not a function of the concentration of the analytes. Preliminary tests confirmed the uniformity of the calibration factors. Thus, all calibration samples were prepared with a constant concentration of analytes of about 1 mol/l. The NMR signal $\overline{S}_i^{NMR,\,cal}$ used for the calibration (see Eq. (2)) is calculated from the mean value of the peak areas in the NMR spectra which were measured while the NMR flow cell was filled with the calibration sample only.

Because of the incomplete equilibrium magnetization of the nuclei in the NMR flow cell, the calibration factors are, however, dependent on the volumetric flow rate, especially at high flow rates (a detailed discussion on the influence of flowing samples on the measured NMR signals is given e.g. in [32,42,43]). Thus, the peak area of at least one analyte was calibrated before (pre-calibration) and after each experiment (post-calibration). If the calibration factors of the pre- and post-calibration run disagreed by more than 3%, the results of that experiment were not evaluated and the whole experiment was repeated.

The comparably fast autocatalytic reaction of methyl formate with water requires that calibration samples with these two species have to be prepared directly before each calibration run. Preliminary calibration experiments, however, confirmed that the calibration factor of methyl formate k_{MF}^{NMR} and the calibration factor of methanol k_{MeOH}^{NMR} agree well within the experimental uncertainty. For that reason and to avoid further autocatalytic reactions, only binary mixtures of water with methanol, with formic acid, with acetic acid or with methyl acetate were used as calibration samples for the pre- and post-calibration runs (see Section 4.2).

The calibration of the RID signal was carried out in a similar way. Binary calibration samples, containing water and one analyte (methyl formate, methyl acetate, methanol, formic acid and acetic acid), were passed through the RID at a constant flow rate. The mean value of the measured refractive index of the analyte in water $\overline{S}_i^{RID,\,cal}$ is related to the known concentration of the analyte, see Eq. (3).

$$c_i^{RID} = k_i^{RID} \cdot S_i^{RID} \quad \text{with:} \quad k_i^{RID} = \frac{c_i^{cal}}{\overline{S}_i^{RID,\,cal}} \tag{3}$$

In contrast to the NMR calibration factors, the RID calibration factors k_i^{RID} are independent of the flow rate (at least within the range of flow rates applied in this work). Furthermore, the RID measurement features a great stability of the calibration factors. Thus, the RID calibration factors were determined prior to the FBCR experiments. More details on the calibration of the RID including a table of the calibration factors are given in the Supplementary data Section S.1.3.

If the product stream contains (besides water) more than one analyte, the signal of the RID is the sum of the contribution of each species. In this case, the concentration of the analytes often cannot be determined by the measured refractive index of the mixture.

4.4. Preliminary tests

4.4.1. Quality of the measurements

Before the reactive chromatography experiments were started, several tests were carried out to assess the quality of the measurements. The accuracy of the measurement of the concentration of analytes using the RID was determined by injecting binary mixtures of water and analyte (prepared as described in Section 4.2) directly into the feed line of the RID. The mean relative deviation between the expected and measured value was found to be ±0.5%.

The error of the concentration of analytes determined by a single scan NMR measurement (as applied in the FBCR experiments) is mainly caused by fluctuation of the peak area in the NMR spectrum. The reasons for these fluctuations are manifold: errors during the processing of the acquired spectrum (e.g. phase and baseline correction), fluctuations in the magnetic field strength etc. The observed scattering of the concentration of the analytes during the calibration run lies within a 95% confidence interval of 0.005 mol/l (a plot of the calibration run is depicted in the Supplementary data Fig. S.1). The small scatter of the NMR spectroscopy based measurements illustrates the high stability of modern high field NMR spectrometers.

Another indicator for the accuracy of the concentration measurements is the error of the mole balance (or component specific mass balance). The error of the mole balance is defined as the difference between the amount of substance of analyte injected into the column and the total amount of substance of analyte that has left the reactor during the measurements. The latter is determined by integrating the measured concentration profile in the product stream over time (see Supplementary data Eq. (S.2)). Details on the experimental parameters and the results are given in the Supplementary data Section S.3.2. The relative error of the mole balance lies in a range of 0.3–2.1% for the NMR measurements and in a range of 0.6–3.5% for the RID measurements. The observed small errors confirm the accuracy and precision of the chosen measurement methods.

The reactive mixture that is analyzed during a FBCR experiment usually contains more species than in the binary mixture applied for the calibration and accuracy test runs. Thus, also more peaks are present in the acquired spectra and the analysis of the NMR spectra becomes more

Table 1
Overview of the conducted FBCR experiments.

Exp. No.	Reaction	varied parameters
MF1-3	I	$\dot{V}$
MF2,4-7	I	T
MF 8-12	I	c_{MF}^{inj}
MA1-3	II	T
MFMA1-3	I + II	c_{MF}^{inj},c_{MA}^{inj}

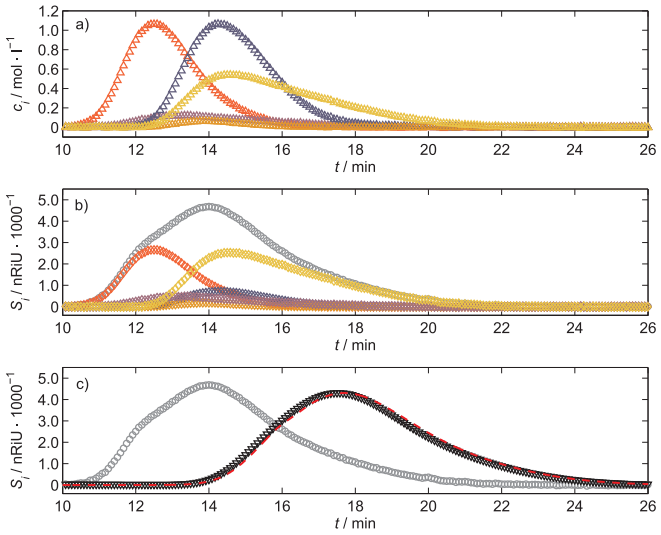

Fig. 3. Comparison of the results that were obtained by NMR spectroscopy and RID measurements for the FBCR experiment MFMA2 of the parallel methyl formate and methyl acetate hydrolysis reaction. Experimental parameters: T = 25 °C,$\dot{V}$ = 300 µl/min, c_{MF}^{inj} = 1.5 mol/l and c_{MA}^{inj} = 1.5 mol/l. (a) Concentration profiles of the analytes measured by NMR spectroscopy as function of time. (b) RID signal simulated from the measured concentration profiles of the analytes in the NMR flow cell as function of time. (c) Comparison of the simulated RID signal and the signal measured in the RID. Symbols: calculated contribution of each analyte to the RID signals (◇), RID signal simulated from the NMR measurements (○) and RID signal simulated from the NMR measurements and from the RTD of the analytes between the NMR flow cell and the RID (▽). Measured RID signal (– – –). Colors of the symbols: FA (—), MF (—), MeOH (—), AA (—), MA (—).

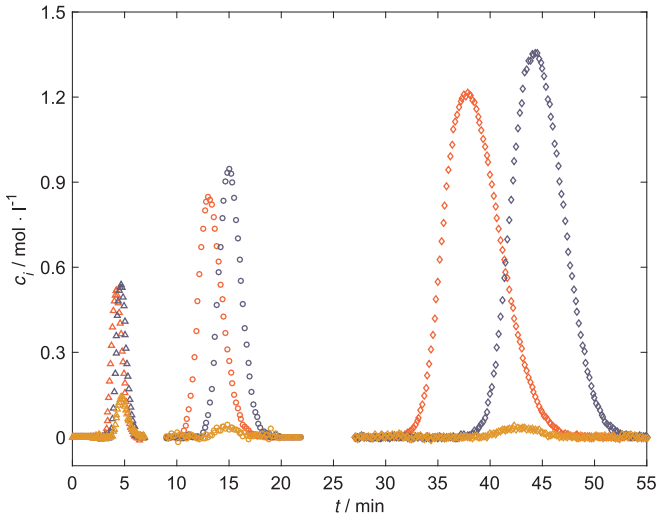

Fig. 4. Influence of the volumetric flow rate on the concentration profiles of the analytes measured with NMR spectroscopy. FBCR experiments MF1-MF3 (hydrolysis of methyl formate). Experimental parameters: $\dot{V}$ = 100 (◇), 300 (○) and 1000 µl/min (△) at T = 25 °C and c_{MF}^{inj} = 1.5 mol/l. Colors of the symbols: FA (—), MF (—), MeOH (—).

difficult e.g. because peaks are not well separated. Therefore, the error of the concentration measurement carried out during the FBCR experiments is larger compared to the concentration measurements carried out during the calibration and test runs. An estimation yields an error of the concentration measurement by NMR of ± 0.02 mol/mol.

4.4.2. Residence time distribution measurements

As the concentration profiles of the analytes are subjected to dispersion while passing from the outlet of the FBCR to the NMR flow cell and further to the RID, the residence time distribution (RTD) from the FBCR outlet to the NMR flow cell and as well as from the NMR flow cell to the RID was determined experimentally. Different binary mixtures of water and an analyte as well as a quaternary mixture of water, methanol, methyl acetate and acetic acid were injected (V^{inj} = 540 µl) into the product stream directly after the FBCR (see Fig. 1) at a constant volumetric flow rate of $\dot{V}$ = 300 µl/min (for details, see Supplementary data Section S.3.1.).

The concentration profiles of the analytes measured with NMR spectroscopy are nearly identical. They are symmetrical and have a Gaussian shape. A plot of the measured concentration profiles is shown in the Supplementary data in Fig. S.2. The mean residence time measured in each experiment gives an averaged value of 4.42 min with a standard deviation of 0.02 min. The variance of the residence time distribution yields an averaged value of only 0.65 min^2 with a standard deviation of 0.05 min^2. The same results were also found for the concentration profiles determined by the RID. These results confirm that no undesired effects such as strong back-mixing or component specific adsorption occur while the analytes are passing from the FBCR to the detector unit. Thus, the applied detector unit comprising the NMR flow cell and the RID is well suited for the investigation of flowing reactive multi-component mixtures.

Assuming the injection of analytes follows a rectangular concentration profile, the measured concentration profiles were applied to parametrize two dispersion models that describe the RTD from the FBCR to the NMR flow cell and the RTD from the NMR flow cell to the RID. Details including the estimated parameters of the dispersion model are given in the Supplementary data Section S.3.1.

To confirm the axial dispersion coefficient inside the FBCR reported by Vu and Seidel-Morgenstern [12], a non-reactive binary mixture of water and methanol was injected before the FBCR reactor applying the same operation conditions as used for the reactive FBCR experiments, and the concentration profile of methanol was measured with NMR spectroscopy. The measured signal was compared to the model prediction (that is the solution of the PDE of the FBCR without reaction which is subjected to the RTD between the FBCR and the NMR flow cell). The good agreement between the model prediction and the experimental results confirms the applied model parameters.

5. Results and discussion

5.1. Overview of experimental studies

The presented FBCR set-up was used to carry out different parameter studies. Both the single reaction of either methyl formate with water (see Reaction I) or of methyl acetate with water (see Reaction II as well as the parallel reaction of methyl formate and methyl acetate with water (i.e. Reaction I + II) were studied. The following parameters were varied: the volumetric flow rate of the mobile phase ($\dot{V}$), the temperature of the FBCR (T) and the concentration of the injected reactants (c_i^{inj} with i = MF, MA). All other parameters such as the injection volume V^{inj} were kept constant. Table 1 gives an overview of the conducted parameter studies and the respective reactive system of the FBCR experiments. Details on the experimental parameters and the determined conversions as well as the corresponding concentration profiles of the analytes are reported in the Supplementary data Section S.3.

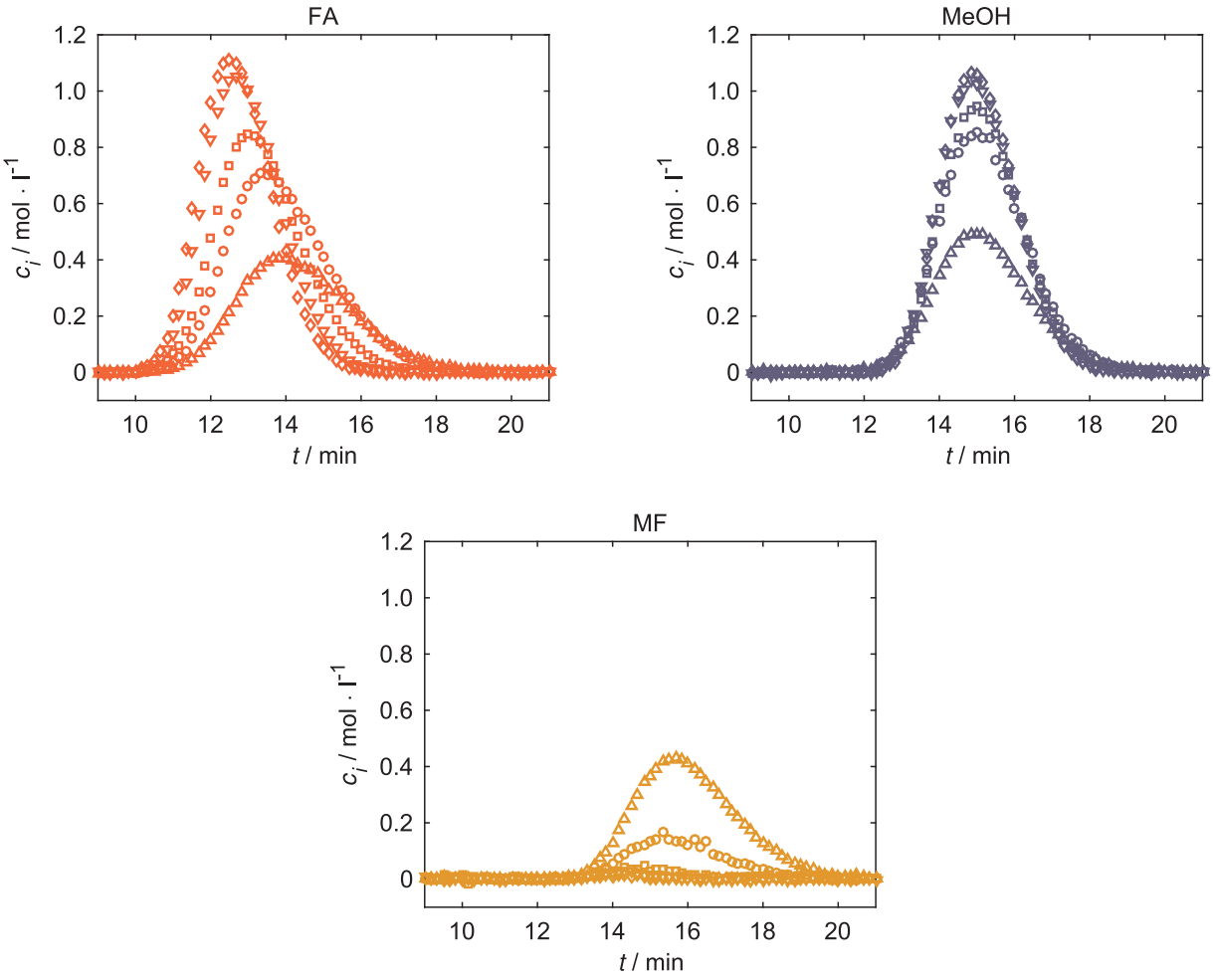

Fig. 5. Influence of the temperature on the concentration profiles of the analytes measured with NMR spectroscopy. FBCR experiments MF2 and MF4-MF7 (hydrolysis of methyl formate). Experimental parameters: T = 5 °C (△), 15 °C (○), 25 °C (□), 35 °C (▽) and 45 °C (◇) at $\dot{V}$ = 300 µl/min and c_{MF}^{inj} = 1.5 mol/l.

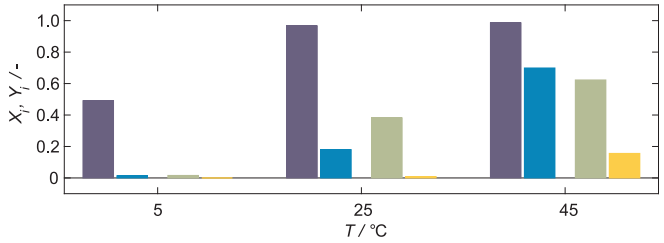

Fig. 6. Comparison of the conversion of ester X_i and the yield of acid Y_i observed at different temperatures for the hydrolysis of methyl formate (FBCR experiments: MF4, MF2 and MF7) and the hydrolysis of methyl acetate (FBCR experiments: MA1, MA2 and MA3). Experimental parameters: c_{MF}^{inj} = 1.5 mol/l, c_{MA}^{inj} = 1.5 mol/l and $\dot{V}$ = 300 µl/min. X_{MF} (▬), X_{MA} (▬), Y_{FA} (▬) and Y_{AA} (▬).

5.2. Comparison of the analysis methods

A comparison of the results that were obtained by NMR spectroscopy and by RID measurements is depicted for a FBCR experiment with parallel hydrolysis of methyl formate and methyl acetate in Fig. 3. The upper part of Fig. 3 shows the concentration of the analytes directly measured by NMR spectroscopy. Using the RID calibration factors, the contribution of each analyte to the RID signal (see Eq. (3)) and the RID signal itself (that is the sum of all contributions), which would be measured in the NMR flow cell, is calculated from the concentration profiles measured using NMR spectroscopy (see middle part of Fig. 3). By means of the function describing the RTD from the NMR flow cell to the RID, which was determined in independent measurements (see Section 4.4.2), the influence of the time delay and the dispersion on the simulated RID signal can be taken into account (for details, see Supplementary data Section S.3.1.) and the measured and the simulated RID signal can be directly compared as shown in the lower part of Fig. 3. The simulated and measured RID signals are in good agreement. The same holds for the other FBCR experiments carried out in this work. In addition, the measured and the simulated RID signals were integrated over time. The mean relative deviation between the two integral values is about 3% for all FBCR experiments carried out in this work (for details, see Supplementary data Section S.3.4).

Furthermore, the experimental results prove the superiority of the NMR spectroscopy measurement compared to the RID measurements. The NMR based analysis method allows determination of concentration profiles of all analytes with a sufficiently high temporal resolution (12 data points per minute) even though the concentration profiles strongly overlap and the concentration of analytes is small. Therefore, important information on the performance of the FBCR such as the extent of the different reactions, the conversion of the reactants and the yield of the products can be determined. Given by the fact that the change of amount of substance of reactants and products, which occurs during a FBCR experiment, can be directly calculated from the measured concentration profiles, it can be tested whether the stoichiometry of the given reaction system is fulfilled. Thereby, an additional and very useful measure to assess the accuracy of the analysis method is provided. This stoichiometric error (details on the definition are given in the Supplementary data Section S.1.2.), averaged over all analytes and FBCR experiments is only about 0.02 mmol (the injected amount of

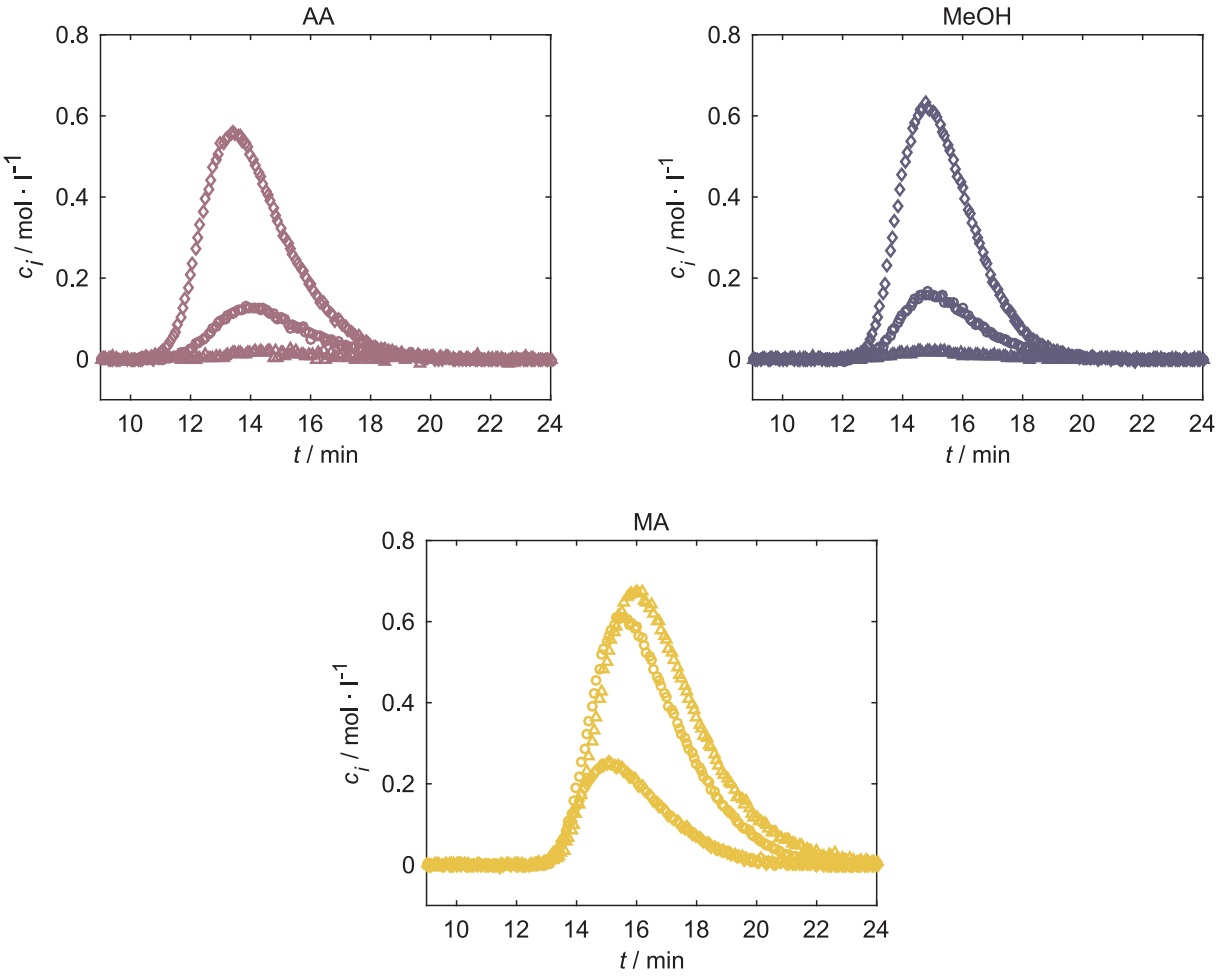

Fig. 7. Influence of the temperature on the concentration profiles of the analytes measured with NMR spectroscopy. FBCR experiments MA1-MA3 (hydrolysis of methyl acetate). Experimental parameters: T = 5 °C (△), 25 °C (○), 45 °C (◇) at $\dot{V}$ = 300 µl/min and c_{MA}^{inj} = 1.5 mol/l.

substance is typically between 0.8 and 1.6 mmol). Related to the converted amount of substance, the mean relative stoichiometric error for most of the FBCR experiments is lower than 3%. Larger relative stoichiometric errors are only observed when the change of amount of substance (i.e. the conversion) is small, for example because of low temperature or short residence time in the FBCR. The stoichiometric error is listed for all experiments in the Supplementary data in Tables S.6–S.8. All in all, these results demonstrate the reliable performance and high accuracy of the NMR spectroscopy based analysis methods.

5.3. Parameter studies

5.3.1. Influence of the volumetric flow rate

Fig. 4 depicts the concentration profiles of the analytes measured with NMR spectroscopy at different volumetric flow rates of the mobile phase (water). The results show that the repetition rate of the NMR measurements is sufficient to fully capture the concentration profiles of the different analytes even at high volumetric flow rates. As expected, the conversion of methyl formate (details on the definition of the conversion are given in the Supplementary data Section S.1.2.3.) and the separation of the products methanol and formic acid increase significantly when the volumetric flow rate of water is decreased from 1000 µl/min to 300 µl/min so that almost complete conversion of methyl formate is achieved. Thus, a further decrease in the volumetric flow rate to 100 µl/min only has a minor influence on the conversion. All FBCR experiments described in the following studies were carried out at a volumetric flow rate of water of 300 µl/min as this flow rate is a good compromise between the conversion of reactants, separation of products and duration of the FBCR experiment.

5.3.2. Influence of the temperature

The concentration profiles of the analytes measured with NMR spectroscopy when the hydrolysis of methyl formate was carried out at different temperatures of the FBCR are plotted in Fig. 5. The conversion of methanol and the yield of formic acid corresponding to these experiments are shown in Fig. 6. Formic and acetic acid are chosen as target products in this work for the sake of illustration. As expected, the concentration of the products increases with temperature caused by acceleration of the rate of reaction. Furthermore, the concentration profile of formic acid shifts significantly towards shorter residence time. In contrast, the concentration profile of methanol hardly shifts. A similar dependence of the concentration profiles on the reactor temperature was also observed by Vu and Seidel-Morgenstern [12]. The higher conversion and the better separation of the reaction products methanol and formic acid is caused by the shift of formic acid towards shorter residence time in the column and results in a higher yield of formic acid at higher temperatures (see Fig. 6).

As the temperature dependence of the adsorption equilibrium constants for this type of catalyst is only marginal [39], the observed shift in the retention time of formic acid is certainly attributable to the temperature dependence of the rate of reaction. If the rate of reaction is increased, formic acid is formed earlier in the column and thus has more time to separate from methanol and methyl formate. As methanol and methyl formate have approximately the same adsorption

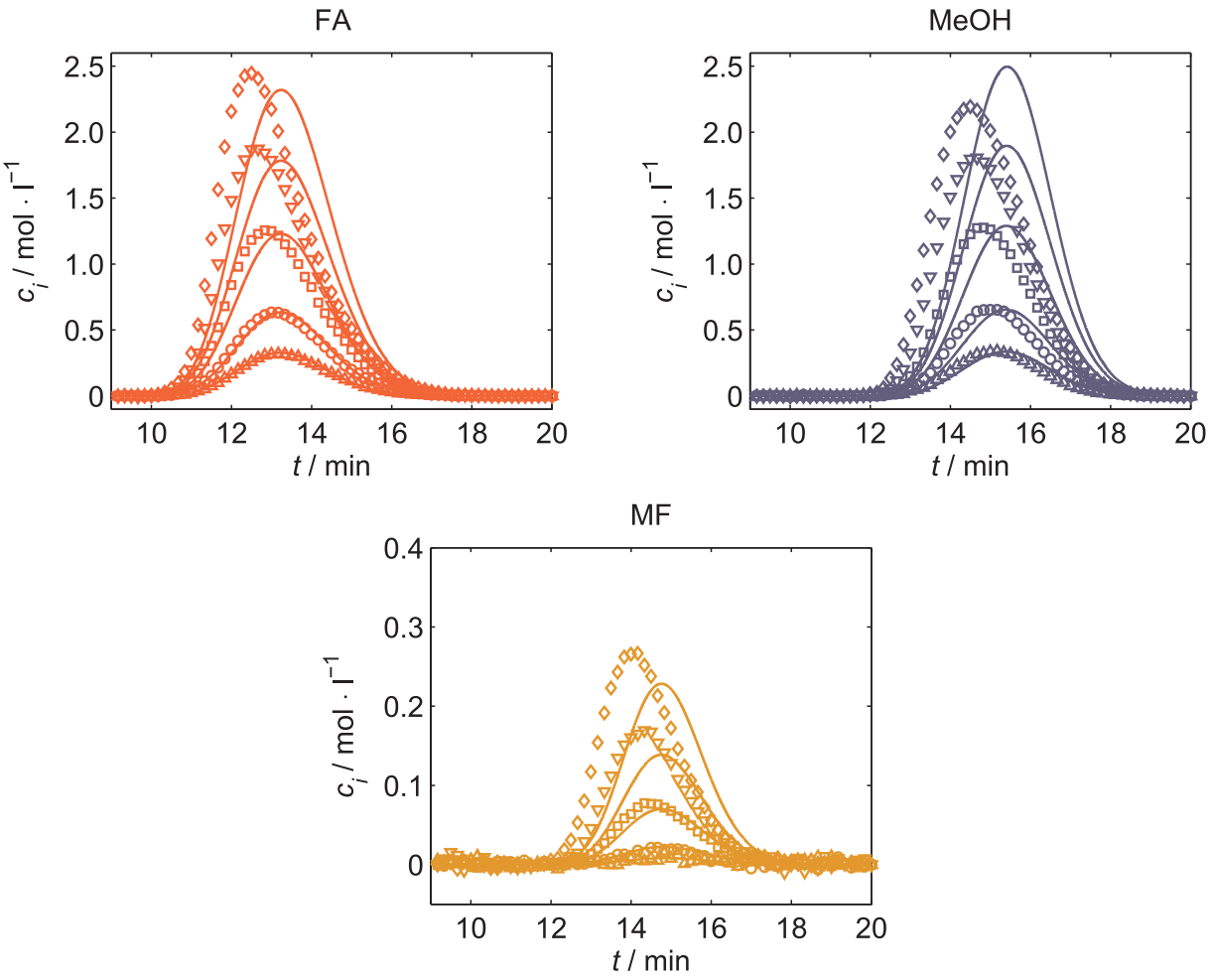

Fig. 8. Influence of the concentration of esters injected into the FBCR on the concentration profiles of the analytes measured with NMR spectroscopy. FBCR experiments MF1-MF5 (hydrolysis of methyl formate). Experimental parameters: c_{MF}^{inj} = 0.5 (△), 1.0 (○), 2.0 (□), 3.0 (▽) and 4.0 mol/l (◇) at $\dot{V}$ = 300 µl/min and T = 25 °C. Lines: model predictions.

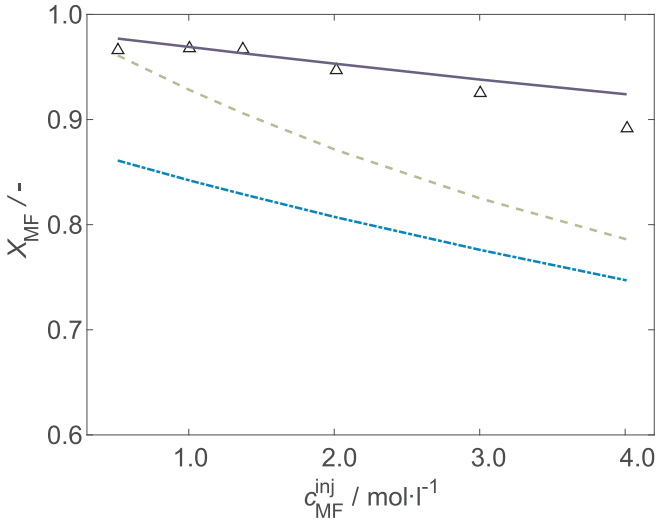

Fig. 9. Conversion of methyl formate as function of the concentration of methyl formate in the mixture injected into the FBCR for the hydrolysis of methyl formate (FBCR experiments: MF2 and MF8-MF12). Experimental parameters: T = 25 °C and $\dot{V}$ = 300 µl/min. FBCR experiments (△), model predictions: FBCR (—), batch reactor after a reaction time corresponding to the hydraulic residence time in the FBCR (– · –), in chemical equilibrium (– – –).

equilibrium constant (cf. Vu [39]), they are hardly separated in the column and methanol is simply formed in the column where methyl formate is present. Since the residence time of methyl formate in the column is hardly influenced by the temperature, the residence time of methanol changes only insignificantly with temperature.

The concentration profiles recorded during the temperature study of the methyl acetate hydrolysis reaction are depicted in Fig. 7. The concentration profile of methyl acetate is clearly unsymmetrical and shows a pronounced tailing. This tailing is attributable to processes occurring inside the FBCR as the residence time distribution of methyl acetate from the FBCR outlet to the detector unit did not show such behavior (see Section 4.4.2). The deviation from a symmetrical concentration profile is most likely caused by non-linear adsorption behavior of methyl acetate in the FBCR. Vu [39] made the same observations and concluded that the assumption of a linear adsorption isotherm of methyl acetate is valid up to a concentration of 0.5 mol/l. Similar to the hydrolysis of methyl formate the conversion of methyl acetate and the yield of acetic acid increases with temperature (see Fig. 6). As expected the conversion of methyl acetate is less than the conversion of methyl formate (at similar temperature) because of its lower rate of reaction. Caused by the higher conversion and the slight shift of the concentration profile of acetic acid to shorter residence time in the column, acetic acid, methyl acetate and methanol are better separated at increasing temperature.

5.3.3. *Influence of the concentration of esters*

Fig. 8 depicts the concentration profiles of analytes that were

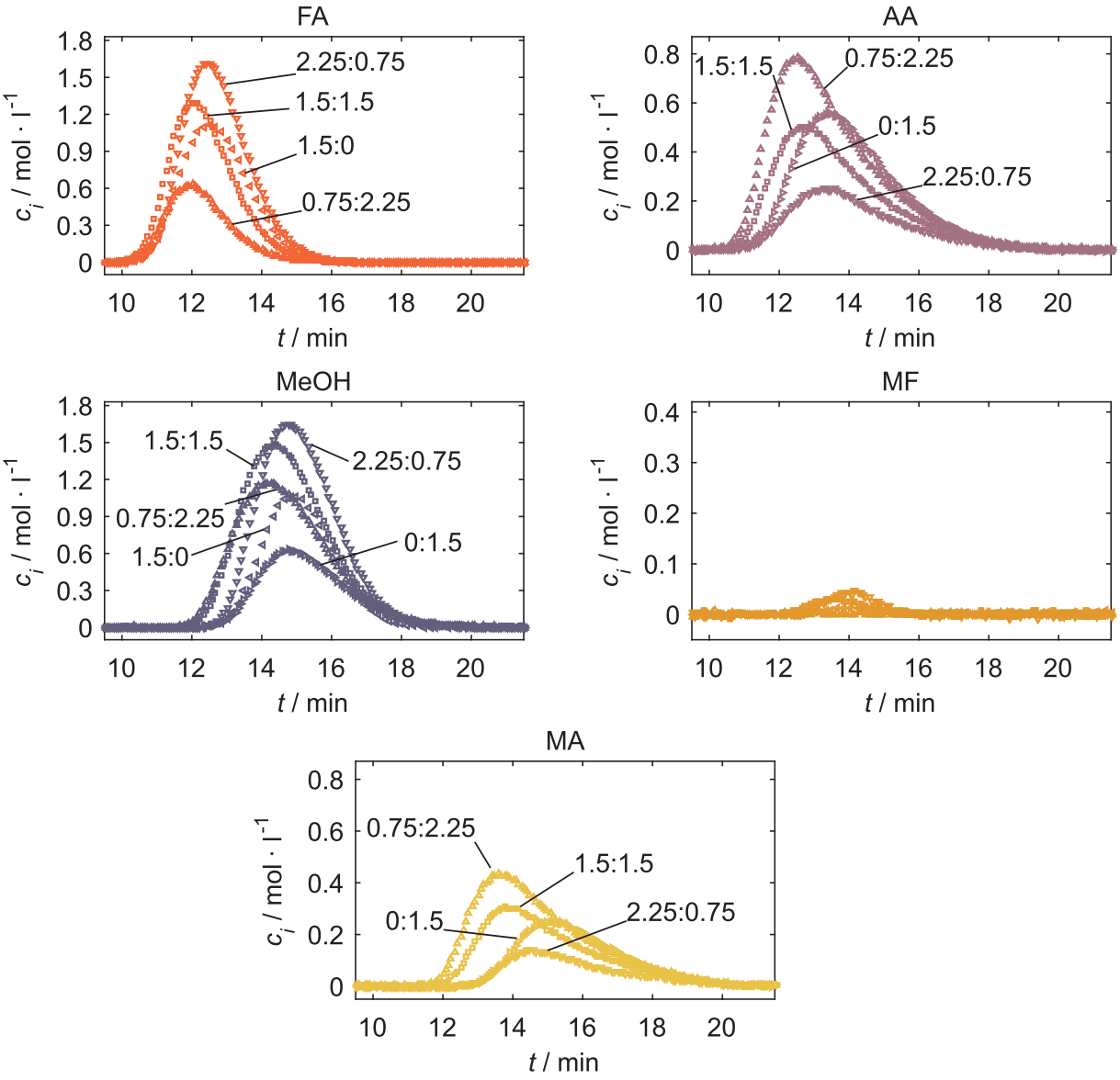

Fig. 10. Influence of the concentration of esters injected into the FBCR on the concentration profiles of the analytes of the parallel reaction (hydrolysis of methyl formate and methyl acetate) measured with NMR spectroscopy. The single reactions (hydrolysis of methyl formate and hydrolysis of methyl acetate) are additionally plotted for comparison. FBCR experiments MFMA1-MFMA3, MF7 and MA3. Experimental parameters: c_{MF}^{inj}: c_{MA}^{inj} = 0.75 mol/l: 2.25 mol/l (△), 1.5 mol/l: 1.5 mol/l (□), 2.25 mol/l: 0.75 mol/l (▽), 1.5 mol/l: 0 mol/l (◁) and 0 mol/l: 1.5 mol/l (▷) at $\dot{V}$ = 300 µl/min and T = 45 °C.

measured with NMR spectroscopy when the concentration of methyl formate injected into the FBCR was varied (hydrolysis of methyl formate only). Additionally, Fig. 8 shows the concentration profiles of analytes predicted by the model of the FBCR. Fig. 9 summarizes the comparison of the conversion of methyl formate experimentally determined and predicted by the model of the FBCR. Additionally, Fig. 9 depicts the conversion of methyl formate that is predicted in case chemical equilibrium would be reached under the given conditions. Furthermore, it shows the conversion of methyl formate that would be observed in an isothermal batch reactor after a reaction time corresponding to the hydraulic residence time in the FBCR if the same initial concentration of methyl formate as in the FBCR experiment was used.

At low concentration of methyl formate the agreement between model prediction and experimental results is good, especially when taking into consideration that all model parameters were adopted from the work of Vu [39] without being fitted to this data set. At higher concentrations of the analytes, however, larger deviations between experiment and simulation are found. The model of the FBCR assumes that the adsorption equilibria can be described by linear adsorption isotherms. This assumption was motivated by the results of adsorption experiments carried out by Vu [39] in a concentration range of adsorbates of 0.1 to 0.5 mol/l. The concentration profiles plotted in Fig. 8, however, show pronounced shifts of the concentration profiles (concentration maxima) with increasing concentration of analytes that cannot be predicted by the model. Obviously, the assumption of a linear adsorption isotherm does only hold for low concentrations of adsorbates. As the description of the adsorption equilibrium influences directly the predicted rates of reaction [12], the deviation between the measured and predicted conversion of methyl formate (see Fig. 9) is most properly also attributable to the lack of accuracy of the adsorption model at higher concentrations of adsorbates.

The experimentally determined conversion of methyl formate decreases with increasing concentration of injected methyl formate (see Fig. 9). The model prediction of the conversion for the FBCR, batch reactor and chemical equilibrium shows the same trend. Thus, the concentration dependence of the conversion of methyl formate is a consequence of the concentration dependence of the rate of reaction. Furthermore, the results show that the conversion in the FBCR is higher

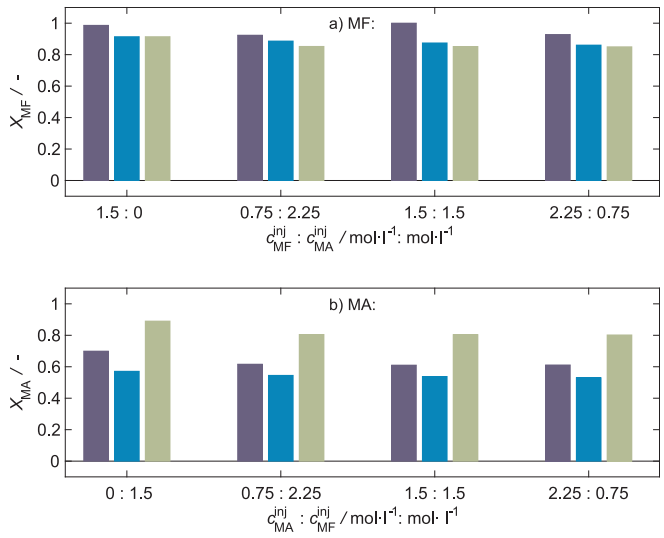

Fig. 11. Results of the concentration study of the FBCR experiments. Conversion of (a) methyl formate and of (b) methyl acetate as function of the concentration of esters in the mixture injected into the FBCR. FBCR experiments MF7, MA3 and MFMA1-MFMA3. Experimental parameters: $T = 45\,^{\circ}C$ and $\dot{V} = 300\,\mu l/min$. FBCR experiment (▬), model prediction: batch reactor after a reaction time corresponding to the hydraulic residence time in the FBCR (▬), in chemical equilibrium (▬).

than in a batch reactor (after a reaction time corresponding to the hydraulic residence time in the FBCR) and even higher than the equilibrium conversion of the given mixture of reactants (see Fig. 9). The high conversion of reactants in the FBCR is the result of the interaction of reaction and separation of reactants and products in the FBCR that keeps the driving force of reaction high and prevents the conversion from being limited by the chemical equilibrium. These results demonstrate the advantage of processes that combine reaction and separation in one apparatus.

Fig. 10 depicts the concentration profiles of the analytes measured with NMR spectroscopy when hydrolysis of methyl formate and methyl acetate take place in parallel. The total concentration of esters in the injected mixture was constant but the ratio of methyl formate to methyl acetate was varied. For comparison, the concentration profiles of the FBCR experiments in which either only methyl formate or methyl acetate was injected are additionally plotted in Fig. 10. The concentration profiles of methyl formate, methanol and formic acid are nearly symmetrical. In contrast, the concentration profiles of methyl acetate and acetic acid are strongly unsymmetrical as already observed in the temperature study of the hydrolysis of methyl acetate (see Fig. 7). As the model of the FBCR assumes linear adsorption isotherms the model cannot describe these strongly unsymmetrical concentration profiles. Therefore, no model prediction of the concentration profiles are shown in Fig. 10. The determined conversion of methyl formate and methyl acetate corresponding to the experiments shown in Fig. 10 are summarized in Fig. 11. In addition, Fig. 11 depicts the predicted conversions in case the reactants would proceed into chemical equilibrium and the conversion that would be be observed in an isothermal batch reactor after a reaction time corresponding to the hydraulic residence time in the FBCR.

Both Fig. 10 and Fig. 11 reveal that the concentration profiles of the analytes and the conversion of reactants are different when two reactions are taking place in parallel in the FBCR instead of one single reaction. A very interesting finding is that the conversion of methyl formate does not decrease when methyl acetate is also present in the FBCR as long as the concentration of injected methyl formate is constant (see Fig. 11 (a)- at $c_{MF}^{inj} = 1.5\,mol/l$). In contrast, the conversion of methyl acetate decreases when the hydrolysis of reaction of methyl formate is taking place simultaneously in the FBCR (see Fig. 11 (b)- at $c_{MF}^{inj} = 1.5\,mol/l$). The same trends are found for the concentration study carried out at lower temperatures ($T = 25\,^{\circ}C$, see plot of the concentration profiles in the Supplementary data Section S.3.7.). The different rates of the two reactions possibly cause this behavior. The rate of the methyl formate hydrolysis is faster than the rate of the methyl acetate hydrolysis. Hence, formic acid is quickly formed and then separated from methanol while passing through the FBCR. Therefore, an increase of the concentration of methanol caused by the parallel reaction of methyl acetate has little impact on the conversion.

In a batch reactor where formic acid is not separated from methanol, an increase of the concentration of methanol caused by the parallel hydrolysis of methyl acetate would force the back reaction (esterification) of formic acid with methanol to methyl formate. Therefore, the conversion of methyl formate first increases in a batch reactor over time, goes through a maximum and finally decreases when further methanol is formed through the slower hydrolysis of methyl acetate occurring in parallel that favors the back reaction of formic acid and methanol. As a consequence, the equilibrium conversion of methyl formate can be even less than the conversion of methyl formate in a batch reactor at a reaction time corresponding to the hydraulic residence time of methyl formate in the FBCR (see Fig. 11 (a)).

The decrease of the conversion of methyl acetate that is observed when the two hydrolysis reactions take place in parallel in comparison to the single hydrolysis of methyl acetate (see Fig. 11 (b)) is most properly attributable to the inferior separation of acetic acid and methanol in the FBCR compared to the separation of formic acid and methanol. Hence, the parallel formation of methanol via the hydrolysis of methyl formate directly reduces the driving force of reaction of the hydrolysis of methyl acetate and thereby causes a reduction of the conversion of methyl acetate.

The comparison of the concentration profiles shown in Fig. 10 reveals that not only the reaction is influenced when the hydrolysis reactions proceed simultaneously but also the retention time of the different analytes. This finding is again an indication that the adsorption of the different species does not follow a simple linear adsorption isotherm and that the interaction of the different adsorbates has to be taken into account when describing the processes that occur in the FBCR.

6. Conclusion

A method based on NMR spectroscopy is presented in this work that facilitates inline analysis of dynamic processes. The method was applied to analyse the product stream of a reactive chromatographic process. Detailed investigations of the quality of the NMR spectroscopy analysis method proved that its accuracy is comparable to the accuracy achievable with measurements using a RID. The NMR spectroscopy method, however, has the advantage that it can resolve different reactants and products accurately, even though two reactions take place simultaneously in the FBCR and the concentration profiles of the different analytes overlap strongly. In contrast, the concentration profiles cannot be derived from the measurements of the RI.

The NMR spectroscopy method was used to study the influence of the volumetric flow rate, the temperature and the concentration of esters in the injected mixture on the performance of the FBCR. The accurate measurement of the concentration profiles of the different reactants and products facilitates studying the interaction of the reaction and separation that occurs simultaneously in the FBCR. The observed trends are in line with findings reported by Vu and Seidel-Morgenstern [12].

The experimental results obtained in this work were compared to predictions using the model of the FBCR developed by Vu and Seidel-Morgenstern [12]. The single hydrolysis of methyl formate can be well described by the model if the concentration of injected methyl formate is low. At higher concentrations of esters, however, especially if both methyl formate and methyl acetate are present, the model fails to predict the experimental results. Obviously, the assumption that the

adsorption of the different adsorbates can be described by a simple linear isotherms does not hold under these conditions. This result, however, is not astonishing as Vu and Seidel-Morgenstern [12] estimated the model parameter and tested the model only at low concentrations of reactants. Furthermore, because of the shortcomings of the RID analysis method applied by Vu and Seidel-Morgenstern [12] they were not able to investigate parallel reactions in the FBCR. By means of the presented NMR spectroscopy method and the measured concentration profiles, the interaction of several adsorbates on the adsorption equilibrium and the kinetics of the occurring reactions can be investigated and finally the model of the FBCR can be improved.

In this work, the experiments were carried out with diluted aqueous solutions to allow a comparison with the results obtained in previous works. In an industrial production process, the concentrations of the reactants and products is generally much higher [8]. Because quantitative NMR spectroscopy is applicable in a wide range of concentrations, as we have demonstrated in many studies (e.g. von Harbou et al. [33], Brächer et al. [27], Scheithauer et al. [28]), the presented inline analysis method is also suitable to study processes with high concentrations of the analytes that are relevant for industrial applications. In fact, the analysis should become even more accurate as the signal-to-noise ratio increases with increasing concentration of the analytes. In future work, an interesting modification of the presented NMR spectroscopy method would be the use of a benchtop NMR spectrometer instead of an high field NMR spectrometer. Benchtop NMR spectrometers are a cost-efficient and more compact alternative to high field NMR spectrometers and they can be operated also in an industrial process environment [44]. Thus, the use of a benchtop NMR spectrometer could significantly widen the range of application of this inline analysis method. The lower sensitivity and spectral resolution of benchtop NMR spectrometers, however, requires in most cases sophisticated methods, such as the method presented by Matviychuk et al. [45], to evaluate the spectroscopic data quantitatively.

To conclude, the presented inline NMR spectroscopy method is a valuable tool to gain insights into complex dynamic processes and to gather accurately experimental data that is necessary for the development of reliable process models.

Acknowledgments

We gratefully acknowledge Flavio Sottile, Nikolas Krüger, Konstantin Sauer and Richard Behrens for their valuable help in establishing and testing the new set-up in various ways. L.M. Kreußer was supported by the UK Engineering and Physical Sciences Research Council (EPSRC) Grant No. EP/L016516/1 for the University of Cambridge Centre for Doctoral Training, the Cambridge Centre for Analysis. E. v. Harbou thanks the German Science Foundation (DFG) for the financial support within the Collaborative Research Center SFB/TRR 173 Spin + X.

Appendix A. Evaluation of the NMR signals

The NMR signal S_i^{NMR} of analyte i was determined from the areas under the corresponding peaks in the NMR spectrum A_j as shown in Table 2. The areas under the peaks were calculated by direct integration of the respective NMR spectrum within the integration limits that are given in Table 2. The concentration of the analyte i is calculated from S_i^{NMR} using Eq. (2).

Table 2
Peak areas used to determine the concentration of the analytes as described in Eq. (2). Details on the peak assignments are given in Fig. 2.

Analyte	Peak areas	Integration limits used
FA	$S_{FA}^{NMR} = A_{FA}^{CH}$	7.53–7.66 ppm
MF	$S_{MF}^{NMR} = \frac{1}{3} \cdot A_{MF1}^{CH3}$	3.10–3.30 ppm
MA	$S_{MA}^{NMR} = \frac{1}{3} \cdot A_{MA2}^{CH3}$	2.94–3.05 ppm
MeOH	$S_{MeOH}^{NMR} = \frac{1}{3} \cdot A_{MeOH}^{CH3}$	2.54–2.87 ppm
AA	$S_{AA}^{NMR} = \frac{1}{3} \cdot A_{AA/MA1}^{CH3} - \frac{1}{3} \cdot A_{MA2}^{CH3}$	1.34–1.46 ppm, 2.94–3.05 ppm

Appendix B. Supplementary data

Supplementary data associated with this article can be found, in the online version, at http://dx.doi.org/10.1016/j.cej.2017.12.004.

References

[1] P. Silveston, R. Hudgins, Periodic Operation of Chemical Reactors, Butterworth-Heinemann, Oxford, U.K., 2013.
[2] D.E. Kowler, R.H. Kadlec, The optimal control of a periodic adsorber: Part I. Experiment, AIChE J. 18 (1972) 1207–1212.
[3] B. Cerkvenik, F. Ziegler, The influence of periodic operation on the characteristics of adsorption devices, Energy Convers. Manage. 47 (2006) 2020–2033.
[4] A.A. Kiss, Cyclic Distillation, Advanced Distillation Technologies, John Wiley & Sons, New York, USA, 2013.
[5] J. Fricke, H. Schmidt-Traub, M. Kawase, Chromatographic Reactors, Ullmann's Encyclopedia of Industrial Chemistry, Wiley-VCH, Weinheim, Germany, 2000.
[6] G. Subramanian, Process Scale Liquid Chromatography, John Wiley & Sons, New York, USA, 2008.
[7] G. Ganetsos, P.E. Barker, Preparative and Production Scale Chromatography vol. 61, Marcel Dekker Inc., New York, USA, 1992.
[8] M. Mazzotti, A. Kruglov, B. Neri, D. Gelosa, M. Morbidelli, A continuous chromatographic reactor: SMBR, Chem. Eng. Sci. 51 (1996) 1827–1836.
[9] B. Reddy, S. Mahajani, Feasibility of reactive chromatography for the synthesis of n-propyl acetate, Ind. Eng. Chem. Res. 53 (2014) 1395–1403.
[10] J. Oh, G. Agrawal, B. Sreedhar, M.E. Donaldson, A.K. Schultz, T.C. Frank, A.S. Bommarius, Y. Kawajiri, Conversion improvement for catalytic synthesis of propylene glycol methyl ether acetate by reactive chromatography: experiments and parameter estimation, Chem. Eng. J. 259 (2015) 397–409.
[11] J. Oh, B. Sreedhar, M.E. Donaldson, T.C. Frank, A.K. Schultz, A.S. Bommarius, Y. Kawajiri, Transesterification of propylene glycol methyl ether in chromatographic reactors using anion exchange resin as a catalyst, J. Chromatogr. A 1466 (2016) 84–95.
[12] T.D. Vu, A. Seidel-Morgenstern, Quantifying temperature and flow rate effects on the performance of a fixed-bed chromatographic reactor, J. Chromatogr. A 1218 (2011) 8097–8109.
[13] P.T. Mai, T.D. Vu, K.X. Mai, A. Seidel-Morgenstern, Analysis of heterogeneously catalyzed ester hydrolysis performed in a chromatographic reactor and in a reaction calorimeter, Ind. Eng. Chem. Res. 43 (2004) 4691–4702.
[14] T.D. Vu, A. Seidel-Morgenstern, S. Grüner, A. Kienle, Analysis of ester hydrolysis reactions in a chromatographic reactor using equilibrium theory and a rate model, Ind. Eng. Chem. Res. 44 (2005) 9565–9574.

[15] T. Falk, A. Seidel-Morgenstern, Comparison between a fixed-bed reactor and a chromatographic reactor, Chem. Eng. Sci. 54 (1999) 1479–1485.
[16] T. Falk, A. Seidel-Morgenstern, Analysis of a discontinuously operated chromatographic reactor, Chem. Eng. Sci. 57 (2002) 1599–1606.
[17] G. Openhaim, E. Grushka, Temperature-dependent refractive index issues using a UV-visible detector in high-performance liquid chromatography, J. Chromatogr. A 942 (2002) 63–71.
[18] R. Thede, D. Haberland, Z. Deng, S.H. Langer, Second-order kinetics in the liquid chromatographic reactor, J. Chromatogr. A 683 (1994) 279–291.
[19] T. Sainio, M. Kaspereit, A. Kienle, A. Seidel-Morgenstern, Thermal effects in reactive liquid chromatography, Chem. Eng. Sci. 62 (2007) 5674–5681.
[20] B.J. Marquardt, P.G. Vahey, R.E. Synovec, L.W. Burgess, A Raman waveguide detector for liquid chromatography, Anal. Chem. 71 (1999) 4808–4814.
[21] R.J. Dijkstra, C.T. Martha, F. Ariese, U.A.T. Brinkman, C. Gooijer, On-line identification method in column liquid chromatography: UV resonance raman spectroscopy, Anal. Chem. 73 (2001) 4977–4982.
[22] C. Kubis, I. Profir, I. Fleischer, W. Baumann, D. Selent, C. Fischer, A. Spannenberg, R. Ludwig, D. Hess, R. Franke, A. Börner, In situ FTIR and NMR spectroscopic investigations on ruthenium-based catalysts for alkene hydroformylation, Chem. Eur. J. 22 (2016) 2746–2757.
[23] J. Cornel, C. Lindenberg, M. Mazzotti, Quantitative application of in situ ATR-FTIR and Raman spectroscopy in crystallization processes, Ind. Eng. Chem. Res. 47 (2008) 4870–4882.
[24] M. Maiwald, H.H. Fischer, H. Hasse, Quantitative high resolution on-line spectroscopy in reaction and process monitoring, Chem. Ing. Tech. 76 (2004) 965–969.
[25] A. Brächer, S. Hoch, K. Albert, H. Kost, B. Werner, E. von Harbou, H. Hasse, Thermostatted micro-reactor NMR probe head for monitoring fast reactions, J. Magn. Reson. 242 (2014) 155–161.
[26] M. Maiwald, T. Grützner, E. Ströfer, H. Hasse, Quantitative NMR spectroscopy of complex technical mixtures using a virtual reference: chemical equilibria and reaction kinetics of formaldehyde-water-1,3,5-trioxane, Anal. Bioanal. Chem. 385 (2006) 910–917.
[27] A. Brächer, R. Behrens, E. von Harbou, H. Hasse, Application of a new micro-reactor ^{1}H NMR probe head for quantitative analysis of fast esterification reactions, Chem. Eng. J. 306 (2016) 413–421.
[28] A. Scheithauer, A. Brächer, T. Grützner, D. Zollinger, W. Thiel, E. von Harbou, H. Hasse, Online ^{1}H NMR spectroscopic study of the reaction kinetics in mixtures of acetaldehyde and water using a new microreactor probe head, Ind. Eng. Chem. Res. 53 (2014) 17589–17596.
[29] A. Nordon, C.A. McGill, D. Littlejohn, Process NMR spectrometry, Analyst 126 (2001) 260–272.
[30] M.A. Bernstein, M. Štefinović, C.J. Sleigh, Optimising reaction performance in the pharmaceutical industry by monitoring with NMR, Magn. Reson. Chem. 45 (2007) 564–571.
[31] M. Maiwald, H.H. Fischer, M. Ott, R. Peschla, C. Kuhnert, C.G. Kreiter, G. Maurer, H. Hasse, Quantitative NMR spectroscopy of complex liquid mixtures: methods and results for chemical equilibria in formaldehyde-water-methanol at temperatures up to 383 K, Ind. Eng. Chem. Res. 42 (2003) 259–266.
[32] A.M.R. Hall, J.C. Chouler, A. Codina, P.T. Gierth, J.P. Lowe, U. Hintermair, Practical aspects of real-time reaction monitoring using multi-nuclear high resolution flow NMR spectroscopy, Catal. Sci., Technol, 2016.
[33] E. von Harbou, R. Behrens, J. Berje, A. Brächer, H. Hasse, Studying fast reaction kinetics with online NMR spectroscopy, Chem. Ing. Tech. 89 (2017) 369–378.
[34] L.A. Cardoza, V.K. Almeida, A. Carr, C.K. Larive, D.W. Graham, Separations coupled with NMR detection, Trends Anal. Chem. 22 (2003) 766–775.
[35] M.E. Lacey, Z. Tan, A.G. Webb, J.V. Sweedler, Union of capillary high-performance liquid chromatography and microcoil nuclear magnetic resonance spectroscopy applied to the separation and identification of terpenoids, J. Chromatogr. A 922 (2001) 139–149.
[36] G. Schlotterbeck, L.-H. Tseng, H. Händel, U. Braumann, K. Albert, Direct On-line coupling of capillary HPLC with ^{1}H NMR spectroscopy for the structural determination of retinyl acetate dimers: 2D NMR spectroscopy in the nanoliter scale, Anal. Chem. 69 (1997) 1421–1425.
[37] K. Albert, On-Line LC NMR Related Techniques, John Wiley & Sons, Chichester, U.K., 2002.
[38] J.C. Lindon, J.K. Nicholson, I.D. Wilson, The development and application of coupled HPLC-NMR spectroscopy, Adv. Chromatogr. 36 (1996) 315–382.
[39] T. Vu, Analysis of Heterogeneously Catalyzed Ester Hydrolysis Reactions in a Fixed-Bed Chromatographic Reactor (Ph.D. thesis), Otto-von-Guericke-University Magdeburg, Germany, 2007.
[40] O. Levenspiel, Chemical Reaction Engineering, John Wiley & Sons, New York, USA, 1999.
[41] Design Institute for Physical Properties Research Sponsored by AIChE, DIPPR Project 801, 2006.
[42] R.L. Haner, W. Llanos, L. Mueller, Small volume flow probe for automated direct-injection NMR analysis: design and performance, J. Magn. Reson. 143 (2000) 69–78.
[43] M. Maiwald, Hochauflösende Online NMR-Spektroskopie für das Reaktions- und Prozessmonitoring, Cuvillier Verlag, Göttingen, Germany, 2012.
[44] E. Danieli, J. Perlo, A.L.L. Duchateau, G.K.M. Verzijl, V.M. Litvinov, B. Blümich, F. Casanova, On-line monitoring of chemical reactions by using bench-top nuclear magnetic resonance spectroscopy, ChemPhysChem 15 (2014) 3060–3066.
[45] Y. Matviychuk, E. von Harbou, D.J. Holland, An experimental validation of a Bayesian model for quantification in NMR spectroscopy, J. Magn. Reson. 285 (2017) 86–100.

Friebel et al., 2017

Reprinted with permission from: A. Friebel, A. Fröscher, K. Münnemann, E. von Harbou, H. Hasse, In situ measurement of liquid-liquid equilibria by medium field nuclear magnetic resonance, Fluid Phase Equilibria, Volume 438, 2017, Pages 44-52, ISSN 0378-3812, DOI 10.1016/j.fluid.2017.01.027

Fluid Phase Equilibria 438 (2017) 44–52

Contents lists available at ScienceDirect

Fluid Phase Equilibria

journal homepage: www.elsevier.com/locate/fluid

In situ measurement of liquid-liquid equilibria by medium field nuclear magnetic resonance

Anne Friebel, Agnes Fröscher, Kerstin Münnemann, Erik von Harbou*, Hans Hasse

Laboratory of Engineering Thermodynamics, University of Kaiserslautern, Erwin-Schrödinger-Straße 44, 67663 Kaiserslautern, Germany

ARTICLE INFO

Article history:
Received 19 December 2016
Received in revised form
30 January 2017
Accepted 31 January 2017
Available online 13 February 2017

Keywords:
NMR spectroscopy
Medium field
Benchtop NMR spectrometer
Quantitative NMR
Liquid-liquid equilibrium
Ternary system
Slope curve method

ABSTRACT

A new method for non-invasive measurement of liquid-liquid equilibria (LLE) using a compact medium field nuclear magnetic resonance (NMR) spectrometer is presented. Mixing of all components, phase separation, and analysis of the composition of the coexisting phases is performed in situ in an NMR glass tube. Thus, the experimental effort is reduced and errors caused by sampling are eliminated. Furthermore, calibration of the analysis method is not necessary as quantitative information is obtained directly from the NMR spectra. The proposed method for studying LLE in situ can be swiftly conducted in standard chemical laboratories as medium field NMR spectrometer do not require dedicated laboratory infrastructure but enable convenient handling and fast analysis of the samples. In the present work, four non-reactive ternary solvent systems with closed miscibility gap (toluene + acetone + water, diethyl ether + acetone + water, diethyl ether + methanol + water, and acetonitrile + ethanol + cyclohexane) and one reactive ternary system (water + acetic acid + acetic anhydride) were investigated at a temperature of 22.0 °C using ^{1}H medium field NMR spectroscopic measurements. For comparison, the composition of the coexisting phases is also examined for one non-reactive system (acetonitrile + ethanol + cyclohexane) using ^{13}C medium field NMR spectroscopy as well as spatially resolved spectroscopy in a conventional high field NMR spectrometer. The comparison of the results of the present work to literature data shows that the new proposed method enables swift and reliable investigations of LLE.

1. Introduction

For process design reliable data on physico-chemical properties are essential. For many processes such as extraction processes or processes with decanter information on the liquid-liquid equilibrium (LLE) is required. Typically, tie lines of the LLE, i.e. the composition of the different coexisting phases, are determined using small thermostated batch vessels [1,2]. A known component mixture is stirred until the equilibrium is reached. Then the phases are separated and a sample is taken from each phase. Subsequently the composition of these samples is analyzed using ex situ analysis methods such as liquid or gas chromatography. This procedure has to be carried out for each tie line, which is time-consuming and prone to experimental errors. Furthermore, in many cases the samples cannot be reused after analysis, which may cause problems if only small amounts of substances are available.

In this work, we present a method to investigate LLE in situ with quantitative NMR spectroscopy. The equilibration, separation of the phases, and analysis of the composition of each phase are carried out directly in the NMR sample tube avoiding most of the problems mentioned above.

NMR spectroscopy is an analytic tool with a wide range of applications in chemistry, biology, and chemical engineering [3,4]. NMR spectroscopy has a high chemical resolution and enables to resolve even chemically similar substances. It is a non-invasive analysis method and facilitates the analysis of complex fluid mixtures in situ without sampling.

The basic idea of the method presented in this work is to equilibrate the two phases in the NMR sample tube and adjust the position of the tube in the NMR spectrometer such that first one and then the other phase is measured. This approach requires no sampling thus eliminating sampling errors and facilitating studies of hazardous substances. Contrarily to optical spectroscopy, no previous calibration is needed for quantitative analysis by NMR spectroscopy.

* Corresponding author.
E-mail address: erik.vonharbou@mv.uni-kl.de (E. von Harbou).

http://dx.doi.org/10.1016/j.fluid.2017.01.027
0378-3812/

The ability to obtain quantitative results without calibration is an important feature of NMR spectroscopy as it reduces the experimental effort significantly and enables the analysis of mixtures containing components, which are not available as pure substances or which cannot be isolated e.g. intermediates. In comparison to typically used setups, the sample volume required for the in situ LLE analysis method is much lower and the sample can be reused for measuring several tie lines simply by adding the desired components. Thus, this method can also be applied if only small amounts of the involved components are available.

The preliminary tests that are necessary to determine the required mixing and settling time of the investigated LLE system can easily be carried out with this in situ analysis method simply by repeating the measurement procedure with the same mixture. Besides, it is possible to obtain the composition of a mixture within seconds because of the short total acquisition time of ^{1}H NMR spectroscopy. Thus, reactions taking place in the different coexisting phases can directly be monitored with the in situ LLE analysis method presented in this work.

In principal, two different types of NMR spectrometers are applicable for the proposed in situ LLE analysis method: high and medium field NMR spectrometer. High field NMR spectrometer have been used in many cases for quantitative investigations and monitoring of reactions and processes by several groups [5–10], listing only a few examples. As described above, the easiest way to analyze the composition of different phases in an NMR sample tube is to change the location of the sample tube within the spectrometer (sample shifting method). However, in commercially available standard NMR probe heads the location of the sample tube cannot be changed significantly. To overcome this obstacle, Leclerc et al. [11] developed a home-built probe head enabling a precise displacement of the sample tube within the NMR active volume. They demonstrated the applicability of this probe head for studying LLE using the system water + toluene as an example. However, only qualitative results and no exact composition of the two coexisting phases were determined. The composition of different phases can also be analyzed in situ in the sample tube using a gradient based spatially selective NMR spectroscopy method (slicing method) as described in Refs. [12–15]. Here, the sample tube does not have to be shifted inside the NMR spectrometer. So far only Mantel et al. [16] have applied spatially selective NMR methods to study liquid phase boundaries, however, without quantifying the concentration of the coexisting phases.

High field NMR spectrometers have the disadvantage that cryogenically cooled super-conducting magnets are required to install high magnetic field strengths of 5 T and more. Thus, high field NMR spectrometers are large and expensive and they need a dedicated laboratory infrastructure such as a vibration free location, constant supply with cryogenic media, and climatisation. In recent years, benchtop NMR spectrometers employing small permanent magnets with high stability and homogeneity of the magnetic field have been developed. These medium field NMR spectrometers have typically magnetic field strengths of 1–1.5 T (corresponding to proton Larmor frequencies of 42.5–60.0 MHz) [17,18]. Furthermore, compared to high field NMR spectrometers, medium field NMR spectrometers have significantly lower investment costs. Without the need of cryogenic media and their small size they are flexible and easily applicable in every day laboratories so that they can be placed for example directly inside a fume hood next to a reactor [19,20]. The lower magnetic field strength and less homogeneity of the magnetic field, however, entail lower sensitivity and chemical resolution compared to high field NMR spectrometers [21]. Nevertheless, it is possible to receive quantitatively evaluable spectra from medium field NMR spectroscopic measurements. Another limitation of the medium field NMR spectrometers being on today's market is the absence of a temperature control for the sample inside. There are workarounds for this problem e.g. by mounting a dewar inside the bore of the magnet, which insulates the NMR sample tube and enables thermostatisation of the sample without evoking a magnetic field drift of the permanent magnet [20,22]. The problem of thermostating the sample, however, is not in the scope of this paper as this restriction does not limit the usefulness of the proposed method in general. In recent years, several groups have employed medium field NMR spectroscopy to investigate and monitor reactions [22–24] and processes [25–27]. To our knowledge, however, medium field NMR spectroscopy has not been used yet to determine physico-chemical properties of multicomponent systems such as phase equilibria.

Therefore, we apply in this work the in situ sample shifting method in combination with medium field NMR spectroscopy to study the composition of the coexisting phases in four non-reactive (toluene + acetone + water, diethyl ether + acetone + water, diethyl ether + methanol + water, and acetonitrile + ethanol + cyclohexane) and one reactive ternary system (water + acetic acid + acetic anhydride). Thereby, we address the question whether the accuracy of the measurement of LLE using medium field NMR spectroscopy can compete with common LLE measurements using ex situ analysis. For comparison one non-reactive ternary system (acetonitrile + ethanol + cyclohexane) is also examined using the sample shifting method with ^{13}C medium field NMR spectroscopy and a slicing method with ^{1}H high field NMR spectroscopy.

The LLE data from the present work are correlated using standard models for the Gibbs excess energy (UNIQUAC and NRTL). Furthermore, the experimental results are compared to experimental data from literature. In this context, the data are also depicted with the slope curve method (SCM) first described by Burger et al. [28] to get more detailed information about the characteristics of the investigated LLE systems. The SCM offers the possibility to rate the quality of measured phase compositions in ternary systems more detailed than in Gibbs ternary diagrams by just comparing the binodal curve. Thus the SCM is a appropriate tool to get an overview of the LLE data and assess the applicability of the system for an extraction process.

2. Experimental section

2.1. Chemicals

Table 1 gives information on the used chemicals, the suppliers and the purities. All purities listed here were adopted from the supplier. All chemicals were used without further purification. Ultrapure water was produced using a Milli-Q integral water purification system from Merck Millipore (Merck, Darmstadt, Germany). During the analysis carried out in the present work no significant amounts of side components were detected.

Table 1
Sample table.

Chemical name	Source	Grade	Purity
Cyclohexane	Sigma-Aldrich	Chromasolv	≥ 0.999 g/g
Diethyl ether	Sigma-Aldrich	ACS reagent	≥ 0.995 g/g
Acetic anhydride	Sigma-Aldrich	ReagentPlus	≥ 0.990 g/g
Deuterium oxide	Sigma-Aldrich	–	≥ 0.999 g/g
Acetonitrile	Carl Roth	Rotisolve	≥ 0.999 g/g
Acetic acid	Carl Roth	Rotipuran	≥ 0.998 g/g
Methanol	Carl Roth	Anhydrous	≥ 0.998 g/g
Ethanol	Merck	Uvasolv	≥ 0.999 g/g
Toluene	Merck	Uvasolv	≥ 0.999 g/g
Acetone	Merck	Uvasolv	≥ 0.999 g/g

2.2. Experimental setup and procedure

2.2.1. Non-reactive systems

The investigation of LLE is carried out in standard 5 mm Wilmad NMR glass tubes closed with gas-tight caps. To determine one tie line the following steps are carried out at ambient temperature (22.0 °C): First, a certain amount of every component, determined gravimetrically using a precision balance by Mettler Toledo (XS603S Delta Range with an absolute error specified by the manufacturer of 0.01 g) is poured in the sample tube. For precise measurements each phase has to be at least 4 cm high to ensure excitation by the radio frequency pulse of the NMR spectrometer in one single phase only. Then, the sample tube is shaken for 10 min to enable the equilibration. Afterwards the sample tube is centrifuged in a modified spinning lab centrifuge to expedite the phase separation. For positioning of the sample tube inside the medium field NMR spectrometer a mounting is used. Two different positions of the tube are employed to analyze the upper and lower phase separately (cf. Fig. 1). After the analysis shaking and separation was repeated two times to check whether the shaking time was chosen long enough to ensure equilibration of the coexisting phases. There were no detectable differences in the composition of the two phases of these three measurements. The results showed that 10 min shaking time was sufficient for all samples in this work.

For the systems diethyl ether + methanol + water and acetonitrile + ethanol + cyclohexane, the first mixture was reused for all tie lines by adding one component (methanol and ethanol, respectively) and thereby changing the overall composition of the sample. For the systems containing acetone every tie line was determined from a freshly prepared mixture using the pure components.

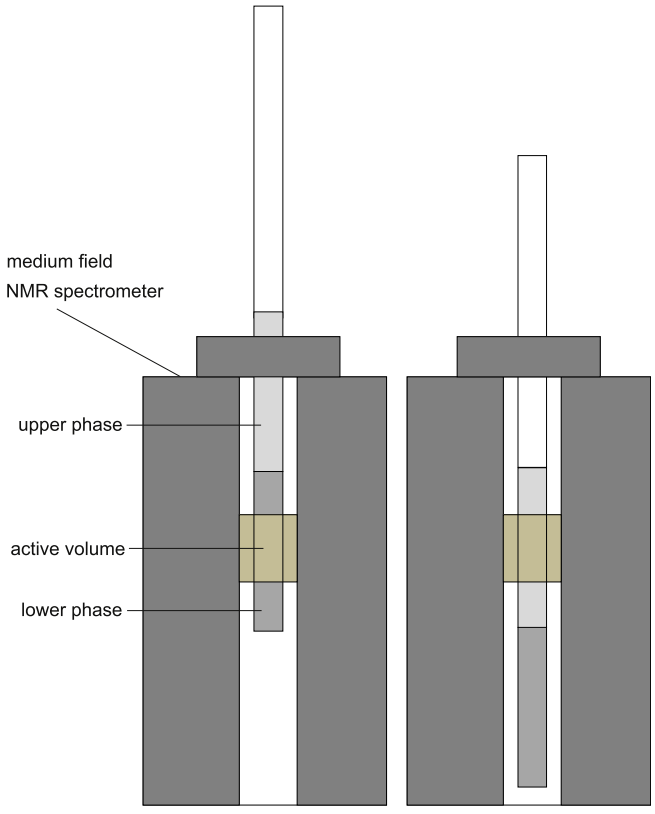

Fig. 1. Different positions of the sample tube inside the medium field NMR spectrometer.

As described above, medium field NMR spectrometers do not facilitate setting the temperature of the sample. The temperature of the permanent magnet is controlled by thermostatisation to 28.5 °C, which is slightly higher than ambient temperature (22.0 °C). A constant liquid temperature of 28.2 °C is reached 10 min after the sample has been placed inside the bore of the medium field NMR spectrometer. This investigation was carried out using a water sample and a thermocouple (Prema 6001 Digital Multimeter with an absolute error specified by the manufacturer of 0.05 °C). Because of the small liquid-liquid interface present in the sample the change of equilibrium composition of the coexisting phases caused by the slight change of liquid temperature takes longer than the measurement time. Thus, the measured composition of the phases corresponds to the equilibrium composition at 22.0 °C. All investigated LLE systems show only a weak temperature dependence. Therefore the error caused by the slight change in temperature are within the accuracy of the analysis method.

2.2.2. Reactive system

The reactive system is investigated in two different ways. First, for determination of the binodal curve the measurement is carried out as described in section 2.2.1 except for the repeated shaking and analysis. Every tie line was determined from a freshly prepared mixture using the pure components. In order to observe the reaction progress in both coexisting phases a second experimental procedure is applied. The reactants (water and acetic anhydride) are mixed by intensive shaking for 30 s and are centrifuged afterward. Every 5 min the composition of both phases is analyzed. During this period any concussions and motions of the sample are avoided to minimize mass transfer between the phases. Thereby the measured change of composition of the phases is attributed to the reactions occurring in the phases. After 30 min the mixture is shaken again for 30 s. This procedure is repeated twice.

2.3. NMR instrument and methods

All spectra are acquired without dilution of the samples with solvents or addition of reference compounds. The ^{1}H medium field NMR measurements using the sample shifting method are carried out on a Magritek Spinsolve® Carbon NMR spectrometer (Magritek, Aachen, Germany) with a field strength of 1 T corresponding to a Larmor frequency of 42.5 MHz for ^{1}H. The ^{1}H spectra of the non-reactive systems are measured with an acquisition time of 6.4 s and 32k data points. The repetition time of the repeated scans is adjusted by measuring the change of peak area as a function of repetition time of the 90° pulse intervals. It was found, that 30 s is an appropriate time interval for all investigated samples, which enables sufficient relaxation of the spins to their thermal equilibrium. To improve the signal to noise ratio (SNR), 32 subsequent scans are accumulated for the non-reactive measurements. Because of the change of the sample composition of the reactive ternary system over time only one scan per spectra is applied for its analysis.

Prior to integration post processing of the obtained NMR spectra is carried out with the MNova software (MestReLabs, Santiago de Campostela, Spain). For baseline correction, a Whittaker smoother algorithm is used. The phase correction is done manually. When evaluating the ^{1}H NMR spectra the ^{13}C satellites are left outside the integration range. The integration method is chosen depending on the system and its spectral resolution. Well separated peaks (distance of the peaks is three times larger than the full width of the peak at half height) are integrated directly. In case of a partial overlap of the peaks the integrals are evaluated with a deconvolution method provided in the software package MNova. This deconvolution method uses Voigt functions for the line fitting.

Completely overlapping peaks are integrated using a corrected direct integration method (see SI for more detailed information).

2.4. Peak assignment and quantification

For each ternary system, a reference sample is prepared with a composition outside the miscibility gap. These reference samples are used for the peak assignment and to verify the accuracy of the quantitative spectroscopic measurements. The structures of all relevant components with assigned peak names are shown in Fig. 2. The ^{1}H NMR spectra of the reference samples acquired with the medium field NMR spectrometer are depicted in Fig. 3. The corresponding peak assignment is listed in Table S1 in the Supplementary Information.

The mole fractions of the different components in the sample can be calculated from the peak area fractions of the corresponding peaks in the NMR spectrum. For components with more than one peak the CH_3 peak is chosen for quantification. Table 2 lists a comparison of the compositions of the reference samples determined by NMR spectroscopy x_i^{NMR} with the compositions expected from the gravimetrical preparation of the samples $x_i^{expected}$. The results show that the absolute deviation of the analysis method is on average 0.8 mol% for ^{1}H (sample shifting method). Because of the continuously changing composition, no reference measurement is possible for the reactive system water + acetic acid + acetic anhydride.

2.5. Correlation

Using the isoactivity criterion, two different g^E-models – the NRTL model and the UNIQUAC model – were parametrized to describe the compositions of the two coexisting phases of the non-reactive systems investigated in this work with ^{1}H medium field NMR spectroscopy. The resulting parameters are listed in the SI.

By means of a coordinate transformation the tie lines and thus the LLE phase behavior can be illustrated using the slope curve method (SCM) which is described in detail by Burger et al. [28]. The resulting slope curve diagrams for every non-reactive system investigated in this work are presented in the SI as well.

3. Results and discussion

3.1. System toluene + acetone + water

Fig. 4 shows the composition of the two phases in the LLE of the system toluene + acetone + water determined in this work at 22.0 °C together with literature data at 20.0 °C, 30.0 °C [29], and 25.0 °C [30], respectively. As already observed by Pavasovic [29], the temperature has no significant influence on the phase composition (cf. Fig. 4). This result is confirmed by additionally published data [31,32] (not shown in Fig. 4). The data of the present work is in good agreement with the literature data of Pavasovic [29], however, the water content in the organic phase is slightly higher than those reported in the literature data. The small deviation can be explained by the low concentration of water measured in the organic phase resulting in a low SNR for the water peak, which slightly increases the inaccuracy of the integration. The slope of the measured tie lines agree with the ones published in the literature. The tie lines measured in this work are located on the overall composition of the mixture given by the initial weight thus the mass balance is fulfilled. The data from the present work can be well correlated with the NRTL-model. Applying the SCM confirms the good agreement of the measured data and the literature data as well. The SCM diagrams of all investigated non-reactive systems are further discussed in the Supplementary information.

3.2. System diethyl ether + acetone + water

Fig. 5 shows the composition of the two phases in the LLE of the system diethyl ether + acetone + water determined in this work using the sample shifting method at 22.0 °C together with literature data at 20.0 °C [33] and 30.0 °C [34], respectively. Acetone is more soluble in the upper diethyl ether rich phase than in the lower water rich phase. The tie lines measured in this work are located on the overall composition of the mixture given by the initial weight thus the mass balance is fulfilled. The literature data reveal, that the temperature has no significant influence on the phase composition in the studied temperature range. The LLE data of this work are in good agreement with the literature data. There are no significant differences in the water rich phase and the tie line direction. Only the water content in the organic phase obtained in the present study is slightly higher then those reported in the literature but the deviation is still within the measurement error taking into account that the inaccuracy of the integration slightly increases with a smaller water peak. The data from the present work can be well correlated with the NRTL-model.

3.3. System diethyl ether + methanol + water

Fig. 6 shows the composition of the two phases in the LLE of the system diethyl ether + methanol + water determined in this work at 22.0 °C together with literature data at 20.0 °C [35] and 25.0 °C

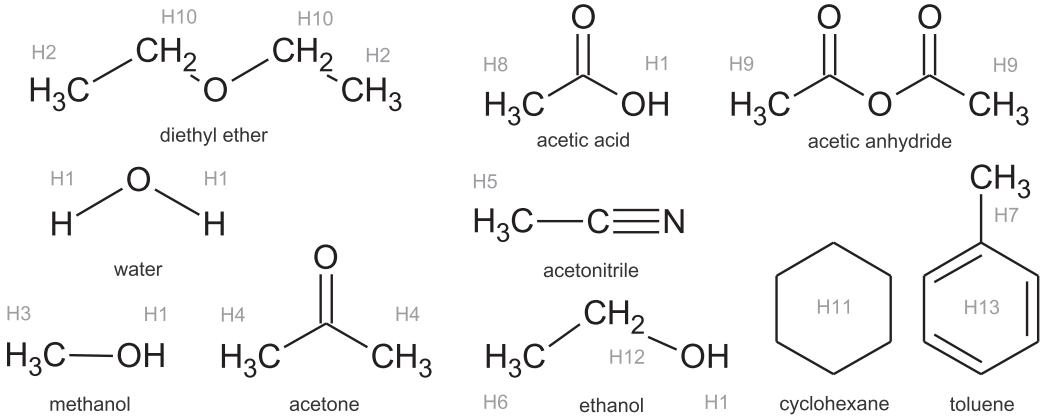

Fig. 2. Chemical structures of the components with labels used for the ^{1}H peak assignment.

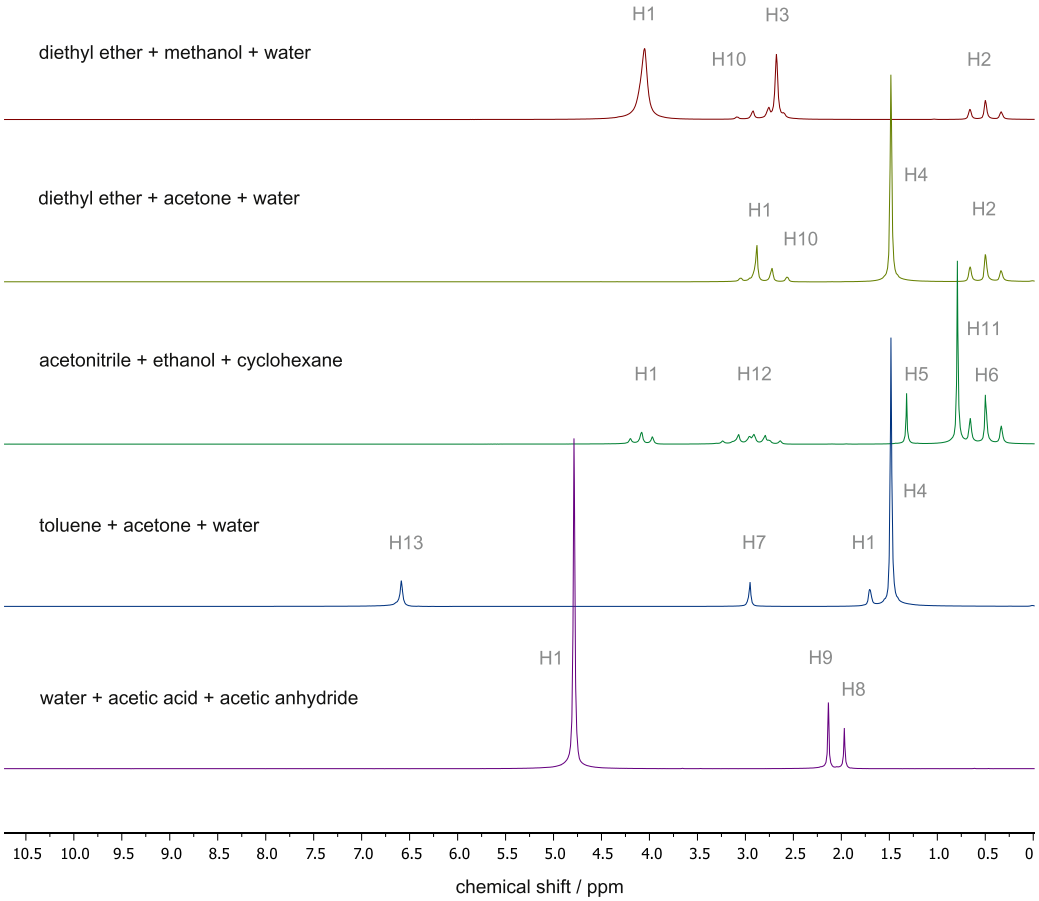

Fig. 3. ^{1}H spectra of the reference samples acquired using medium field NMR spectroscopy.

[2], respectively. The corresponding tie lines determined in this work are located on the overall composition of the mixture given by the initial weight thus the mass balance is fulfilled. The literature data for the LLE are contradictory to the results of the present study. Neither the enrichment of methanol in one of the phases nor the slope of the tie lines match. The data from the present work confirm the shape of the binodal curve in the organic phase measured by Merzougui et al. [2], though other results are found for the slope of the tie lines. Possibly the enrichment of methanol in one of the coexisting phases is highly sensitive to the experimental conditions. The data from the present work can be well correlated with the NRTL-model. However the predicted binodal curve from this work is not as flat as those from the literature data.

Table 2
Compositions of the reference samples expected from the gravimetrical sample preparation $x_i^{expected}$ and determined by ^{1}H medium field NMR spectroscopy x_i^{NMR}. Used integration methods: ^{DI} - direct integration, ^{DEC} - deconvolution, ^{CDI} - corrected direct integration.

Component	Evaluated peak	$x_i^{expected}$ mol mol^{-1}	x_i^{NMR} mol mol^{-1}	$\lvert\Delta x_i^{sbol.}\rvert$ mol mol^{-1}	$\lvert\Delta x_i^{rel.}\rvert$ %
toluene	H7 ^{DI}	0.136	0.134	0.002	1.3
acetone	H4 ^{DI}	0.665	0.666	0.001	0.1
water	H1 ^{DI}	0.199	0.200	0.001	0.5
diethyl ether	H2 ^{DI}	0.206	0.218	0.012	5.8
acetone	H4 ^{DI}	0.582	0.565	0.017	2.9
water	H1 ^{CDI}	0.212	0.217	0.005	2.3
diethyl ether	H2 ^{DI}	0.289	0.293	0.004	1.5
methanol	H3 ^{CDI}	0.404	0.401	0.003	0.7
water	H1 ^{CDI}	0.307	0.305	0.001	0.5
acetonitrile	H5 ^{DI}	0.199	0.206	0.007	3.6
ethanol	H6 ^{DEC}	0.606	0.595	0.011	1.8
cyclohexane	H11 ^{DEC}	0.195	0.199	0.004	1.9

3.4. System acetonitrile + ethanol + cyclohexane

Fig. 7 shows the compositions of the two phases in the LLE of the system acetonitrile + ethanol + cyclohexane determined in this work at 22.0 °C using the sample shifting method together with literature data at 25.0 °C [36]. The measured phase compositions are in good agreement with the data of Nagata and Katoh [36], though the compositions of both phases scatter slightly about the continuous shape of the binodal curve. The slope of the measured tie lines differs only slightly from the ones determined by Nagata and Katoh [36]. Also in this system, the total initial weight of both phases is located on the measured tie lines. This result confirms the accuracy and consistency of the measurement method.

This system is also examined using the sample shifting method with ^{13}C medium field NMR spectroscopy and a the slicing method with ^{1}H high field NMR spectroscopy. Both alternative measurement methods do not achieve the accuracy of the proposed ^{1}H medium field sample shifting method. Moreover, the experimental effort for both alternative measurement methods was higher than for the proposed one. A detailed description of the methods and a comparison of the results is shown in the Supplementary Information.

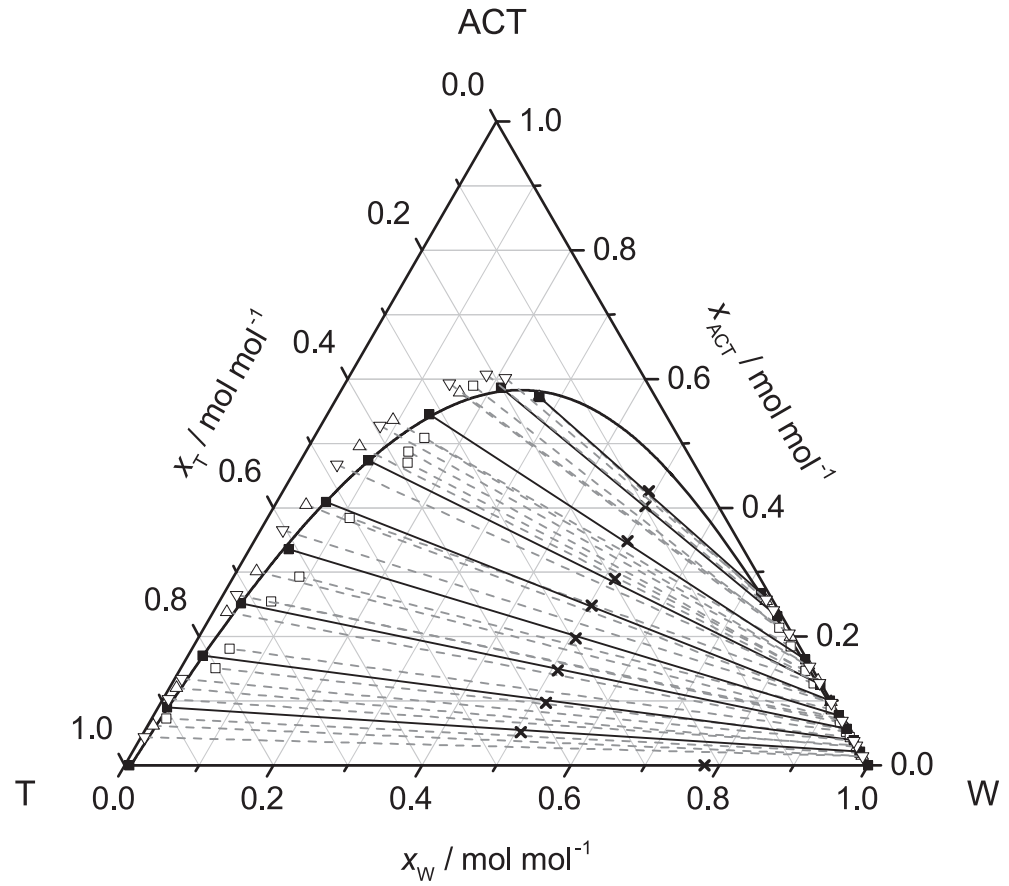

Fig. 4. Liquid-liquid phase equilibrium of the system toluene (T) + acetone (ACT) + water (W) at different temperatures. Compositions measured at 22.0 °C in the present work: (×) initial weight, (■) upper and lower phase determined with the sample shifting method in combination with medium field ^{1}H NMR spectroscopy. (—) NRTL parametrized in this work. Literature data: (□) Afolabi and Edewor [30] at 25.0 °C, (▽) at 20.0 °C and (△) at 30.0 °C (both Pavasovic [29]).

3.5. *Reactive system water + acetic acid + acetic anhydride*

Fig. 8 shows the results of the in situ investigation of the reaction of water and acetic anhydride to acetic acid (Reaction I) in the coexisting liquid phases using the sample shifting method.

$$\underset{\text{acetic anhydride}}{(CH_3CO)_2O} + \underset{\text{water}}{H_2O} \rightarrow \underset{\text{acetic acid}}{2CH_3COOH} \quad (1)$$

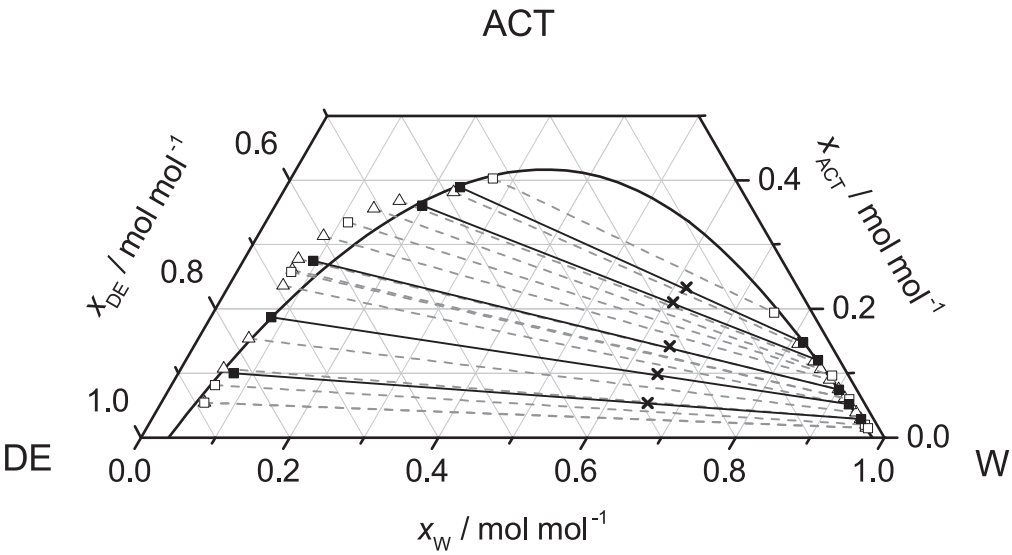

Fig. 5. Liquid-liquid phase equilibrium of the system diethyl ether (DE) + acetone (ACT) + water (W) at different temperatures. Compositions measured at 22.0 °C in the present work: (×) initial weight, (■) upper and lower phase determined with the sample shifting method in combination with medium field ^{1}H NMR spectroscopy. (—) NRTL parametrized in this work. Literature data: (□) Sokolov et al. [33] at 20.0 °C, (△) Krishnamurty et al. [34] at 30.0 °C.

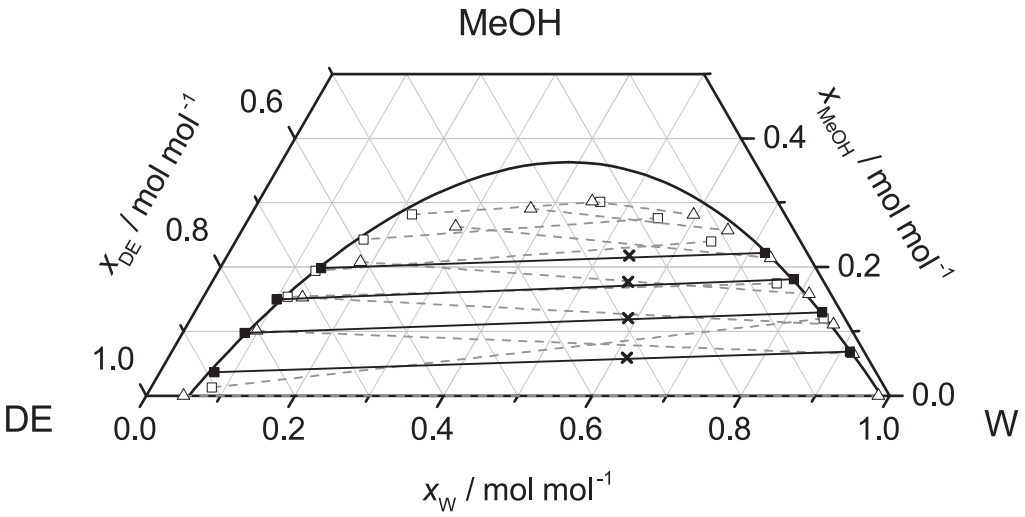

Fig. 6. Liquid-liquid phase equilibrium of the system diethyl ether (DE) + methanol (MeOH) + water (W) at different temperatures. Compositions measured at 22.0 °C in the present work: (×) initial weight, (■) upper and lower phase determined with the sample shifting method in combination with medium field ^{1}H NMR spectroscopy. (—) NRTL parametrized in this work. Literature data: (□) Merzougui et al. [2] at 20.0 °C, (△) Letcher et al. [35] at 25.0 °C.

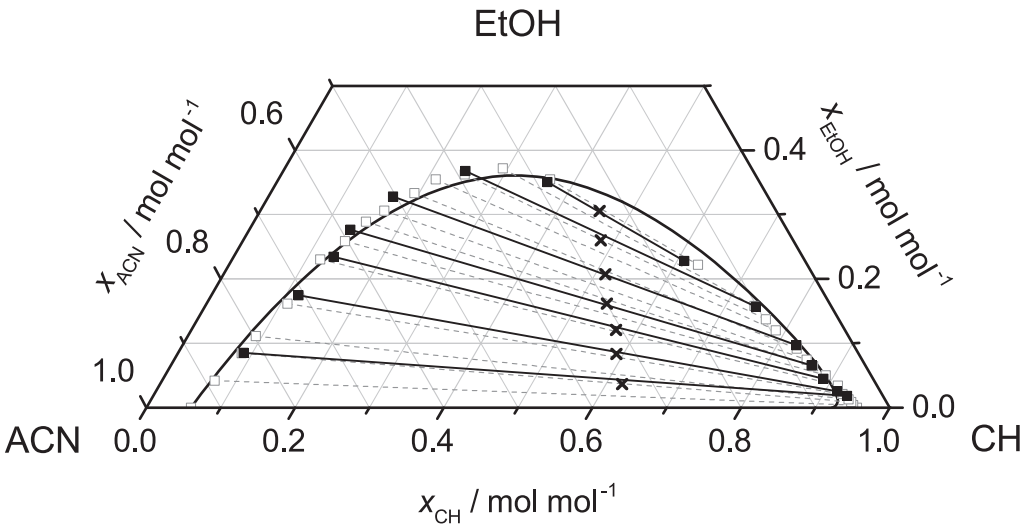

Fig. 7. Liquid-liquid phase equilibrium of the system acetonitrile (ACN) + ethanol (EtOH) + cyclohexane (CH) at different temperatures. Compositions measured at 22.0 °C in the present work: (×) initial weight, (■) upper and lower phase determined with the sample shifting method in combination with medium field ^{1}H NMR spectroscopy. (—) NRTL parametrized in this work. Literature data: (□) Nagata and Katoh [36] at 25.0 °C.

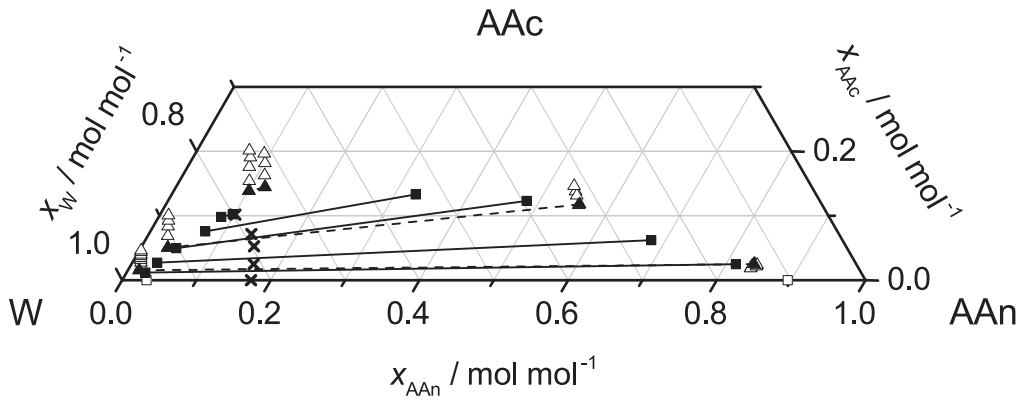

Fig. 8. Liquid-liquid phase equilibrium of the reactive system water (W) + acetic acid (AAc) + acetic anhydride (AAn) at 22.0 °C. Compositions of the coexisting phases measured in the present work with medium field ^{1}H NMR spectroscopy: (×) initial weight, (■) upper and lower phase determined with the sample shifting method in combination with medium field NMR spectroscopy. Measurement of the progress of reaction: (▲) first data point of the phase composition after mixing the reactants, (△) repeated measurements of the composition during reaction. Literature data: (□) Interpolation of binary LLE data from Marek [37].

The literature data shown in Fig. 8 results from a linear interpolation between 18.2 °C and 38.7 °C [37].

With the standard ^{1}H NMR method the LLE is investigated. The fast ^{1}H NMR method is used to monitor the reaction progress in both phases (cf. 2.2.2).

To our knowledge the LLE of the reacting biphasic system of water and acetic anhydride to acetic acid is determined for the first time in this work. The measured compositions of the upper and lower phase in the LLE indicate a miscibility gap that narrows with increasing acetic acid concentration. As shown in Fig. 8, the tie lines are not located on the overall composition given by the initial weights which indicates that the chemical reaction takes place in the phases during preparation and measurement.

The results of the reaction progress monitoring are depicted in Fig. 8 as well. The change of the composition caused by reaction follows a vertical line. This vertical line is in agreement with the stoichiometric lines of the given reaction I. It can be concluded from the observed change of composition that the rate of acetic acid formation is greater in the water rich phase than in acetic anhydride rich phase. Obviously, the dissociation of acetic acid in water and the formation of protons catalyze the reaction. The comparison of the different measurement results (LLE and progress of the reaction) reveals that the miscibility gap narrows upon the reaction.

4. Conclusion

In the present work, we demonstrated that the sample shifting method in combination with medium field NMR spectroscopy is an appropriate approach for in situ investigations of multicomponent LLE at ambient temperature. The great advantage of the method is the non-invasive measurement of the composition of the two coexisting phases. Equilibration, phase separation, and analysis are carried out in a 5 mm NMR glass tube. The method requires only small amounts of chemicals and is also suitable for hazardous substances. Moreover, no sampling and calibration is necessary which reduces the experimental error and the time effort. Another advantage of the new method is the possibility to quickly determine the time which is needed for equilibration of the phases just by repeated measurements. However the feasibility of the method is strongly dependent on the chemical resolution of the investigated components and should be checked previously.

In contrast to the slicing method, the sample shifting method requires less preparation and shimming effort as well as the line shape of the resulting spectrum is much better than with spatially resolved spectroscopy. Moreover, the application of the sample shifting method is straight forward and does not require a specially trained operator. With a particularly designed probe head (an example is given by Leclerc et al. [11]) the sample shifting can be carried out in a high field NMR spectrometer as well and a thermostatisation of the sample can be provided in a large temperature range.

As a proof of concept four non-reactive and one reactive ternary solvent systems with a miscibility gap were examined. The measured compositions of the reference samples were in good agreement with the ones expected from the gravimetrical preparation of the samples which demonstrates the accuracy of the measuring method (the absolute deviation was on average smaller than 1 mol%). For the non-reactive systems containing water the water content in the organic phase was slightly higher then those reported in the literature. The small deviation can be explained by the low concentration of water measured in the organic phase resulting in a low SNR for the water peak which slightly increases the inaccuracy of the peak integration. Except of these deviations the resulting phase compositions were in good agreement with published literature data. With the chosen NMR medium field method low concentrations up to 2 mol% and 5 mol% are quantitatively measurable with ^{1}H and ^{13}C NMR spectroscopy, respectively. By increasing the number of subsequent scans also lower concentrations would be detectable. For the biphasic formation of acetic acid from water and acetic anhydride, the ternary phase compositions were measured for the first time. Furthermore, the extent of reaction as well as the reactivities were followed in the two coexisting phases. The observed change of the composition of the reacting mixtures follows well the stoichiometry of the reaction. In addition, g^{E}-models (NRTL and UNIQAC model) were fitted to the non-reactive ternary experimental data. The SCM was applied to compare and assess the measured data, the data from literature as well as the prediction using the models parametrized in this work.

These results evidence that the proposed sample shifting method can be well used in combination with medium field NMR spectroscopy. Hence, the proposed measuring method was applied for further systems containing water and different poly(oxymethylene) dimethyl ethers [38]. Thus, the proposed measuring method is an valuable tool to receive a swift overview of the physico-chemical properties of biphasic multicomponent systems.

Acknowledgments

The authors thank the German Science Foundation (DFG) for the financial support within the Collaborative Research Center SFB/TRR 173 Spin + X. The authors thank Daniel Holland (University of Canterbury, Christchurch, New Zealand) for the fruitful discussion on the implementation of the slicing NMR spectroscopy method.

Appendix A. Supplementary data

Supplementary data related to this article can be found at http://dx.doi.org/10.1016/j.fluid.2017.01.027.

References

[1] M. Schmitt, H. Hasse, J. Chem. Eng. Data 50 (2005) 1677–1683, http://dx.doi.org/10.1021/je050141m.
[2] A. Merzougui, A. Hasseine, A. Kabouche, M. Korichi, Fluid Phase Equilibria 309 (2011) 161–167, http://dx.doi.org/10.1016/j.fluid.2011.07.011.
[3] D. Marion, Mol. Cell. Proteomics 12 (2013) 3006–3025, http://dx.doi.org/10.1074/mcp.O113.030239.
[4] O. Zerbe, S. Jurt, Applied NMR Spectroscopy for Chemists and Life Scientists, Wiley-VCH Verlag GmbH & Co. KGaA, 2014.
[5] A. Scheithauer, E. von Harbou, H. Hasse, T. Grützner, C. Rijksen, D. Zollinger, W.R. Thiel, AIChE J. 61 (2015) 177–187, http://dx.doi.org/10.1002/aic.14623.
[6] A. Brächer, S. Hoch, K. Albert, H.J. Kost, B. Werner, E. von Harbou, H. Hasse, J. Magnetic Reson. 242 (2014) 155–161, http://dx.doi.org/10.1016/j.jmr.2014.02.013.
[7] E.J. Kibrik, O. Steinhof, G. Scherr, W.R. Thiel, H. Hasse, Industrial Eng. Chem. Res. 53 (2014) 12602–12613, http://dx.doi.org/10.1021/ie5001746.
[8] M. Maiwald, Hochauflösende online NMR-Spektroskopie für das Reaktions- und Prozessmonitoring, Cuvillier Verlag, Göttingen, 2012.
[9] M.A. Bernstein, M. Stefinović, C.J. Sleigh, Magnetic Reson. Chem. 45 (2007) 564–571, http://dx.doi.org/10.1002/mrc.2007.
[10] M. Maiwald, H.H. Fischer, M. Ott, R. Peschla, C. Kuhnert, C.G. Kreiter, G. Maurer, H. Hasse, Industrial Eng. Chem. Res. 42 (2003) 259–266, http://dx.doi.org/10.1021/ie0203072.
[11] S. Leclerc, G. Trausch, B. Cordier, D. Grandclaude, A. Retournard, J. Fraissard, D. Canet, Magnetic Reson. Chem. 44 (2006) 311–317, http://dx.doi.org/10.1002/mrc.1757.
[12] R. Freeman, Concepts Magnetic Reson. 38A (2011) 1–6, http://dx.doi.org/10.1002/cmr.a.20199.
[13] G.E. Wagner, P. Sakhaii, W. Bermel, K. Zangger, Chem. Commun. 49 (2013) 3155–3157, http://dx.doi.org/10.1039/c3cc39107h.
[14] E.H.L. Yuen, A.J. Sederman, L.F. Gladden, Appl. Catal. A General 232 (2002) 29–38, http://dx.doi.org/10.1016/S0926-860X(02)00064-9.
[15] E. von Harbou, H.T. Fabich, M. Benning, A.B. Tayler, A.J. Sederman, L.F. Gladden, D.J. Holland, J. Magnetic Reson. 261 (2015) 27–37, http://dx.doi.org/10.1016/j.jmr.2015.09.013.
[16] C. Mantel, P.-A. Bayle, S. Hediger, C. Berthon, M. Bardet, Magnetic Reson. Chem. 48 (2010) 600–606, http://dx.doi.org/10.1002/mrc.2628.

[17] B. Luy, Angew. Chem. 123 (2011) 371–373, http://dx.doi.org/10.1002/ange.201005976.
[18] E. Danieli, J. Perlo, B. Blümich, F. Casanova, Angew. Chem. 122 (2010) 4227–4229, http://dx.doi.org/10.1002/ange.201000221.
[19] S.K. Küster, E. Danieli, B. Blümich, F. Casanova, Phys. Chem. Chem. Phys. 13 (2011) 13172–13176, http://dx.doi.org/10.1039/C1CP21180C.
[20] F. Dalitz, L. Kreckel, M. Maiwald, G. Guthausen, Appl. Magn. Reson. 45 (2014) 411–425, http://dx.doi.org/10.1007/s00723-014-0522-x.
[21] M.V. Silva Elipe, R.R. Milburn, Magnetic Reson. Chem. 54 (2016) 437–443, http://dx.doi.org/10.1002/mrc.4189.
[22] N. Zientek, C. Laurain, K. Meyer, M. Kraume, G. Guthausen, M. Maiwald, J. Magnetic Reson. 249 (2014) 53–62, http://dx.doi.org/10.1016/j.jmr.2014.10.007.
[23] M. Goldbach, E. Danieli, J. Perlo, B. Kaptein, V.M. Litvinov, B. Blümich, F. Casanova, A.L.L. Duchateau, Tetrahedron Lett. 57 (2016) 122–125, http://dx.doi.org/10.1016/j.tetlet.2015.11.077.
[24] V. Sans, L. Porwol, V. Dragone, L. Cronin, Chem. Sci. 6 (2015) 1258–1264, http://dx.doi.org/10.1039/C4SC03075C.
[25] T. Parker, E. Limer, A.D. Watson, M. Defernez, D. Williamson, E.K. Kemsley, Trends Anal. Chem. 57 (2014) 147–158, http://dx.doi.org/10.1016/j.trac.2014.02.006.
[26] D. Kreyenschulte, E. Paciok, L. Regestein, B. Blümich, J. Büchs, Biotechnol. Bioeng. 112 (2015) 1810–1821, http://dx.doi.org/10.1002/bit.25599.
[27] M.R.M. Koos, E. Danieli, F. Casanova, B. Blümich, B. Luy, Magnetic Reson. Chem. 54 (2016) 527–530, http://dx.doi.org/10.1002/mrc.4222.
[28] J. Burger, M. Kaul, H. Hasse, Chem. Eng. Sci. 143 (2016) 105–113, http://dx.doi.org/10.1016/j.ces.2015.12.008.
[29] V. Pavasovic, Equilibrium Properties of the System Toluene-acetone-water, Chemical Dynamics Laboratory Boris Kidric Institute, 1974.
[30] T.J. Afolabi, T.I. Edewor, Int. J. Chem. Mol. Nucl. Mater. Metallurgical Eng. 5 (2011) 1124–1127.
[31] H.W. Brandt, J. Schröter, G. Strauss, Testsysteme für die Flüssig-flüssig Extraktion, Report Farbenfabriken Bayer, 1975.
[32] A. Hackl, W. Solar, G. Ziebland, Determination of the Test System Water - Acetone - Toluene, Institut für Verfahrenstechnik und Technologie der Brennstoffe, TH Wien, 1975.
[33] N. Sokolov, I. Borisova, V. Vatskova, M. Erlykina, V. Mikhailov, Khimichskaya Promyshlennost (1987) 17–18.
[34] V. Krishnamurty, P. Murti, R. Venkata, J. Sci. Industrial Res. B Phys. Sci. 12 (1953) 583–590.
[35] T.M. Letcher, J.D. Sewry, D. Naran, Fluid Phase Equilibria 49 (1989) 187–193, http://dx.doi.org/10.1016/0378-3812(89)80015-9.
[36] I. Nagata, K. Katoh, Thermochim. Acta 39 (1980) 45–62, http://dx.doi.org/10.1016/0040-6031(80)80055-4.
[37] J. Marek, Collect. Czechoslov. Chem. Commun. 21 (1956) 269–280, http://dx.doi.org/10.1135/cccc19560269.
[38] N. Schmitz, A. Friebel, E. von Harbou, J. Burger, H. Hasse, Fluid Phase Equilibria 425 (2016) 127–135, http://dx.doi.org/10.1016/j.fluid.2016.05.017.

von Harbou et al., 2015

Reprinted with permission from: E. von Harbou, H. T. Fabich, M. Benning, A. B. Tayler, A. J. Sederman, L. F. Gladden, D. J. Holland, Quantitative mapping of chemical compositions with MRI using compressed sensing, Journal of Magnetic Resonance, Volume 261, 2015, Pages 27-37, ISSN 1090-7807, DOI 10.1016/j.jmr.2015.09.013

Journal of Magnetic Resonance 261 (2015) 27–37

Contents lists available at ScienceDirect

Journal of Magnetic Resonance

journal homepage: www.elsevier.com/locate/jmr

Quantitative mapping of chemical compositions with MRI using compressed sensing

Erik von Harbou [a], Hilary T. Fabich [b], Martin Benning [b,1], Alexander B. Tayler [b], Andrew J. Sederman [b], Lynn F. Gladden [b], Daniel J. Holland [b,*]

[a] Laboratory of Engineering Thermodynamics, University of Kaiserslautern, Erwin-Schrödinger-Straße 44, 67663 Kaiserslautern, Germany
[b] Department of Chemical Engineering and Biotechnology, University of Cambridge, Pembroke Street, Cambridge CB2 3RA, United Kingdom

ARTICLE INFO

Article history:
Received 20 July 2015
Revised 21 September 2015
Available online 19 October 2015

Keywords:
Concentration mapping
Compressed sensing
Fast acquisition
Quantitative MRI
Total variation
Bregman iteration

ABSTRACT

In this work, a magnetic resonance (MR) imaging method for accelerating the acquisition time of two dimensional concentration maps of different chemical species in mixtures by the use of compressed sensing (CS) is presented. Whilst 2D-concentration maps with a high spatial resolution are prohibitively time-consuming to acquire using full **k**-space sampling techniques, CS enables the reconstruction of quantitative concentration maps from sub-sampled **k**-space data. First, the method was tested by reconstructing simulated data. Then, the CS algorithm was used to reconstruct concentration maps of binary mixtures of 1,4-dioxane and cyclooctane in different samples with a field-of-view of 22 mm and a spatial resolution of 344 μm × 344 μm. Spiral based trajectories were used as sampling schemes. For the data acquisition, eight scans with slightly different trajectories were applied resulting in a total acquisition time of about 8 min. In contrast, a conventional chemical shift imaging experiment at the same resolution would require about 17 h. To get quantitative results, a careful weighting of the regularisation parameter (via the L-curve approach) or contrast-enhancing Bregman iterations are applied for the reconstruction of the concentration maps. Both approaches yield relative errors of the concentration map of less than 2 mol-% without any calibration prior to the measurement. The accuracy of the reconstructed concentration maps deteriorates when the reconstruction model is biased by systematic errors such as large inhomogeneities in the static magnetic field. The presented method is a powerful tool for the fast acquisition of concentration maps that can provide valuable information for the investigation of many phenomena in chemical engineering applications.

1. Introduction

Maps of chemical compositions can provide valuable information for many applications, especially in chemical engineering. They can be used to gain a rigorous understanding of chemical processes and mass transfer phenomena occurring, for example, in catalyst beds, along interfaces, or in and near membranes. This understanding is important for a reliable design and scale-up of chemical processes. Taking samples and analysing them *ex situ* is often not feasible because the sampling disturbs the system and the effort is immense to obtain sufficient spatial resolution to resolve the processes. In this application, magnetic resonance imaging (MRI) offers great potential as it is a non-invasive, spatially resolved measurement technique able to probe optically opaque environments like reactors. In situ MRI has been successfully applied to study conversion and composition profiles or local reaction rates along fixed-bed reactors for various reactions using spatially resolved ^{1}H NMR-spectroscopy [1,2] and ^{13}C NMR-spectroscopy [3–5] also called chemical shift imaging (CSI). The acquisition time needed to obtain multidimensional, fully sampled concentration maps, however, may take several hours [3] which can be detrimental. First, the process has to be operated steadily for several hours so the consumption of chemicals is high which is costly and undesirable concerning the safety in laboratories. Second, transient phenomena that take place within minutes cannot be studied with this technique. This paper presents a method for accelerating the acquisition of spatially resolved concentration maps by the use of compressed sensing (CS).

CS enables the accurate reconstruction of an under-sampled signal by utilising the prior knowledge that the signal is compressible

* Corresponding author at: Department of Chemical and Process Engineering, University of Canterbury, Private Bag, 4800 Christchurch, New Zealand.
E-mail address: daniel.holland@canterbury.ac.nz (D.J. Holland).
[1] Current address: Department of Applied Mathematics and Theoretical Physics, University of Cambridge, Wilberforce Road, CB3 0WA Cambridge, United Kingdom.

http://dx.doi.org/10.1016/j.jmr.2015.09.013
1090-7807/

or sparse with respect to a specific representation [6,7]. As undersampled signals can be used, CS provides a method of reducing the data acquisition times characteristic of many imaging techniques. CS has been successfully applied to reduce the acquisition time of MR images [8,9]. Holland et al. [10] and Tayler et al. [11] demonstrated the potential of CS by reconstructing velocity images in fixed-bed reactors and of multiphase flow, respectively from fast and under-sampled phase-encoded MR measurements. Furthermore, Holland et al. [12] and Kazimierczuk and Orekhov [13] applied CS for fast multidimensional NMR spectroscopy. Hu et al. [14] and Kampf et al. [15] used CS for the accurate reconstruction of three dimensional chemical shift imaging (CSI) of ^{13}C and ^{19}F markers, respectively from under-sampled data sets. When the chemical shift information of the observed chemical species is known and is incorporated into the model used for the reconstruction, images showing different species can be directly recovered with high resolution from the under-sampled signals by CS. Good results with a significant reduction of the scanning time compared to conventional methods have been achieved in medical applications with this method for imaging water and fat [16–18]. The focus of these works was to get a good separation of water and fat in the reconstructed images and not to obtain quantitative information on the composition.

In this work, we apply CS reconstruction to resolve spatially and quantitatively the compositions of different species in mixtures. This method enables the mapping of the composition directly as a function of space. Only the information about the chemical shift of the observed species are required for the reconstruction; there is no need for calibration prior to the analysis. This feature of the presented method is beneficial for many applications in chemical engineering where unstable intermediates are formed during the process that make a calibration impossible. To achieve a high accuracy of the concentration map, however, the parameters of the CS algorithm have to be correctly set. As mentioned above, CS exploits prior knowledge of the signal. This prior knowledge is integrated in the CS solver with a regulariser [6,7]. To get quantitative results, the systematic bias of the CS reconstruction has to be minimised, either by carefully weighting the regulariser or by applying contrast-enhancement approaches. Different generic approaches exist for the identification of good regularisation parameters. In the present work, two different approaches, the L-curve approach [19] and the Bregman iterations [20], are applied for the reconstruction of simulated data of a phantom sample and for the reconstruction of measured data from binary mixtures in different test samples. These results are used to assess the robustness of the approaches to yield concentration maps with a high accuracy. Finally, we present a discussion of the strengths and limitations of the method for the spatial quantification of chemical species.

2. Reconstruction using compressed sensing

2.1. Model equations

The measured **k**-space signal **S** at the echo time t is related to the concentration maps $\mathbf{x}_k$ of all species $k = 1,\dots,M$ via the signal model [16]

$$\mathbf{S}(t) = \sum_{k=1}^{M}\left(\sum_{j=1}^{L_k} w_{k,j}\exp\left(2\pi i\,\delta_{k,j}t\right)\exp\left(-\frac{t+2\tau}{T_2^*}\right)\times\int_{\Omega}\mathbf{x}_k(\mathbf{r})\exp\left(2\pi i\,\mathbf{k}(\mathbf{t})\cdot\mathbf{r}\right)\mathrm{d}\mathbf{r}\right)+\mathbf{v} \tag{1}$$

with

$$\mathbf{k}(t) = \frac{1}{2\pi}\int_0^t \gamma\mathbf{G}(t')\mathrm{d}t' \quad\text{and}\quad \Omega\subset\mathbb{R}^2. \tag{2}$$

In Eq. (1), $\mathbf{v}$ is the noise. $\delta_{k,j}$ denotes the relative chemical shift (related to the resonance frequency of the spectrometer) of the j-th group (peak) that belongs to species k. $w_{k,j}$ is the group weighting factor that exists for all groups $j = 1,\dots,L_k$ of species k. It describes the mole of the nuclei (here ^1H: $n^{^1H}$) in the j-th group per mole of species k (n_k^{species}), see Eq. (3). To get quantitative results from the measured **k**-space signal, the group weighting factors have to be set correctly.

$$w_{k,j} = \frac{n^{^1H}}{n_{k,j}^{\text{group}}}\frac{n_{k,j}^{\text{group}}}{n_k^{\text{species}}}. \tag{3}$$

In Eq. (2), 2τ denotes the time from the excitation pulse to the centre of the echo and T_2^* denotes the apparent T_2-relaxation time. **G** is the vector of the magnetic field gradient that acts at the echo time t. Here, we subsample the **k**-space $S_{p,q}$ as $S(t)$. Eq. (1) can be abbreviated with linear operators, see Eq. (4). The explicit equations for the operators are given in Appendix A.

$$\mathbf{S} = \mathbf{CHS}\cdot\mathcal{F}_u\cdot\mathbf{x}+\mathbf{v}. \tag{4}$$

In Eq. (4), **CHS** denotes the chemical shift operator, $\mathcal{F}_u$ is the undersampled Fourier transform, and **x** is the concatenated matrix of all concentration maps $\mathbf{x}_k$ with $k = 1\dots M$. Eq. (4) can only be applied when spatial and temporal inhomogeneities in the $\mathbf{B}_0$-field are negligible.

2.2. Solving strategy

The goal of the reconstruction is to find well resolved concentration maps **x** from the under-sampled **k**-space measurements **S** so that the signal model according to Eq. (4) is fulfilled. In CS, the reconstruction is obtained by solving a Tikhonov-type optimisation problem of the form (for details, see e.g. Benning et al. [21]):

$$\mathbf{x}_{\text{reconstructed}} = \arg\min_{\mathbf{x}}\left\{\frac{1}{2}\|\mathbf{S}-\mathbf{CHS}\cdot\mathcal{F}_u\cdot\mathbf{x}\|_2^2+\sum_{k=1}^{M}\alpha_k J(\Psi\mathbf{x}_k)\right\}. \tag{5}$$

The first term in Eq. (5) is the fidelity term that models Eq. (1). Here $\|v\|_2 := \sqrt{\sum|v(i)|^2}$ is the standard Euclidean 2-norm. The second term is the regularisation with $J(\Psi\mathbf{x}_k)$ as regularisation functional that enables the incorporation of prior information on the reconstruction. Ψ is a linear operator that transforms the concentration maps **x** to another domain where they are sparse. Thus, the solution of Eq. (5) yields concentration maps that have a sparse representation in the transform domain and that are, according to Eq. (1), consistent with the measured **k**-space data in the least squares sense. The parameter α_k is a positive regularisation parameter that weights the influence of the fidelity and the regularisation term. We found that quantitative reconstruction results are only obtained when the parameters $\alpha_1,\alpha_2,\dots,\alpha_M$ are not chosen independently but based on the group weighting factors $w_{k,j}$ and a constant positive regularisation parameter α,

$$\alpha_k = \alpha\sum_{j=1}^{L_k} w_{k,j}. \tag{6}$$

The concentration maps of the test samples used in the present work to test the method contain sharp edges. Thus, a finite-difference approximation of the gradient operator is used as the sparsifying transform Ψ for all reconstructions carried out in this work. For a discrete, isotropic total variation the regularisation functional becomes $J(\Psi x_k) = \|\Psi x_k\|_{2,1} = \||\Psi x_k\|_2\|_1$. (details of the computation of this term are given in Appendix B) Depending on the features of the concentration maps, further sparsifying transforms, such as wavelet transforms, which are used for smooth changes in the concentration maps, or other one-norm-based

regularisers like the Total Generalised Variation can be chosen as well. A detailed discussion of different regularisers and their implementation is given, for example, by Benning et al. [21].

To solve Eq. (5), we used an inhouse-code written in MATLAB (product of MathWorks, Natick, USA) that is based on a scaled alternating direction method of multipliers (ADMM) [22]. The under-sampled Fourier transformation was performed using a non-uniform fast Fourier transform algorithm that had been developed by Fessler and Sutton [23] and that is accessible online as an open source toolbox [24]. The concentration map $\mathbf{x}_k$ obtained by solving Eq. (5) is given in arbitrary units (a.u.). To get the concentration map $\mathbf{x}_k^{(\mathrm{n})}$ in mole fractions, the concentration $x_k(p)$ of species k has to be scaled in each pixel p,

$$x_k^{(\mathrm{n})}(p) = \frac{x_k(p)}{\sum_{k=1}^{M} x_k(p)}. \tag{7}$$

If pixel p^{out} lies outside the sample where none of the species are present, the sum $\sum_{k=1}^{M} x_k(p^{\mathrm{out}})$ of a well reconstructed concentration map approaches zero and here the concentration of each species $x_k^{(\mathrm{n})}(p^{\mathrm{out}})$ is set to zero by default. In this work, the pixels that lie outside the sample were identified from the "best" of the Bregman iteration reconstructions. The same pixels were set to zero in all reconstructions. It would also be possible and potentially advantageous to identify these pixels from an independent experiment, see for example [10,25], however that was not done here.

The correct choice of the regularisation parameter α is not trivial. In this regard, different approaches have been described in literature. For example, Holland et al. [10] used simulated data to determine the regularisation parameter that yielded the best reconstruction results for a given signal to noise ratio (SNR). The drawback to this approach is that it is always necessary to simulate data very similar to the system under investigation. Hansen [19] suggested the L-curve as a more generic approach to choose a regularisation parameter. The L-curve plots the regularisation term – l_1-norm, here: $\sum_{k=1}^{M}\sum_{j=1}^{L_k} w_{kj}\|\Psi\mathbf{x}_k\|_{2,1}$ – versus the norm of the fidelity term – l_2-norm, here: $\|\mathbf{S} - \mathbf{CHS}\cdot\mathcal{F}_{\mathrm{u}}\cdot\mathbf{x}\|_2$. An example of an L-curve is depicted in Fig. 1. The L-curve starts at low values of the fidelity term and high values of the regularisation term. In other words, the reconstruction fits the measurements precisely but the image likely contains a lot of noise or artefact as it is not well regularised. As the value of α increases, the l_1-norm of the regularisation term decreases. Initially large changes in the l_1-norm are associated with only small changes in the data fidelity term, thus the curve is steep. At some value of α, further increases in α result in small decreases in the l_1 term and large increases in the l_2 term, thus the curve becomes flat. The resulting curve looks approximately "L"-shaped. The point at which the curve turns from a sharp decrease to a flat line is known as the corner of the L-curve, and is indicated by the arrow on Fig. 1. This L-curve represents the range of possible solutions that provide a compromise between the two-norm of the fidelity and the one-norm of the regularization and as such is often considered as a Pareto frontier [26]. The best regularisation parameter corresponds to the reconstruction result that appears on the L-curve in that corner (or a little bit to the right) [19]. Thus, by varying the regularisation parameter in a broad range and plotting the L-curve, a selection criterion for an optimal regularisation parameter is provided.

Benning et al. [21] applied a different approach called Bregman iterations to obtain quantitative phase reconstruction from velocity-encoded MRI measurements. For Bregman iteration, the regulariser is replaced by its Bregman distance in order to create an iterative procedure that refines the solution the further one iterates. For this approach, the regularisation parameter α is set to a value that strongly overweights the regularisation term (cf. Eq. (5)) and the following iterative procedure is carried out [27]:

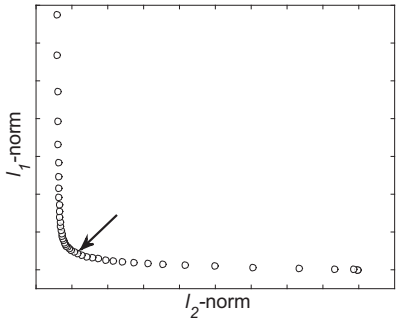

Fig. 1. An example of an L-curve. By varying the regularisation parameter α, the regularisation term can be plotted versus the norm of the fidelity term. The arrow indicates the corner of the L-curve which corresponds to the optimal regularisation parameter α.

$$\mathbf{x}^m = \arg\min_{\mathbf{x}}\left\{\frac{1}{2}\left\|\mathbf{S}^{m-1} - \mathbf{CHS}\cdot\mathcal{F}_{\mathrm{u}}\cdot\mathbf{x}\right\|_2^2 + \alpha\sum_{k=1}^{M}\sum_{j=1}^{L_k} w_{kj}\|\Psi\mathbf{x}_k\|_{2,1}\right\} \tag{8a}$$

$$\mathbf{S}^m = \mathbf{S}^{m-1} + (\mathbf{S} - \mathbf{CHS}\cdot\mathcal{F}_{\mathrm{u}}\cdot\mathbf{x}^m) \quad \text{with} \quad \mathbf{S}^0 = \mathbf{S} \tag{8b}$$

The iteration given in Eqs. (8a) and (8b) is repeated until a stop criterion is satisfied. Benning et al. [21] and Yin et al. [27] demonstrated that Morozov's discrepancy principle [28], given in Eq. (9), yielded satisfactory reconstruction results in combination with the Bregman iteration.

$$\|\mathbf{S} - \mathbf{CHS}\cdot\mathcal{F}_{\mathrm{u}}\cdot\mathbf{x}\|_2 \leqslant \sigma\sqrt{N_{\mathrm{samples}}} \tag{9}$$

In Eq. (9), σ denotes the standard deviation of the noise and N_{samples} is the number of samples. Thus, the right hand side of Eq. (9) refers to the noise level. Morozov's discrepancy principle states that the error between the sub-sampled Fourier transform of the reconstruction and the measured **k**-space data differ by less than the normally distributed noise (which has mean zero and standard deviation σ). As long as this deviation is larger, data and reconstruction will differ by more than just noise. This stopping criterion is also applicable for selecting the optimum α value using the L-curve approach. It has the advantage that it is mathematically well-defined compared to the selection criterion "in the corner of the L-curve".

The L-curve and Bregman iterations were applied in the present work to reconstruct quantitatively maps of the composition of simulated data and data from real measurements of test samples. By comparing the obtained maps of the composition with the expected values, the performance of both approaches and the applicability of the selection criterion (in the corner of the L-curve) and the stopping criterion (Morozov's discrepancy principle) is assessed.

3. Experiments

All experiments were performed on a Bruker AV-400 spectrometer (Rheinstetten, Germany) operating at a ^{1}H resonance frequency of 400.25 MHz with a vertical 9.4 T superconducting magnet. The spectrometer was equipped with a 25 mm diameter birdcage radio-frequency coil and with a shielded and water cooled gradient system producing a maximum gradient strength of 1.46 T/m in the x, y, and z directions.

3.1. Sampling scheme and acquisition parameter

The concentration maps were obtained with a slice selective two-dimensional spin echo pulse sequence using a 90° hard pulse and a 180° gaussian shaped soft pulse. Spiral trajectories were chosen to subsample **k**-space. As demonstrated by Tayler et al. [11], spiral trajectories present a suitable sampling scheme for CS. In

the present work, however, two different spirals strung together into a single trajectory were used to ensure the centre of the echo was formed near the centre of **k**-space. The spirals were constructed using an algorithm that had been developed by Lustig et al. [29] and that is accessible online as open source toolbox [30]. Two different basic types of trajectories (type A and type B) were designed. Type A starts at the centre of **k**-space, spirals out, comes back straight, goes through the centre of **k**-space, out again, and finally, it spirals back to the centre of **k**-space. Trajectory B is simply the opposite. Starting at the centre of **k**-space, it goes straight out, spirals back to the centre of **k**-space, spirals out again, and comes straight back to the centre of **k**-space. The entire sampling scheme employed for the concentration map consists of eight trajectories (four of type A and four of type B). Each trajectory is turned about the centre of **k**-space by a different angle so that a good coverage of **k**-space is achieved. To increase the randomness of the sampling scheme, the spirals are distorted with a sinusoidal oscillation at a higher frequency and lower amplitude than the main spiral trajectory. The direction of the oscillation was chosen such that it was perpendicular to the direction of the main spiral at all times. The amplitude and frequency were different for each spiral. Furthermore, different numbers of points were added at the beginning and/or removed at the end of each of the eight trajectories. In this way, all eight trajectories have the same length (number of points) but the centre of the echo is formed at different locations that are distributed around the centre of **k**-space. A better resolution of the chemical shift information is obtained in experiments using this type of trajectory compared to experiments with trajectories where the echo is always formed in the centre of **k**-space. The trajectories were then further processed using the algorithms of Lustig et al. [29]. By adding and removing points within the trajectories the algorithm ensures that the trajectories yield the desired field-of-view (FOV) and that they do not exceed the maximum gradient strength and slew rate achievable by the hardware. Other sampling schemes based on Lissajou curves or lemniscates were tested as well but gave significantly worse results compared to the results obtained with the spiral based trajectories.

For a good reconstruction of the concentration maps, the trajectories generated by the gradients during the acquisition have to be known very precisely. For that reason, the trajectories were measured using the technique of Duyn et al. [31]. To reduce errors in the phase measurement associated with inhomogeneities in the $\mathbf{B}_0$-field, the technique was slightly modified and a volume selective excitation was used as suggested by Tayler et al. [32].

In the present work, a sampling scheme designed as described above was employed with 8×551 complex data points and a dwell time of 2.5 μs. The sampling scheme is depicted in Fig. 2. The concentration maps were obtained with a field-of-view of 22 mm × 22 mm and a resolution of 344 μm × 344 μm for a slice thickness of 0.5 mm. The repetition time of the experiment was approximately 15 s and a 4 step phase-cycle was used, giving a total acquisition time of about 8 min.

The sampling scheme is obtained by integration (cumulative summation) of the acquire data as describe by Duyn et al. [31]. Thus the small measurement errors add up so that points at the end of the sampling scheme are subjected to larger errors than points earlier in the sampling scheme. For that reason, the reproducibility in the measurements at the same values of k_x and k_y is better in the part of the sampling scheme shown in Fig. 2 (b) at $k_x \approx 7.5\ \mathrm{cm}^{-1}$ and $k_y \approx -6\ \mathrm{cm}^{-1}$ when compared to the part of the sampling scheme at $k_x \approx 8\ \mathrm{cm}^{-1}$ and $k_y \approx -5\ \mathrm{cm}^{-1}$; the latter points being acquired much later during the acquisition.

3.2. Generation of simulated data

To generate simulated data, first, phantom concentration maps of a binary mixture of species A and B were created. In the present work, the concentrations were set to a constant value ($x_A^{(n)} = 0.667$ mol/mol, $x_B^{(n)} = 0.333$ mol/mol). The relative chemical shifts and group weighting factors of species A were $\delta_A = (800\ \mathrm{Hz}, 200\ \mathrm{Hz}, -400\ \mathrm{Hz})$ and $\mathbf{w}_A = (3/8, 1/4, 1/8)$, respectively. The relative chemical shift and weighting factor of species B was $\delta_B = 0$ Hz and $w_B = 1/4$, respectively. The image size was set to 64×64 pixels. The phantom concentration map of species A is shown in Fig. 3.

By means of Eq. (4), simulated data were generated for these phantom concentration maps. The noise **v** was Gaussian distributed and the noise level was set according to the experimental noise level determined by repeated measurements.

3.3. Preparation of test samples

To test the reconstruction method experimentally, two different test samples of about 5 ml were prepared in vials (inner diameter: 19 mm). Test sample A was a binary homogeneous mixture of cyclooctane and 1,4-dioxane ($x_{\mathrm{dioxane}} = 0.761$ mol/mol). For the preparation of test sample B, a small vial (inner diameter: 11 mm) was inserted into the large vial. Both vials were filled with binary homogeneous mixtures of cyclooctane and 1,4-dioxane with different compositions. The concentration of 1,4-dioxane in the small, inner vial was $x_{\mathrm{dioxane}}^{\mathrm{inner}} = 0.666$ mol/mol and in the large, outer vial $x_{\mathrm{dioxane}}^{\mathrm{outer}} = 0.415$ mol/mol. Additionally, a Teflon tube

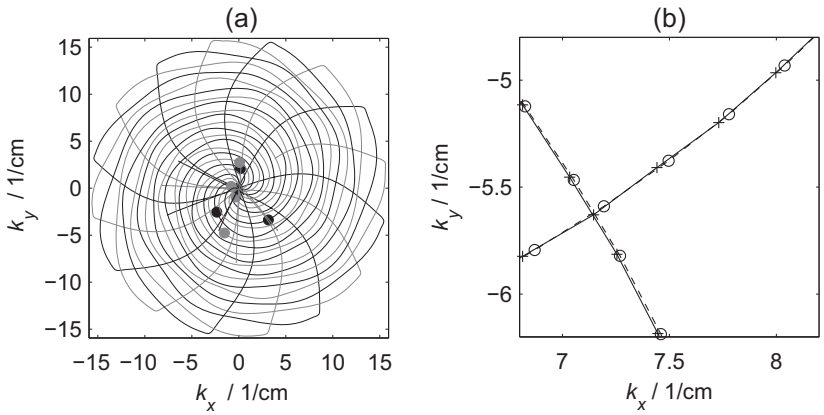

Fig. 2. (a) Spiral based sampling scheme with 8×551 data points. The bullets indicate the location of the centre of the spin echo. (b) Zoomed view of a comparison of repeated measurements (+/○). The measured points in k-space are indicated by the symbols; the lines are linear interpolations to guide the eye.

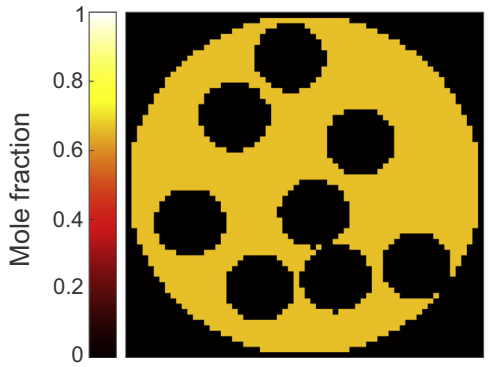

Fig. 3. Phantom concentration map of species A with $x_A^{(n)} = 0.667$ mol/mol. Image size: 64 × 64 pixels.

(inner diameter 4 mm) was inserted into the large, outer vial to test the resolution of the reconstruction method. As the Teflon tube was open at the ends, the composition of the liquid inside the Teflon tube was the same as the composition of the liquid contained in the large, outer vial.

The chemical shift of interest in these reconstructions is the chemical shift relative to the resonant frequency of the acquisition. This chemical shift is measured relative to one of the frequencies in the sample, and not relative to a standard reference species, such as tetramethylsilane. In this case, we set the resonant frequency of the instrument to the frequency of the peak for 1,4-dioxane. The relative chemical shift for the binary mixture of 1,4-dioxane and cyclooctane was then determined by the acquisition of a standard ^{1}H-spectrum of the sample. The results are summarised in Table 1.

4. Results and discussion

4.1. Reconstruction of simulated data

Fig. 4(a) shows the relative error of the reconstructed concentration map of species A compared to the concentration map that was input to the simulation as shown in Fig. 3. In Fig. 4(b), a comparison of the reconstructed concentration profile compared to the input concentration profile in the middle of the sample is depicted. The reconstruction was carried out with a regularisation parameter $\alpha = 0.004$ determined by the L-curve approach (for details, see below). The results demonstrate that both a good spatial resolution is achieved in the reconstructed image and that the reconstruction yields almost perfect quantitative results. Only at the corners and edges larger deviations occur in the reconstructed concentration map. The reason for this behaviour is a systematic error that is introduced because of the discretisation of the gradient operator Ψ with finite differences (cf. Eq. (5)). Other discretisation approaches exist with a lower systematic error [33]. The optimisation of the gradient operator, however, is not in the scope of this paper. The reconstruction results using 19 Bregman iterations give similar results (not shown here).

Table 1
Measured relative chemical shift and weighting factor (mole of ^{1}H per mole of the species).

Species	Group	Rel. chem. shift (Hz)	Weighting
1,4-Dioxane	CH_2	0	8
Cyclooctane	CH_2	−814	16

4.1.1. Optimisation of reconstruction

As mentioned above, both the L-curve approach and Bregman iterations were applied to reconstruct the simulated data of the phantom concentration maps. The reconstruction results are summarised in Fig. 5 for the L-curve approach and in Fig. 6 for the Bregman iterations. Figs. 5(a/b) and 6(a/b) show the reconstructed mean mole fraction of species A and the standard deviation of the mole fraction of species A (related to the true value) as a function of the regularisation parameter and number of Bregman iterations, respectively. Fig. 5(c) shows the L-curve and Fig. 6(c) shows the l_2-norm as a function of the number of Bregman iteration. As expected, the reconstruction results depend strongly on the chosen regularisation parameter α and on the number of Bregman iterations m_{Bregman}, respectively. However, when the stop or selection criteria discussed above are applied, a parameter (α and m_{Bregman}, respectively) can be found for both approaches that yield a concentration map which represents an almost perfect reconstruction of the phantom concentration map.

The regularisation parameter that corresponds to the corner in the L-curve (cf. Fig. 5(c)) is about $\alpha = 0.004$. This regularisation parameter was used for the reconstruction of the concentration map shown in Fig. 4. Morozov's discrepancy principle (cf. Eq. (9)) is also applicable for the L-curve approach as the noise level intersects with the corner of the L-curve. For this value of the regularisation parameter ($\alpha = 0.004$), the relative error in the reconstructed mean mole fraction of species A is 0.05% and the standard deviation of the reconstructed mole fractions (related to

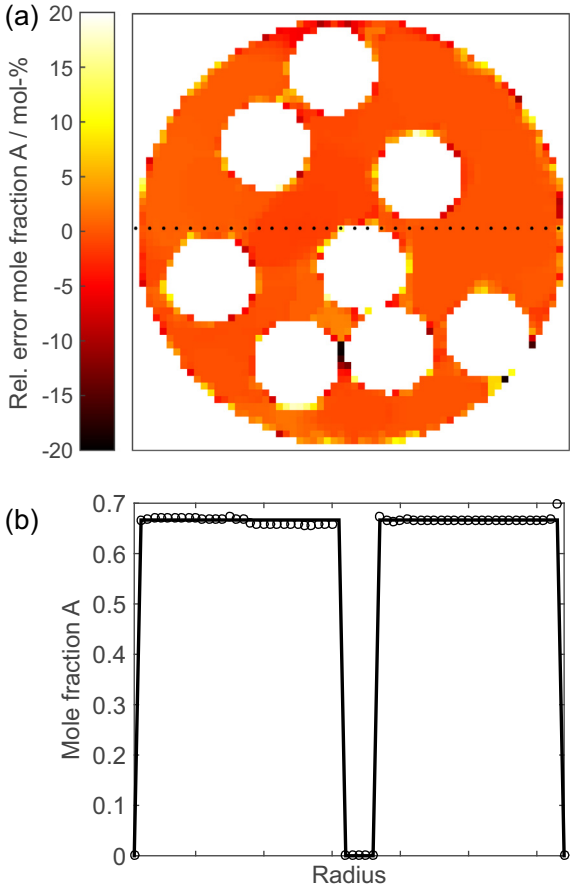

Fig. 4. (a) Relative error of the reconstructed concentration map compared to the set concentration map of species A in the phantom. (b) Radial concentration profile of species A through the sample at the location indicated with a dotted line in the part (a) of the figure. The reconstruction was carried out with $\alpha = 0.004$ (L-curve apporach). ∘ reconstructed mole fraction, – set mole fraction.

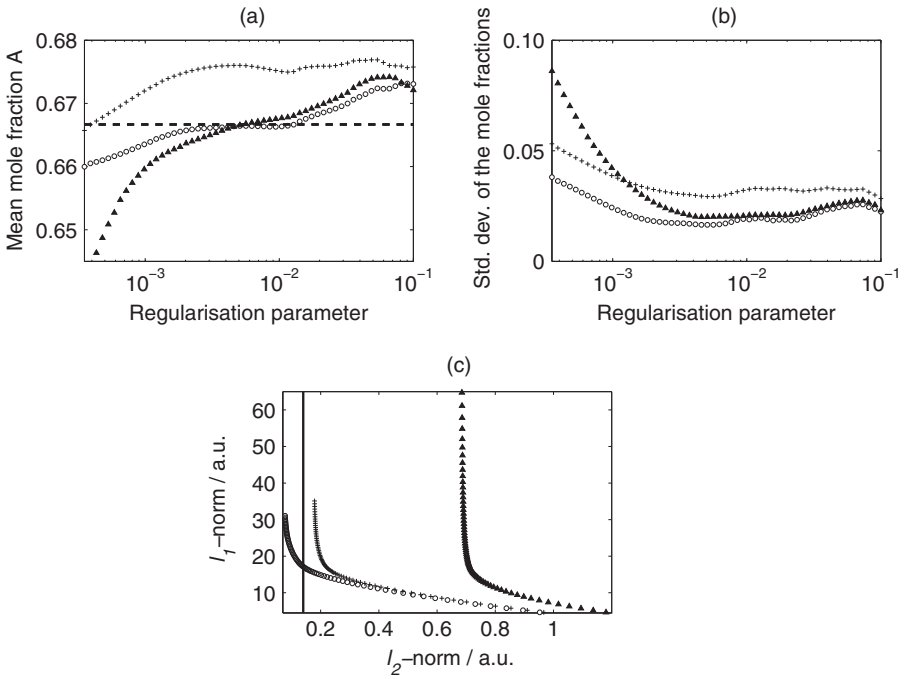

Fig. 5. (a) Mean mole fraction of species A in the reconstructed phantom concentration map, (b) the standard deviation of the reconstructed mole fractions of species A as a function of the regularisation parameter and (c) illustration of the "L-curve" approach whereby the regularisation term (l_1-norm) is shown as a function of the fidelity term (l_2-norm). The optimum regularisation parameter would correspond to the value required to obtain a result at the corner of the l-shaped curves shown. ∘ without systematic error, + systematic error in the chemical shift, ▲ systematic error in the sampling scheme, – – true mole fraction, — noise level.

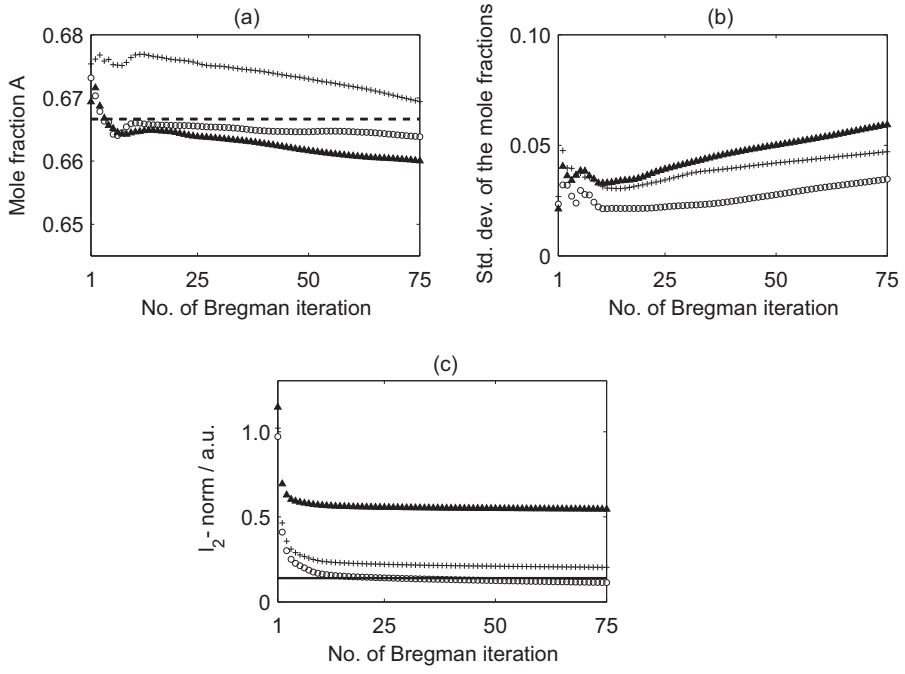

Fig. 6. (a) Mean mole fraction of species A in the reconstructed phantom concentration map, (b) and the standard deviation of the reconstructed mole fractions of species A, and (c) the fidelity term (l_2-norm) as a function of the number of Bregman iterations. ∘ without systematic error, + systematic error in the chemical shift, ▲ systematic error in the sampling scheme, – – true mole fraction, — noise level.

the set mole fraction) exhibits a minimum with a value of 4×10^{-4} mol/mol. The same is true for the approach using Bregman iterations. After 19 iterations, the l_2-norm intersects the noise level and the stop criterion given in Eq. (9) is fulfilled. Here, the relative error in the reconstructed mean mole fraction of species A and the standard deviation of the reconstructed mole fractions show again a minimum (cf. Fig. 6(a/b)). The relative error in the mean mole fraction is 0.3% and the standard deviation of the reconstructed mole fractions is 5×10^{-4} mol/mol showing that an almost perfect reconstruction of the concentration map is achieved.

With respect to the robustness of the two approaches, it is important to evaluate the sensitivity of the reconstruction results on the chosen regularisation parameter and number of Bregman

iterations, respectively. As can be seen in Figs. 5 and 6, the mean mole fraction and the standard deviation are almost constant for a range near the regularisation parameter or number of Bregman iterations that are chosen according to the selection criterion. Hence, the quality of the reconstruction results is not very sensitive to the choice of the regularisation parameter or the number of Bregman iterations, as long as this choice is in a range near the optimal values. This low sensitivity of the reconstruction results on the regularisation parameter near the optimal regularisation parameter is a very important feature of the L-curve approach, since the corner in the L-curve shown in Fig. 5 is not sharp and thus its location is not exactly defined.

Additionally, the optimal range of regularisation parameters or the number of Bregman iterations can be quite well estimated by evaluating the reconstructed images. If the regularisation parameter is chosen too high or the number of Bregman iterations are too few, the image is oversmoothed and the spatial resolution deteriorates significantly caused by the overweighted TV operator. On the other hand, if the regularisation parameter is chosen too small or the number of Bregman iterations are too many, the fidelity term is overweighted and the resulting image looks pixelated. Thus, as expected, when an image with good spatial resolution is obtained (neither oversmoothed nor pixelated) the quantitative information, i.e. the concentration map, is correctly recovered.

4.1.2. Sensitivity to systematic errors

To test the sensitivity of the reconstruction, the simulated data was reconstructed with systematic errors introduced to the model. First, the concentration map was reconstructed with a biased relative chemical shift of species A and B ($\delta_A^{\text{biased}} = \delta_A - 20\,\text{Hz}$, $\delta_B^{\text{biased}} = \delta_B + 30\,\text{Hz}$). The line widths of the NMR samples studied were typically about 100 Hz, therefore the combined shift of 50 Hz in the estimated frequency corresponds to a worst case estimate of the expected error in the chemical shift. Second, the concentration map was reconstructed assuming that there were errors in the measured trajectory map. In order to simulate error in the trajectory map, the reconstructions were performed using an effective sampling scheme given by $\mathbf{k}^{\text{eff}} = \mathbf{k} + \mathbf{v}$ with $\mathbf{v}$ as Gaussian distributed noise. The standard deviation of the noise was determined by repeated measurements of the sampling trajectories as shown in Fig. 2(b). Also the influence of the apparent T_2-relaxation time on the reconstruction results was examined. Since the time to acquire data along a sampling trajectory is only 1.4 ms (i.e. short compared with the T_2-relaxation time of the samples considered in this work), the term $\exp\left(-\frac{t+2\tau}{T_2}\right)$ can be neglected and the chosen value of the apparent T_2-relaxation time has no effect on the reconstruction results. The reconstruction results biased by systematic errors are included both for the L-curve approach and for the Bregman iteration approach in Figs. 5 and 6, respectively.

An error in the chemical shift has a large impact on the reconstructed mole fractions (cf. Figs. 5(a) and 6(a)) whilst the spatial resolution is nearly unaffected. To demonstrate the effect of a systematic error in the chemical shift on the spatial resolution, Fig. 7 shows the sum of the unscaled concentration maps of species A and B when the reconstruction is carried out without systematic errors (Fig. 7(a)) and with a systematic error in the chemical shift (Fig. 7(b)). In both figures the spatial resolution is good and the sum of the concentration maps of species A and species B is almost the same. The systematic error of the chemical shift results in a small amount of signal being incorrectly assigned outside the sample and changes the ratio of species A to species B. These changes cause the concentration of species A and B to be estimated incorrectly (cf. Fig. 5(a)), though the effect is not too severe (1%); the spatial resolution of the image is almost unaffected by a systematic error in the chemical shift.

A systematic error in the sampling scheme causes the reconstruction results to deteriorate compared to the reconstruction without systematic error. The systematic error in the k-space trajectory causes a large shift in the l_2-norm, and hence the L-curve (cf. Figs. 5(c) and 6(c)). The shift of the L-curve does not effect the shape of the L-curve (cf. Fig. 5) and the optimum regularisation parameter α is still located in the corner of the L-curve. The value of α that corresponds to the corner of the L-curve is about 0.007 (the optimal value of α in the corner of the L-curve obtained without systematic error is 0.004). Thus the change of the optimal value of α caused by an introduction of a systematic error is only minor (the overall variation of the value of α along the L-curve is from 1×10^{-1} to 5×10^{-5}). By contrast, Morozov's discrepancy principle, cf. Eq. (9), is not applicable now since the l_2-norm and the noise level do not intersect. However, the L-curve approach can be adapted for use with Bregman iterations. A plot of the l_2-norm versus the number of Bregman iterations shows a corner, as with the L-curve. Here, the optimal range for the number of Bregman iterations is located a little bit to the right of that corner (cf. Fig. 6(c)). The optimal range for the number of Bregman iterations can also be identified by evaluating the reconstructed images. To the left of the optimal range in (i.e. $m_{\text{Bregman}} < 10$), where the l_2-norm has a steep slope (cf. Fig. 6 (c)), the reconstructed images are oversmoothed and to the right of the optimal range (i.e. $m_{\text{Bregman}} > 30$), where the l_2-norm reaches a constant level, the reconstructed images are pixelated. Within the range ($10 < m_{\text{Bregman}} < 30$), little change is seen between images.

4.1.3. Conclusions from simulations

The simulations demonstrate the potential of this Compressed Sensing based technique to reconstruct concentration maps accurately from significantly less data than would be required to obtain a full chemical shift image. The correct weighting of the fidelity term and the regularisation term is important for a good reconstruction result both concerning the spatial resolution and the quantitative information (concentration). Both approaches used in the present work facilitate the identification of an optimal range for the weighting that yield a good reconstruction result for the concentration maps. These two approaches are still applicable when the model used for the reconstruction is biased by systematic errors. An error in the relative chemical shift has a large effect on the reconstructed concentration map but only a minor effect on the l_2-norm of the fidelity term. In contrast, small deviations of the sampling schemes cause a large shift of the l_2-norm of the fidelity term but only minor shift of the reconstructed concentration.

4.2. Reconstruction of measured data

Fig. 8 shows the reconstructed concentration map of dioxane for the experimental test sample A (a binary homogeneous mixture of cyclooctane and 1,4-dioxane) that was obtained using Bregman iterations in combination with the selection criterion discussed above. The results are similar when the L-curve approach is applied and they are not shown here. The relative error of the reconstructed mean mole fraction of dioxane is 1.3% and the spatial deviations are low. This result demonstrates that the composition of samples can be spatially resolved with a high accuracy with the presented method.

As described above, the total acquisition time to obtain a concentration map was approximately 8 min. The recycle delay of 15 s before each acquisition had the main contribution to the total acquisition time along a sampling trajectory. The recycle delay was chosen to allow sufficient relaxation ($5 \times T_1$) such that quantitative

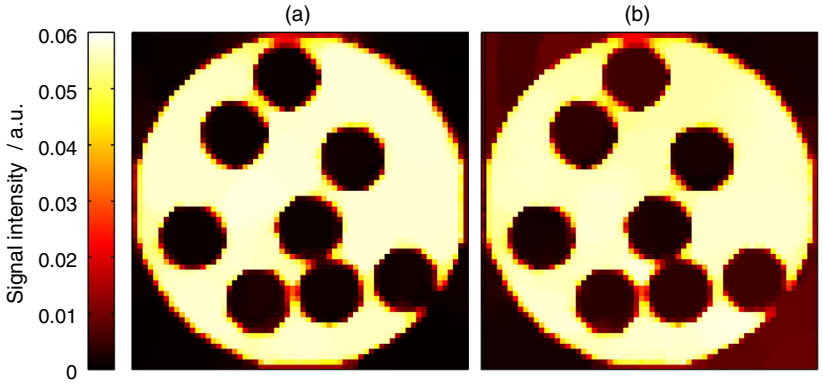

Fig. 7. Sum of the unscaled concentration maps of species A and B obtained by reconstruction of the simulated data: (a) without systematic error, (b) with systematic error in the chemical shift (b). The reconstruction was carried out with $\alpha = 0.004$ (L-curve approach). Image size: 64×64 pixels.

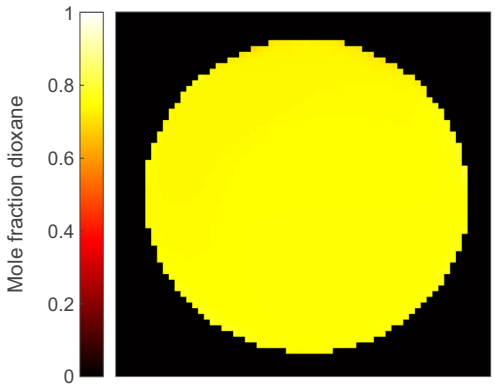

Fig. 8. Reconstructed concentration map of dioxane for test sample A using Bregman iteration. The resolution of the image was 344 μm × 344 μm. The concentration of dioxane in the sample was 0.761 mol/mol.

measurements were obtained. In some cases other approaches might be available to reduce the total acquisition time further. For example, a shorter phase cycle may be used or if the T_1-relaxation time of all species is approximately constant, a shorter recycle delay can be chosen.

To reconstruct the data acquired for the experimental test sample A, both the L-curve approach and Bregman iterations were applied. The reconstruction results are summarised in Fig. 9 for the L-curve approach and in Fig. 10 for the Bregman iteration. Figs. 9(a/b) and 10(a/b) show the reconstructed mean mole fraction of dioxane and the standard deviation of the mole fraction of dioxane (related to the expected mole fraction of dioxane) as a function of the regularisation parameter and number of Bregman iterations, respectively. Fig. 9(c) shows the L-curve and Fig. 10(c) the l_2-norm as a function of the number of Bregman iterations. The plots are very similar to the plots shown in Figs. 5 and 6 that were obtained for the simulated data. Also here, a range of regularisation parameters are given by the corner in the L-curve that yield good reconstruction results both concerning the spatial resolution and the accuracy of the concentration (cf. Fig. 9). For a regularisation parameter of about $\alpha = 0.012$, which corresponds to a result located in the corner of the L-curve, the relative error of the mean mole fraction of dioxane is 1.3% and the standard deviation shows a minimum.

The concentration maps that were reconstructed using Bregman iterations are also well resolved and a parameter set ($12 < m_{\text{Bregman}} < 30$) exists that yields a relative error in the mean fraction of dioxane of 1.4% and that has a minimum in the standard deviation of the mole fractions. The l_2-norm of the reconstruction result, however, is significantly larger than the estimated noise level (cf. Fig. 10) and hence the stopping criterion (Morozov's discrepancy principle) as defined in Eq. (9) is not applicable. As demonstrated in Section 4.1, the deviations in the reconstructed concentration and the large values for the l_2-norm of the fidelity term are attributable to systematic errors in the model. To verify this, the relative chemical shift of cyclooctane used in the model to reconstruct the concentration maps was decreased by 5%, which corresponds to 41 Hz. The results are included for both approaches in Figs. 9 and 10. The reconstructed concentration map when using a chemical shift that was 41 Hz lower than that measured relative chemical shift matches the known concentration more closely than the original chemical shift value. This change in chemical shift is attributed to errors in the shim of the sample making it difficult to identify the true chemical shift accurately. Interestingly, this small change of the chemical shift has no significant influence on the l_2-norm as shown in Figs. 9(c) and 10(c). However, when the sampling trajectory is slightly disturbed by noise, the whole curve of the l_2-norm is shifted significantly but there is almost no effect on the reconstructed concentration. In this case, the noise in the sampling trajectory was estimated from repeated measurements (see Fig. 2(b)). These results indicate that the quality of the reconstruction would likely be improved by more accurate measurement of the k-space trajectory.

Nevertheless, the Bregman iteration approach can still be used even though the stopping criterion is not applicable. As discussed above, the optimal range for the number of Bregman iterations can be identified both by evaluating the plot of the l_2-norm versus the number of Bregman iterations (the optimal range is here located a little bit to the right of the corner) or by evaluating the reconstructed images. The concentration map that has the best spatial resolution is also the concentration map that yields the best agreement with the expected concentration. As mentioned above, the reconstructed image is oversmoothed if the number of Bregman iterations is chosen too low and it becomes pixelated if it is too high.

Fig. 11 shows the reconstructed concentration map of dioxane for test sample B that was obtained using Bregman iterations in combination with the selection criterion discussed above. The results are similar when the L-curve approach is applied and they are not shown here. Table 2 lists a comparison of the reconstructed mean mole fraction with the expected mole fraction of dioxane. The results show that the concentration in the inner vial is well recovered (relative error less than 1%). In the outer vial, however, the error is larger (about 11%). Two reasons are presented for the larger error of the reconstructed concentration in the outer vial

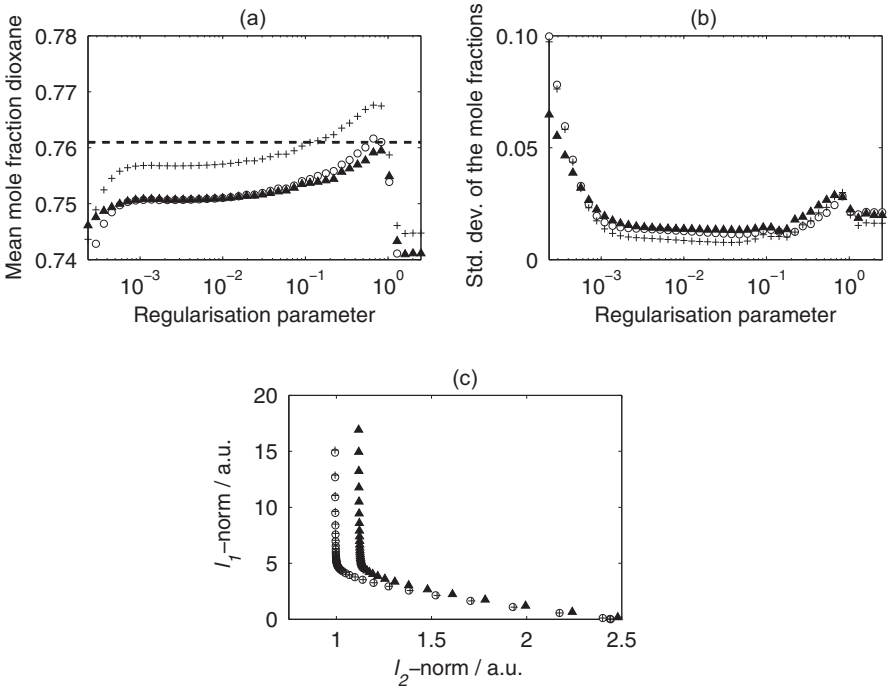

Fig. 9. (a) Mean mole fraction of dioxane in the reconstructed concentration map of test sample A and (b) the standard deviation of the reconstructed mole fractions of dioxane as a function of the regularisation parameter. (c) The regularisation term (l_1-norm) as a function of the fidelity term (l_2-norm) (c). ∘ reconstruction with measured relative chemical shift, + relative chemical shift of cyclooctane decreased by 5%, ▲ systematic error in the sampling scheme, – – expected mole fraction of dioxane in test sample A.

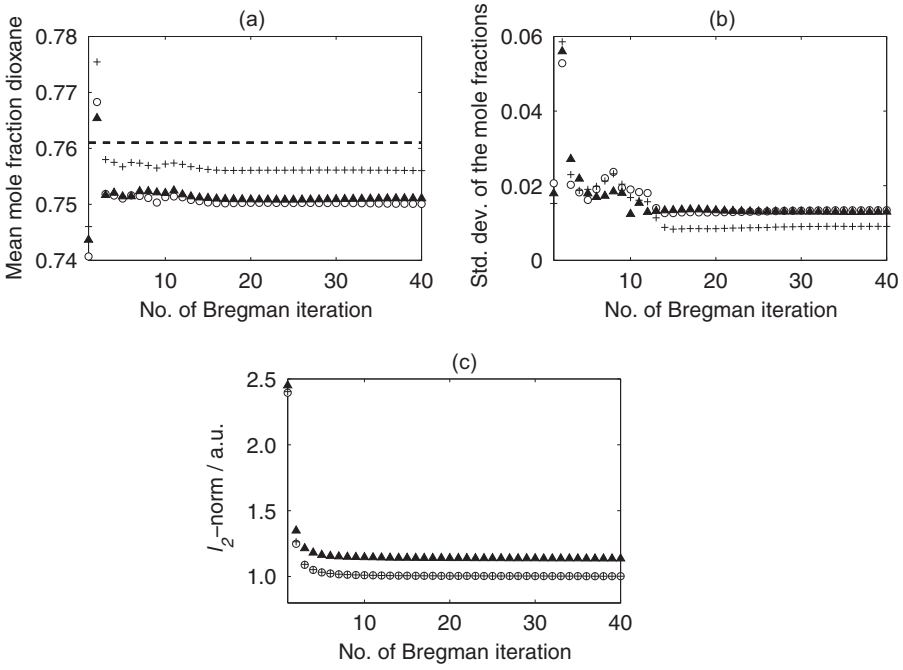

Fig. 10. (a) Mean mole fraction of dioxane in the reconstructed concentration map of test sample A, (b) the standard deviation of the reconstructed mole fractions of dioxane, and (c) the fidelity term (l_2-norm) as a function of the number of Bregman iterations. ∘ reconstruction with measured relative chemical shift, + relative chemical shift of cyclooctane decreased by 5%, ▲ systematic error in the sampling scheme, – – expected mole fraction of dioxane in test sample A.

compared to the inner vial. First, sharp corners are present in the outer vial, and as shown in Fig. 4 and by Benning et al. [21], sharp corners and confined spaces are challenging for the reconstruction algorithm and thus they are often not correctly recovered even though no systematic error is present in the model. Second, spatial inhomogeneities are present in the $\mathbf{B}_0$-field. These inhomogeneities are interpreted by the model as a relative chemical shift and thus they have a similar effect on the reconstruction result as an error in the chemical shift, namely the accuracy of the quantitative information, i.e. the concentration, deteriorates whilst the spatial resolution remains good. Thus, these inhomogeneities cause differences in the reconstructed concentration between the upper part of the image and the lower part of the image where there should be none.

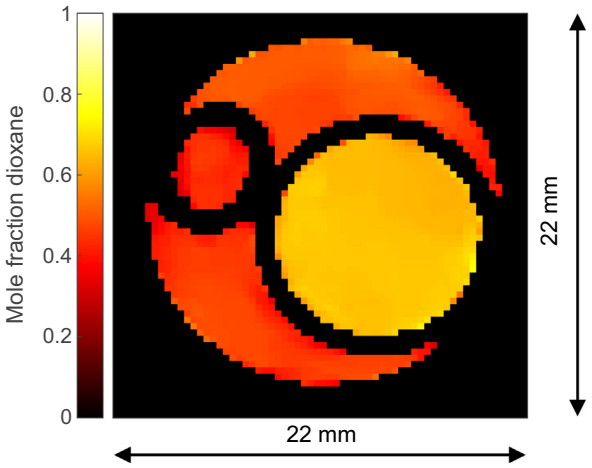

Fig. 11. Reconstructed concentration map of dioxane for test sample B using Bregman iteration. The resolution of the image was 344 μm × 344 μm.

Table 2
Comparison of the mean mole fraction in the reconstructed concentration map with the expected mole fraction of dioxane in test sample B. The error of the expected value is estimated based on the accuracy of the used scale.

Location	Mean mole fraction dioxane	
	Expected	Measured
Inner vial	0.666 ± 0.001	0.66
Outer vial	0.415 ± 0.002	0.46

It may be possible to improve the reconstruction shown in Fig. 11 by incorporating the spatial inhomogeneities of the magnetic field in the model. In this case, the concentration map and the map of the field inhomogeneities have to be reconstructed from the measured signal data by the solution algorithm. This additional reconstruction of the map of the field inhomogeneities is numerically expensive as the order of the chemical shift operator and the undersampled Fourier transform in Eq. (4) have to be changed and thus the Fourier transform has to be performed not only M times (M – number of species, here 2) as it is done in Eq. (4) but N_t times (N_t – number of data points in each trajectory, here 551). Furthermore, when the map of the field inhomogeneities is included in the model, the equation becomes non-linear which makes the solution algorithm more challenging compared to the algorithm used in the present work. As the scope of this paper is to show the principle of quantitative concentration mapping with MRI using compressed sensing, we refrain from a detailed discussion on solution algorithms for non-linear equations which include the reconstruction of the map of the field inhomogeneities. More details on that topic are given for example by Doneva et al. [16].

5. Conclusion

A fast MR imaging method is presented that enables the composition of mixtures of chemical species to be resolved. The method enables acquisition of quantitative maps of the chemical composition in as little as 8 min, when a full chemical shift image at the same resolution would require 17 h. The method is fast because it is based on a compressed sensing algorithm that uses prior-knowledge to obtain the concentration image from under-sampled data. Further reductions in acquisition time may be possible through optimisation of the pulse sequence. No calibration is necessary prior to the analysis in order to get quantitative information with an accuracy of ±2 mol-%. Therefore, the method is valuable for many applications, e.g. in chemical engineering where unstable intermediates may form during the process and hence prohibit a calibration or in medical sciences and biology.

The prior-knowledge that is necessary for the reconstruction of information from under-sampled data is incorporated in the algorithm via a regularisation term. In this work, a spatial finite differences ("total variation") based regularisation is used as images are piece-wise constant. For other systems, regularisers such as Total Generalised Variation or wavelets may be preferable. Regardless of the form of the regularisation function, the weighting has to be carefully chosen in order to get both a good spatial resolution and a high quantitative accuracy in the concentration map. In the present work, the L-curve approach and Bregman iterations, and different selection and stop criteria were used to find an optimal weight for the regularisation term. The two approaches and the selection and stop critera were tested by reconstructing both simulated data from a phantom concentration map and measured data from different samples of binary mixtures.

The mathematically well-defined stopping criterion that is based on Morozov's discrepancy principle is not applicable to the experimental data owing to systematic errors in the model, mainly deviations in the measured sampling trajectories. Nevertheless, the selection criterion that is based on a graphical evaluation of the reconstruction results enables well resolved concentration maps to be obtained using both the L-curve and the Bregman iteration approaches. Furthermore, the fact that the optimal parameters for the regularisation are based on a selection criterion that requires a graphical evaluation of the reconstruction results is not disadvantageous for the quality of the results because the reconstruction result is insensitive to the choice of these parameters in an interval near the optimal parameters. Thus, both the L-curve and the Bregman iteration are generic and robust approaches to achieve quantitative results.

To conclude, the presented method is a powerful tool for the fast acquisition of concentration maps. These concentration maps can provide valuable information for the investigation of many phenomena in chemical engineering applications.

Acknowledgments

Financial support was provided by Microsoft Research Cambridge, Cambridge, and the EPSRC (EP/K039318/1 and EP/K008218/1). Erik von Harbou was the recipient of a scholarship from the German Academic Exchange Service (DAAD).

Appendix A. Description of the linear operators

The transformation of the M concentration maps $\mathbf{x}_k$ into the signal $\mathbf{S}$ shown in Eq. (1) can be abbreviated by linear operators, see Eq. (4). First, the concentration maps are subjected to a Fourier transformation,

$$\mathbf{S}_k^* = \mathcal{F}_u\{\mathbf{x}_k\} \quad \text{with}: \ \mathbf{x}_k \in \mathbb{R}^{N\times N}, \quad \mathbf{S}_k^* \in \mathbb{C}^{[N_{\text{samples}}\times 1]} \text{ and } k = 1,\ldots,M$$

$\mathcal{F}_u$ is the discrete non-uniform Fourier transform operator that is described in detail by Fessler and Sutton [23]. $N \times N$ is the size (number of pixels) of the concentration map $\mathbf{x}_k$. N_{samples} is the number of samples.

To get the signal $\mathbf{S}$, the chemical shift operator **CHS** is applied to the Fourier transformed concentration map $\mathbf{S}_k^*$:

$$\mathbf{S} = \mathbf{CHS} \cdot \begin{pmatrix} \mathbf{S}_1^* \\ \vdots \\ \mathbf{S}_M^* \end{pmatrix} \quad \text{with}: \ \mathbf{S} \in \mathbb{C}^{N_{\text{samples}}\times 1}$$

The chemical shift operator **CHS** is a matrix:

$$\mathbf{CHS} = \Big[\mathrm{diag}\Big(CHS_1(t_1),\ldots,CHS_1(t_{N_{\mathrm{samples}}})\Big),\ldots,\mathrm{diag}(CHS_M(t_1),\ldots,CHS_M(t_{N_{\mathrm{samples}}}))\Big] \text{ with : } \mathbf{CHS} \in \mathbb{C}^{N_{\mathrm{samples}}\times N_{\mathrm{samples}}\cdot M}$$

Here, the operator $CHS_k(t_j)$ is defined as

$$CHS_k(t_l) = \sum_{j=1}^{L_k} w_{kj} \exp\left(2\pi i\, \delta_{kj} t_l\right) \exp\left(-\frac{t_l + 2\tau}{T_2^*}\right).$$

Appendix B. Description of the total variation regularisation

Total variation regularisation is the 1-norm penalty on a discrete finite difference approximation of the two-dimensional gradient ∇ [21]. The two-dimensional gradient is defined as

$$\nabla_1 x_k(i,j) = \begin{cases} x_k(i+1,j) - x_k(i,j) & \text{if } i < n_1 \\ 0 & \text{if } i = n_1 \end{cases}$$
$$\nabla_2 x_k(i,j) = \begin{cases} x_k(i,j+1) - x_k(i,j) & \text{if } j < n_2 \\ 0 & \text{if } j = n_2 \end{cases}$$

for $i = 1,\ldots,n_1$ and $j = 1,\ldots,n_2$.

Thus the discrete total variation functional is given by

$$J(\Psi x_k) = \|\Psi x_k\|_{2,1} = \|\nabla x_k\|_{2,1} = \sum_{i,j} \sqrt{|\nabla_1 x_k(i,j)|^2 + |\nabla_2 x_k(i,j)|^2}.$$

References

[1] E. Yuen, A. Sederman, L. Gladden, Appl. Catal. A: Gen. 232 (2002) 29–38.
[2] I. Koptyug, A. Lysova, A. Kulikov, V. Parmon, R. Sagdeev, Appl. Catal. A: Gen. 267 (2004) 143–148.
[3] B.S. Akpa, M.D. Mantle, A.J. Sederman, L.F. Gladden, Chem. Commun. (2005) 2741–2743.
[4] A.J. Sederman, M.D. Mantle, C.P. Dunckley, Z. Huang, L.F. Gladden, Catal. Lett. 103 (2005) 1–8.
[5] L.F. Gladden, F.J. Abegão, C.P. Dunckley, D.J. Holland, M.H. Sankey, A.J. Sederman, Catal. Today 155 (2010) 157–163.
[6] D. Donoho, IEEE Trans. Inf. Theory 52 (2006) 1289–1306.
[7] E. Candes, J. Romberg, T. Tao, IEEE Trans. Inf. Theory 52 (2006) 489–509.
[8] M. Lustig, D. Donoho, J.M. Pauly, Magn. Reson. Med. 58 (2007) 1182–1195.
[9] R. Otazo, D. Kim, L. Axel, D.K. Sodickson, Magn. Reson. Med. 64 (2010) 767–776.
[10] D. Holland, D. Malioutov, A. Blake, A. Sederman, L. Gladden, J. Magn. Reson. 203 (2010) 236–246.
[11] A.B. Tayler, D.J. Holland, A.J. Sederman, L.F. Gladden, Phys. Rev. Lett. 108 (2012) 264505.
[12] D.J. Holland, M.J. Bostock, L.F. Gladden, D. Nietlispach, Angew. Chem. Int. Ed. 50 (2011) 6548–6551.
[13] K. Kazimierczuk, V.Y. Orekhov, Angew. Chem. Int. Ed. 50 (2011) 5556–5559.
[14] S. Hu, M. Lustig, A.P. Chen, J. Crane, A. Kerr, D.A. Kelley, R. Hurd, J. Kurhanewicz, S.J. Nelson, J.M. Pauly, D.B. Vigneron, J. Magn. Reson. 192 (2008) 258–264.
[15] T. Kampf, A. Fischer, T. Basse-Lüsebrink, G. Ladewig, F. Breuer, G. Stoll, P. Jakob, W. Bauer, J. Magn. Reson. 207 (2010) 262–273.
[16] M. Doneva, P. Börnert, H. Eggers, A. Mertins, J. Pauly, M. Lustig, Magn. Reson. Med. 64 (2010) 1749–1759.
[17] S.D. Sharma, H.H. Hu, K.S. Nayak, Magn. Reson. Med. 67 (2012) 650–659.
[18] S.D. Sharma, H.H. Hu, K.S. Nayak, Magn. Reson. Med. 69 (2013) 456–466.
[19] P. Hansen, SIAM Rev. 34 (1992) 561–580.
[20] S. Osher, M. Burger, D. Goldfarb, J. Xu, W. Yin, Multiscale Model. Simul. 4 (2005) 460–489.
[21] M. Benning, L. Gladden, D. Holland, C.-B. Schönlieb, T. Valkonen, J. Magn. Reson. 238 (2014) 26–43.
[22] D. Gabay, in: M. Fortin, R. Glowinski (Eds.), Augmented Lagrangian Methods: Applications to the Numerical Solution of Boundary-Value Problems, vol. 15, Elsevier, 1983, pp. 299–331.
[23] J. Fessler, B. Sutton, IEEE Trans. Signal Process. 51 (2003) 560–574.
[24] J.A. Fessler, Nonuniform FFT (NUFFT) Matlab Toolbox <http://web.eecs.umich.edu/fessler/irt/fessler.tgz>, October 2012.
[25] T.Z. Teisseyre, J.L. Paulsen, V.S. Bajaj, N.W. Halpern-Manners, A. Pines, J. Magn. Reson. 216 (2012) 13–20.
[26] E. van den Berg, M. Friedlander, SIAM J. Sci. Comput. 31 (2008) 890–912.
[27] W. Yin, S. Osher, D. Goldfarb, J. Darbon, SIAM J. Imag. Sci. 1 (2008) 143–168.
[28] V.A. Morozov , Soviet Math. Dokldy 7 (1966) 414–417.
[29] M. Lustig, S.-J. Kim, J. Pauly, IEEE Trans. Med. Imag. 27 (2008) 866–873.
[30] M. Lustig, Time Optimal Gradient Design <http://www.eecs.berkeley.edu/mlustig/Software.html>, October 2012.
[31] J.H. Duyn, Y. Yang, J.A. Frank, J.W. van der Veen, J. Magn. Reson. 132 (1998) 150–153.
[32] A.B. Tayler, D.J. Holland, A.J. Sederman, L.F. Gladden, J. Magn. Reson. 211 (2011) 1–10.
[33] A. Chambolle, S. Levine, B. Lucier, SIAM J. Imag. Sci. 4 (2011) 277–299.

Curriculum vitae

Personal information

Name:	Erik von Harbou
Nationality:	german, swedish

Education

2001 – 2002	University of Technology Berlin Course: Chemistry
2003 – 2008	University of Technology Hamburg-Harburg Course: Chemical Engineering Final degree: Dipl.-Ing.
2008 – 2012	Research assistant Laboratory of Engineering Thermodynamics Technische Universität Kaiserslautern Prof. Dr.-Ing. H. Hasse
2012 – 2013	Postdoctoral research fellow Magnetic Resonance Research Centre University of Cambridge, UK Prof. Dr. L. Gladden, Dr. D. Holland
2013 – 2017	Junior Professor for Chemical System Engineering Laboratory of Engineering Thermodynamics Technische Universität Kaiserslautern
since 2018	Engineer in Research and Development Reaction Engineering Group BASF SE, Ludwigshafen, Germany

In this work, new methods are presented that facilitate the application of Nuclear Magnetic Resonance (NMR) spectroscopy for monitoring of reactions and processes. NMR spectroscopy has the advantage that it enables both elucidation of species and their following quantification in a reacting mixture in situ without the need of prior calibration. New post-processing methods were developed that enable handling of large sets of NMR spectra and that reduce influence of the user on the outcome of the measurements of the composition. Furthermore, a spectral analysis method was introduced and tested that allows evaluating the acquired NMR signals quantitatively even if the peaks in the NMR spectrum are distorted and the concentration of analytes becomes very small. As the standard NMR equipment is mostly designed for structure elucidation purposes but not for reaction and process monitoring, the apparatuses were tailored in this work. A liquid thermostatted NMR probe head is presented, in which fast reactions can be monitored under isothermal conditions. Methods and experimental procedures were established to investigate chemical equilibria of different industrial relevant systems in situ. Examples are: the formation of intermediates in the reaction system that is found in the synthesis of crotonaldehyde from acetaldehyde and water, and the reaction that take place in aqueous methyl diethanolamine solutions when loaded with carbon dioxide. Furthermore, an inline analysis method for monitoring dynamic processes reliably with a high chemical and temporal resolution is presented. To demonstrate the potential of this method, the complex interactions of reaction and separation in a fixed-bed chromatographic reactor process were studied. Furthermore, a benchtop NMR spectrometer was employed to study liquid-liquid phase equilibria in situ in different systems. This new type of spectrometer are an interesting alternative to the high-field NMR spectrometer because of its smaller size and lower costs. The results show that benchtop NMR spectrometers have the potential to widen the range of application of NMR spectroscopy for reaction and process monitoring significantly. This works demonstrate that NMR spectroscopy is a useful tool in chemical reaction engineering as it enables detailed insights into complex reactions and processes and provides data that is essential for the development of reliable process models.

ISBN: 978-3-95974-159-0
ISSN: 2748-7458